THÈSE

En vue de l'obtention du

DOCTORAT DE L'UNIVERSITÉ DE TOULOUSE

Délivré par :

Institut National Polytechnique de Toulouse (Toulouse INP)

Discipline ou spécialité :

Energétique et Transferts

Présentée et soutenue par :

M. FELIX COLLIN
le mardi 28 mai 2019

Titre :

Modeling and Numerical Simulations of Two-Phase Ignition in Gas Turbine

---

Ecole doctorale :
Mécanique, Energétique, Génie civil, Procédés (MEGeP)

Unité de recherche :
Centre Européen de Recherche et Formation Avancées en Calcul Scientifique (CERFACS)

Directeur(s) de Thèse :
MME BENEDICTE CUENOT
MME ELEONORE RIBER

Rapporteurs :
M. BENOIT FIORINA, CENTRALESUPELEC GIF SUR YVETTE
M. EPAMINONDAS MASTORAKOS, UNIVERSITE DE CAMBRIDGE

Membre(s) du jury :
M. MARC BELLENOUE, ENSMA POITIERS, Président
M. ALAIN CAYRE, GROUPE SAFRAN, Invité
M. BRUNO RENOU, INSA ROUEN, Membre
Mme BENEDICTE CUENOT, CERFACS, Membre
Mme CORINE LACOUR, INSA ROUEN, Membre

Abstract

In order to meet the new international environmental regulations while maintaining a strong economic competitiveness, innovative technologies of aeronautical combustion chambers are developed. These technologies must guarantee fast relight in case of extinction, which is one of the most critical and complex aspects of engine design. Control of this phase involves a thorough understanding of the physical phenomena involved. In this thesis the full two-phase ignition sequence of an aeronautical engine has been studied, from the breakdown of the spark plug to the propagation of the flame in the complete engine. For this purpose, Large-Eddy Simulations (LES) using a detailed description of the liquid phase (Euler-Lagrange formalism) and of the combustion process (Analytically Reduced Chemistry) were performed. The results also led to the development of a simplified model for the prediction of ignition probability map, which is particularly useful for the design of combustion chambers.

Résumé

Afin de répondre aux nouvelles réglementations environnementales internationales tout en maintenant une forte compétitivité économique, des technologies innovantes de chambres de combustion aéronautiques sont développées. Ces technologies doivent garantir un rallumage rapide en cas dextinction, qui est un des aspects les plus critiques et complexes de la conception moteur. La maîtrise de cette phase implique une compréhension approfondie des phénomnes physiques mis en jeu. Dans cette thèse la séquence dallumage diphasique de moteur aéronautique a été étudiée dans son intégralité, du claquage de la bougie la propagation de la flamme dans le moteur complet. Dans cet objectif, des Simulations aux Grandes Échelles (SGE) utilisant une description détaillée de la phase liquide (formalisme Euler-Lagrange) et du processus de combustion (Chimie Analytiquement Réduite) ont été réalisées. Les résultats ont également permis de développer un modèle simplifié pour la prédiction de carte de probabilité dallumage, particulièrement utile pour le dimensionnement et la conception des chambres de combustion.

Acknowledgements

Dernière partie de ce manuscrít à être rédigée mais celle-ci devrait être la plus facile.

Tout d'abord je souhaite remercier les rapporteurs de mon manuscrit, Epaminondas Mastorakos et Benoît Fiorina, pour avoir lu mon manuscrit et évalué mon travail. Je remercie également Corine Lacour, Marc Bellenoue et Brunon Renou pour avoir évalué ma soutenance et s'être joint aux rapporteurs pour la discussion ayant suivi la soutenance.

Je remercie ensuite Bénédicte Cuenot, Eleonore Riber et Olivier Vermorel. Merci pour votre encadrement quotidien toujours dans la bonne humeur, et vos conseils scientifiques qui m'ont permis de découvrir les joies de la simulation numérique, de la combustion jusqu'à la jolie ville de Dublin! Merci également à Stéphane Richard et Alain Cayre pour votre encadrement du côté industriel qui a été constant et que j'ai particuliérement apprécié.

Merci également à Thierry Poinsot de m'avoir acceuilli au sein de l'équipe CFD du Cerfacs, et un grand merci à Gérald Debenest et son équipe (Jacques Franc, Pierre Horgue, Romain Guibert) de l'IMFT pour m'avoir mis le pied à l'étrier dans le monde de la recherche!

Je souhaite également remercier toutes les personnes avec qui j'ai pu travailler au Cerfacs: Marie, Nicole, Chantal, Michèle et toute l'équipe administrative grâce à qui nous travaillons sans avoir à nous soucier d'autre chose que de nos travaux de recherches et c'est un luxe. De manière similaire, je remercie également grandement Isabelle, Gérard, Fabrice, Fred et toute l'équipe CSG qui nous facilite notre vie informatique. Merci aux séniors CFD de leur disponibilité lorsque l'on a besoin d'eux: Antony, Nicolas, Laurent, Jérôme, Marc, Gab, Antoine, Florent.

J'en viens maintenant aux remerciements des doctorants, post-doctorants, ex-doctorants que j'ai pu cotoyer au cours de mon séjour de 4 ans au Cerfacs. Les noms me viendront dans le désordre: Lulu, j'espère que tu tiens ton rythme de 1 page par jour. Tu feras un bon docteur j'en suis certain, mais pense à m'envoyer ton modèle stp... O'Malé, prends exemple sur ton cobureau si tu veux boucler ton PhD: essaies d'arriver avant 11h. Hum, pas le meilleur exemple en fait. La Bizz', calme toi sur les échauffements, avec l'âge il faut savoir lever le pied. Regarde Valou, jamais plus d'entrainement qu'il n'en faut, il ne faudrait pas risquer une blessure bête... Dans le thème football qui rassemble beaucoup de souvenir avec l'EAC: Maxou, ravi d'avoir été sur le même terrain que toi si longtemps, dommage que tu n'ais pas trouvé le temps de me faire une passe. Et pourtant je suis resté suffisamment longtemps au club pour voir Kelu mettre un but, c'est dire... Je tiens à citer quelques piliers pour l'avenir de ce club: Vic gradelinho, les hommes-glaçons Camille et Nico ainsi que quelques membres all-star: La Frite j'espère que tu n'en veux plus au public d'avoir rigolé sur le bord du terrain, Terrible moment... Luis, ce paragraphe est long c'est vrai, prend un moment pour souffler avant de continuer... Greg, quel jubilé tu nous as fait. J'ai toujours pas compris si t'étais heureux ou pas à cette soirée. Pendolino, je dois avouer que c'est moi qui te mettais des 1 sur sporteasy. J'aimais trop te voir crier sur Biolchi et voir Melissa te défendre... En parlant d'anciens: Biolchi, honnêtement, tu progresses vraiment au tennis, je sens que d'ici quelques semaines tu pourras me battre sur plus qu'un set. Non je rigole, j'ai de la marge :) Majd, prépare ton maillot du Paris FC, bientôt la reprise. Pedro le T-rex du Cerfacs, aaah la la... JarJar, la légende auto-proclamée. En même temps, pas faux... Passons maintenant aux personnes n'ayant aucun rapport de près comme de loin avec l'EAC: Douds, si je suis un escroc, tu es à toi tout seul une escroquerie. Bravo. D'ailleurs Jaouen tu as été vaillant pour tenir aussi longtemps dans ce bureau... Grosnick, j'ai mis en route ma station météo. I'm back. Laure et Pierre, j'essaierai de vous envoyer ces remerciements par charrue pour que le vide technologique rural ne soit pas un frein à notre amitié. Lola, quand tu veux pour un combat de pokemon-Cerfacs. Je finirai par citer certains de ma génération (ou presque): Bastien, Robin, Maël, Gauthier, Astoul, Flo, Charlélie, Fabien, Paco et Quegi. J'en oublie c'est certain donc je remercie tous ceux que j'ai oublié.

Enfin un grand merci à ma famille qui m'aura accompagné tout au long de ces 4 années et en particulier Eva. Tu m'as montré la voie il y a 18 mois. Nous allons maintenant tracer notre route enfin réunis.

Contents

1 Introduction **7**

1.1 Industrial context: Aeronautical gas turbines 7

1.2 A crucial constraint: high altitude engine relight capability 14

1.3 Role of numerical simulation 17

1.4 Objectives and organisation of the thesis 17

I Turbulent two-phase reactive flows **19**

2 Theoretical concepts of combustion **21**

2.1 Laminar flames 21

2.2 Turbulent flames 27

2.3 Spray flames 32

3 Equations and models for gaseous turbulent reactive flows **39**

3.1 Conservative equations for gaseous flows 39

3.2 Large Eddy Simulation equations 45

4 Equations and models for the liquid phase **55**

4.1 Euler-Lagrange modeling 55

4.2 System of equations 56

4.3 Exchange terms 57

4.4 Coupling with the gaseous phase 62

4.5 Droplet injection 63

II From the spark to the flame kernel **65**

5 Literature review **67**

5.1 General phenomenology 68

5.2 Concept of Minimum Ignition Energy 72

5.3 Ignition of mists of fuel droplets 75

5.4 Inclusion of detailed chemistry and plasma phase 79

5.5 Numerical models 82

5.6 Conclusions 87

6 Numerical simulations of spark ignition 89
6.1 Objectives 89
6.2 Spark ignition modeling 90
6.3 Chemistry modeling 91
6.4 Experimental set-up 96
6.5 Numerical set-up 96
6.6 Ignition sequence dynamics 98
6.7 Influence of plasma chemistry on spark ignition 102
6.8 High temperature Energy Deposition model for LES: A new methodology 107
6.9 Conclusions 109

III Flame growth and propagation towards the nearest injector 111

7 Literature review 113
7.1 Stochastic behaviour of ignition 114
7.2 Local competition between flammability and turbulence 115
7.3 Kernel evolution in recirculating flows 119
7.4 Ignition probability prediction models 126
7.5 Conclusions 130

8 LES of two-phase ignition of the KIAI single burner 133
8.1 Objectives 133
8.2 Experimental set-up 134
8.3 Numerical set-up 137
8.4 Non-reacting flow analysis 142
8.5 Stable reacting flow 149
8.6 Quantitative comparison of spray ignition sequences between LES and experiments 154
8.7 Identification of key mechanisms controlling ignition success or failure . 159
8.8 Conclusions 174

9 Prediction of two-phase ignition probability 177
9.1 Objectives 177
9.2 Test configuration 178
9.3 Model for Ignition STatistics (MIST) 182
9.4 Application to the KIAI burner 189
9.5 Application to a real combustor 194
9.6 Conclusions 208

IV Light-round 211

10 Literature review 213

10.1 Multi-burners non-reacting flow topology 214

10.2 Overview of inter-sector flame propagation 215

10.3 Mechanisms driving flame propagation 218

10.4 Conclusions 222

11 Inter-sector flame propagation: CORIA Linear Swirled Spray Burner 225

11.1 Objectives 225

11.2 Experimental set-up 226

11.3 Numerical set-up 228

11.4 Influence of the inter-injector spacing on ignition 230

11.5 Influence of fuel volatility 243

11.6 Conclusions 245

12 Light-round: MICCA annular combustion chamber 247

12.1 Objectives 247

12.2 Experimental set-ups 248

12.3 Numerical set-up 250

12.4 Validation of the non-reacting and stable flame cases on the SICCA configuration 254

12.5 MICCA-Spray light-round 259

12.6 Conclusions 271

13 General Conclusions 273

Bibliography 277

Appendices 301

A Derivation of the combustion-plasma chemistry 303

B Article on spark ignition (phase 1 of ignition) 305

C Article on spray ignition (phase 2 of ignition) 315

List of symbols

Roman characters

Symbol	Description	Unit
a	Strain rate	[s^{-1}]
c	Flame progress variable	[-]
d_p	Liquid droplet diameter	[m]
$\mathcal{F}$	Thickening factor	[-]
F_f	Flammability factor	[-]
Hr	Heat release rate	[W/m^3]
h_s	Sensible enthalpy	[J/kg]
l_κ	Kolmogorov scale	[m]
l_t	Integral length scale	[m]
L_v	Latent heat of evaporation	[J/kg]
m_p	Mass of a Lagrangian particle	[kg]
$\dot{m}_p$	Rate of change of droplet mass	[kg/s]
P	Pressure	[Pa]
P_{ign}	Ignition probability	[-]
r_p	Liquid droplet radius	[m]
S_a	Absolute flame speed	[m/s]
S_c	Flame consumption speed	[m/s]
S_d	Flame displacement speed	[m/s]
S_d^*	Weighted flame displacement speed	[m/s]
S_{ij}	Strain rate tensor	[s^{-1}]
s_l^0	Laminar unstrained flame velocity	[m/s]
s_l^{tp}	Laminar unstrained two-phase flame velocity	[m/s]
s_t	Turbulent flame velocity	[m/s]
t	Time	[s]
T	Gaseous temperature	[K]
T_p	Liquid droplet temperature	[K]
u_i	Gaseous velocity vector	[m/s]
u_p	Velocity vector of a Lagrangian particle	[m/s]
W	Molecular weight	[kg/mol]
x_i	Spatial coordinate (vector)	[m]
$\mathbf{x}$	Spatial coordinate (vector)	[m]
X_k	Molar fraction of species k	[$-$]
X_p	Position vector of a Lagrangian particle	[m]
Y_k	Mass fraction of species k	[$-$]
z	Mixture fraction	[$-$]

Greek characters

Symbol	Description	Unit
α_l	Liquid volume fraction	$[-]$
δ_{ij}	Kronecker symbol	$[-]$
δ_l^0	Laminar unstrained flame thickness	[m]
δ_l^{tp}	Laminar unstrained Two phase flame thickness	[m]
$\mathcal{E}$	Efficiency function	[-]
ζ	Glow efficiency coefficient	[-]
η	Breakdown efficiency coefficient	[-]
κ	Flame stretch	[s^{-1}]
$\mathcal{K}$	Flame curvature	[m^{-1}]
λ	Heat conduction coefficient	[W/m/K]
μ	Molecular viscosity	[Pa s]
μ_t	Turbulent viscosity	[Pa s]
ρ	Gaseous density	[$\mathrm{kg/m^3}$]
ρ_k	Density of the gaseous species k	[$\mathrm{kg/m^3}$]
ρ_l	Liquid phase density	[$\mathrm{kg/m^3}$]
τ_{ev}	Characteristic evaporation time	[s]
τ_{ij}	Stress tensor	[$\mathrm{N/m^2}$]
τ_{ij}^t	Turbulent stress tensor	[$\mathrm{N/m^2}$]
τ_p	Particle relaxation timescale	[s]
ϕ	Equivalence ratio	[-]
ϕ_l	Liquid equivalence ratio	[-]

Dimensionless numbers

Symbol	Description
B_M	Spalding number for mass transfer
B_T	Spalding number for heat transfer
Da	Damköhler number
Le	Lewis number
Nu	Nusselt number
Pr	Prandtl number
Pr_t	Turbulent Prandtl number
Re	Reynolds number
Re_t	Turbulent Reynolds number
Re_p	Particle Reynolds number
Sc	Schmidt number
Sh	Sherwood number
St	Stokes number
TI	Takeno Index

Indices and superscripts

Symbol	Description
F	Index of a fuel quantity
g	Index of a gaseous phase quantity
$glob$	Index of a quantity at global equivalence ratio
l	Index of a liquid phase quantity
O	Index of an oxidiser quantity
p	Index of a particle quantity
st	Index of a quantity at stoichiometric equivalence ratio
tot	Superscript of a total (gas + liquid) quantity

Acronyms

Acronym	Definition
ARC	Analytically Reduced Chemistry
BPR	ByPass Ratio
CFD	Computational Fluid Dynamics
CFL	Courant-Friedrichs-Lewy
CLSSB	Coria Linear Swirled Spray Burner
DNS	Direct Numerical Simulation
DRG	Directed Relation Graph method
DRGEP	DRG with Error Propagation
DTFLES	Dynamically Thickened Flame model for LES
EE	Euler-Euler
ED	Energy Deposition
ED_HT	Energy Deposition for High Temperature
EL	Euler-Lagrange
FIM-UR	Fuel Injection Method by Upstream Reconstruction
GRC	Globally Reduced Chemistry
HBR	High Bypass Ratio
IRZ	Inner Recirculation Zone
KIAI	Knowledge for Ignition, Acoustics and Instabilities
KC	Kernel Convection mechanism
LES	Large Eddy Simulation
LKG	Local Kernel Growth mechanism
LKS	Local Kernel Shrinking mechanism
LP	Leading Point
LPP	Lean-Premixed Prevaporized
LRZ	Lateral Recirculation Zone
LW	Lax-Wendroff
MIE	Minimum Ignition Energy
MIST	Model for Ignition STatistics
NSCBC	Navier-Stokes Characteristic Boundary Conditions
OPR	Overall Pressure Ratio
ORZ	Outer Recirculation Zone
PDA	Phase Doppler Anemometry
PDF	Probability Density Function
PIV	Particle Image Velocimetry
PLIF	Planar Laser-Induced Fluorescence
PVC	Precessing Vortex Core
QSS	Quasi-Steady State
QSSA	QSS Approximation
RANS	Reynolds Average Navier-Stokes
RQL	Rich-burn, Quick-Quench, Lean-Burn
RMS	Root-Mean-Square
SJZ	Swirled Jet Zone
TIMBER	Two-phase Ignition and propagation in Multi-BurnER
TF	Thickened Flame
TFLES	Thickened Flame model for LES
TTGC	Two-step Taylor-Galerkin scheme version C

Chapter 1

Introduction

Contents

1.1 Industrial context: Aeronautical gas turbines 7
  1.1.1 Civil air traffic challenges 7
  1.1.2 Evolution of propulsive system technologies 9
1.2 A crucial constraint: high altitude engine relight capability 14
  1.2.1 Overview of an ignition sequence 14
  1.2.2 Effects of new engine concepts on ignition performance 16
1.3 Role of numerical simulation 17
1.4 Objectives and organisation of the thesis 17

1.1 Industrial context: Aeronautical gas turbines

1.1.1 Civil air traffic challenges

The civil aerospace market is constantly growing. A revenue passenger kilometers (RPK) growth of +4.3 % is expected between 2017 and 2037 along with a global fleet growth of ×1.8 to the end of 2037. A strong economic competition comes with this thriving market. Historic aircraft manufacturers such as Airbus and Boeing face new entrants coming from Brazil, Turkey, Russia, Japan or China. To remain competitive, each market player has to constantly increase its development efforts, leading to an overall very dynamic aerospace sector.

The boom of the aircraft industry also raises important worldwide issues. Environmental consequences are tremendous at high altitude inducing global atmospheric changes, but also locally around airports deteriorating the air quality and bringing an important noise pollution to the neighbourhood. Figure 1.1 presents pollutant emissions from a typical two-engine jet aircraft during 1-hour flight with 150 passengers. Emissions are huge, and will increase with the aerospace market. To meet the growing demand, traditional scheduled carriers used 3.7 flights/day/aircraft in 2014 instead of 3.1 in 2005, causing an increase of flights in the early morning and late evening as shown in Fig. 1.2. Very strict regulations on some aircraft pollutant and noise emissions have thus been progressively settled. Objectives for 2050 compared to 2000 are given by the Committee on Aviation Environmental Protection (CAEP) and the Advisory Council for Aviation Research and Innovation in Europe (ACARE):

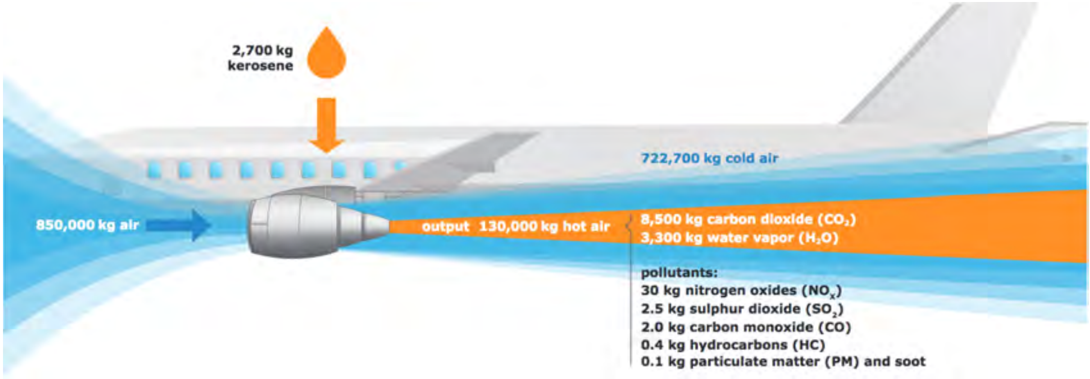
2,700 kg kerosene
722,700 kg cold air
850,000 kg air
output 130,000 kg hot air
8,500 kg carbon dioxide (CO2)
3,300 kg water vapor (H2O)
pollutants:
30 kg nitrogen oxides (NOx)
2.5 kg sulphur dioxide (SO2)
2.0 kg carbon monoxide (CO)
0.4 kg hydrocarbons (HC)
0.1 kg particulate matter (PM) and soot

Figure 1.1: Emissions from a typical two-engine jet aircraft during 1-hour flight with 150 passengers. Extracted from the European Aviation Environmental Report 2016.

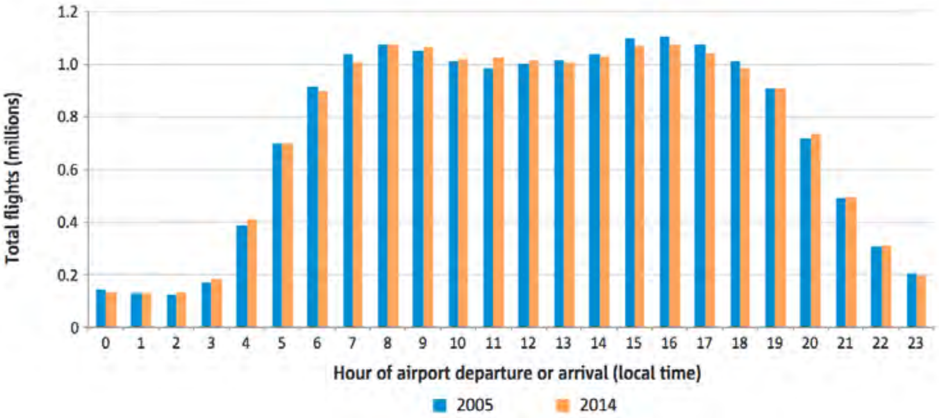

Figure 1.2: Total number of flights per hour of airport departure or arrival. Extracted from the European Aviation Environmental Report 2016.

- 75 % reduction of CO_2 emissions.
- 90 % reduction of NO_x emissions.
- 65 % reduction of noise emissions.
- 0 emissions during taxiing.

Of course, one of the most important source of noise and atmospheric pollution of the aircraft is its propulsion system. In addition, it is the most expensive part of the plane, representing up to 1/3 of the final aircraft cost. The increasing price of kerosene also makes fuel consumption reduction a determinant challenge. It is thus clear that the engine is a key point of the current aeronautical challenge. Engine manufacturers are major layers for future of the aerospace sector, leading mandatory developments on propulsive systems.

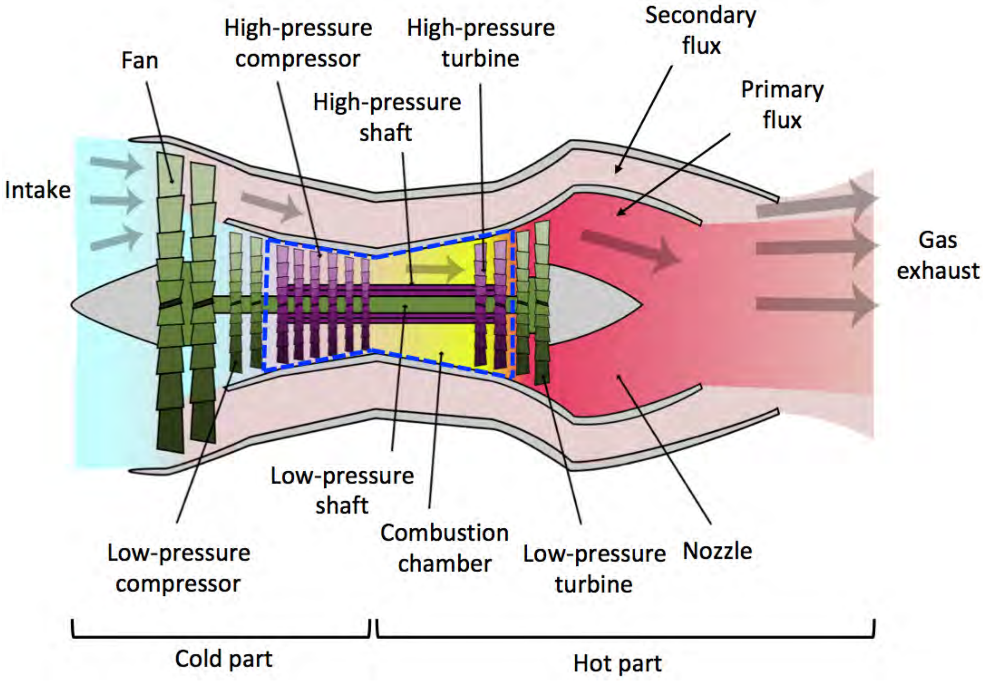
Fan
High-pressure compressor
High-pressure turbine
Secondary flux
Primary flux
High-pressure shaft
Intake
Gas exhaust
Low-pressure shaft
Combustion chamber
Low-pressure compressor
Low-pressure turbine
Nozzle
Cold part
Hot part

Figure 1.3: Scheme of a conventional double-flux gas turbine engine.

1.1.2 Evolution of propulsive system technologies

1.1.2.1 Conventional combustor design

Conventional gas turbines design is first introduced in Fig. 1.3. Current civil aircrafts use double-flux gas turbines. Air entering the primary flux by the fan is pressurized by the low and high pressure compressors to optimize the thermodynamic cycle. In the combustion chamber, it is rapidly mixed with injected kerosene and the mixture is burnt producing very hot combustion products at high velocity. These accelerated hot products then transfer their kinetic energy to high and low pressure turbines before

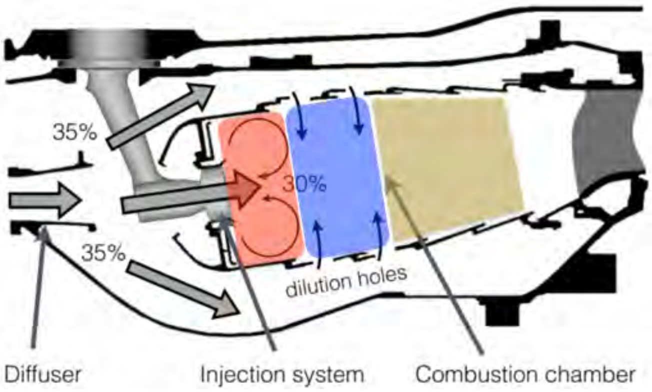
35%
30%
35%
dilution holes
Diffuser
Injection system
Combustion chamber

Figure 1.4: Scheme of a conventional RQL combustion chamber design. Extracted from [1].

being released through the nozzle. The turbine drives the compressor and the fan thanks to axial shafts. This is actually the main role of the primary flux. Then, the major part of the engine thrust is produced by the action-reaction principle: the secondary flux is ejected at a much higher velocity than at intake thanks to the energy transfer from the fan to the secondary flux gases.

The engine is often split in two parts: the Low Pressure (LP) and High Pressure (HP) components. The HP part is highlighted by a dashed blue frame in Fig. 1.3. It is only made of elements from the primary flux, namely the HP compressor, the combustion chamber, and the HP turbine. A zoom on a conventional combustion chamber is proposed in Fig. 1.4. It is named a Rich Burn, Quick-Mix, Lean Burn (RQL) system. Air enters the plenum by a diffuser and is then distributed to the flame tube by many sources. Around 30 % comes from the injection system and is mixed with kerosene. The overall rich mixture burns in the primary zone (coloured in red in Fig. 1.4). An important part of the incoming air then enters the flame tube by dilution holes placed on lateral walls. These fresh gases quench the flame (blue zone) and mix with unburned products that are finally consumed by overall lean combustion in the secondary zone (coloured in yellow).

To meet requirements in terms of pollutant emissions and to stay competitive, engine manufacturers try to reduce their fuel consumption by optimizing the efficiency of the engine. Two sources must be distinguished: optimisation of the propulsive efficiency and optimisation of the engine core efficiency. They are respectively related to the LP system and the HP system. It is proposed here to review briefly long-term disruptive concepts and short-term incremental evolutions that are planned by industrial actors.

1.1.2.2 Disruptive concepts

Concepts presented here are only long-term potential solutions that will not be commonly used before 2040 or later. First, low carbon fuels such as cryogenic CH_4 of H_2 would be very good candidates to replace kerosene. Their energy density per unit mass (green dots) is higher than kerosene (blue dot) as shown in Fig. 1.5, abundant resources can be found on Earth and they would reduce drastically pollutant emissions in terms of CO_2, NO_x, and particles. However, changing the fuel type raises major issues for the aircraft integration, for example to include cryogenic fuel storage. Working with full electric energy will not be a mature technology before 2040. Indeed, the energy density of current batteries used for automotive transport is around 60 times lower than kerosene (see red circle in Fig. 1.5). Even the best prevision on battery improvement with known technologies brings the energy density of batteries to be still 24 times lower than kerosene in 2035 (orange circle). Therefore, the use of electric energy for

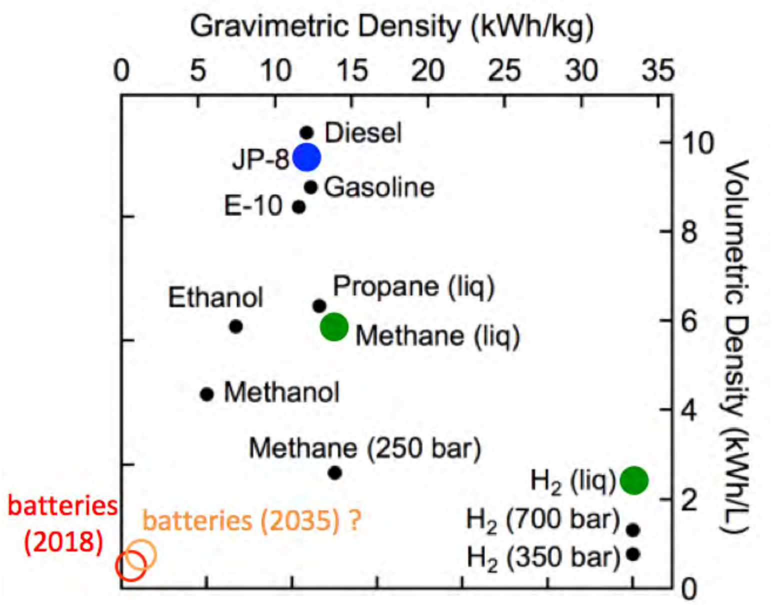

Figure 1.5: Energy densities for many sources of energy.

aircraft propulsion will first consider electric taxing, and then micro-hybrid propulsion (600 kW, 5 % e-propulsion), expected by 2030. Alternative combustion modes are also progressively matured to be used after 2040. Pulse detonation combustors and constant volume combustion are among the most advanced technologies. By working on a modified thermodynamic cycle, they allow to improve drastically the performance of the engine.

1.1.2.3 Incremental evolutions

On propulsive efficiency

For standard gas turbine designs, the propulsive efficiency is mainly controlled by the ByPass Ratio (BPR) between the mass flow rates going through the secondary flux and the primary flux. Increasing the BPR allows to lower the fuel consumption for the same thrust. Entered in service in 1982, the best seller Safran Aircraft Engines-General Electrics CFM-56 engine equipping for instance the Airbus A320/A340 and Boeing 737 operates with a BPR of 5:1 to 6:1. With the CFM LEAP engine, designed to replace the CFM-56 and operated since 2013, the BPR raises up to 11:1 (High Bypass Ratio, HBR). Using such technology, the fuel consumption is reduced by 15 % as well as CO_2 emissions. However, upgrading the BPR is limited. A compromise must be found as it also implies a heavier engine because of the large nacelle, as well as an increased drag force. An optimum BPR of 12:1 to 15:1 was found and leads to the so-called Ultra High Bypass Ratio (UHBR) designs illustrated in Fig. 1.6. Such high BPR should allow to

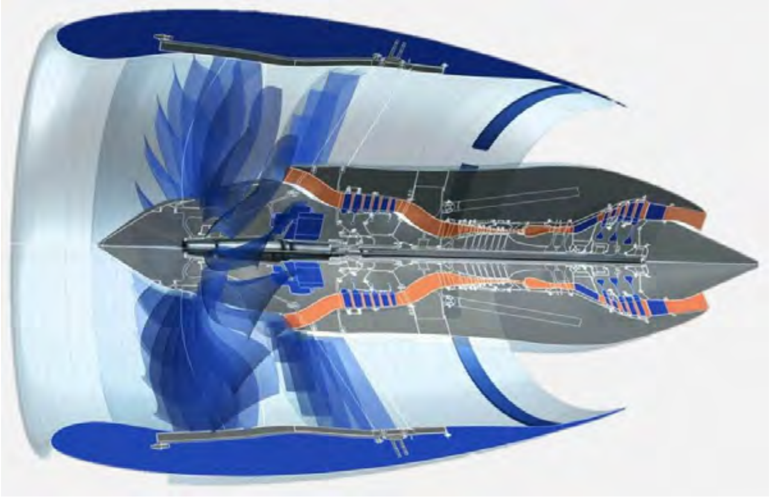

Figure 1.6: Scheme of an Ultra High Bypass Ratio (UHBR) engine. Courtesy of Safran Aircraft Engines.

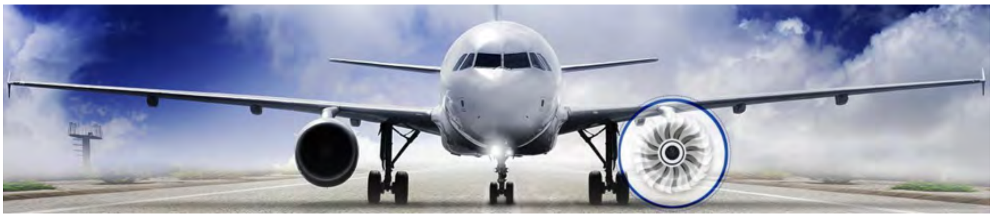

Figure 1.7: Illustration (NIPSE project) of aircraft integration issue with the UHBR concept.

lower the fuel consumption by 5 % - 10 % compared to the LEAP engine. However, the increase of the nacelle diameter brings aircraft integration issues for UHBR: positioning engines under the plane wings will still be possible, but requires design evolutions of the wings shape as landing gears would be too short with conventional wings as illustrated in Fig. 1.7.

The limited optimized BPR ratio mainly comes from the increase of the nacelle weigh. Therefore, in the context of the Clean Sky 2 European research programme, the Open Rotor concept showcased in Fig. 1.8 is developed. This engine operates with a turbine driving a pair of unducted counter-rotating fans, and leads to drastic weight reduction and potential BPR over 30:1. It is the only architecture proving a 15 % reduction of fuel consumption and CO_2 emissions compared to the LEAP engine. To obtain such high BPR, the diameter of the fan is significantly increased from 1.6 m for the CFM-56 to 4.3 m for the Open Rotor concept. It will require to place engines at the rear of fuselage, instead of under the wings. This unconventional positioning is a real challenge for engine manufacturers. Besides, the nacelle also limits risks for passengers in case of blade rupture, a protection that disappears with the Open Rotor. For these

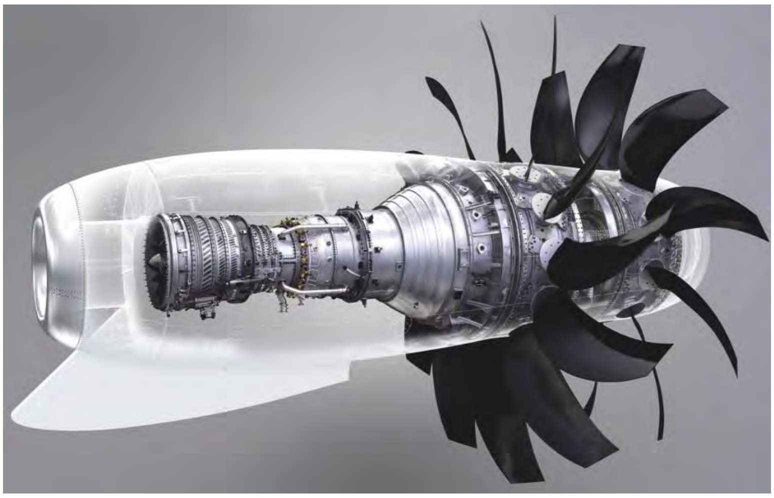

Figure 1.8: Scheme of the Safran Open Rotor engine. Courtesy of Safran Aircraft Engines.

reasons, the Open Rotor is a long-term project, expected to be commercialized as from 2035. Still, it achieved the TRL5 level on the Technology readiness levels (TRL) on a scale of 9, proving its potential and already high maturity.

On engine core efficiency

The engine core efficiency is directly controlled by the Overall Pressure Ratio (OPR) between measured pressure upstream and downstream the compressor. Over years, this OPR has been increased in standard RQL designs. However, as fresh gases are more pressurized, combustion leads to higher maximum temperatures in the combustion chamber, which directly increase NO_x emissions. To keep optimizing the engine core efficiency while meeting pollutant emissions targets, new combustor designs alternative to RQL, must be developed. Many low-NO_x combustor designs are proposed, as the Lean Direct Injection (LDI) concept, the Lean Premixed Pre-vaporized (LPP) concept, or the multipoint injection system. All of them tend to reduce the overall equivalence ratio in the chamber to burn in lean conditions. This leads to a lower maximum temperature and lower induced NO_x emissions. A Low-NO_x combustion chamber design is given in Fig. 1.9. As compared to conventional combustors, leaner conditions are achieved by increasing the amount of fresh air through the injection system and that mixes with kerosene (over 70 %). Moreover, as NO_x formation is function of the residence time in the combustor, the length of the flame tube is reduced. Such designs introduce new issues. For instance, because the flame tube is much smaller, temperature heterogeneities after combustion can remain until the HP turbine. An efficient cooling of turbine blades must then be used to avoid structural damages. In addition,

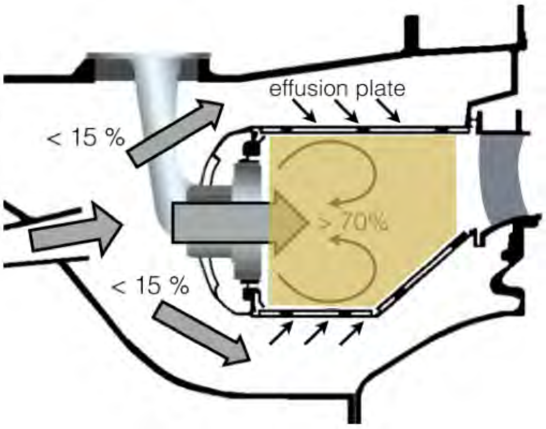

Figure 1.9: Scheme of a Low-NO$_x$ combustion chamber design. Extracted from [1].

the leaner flame is less stable and more subjected to thermo-acoustic instabilities that are very dangerous for the whole engine integrity. Finally, as detailed below, ignition is more difficult.

1.2 A crucial constraint: high altitude engine relight capability

Even if dramatically improved over years, aviation safety remains decisive before considering any technological change. Efforts to limit hazards are being made by manufacturers, for instance to increase the resistance of aircraft engines to bird strikes, abnormal volcanic ash intake, or ice ingestion. Nevertheless, zero risk cannot be achieved and engine relight performance in case of high altitude emergency failure is primordial. Safety regulations impose high altitude engine relight capability in case of flame-out for the certification of an engine. This is often based on a range of reliable flight conditions, for which relight performance must be guaranteed. The certification procedure is an engine test in sub-atmospheric experimental test bench reproducing the desired altitude conditions. Sub-atmospheric conditions (0.3 $bars$, -50° C) are very unfavourable to ignition as evaporation and combustion processes are slowed down. Multiple reasons of relight failure can be identified and are presented in the following section.

1.2.1 Overview of an ignition sequence

Aeronautical engines are ignited with one or several igniting systems, spark plugs or hot gas jet. The ignition sequence can be divided in three main parts, illustrated in Fig. 1.10, that must all be successful to correctly ignite or relight the combustor:

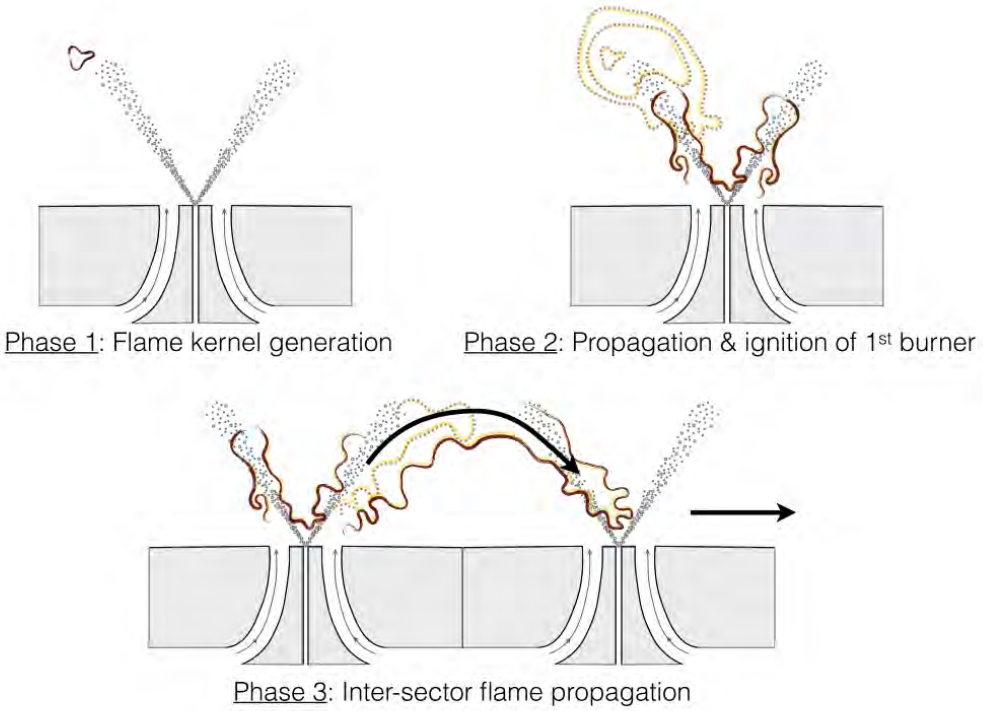
Phase 1: Flame kernel generation
Phase 2: Propagation & ignition of 1st burner
Phase 3: Inter-sector flame propagation

Figure 1.10: Scheme of the three main phases of forced spark ignition in an aeronautical gas turbine: Phase 1: kernel formation, Phase 2: growth and propagation up to the nearest fuel injector, Phase 3: Light-round. Extracted from [1].

- **Phase 1.** The first step is the flame kernel formation following the electric discharge at the spark plug. Many influencing parameters are involved during this phase as the local fuel/air mixing at the spark, and of course igniter related parameters such as the spark duration and power.
- **Phase 2.** The second step is the growth and propagation of the flame kernel up to the nearest fuel injector. The kernel is weak at this time and is convected in the chamber, encountering various local flow conditions. Flow properties controlling the success of this phase are essentially the mean local velocity, the spray evaporation, the local fuel/air mixing and turbulence properties along the flame kernel path.
- **Phase 3.** Finally the third phase is the light-round phase. In this phase, the flame propagates from one injector to the other to ignite the entire combustion chamber. The efficiency (speed, reliability) of this phase is mainly controlled by the injector-to-injector distance that changes mixture flammability, spray and flow aerodynamic properties.

In the entire manuscript, these three steps will be regularly referred to as Phase 1, Phase 2 and Phase 3.

1.2.2 Effects of new engine concepts on ignition performance

Engine ignition capacity is challenged by design innovations induced by the reduction of fuel consumption, pollutant emissions, and by operating costs. Typically, new Low-NO_x burners are quite detrimental to relight performance compared to RQL designs. Indeed, the increased velocity and turbulence at the spark igniter position (due to the important amount of air coming from the injector) as well as the leaner equivalence ratio are prejudicial for ignition. Reducing the number of injectors in an annular combustion chamber lowers the cost but dramatically impacts the light-round phase as it increases injectors spacing limiting the flame propagation ability. A last example is the spark plug, which needs to be often changed due to erosion. Lowering the power of the spark or changing the spark plug position limits erosion but leads to a weaker kernel.

For conventional systems, empirical correlations have been developed over the years, allowing to anticipate ignition behaviour changes with small design adjustments. However, these correlations do not hold for new burner designs. To avoid expensive and time wasting iterations between conception phases and certification tests, increased theoretical knowledge and modeling of ignition in conditions representative of Low-NO_x systems is now required.

In conclusion, the development of future combustion chamber designs is obviously a trade-off between many objectives and limitations:

- Satisfy the growing aircraft market demand.
- Reach challenging noise and pollutant emission regulation constraints.
- Limit fuel consumption.
- Consider aircraft integration.
- Minimize maintenance cost.
- Guarantee absolute safety, in particular concerning the most stringent operability requirement that is relight capability.

Developing a design that satisfies all these constraints in a limited time and with limited fund resources requires advanced tools such as numerical simulations which are increasingly used in the industrial world.

1.3 Role of numerical simulation

Relight certification tests only occur at the end of the entire conception phase, and intermediate experimental tests can not be always used to make adjustments. It is then more and more common to rely on numerical tools able to predict burner behaviour in an accurate and reliable way. In particular, the prediction of the ignition probability map of a combustor is a very precious tool in order for example to optimize the spark plug position.

In order to be used by engine manufacturers, numerical simulation tools must of course prove their accuracy. Validation is therefore a crucial step in model developments. This is why early numerical tool developments are mostly done in an academic context, and only when sufficiently mature, transferred to be used by industrials. Developed since the sixties, Computational Fluid Dynamics (CFD) is now a very mature complementary analysis tool to experiment, with reasonable cost and restitution time. CFD has been used in the aerospace industry since the beginning, to limit very expensive experimental tests with engine prototypes. This early use leads today to its widespread deployment in this industry. The continuously growing CPU technologies and resources allow more and more accurate numerical methods such as Large Eddy Simulations (LES), including multi-physics.

1.4 Objectives and organisation of the thesis

This PhD work was sponsored by Safran Aircraft Engines and is linked to two national research projects: TIMBER (Two-phase Ignition and propagation in Multi-BurnER combustors) and FAMAC (ignition fundamentals for internal combustion engines). Because of the two-sided context (academic and industrial) of this work, two main objectives have emerged:

- Confirm and improve the ability of Large Eddy Simulations (LES) to be used in the context of gas turbine ignition. LES is progressively becoming standard in the industrial context but still requires a lot of strengthening and validations to reach higher levels of TRL. Ignition is a particular field of interest regarding LES as this transient stochastic phenomenon can not be accurately captured by more standard methods such as Reynolds-averaged Navier-Stokes (RANS) simulations.
- Improve the knowledge of all phases of gas turbine ignition. This is encouraged by the development of new combustor designs that are constrained by relight capability requirements. The LES solver AVBP developed at CERFACS is a good candidate for such investigations as it has already been successfully used in many ignition studies of increasing complexity over the years. Results may also serve as academic databases in the future.

This PhD thesis directly follows the work of Esclapez [1] who studied ignition in the context of the LEMCOTEC FP7 European project. Esclapez investigated phases 2 & 3 of ignition in gaseous premixed and non-premixed conditions. In this work, it is proposed to extend this work to spray conditions, by also adding a more complex description of the combustion chemistry using Analytically Reduced Chemistry (ARC). It is also proposed to investigate phase 1 of ignition in gaseous premixed conditions.

The manuscript is organized as follows. Before dealing specifically with ignition, the necessary theoretical backgrounds on turbulent two-phase combustion and CFD are introduced in **Part. I**. Then, **Parts. II - III - IV** respectively focus on ignition **Phases 1 - 2 - 3**, in their chronological order. Each part (II - III - IV) begins with a dedicated literature review to put into context the work and highlight the state of the art and missing knowledge that should be further investigated. **Part. II** is made of one result chapter where numerical simulations of spark ignition are performed in a simplified anode-cathode geometry, and confronted to experimental results. **Part III** is made of two result chapters. The first one is dedicated to numerical simulations of two-phase ignition in the KIAI-Spray single burner. The experimental work of Marrero-Santiago [2] on this configuration is extensively used for comparison. The second chapter focuses on the extension and application to two-phase flow conditions of the MIST model for ignition probability prediction initially developed by Esclapez [1] for gaseous flows. Finally, **Part IV** is comprised of two result chapters. In the first one, two-phase light-round is studied in the CLSSB burner (linear arrangement) investigated by Marrero-Santiago [2]. Then the MICCA-spray burner (annular arrangement) is studied. Results are here compared to experimental data from Prieur [3] and numerical results from Lancien [4].

Part I

Turbulent two-phase reactive flows

Chapter 2

Theoretical concepts of combustion

Contents

2.1 Laminar flames 21
  2.1.1 Laminar premixed flames 22
  2.1.2 Laminar diffusion flames 25
2.2 Turbulent flames 27
  2.2.1 Turbulence basis 27
  2.2.2 Turbulent premixed flames 28
  2.2.3 Turbulent diffusion flames 30
  2.2.4 Partially-premixed flames in real systems 31
2.3 Spray flames 32
  2.3.1 Laminar two-phase flames 32
  2.3.2 Turbulent two-phase flames 35

The objective of this chapter is to introduce basic concepts of combustion in canonical cases, before dealing specifically with ignition in the core of this manuscript. This chapter does not pretend to be extensive but only to provide the necessary knowledge on combustion for the comprehension of this work. The global context of this thesis is two-phase ignition in aeronautical gas turbines. The reacting flow in such combustor is highly turbulent and two kinds of combustion regime may be encountered: premixed and diffusion flames.

First, laminar premixed and non-premixed flames are introduced. The interaction of the flame with the turbulent structures of the flow is presented next and finally, the specificity of spray flames is discussed in the last part.

2.1 Laminar flames

A flow characterized by low velocities is called laminar when small perturbations are dumped by the molecular viscosity of the mixture. The flow stays well structured, with regular streamlines. Combustion analysis is first made in such simple flows.

2.1.1 Laminar premixed flames

Flame structure

A premixed flame can appear when fuel and oxidiser are mixed before being heated. The simplest structure of laminar unstretched premixed flame is represented in Fig. 2.1. The fresh and burnt gases are separated by the flame. Three layers can be seen:

- The preflame zone essentially made of fresh gases. When getting closer to the flame, fresh gases are heated due to thermal diffusion.
- When the temperature is high enough, first chemical reactions are triggered consuming the fuel and the oxidiser. Highly reacting radical species (O, OH, C_2H_2, ...) are produced and consumed due to hundreds of elementary reactions. This reaction zone is very thin, of the order of hundreds of microns.
- When final stable products (H_2O, CO_2, CO) are produced, the overall reactivity decreases, which corresponds to the post-flame region. Some slow reactions can still occur, for example producing NO_x products.

The flame structure can also be analysed as a function of c, the progress variable which evaluates the advancement of the combustion process. It can be defined based on the temperature:

$$c = \frac{T - T_f}{T_b - T_f} \tag{2.1}$$

with T_f and T_b respectively the fresh gases and burnt gases temperatures, or based on the mixture composition evolution:

$$c = \frac{Y_c}{Y_c^{eq}} \tag{2.2}$$

with Y_c a composition index bounded between 0 in fresh gases and Y_c^{eq} in the mixture at equilibrium. Typically, combustion products are used for instance $Y_c = Y_{CO} + Y_{CO_2} + Y_{H_2O}$. Based on either temperature or composition, the progress variable evolves from 0 in the fresh gases to 1 in the burnt gases. It allows to compare flames independently of their thickness. An iso-c line can be used to localise the flame front and the gradient of c can be used to localize the local normal direction of the flame towards fresh gases:

$$\mathbf{n} = -\frac{\nabla c}{|\nabla c|}. \tag{2.3}$$

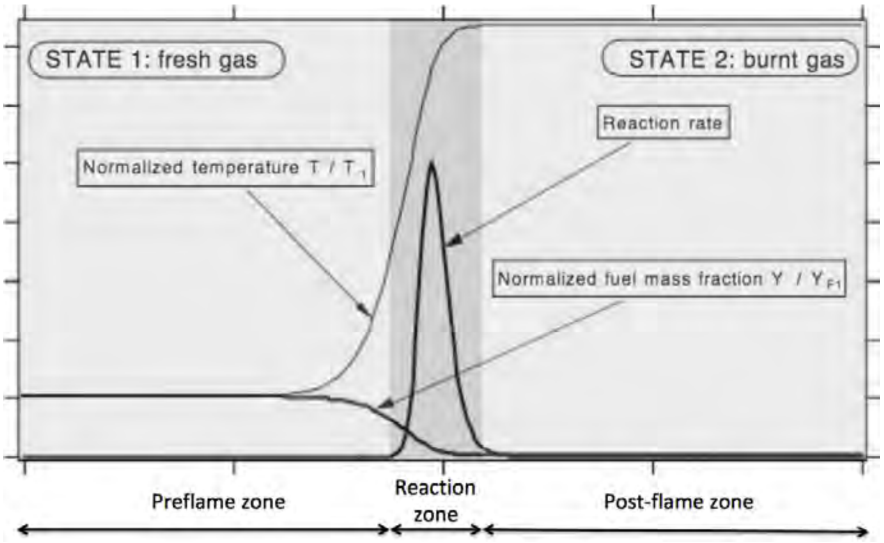

Figure 2.1: Laminar premixed flame structure. Extracted from Poinsot & Veynante [5].

Flame properties

Parameters driving the flame properties are essentially the fresh state pressure P_f, temperature T_f, and mixing properties often described by the equivalence ratio ϕ linking the fuel mass fraction Y_F and the oxidiser mass fraction Y_O:

$$\phi = s\frac{Y_F}{Y_O}. \tag{2.4}$$

The parameter introduced s is the mass stoichiometric ratio defined as:

$$s = \left(\frac{Y_O}{Y_F}\right)_{st} = \frac{\nu'_O W_O}{\nu'_F W_F}. \tag{2.5}$$

ν'_F and ν'_O are the fuel and oxidiser stoichiometric coefficient of the global reaction considered and W_F and W_O are the molecular weights of the fuel and oxidiser. When burning a mixture with exactly s times more oxidiser than fuel (in mass), all the oxidiser and the fuel will be consumed. This situation corresponds to a stoichiometric case: $\phi = 1$. When decreasing the initial amount of fuel, oxidiser will be left at the end of the combustion. This is called lean combustion: $\phi < 1$. Finally, if fuel is provided in excess, rich combustion occur: $\phi > 1$ and fuel will be left at the end of combustion.

P_f, T_f, ϕ influence the two main global properties of the flame: its laminar speed s_l^0 and thickness δ_l^0. Different definitions of the flame thickness exist. The most common one uses the thermal profile of the flame:

$$\delta_l^0 = \frac{T_b - T_f}{\max\left(\left|\frac{\partial T}{\partial x}\right|\right)}. \tag{2.6}$$

Assuming a global one-step chemistry, one can show that:

$$\delta_l^0 \propto \sqrt{\frac{D_{th}}{A}} \tag{2.7}$$

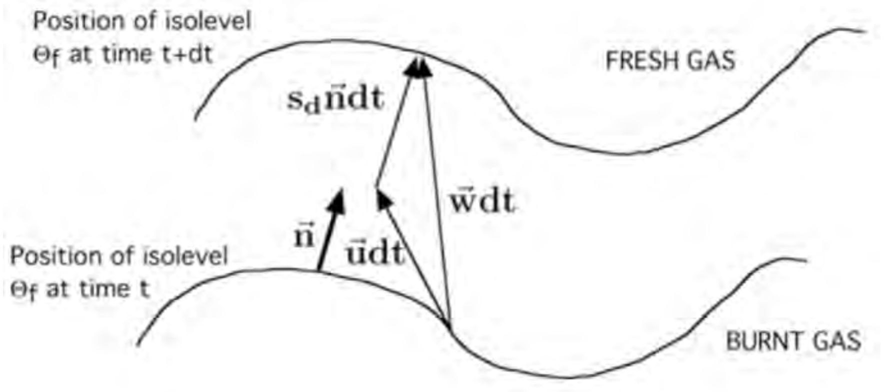

Figure 2.2: Flame speed definitions. Extracted from Poinsot & Veynante [5].

with the thermal diffusivity $D_{th} = \lambda/\rho_f C_p$, λ the thermal conductivity (Eq. 3.13), ρ_f the fresh gases density, C_p the heat capacity at constant pressure of the mixture and A the Arrenhius pre-exponential constant of the global reaction. Equivalently,

$$s_l^0 \propto \sqrt{D_{th} A}. \tag{2.8}$$

The flame speed s_l^0 is actually a concept that can have various definitions depending on the reference frame. With notations introduced in Fig. 2.2:

- The absolute flame velocity $S_a = \mathbf{w} \cdot \mathbf{n}$ is the flame front speed relative to a fixed reference frame.
- The displacement flame speed $S_d = (\mathbf{w} - \mathbf{u}) \cdot \mathbf{n} = S_a - \mathbf{u} \cdot \mathbf{n}$ is the flame front speed relative to the local flow. A density weighted displacement speed is also often used defined as $S_d^* = \rho_b/\rho_f S_d$ in order to take into account the gases dilatation created.
- The consumption speed S_c is the speed at which reactants are consumed.

Contrary to S_a and S_d that are local, the consumption speed is a global quantity expressed as:

$$S_c = -\frac{1}{\rho_f Y_F^f} \int_{-\infty}^{+\infty} \dot{\omega}_F d\mathbf{n} \tag{2.9}$$

with $\dot{\omega}_F$ the fuel consumption rate. S_c represents the fuel consumption integrated in the normal direction of the flame.

Stretch effect

The example of the unstretched laminar flame is a particular case for which the flame surface stays constant. More generally, the flame surface may change with time due to the flame stretch κ:

$$\kappa = \frac{1}{A} \frac{dA}{dt} \tag{2.10}$$

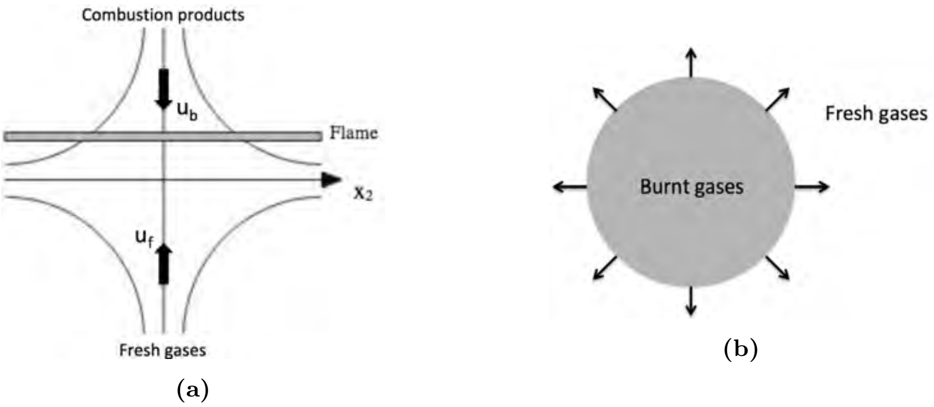

Figure 2.3: Canonical stretched premixed flame: (a) Strained flame, (b) Curved flame.

with A the flame surface. κ can be splitted in two componants [6]:

$$\kappa = \underbrace{(\delta_{ij} - n_i n_j)\frac{\partial u_i}{\partial x_j}}_{\text{Tangential strain rate}} + \underbrace{S_d \frac{\partial n_i}{\partial x_i}}_{\text{Curvature effect}} = a_t + 2S_d\mathcal{K}. \tag{2.11}$$

Two terms are revealed: a_t the tangential strain rate, and $\mathcal{K}$ the flame front curvature. Strain and curvature can modify the flame speed depending on the fuel Lewis number $Le_F = D_{th}/D_F$ comparing the thermal and fuel diffusion coefficients. For fuels with $Le_F < 1$, the consumption speed increases with the stretch. A linear dependence is even found for small stretches. On the contrary, for fuels with $Le_F > 1$, S_c decreases when the stretch increases, and can even lead to flame extinction for too high stretch levels. Figure 2.3 shows two archetypes of premixed flame subjected to stretch. In Fig. 2.3a a flame is subjected to strain only, without curvature effect. Fresh premixed gases are provided from one side of the flame. Products of combustion are brought from the other side. In Fig. 2.3b, an expanding spherical flame subjected to curvature only. These simple configurations are useful to isolate strain and curvature effects on the flame response. For the strained flame, a strain rate

$$a = \frac{u_f + u_b}{L} \tag{2.12}$$

is generally defined with u_f, u_b the fresh gases and burnt gases inlet velocity and L the distance between the two inlets.

2.1.2 Laminar diffusion flames

Contrary to a premixed flame, a diffusion flame appears when fuel and oxidiser are not mixed. The flame actually separates the fresh pure fuel on one side and the fresh pure oxidiser on the other side as sketched in Fig. 2.4. In the reaction zone, fuel and oxidiser burn around stoichiometry. Heat is diffused to both sides. Contrary to premixed flames,

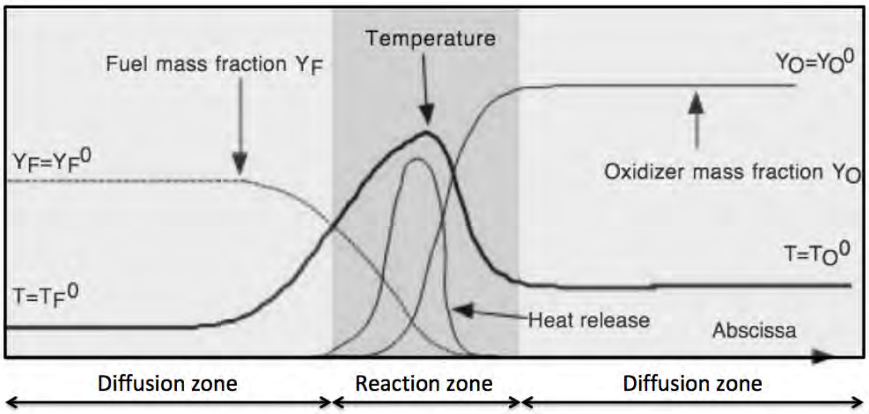

Figure 2.4: Laminar diffusion flame structure. Extracted from Poinsot & Veynante [5].

diffusion flames do not have intrinsic propagation speed and flame thickness. The rate of reaction is mainly controlled by the mixing of fuel and oxidiser along the flame that is driven by the inlet fuel and oxidiser flow rates. A typical diffusion flame is the stretched flame shown in Fig. 2.5. Usually, a strain rate

$$a = \frac{u_F + u_O}{L} \tag{2.13}$$

is defined with u_F, u_O the fuel and oxidiser inlet velocities and L the distance between the two inlets. Considering infinitely fast chemistry, and supposing that all species diffusivities are equal to the thermal diffusivity ($D_k = D_{th} = D$), the flame consumption speed can be evaluated as

$$S_c \propto \sqrt{aD}. \tag{2.14}$$

This expression shows that the fuel consumption is controlled by the local flow condition for diffusion flames. The burning rate is increased when reactants are brought faster in the reaction zone and when their mixing is faster. When considering real finite rate chemistry, a competition between mixing time and chemical time arises and the fuel consumption rate can also be limited by chemistry.

An essential quantity to study diffusion flames is the mixture fraction z. The flame structure is often studied in the z-space. z is adequately defined by Bilger [7]:

$$z = \frac{\beta - \beta_O}{\beta_F - \beta_O} \tag{2.15}$$

with the coupling function:

$$\beta = \sum_{i=1}^{n_{spec}} \gamma_i \sum_{j=1}^{N_a} n_{ij} \frac{W_i Y_j}{W_j}. \tag{2.16}$$

Here, n_{ij} is the number of atoms of the ith element in the jth species and N_a is the total number of atoms. γ_i are weighting factors, with values $\gamma_C = 2/W_C$, $\gamma_H = 1/(2W_H)$

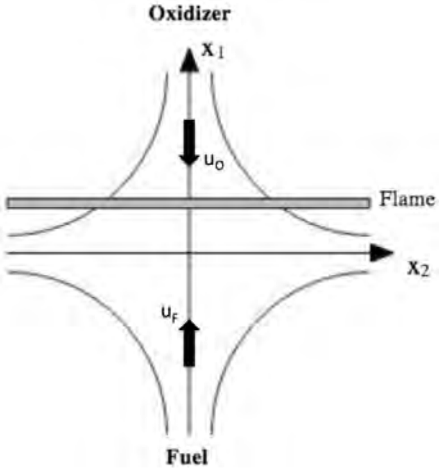

Figure 2.5: Canonical laminar stretched flame. Extracted from Poinsot & Veynante [5].

and $\gamma_O = 1/W_O$. β_F and β_O are the values obtained in the incoming fuel stream and incoming oxidiser stream. A link between ϕ and z can be made with:

$$\phi = \frac{z}{1-z}\frac{1-z_{st}}{z_{st}}. \tag{2.17}$$

2.2 Turbulent flames

2.2.1 Turbulence basis

Combustion is almost never found in a laminar flow. Most of the time, it is found in turbulent conditions. In such flow, velocity is high, creating important velocity fluctuations that cannot be dumped by the molecular viscosity. The flow is no more well structured in appearance, with disorganised large and small scales of flow perturbation. The turbulent nature of the flow is often characterized by comparing the inertia forces that tend to disrupt the organisation of the flow with the viscous forces than try to smooth all perturbations to recover a laminar flow. This is done by the well-known Reynolds number:

$$Re = \frac{U\,L}{\nu} \tag{2.18}$$

with U and L characteristic velocity and length of the flow studied and ν the kinematic viscosity of the fluid. The exact transition from laminar to turbulent regime is only known in few academic configurations (such as pipe flows). In all cases, a high Re number characterizes a highly turbulent flow while when Re tends to 1, the flow is laminar. The mechanisms linking large scale deformations of the flow with the smallest scales are described by the Kolmogorov theory. The energetic cascade, drawn in Fig. 2.6, represents the progressive decay of large structures (small wave number k) into small ones (large wave number k). This energy spectrum is made of three parts:

- The integral zone corresponding to the largest turbulent scales. These scales are also the most energetic ones. They are characterised by l_t the integral length scale and u' the characteristic large scale velocity fluctuation. A corresponding time scale $\tau_l = u'/l_t$ can be deduced. A turbulent Reynolds number is defined for these largest scales: $Re_t = u'l_t/\nu$.
- The inertial zone where large eddies break to form smaller eddies. Energy is just transferred to the new eddies but is not dissipated yet. The rate of energy transfer is constant following a $k^{-5/3}$ law in homogeneous isotropic turbulence [8].
- The dissipation zone corresponds to the smallest eddies of the flow, with a size close to the Kolmogorov length scale l_κ and a characteristic velocity u_κ. A corresponding time scale $\tau_\kappa = u_\kappa/l_\kappa$ can be deduced. These eddies are not broken into smaller ones but are dissipated by the molecular viscosity. The Reynolds number associated to these scales writes $Re_\kappa = u_\kappa l_\kappa/\nu = 1$.

In homogeneous isotropic turbulence, links can be done between integral and Kolmogorov length and velocity scales thanks to the constant dissipation rate ϵ of the kinetic energy. This dissipation rate can be estimated from the largest scale for instance:

$$\epsilon = 2\nu S_{ij} S_{ij} \tag{2.19}$$

with S_{ij} the deformation tensor:

$$S_{ij} = \frac{1}{2}\left(\frac{\partial u_j}{\partial x_i} + \frac{\partial u_i}{\partial x_j}\right). \tag{2.20}$$

It is found for example that

$$\frac{l_t}{l_\kappa} = Re_t^{3/4} \tag{2.21}$$

meaning that large Reynolds number flows create the biggest energy cascade. Turbulent structures of various size may thus interact with the flame changing its structure and properties as compared to the laminar case.

2.2.2 Turbulent premixed flames

All turbulence length scales from l_t to l_κ may interact with the flame. Therefore, two dimensionless numbers are introduced:

- The Damkhler number which is the ratio between the time scale associated to the integral scale and the chemical time scale:

$$Da = \frac{\tau_t}{\tau_c} = \frac{l_t}{\delta_l^0}\frac{s_l^0}{u'} \tag{2.22}$$

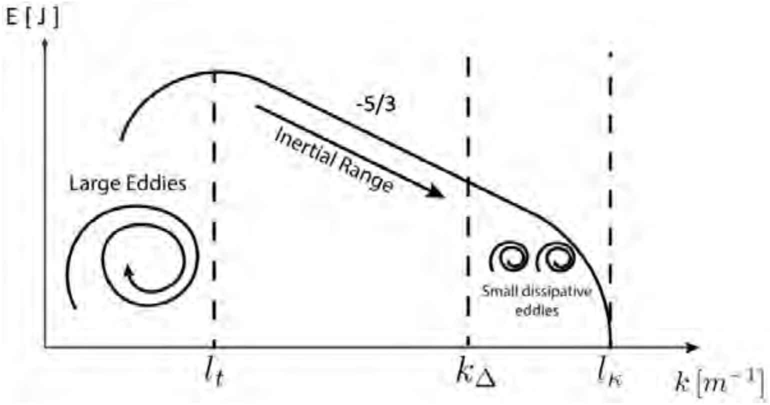

Figure 2.6: Scheme of the turbulent energetic spectrum along the energetic cascade.

- The Karlovitz number which is the ratio between the chemical time scale and the time scale corresponding to the Kolmogorov eddies:

$$Ka = \frac{\tau_c}{\tau_\kappa} = \frac{\delta_l^0}{l_\kappa}\frac{u^\kappa}{s_l^0} \tag{2.23}$$

By combining Da and Ka, it possible to rewrite

$$Re_t = Da^2 Ka^2. \tag{2.24}$$

Many combustion diagrams have been proposed in the literature to summarize possible flame-turbulence interactions as function of Ka and Da, for example the one of Peters shown in Fig. 2.7. The first important regime is the flamelet regime or thin wrinkled flame regime, corresponding to $Ka < 1$ and so necessarily $Da \gg 1$. In this regime, all turbulent time scales are larger than the flame time scale. The flame surface is then modified by the large eddies but the inner flame structure is unaffected by these turbulent structures: the turbulent flame front can be seen as an ensemble of flamelets, or laminar flames distributed along a stretched and wrinkled front. The opposite case is found when $Da < 1$ and so necessarily $Ka \gg 1$. Turbulent mixing occurs faster than chemical reactions. Turbulent structures can penetrate the reaction zone and preheat zone, increasing turbulent diffusion. It is called the well stirred reactor regime or thickened flame regime. The intermediate regime is the thickened-wrinkled flame regime for which $Ka > 1$ and $Da > 1$. The flame thickness is larger than the Kolmogorov scale so small structures can penetrate the preheat zone and increase heat diffusion leading to a thicker flame. However, the flame thickness remains smaller than the integral length scale so the flame keeps its laminar structure.

In most of practical hydrocarbon oxidation processes, the flamelet regime is the most relevant one. Thus, this one has been studied intensively, especially numerically.

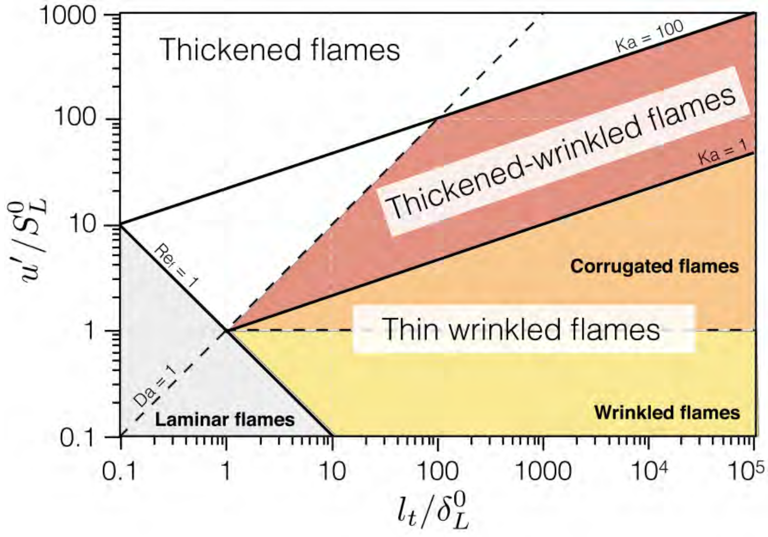

Figure 2.7: Combustion diagram for premixed turbulent combustion [9].

A particular effect of turbulence is to increase the flame surface area by flame stretching. The direct consequence is an increase of flame speed. A turbulent flame speed s_T has been proposed by Abdel-Gayed [10] using the integral scale velocity fluctuation and the laminar flame speed:

$$\frac{s_T}{s_l^0} \propto 1 + \frac{u'}{s_l^0}. \tag{2.25}$$

For high velocity fluctuations, s_T reaches a plateau and can even drop at one point corresponding to flame quenching. This comes from a too high turbulent thermal diffusion that takes the energy away from the flame front faster that it is produced by the flame.

2.2.3 Turbulent diffusion flames

Even if diffusion flames do not have intrinsic time and length scales, similar combustion diagrams as for premixed flames have been derived. Based on a calibrated flame/vortex case where a flame thickness could be established, Cuenot & Poinsot [11] proposed the combustion diagram shown in Fig. 2.8. Its genericity for all diffusion flames is of course not guaranteed but it offers a good description of controlling numbers. For a sufficient turbulent Reynolds number Re_t, three regimes are found and only depend on the Damkohler number of the diffusion flame. For high Da, the flame keeps a structure similar to its laminar structure. On the contrary, for low Damkohler number, quenching occurs because the chemical time scale is too high compared to the turbulent time scale. The intermediate case corresponds to a situation with strong unsteady effects. The flame is not quenched.

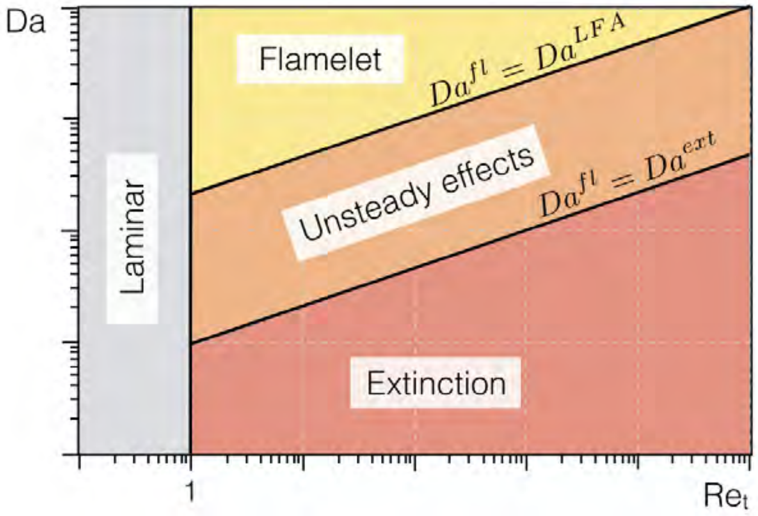

Figure 2.8: Combustion diagram for non-premixed turbulent combustion [11].

2.2.4 Partially-premixed flames in real systems

Only purely premixed and purely diffusion flames have been discussed so far. Actually, in real systems such as aeronautical gas turbines, combustion occurs in a partially-premixed regime. The ideal situation would be to use premixed fuel-air mixture to optimise the combustion efficiency. However, having a premixed fuel-air mixture before entering the combustion chamber is unsafe as it can ignite accidentally the tank and destroy the engine. For this reason, the mixing is only done when entering the combustion chamber. Systems such as highly turbulent swirlers are used to mix fuel and air as fast as possible before reaching the flame. Still, because of an incomplete mixing, a non-negligible part of the combustion occurs in a diffusion mode. As liquid fuels are used in such device, non-uniformity of the mixture fraction near the flame is certain: the evaporation process depends on local conditions and is therefore non-homogeneous. The gaseous mixture presents more or less heterogeneity depending on the quality of the evaporation process and its time scale as compared to the mixing time scale. If the evaporation time scale is too large, droplets can even cross the flame front creating spray flames studied in the following section.

To distinguish premixed from diffusion combustion, the Takeno index [12] TI can be used:

$$\mathrm{TI} = \frac{\nabla Y_F \cdot \nabla Y_O}{|\nabla Y_F \cdot \nabla Y_O|}. \tag{2.26}$$

Considering that in a premixed one-dimensional flame, the gradients of the oxidizer and the fuel mass fractions have the same sign while it is the opposite in a diffusion flame, the Takeno Index ranges from -1 for diffusion flames to $+1$ for premixed flames. The Takeno index weighted by the heat release rate (in order to dump non relevant

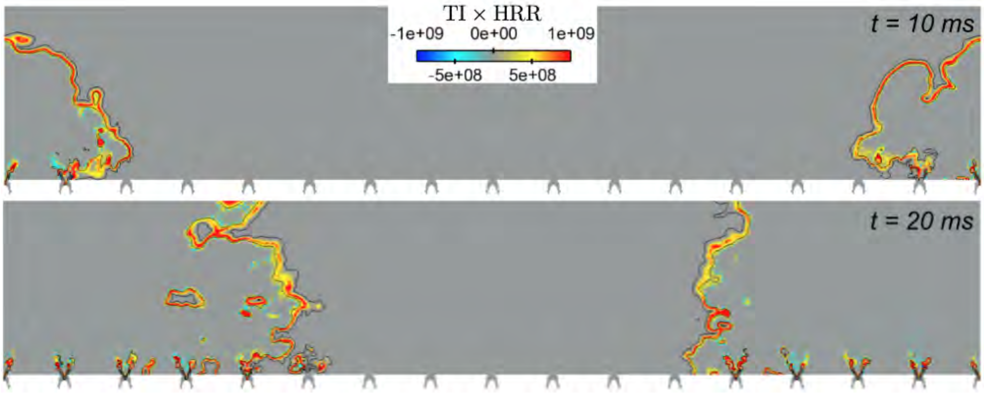

Figure 2.9: Takeno index weighted by the heat release rate during the flame propagation in an annular chamber. The central cut is shown, unfolded on a plane surface [4].

values) during the flame propagation in an annular chamber is shown in Fig. 2.9. The central cut of the annular chamber is shown, unfolded on a plane surface. It can be seen that both premixed and diffusion regimes are found. In particular, some diffusion spots are found in the post-flame region, where droplets cross the flame front.

2.3 Spray flames

2.3.1 Laminar two-phase flames

2.3.1.1 Two-phase flame structure

Compared to gaseous flames, a new important parameter needs to be considered: the evaporation process. A characteristic evaporation time τ_{ev} is introduced to qualitatively understand the behaviour of spray flames. A classical expression is

$$\tau_{ev} = \frac{\rho_l d_p^2}{8\rho_g D_F \ln(1 + B_M)} \tag{2.27}$$

with ρ_l and ρ_g the liquid and gaseous densities, d_p the droplets diameter, D_F the fuel diffusivity and B_M the Spalding mass transfer number. This time should be evaluated compared to a characteristic residence time τ_{res} of droplets between injection and arrival at the flame front. 1D two-phase laminar flames are useful to understand the structure of spray flames. In Fig. 2.10, three flames are presented for different ratios τ_{ev}/τ_{res}. The two-phase flame velocity and thickness are denoted respectively s_l^{tp} and δ_l^{tp}. For all cases, fuel droplets are injected along with fresh gases from the left and the injection velocity is s_l^{tp} so that the flame is stabilized. The residence time is in this case $\tau_{res} = L/s_l^{tp}$.

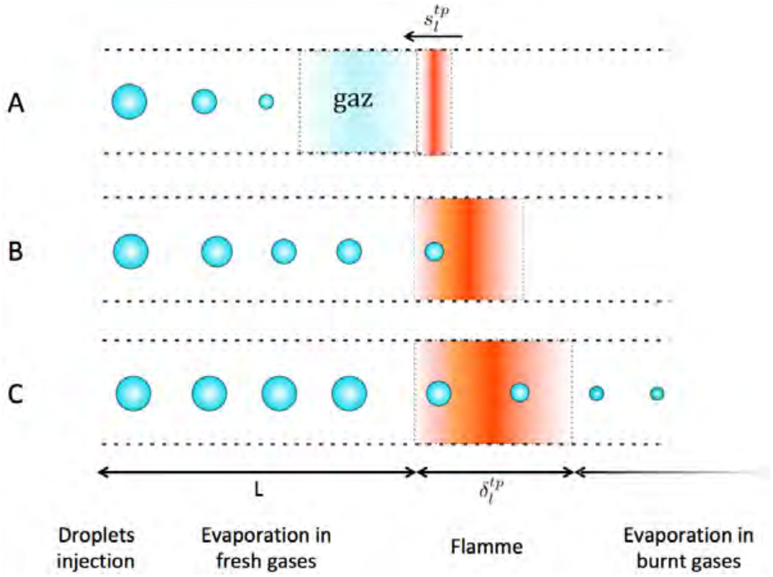

Figure 2.10: Two-phase laminar flame topology depending on τ_{ev}.

- For case A, $\tau_{ev}/\tau_{res} < 1$. In this case, droplets are already fully evaporated when reaching the flame front. The flame is then similar to a gaseous flame. If the mixing time between gaseous fuel and air is fast, the flame is premixed. In the contrary, a non-premixed flame is found.

- For case B, $\tau_{ev}/\tau_{res} \approx 1$. Droplets evaporate principally in the preheat zone of the flame but are not able to cross the flame front. Still, in addition to pre-vaporized fuel, the reactive zone of the flame sees droplets of fuel that change the structure of the flame.

- For case C, $\tau_{ev}/\tau_{res} > 1$. This case can be found for instance for large droplets or if the droplets velocity is much higher than the gaseous one. Here, droplets are not fully evaporated at the end of the flame front so that evaporation continues in the burnt gases. Because gaseous fuel appears after the reactive zone, it may burn if oxidiser is available leading to a thickened flame compared to a gaseous one.

2.3.1.2 Two-phase flame properties

Two-phase flame properties such as s_l^{tp} and δ_l^{tp} can be very different than gaseous flame properties. δ_l^{tp} is higher than δ_l^0 if some droplets burn after the main flame front. The most important parameter is s_l^{tp}. Different studies tried to model s_l^{tp} as function of s_l^0 and different liquid properties. Ballal & Lefebvre [13] proposed the following

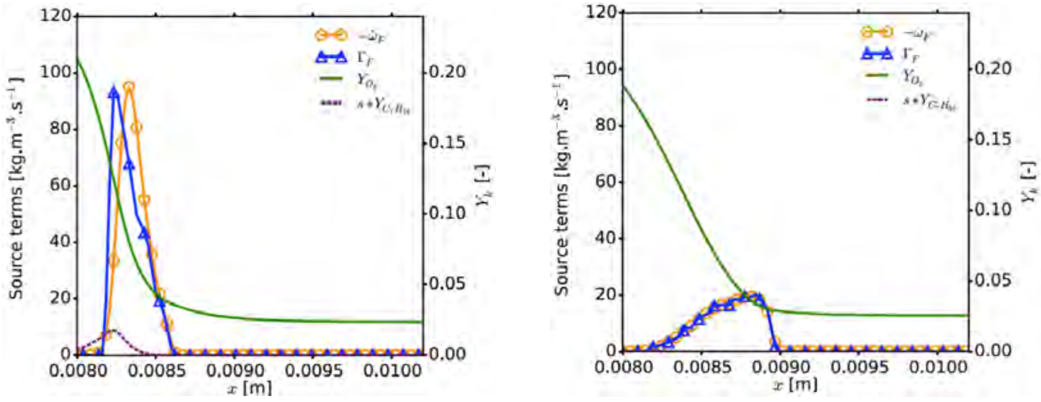

(a)

(b)

Figure 2.11: Two archetypes of spray flame structures extracted from Rochette et al. [15]. (a) Flame weakly controlled by evaporation. (b) Flame controlled by evaporation. Solid line: Oxidiser mass fraction. Dashed line: gaseous fuel mass fraction. Circles: fuel consumption rate. Triangles: evaporation rate.

correlation:

$$s_l^{tp} = \left(\frac{\tau_{ev}}{D_{th}} + \frac{1}{s_l^{0\,2}} \right)^{-\frac{1}{2}} . \tag{2.28}$$

Experimental spray flame velocities were recovered with this correlation for a large range of droplets diameter but only for overall lean mixtures. For rich mixtures, large discrepancies appeared showing the limitation of this formulation. Neophytou et al. [14] investigated numerically two-phase flames and evaluated the theoretical formula of Ballal & Lefebvre (Eq. 2.28) for different fuels. It was confirmed that lean combustion was well captured but that this formula was not able to catch effects created in rich conditions. The study of Neophytou et al. also demonstrated some features of spray flames. Spray flames can exist over the rich gaseous flammability limit at the equivalent overall equivalence ratio $\phi_{tot} = \phi_g + \phi_l$. Furthermore, it was shown that s_l^{tp} could become higher that s_l^0 for instance for large droplets or for $\phi_{tot} > 1$. These behaviours were explained quantitatively by Rochette et al. [15] and incorporated in an analytical expression for s_l^{tp}. 1D laminar spray flames were investigated numerically by varying the initial droplets diameter ($5 - 80\,\mu m$), the liquid/gas relative velocity ($1 < u_l/u_g < 80$), the initial gaseous equivalence ratio at injection ($0 < \phi_g < 0.8$) and the initial liquid equivalence ratio at injection ($0.1 < \phi_l < 1.3$). Among all these cases, two spray flame archetypes were identified and are shown in Fig. 2.11: **evaporation controlled flames** and **weakly evaporation controlled flames**.

A **Weakly evaporation controlled flame** is sketched in Fig. 2.11a. Such flames can be found if the initial gaseous mixture is already flammable or if droplets evaporation is required to reach the lean flammability limit ϕ_{lean} but evaporation is very fast. Its structure is very close to a gaseous flame and the evaporation rate differs from the fuel consumption rate. This means that first droplets evaporate and in a second step, the fuel vapor burns. The flame thickness and consumption speed are the ones of the equivalent gaseous flame at an effective equivalence ratio ϕ_{eff} corresponding to the total quantity of fuel (gaseous + evaporating) consumed within a consumption zone of length δ_l^{tp}, assumed very close to δ_l^0. Rochette et al. proposed:

$$\phi_{eff} = \left(\frac{\delta_l^0}{\max\left(\delta_{ev}, \delta_l^0\right)} \right)^{2/3} \phi_l + \phi_g \tag{2.29}$$

with $\delta_{ev} = u_l * \tau_{ev}$ an evaporation length. ϕ_{eff} is necessary smaller than ϕ_{tot}. Therefore, for overall rich flames ($\phi_{tot} > 1$), ϕ_{eff} can be close to stoichiometry and lead to $s_l^{tp} > s_l^0(\phi_{tot})$.

An **evaporation controlled flame** is sketched in Fig. 2.11b. In this case, the gaseous mixture is below the lean flammability limit and evaporation is the controlling parameter of the flame speed. This can be observed with the profiles of evaporation rate and fuel consumption rate which superpose exactly. This corresponds to the situation $\tau_c < \tau_{ev}$ with τ_c the characteristic chemical time that can be roughly evaluated using s_l^0 and δ_l^0. The flame structure is then very different than a purely gaseous one. The flame is much thicker and droplets can even continue to burn in the post-flame region if oxidiser is available. The two-phase flame laminar speed can not be recovered using equivalent gaseous flame properties as it is too different. s_l^{tp} is much smaller that s_l^0 and can be estimated by simply replacing τ_c by τ_{ev} in the definition of the flame speed:

$$S_l^{tp} = \frac{\delta^0_{l,\phi_g = \min(\phi_{tot},1)}}{\tau_{ev}} \tag{2.30}$$

These two-phase laminar flame properties will be used in Chap. 9 for the elaboration of a model to predict two-phase ignition probability.

2.3.2 Turbulent two-phase flames

Ideally, in aeronautical combustors, a gaseous fuel-air mixture should be obtained before burning. To enhance evaporation, turbulence is necessary. As sketched in Fig. 2.12, the first effect of turbulence is to destabilize the liquid sheet coming from the injector. Ligaments of liquid are created in the primary atomisation zone. The spray is very dense here with liquid volume fraction $\alpha_l > 1e^{-3}$. Ligaments break in the secondary atomisation zone because of the stretch imposed by local turbulent flow structures creating a mist of fuel droplets of inhomogeneous size. A dilute spray is formed $1e^{-6} < \alpha_l < 1e^{-3}$ which eventually reaches very low liquid volume fraction $\alpha_l < 1e^{-6}$ for which evaporation is much faster ($\tau_{ev} \propto d_l^2$).

The second effect of turbulence on sprays is the possible preferential segregation that can occur as illustrated in Fig. 2.13. This phenomenon occurs when particle inertia is

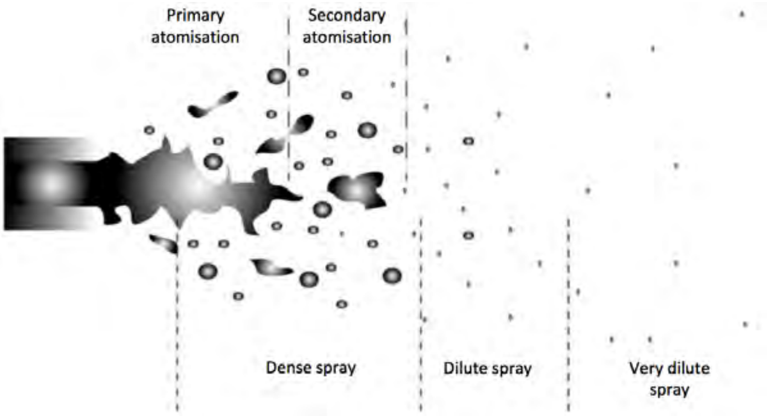
Primary atomisation
Secondary atomisation
Dense spray
Dilute spray
Very dilute spray

Figure 2.12: Atomisation process of sprays and corresponding spray density.

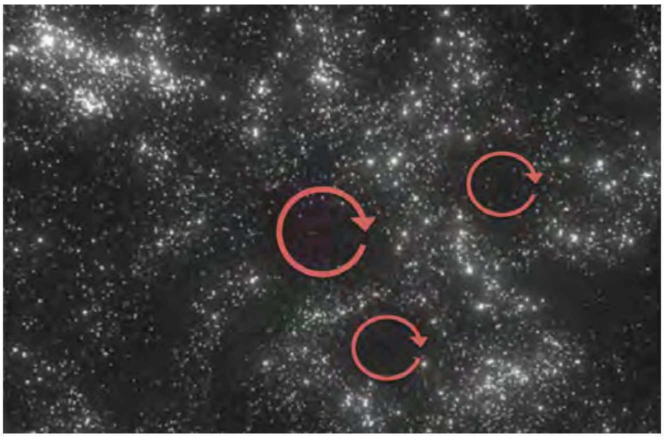

Figure 2.13: Preferential segregation of droplets in homogeneous isotropic turbulence, extracted from Wood et al. [16] . Large scale turbulent structures are modelled with red arrows.

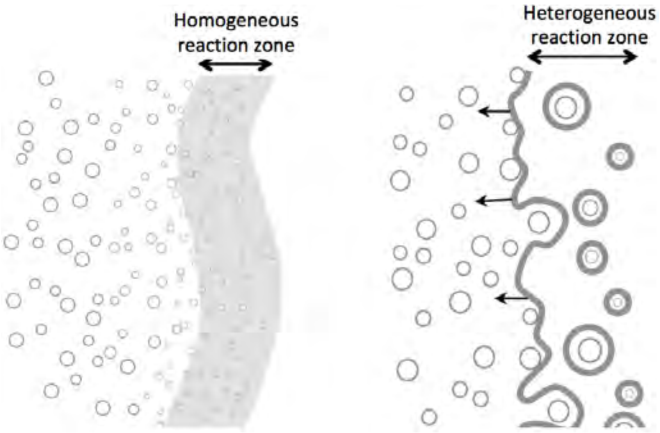

Figure 2.14: (Left) Homogeneous two-phase flow combustion. (Right) Heterogeneous two-phase flow combustion. Adapted from Paulhiac [17].

small. This is characterized with the Stokes number of the particle S_t which compares characteristic times of particle and gaseous dynamics. Large inertial particles are not subject to preferential segregation as their trajectories are independent of the flow. On the other hand, small droplets can exhibit a coherent motion and agglomerate in zones of lowest vorticity, trapped by large scale turbulent structures. This segregation implies strong inhomogeneities of fuel distribution as small droplets and large droplets are found in separate zones. This is true for gaseous fuel distribution as well as liquid fuel distribution. Evaporation properties are directly changed and can modify the flame structure. Another effect of turbulence on sprays is to create a local relative difference between the liquid and the gaseous velocities. This relative velocity difference is a factor driving the two-phase flame structure as detailed in Sec. 2.3.1.

Because of the inhomogeneities of mixture and flow properties created by turbulence, and also depending on the local liquid volume fraction, spray flame regimes can differ as represented in Fig. 2.14. If a globally dilute homogeneous spray reaches the flame front, a homogeneous reaction zone is preferentially found. The flame is not bended near droplets. On the contrary, in a very poly-disperse flow with a large range of droplet velocities, the flame may be bended near large droplets. The largest droplets can even cross the flame and single droplet evaporation might occur in the post-flame region generating diffusion flames. This regime is called heterogeneous combustion.

Chapter 3

Equations and models for gaseous turbulent reactive flows

Contents

3.1 Conservative equations for gaseous flows 39

3.1.1 Navier-Stokes equations 39

3.1.2 Flux description 40

3.1.3 Transport modeling 41

3.1.4 Chemical kinetics 42

3.2 Large Eddy Simulation equations 45

3.2.1 Concept of LES 45

3.2.2 Filtered LES equations 46

3.2.3 Closure of filtered viscous terms 47

3.2.4 Closure of subgrid fluxes 48

3.2.5 Combustion modeling 49

3.2.6 Numerics 53

This chapter is divided in two sections. In the first one, the Navier-Stokes equations describing gaseous turbulent reactive flows are presented. In the second section, the main concepts of Large Eddy Simulation are introduced and the corresponding filtered Navier-Stokes equations are given, along with associated numerical details. A particular focus is made on the modelling of the combustion source term.

3.1 Conservative equations for gaseous flows

3.1.1 Navier-Stokes equations

The Navier-Stokes equations for multi-species reacting flows arise from conservation laws for mass, momentum and energy. They are recalled here in their conservative form:

- Mass conservation

$$\frac{\partial \rho}{\partial t} + \frac{\partial}{\partial x_j}\left(\rho u_j\right) = 0 \tag{3.1}$$

  with ρ the density and u_j the jth velocity component.

- Species conservation

$$\frac{\partial \rho Y_k}{\partial t} + \frac{\partial \rho Y_k u_j}{\partial x_j} = -\frac{\partial}{\partial x_j} J_{jk} + \dot{\omega}_k, \qquad \text{for } k = 1, n_{spec} \tag{3.2}$$

  with Y_k the mass fraction of species k, J_{jk} the species diffusive flux and $\dot{\omega}_k$ the kth species source term.

- Momentum conservation

$$\frac{\partial \rho u_i}{\partial t} + \frac{\partial \rho u_i u_j}{\partial x_j} = -\frac{\partial}{\partial x_j} \left(P\delta_{ij} - \tau_{ij} \right), \text{ for } i = 1, 2, 3 \tag{3.3}$$

  with $P\delta_{ij}$ the pressure flux tensor and τ_{ij} the viscous momentum flux tensor. δ_{ij} is the Kronecker symbol equals to 1 if $i = j$ and 0 otherwise.

- Energy conservation

$$\frac{\partial \rho E}{\partial t} + \frac{\partial}{\partial x_j} \left(\rho E u_j \right) = -\frac{\partial}{\partial x_j} \left(u_i \left(P\delta_{ij} - \tau_{ij} \right) + q_j \right) + \dot{\omega}_T \tag{3.4}$$

  with E the total energy, q_j the energy flux, and $\dot{\omega}_T$ the energy source term.

The equation of state for perfect gases is used to close this set of equations:

$$P = \rho r T \tag{3.5}$$

with $r = \mathcal{R}/W$. $\mathcal{R} = 8.314\, J.mol^{-1}.K^{-1}$ is the universal gas constant, and W is the mean molecular weight:

$$\frac{1}{W} = \sum_{k=1}^{n_{spec}} \frac{Y_k}{W_k} \tag{3.6}$$

with W_k the molecular weight of the kth species.

3.1.2 Flux description

3.1.2.1 Species diffusion flux

The species diffusion flux is found using the Hirschfelder Curtis approximation:

$$J_{jk} = -\rho \left(D_k \frac{W_k}{W} \frac{\partial X_k}{\partial x_j} - Y_k V_j^c \right). \tag{3.7}$$

D_k is the diffusivity of the kth species and $X_k = Y_k W / W_k$ is the mole fraction of the kth species. The velocity V_j^c ensures mass conservation:

$$V_j^c = \sum_{k=1}^{N} D_k \frac{W_k}{W} \frac{\partial X_k}{\partial x_j}. \tag{3.8}$$

3.1.2.2 Viscous momentum flux

The viscous momentum flux tensor writes:

$$\tau_{ij} = 2\mu \left(S_{ij} - \frac{1}{3}\delta_{ij} S_{ll} \right) \tag{3.9}$$

with μ the molecular viscosity and S_{ij} the strain rate tensor:

$$S_{ij} = \frac{1}{2} \left(\frac{\partial u_i}{\partial x_j} + \frac{\partial u_j}{\partial x_i} \right) \tag{3.10}$$

3.1.2.3 Energy flux

The energy flux is made of two parts. A term for heat diffusion and a second term for species diffusion:

$$q_j = -\lambda \frac{\partial T}{\partial x_j} + \sum_{k=1}^{N} J_{jk} h_{s,k}. \tag{3.11}$$

λ is the heat conduction coefficient and $h_{s,k} = \int_{T_0}^{T} C_{p,k} dT$ is the sensible enthalpy of the kth species and $C_{p,k}$ the constant pressure mass heat capacity of the kth species.

3.1.3 Transport modeling

In the flux expressions given above, three transport coefficients need to be determined: D_k, μ and λ. In kinetics solvers, D_k is calculated as a function of the binary coefficients D_{ij} obtained from kinetic theory (Hirschfelder et al. [18]). The strategy in this work is to simplify this estimation by assuming a constant Schmidt number $S_{c,k}$ for each species so that:

$$D_k = \frac{\mu}{\rho S_{c,k}}. \tag{3.12}$$

Similarly, λ is computed assuming a constant Prandtl number Pr of the mixture:

$$\lambda = \frac{\mu C_p}{Pr} \tag{3.13}$$

with $C_p = \sum_{k=1}^{n_{spec}} C_{p,k} Y_k$ the heat capacity of the mixture. The Schmidt number comparing the viscous and species diffusion rates, and the Prandtl number comparing the viscous and thermal diffusion rates, are related by:

$$Le_k = \frac{Sc_k}{Pr} \tag{3.14}$$

with Le_k the Lewis number that compares thermal and species diffusion rates.

Finally, the dynamic viscosity μ is obtained using a simple power law:

$$\mu = \mu_0 \left(\frac{T}{T_0} \right)^b \tag{3.15}$$

with b a parameter to calibrate. This simple modelling is used throughout this work. For some parts of this work, a more complex strategy is used, in which case it is explicitly

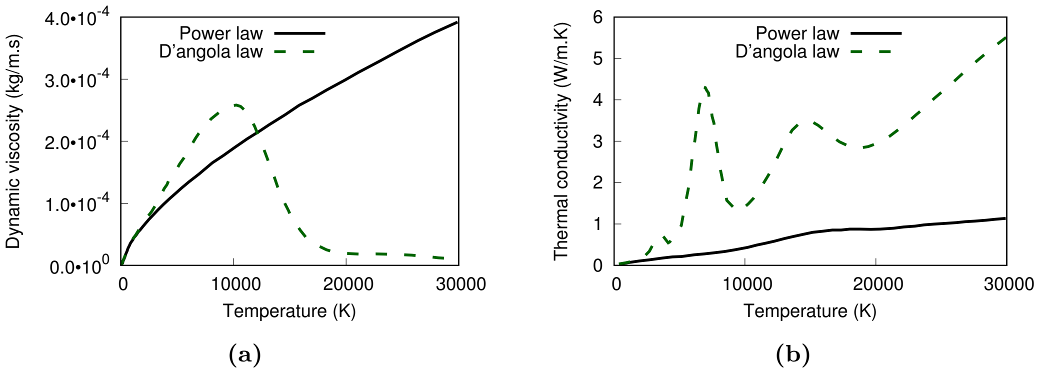

(a) **(b)**

Figure 3.1: Profiles of (a) dynamic viscosity μ and (b) thermal conductivity λ as functions of temperature for both classical power law and d'Angola law [19] for an air mixture.

mentioned. When temperatures higher than $3\,000\,K$ are reached which typically occurs during the first stage of a spark ignition, μ and λ are calculated using the d'Angola law. As shown in Fig. 3.1, differences are visible only over $3\,000\,K$ and can be very important above this temperature, justifying the use of this law, which takes into account species dissociation to obtain a more accurate estimation of transport properties. The mixture transport coefficients are considered independent of the composition and are assumed close to the ones of pure air.

3.1.4 Chemical kinetics

The final terms to be explored in the N-S equations are the energy source term $\dot{\omega}_T$ and specie source terms $\dot{\omega}_k$. They are directly related by:

$$\dot{\omega}_T = -\sum_{k=1}^{N} \Delta h^0_{f,k} \dot{\omega}_k \tag{3.16}$$

with $\Delta h^0_{f,k}$ the formation enthalpy of the kth species at reference temperature T_0. The expression of $\dot{\omega}_k$ is given for different chemistry descriptions: very accurate detailed chemistry, simplified Globally Reduced Chemistry (GRC) and finally Analytically Reduced Chemistry (ARC) which is a good compromise between accuracy and cost of the description. ARC is used throughout this work except for Chap. 12, where a GRC is used in order to allow comparison with other relevant studies. The main features of these three chemistry descriptions are given below.

3.1.4.1 Detailed Chemistry

Detailed schemes are useful to perform very accurate simulations focusing on the chemical processes of combustion. Hundreds of species are considered for heavy hydrocarbon fuels and thousands of elementary reactions are involved. The computational cost of a detailed chemistry is however prohibitive for most numerical studies except in simplified configurations. It comes from three sources:

- A large number of species implies a large number of equations to be solved and a large number of reaction source terms to compute.
- Among the species considered in typical detailed scheme, highly reacting radical species involved in the fuel oxidation have very short life times and require a very short time step ($\Delta t < 1\, ns$).
- These radicals are also associated to very short length scales so that a very short space discretization ($\Delta x < 10\, \mu m$) has also to be used.

Detailed chemistries are however very useful to understand chemical processes in canonical cases (0D reactors, 1D flames, or very simple 2D/3D cases) and to validate simplified chemistries. The calculation of $\dot{\omega}_k$ for detailed chemistry is given considering M reactions involving N species:

$$\sum_{k=1}^{N} \nu'_{kj}\mathcal{M}_k \Longleftrightarrow \sum_{k=1}^{N} \nu''_{kj}\mathcal{M}_k \quad \text{for } j = 1, M. \tag{3.17}$$

Here, $\mathcal{M}_k$ is the kth species, and ν'_{kj}, ν''_{kj} are the molar stoichiometric coefficients of $\mathcal{M}_k$ in the jth reaction. The coefficient $\nu_{kj} = \nu''_{kj} - \nu'_{kj}$ will be used further. With these notations, the species source term $\dot{\omega}_k$ is the sum of the species source terms $\dot{\omega}_{k,j}$ for the M reactions:

$$\dot{\omega}_k = \sum_{j=1}^{M} \dot{\omega}_{k,j} = W_k \sum_{j=1}^{M} \nu_{kj}\mathcal{Q}_j \tag{3.18}$$

The progress rate $\mathcal{Q}_j$ of reaction j is introduced and given by:

$$\mathcal{Q}_j = K_{fj} \prod_{k=1}^{N} \left(\frac{\rho Y_k}{W_k}\right)^{\nu'_{kj}} - K_{rj} \prod_{k=1}^{N} \left(\frac{\rho Y_k}{W_k}\right)^{\nu''_{kj}} \tag{3.19}$$

with K_{fj} and K_{rj} respectively the forward and reverse reaction rates of the j_{th} reaction. K_{fj} is defined using the standard Arrhenius law:

$$K_{fj} = \mathcal{A}_j T^{\beta,j} \exp\left(-\frac{E_{aj}}{\mathcal{R}T}\right) \tag{3.20}$$

with $\mathcal{A}_j$, β, j and E_{aj} the pre-exponential factor, temperature exponant and activation energy associated to the jth reaction. Forward and reverse reaction rates are linked to each other thanks to an equilibrium constant defined by Kuo [20]:

$$K_{eq,j} = \left(\frac{P_0}{\mathcal{R}T}\right)^{\sum_{k=1}^{N}\nu_{kj}} \exp\left(\frac{\Delta S_j^0}{\mathcal{R}} - \frac{\Delta H_j^0}{\mathcal{R}T}\right). \tag{3.21}$$

P_0 is taken equal to $1\,bar$ and ΔS_j^0, ΔH_j^0 are respectively the entropy and enthalpy changes for the jth reaction:

$$\Delta S_j^0 = \sum_{k=1}^{N} \nu_{kj} W_k s_k(T) \tag{3.22}$$

$$\Delta H_j^0 = h(T) - h(0) = \sum_{k=1}^{N} \nu_{kj} W_k \left(h_{s,k} + \Delta h_{f,k}^0\right) \tag{3.23}$$

with s_k the entropy of the kth species.

3.1.4.2 Globally Reduced Chemistry

Globally Reduced Chemistries (GRCs) are made of few (1-4) artificial steps fitted to reproduce global properties of combustion such as laminar flame speed or adiabatic temperature. The major advantage of GRCs is the low cost of the method as only few species and reactions are considered. However, many important mechanisms may be badly reproduced (auto-ignition delays, response of the flame to stretch). This kind of chemistry description has been used intensively in the past for many fuels, from light fuels [21] to heavy aviation fuels such as Kerosene [22]. The methodology to build a GRC is to presume the form of the mechanism, for example using two reactions: one for the fuel oxidation and one for the CO-CO_2 equilibrium:

$$\mathrm{F + xO_2 \longrightarrow yCO + zH_2O} \tag{3.24}$$

$$\mathrm{CO + 0.5O_2 \longleftrightarrow CO_2}. \tag{3.25}$$

The constants of each reaction progress rate are fitted manually to match specified targets (laminar flame speed or adiabatic temperature) and to ensure that the scheme can be used in a large range of pressure-temperature-equivalence ratio conditions. A modified Arrhenius-like expression is built, for example for the fuel oxidation reaction:

$$\mathcal{Q}_1 = f_1(\phi) k_1 [F]^{n_1} \, [\mathrm{O_2}]^{n_2} \, T^{\beta_1} \exp\left(\frac{-E_{a,1}}{RT}\right) \tag{3.26}$$

with $f_1(\phi)$, k_1, n_1, n_2, β_1, $E_{a,1}$ adjustable parameters.

3.1.4.3 Analytically Reduced Chemistry

Contrary to GRCs that have no direct link with detailed chemistry, Analytically Reduced Chemistries (ARCs) are derived from detailed schemes. The objective is to keep only relevant species and reactions for the targeted application. It is possible to reduce drastically the cost of computation as only $15-40$ species and hundreds of reactions are kept. Depending on the required accuracy, the scheme can be more or less detailed. A scheme derived to study ignition in turbulent flows and able to describe NO_x

formation and flame extinction in atmospheric plus sub-atmospheric conditions will be much heavier than a simpler one dedicated to steady flame study at one operating point only. Different techniques of reduction are used to discard useless species and reactions such as the DRGEP method as in Pepiot-Desjardins et al. [23]. The obtained scheme is known as a *skeletal mechanism.* Most very stiff radicals of the detailed mechanism are removed, but a few are kept as they are important to ensure correct prediction of targets. A second operation is thus performed leading to an *analytically reduced chemistry.* Species with too small time scales are considered in the Quasi-Steady State Approximation (QSSA) [24]. Such QSS species are assumed to be always present in low concentration, with a net production rate that is low compared to its creation and destruction rates, and therefore set to 0. As a consequence, their concentration can be calculated analytically using other species concentrations and reaction rates, and there is no need to solve a transport equation for them. QSS species are selected using the Level of Importance (LOI) technique [25, 26].

3.2 Large Eddy Simulation equations

3.2.1 Concept of LES

Different strategies are possible to solve numerically the Navier-Stokes equations. Due to turbulence, the evolution of variables over time can be decomposed in a mean part plus a fluctuation $X(t) = \bar{X} + x'$ as sketched in Fig. 3.2. The first option is to resolve all the turbulent scales of the flow from the integral length scale l_t to the Kolmogorov scale l_κ. This is called **Direct Numerical Simulation** (DNS). This method is of course the most accurate but is still too expensive nowadays for aeronautical combustor applications. In such flows, the smallest scales that should be resolved are of the order of tens of microns and the volume of combustion chambers of around $10^{-6}\, m^3$. A discretization of approximately 10^{15} cells would be required which is out of reach with current computing resources. A maximum of $10^{11} - 10^{12}$ cells could be used with the most powerful computers in the world. Therefore, two methods have been introduced to reduce the cost of numerical simulations:

- In **Reynolds-Averaged Navier Stokes** (RANS) simulations, an averaging procedure is used over all scales of turbulence so that only the mean quantities of all conserved variables are solved. Fluctuations are then ignored in a first step as shown in Fig. 3.2. As the entire turbulent spectrum is modelled, the accuracy of RANS is limited, especially when considering very turbulent flows with strong flame-turbulence coupling as in aeronautical gas turbines.

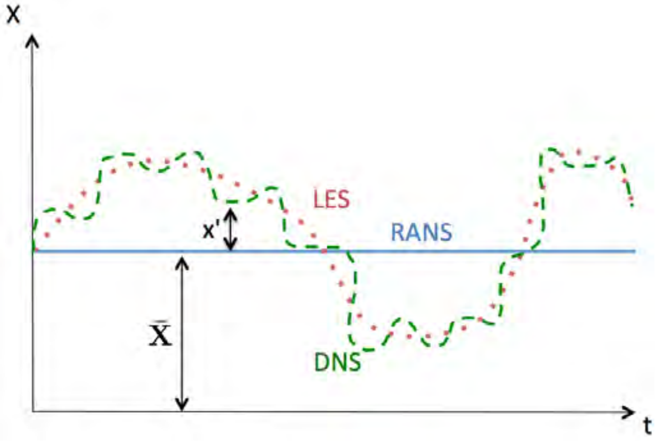

Figure 3.2: Evolution of variables over time and modelisation in RANS, LES, and DNS formulations.

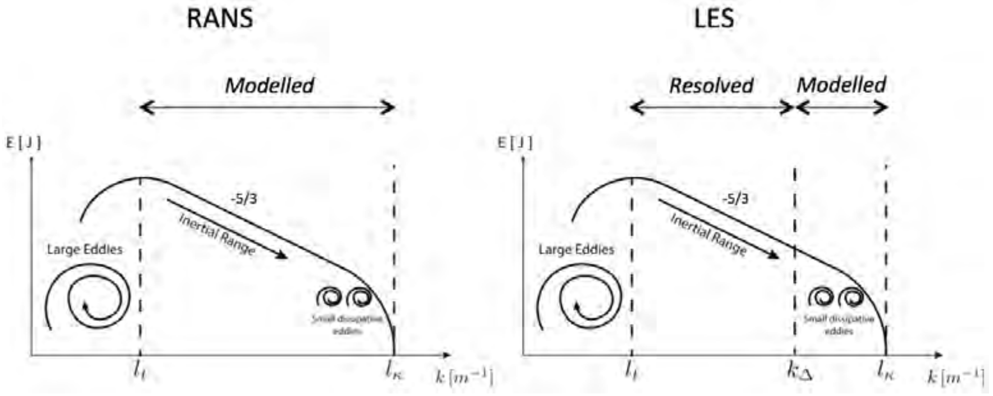
RANS
Modelled
LES
Resolved
Modelled
E [J]
-5/3
Inertial Range
Large Eddies
Small dissipative eddies
l_t
l_K
k_Δ
$k\,[m^{-1}]$

Figure 3.3: Resolved and modelled scales of turbulence in the RANS and LES contexts.

- In **Large Eddy Simulation** (LES), the largest turbulent structures are resolved and only the smallest ones are modelled as illustrated in Fig. 3.3. A cut-off length scale k_Δ separating resolved and modelled scales is used. In practice, the cut-off length scale is the cell size Δ_x of the grid. The quality of the LES is then directly linked to the resolution of the mesh. For very refine grids, DNS is recovered. LES is then a good compromise allowing to catch the mean information missing in RANS simulations for a reasonable cost. The filtering procedure of the N-S equations is presented in Sec. 3.2.2.

3.2.2 Filtered LES equations

For a given variable Ω, the filtering operation denoted $\bar{\cdot}$ reads:

$$\overline{\Omega}(\mathbf{x}) = \int \Omega(\mathbf{y}) F_\Delta(\mathbf{x}-\mathbf{y})\mathbf{dy} \tag{3.27}$$

with F_Δ the filter kernel and Δ the filter width. As variable density flows is considered, a Favre-filtering operation (weighted by the density) denoted $\widetilde{\cdot}$ is preferred. The resulting filtering operation on Ω reads:

$$\overline{\rho}\widetilde{\Omega}(\mathbf{x}) = \int \rho\Omega(\mathbf{y})F_\Delta(\mathbf{x}-\mathbf{y})\mathbf{dy} \tag{3.28}$$

Applied to the N-S equations, the filtering procedure gives:

- Filtered Mass conservation

$$\frac{\partial\overline{\rho}}{\partial t} + \frac{\partial}{\partial x_j}\left(\overline{\rho}\widetilde{u}_j\right) = 0. \tag{3.29}$$

- Filtered Species conservation

$$\frac{\partial\overline{\rho}\widetilde{Y}_k}{\partial t} + \frac{\partial\overline{\rho}\widetilde{Y}_k\widetilde{u}_j}{\partial x_j} = -\frac{\partial}{\partial x_j}\left(\overline{J}_{j,k} + \overline{J}^t_{j,k}\right) + \overline{\dot{\omega}}_k, \qquad \text{for } k = 1, n_{spec}. \tag{3.30}$$

- Filtered Momentum conservation

$$\frac{\partial\overline{\rho}\widetilde{u}_i}{\partial t} + \frac{\partial\overline{\rho}\widetilde{u}_j\widetilde{u}_i}{\partial x_j} = -\frac{\partial}{\partial x_j}\left(\overline{P}\delta_{ij} - \overline{\tau}_{ij} - \overline{\tau}^t_{ij}\right), \qquad \text{for } i = 1,2,3. \tag{3.31}$$

- Filtered Energy conservation

$$\frac{\partial\overline{\rho}\widetilde{E}}{\partial t} + \frac{\partial}{\partial x_j}\left(\overline{\rho}\widetilde{E}\widetilde{u}_j\right) = -\frac{\partial}{\partial x_j}\left(\overline{u_i\left(P\delta_{ij} - \tau_{ij}\right)} + \overline{q_j} + \overline{q_j}^t\right) + \overline{\dot{\omega}_T}. \tag{3.32}$$

3.2.3 Closure of filtered viscous terms

Expressions of the filtered viscous terms $\overline{J}_{j,k}$ $\overline{\tau}_{ij}$ and $\overline{q}_j$ are given here. High order cross terms are neglected to obtain these expressions.

- Diffusive species flux vector:

$$\overline{J}_{j,k} \simeq -\overline{\rho}\left(\overline{D}_k\frac{W_k}{\overline{W}}\frac{\partial\widetilde{X}_k}{\partial x_j} - \widetilde{Y}_k\widetilde{V}^c_j\right) \tag{3.33}$$

  with

$$\widetilde{V}^c_j = \sum_{k=1}^{n_{spec}}\overline{D}_k\frac{W_k}{\overline{W}}\frac{\partial\widetilde{X_k}}{\partial x_j} \text{ and } \overline{D}_k \simeq \frac{\overline{\mu}}{\overline{\rho}Sc_k}. \tag{3.34}$$

- Laminar filtered stress tensor:

$$\overline{\tau}_{ij} \simeq 2\overline{\mu}\left(\widetilde{S}_{ij} - \frac{1}{3}\delta_{ij}\widetilde{S}_{ll}\right) \tag{3.35}$$

  with

$$\widetilde{S}_{ij} = \frac{1}{2}\left(\frac{\partial\widetilde{u}_j}{\partial x_i} + \frac{\partial\widetilde{u}_i}{\partial x_j}\right) \text{ and } \overline{\mu} \simeq \mu(\widetilde{T}). \tag{3.36}$$

- Filtered heat flux vector

$$\overline{q}_j \simeq -\overline{\lambda}\frac{\partial\widetilde{T}}{\partial x_j} + \sum_{k=1}^{n_{spec}}\overline{J}_{jk}\widetilde{h_{sk}} \tag{3.37}$$

  with

$$\overline{\lambda} = \frac{\overline{\mu}\,\overline{C_p}(\widetilde{T})}{\mathrm{Pr}}. \tag{3.38}$$

3.2.4 Closure of subgrid fluxes

Expressions of the unresolved Sub Grid Scale (SGS) fluxes $\overline{J}^t_{j,k}$, $\overline{\tau}^t_{ij}$ and $\overline{q}^t_j$, are given here.

- The SGS Reynolds stress tensor is expressed as a diffusion contribution by introducing a turbulent viscosity μ_t. All unresolved small scales are then assumed to dissipate fluctuations while with a DNS formalism, only the Kolmogorov scales l_κ are dissipative. The form given to the SGS contribution is similar to the laminar one:
$$\overline{\tau}^t_{ij} = -\overline{\rho}\left(\widetilde{u_i u_j} - \tilde{u}_i \tilde{u}_j\right) = 2\mu_t\left(\widetilde{S}_{ij} - \frac{1}{3}\delta_{ij}\widetilde{S}_{ll}\right). \tag{3.39}$$
A lot of turbulent viscosity models to estimate μ_t are available in the literature such as the **Smagorinsky model** [27] that is efficient in homogeneous isotropic turbulence but was shown too be too dissipative for wall-bounded flows. This issue was corrected with the **WALE model** proposed by Ducros et al. [28]. Finally, Nicoud et al. again proposed an improvement for rotating flows with the **SIGMA model** [29]. As this work focuses on flows in aeronautical combustors which are confined and where swirling flows are generated, the **SIGMA model** is used throughout this work except if stated otherwise. The singular values $\sigma_1 \geq \sigma_2 \geq \sigma_3$ of the velocity gradient tensor $\partial u_i/\partial x_j$ are used:
$$\mu_t = \rho\left(C_\sigma \Delta\right)^2 \frac{\sigma_3\left(\sigma_1 - \sigma_2\right)\left(\sigma_2 - \sigma_3\right)}{\sigma_1^2} \tag{3.40}$$
with $C_\sigma = 1.35$ and Δ the characteristic filter width based on the mesh cell size.

- The SGS species fluxes vector is also represented as a diffusive contribution with an associated turbulent species diffusivity D^t_k written similarly to the laminar species diffusivity:
$$\overline{J}^t_{j,k} = \overline{\rho}\left(\widetilde{u_j Y_k} - \widetilde{u_j}\widetilde{Y_k}\right) = -\overline{\rho}\left(D^t_k \frac{W_k}{\overline{W}}\frac{\partial \widetilde{X}_k}{\partial x_j} - \widetilde{Y}_k \widetilde{V}_j^{c,t}\right) \tag{3.41}$$
with
$$D^t_k = \frac{\mu_t}{\rho Sc^t_k} \text{ and } \tilde{V}^{c,t}_j = \sum_k D^t_k \frac{W_k}{\overline{W}}\frac{\partial \widetilde{X_k}}{\partial x_j}. \tag{3.42}$$
A turbulent Schmidt number Sc^t_k is introduced linking the species turbulent diffusivities to the turbulent viscosity μ_t. In practice, $Sc^t_k = 0.60$ is used in this work. The turbulent correction velocity $\widetilde{V}_j^{c,t}$ is used to ensure mass conservation.

- Finally, the SGS energy flux vector is again represented as a diffusive contribution with an associated turbulent heat conduction coefficient λ_t linked to the turbulent viscosity μ_t with a turbulent Prandtl number $Pr^t = 0.60$ fixed in this work.

$$\overline{q}_j^t = -\overline{\rho}\left(\widetilde{u_j E} - \widetilde{u}_j \widetilde{E}\right) = -\lambda_t \frac{\partial \widetilde{T}}{\partial x_j} + \sum_{k=1}^{N} \overline{J}_{j,k} \tilde{h}_{s,k} \tag{3.43}$$

with

$$\lambda_t = \frac{\mu_t \overline{C_p}}{Pr^t}. \tag{3.44}$$

3.2.5 Combustion modeling

The final unclosed terms to be detailed are the filtered chemical source terms $\overline{\dot{\omega}_k}$ and $\overline{\dot{\omega}_T}$. The flame front in typical applications is smaller than $1\,mm$, and requires to be sufficiently discretized. When considering ARCs, more than $10 - 20$ points could be needed to resolve all species profiles across the flame. This level of discretization in LES is hardly feasible so $\overline{\dot{\omega}_k}$ and $\overline{\dot{\omega}_T}$, named $\overline{\dot{\omega}}$ in the rest of this section, need to be modeled as function of resolved fields. Combustion models have thus been derived for either premixed and non-premixed combustion. A comprehensive review of models can be found in the book of Poinsot & Veynante [5].

- For premixed combustion, one option is to consider the reaction zone as infinitely thin. Models such as the **Bray-Moss-Libby model** [30] or the **G-equation model** [31] use this assumption. The second option is on the contrary to account for a flame thickness and potential stretching by turbulence. The **F-TACLES** [32] and **Thickened Flame** [33] models are among the most used approaches.

- For non-premixed combustion, the reaction rate is known to be essentially controlled by the mixing as chemistry is much faster than mixing. Then, a method named **Probability Density Function** (PDF) methods is to transport an additional equation (with the N-S equations) for the mixture fraction z. A presume PDF of the subgrid scale mixture fraction $P(z, x, t)$ is reconstructed with a β-function for instance and the filtered chemical source terms are estimated with

$$\overline{\dot{\omega}}(x, t) = \int_0^1 \dot{\omega}(z) P(z, x, t) dz \tag{3.45}$$

  with $\dot{\omega}(z)$ the resolved reaction rate obtained from an external flamelet library [34]. Finite rate chemistry can even be encompassed by extending the external flamelet library [35].

3.2.5.1 Thickened Flame model

The **Thickened Flame** (TF) [33] model was derived in the premixed framework. Still, it has been used in many partially-premixed configurations showing reasonably good results. It is then used in Part. IV of this work dealing with two-phase light-round LES simulations. The TF model is explained here for gaseous flows and its extension for spray flames is detailed in Sec. 4.3.3. The main idea of the TF model is to artificially thicken the flame front in order to be able to resolve it with the LES grid considered. The flame thickness δ_l is the only parameter that should be changed. In particular, the flame speed s_l should remain unaffected by the flame thickening. Equations 2.7 and 2.8 can be rewritten

$$\delta_l \propto \sqrt{\frac{D_{th}}{\dot{\omega}}} \tag{3.46}$$

$$s_l^0 \propto \sqrt{D_{th}\dot{\omega}}. \tag{3.47}$$

showing that applying the transformation $D \to \mathcal{F}D$ and $\dot{\omega} \to \dot{\omega}/\mathcal{F}$ to diffusivities and source terms in the LES equations, the obtained flame is thickened by the value $\mathcal{F}$ while keeping the same laminar speed. $\mathcal{F}$ is then an adjustable parameter to obtain exactly the desired number of grid points in the thickness of the flame. A limitation of the TF model arises for turbulent flames: it was shown in Sec. 2.2.2 that the wrinkling of the flame induced by turbulence increases the flame surface leading to a turbulent flame speed greater than the laminar one. The stretching of the flame by turbulent structures is directly controlled by the relative size of vortices compared to the flame thickness. As sketched in Fig. 3.4, a thickened flame is much less wrinkled than a thin one as only the largest turbulent structures are able to deform it. The flame surface deficit induced by the artificial thickening operation should thus be accounted for. This is done in practice using an efficiency function $\mathcal{E}$: $D \to \mathcal{F}\mathcal{E}D$ and $\dot{\omega} \to \mathcal{E}\dot{\omega}/\mathcal{F}$. This way, the flame thickness is still

$$\delta_l \to \mathcal{F}\delta_l \tag{3.48}$$

but the flame speed of the thickened flame is multiplied by $\mathcal{E}$:

$$S_l \to \mathcal{E}S_l. \tag{3.49}$$

$\mathcal{E}$ is simply the ratio between the wrinkling of the non-thickened flame and the thickened one:

$$\mathcal{E} = \frac{\Xi\left(\delta_l\right)}{\Xi\left(\mathcal{F}\delta_l\right)}. \tag{3.50}$$

The wrinkling factor Ξ, which is function of the flame thickness, is estimated assuming that there is no creation or destruction of flame surface at the subgrid scale level (an

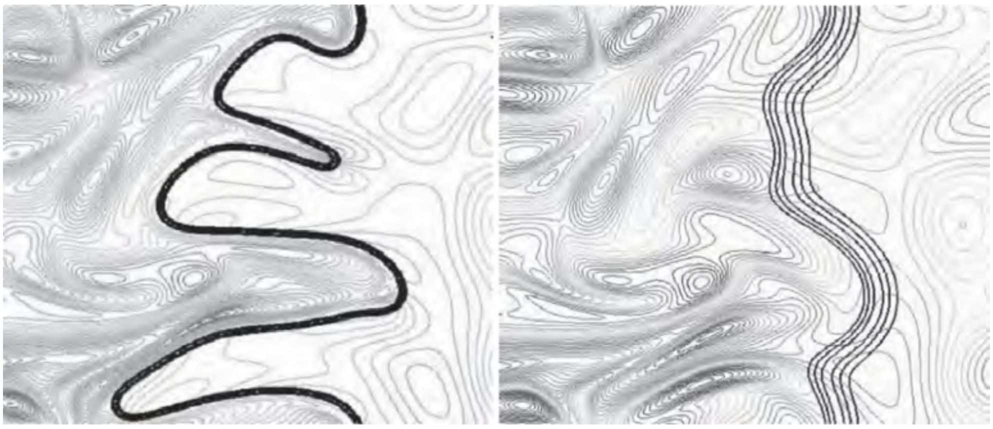

Figure 3.4: Flame-turbulence interaction for a thin and artificially thickened flame, studied by DNS [33].

equilibrium is reached) and calculating a characteristic turbulent velocity u'_Δ, at the filter scale Δ, given by Colin et al. [33]. In practice, the filter scale is taken as $\Delta = \mathcal{F}\delta_l$.

Numerous formulations have been proposed in the literature for Ξ and interested readers are referred to [36]. One of the most used is the one of Colin et al. [33]:

$$\Xi\left(\delta_l\right) = 1 + \alpha\left(Re_t\right)\Gamma\left(\frac{\Delta}{\delta_l}, \frac{u'_\Delta}{S_l}\right)\frac{u'_\Delta}{S_l} \tag{3.51}$$

with α a parameter depending on the turbulent Reynolds number and Γ a function that mimics the unresolved strain rate that is function of the subgrid velocity fluctuations and the filter size. The second standard Ξ formulation was proposed by Charlette et al. [37]:

$$\Xi\left(\delta_l\right) = \left(1 + \min\left[\frac{\Delta}{\delta_l}, \Gamma\left(\frac{\Delta}{\delta_l}, \frac{u'_\Delta}{S_l}, Re_{\Delta_e}\right)\frac{u'_\Delta}{S_l}\right]\right)^\beta \tag{3.52}$$

with β the exponent parameter. In the static version of the Charlette model, $\beta = 0.5$ is imposed. A Charlette Dynamic version [38, 39] was also proposed, recognizing that in most application, u'_Δ/S_l is large. In such case,

$$\Xi_\Delta = \left(\frac{\Delta}{\delta_L^0}\right)^\beta \tag{3.53}$$

is found. The wrinkling therefore depends almost solely on the β factor. Instead of fixing its value, β is here estimated dynamically in space and time using the resolved progress variable field. The additional computational cost is only $5 - 10\,\%$ and allows to be much more insensitive to numerical inputs compared to the statistical approach.

3.2.5.2 Dynamic Thickened Flame model

When applying the modifications $D \rightarrow \mathcal{F}\mathcal{E}D$ and $\dot{\omega} \rightarrow \mathcal{E}\dot{\omega}/\mathcal{F}$ in the LES equations, mixing properties in non-premixed regime are modified in the entire domain including the non-reacting fresh gases and burnt gases. Fluctuations of mixture fraction are dumped as the diffusivity is increased. The avoid this issue, a dynamic (not to be confused with the Charlette dynamic model) thickening procedure is used to modify diffusivities and source terms only in the flame region. This **Dynamic Thickened Flame model** (DTFLES) [40] needs a sensor $\mathcal{S}$ to detect the flame front. The local thickening factor is then:

$$\mathcal{F} = 1 + (\mathcal{F}_{\max} - 1)\,\mathcal{S} \tag{3.54}$$

with $\mathcal{F}_{max} = N_c \Delta_x / \delta_l$ a local estimation of the thickening factor required to obtain the desired number of grid points N_c in the flame front. N_c is generally close to 5 for GRCs, or $5 - 10$ for ARCs in order to thicken radical species profiles. The sensor definition depends on the type of chemistry description used. Expressions for GRCs and ARCs are presented here as they will be used in this work.

Sensor for GRCs For GRCs, the sensor $\mathcal{S}$ is based on one of the global reaction steps. For example, choosing the fuel consumption reaction, a local reaction rate:

$$\Omega = Y_F^{n_F} Y_O^{n_O} \exp\left(-\Gamma \frac{E_a}{RT}\right) \tag{3.55}$$

is calculated and compared to a reference value Ω_0 pre-determined with a 1D flame calculation. The sensor is written:

$$\mathcal{S} = \tanh\left(\beta' \frac{\Omega}{\Omega_0}\right) \tag{3.56}$$

with $\beta' \approx 50$.

Sensor for ARCs The sensor based on a reaction rate is not adapted for ARCs as it is difficult to know which reaction is the most appropriate among all reactions in the ARC scheme. In the flame profile, reactions rates are not superposed. Some reactions occur in the pre-flame region while others are in the post-flame region. Thickening the flame front based on one reaction rate would lead to an unsatisfactory behaviour. An alternative procedure to tackle this issue is to thicken the flame front based on the fuel source term $|\dot{\omega}_F|$ as proposed by Jaravel [41]. Again a comparison between local values and maximum value $|\dot{\omega}_F|_{1D}^{\max}$ found in a 1D flame in representative conditions is used. The sensor writes:

$$\mathcal{S} = \max\left[\min\left(2\frac{\mathcal{F}_{\max}\,|\dot{\omega}_F|}{|\dot{\omega}_F|_{1D}^{\max}} - 1, 1\right), 0\right]. \tag{3.57}$$

Based on the fuel source term, this sensor however does not cover the entire flame region but only the very sharp zone of strong temperature gradient. The pre-flame and post-flame region are not well captured. In order to obtain a wider thickened region, a filtering procedure is applied on the sensor by using a passive scalar that is transported. A source term for the passive scalar is added in the region where $\mathcal{S} > 0.8$ and its diffusion is calibrated to capture the desired zone around the flame.

3.2.6 Numerics

Throughout this work, all canonical cases including 0D reactors and 1D flames are simulated using the open-source software Cantera [42] dedicated to chemical kinetics, thermodynamics, and transport processes. For the reduction of ARCs that are used in this work, the YARC reduction tool developed by Pepiot-Desjardins [43] is used. For all Large Eddy Simulations, the LES parallel code AVBP [44] co-developed by CERFACS and IFPEN is used on the national HPC resources of CINES (Occigen computer), IDRIS (Turing computeur), CEA-TTGC (Curie and Irene computers) and local CERFACS computers. AVBP solves the fully compressible multispecies Navier Stokes equations on unstructured hybrid grids. The main numerics features of AVBP are presented by Lamarque [45]. Boudary conditions are based on the NSCBC formalism [46]. The numerical scheme for diffusive fluxes is a 2nd order scheme in space while two schemes are used in this work for the space and time discretization of the convective fluxes: the explicit Lax-Wendroff scheme [47] (2nd order in time and space) and the explicit Taylor-Galerkin TTGC scheme [48] (3rd order in space and time). An artificial viscosity operator is used to ensure the stability of the explicit numerical schemes used. Finally, the description of the liquid phase and its coupling with the gaseous phase is detailed in Chap. 4.

Chapter 4

Equations and models for the liquid phase

Contents

4.1 Euler-Lagrange modeling **55**
4.2 System of equations **56**
  4.2.1 Assumptions 56
  4.2.2 Equations 56
4.3 Exchange terms **57**
  4.3.1 Drag force 57
  4.3.2 Evaporation 58
  4.3.3 Correction of drag and evaporation for the TF model 61
4.4 Coupling with the gaseous phase **62**
4.5 Droplet injection **63**

4.1 Euler-Lagrange modeling

In order to account for the spray in the LES equations, two main methodologies are available:

- In the Eulerian (EE) formalism, the liquid phase is considered as a continuous phase, that is resolved on the same grid than the gaseous phase.
- In the Lagrangian (EL) formalism, the spray is viewed as a discrete phase, composed of an ensemble of droplets that are tracked individually.

The main advantage of the EE formalism is to be very scalable in a parallel solver as the liquid and gaseous phases are solved on the same grid. This method has therefore been used in many applications including aeronautical configurations. However, an important limitation of EE simulation is its mono-dispersed character. At each grid point and at each time, only a mean droplet diameter is known. The poly-dispersion of the spray can be recovered using sectional methods that involve to solve multiple liquid phases and implies an important numerical cost. In order to take into account the poly-dispersion of the spray that must be considered in the ignition phase of aeronautical engines, the Lagrangian formalism implemented in the AVBP code [17, 49, 50, 51, 52, 53, 54] is retained in this work.

This chapter starts by describing in Sec. 4.2 the set of equations solved for the dispersed phase. Exchange terms between phases are presented in Sec. 4.3, along with the coupling with the gaseous phase in Sec. 4.4. Finally, the injection model used in this work is explained in Sec. 4.5.

4.2 System of equations

4.2.1 Assumptions

In the EL formalism, different levels of coupling between the gaseous and liquid phases depend on the dispersed phase density.

- For very dilute sprays ($\alpha_l < 1e^{-6}$), the liquid phase is not dense enough to have any impact on the gas phase. However, the droplets dynamics are influenced by the gas. This is called a **one-way coupling**.
- For moderately dense sprays, ($1e^{-6} < \alpha_l < 1e^{-3}$), the liquid phase acts on the gas dynamics by a retro-coupling force (fuel evaporation and drag force for instance). Thus, it is called a **two-way coupling.**
- Finally, for very dense sprays, ($\alpha_l > 1e^{-3}$), droplets are so close from each other that they interact. This level of coupling is named **four-way coupling**.

The strategy retained here is the two-way coupling that is relevant in typical aeronautical applications, where the fuel is injected by spray atomizer creating a mist of small droplets. The primary and secondary breakup phenomena are skipped. Collisions between droplets are neglected as the spray is sufficiently diluted. Particles just do not see the other particles. The evolution of the spray is then described by resolving the evolution of each single droplet individually. Droplets are seen as simple material points that are tracked, with their inherent properties (temperature, size, etc). Considering the small size of droplets, they are also considered as spherical due the high surface tension forces.

4.2.2 Equations

With the assumptions previously given, the radius (equivalent to volume, considering the spherical assumption), temperature and position of droplets are transported thanks to this set of equations:

$$\frac{\mathcal{D}X_{p,i}}{\mathcal{D}t} = u_{p,i}, \text{ for } i = 1,2,3 \tag{4.1}$$

$$\frac{\mathcal{D}m_p u_{p,i}}{\mathcal{D}t} = F^{ext}_{p,i}, \text{ for } i = 1,2,3 \tag{4.2}$$

$$\frac{\mathcal{D}m_p}{\mathcal{D}t} = \dot{m}_p \tag{4.3}$$

$$\frac{\mathcal{D}m_p h_{s,p}}{\mathcal{D}t} = \dot{\Phi}_p \tag{4.4}$$

with X_p, u_p, m_p, $h_{s,p}$ respectively the position, velocity, mass, and sensible enthalpy of particle p, and F^{ext}_p, $\dot{m}_p$, and $\dot{\Phi}_p$ respectively the forces acting on the particle, and variation of mass and sensible enthalpy of the droplet. These three last terms are explicitly derived in Sec. 4.3.

4.3 Exchange terms

4.3.1 Drag force

Single droplet dynamics have been studied widely and are then well documented now. Various forces can be take into account in F^{ext}_p in Eq. 4.2. Buoyancy and gravity forces combine and write:

$$\vec{F}_{G+arch} = \rho_l V_p \vec{g} \left(1 - \frac{\rho_g}{\rho_l}\right) \tag{4.5}$$

with ρ_l and ρ_g the liquid and gaseous densities, V_p the volume of the particle, and $\vec{g}$ the gravity. Considering the ratio of densities between air and fuels, the buoyancy force can be neglected. The unsteady virtual mass effect and Basset force, created by a change of the relative velocity between the droplet and the gas are also easily neglected [55] considering the density ratio in our application. Finally, the most important force is the drag force $\vec{F}_D$ applied on a droplet having a velocity $\vec{u}_p$ in a gaseous environment at velocity $\vec{u}_g$. The very general formulation of this force is:

$$\vec{F}_D = \frac{1}{2}\rho_g \mathcal{C}_D A \left\|\vec{u}_g - \vec{u}_p\right\| \left(\vec{u}_g - \vec{u}_p\right) \tag{4.6}$$

with $A = \Pi d_p^2/4$ the projected area of the spherical droplet and $\mathcal{C}_D$ the drag coefficient. This drag coefficient is very dependent on the relative velocity between the droplet and the gas as shown in Fig. 4.1 showing the evolution of $\mathcal{C}_D$ as function of the Reynolds number based on the particle defined as:

$$\Re e_p = \frac{\rho_g d_p \left\|\vec{u}_g - \vec{u}_p\right\|}{\mu_g} \tag{4.7}$$

with d_p the diameter of the particle and μ_g the gaseous dynamic viscosity. In typical aeronautical applications, Re_p stays under 500. Correlations have been derived in the

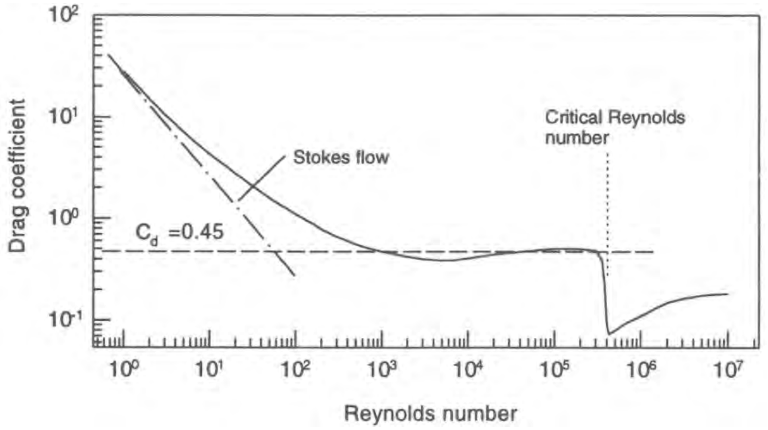

Figure 4.1: Drag coefficient $\mathcal{C}_D$ as function of the particle Reynolds number Re_p. Extracted from Crowe et al [55].

literature starting from Stokes in 1851. In 1927, Oseen [56] proposed:

$$\mathcal{C}_D = \frac{24}{\mathcal{R}e_p}\left(1 + \frac{3}{16}\mathcal{R}e_p\right) \tag{4.8}$$

but this law is valid only for $Re_p < 5$. In 1935, Schiller & Naumann [57] extended this law to $Re_p < 800$ with their empirical drag correlation:

$$\mathcal{C}_D\left(\mathcal{R}e_p\right) = \frac{24}{\mathcal{R}e_p} f\left(\mathcal{R}e_p\right) \tag{4.9}$$

$$f\left(\Re e_p\right) = \left(1 + 0,15\mathcal{R}e_p^{0,687}\right). \tag{4.10}$$

This law is one of the most used in aeronautical applications as it showed its good behaviour in the past. Equation 4.2 finally writes:

$$\frac{\mathcal{D}u_{p,i}}{\mathcal{D}t} = \frac{1}{\tau_p}\left(u_{g,i} - u_{p,i}\right) + g_i. \tag{4.11}$$

In this form, a characteristic droplet time τ_p is evidenced:

$$\tau_p = \frac{\rho_l d_p^2}{18\mu_g f\left(\mathcal{R}e_p\right)}. \tag{4.12}$$

τ_p can be compared to a characteristic gaseous time τ_g via the Stokes number $S_t = \tau_p/\tau_g$. For low S_t numbers, the droplet behaves like a tracer, which means that the velocity if the droplet follows the gaseous one. On the contrary, for high S_t number, the particle is not affected by the gaseous dynamics and its trajectory is dictated by its inertia.

4.3.2 Evaporation

4.3.2.1 Spalding model

Evaporation is responsible for the exchange terms $\dot{m}_p$ and $\dot{\Phi}_p$. The analytical Spalding model [58] for isolated spherical droplet evaporation is recalled here as it is the basis

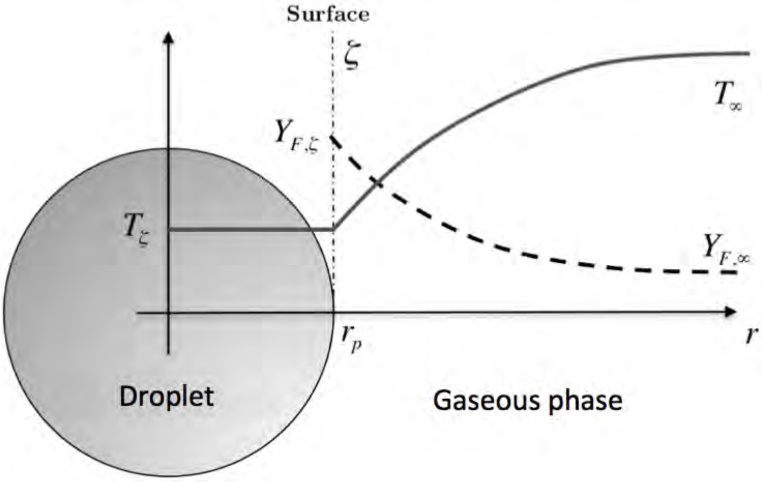

Figure 4.2: Radial profile of temperature T and fuel mass fraction Y_F around a droplet.

of the evaporation model that is used in this work. Some hypotheses are required: the temperature inside the droplet is considered homogeneous (the thermal conductivity is infinite), and the gas and the droplet are considered at rest, so that the gas has a quasi-static evolution. These hypothesis allow to solve the mass and thermal evolution of the droplet in its spherical reference frame and to only consider radial variations as illustrated in Fig. 4.2. Momentum, species and energy conservation is written between the surface of the droplet, denoted ζ, and the infinite ∞:

$$\rho_g u_g r^2 = \text{ constant } = \frac{\dot{m}_F}{4\pi} \tag{4.13}$$

$$\rho_g u_g r^2 \frac{dY_F}{dr} = \frac{d}{dr}\left(r^2 \left[\rho_g D_F\right] \frac{dY_F}{dr}\right) \tag{4.14}$$

$$\rho_g u_g r^2 \frac{dC_P T}{dr} = \frac{d}{dr}\left(r^2 \frac{\lambda}{C_P} \frac{dC_P T}{dr}\right). \tag{4.15}$$

In the above conservation laws, r is the radial coordinate, $\dot{m}_F$ is the gaseous fuel flux at the surface, Y_F the fuel mass fraction, D_F the fuel diffusivity, C_p the heat capacity of the mixture, T the gas temperature, and λ the thermal diffusivity. Note that $[\rho_g D_F]$ and λ/C_P are evaluated at infinite (for $Y_{F,\infty}$ and T_∞) and are supposed constant along the radial profile. Latter, this point was improved by Miller et al. [59] that proposed to evaluate these values between the droplet surface and the infinite with a $1/3-2/3$ law. The reference temperature T_R and fuel mass fraction $Y_{F,R}$ at which transport and thermodynamic properties are evaluated write:

$$T_R = T_\zeta + \frac{1}{3}\left(T_\infty - T_\zeta\right) \tag{4.16}$$

$$Y_{F,R} = Y_{F,\zeta} + \frac{1}{3}\left(Y_{F,\infty} - Y_{F,\zeta}\right). \tag{4.17}$$

$[\rho_g D_F]$ and λ/C_P are finally obtained introducing a Schmidt number Sc_F and a Prandtl number Pr:

$$\rho_g D_F = \frac{\mu(T_R)}{Sc_F} \tag{4.18}$$

$$\frac{\lambda}{C_P} = \frac{\mu(T_R)}{Pr}. \tag{4.19}$$

The Schmidt and Prandtl numbers for the gaseous phase transport can be used or a specific evaluation of these numbers is proposed by Sierra et al. [52] to take into account complex transport effects. A better calculation of the viscosity of the mixture following Wilkes equation [60] is also used in this case.

4.3.2.2 Droplet mass and temperature evolution

The integration of Eq. 4.14 between the infinite and the droplet surface leads to the expression of the evaporation rate of Eq. 4.3:

$$\dot{m}_p = -2\pi d_p \left[\rho \mathcal{D}_F\right] \ln\left(B_M + 1\right) \tag{4.20}$$

with B_M the mass Spalding transfer number:

$$B_M = \frac{Y_{F,\zeta} - Y_{F,\infty}}{1 - Y_{F,\zeta}}. \tag{4.21}$$

$Y_{F,\zeta}$ is obtained by considering the Clausius-Clapeyron equation considering that the droplet interface is in thermodynamic equilibrium. The evolution of the droplet diameter is easily recovered:

$$d_p^2 = d_{p,0}^2 - \frac{8\rho_g \mathcal{D}_F}{\rho_l} \ln\left(B_M + 1\right) \times t \tag{4.22}$$

with $d_{p,0}$ the initial droplet diameter. The classic d^2 evaporation law is found when the droplet temperature T_p is constant. A characteristic evaporation time τ_{ev} can also be highlighted thanks to Eq. 4.22:

$$\tau_{ev} = \frac{\rho_l d_{p,0}^2}{8\rho_g D_F \ln\left(B_M + 1\right)}. \tag{4.23}$$

The evolution of the droplet temperature is found recalling its energy conservation equation (Eq. 4.4):

$$\frac{\mathcal{D} m_p h_{s,p}}{\mathcal{D}t} = \dot{\Phi}_p. \tag{4.24}$$

By combining this thermal balance at the droplet interface where no energy is stored with the integration of Eq. 4.15, the evolution of T_p is found:

$$\frac{dC_{p,l}T_p}{dt} = \frac{1}{m_p}\left(\dot{m}_p L_v\left(T_p\right) - 4\pi r_p \frac{\lambda}{C_P}\left(C_P\left(T_p\right)T_p - C_P\left(T_\infty\right)T_\infty\right)\frac{\ln\left(B_T + 1\right)}{B_T}\right). \tag{4.25}$$

In the above expression, $L_v\left(T_p\right)=h_{s,g}\left(T_p\right)-h_{s,l}\left(T_p\right)$ is the latent heat of evaporation, r_p is the droplet radius, and $B_T=\left(1+B_M\right)^{\frac{1}{\mathcal{L}e_F}}-1$ is the temperature Spalding transfer number. The simultaneous integration of Eq. 4.20 and 4.25 allows to track the temporal evolution of the droplet using the Spalding evaporation model.

4.3.2.3 Abramzon & Sirignano correction

One of the hypotheses of the Spalding evaporation model is that the droplet and the gas are at rest. However, in practical applications, an important relative velocity between the gas and the droplet can be found, leading to Reynolds number based on the particle up to $Re_p \approx 500$. This flow enhances the evaporation process and must be included to better model the mass and thermal transfers between phases. Ranz & Marshall [61] introduced a Sherwood number and a Nusselt number as:

$$Sh = 2 + 0.55\mathcal{R}e_p^{1/2}\left(Sc_F\right)^{1/3} \tag{4.26}$$

$$Nu = 2 + 0.55\mathcal{R}e_p^{1/2}Pr^{1/3} \tag{4.27}$$

to take into account the local Re_p value. Eq. 4.20 and 4.25 are modified as follows:

$$\dot{m}_p = -Sh\pi d_p\left[\rho\mathcal{D}_F\right]\ln\left(B_M+1\right) \tag{4.28}$$

$$\frac{dC_{p,l}T_p}{dt} = \frac{1}{m_p}\left(\dot{m}_p L_v\left(T_p\right) - 2Nu\pi r_p\frac{\lambda}{C_P}\left(C_P\left(T_p\right)T_p - C_P\left(T_\infty\right)T_\infty\right)\frac{\ln\left(B_T+1\right)}{B_T}\right). \tag{4.29}$$

Finally, Abramzon & Sirignano [62] again modified the Sh and Nu numbers to take into account a boundary layer around the droplet allowing to estimate more accurately mass and thermal fluxes:

$$Sh^* = 2 + \left(Sh-2\right)/F_M \tag{4.30}$$

$$Nu^* = 2 + \left(Nu-2\right)/F_T \tag{4.31}$$

with

$$F_M = \left(1+B_M\right)^{0,7}\frac{\ln(1+B_M)}{B_M} \tag{4.32}$$

$$F_T = \left(1+B_T\right)^{0,7}\frac{\ln(1+B_T)}{B_T}. \tag{4.33}$$

4.3.3 Correction of drag and evaporation for the TF model

When using the Thickened flame model presented in Sec. 3.2.5.1, the interaction of droplets with the flame front is artificially modified. Corrections introduced by Boileau [63] and Paulhiac [17] must be used to recover the correct behaviour. As the flame is F

times thicker, droplets must evaporate F times slower than in reality and must be subjected to a drag force F times lower than the real drag force. The correction is done by again modifying the equations governing the droplet mass and temperature evolution:

$$\dot{m}_p = -Sh\pi d_p \left[\rho \mathcal{D}_F\right] \ln\left(B_M + 1\right) \frac{1}{\mathcal{F}} \tag{4.34}$$

$$\frac{dC_{p,l}T_p}{dt} = \frac{1}{m_p}\left(\dot{m}_p L_v\left(T_p\right) - 2Nu\pi r_p \frac{\lambda}{C_P}\left(C_P\left(T_p\right)T_p - C_P\left(T_\infty\right)T_\infty\right)\frac{\ln\left(B_T+1\right)}{B_T}\frac{1}{\mathcal{F}}\right) \tag{4.35}$$

as well as the drag force:

$$\frac{\mathcal{D}u_{p,i}}{\mathcal{D}t} = \frac{1}{\mathcal{F}\tau_p}\left(u_{g,i} - u_{p,i}\right) + g_i. \tag{4.36}$$

4.4 Coupling with the gaseous phase

The coupling between the liquid and gaseous phases is simply done by transferring conservatively F_p^{ext}, $\dot{m}_p$, and $\dot{\Phi}_p$ for all droplets to the gaseous phase thanks to source terms in the gaseous conservation equations.

- Source term for mass conservation **and** fuel species conservation:

$$S_m^{l\to g} = \frac{1}{\Delta V}\sum_{p=1}^{N} \Psi_p \dot{m}_p. \tag{4.37}$$

- Source term for momentum:

$$S_{qdm,i}^{l\to g} = \frac{1}{\Delta V}\sum_{p=1}^{N} \Psi_p\left(-m_p F_{p,i}^{ext} + \dot{m}_p u_{p,i}\right). \tag{4.38}$$

- Source term for energy:

$$S_E^{l\to g} = \frac{1}{\Delta V}\sum_{p=1}^{N} \Psi_p\left(-m_p \vec{F}_p^{ext}\cdot\vec{u}_p + \frac{1}{2}\dot{m}_p\left\|\vec{u}_p\right\|^2 - \dot{\Phi}_p\right). \tag{4.39}$$

ΔV is the control volume of the grid node considered and N is the total number of droplets in this control volume. Ψ_p is the interpolation function used. In this work, an inverse distance interpolation, illustrated in Fig. 4.3 is used.

$$\Psi_{p,j} = \frac{1/d_j}{\sum_{k=1}^{N_v} 1/d_k} \tag{4.40}$$

$\Psi_{p,j}$ is the particle weight associated to the vertex j of the element containing the droplet. d_j is the distance between the particle and the vertex j, and N_v is the number of vertices of the element. Note that when gaseous properties at the particle position are required, the same inverse distance interpolation is used.

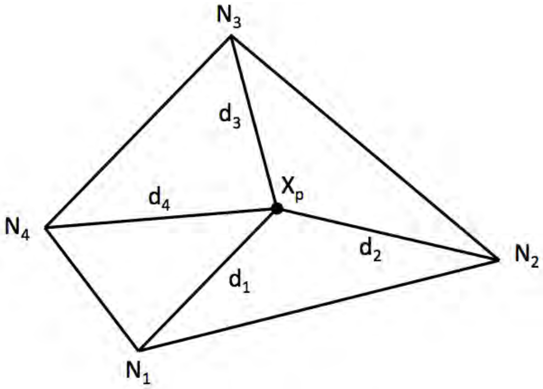

Figure 4.3: Particle source term projection on the nodes of the gaseous grid.

4.5 Droplet injection

In order to accurately simulate pressurized liquid injectors that are often used in aeronautical combustors, primary and secondary breakup phenomena should be taken into account. However, these steps are not resolved with the Euler-Lagrange formalism used here. Sanjosé et al. [64] proposed a method imposing velocity and grain size profiles at the injector outlet without resolving atomisation. This FIM-UR (Fuel Injection Model by Upstream Reconstruction) model needs the liquid flow and injector geometry properties as inputs. θ_s is the mean half angle made by particles after their injection. R_a and R_0 are respectively the inner and outer radius of the liquid injection ring. Indeed, due to the swirling motion, an air core is form in the center of the injector, and the liquid is pushed against the outer surface. A ratio variable is defined:

$$X = \frac{R_a^2}{R_0^2} = \frac{sin^2\theta_s}{1 + cos^2\theta_s} \tag{4.41}$$

In the Lagrangian formalism, only the injector parameters R_a, R_0, the liquid mass flow rate $\dot{m}_l$ and the spray characteristic θ_S are needed to determine the velocity imposed at the injection outlet ($x = x_0$). For one particle injected randomly in the injection ring :

$$u^0_{l,x}(\theta, r_0) = \frac{\dot{m}_l}{\rho_l \pi R_0^2 (1 - X)} \tag{4.42}$$

$$u^0_{l,r}(\theta, r_0) = 0 \tag{4.43}$$

$$u^0_{l,\theta}(\theta, r_0) = \tan(\theta) u^0_{l,x}(\theta, r_0) \tag{4.44}$$

where θ is the half angle made by the particle considered. The axial component is derived thanks to conservation laws. The radial component is null initially while the tangential one is set to respect the mean half angle of the injector imposed by the user to mimic the injection half angle of the target configuration. Finally, the grain size distribution must also be arbitrary given by the user.

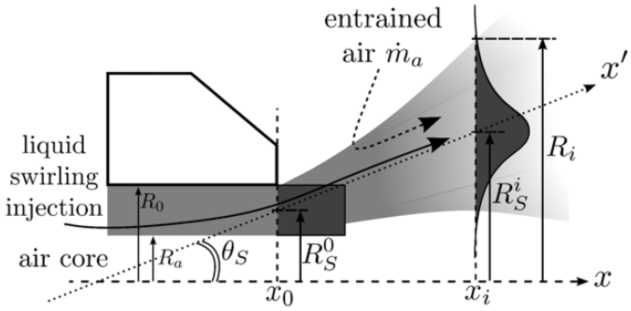
entrained
air $\dot{m}_a$
x'
liquid
swirling
injection
R_0
R_i
R_S^i
air core
R_a
θ_S
R_S^0
x
x_0
x_i

Figure 4.4: Scheme of the FIM-UR injection.

Part II

From the spark to the flame kernel

Chapter 5

Literature review

Contents

5.1 General phenomenology 68

5.1.1 Spark ignition 68

5.1.2 Laser ignition 70

5.1.3 Energy losses 71

5.2 Concept of Minimum Ignition Energy 72

5.3 Ignition of mists of fuel droplets 75

5.4 Inclusion of detailed chemistry and plasma phase 79

5.5 Numerical models 82

5.5.1 Low-order models 83

5.5.2 Energy Deposition model 85

5.6 Conclusions 87

As introduced in Chap. 1, the full relight sequence of an aeronautical combustor can be decomposed as follows:

- Kernel generation by an external source of energy.
- Kernel growth and propagation towards the nearest fuel injector.
- Azimuthal flame propagation until flame stabilisation above all fuel injectors of the annular combustor.

This chapter aims at presenting the state of the art regarding the first phase of external source ignition and understanding which are the topics that still require research work. Note that if auto-ignition has been extensively studied [65, 66, 67, 68], in particular for Internal Combustion engine applications, it is not reviewed in this work.

Different kinds of devices can be used to ignite a flammable mixture: torch igniters [69], plasma jet igniters [70] or flammable chemical products [69]. However, their use in aeronautical combustor is proscribed because of their size, durability, or potential threat to the turbine. Laser can also be used as an igniter device. It is particularly useful because it is not intrusive and allows a full optical access to the developing flame. Morevover, the ignition position can be changed very easily. Thus, it has been widely used in many lab-scale experiments. However, since optical access to the chamber is by definition necessary, its application in real combustors is also prevented. Finally, the

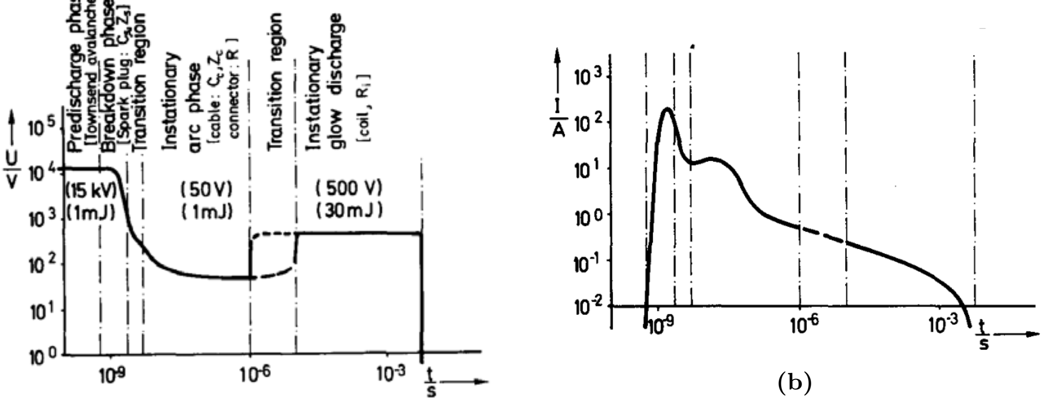

(b)

(a)

Figure 5.1: Diagram of (a) voltage and (b) current during ignition, differenciating well the three steps of ignition [72].

last classic device for combustion initiation is the spark plug. It is actually the technology that equips aeronautical gas turbines. For this reason, spark plug ignition has also been extensively studied since the beginning of the aeronautical industry development.

The phenomenology of spark plug and laser ignition is actually similar. Both are presented in Sec. 5.1. A large part of studies dealing with flame kernel generation focused on the concept of Minimum Ignition Energy [71] (MIE) which is the minimum energy an external source should deliver to the mixture to initiate a sustainable flame kernel. These studies aimed at understanding the main dependencies of MIE to flow and/or igniter device parameters. Derivations of analytical models and first numerical simulations of the early development of the flame front and the shock wave generated were proposed. The important conclusions of these studies are summarized in Sec. 5.2. Then a particular focus is made here on two topics. The first one is the inclusion of accurate thermodynamics, transport and chemistry in the numerical simulations of this phase, during which very high temperatures can be reached. This point is reviewed in Sec. 5.4. The second topic is the ignition of droplet mists, detailed in Sec. 5.3. Finally, models that can be used to mimic flame kernel generation in 3D numerical simulations focusing on phase 2 of ignition are presented in Sec. 5.5.

5.1 General phenomenology

5.1.1 Spark ignition

Spark ignition can be mainly split in three steps [72, 73, 74, 75]: the pre-breakdown and breakdown phase ($t \propto 10^{-9}\, s$), the arc phase ($t \propto 10^{-6}\, s$), and the glow phase ($t \propto 10^{-3}\, s$).

In the pre-breakdown phase, because of the very high voltage applied between electrodes (up to $10\,kV$ as shown in Fig. 5.1), free electrons move rapidly from the cathode towards the anode. On their way, some of them may collide with gas molecules releasing other electrons and negative ions that are attracted as well by the anode. This electronic avalanche forms small cylindrical streamers from the cathode to the anode. At this point, the electronic avalanche is not massive yet, and a cold plasma is formed. A plasma is a ionized mixture, containing charged ions and free electrons that have been removed from atoms. Free electrons have a very high temperature due to their activity. Other species can be at thermal equilibrium with electrons (meaning at high temperature too), in which case it is named a hot or equilibrium plasma. However, at the beginning of the electronic avalanche, only electrons are very reacting, and other species stay at low temperature ($1000\,K$). This cold (or non-equilibrium) plasma state is typically conserved in Nanosecond Repetitively Pulsed (NRP) Discharges as discharges are short and not as intense as conventional sparks.

The breakdown phase occurs at the time a continuous streamer joins the cathode and the anode so that the gap is bridged (after around $1\,ns$). The gap impedance drops, the voltage diminishes and the current is dramatically boosted for $20 - 60\,ns$ up to $200\,A$. The streamer joining the cathode and the anode can be assimilated to a cylinder of diameter around $10 - 100\,\mu m$. These very small dimensions and time scales illustrate the need for numerical models: in a LES, it is still out of reach today to resolve spatially and numerically this kernel generation. The strong collisions and the ionization cascade lead to the warming of the plasma up to $60\,000\,K$ (hot equilibrium plasma). At such temperatures, the gas can be considered as fully dissociated and ionized. The gas dilatation due to the temperature increase induces a strong blast wave expanding in all directions with an initial pressure up to $100\,bars$. At early times, the kernel front displacement is controlled by the shock expansion.

After the breakdown, the electric power level is reduced by 2-3 orders of magnitude. This is the arc phase. During this period, the ionized gas cools down progressively towards the adiabatic flame temperature. Ionized species thus recombinate into uncharged species. The effect of the blast wave on the flame kernel front evolution vanishes since the blast wave is much faster and detaches from the kernel. At this time, the control parameter of the front evolution is the competition between heat release by combustion and thermal diffusion. The transition time between the initial blast wave controlled phase and the diffusion controlled kernel propagation is $t \propto 10^{-5}\,s$ [76], corresponding to the arc phase.

Finally, the end of the spark is the glow phase. The power level is again reduced but as this period is much longer ($t \propto 10^{-3}\,s$), this phase is the one providing most of the external energy to the gas. Releases of hot gases forming a torus are typically

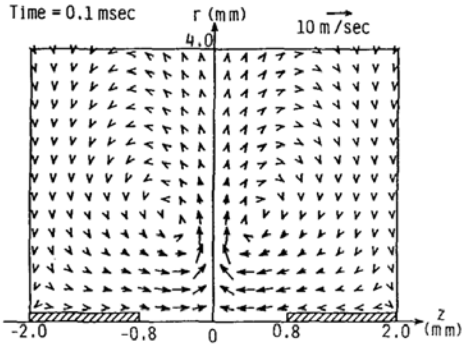

(a) Velocity field

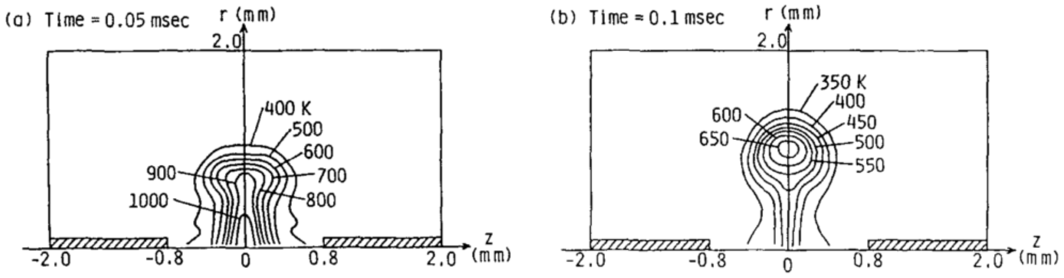

(b)

(c)

Figure 5.2: (a) Velocity field and (b)-(c) kernel position and shape following a spark ignition at two different times [77].

observed [77] as shown in Fig. 5.2c. This displacement of hot gases is linked to the blast wave produced during the breakdown expanding from the spark gap. Outward expansion of gases leads to a pressure deficit at the spark gap inducing an inwards gaseous flow along electrodes, as illustrated in Fig. 5.2a. After this torus release, the kernel growth is mainly spherical and the flame front velocity reaches its steady state. Transition from laminar to turbulent regime may happen later if sparking in turbulent conditions.

5.1.2 Laser ignition

The phenomenology of laser ignition is simpler than that of spark ignition. It can be mainly assimilated to a breakdown phase of around $10\,ns$ during which an electronic cascade leads to a totally ionized plasma at the focusing point of the laser. This zone is actually an elipsoid elongated in the focusing direction. Similarly to spark ignition, the temperature reaches very high values, up to $100\,000\,K$, and a strong shock is formed, with initial pressures up to $100\,bars$ [78, 79]. While the shock expands quickly, the temperature of the hot gas kernel reduces progressively. The ionized plasma recombinates to form a flame at classic adiabatic temperature. The dynamic of ignition is characterised by the third lobe formation [80, 81] as illustrated in Fig. 5.3. Two vortices are created just after energy deposition. However, the laser absorption is non-

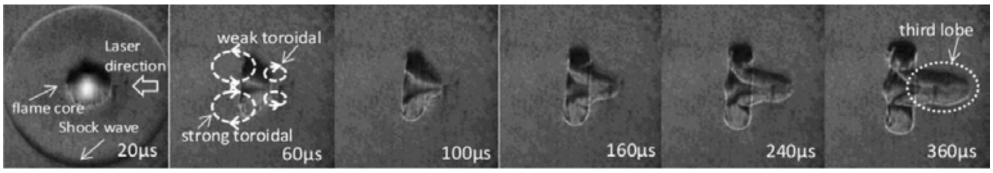

Figure 5.3: Third lobe formation following a laser ignition of methane-air mixture [81].

uniform in the gas so vortices are unbalanced, and a third lob is generated. This third lob makes the surface of the kernel bigger increasing thermal diffusion and potential thermal quenching. However reactivity is also enhanced by the increase of the flame surface area increase.

5.1.3 Energy losses

Energy losses during either spark or laser ignition are very important to analyse. A large amount of the electric/photonic energy released can be lost or, even if transmitted, useless for combustion initiation. During a spark ignition, the breakdown phase provides to the gas roughly 3 % of the total energy because, even if very powerful, this phase is extremely short. The arc phase also gives about 3 % of the energy and the glow phase is the most energetic one, with about 94 % of the total energy. Of course for laser ignition, all the energy is given in only one phase: the breakdown. The first source of energy losses is the efficiency of the energy transmission to the gas. The energy transmitted to the gas in a spark ignition is variable and represents about 60 % of the primary electric energy available [82] due to losses in the electric circuit. For a laser ignition, the transmission efficiency is also very variable, depending on the laser characteristics and also the gas properties (temperature, composition, equivalence ratio). Reported values range from 10 % – 50 % [83] to 92.5 % [79]. Once transmitted to the gas, a large part of this remaining energy can be lost during spark ignition, mainly by conduction to the electrodes but also at a limited level by radiation. The breakdown phase is actually very efficient [72, 80, 84, 85], above 95 % efficiencies, because it is very short. The arc phase is less efficient (50 %) and the glow phase is even worse (30 %) as it is the longest phase. In this phase, losses by conduction at electrodes are dominant. All the remaining energy is given to the gas but not all of it is actually useful for combustion initiation. First, 50 % – 80 % of the remaining energy is transmitted to the gas by the shock wave that propagates away from the kernel in a few microseconds [78, 86, 87, 88, 89]. This energy is thus considered useless for ignition as it does not contribute to the flame kernel expansion. Finally, an important part of the deposited energy contributes to the ionisation of the gases, which is an endorthermic

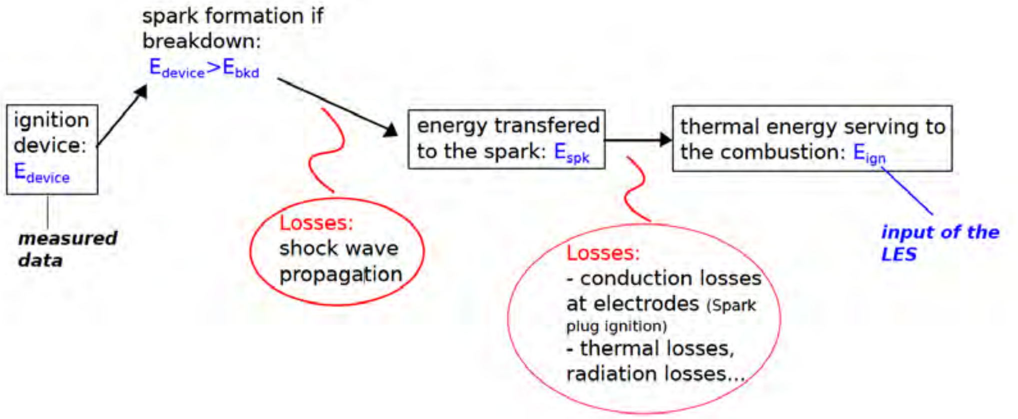
spark formation if breakdown: E_device>E_bkd
ignition device: E_device
measured data
Losses: shock wave propagation
energy transfered to the spark: E_spk
Losses: - conduction losses at electrodes (Spark plug ignition) - thermal losses, radiation losses...
thermal energy serving to the combustion: E_ign
input of the LES

Figure 5.4: Illustration of energy transfers occuring from electric input energy to thermal energy available to ignite gases [91].

process. The stored chemical energy is of course released when the temperature decreases leading to the recombination of ionized species and radicals. However, if this recombination occurs when the flame already left, the energy used to dissociate gases can be considered as useless for ignition. Ultimately, the energy given to the gas and useful for ignition E_{ign} is very low for both spark and laser ignition techniques and very difficult to estimate as schemed in Fig. 5.4 for spark ignition. Overall energy efficiencies of around $7\,\% - 15\,\%$ are reported for laser ignition [78, 79, 90] and of $10\,\% - 30\,\%$ for spark ignition [72, 89].

Quantifying energy losses is very important to adjust the power of the ignition device. In practical applications (internal combustion engines or gas turbine relight), good ignition performances are mandatory. Losses must correctly be estimated to be sure to provide enough energy to ignite. For research applications, a precise estimation of losses is also required to better understand the phenomenology of this phase. If energy losses are very fluctuating, the energy required to ignite a flammable gas is also not well known: this is the topic of many researches discussed in Sec. 5.2.

5.2 Concept of Minimum Ignition Energy

Here is a list of some parameters influencing the spark/laser ignition process [92]. These parameters can be separated in three main groups:

- *Ignition source parameters* including its geometry (pin-pin gap and electrode size for spark plugs), duration, input energy, frequency if multiple sparks are considered (Nanosecond Repetitively Pulsed Discharges).

- *Gas-phase parameters* including mean velocity, turbulence intensity, temperature, pressure, fuel-air mixing.
- Possibly *Liquid-phase parameters* considered in Sec. 5.3 including fuel volatility and spray characteristics such as droplet density and size distribution.

The influence of all these parameters on ignition was often investigated by referring to the MIE. If the precise definition of MIE varies from one author to the other, the most common definition is this one: the MIE represents the transmitted energy to the fluid leading to 50% of successful ignition (and so 50% of misfiring). A theoretical formula for the MIE was proposed by Glassman et al. [93]:

$$MIE = \frac{4}{3\pi r_c^3}\rho_g C_{p,g}(T_a - T_0) \tag{5.1}$$

with ρ_g, $C_{p,g}$, T_a and T_0 the density, heat capacity of the mixture, adiabatic flame temperature and fresh gas temperature respectively. Finally, the last parameter r_c is the quenching distance, i.e. the critical radius the kernel should reach to become a sustainable flame. r_c corresponds to the kernel size for which heat release is balanced by heat losses. Under this critical size, thermal diffusion is too high and the kernel can't survive. This parameter has also been investigated by many groups [94, 95] that proposed theoretical formulations for gaseous mixtures and compared their results to experiments. r_c is found to be of the order of magnitude of the laminar flame thickness δ_l^0. The development of 1D-2D analytical models able to predict the MIE or r_c, and track the flame kernel front and blast wave for spark/laser ignitions was extensively studied [73, 74, 96, 97, 98, 99, 100, 101]. Many conditions were investigated: quiescent and flowing mixtures, gaseous premixed, non-premixed and two-phase mixtures, atmospheric conditions or low temperature-pressure environments. These pioneer models helped to understand the main correlations linking ignition behaviour to mixture and igniter properties detailed in this section. These models were developed and validated thanks to numerous experimental studies such as [102, 103, 104] as well as studies used for the phenomenological description of Sec. 5.1.

The influence of the fresh gas temperature on MIE is found thanks to Eq. 5.1: increasing the fresh gas temperature facilitates ignition. The existence of an optimal value of spark duration that minimizes the MIE has been shown [99, 105] as illustrated in Fig. 5.5a. Indeed, for short duration sparks, a large part of the energy is lost due to the shock wave. On the contrary, for long sparks, a part of the energy released is wasted since it is added once ignition is complete. The optimal value of spark duration increases near stoichiometry which is logical as reactivity is enhanced. The pressure dependence is one important parameter when thinking about high altitude relight where pressures around 0.3 $bars$ are encountered. MIE is found to increase with

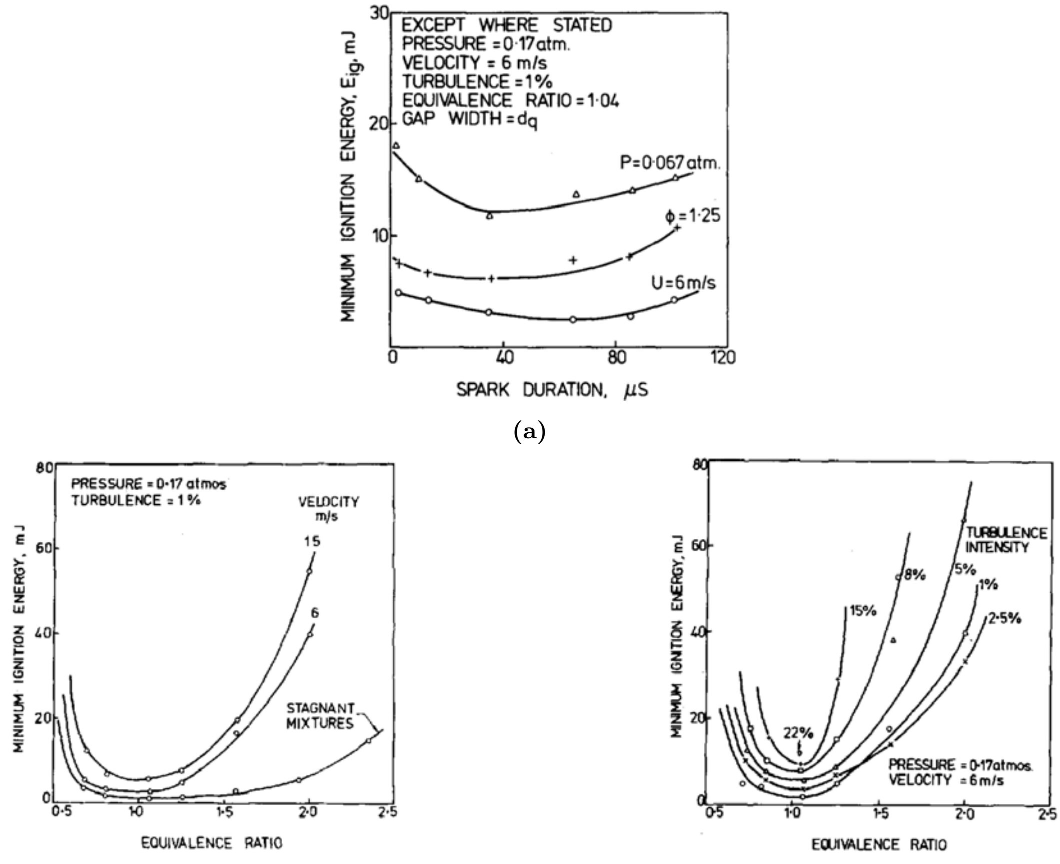

(a)

(b) (c)

Figure 5.5: Influence of (a) spark duration, (b) mainstream velocity and (c) turbulence intensity on the MIE [105].

decreasing pressure. A relation $MIE \propto P^{-2}$ was proposed by Ballal [105] for propane-air mixtures. This law directly comes from the inversely proportional dependence of the thermal diffusion to pressure. For spark ignition specificaly, an optimal spark gap width is also evidenced, and both r_c and MIE are shown to be higher with larger electrode diameters, as a higher diameter leads to more heat losses by conduction. The adverse effect of turbulence intensity on ignition is often reported, as it mainly promotes heat losses from the spark kernel to the surrounding mixture. This effect is smaller near stoichiometry as shown in Fig. 5.5c as ignition is eased by perfect mixing properties. Finally, advection of the kernel away from the energy release zone also promotes thermal diffusion as illustrated by Fig. 5.5b. However, in the case of spark ignition, the kernel is also moved away from electrodes where most of the energy is lost by conduction. Therefore it could be a key positive parameter in this case [106].

Maly [107] also investigated MIE dependancies by proposing an ignition model for quiescent and flowing mixtures. He concluded that an important factor to optimize ignition is to increase the energy deposition density in space and time, more than increasing the total amount of energy itself. This is confirmed by other works [72, 73]

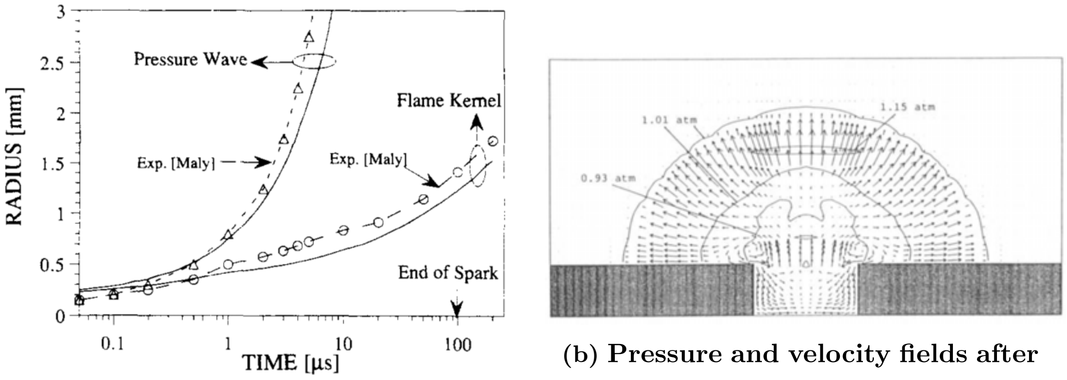

(a) Flame kernel and blast wave radius.

(b) Pressure and velocity fields after $4\,\mu s$.

Figure 5.6: Initiation of a spark kernel and its propagation in a quiescent stoichiometric methane-air mixture [100].

stating the importance of the temporal distribution of energy deposition on the ignition outcome. In particular, ignition success was shown to be linked to the amount of energy supplied during the breakdown phase. The blast wave expansion as well as the flame kernel propagation were also recovered by numerical simulations with good accuracy [100] as shown in Fig. 5.6. However these studies often made strong assumptions, using simplified energy deposition models and neglecting the plasma phase for instance. Studies particularly dedicated to a better description of the plasma chemistry activities are summarized in Sec. 5.4. In the next section, two-phase ignition studies are presented as they present an additional complexity representative of high altitude relight.

5.3 Ignition of mists of fuel droplets

Ignition of droplets can be of three forms: isolated droplet ignition, droplet cloud ignition, or dilute spray ignition. The ignition mode actually occurring depends on gaseous and two-phase flow parameters. The first ignition mode is characterised by a flame envelop around the droplet [17, 108] (or a wake flame, if the gaseous velocity is high enough), having a size of the order of the droplet. The third one corresponds to the apparition of a global flame around the spray [109], not bent near droplets. In this case, the flame kernel characteristic size is one or two orders of magnitude larger than the mean droplet diameter. The droplet cloud ignition mode is the intermediate situation between the two modes described above. Determining the dominant ignition mode [110] is of great importance because it influences in particular the spray flame structure, the pollutant emission characteristics, or the flame stability. For example, NOx emission levels are increased when isolated droplet combustion occurs. Besides,

MIE values for dilute spray ignition is much lower than for isolated droplet ignition. In practice, dilute spray ignition is the most encountered mode and is therefore focused in what follows.

When considering ignition in a mist of fuel droplets, conclusions for gaseous ignition of Sec. 5.2 are qualitatively unchanged but can be quantitatively significantly impacted. For instance, considering the influence of mixture pressure on MIE, it is found that when considering ignition in a two-phase flow, $MIE \propto P^{-0.5}$ instead of $MIE \propto P^{-2}$ [69]. In practice, most of the studies were dedicated to finding the influence of fuel volatility, droplet size or fuel inhomogeneities on MIE [111, 112, 113, 114, 115, 116, 117, 118, 119]. Most of them are summarized in the reviews of Aggarwal and Mastorakos [120, 121].

Keeping in mind the importance of relight capability in aircraft applications, Ballal and Lefebvre[111] investigated experimentally ignition in lean two-phase mixtures at sub-atmospheric conditions that can be encountered in gas turbine combustors for instance. In such conditions, the evaporation rate is very low leading to a decisive competition between chemistry and evaporation time scales. MIE is found to increase with an increase of spray Sauter Mean Diameter (SMD) as shown in Fig. 5.7b, confirming the benefits of a good atomization process in aircraft applications. Compared to gaseous ignition, as high velocity enhances evaporation and tends to reduce the spray SMD by promoting droplet collision, MIE sometimes decreases with an increase of velocity. An important fuel volatility also promotes easier ignition (Fig. 5.7a). Equation 5.1 was reworked to be used for two-phase ignition of quiescent flows and a theoretical formulation of the quenching distance, or critical kernel radius r_c was also proposed. Infinitely fast chemistry was considered to build this analytical model:

$$r_c = D[\frac{\rho_l}{\rho_g \; \phi_g \; \ln(1+B_{st})}]^{0.5} \tag{5.2}$$

$$MIE = [\frac{(\frac{1}{6}\pi)C_{p,g}(T_a - T_0)D^3}{\rho_g^{0.5}}][\frac{\rho_l}{\phi \ln(1+B_{st})}]^{1.5}. \tag{5.3}$$

with D the mean droplet diameter, ρ_l and ρ_g respectively the density of fuel and gas, B_{st} the mass transfer number and ϕ the total equivalence ratio. Note that here, no pre-evaporated fuel is considered, but only a liquid fuel so they don't degenerate towards purely gaseous expressions considering no liquid. These analytical expressions showed a good agreement with the experimental dependancies highlighted above. Ballal and Levebvre [112] continued their experimental and analytical analyses on ignition by extending it to turbulent heterogeneous flows. Authors exhibited that r_c and MIE tend to increase with increasing mean flow velocity and turbulent intensity. The influence of the mean droplet size D is even stronger in the turbulent case ($MIE \propto D^{4.5}$ instead

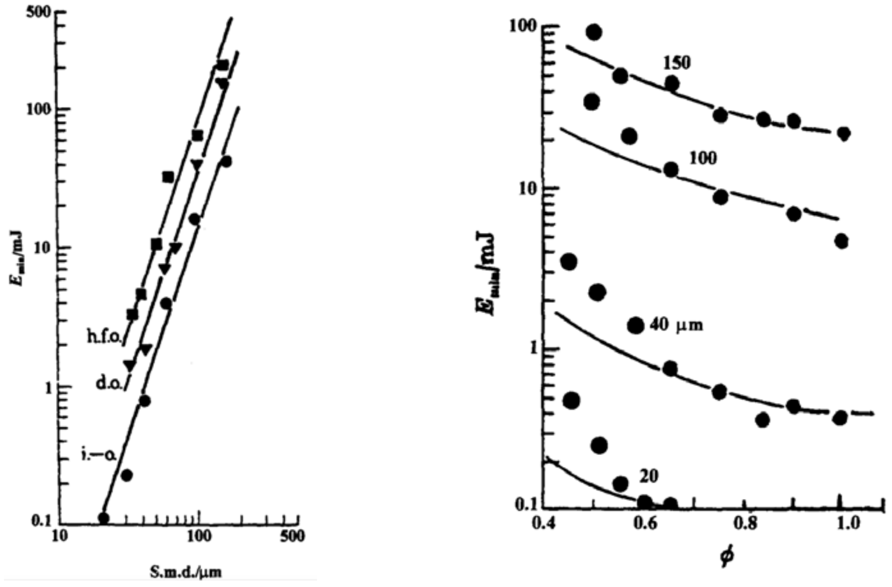

(a) (b)

Figure 5.7: (a) MIE versus SMD for iso-octane (i.-o.), diesel oil (d.o.), and heavy fuel oil (h.f.o.) at $\phi = 0.65$. (b) MIE versus ϕ for iso-octane (i.-o.)-air mixture and for different SMD [122].

of $MIE \propto D^3$ in the laminar case). Finally, Ballal and Lefebvre further improved their model by removing the infinitely fast chemistry assumption [113] and adding the possible presence of pre-evaporated gaseous fuel in the mixture. This new model was validated using experiments showing better agreement than with their previous model. In particular, the new model raised the importance of the pre-evaporation on ignition as well as the competition between evaporation and chemical times.

The phenomenological model of Ballal and Lefebvre didn't provide any details about the temporal evolution of ignition. The first detailed numerical analysis of the transient ignition phenomenon in two-phase flow was done by Aggarwal and Sirignano [114]. It was shown for exemple that MIE and ignition time delays can be reduced in spray cases compared to premixed cases, at certain equivalence ratios. This property was found because a large range of equivalence ratio up to rich mixtures was investigated, contrary to Ballal and Levebvre [112] who limited their study to very lean mixtures making impossible the detection of these optimum. Similarly, droplet diameter and overall (liquid+gas) equivalence ratio optimum were found to minimize the MIE. These key properties were determined for mono-dispersed and poly-dispersed sprays and for quiescent and flowing mixtures [115, 116, 117, 118]. A summary of these results can be found in Fig. 5.8.

Almost all experimental and numerical studies dedicated to two-phase ignition considered fuels such as heptane, decane or surrogates, and used to keep the same fuel for the entire study. Fuels used in aeronautical gas turbines are surrogates of several

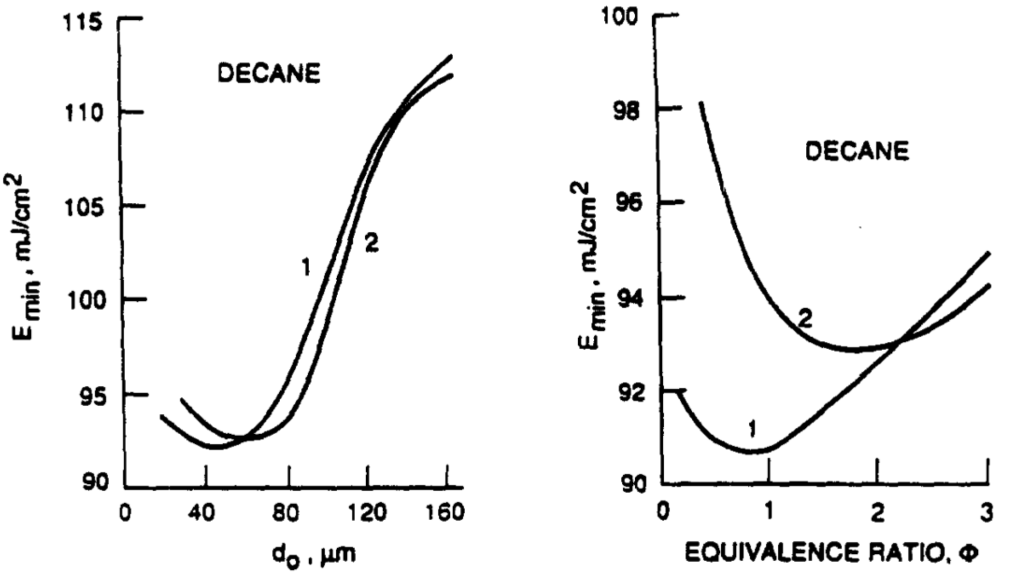

(a) $\phi = 1$ (curve 1) and $\phi = 2$ (curve 2).

(b) $d_0 = 40\,\mu s$ (curve 1) and $d_0 = 80\,\mu s$ (curve 2).

Figure 5.8: Dependence of the MIE to (a) N-decane droplet diamater and (b) total (gas+liquid) equivalence ratio [118].

pure fuels having different volatility properties. This multicomponent character has an important impact on ignition behaviour compared to single-component fuels. Aggarwal studied the ignition of a two-component fuel made of hexane (high volatility) and decane (low volatility) [123]. It was shown that the volatility of the surrogate is not linearly dependent on pure fuel volatilities. For example, adding only a small amount ($< 20\,\%$) of volatile fuel in a relatively non-volatile mixture strongly enhances its ignitability as presented in Fig. 5.9. This property is particularly true when considering large droplets. Indeed, two-phase ignition characteristic time is the sum of atomization, evaporation, fuel-air mixing and chemical times. For small droplets, ignition is controlled by mixing and chemistry only, and not by evaporation. Then, volatility properties of the mixture have almost no effect.

Thanks to new high quality diagnostics, the beneficial effect of the presence of droplets in the energy deposition zone was shown experimentally [124]. The effect of the blast wave on droplets was also tackled [88, 125], to understand if droplets could be ejected away from the sparking zone for instance, or quickly evaporated. Different scenarii were as shown and are reported in Fig. 5.10. At $5\,mm$ from the blast wave origin, droplets are rapidly deformed and show catastrophic breakup after $5\,\mu s$. The two large spherical droplets are disintegrated forming a homogeneous mist of very small droplets after tens of microseconds. This is of course a favourable mechanism for spray ignition in a lean mixture as secondary droplets evaporate much faster than the initial ones, thus providing more fuel vapour. It is also remarkable that no droplets enter

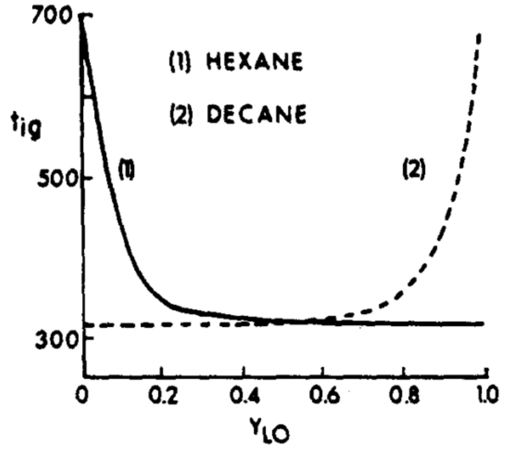

Figure 5.9: Normalized ignition delay time versus initial mass fraction of hexane and decane. Injection droplet diameter is $100\,\mu s$ [123].

the observation box from the top, certainly because the droplets evaporate over a very short distance ($< 5\,mm$ from the focal point), due to either the blast wave or the plasma. Further, $10\,mm$ under the sparking position, droplets are affected by the blast wave only after $12\,\mu s$. Droplets are first deformed, they exhibit oscillations of shape and position and eventually break into 2 or 3 small secondary droplets. Even further, $15-20\,mm$ under the sparking position, only shape deformation is sometimes observed but the droplets finally recover their initial spherical shape.

5.4 Inclusion of detailed chemistry and plasma phase

A major issue with many past numerical studies on laser/spark ignition is the overly simplified description of the chemistry and breakdown phase. This point is investigated here.

Sloane and Ronney [126] discussed why using too simplified kinetic schemes along with simplified thermodynamic and transport properties, as in several studies, makes impossible any correct evaluation of MIE. One-step schemes are well calibrated to fit steady unstretched flame properties but are not sufficient to recover unsteady kernel development properties. Sloane and Ronney studied CH_4-air ignition at ambient conditions first with a one-step global reaction and simplified thermodynamic and transport models and secondly with a detailed chemical scheme along with accurate transport and thermodynamic properties. Figure 5.11 presents the MIE as a function of the energy deposition radius with the detailed model (circles) and with the simplified model (line). The open circles indicate energies where ignition occurred, and the filled circles indicate energies where ignition did not occur. The only experimental MIE available is $0.4\,mJ$ for low radius, while the simplified model predicted $0.007\,mJ$ and the detailed

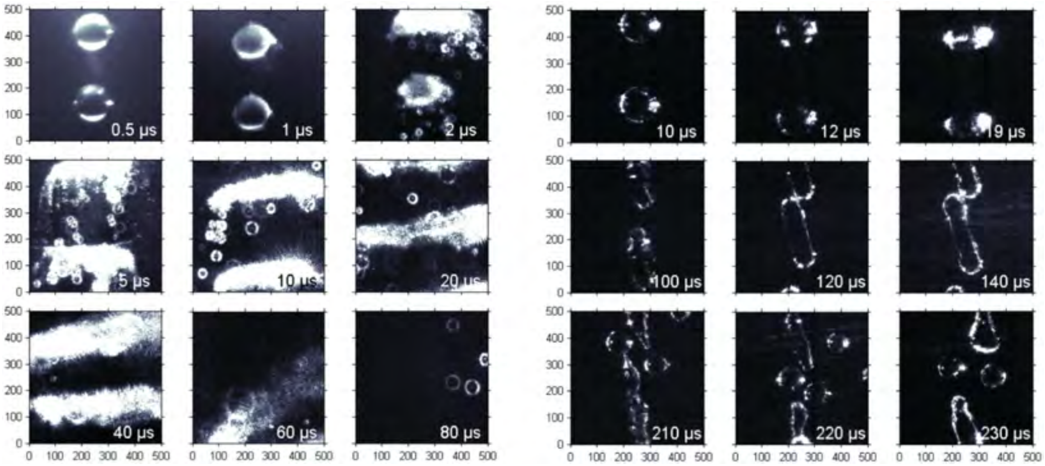

Figure 5.10: Mie scattering of Jet A-1 droplet breakup in boxes (Left) 5 mm and (Right) 10 mm below the breakdown focus. Dimensions are given in μm [125].

model gave $0.1\,mJ$. Using a detailed model therefore improved results by at least one order of magnitude for low energy deposition radius. Even at higher radius, results were improved by a factor of 2. By analysing temperature and chemical energy release profiles for the detailed and simplified kinetic schemes, the authors explained these differences by the endothermic reactions of radical formation preceding the exothermic reactions at the beginning of the the ignition process. These reactions are missing in the one-step chemistry which contains only one exothermic reaction instead of the long full chain-branching chemical process. Therefore, chemical run-away occurs too early. For the detailed model, the temperature rise is limited by these endothermic reactions which is not the case for the simplified model leading to too high temperatures. As there is no need to create the radical pool, less spark energy is needed to obtain a successful ignition with the simplified scheme, which explains smaller MIE values. In other words, for the same amount of deposited energy, ignition success can be predicted with the simplified scheme while failure is reported by the detailed one.

If including detailed chemistry in numerical simulation has progressively become a standard practice [91, 100, 127], avoiding an excessive simplification of the first nanoseconds of the energy discharge is still a challenge. The very small length and time scales of the breakdown phase that are difficult to resolve, as well as the lack of accurate models on what happens at very high temperatures, explain the choice of many studies to simplify as much as possible the modeling of this phase. Similarly to several works, Sloane [98] adapted his numerical set-up by increasing the breakdown phase duration from $10-40\,ns$ to $1\,\mu s$ and expanding the energy deposition in space so that the peak temperature does not exceed $3500-4000\,K$. This numerical artefact avoids having

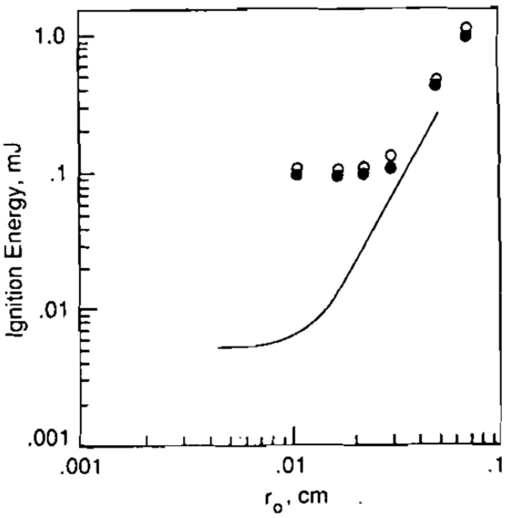

Figure 5.11: MIE as a function of the energy deposition radius with the detailed model (circles) and the simplified model. For comparison, the lowest experimental result (not shown) found at low radius was about $0.4\,mJ$ [126].

to prescribe transport properties and chemical reaction rates at higher temperatures. Even recently, simulation of the breakdown phase itself is not commonly found in the literature. A more standard procedure [84, 128, 129] is to simulate the arc and glow phases only, starting from an initial state (volume V_i of hot gases of composition X_i at temperature T_i and pressure P_i) corresponding to the end of the breakdown. If this initial state is taken too early, the plasma phase can not be neglected, in particular its thermodynamics and transport properties as well as its chemistry. Sher et al. [75] justified this need showing the mixture composition versus temperature of an initial 79% nitrogen-21% oxygen mixture at $300\,K - 1\,bar$ in a constant pressure chamber (Fig. 5.12a). A fully dissociated mixture is found from $10\,000\,K$ and a fully ionized state from $20\,000\,K$. Heat capacity also reveals a non-monotone dependence on temperature (see Fig. 5.12b) as well as on pressure (not shown), each peak corresponding to a dissociation level. The same behaviour is observed for thermal conductivity and electric conductivity [19]. An estimation of V_i and T_i without adequate thermodynamics and transport can therefore lead to erroneous results. Refael et al. [73] proposed analytical estimations of V_i and T_i using JANAF thermodynamics properties for high temperatures [130]. Finally, the composition X_i of the initial kernel can be obtained using 0D simulation and dedicated plasma mechanisms [131, 132, 133, 134] or chemical equilibrium codes [135]. Very few numerical works, such as the one of Thiele et al. [136], actually simulated the entire breakdown phase with its associated plasma chemistry or try to take into account the effect of the electric and magnetic fields [137, 138]. The impact of electric and magnetic fields is found negligible for the flame initiation. Con-

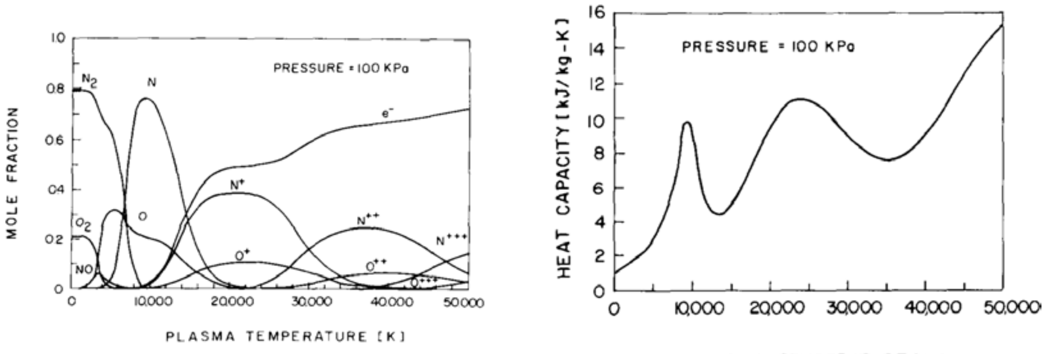

(a)

(b)

Figure 5.12: (a) Mixture composition versus temperature of an initial 79% nitrogen-21% oxygen mixture at $300\,K - 1\,bar$ in a constant pressure chamber. (b) Evolution of heat capacity versus plasma temperature [75].

cerning the chemistry description, using a detailed chemical scheme (encompassing dissociation and recombination reactions) with accurate transport and thermodynamic properties is mandatory, but the interest of adding the chemistry of the plasma phase (i.e. adding the charged species complexity with ionization reactions) is still an open question.

5.5 Numerical models

If a lot of studies focused on the creation of the kernel, as summarized in Sec. 5.1-5.4, plenty of them were also dedicated to the kernel growth phase. Indeed, due to its stochastic nature (see Sec. 7.1), this phase mainly controls the ignition probability. When investigating kernel growth using LES or RANS simulations, a critical issue is the large range of space and time scales to consider from a few millimetres and nanoseconds when the kernel is created to a few tens of centimetres and milliseconds at the end of the growth phase. In practice, the creation phase of the kernel can not be resolved either temporally of spatially. Two methods can be used to solve this problem:

- Computing the temporal and spatial kernel expansion with an external low-order model until it can be resolved on the LES mesh. The creation phase of the kernel is fully calculated with the low order model and only the growth phase is resolved with LES.

- Refining the mesh around the sparking position to resolve as much as possible the kernel evolution, including the kernel creation phase. A *filtered* kernel evolution is then resolved as the smallest time and length scales are unreachable. In practice, a source term $\dot{Q}$ in the energy equation that simplifies the real energy delivered by the external source.

Both methods require an estimation of the thermal energy E_{ign} used to initiate the flame (see Fig. 5.4). Accurate models must also take into account the temporal evolution of E_{ign}. First, low-order numerical models solving the kernel expansion until it can be resolved by an LES mesh are presented. Such models are particularly used with the Flame Surface Density (FSD) approach. Then, the Energy Deposition model (ED) is presented.

5.5.1 Low-order models

Boudier et al. [101] coupled a 0-D solver (called LI model) for the laminar kernel creation to the turbulent propagation Coherent Flame Model (CFM). Important assumptions are made in the LI model such as spherical symmetry, no blast wave effect, simple model for heat losses to electrodes and no plasma effect. Using some input parameters (flame speed s_l, flame thickness δ_l, burnt/fresh gases temperature ratio $\frac{T_2}{T_1}$, activation energy E_a, Lewis number Le, $E_{ign}(t)$, spark duration t_s and initial plasma radius r_s) this model provides the flame radius at the end of the laminar phase and the duration of this phase. The LI model was validated by comparing critical ignition energies and times with values of Champion et al. [94]. Then the CFM model is used to describe the rest of the kernel growth, which occurs in a fully turbulent regime. The transition between the LI solver and the CFM solver in the global LI-CFM model occurs when the laminar flame stretch K_l becomes smaller than the turbulent K_t one with

$$\frac{K_t}{\epsilon/k} = f\left(\frac{u'}{s_L}, \frac{L}{\delta_l}\right) \tag{5.4}$$

$$K_l = \frac{2}{r}\frac{dr}{dt} = 2\,\frac{T_2}{T_1}\frac{s_L}{r} \tag{5.5}$$

and ϵ the turbulent dissipation rate, k the turbulent kinetic energy, u' the RMS turbulent velocity and L the integral scale. In the laminar-turbulent phase (Fig. 5.13), both laminar and turbulent effects are taken into account and compete. A similar ignition model was developed at ONERA for RANS simulations which couples a 1-D model [139, 140] solving the kernel expansion in a mist of fuel droplets to their in-house CFD code CEDRE. In the absence of information on E_{ign}, experimental visualisations are used to initialize a kernel of correct size. Another model was proposed by Tan et al. [141]: the Discrete Particle Ignition Kernel (DPIK model). The flame surface is tracked with passive lagrangian tracers initially placed spherically around the sparking position. Kernel particles evolve radially with a velocity that is the sum of the turbulent flame speed and a plasma velocity calculated thanks to E_{ign} considered to be around $30\,\% E_{spark}$. Once the flame surface (joining these particles) can be resolved on the

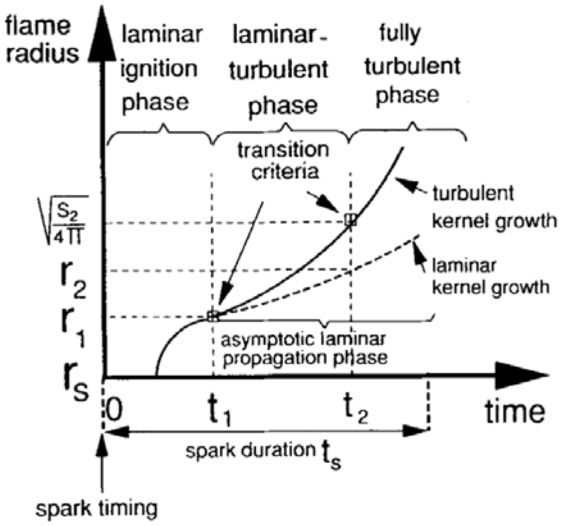
flame radius
laminar ignition phase
laminar-turbulent phase
fully turbulent phase
transition criteria
turbulent kernel growth
laminar kernel growth
$\sqrt{\frac{S_2}{4\pi}}$
r_2
r_1
r_s
asymptotic laminar propagation phase
0
t_1
t_2
time
spark duration t_s
spark timing

Figure 5.13: Illustration of the coupling between the LI solver and the CFM model presented by Boudier et al. [101].

mesh, an interpolation is performed to reconstruct the interface between fresh gases and burnt gases. The propagation of this interface is then tracked with a Level-Set method.

Duclos & Colin [142] also derived a low-order model called AKTIM (Arc and Kernel Tracking Ignition Mode) for the initial kernel expansion, dedicated to RANS simulations. In this model, E_{ign} is no longer a user input but is reconstructed from an electric circuit model. Moreover, $E_{ign}(t)$ varies in time to mimic a two-step process: breakdown phase and glow phase. $E_{ign}(t)$ is calculated using the voltage and current as function of time and coefficients accounting for losses by conduction to electrodes, shock wave, radiation and also electric losses in the circuit. As presented in Fig. 5.14, the AKTIM model also models the geometry of the spark plug with lagrangian markers to take into account the modification of the flow due to the spark plug. The electric arc is not only modeled as a fixed cylinder between both electrodes but is tracked by lagrangian tracers too. The flow can deform the arc and thus change the voltage between electrodes and the $E_{ign}(t)$ signal. Finally, a high number of potential flame kernels are modeled with lagrangian tracers and are initiated along the arc at the moment of breakdown. Kernels are characterized by an initial energy (delivered during the breakdown+arc phases) and an initial burnt gas mass (null initially) and evolve in time. Their energy grow with time thanks to $E_{ign}(t)$ but also decrease by conduction to electrodes for example. If the energy of a kernel reaches an arbitrary critical energy E_{crit}, ignition is considered successful and the mass of burnt gases it transports is used as an initial condition for the 3D solver. Latter, the AKTIM model was modified by Richard et

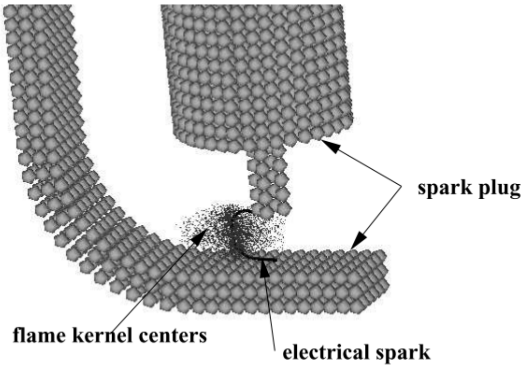

Figure 5.14: 3D view of the AKTIM model [142].

al. [143] (AKTIMeuler) to be used with a LES Flame Surface Density approach. The main difference is that no lagrangian tracers are used for describing the flame kernels. Instead, the Eulerian progress variable field is chosen. Finally, Colin & Truffin [144] improved the AKTIMeuler model. The new ISSIM-LES model is now used in many spark ignition studies [145]. It should be noted that all these low-order models rely heavily on user coefficients and parameters that are subject to large uncertainties (e.g., loss coefficients, see Fig. 5.4) and can therefore strongly limit their accuracy.

5.5.2 Energy Deposition model

An alternative to all these ignition models is to resolve on a refined grid a filtered kernel evolution from its creation by providing E_{ign} as a source term in the energy equation:

$$\rho\frac{DE}{Dt} = \dot{w_T} + \frac{\partial}{\partial x_i}(\lambda\frac{\partial T}{\partial x_i}) - \frac{\partial}{\partial x_i}(\rho\sum_{k=1}^{N} h_{s,k}Y_kV_{k,i}) + \frac{\partial}{\partial x_j}(\sigma_{ij}u_i) + \dot{E}_{ign} \tag{5.6}$$

where

$$\dot{E}_{ign} = \frac{E_{ign}(t)}{dt} \tag{5.7}$$

Sloane [146] proposed a slightly modified version in which an arbitrary part of the input energy is actually used for the creation of a radical pool (H, O, OH species). As for low-order models, such model requires an estimate of E_{ign} by the user. The major drawback is that the mesh must be refined (10 points in the deposition zone) around the spark position. It is however possible to latter interpolate the kernel on a classic LES grid when it is large enough. However it has many advantages and has therefore been used in many DNS [147, 148, 149] and LES studies [150, 151]. 1- The modeling is much simpler that a low-order model. 2- No assumptions are needed about when the low-order model should be coupled to the 3D LES solver. 3- By definition, the kernel expansion is fully resolved so no arbitrary criterion about flame success or failure is necessary. 4- Such model allows to consider arbitrary temporal and spatial shapes of

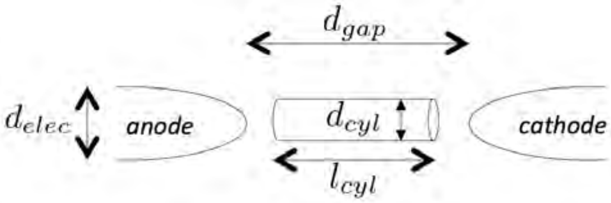

Figure 5.15: Sketch of a cylindrical zone where energy can be deposited using an ED model to mimic spark ignition.

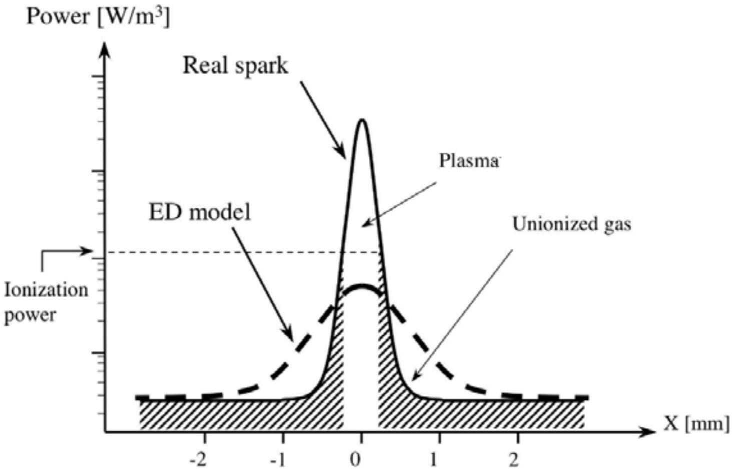

Figure 5.16: Sketch of the gaussian ED model and real spark power as proposed by Lacaze et al. [151]. The same idea is applied for the temporal shape.

energy deposition. For instance can be represented by considering an energy deposition in a cylinder between two electrodes as proposed in Fig. 5.15 with a temporal signal decomposed in a breakdown phase plus a glow phase. However, to avoid dealing with too high temperatures for many reasons explained in Sec. 5.4 (adapted thermodynamics, transport properties and kinetics schemes required), the energy deposition shape in time and space is often smoothed, as in the Energy Deposition model (ED model) used by Lacaze et al. [151]. The main idea sketched in Fig. 5.16 is to deliver the energy profile that would exist following a real spark once the temperature has dropped below the ionization temperature, thereby ignoring the plasma phase. In other terms, the ED model does not consider breakdown plus glow phases but only one glow phase during which E_{ign} is smoothly deposited.

The form of the source term chosen by Lacaze et al. [151] is Gaussian in space and time. $\frac{E_{ign}}{E_{spark}} = 10 - 30\%$ is proposed taking values from the literature. The diameter of the initial ignition sphere Δ_s is deduced from E_{ign} and from the temperature in the center of the deposition sphere $T_{k_{max}}$ [151] which is found neglecting heat losses by conduction in the mixture:

$$T_{k_{max}} \approx \frac{1}{\rho C_p} \frac{E_{ign}}{(2\pi)^{3/2}\sigma_s^3} + T_0 \tag{5.8}$$

with ρ and C_p the density and heat capacity of the fresh mixture at the ignition location, T_0 the temperature of fresh gas, and $\sigma_s = \Delta_s/(4\sqrt{ln(10)})$. For spark ignition, Δ_s is typically of the order of the electrode gap.

Figure 5.17 illustrates the phenomenology following a 1D energy deposition. During the energy deposition, the temperature increases abruptly in the kernel. This energy is then transferred to the surroundings by diffusion, leading to a decrease of the maximal temperature. After a moment, if its temperature is still high enough, the first chemical reactions may occur, leading to the chemical run-away and eventually to the formation of the flame kernel. This artificial period between energy deposition and chemical run-away, due to a deliberately low maximum temperature reached, is called induction time. It allows a good understanding of the balance between thermal losses by diffusion and chemical heat release which must be positive to result in a successful ignition. After the chemical run-away led to the kernel formation, the flame grows, becomes turbulent, and propagates. If the total amount of energy transmitted to the mixture E_{ign} is too small, chemical reactions are never triggered. The added energy is then simply diffused in the domain. If ignition occurs, the artificial induction time is reduced by increasing the deposited energy as the chemical run-away is accelerated. The ED model was validated by Enaux [152] by comparing laminar flame growths in the ARC experimental configuration of CORIA [153].

5.6 Conclusions

The first phase of ignition during which a small flame kernel is created thanks to an external source of energy has been studied for years as it is of practical interest for IC engines as well as gas turbine combustors. The very short time and space scales of this phase make its full comprehension still a challenge. Few nanoseconds after breakdown, a very hot ionized plasma phase is created. This phase is still not well understood and thus requires further investigations. After this short period, the temperature drops and a flame kernel might be created depending on local mixture properties (temperature, mixture fraction, turbulence level, presence of fuel droplets and so on). The probability of ignition as function of local properties has been studied intensively and is now quite well documented, partly thanks to accurate numerical investigations. Still, uncertainties in numerical simulations arise from few sources. For instance, estimating the quantity of energy the external source actually transmits to the fluid is not trivial and including an accurate description of the plasma chemistry

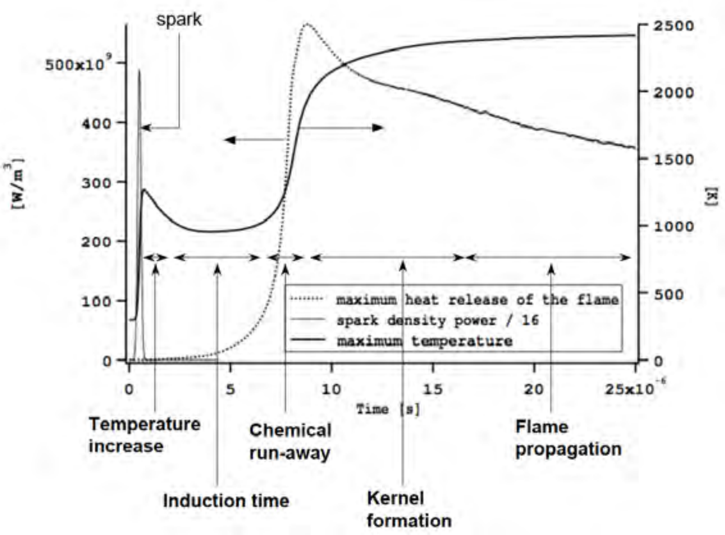

Figure 5.17: Evolution of the maximal temperature, spark density power and maximum heat release of the flame following a 1D ignition with the ED model [154].

is not straightforward neither. To be able to investigate full ignition sequences despite this lack of knowledge, simple ignition models have been developed, recovering the flame state at the end of the kernel generation phase with good accuracy. Nevertheless, precise numerical simulations are still required to improve our understanding of this early phase and to propose better ignition models for future LES of ignition. Thus, Chap. 6 focuses on investigating with DNS simulations this early ignition phase, and in particular bringing new insights on the impact of plasma chemistry on the flame initiation.

Chapter 6

Numerical simulations of spark ignition

Contents

6.1 Objectives 89

6.2 Spark ignition modeling 90

6.3 Chemistry modeling 91

6.3.1 Combustion ARC 91

6.3.2 Plasma chemistry 92

6.3.3 Merged combustion-plasma ARC 94

6.4 Experimental set-up 96

6.5 Numerical set-up 96

6.6 Ignition sequence dynamics 98

6.6.1 Discharge in air 98

6.6.2 Propane-air ignition 101

6.7 Influence of plasma chemistry on spark ignition 102

6.8 High temperature Energy Deposition model for LES: A new methodology 107

6.9 Conclusions 109

6.1 Objectives

This chapter focuses on the first phase of ignition that has been widely studied in the litterature [73, 96, 100, 155] as summarized in Chap. 5. During this period, a spark plug delivers a very short and powerful electrical discharge to the mixture. A high temperature plasma [72, 77] is thus generated for a very short time as well as a propagating shock. This plasma phase therefore induces a thermal effect, a mechanical effect associated with the shock, and a high chemical activity. Among the questions still open, the impact of the plasma chemistry on the combustion initiation is a subject that is not well covered in the literature. It is proposed in this chapter to address this issue in a simple academic configuration.

Numerical simulations are ideally suited for the very small time and space scales of this phase in order to better understand the main mechanisms driving this complex transient phenomenon. Accurately treating this phase however requires an adequate description of the spark and the plasma chemistry. The spark can be modeled with an energy deposition model. To describe the plasma chemistry (including charged species evolution), suitable chemical kinetics should be used. Exhaustive mechanisms are however too complex and too CPU time consuming to be directly used. One affordable solution is to use Analytically Reduced Chemistries (ARC) (see Sec. 3.1.4.3) which keep the main chemical paths of interest. ARCs have already been successfully used in the context of combustion [24, 156] and are particularly well suited for the study of ignition. The novelty of this work is to apply this in the context of plasma chemistry.

First, the development of an appropriate energy deposition model needed to mimic the spark discharge is presented. Second, the derivation and validation of two ARCs are detailed (one for combustion only and another one describing both combustion and plasma chemistries), as well as the associated thermodynamic and transport properties. Numerical simulations of an anode-cathode configuration are then performed with and without plasma chemistry. Results are compared and analysed in terms of temperature and mixture composition evolution to understand the impact of the plasma phase on the combustion initiation. Finally, an improved methodology based on the standard ED model [151] is proposed to better mimic a spark or laser energy deposition in a Large Eddy Simulation context.

This chapter is adapted from a published article [157] available in Appendix. B:
F. Collin-Bastiani, O. Vermorel, C. Lacour, B. Lecordier, B. Cuenot, DNS of spark ignition using Analytically Reduced Chemistry including plasma kinetics, Proceedings of the Combustion Institute (2018),
https://doi.org/10.1016/j.proci.2018.07.008

6.2 Spark ignition modeling

As mentioned in Sec. 5.1, the first phase of spark ignition can be divided in 3 main steps [72, 73, 74, 75]: during breakdown ($1 - 10$ ns), a small amount of energy is delivered to the mixture. The energy deposition density is high as it occurs in a very small volume and for a very short time, so the energy transfer is very efficient. Temperatures up to $20,000$ K or more can be reached in the inter-electrode zone leading to an intense shock wave, molecular dissociations and the creation of a radical pool. Following the breakdown, the arc phase lasts longer (≈ 1 μs), but with lower energy deposition density and efficiency. Finally, the glow phase is characterized by a lower power compared to the arc phase and important losses due to conduction to the electrodes. However, the long duration of the glow phase ($\approx 1\ ms$) allows to transfer a significant amount of energy to the gas. This transfer is slow enough for the mixture to cool down by heat diffusion.

To properly model the phenomenology of a spark, an adaptation of the 1-step Energy Deposition (ED) model is used here [151]. Unlike the original model, energy is here deposited in 2 steps: the breakdown phase and the merged arc and glow phases, called glow hereafter for simplicity. The breakdown is too short to allow detailed measurements but the amount of electrical energy provided during this phase E_{bd} as well as the phase duration t_{bd} are known from experiments [158]. For the glow phase, the total electrical energy E_{glow} as well as the phase duration t_{glow} are also given experimentally [158]. In addition, it is observed that the electrical power is almost linearly decreasing. From these experimental observations, the time derivative of the electrical energy given to the electrodes $E_s(t)$ during the breakdown (Eq. 6.1) and glow (Eq. 6.2) phases are written respectively:

$$\frac{dE_s(t)}{dt} = \frac{E_{bd}}{t_{bd}} \tag{6.1}$$

$$\frac{dE_s(t)}{dt} = \frac{2\ E_{glow}}{{t_{glow}}^2}(t_{spark} - t). \tag{6.2}$$

with t_{spark} the end of the spark. The actual energy $E_{ign}(t)$ transferred to the mixture is then obtained by applying breakdown and glow efficiency coefficients:

$$E_{ign}(t) = \eta\, E_s(t), \text{ breakdown phase} \tag{6.3}$$

$$E_{ign}(t) = \zeta\, E_s(t), \text{ glow phase} \tag{6.4}$$

where η and ζ are estimated following the literature [72, 80, 84, 85]. The influence of these two coefficients will be assessed in Sec. 6.6.1. The energy deposition volume is approximated by a cylinder between the two electrodes as represented in Fig. 6.4.

6.3 Chemistry modeling

6.3.1 Combustion ARC

Using a DRGEP method and Quasi-Steady State Approximations (QSSA) [23, 24], an ARC (called COMB25) made of 25 transported species (for which conservation equations are solved), 292 irreversible reactions and 16 species in QSSA (for which concentrations are calculated analytically), dedicated to propane combustion in air, is derived starting from the detailed LLNL mechanism [159]. All thermodynamic properties are extracted from the reference NASA database [135]. Properties of several species are available up to $20,000\ K$. However, for some species used in our study, properties are only given up to $6,000\ K$. In such cases, extrapolation is performed

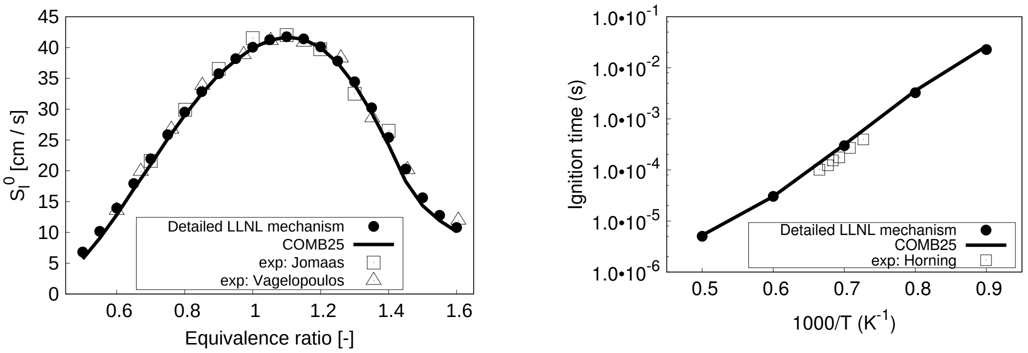

(a) **(b)**

Figure 6.1: Comparison between detailed chemistry, ARC and experiments on (a) Laminar flame speed for an unstrained premixed flame at $1\,bar$ and $298\,K$, and (b) ignition delay time at $1\,bar$ and $\phi = 1$ as function of the temperature.

from $6,000$ K to $20,000$ K. Viscosity and thermal conductivity of the mixture are derived from high temperature equilibrium air plasmas as in D'Angola [19], as classical viscosity laws such as the Sutherland law [160] do not behave correctly in such extreme conditions (see Sec. 3.1.3).

For validation, COMB25 is used to compute laminar unstrained premixed flames at 1 bar and 298 K [161, 162]. A very good agreement with both the detailed mechanism and experimental data is obtained with less than 5 % relative error for equivalence ratios $0.6 < \phi < 1.4$ as shown in Fig. 6.1a. Mass fraction profiles of important species, such as C_3H_8, CO_2, CO but also OH and O that are known to be important for ignition, are also well predicted (not shown). In addition, ignition delay times at 1 bar and $\phi = 1$ are well recovered with relative errors below 15 % for $1,100$ $K < T < 2,000$ K compared to both the detailed mechanism and experimental data [163] as presented in Fig. 6.1b.

6.3.2 Plasma chemistry

The original set of plasma chemical reactions [132], called PLASMA38 hereafter, contains 38 species and 334 irreversible reactions and has already been successfully used in previous plasma studies [164]. It is a comprehensive concatenation of elementary plasma reactions extracted from several publications of reference [133, 134, 165]. To highlight the correct behaviour of PLASMA38 in the context of our study, it is here assessed at temperatures where ionization and dissociation reactions take place, i.e. for $T > 3,000$ K. Constant pressure reactors are advanced in time and the final compositions obtained with the software Cantera [166] are compared to reference solutions given by the NASA Chemical Equilibrium with Applications (CEA) reference code [167], in the absence of available experimental measurements. Different test cases of increasing

$T_{ini}\,(K)$	3,000	5,000	15,000	20,000
ε_T	$5.1\ e^{-4}$	$-3.2\ e^{-4}$	$-1.1\ e^{-2}$	$-7.1\ e^{-3}$
ε_X	$2.3\ e^{-3}$	$9.3\ e^{-3}$	$4.7\ e^{-2}$	$2.1\ e^{-2}$

Table 6.1: Validation of PLASMA38: Case A. Relative errors between Cantera and CEA on the final temperature T_{final} and species molar fractions X^k_{final} obtained for various values of T_{ini}.

complexity have been considered to ensure the robustness of the chemical system in case of acceptable departure from equilibrium during calculation.

Three cases of increasing difficulty are considered. In case A, the simulation starts at temperature T_{ini} with the equilibrium composition at T_{ini} calculated by the CEA code from an initial stoichiometric C_3H_8-air mixture. It is then expected that the final temperature T_{final} and final composition X_{final} do not deviate from the initial state. Table 6.1 shows the relative errors on the temperature ε_T (Eq. 6.5) and species molar fractions ε_X (Eq. 6.6) obtained for various values of T_{ini}:

$$\varepsilon_T = \frac{T_{final} - T_{ini}}{T_{ini}} \tag{6.5}$$

$$\varepsilon_X = \frac{1}{N_{spec}} \sum_{k=1}^{N_{spec}} \frac{X^k_{final} - X^k_{ini}}{X^k_{ini}} \tag{6.6}$$

In the above expressions, N_{spec} is the number of transported species. In all cases of Tab. 6.1, the final temperature given by Cantera remains close to T_{ini} with a maximum 1 % relative error. The composition stays close to the equilibrium composition at T_{ini} with errors below 5 %. For temperatures below $5,000\ K$, all major species (N_2, H_2, H, O, OH, H_2O, O_2, CO, CO_2, NO) are accurately predicted. At higher temperatures ($15,000\ K$-$20,000\ K$), only few species such as C, N or O have larger errors but they are only minor species ($X^k_{ini} < 0.01$). The electro-neutrality is preserved as well.

In a second case B, the initial state is set as in case A but the final temperature T_{final} is forced to a different value than T_{ini}. The final composition should correspond to the equilibrium composition at T_{final}. The relative error between Cantera and CEA ε_X defined in Eq. 6.7 is reported for various values of the couple (T_{ini}/T_{final}) in Tab. 6.2.

$$\varepsilon_X \quad = \tfrac{1}{N_{spec}} \textstyle\sum_{k=1}^{N_{spec}} \tfrac{X^k_{final} - X^k_{eq}(T_{final})}{X^k_{eq}(T_{final})} \tag{6.7}$$

Even with important temperature differences, leading to large differences between the initial and final compositions, the equilibrium composition given by CEA is always well recovered with Cantera. For example, for $(T_{ini}/T_{final}) = (10,000\,K/3,000\,K)$, the molar fraction of almost all species undergoes a huge variation due to recombination reactions, like the molar fraction of OH which goes from $4e^{-6}$ to $3e^{-2}$. Nevertheless,

(T_{ini}/T_{final})	20,000/15,000	15,000/20,000	10,000/3,000	3,000/10,000
ε_X	0.094	0.082	0.009	0.086

Table 6.2: Validation of PLASMA38: Case B. Relative error between CANTERA and CEA on the final composition X^i_{final} for various values of $(T_{ini}/T_{final})(K)$.

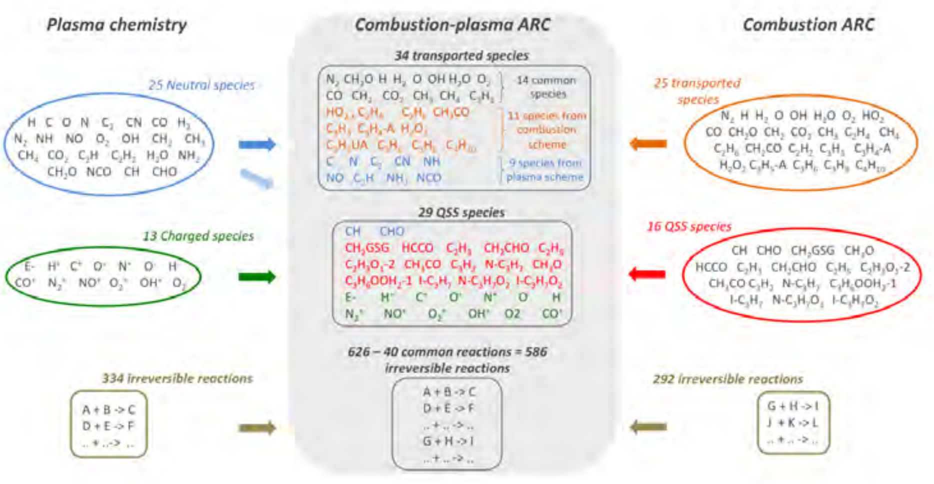
Plasma chemistry
25 Neutral species
H C O N C2 CN CO H2 N2 NH NO O2 OH CH2 CH3 CH4 CO2 C2H C2H2 H2O NH2 CH2O NCO CH CHO
13 Charged species
E- H+ C+ O+ N+ O- H- CO+ N2+ NO+ O2+ OH+ O2-
334 irreversible reactions
A + B -> C
D + E -> F
.. + .. -> ..
Combustion-plasma ARC
34 transported species
N2 CH2O H H2 O OH H2O O2 CO CH2 CO2 CH3 CH4 C2H2
14 common species
HO2 , C2H4 C2H6 CH2CO C3H3 C3H4-A H2O2 C3H5UA C3H6 C3H8 C4H10
11 species from combustion scheme
C N C2 CN NH NO C2H NH2 NCO
9 species from plasma scheme
29 QSS species
CH CHO
CH2GSG HCCO C2H3 CH3CHO C2H5 C3H3O2-2 CH3CO C3H2 N-C3H7 CH3O C3H6OOH2-1 I-C3H7 N-C3H7O2 I-C3H7O2
E- H+ C+ O+ N+ O- H- N2+ NO+ O2+ OH+ O2 CO+
626 – 40 common reactions = 586 irreversible reactions
A + B -> C
D + E -> F
.. + .. -> ..
G + H -> I
.. + .. -> ..
Combustion ARC
25 transported species
N2 H H2 O OH H2O O2 HO2 CO CH2O CH2 CO2 CH3 C2H4 CH4 C2H6 CH2CO C2H2 C3H3 C3H4-A H2O2 C3H5-A C3H6 C3H8 C4H10
16 QSS species
CH CHO CH2GSG CH3O HCCO C2H3 CH3CHO C2H5 C3H3O2-2 CH3CO C3H2 N-C3H7 C3H6OOH2-1 I-C3H7 N-C3H7O2 I-C3H7O2
292 irreversible reactions
G + H -> I
J + K -> L
.. + .. -> ..

Figure 6.2: Sketch of the merging procedure to obtain the MERGED34 kinetic scheme.

the final composition of the mixture is recovered with a deviation from equilibrium of only 1 %.

Finally a third case C has been performed showing that starting at T_{ini} and with a composition different from the equilibrium composition at T_{ini}, the equilibrium state is recovered with good accuracy provided that the initial departure from equilibrium composition is not too large.

6.3.3 Merged combustion-plasma ARC

To couple combustion and plasma chemistries, PLASMA38 is simply merged to COMB25 as illustrated in Fig. 6.2 where all involved species are recalled. All 13 charged species of PLASMA38, known to be very reactive, are put in QSSA. The resulting merged mechanism (named MERGED34) is finally made of 586 irreversible reactions, 29 species in QSSA and 34 transported species. Among them, 14 species (N_2, H, H_2, O, OH, H_2O, O_2, CO, CO_2, CH_2, CH_3, CH_4, C_2H_2 and CH_2O) are essential as they appear in both combustion and plasma chemistries and constitute the coupling between the two chemistries. Similarly, among the 586 irreversible reactions of MERGED34, 40 reactions are common to both combustion and plasma databases. When species are found in both databases, their thermodynamic and transport properties are taken from

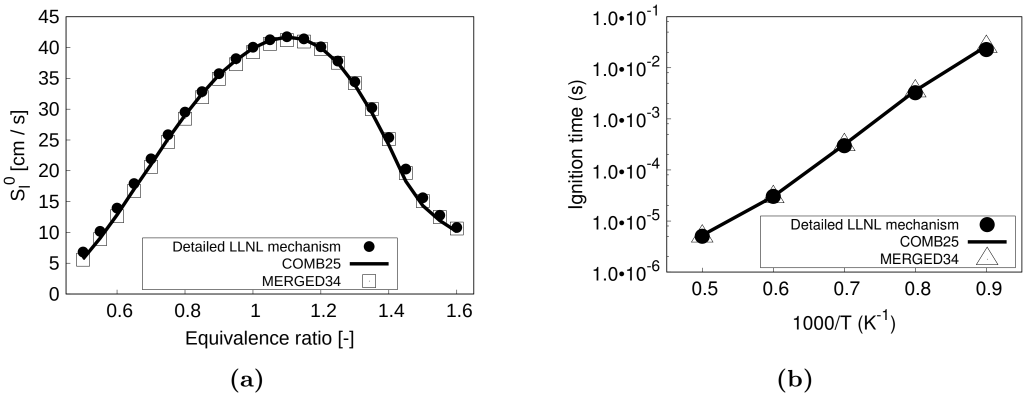

Figure 6.3: Comparison between detailed chemistry, reduced combustion chemistry and reduced combustion-plasma chemistry on (a) laminar flame speed for an unstrained premixed flame at $1\,bar$ and $298\,K$, and (b) ignition delay time at $1\,bar$ and $\phi = 1$ as function of the temperature.

the combustion database. The same applies to rate coefficients of common reactions. In practice, differences are found to be negligible and do not affect the behaviour of the final merged mechanism. All details about the merging procedure are provided in Appendix. A.

At this point, a few verifications are required to ensure that PLASMA38 does not interfere with COMB25 at low temperature and conversely that COMB25 does not disrupt PLASMA38 at high temperature. For $T < 3,000\ K$ where combustion only is expected, MERGED34 is compared to the detailed LLNL mechanism and to COMB25 in terms of both laminar flame speed at $1\,bar$ and $298\,K$ (see Fig. 6.3a) and ignition delay time at $1\,bar$ and $\phi = 1$ (see Fig. 6.3b). No difference is observed confirming that plasma chemistry is inactive at low temperatures. Similarly to PLASMA38, verifications of MERGED34 at higher temperatures are based on constant pressure reactors simulated with Cantera, starting with a stoichiometric C_3H_8-air mixture at $T_{ini} = 300\ K$, and progressively increasing temperature up to $T_{final} = 10,000\ K$. The final composition is compared to the equilibrium composition at T_{final} given by the CEA code. The relative errors ε_X^k (Eq. 6.8) on the final molar fractions of the 4 major transported species k remaining at this temperature, are given in Tab. 6.3.

$$\varepsilon_X^k = \frac{X_{final}^k - X_{eq}^k(T_{final})}{X_{eq}^k(T_{final})} \tag{6.8}$$

An overall good agreement is obtained for the considered species. The mean relative error is 7 % with a maximum of 17 % for the atomic carbon molar fraction. This error is non negligible and is linked to the uncertainties of plasma chemistry. However it is expected not to change the overall system behaviour. This shows that the addition of species coming from the combustion scheme does not change high temperature chemical equilibrium.

species	C	N	O	H
ε_X^k	0.17	0.07	0.015	0.037

Table 6.3: Validation of MERGED34. Relative errors ε_X^k between Cantera and CEA on the molar fractions of the 4 major transported species k, starting with a stoichiometric $C_3H_8 - air$ mixture at $T_{ini} = 300\ K$.

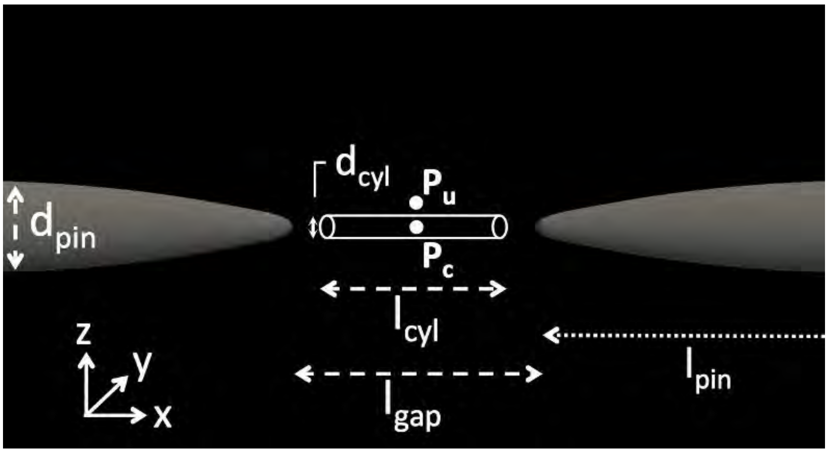

Figure 6.4: Sketch of the studied anode-cathode configuration.

6.4 Experimental set-up

The configuration studied here is an academic set-up experimented at CORIA laboratory [158, 168]. It is made of two facing parabolic electrodes of length $l_{pin} = 2.2\ cm$ as illustrated in Fig. 6.4, with radius of curvature of 150 μm. The maximum diameter of the electrodes is $d_{pin} = 1.6\ mm$ and the electrode gap is $l_{gap} = 3\ mm$. Two operating conditions are investigated: a non-reacting case of discharge in pure quiescent air at atmospheric conditions and a reacting case where the volume is initially filled with a quiescent flammable propane-air mixture at $\phi = 0.75$ and at atmospheric conditions.

6.5 Numerical set-up

Neglecting the temperature gradient that may appear after ignition between the two electrode heads, the configuration has a spherical symmetry (P_c [0,0,0] is the symmetry point). This temperature gradient may slightly modify the dynamics of the kernel development. However, as the focus is made here on the impact of plasma chemistry, this simplification does not change the conclusions but allows to reduce drastically the computational domain size to $1/8^{th}$ of a sphere of radius 10 cm as sketched in Fig. 6.5.

Simulations are performed with AVBP. The second-order explicit Lax & Wendroff scheme is used with a time step imposed by the CFL number but also by the chemical

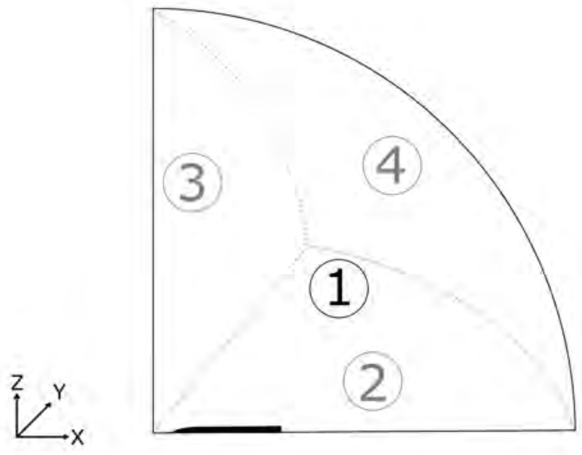

Figure 6.5: Scaled representation of the numerical domain.

system: time steps range from 0.2 ns during the breakdown phase to 2.5 ns in the glow phase. Chemistry sub-cycling is also used to improve the stability of the explicit time integration scheme. Symmetry conditions are applied on faces 1, 2 and 3 of the domain shown in Fig. 6.5 and an NSCBC condition [46] is employed for the outlet face 4, fixing pressure to 1 bar. The electrode surfaces are modelled as no-slip adiabatic walls. Indeed, losses at the walls are already accounted for by the efficiency coefficients η and ζ. Simulations are performed on a 2.1 million tetrahedral cells mesh with a characteristic grid size of 15 μm in the inter-electrodes gap. Such a small grid size is required during the breakdown phase to resolve the strong gradients and chemical source terms.

5 simulations have been performed: 3 non reacting simulations and 2 reacting simulations. In the 3 inert calculations, different values for the efficiency parameters η and ζ are used to investigate their influence on the flow dynamics as shown in Tab. 6.4. For the 2 reacting cases, standard values from the litterature are used. The 2-step Energy Deposition model presented in Sec. 6.2 is applied in the five simulations. The energies deposited in each phase as well as the deposit times are provided by experimental measurements. The breakdown time t_{bd} is thus fixed to 20 ns, according to Lacour et al. [158] for this particular case. t_{bd} obviously imposes the time when temperature is maximum. The influence of this parameter has not been assessed and would require a dedicated study. The length of the energy deposition cylinder l_{cyl} is 2.4 mm and its diameter d_{cyl} is 150 μm, following experimental recommendations. Finally, no electromagnetic activity is considered. The electromagnetic field generated by the discharge implies non-thermal equilibrium for only very few nanoseconds. This hypothesis appears to be justified in the context of this work [138].

Case	**Conditions**	E_{bd}	t_{bd}	E_{glow}	t_{glow}	η	ζ
Low ζ	Non-reacting	$2.8\,mJ$	$20\ ns$	$77\,mJ$	$2.7\,ms$	$60\ \%$	$10\ \%$
Intermediate η & ζ	Non-reacting	$2.8\,mJ$	$20\ ns$	$77\,mJ$	$2.7\,ms$	$60\ \%$	$25\ \%$
High η	Non-reacting	$2.8\,mJ$	$20\ ns$	$77\,mJ$	$2.7\,ms$	$95\ \%$	$25\ \%$
C_3H_8-air	Reacting	$5.0\,mJ$	$20\ ns$	$85\,mJ$	$2.6\,ms$	$95\ \%$	$30\ \%$

Table 6.4: ED model parameters for the three non-reacting cases and the two reacting cases investigated.

6.6 Ignition sequence dynamics

6.6.1 Discharge in air

Before simulating propane-air ignition sequences, non-reacting discharges in air are first investigated to understand the impact of the spark on the flow dynamics and to assess the influence of the energy deposition efficiency parameters. Electrodes are surrounded by quiescent air at atmospheric conditions. Using the "Intermediate η & ζ" case of Tab. 6.4, a qualitative description of the flow motion induced by the discharge is first given in Fig. 6.6 for $t < 1\ ms$ and in Fig. 6.7 for $t > 1\ ms$. Cuts of temperature fields at 7 moments after the beginning of the discharged are displayed. The hot gas expansion is first controlled by the shock wave during the first microseconds. Tens of microseconds after the discharge starts, a depression following the shock wave is observed between the two electrodes. This depression leads to an inward gaseous flow along the electrodes, described by white arrows at $t = 33.9\ \mu s$, with counter-rotating vortices. Fresh gases leave the inter-electrode gap with a radial velocity resulting in the separation of a hot gas torus from the central core as shown at $t = 75.6\ \mu s$ and already observed in the literature [77, 155]. After this torus separation, the flow motion is much more quiescent. The temperature field is only governed by the competition between the energy source term and thermal diffusion. The central hot gas pocket extends slowly until the end of the glow phase at $2.7\ ms$. At this time a diamond shaped hot gas zone is formed as presented at $t = 5\ ms$. After the end of the energy deposition, only thermal diffusion controls the temperature field leading to a fast cooling of the inter electrodes region. After $7\ ms$, the temperature falls below $1000\ K$.

The influence of the ED model efficiency parameters η & ζ presented in Sec. 6.2 is now studied by comparing three simulations for which η & ζ are varied according to Tab. 6.4. The evolution of the temperature at point $P_A : x = 150\ \mu m;\ z = 750\ \mu m$ is compared with experimental measurements in Fig. 6.8. Compared to the

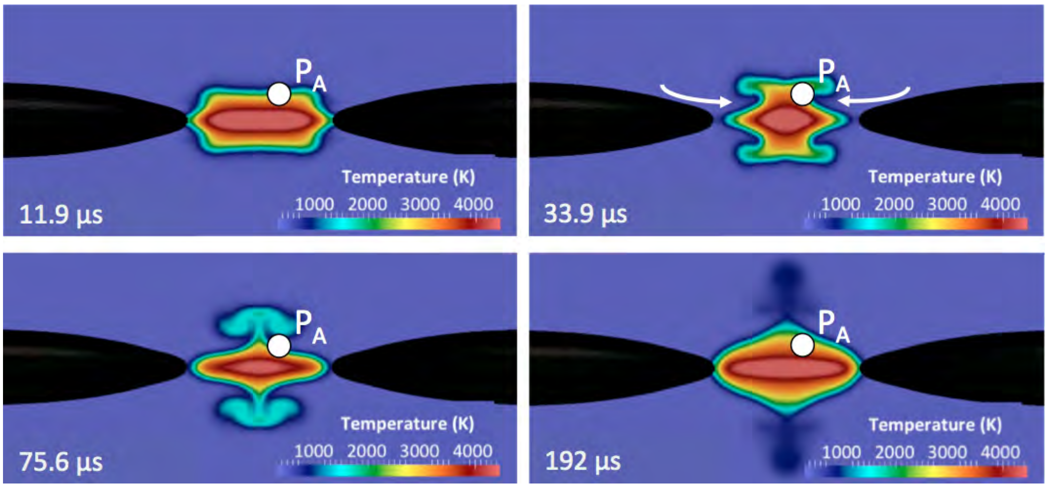

Figure 6.6: Temperature fields at 4 moments after the start of the discharge in air for $t < 1\ ms$.

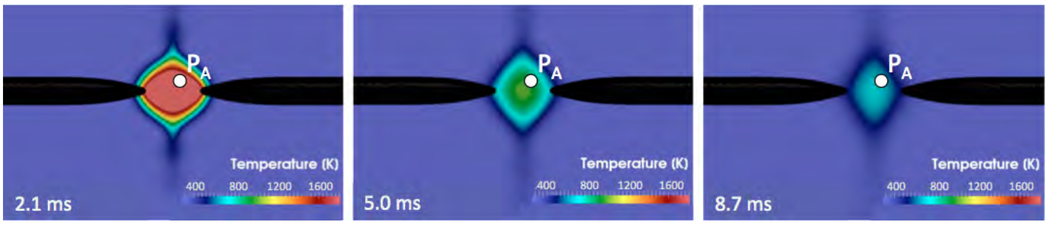

Figure 6.7: Temperature fields at 3 moments after the start of the discharge in air for $t > 1\ ms$.

"Intermediate" case ($\eta = 60$ %, $\zeta = 25$ %), the breakdown efficiency is increased to $\eta = 95$ % in the "High η" simulation and the glow efficiency is decreased to $\zeta = 10$ % in the "Low ζ" case. First, all simulations recover the "double-peak" shape of the experimental temperature evolution at P_A. This characteristic evolution is due to the hot gas torus detachment shown in Fig. 6.6. The hot gas kernel pushed radially reaches P_A leading to the first peak of temperature. Then the inward gaseous flow along the electrodes brings fresh gases at P_A cooling down the mixture. The expanding diamond-shaped hot gas zone leads to the second peak of temperature. Thermal diffusion finally contributes to the temperature drop observed after the end of the energy deposition. If the shape of the temperature evolution at P_A is correctly recovered for the three simulations, the agreement with experiments on the timings and magnitudes of the first and second temperature rises are very dependant on the efficiency parameters. For the "Intermediate" case ($\eta = 60$ %, $\zeta = 25$ %), the first temperature rise is over-estimated and occurs too early compared to experiments. The second temperature elevation also appears much too early but leads to a correct maximum temperature. By reducing the glow efficiency coefficient ($\zeta = 10$ %), the correct maximum temperature for the first peak and the correct timing of temperature rise for the second peak are recovered. However, the temperature elevation during the second peak is this time very under-estimated and the first peak still happens a little bit too early. By increasing the breakdown efficiency coefficient ($\eta = 95$ %), results are not improved compared to experiments. This highest efficiency results in more energy deposited in the mixture and a more powerful induced shock wave. Consequently, the inward gaseous flow along the electrodes bringing fresh gases at P_A is also stronger explaining the 1200 K temperature decrease just after the first peak compared to the 400 K decrease with $\eta = 60$ %.

A lot of η - ζ combinations have been tested but none of them led to accurate timings and maximum temperatures for both peaks. This shows the limitation of the 2-step Energy Deposition model used in this work. In particular, fixing the ED cylinder diameter d_{cyl} to 150 μm during the whole spark ignition scenario appears to be a strong assumption that should be investigated further. Indeed, as explained in Sec. 5.1, the spark begins when the electronic avalanche forms small streamers joining the cathode and the anode. Initially, these streamers made by electrons are much thinner than the 150 μm considered in the model. Ideally, the diameter of the ED cylinder should thus increase over time starting from a negligible diameter. Of course this would require a much more refined grid, leading to expensive simulations. Nevertheless, this 2-step Energy Deposition model is able to recover the main features of a spark discharge and appears sufficiently accurate to investigate the influence of plasma chemistry on propane-air spark ignition in the next section.

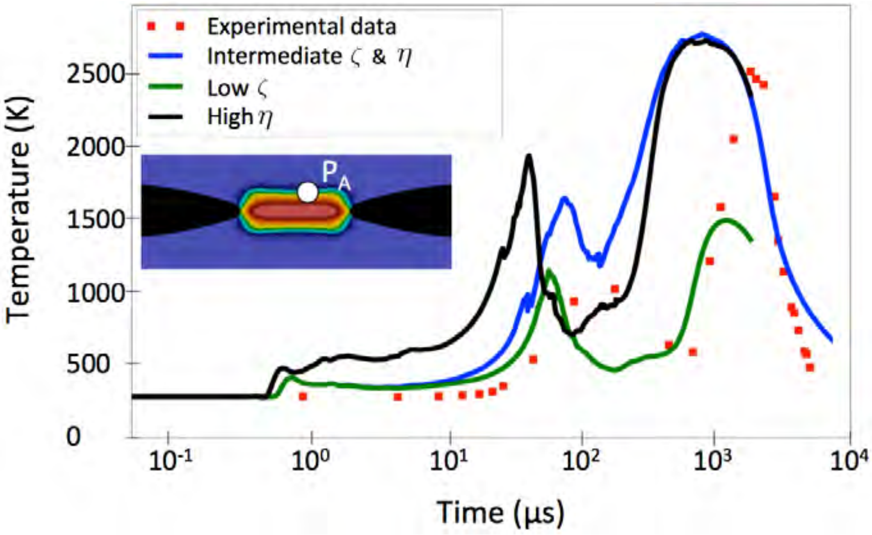

Figure 6.8: Evolution of the temperature at point $P_A : x = 150\ \mu m;\ z = 750\ \mu m$ after a spark discharge in air. Comparison between experimental measurements and three simulations using different efficiency parameters η & ζ (see Tab. 6.4).

6.6.2 Propane-air ignition

For the reacting case, the volume around the electrodes is initially filled with a quiescent flammable propane-air mixture at $\phi = 0.75$ and at atmospheric conditions. Two simulations are performed using COMB25 and MERGED34 to assess the impact of plasma kinetics on the ignition sequence. A first qualitative description of the flow motion during the ignition sequence with COMB25 is proposed in Fig. 6.9 (Left). The same evolution is observed with MERGED34 (not shown). Similarly to the non-reacting discharge in air, the flow is governed by the gas expansion at early times (10 μs). Later, the depression following the shock wave induces an inward flow along the electrodes, forcing the hot gas region to expand in the radial direction (500 μs) as in the non-reacting case. This results in an elongated flame shape, forming a torus around the electrodes axis that does not separate from the central core, contrary to the discharge in pure air. Then the flame progressively evolves to a classical spherical flame.

During the ignition sequence, temperature and pressure in the energy deposition zone reach very high levels in a few nanoseconds. Such short time-scales must be reproduced by the ignition model, as does the 2-step ED model used in this work. Indeed, a simple 1-step model would delay too much the energy supply leading to an overestimation of the ignition time. Besides, the initial flame propagation is directly dictated by the convective motion induced by the shock. Considering a too large deposition volume would lead to a too weak shock and a wrong initial flame motion. To further assess the validity of the ED model, the numerical ignition sequence is

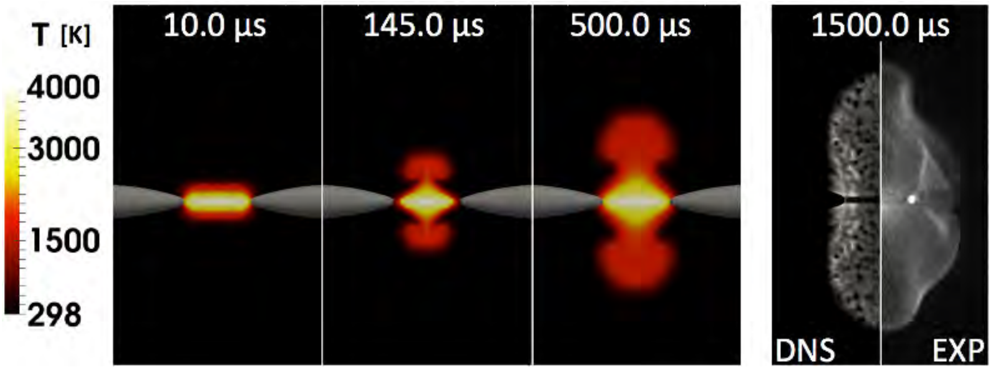

Figure 6.9: (Left): Temperature fields at 3 instants after the start of the ignition sequence, using COMB25. The same temperature fields are obtained with MERGED34 and are thus not shown. (Right): Integrated flame emission $1.5\ ms$ **after the ignition starts obtained numerically (with COMB25) and experimentally.**

qualitatively compared to experimental visualizations (Fig. 6.9 Right) in terms of flame evolution at longer time ($\geq 1\ ms$). In the experiment, the integrated flame emission corresponds to the direct emission from radicals (OH^*, CH^*, C_2^*) integrated along the camera axis. This is compared to the numerical OH mass fraction similarly integrated in the same direction. A good agreement is obtained, in particular in terms of flame velocity in the radial direction.

6.7 Influence of plasma chemistry on spark ignition

In order to quantify the impact of plasma kinetics, the time evolution of the temperature at P_c (symmetry point, see Fig. 6.4) with and without plasma chemistry is displayed in Fig. 6.10 during the first $2\ \mu s$. To explain why plasma kinetics impact so drastically the temperature field, radial profiles (starting from P_c) of temperature and O_2, O, N_2 and N mass fractions obtained with MERGED34 are presented in Fig. 6.11 (top). Absolute differences between results of MERGED34 and COMB25 are also shown in Fig. 6.11 (bottom). $8\ ns$ after ignition starts, the level of O_2 is similar in both simulations even if the temperature is high, close to $8,000\ K$. Indeed, COMB25 contains part of the dissociation reactions such as $H{+}O_2 \rightarrow O{+}OH$ or $OH{+}O_2 \rightarrow HO_2{+}O$. On the contrary, N_2 dissociation is present only in MERGED34. As N_2 dissociation has not started yet, no significant difference in mixture composition is observed explaining the similar temperature with both chemistries. After $20\ ns$, the dissociation process of O_2 is almost completed with MERGED34 as observed in Fig. 6.11: at P_c $[z = 0]$, $Y_{O_2} = 0.003$ and $Y_O = 0.16$. The conversion rate of O_2 into mono-atomic O is around 72 %. On the contrary, with COMB25, the dissociation process of O_2 is incomplete: $Y_{O_2} = 0.02$ at P_c and the O_2-O conversion rate is around 64 %. This is due to the

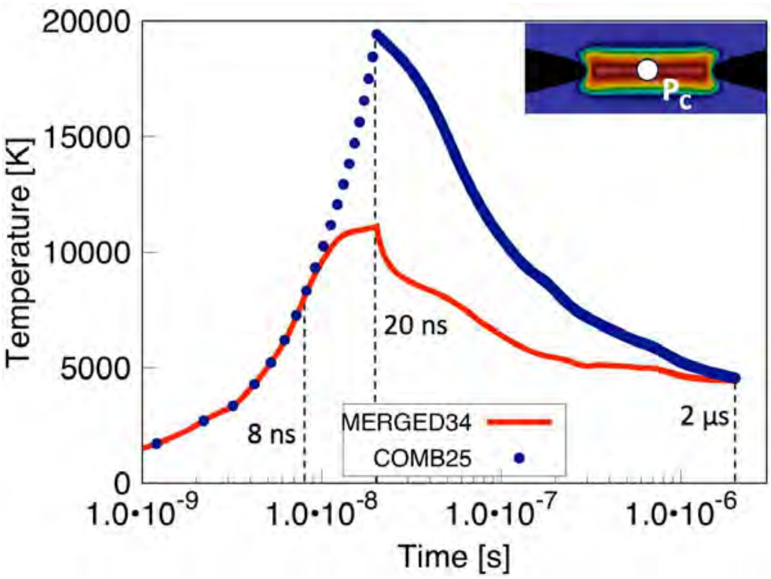

Figure 6.10: Evolution of the temperature at P_c versus time during the ignition sequence using MERGED34 and COMB25.

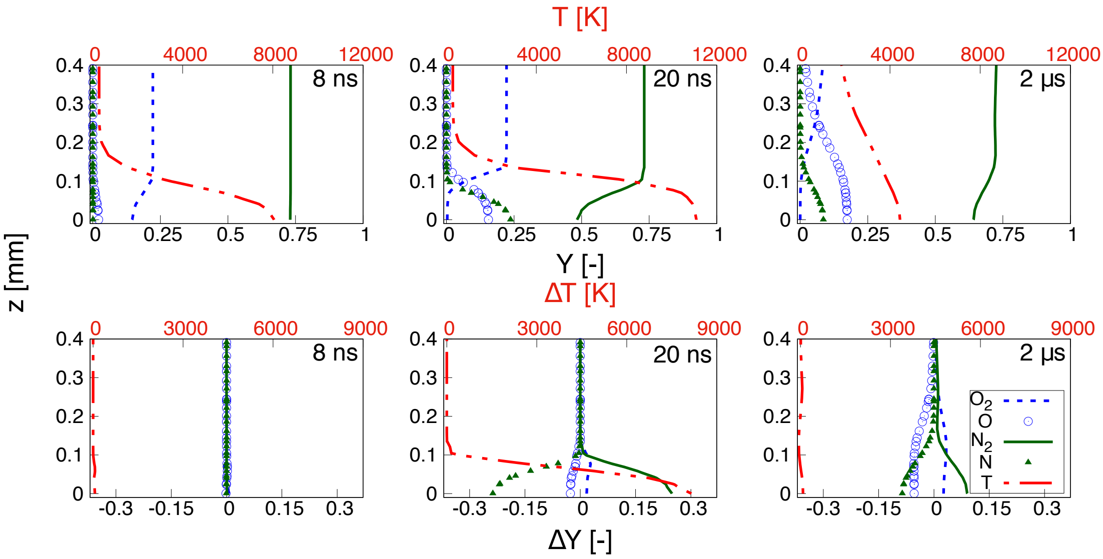

Figure 6.11: Radial profiles (at $x = 0$) of temperature and species mass fraction obtained with MERGED34 at three different instants of the ignition sequence (top) and absolute differences between calculations with COMB25 and MERGED34 (bottom). $\Delta T = T_{COMB25} - T_{MERGED34}$; $\Delta Y = Y_{COMB25} - Y_{MERGED34}$.

simplified O_2 dissociation chemical pathways in COMB25, which produce OH instead of O. Around 36 % of the mass of oxygen atom is stored in other forms such as OH or CO. In MERGED34, where all O_2 dissociation chemical pathways are included, a smaller portion of the mass of oxygen atom, around 28 %, is stored in OH, CO, NO but also O^+ as ionisation reactions appear above $10,000\ K$. Nevertheless, this discrepancy in the O_2 dissociation process remains small. The major difference between the two simulations concerns N_2 dissociation that is totally ignored in COMB25 and that starts around $7,500\ K$. More than 20 % of the N_2 mass is transformed in N after 20 ns with MERGED34. As dissociation and ionisation reactions are strongly endothermic, neglecting this kinetic activity in COMB25 leads to a higher temperature ($19,200\ K$ compared to $11,100\ K$ with MERGED34) at P_c at the end of the breakdown. This thermal difference has a direct consequence on the mechanical effect: the shock amplitude is much higher with COMB25 ($P_{max} = 84\ bar$) than with MERGED34 ($P_{max} = 60\ bar$). At 2 μs, the exothermic recombination of N_2 is almost completed and the radial profiles of species mass fractions in both simulations are again very close leading to similar temperature levels ($\approx 4,500\ K$) at P_c. From this moment, plasma effects become negligible again as temperature is too low to activate plasma reactions.

The impact of plasma chemistry on the heat release during ignition is shown in Fig. 6.12. Until the end of the breakdown, temperatures are very high with mostly endothermic reactions, so that only the negative heat release contribution is displayed in Fig. 6.12 a. At later times, exothermic combustion reactions occur and only the positive heat release contribution is displayed in Fig. 6.12 b. After 20 ns (i.e. at the end of the breakdown), the negative heat release is strong in the region heated by the energy deposition with MERGED34, indicating strong dissociation or ionization reactions. As already discussed, negative heat release is also present but lower using COMB25. After the end of the breakdown, the temperature starts to fall rapidly. At 32 ns, i.e., 12 ns after the end of the breakdown, the order of magnitude of negative heat release in the inter-electrode region has been reduced by a factor 100 showing that endothermic reactions have stopped. After tens of nanoseconds, first exothermic reactions appear. Two zones of reaction are highlighted in Fig. 6.12 (b): i) a zone of exothermic reactions around the energy deposition region, only present with MERGED34. This zone corresponds to molecule recombinations during the temperature drop following the breakdown phase. ii) An outer envelop of exothermic reactions, similar in both simulations. This positive heat release corresponds to the propagating flame created by the runaway of combustion reactions triggered at the border of the energy deposition zone by the hot gas kernel. Indeed, at this position, the temperature elevation is moderate ($1,000\ K < T < 2,000\ K$), too low to activate plasma chemistry but high enough for the mixture to burn.

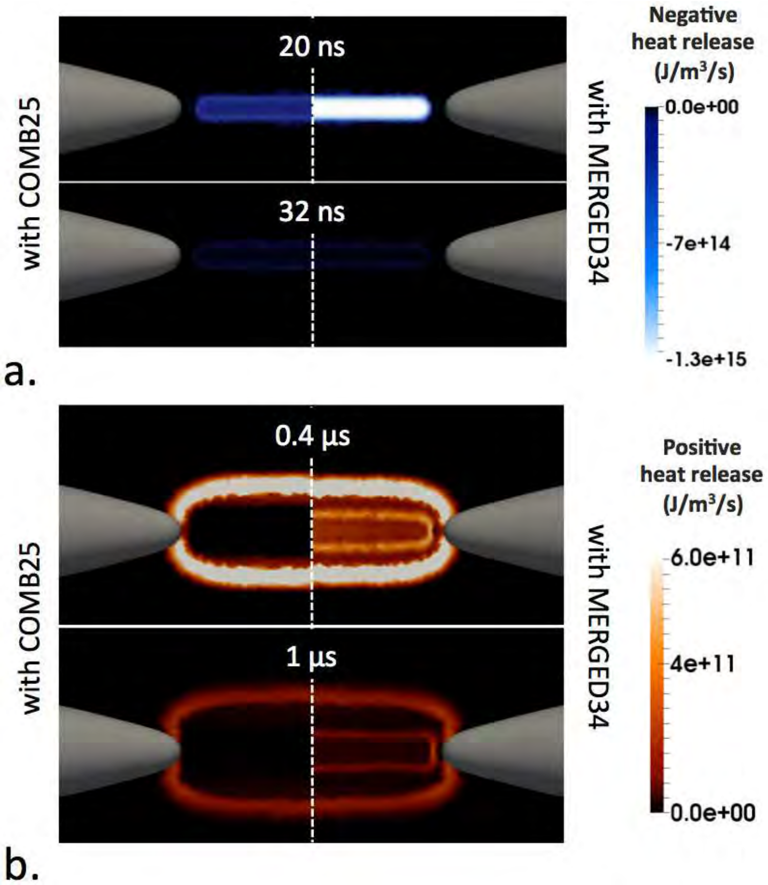

Figure 6.12: Fields of negative (a) and positive (b) heat release at different instants of the ignition sequence with the kinetic schemes COMB25 (left halves) and MERGED34 (right halves).

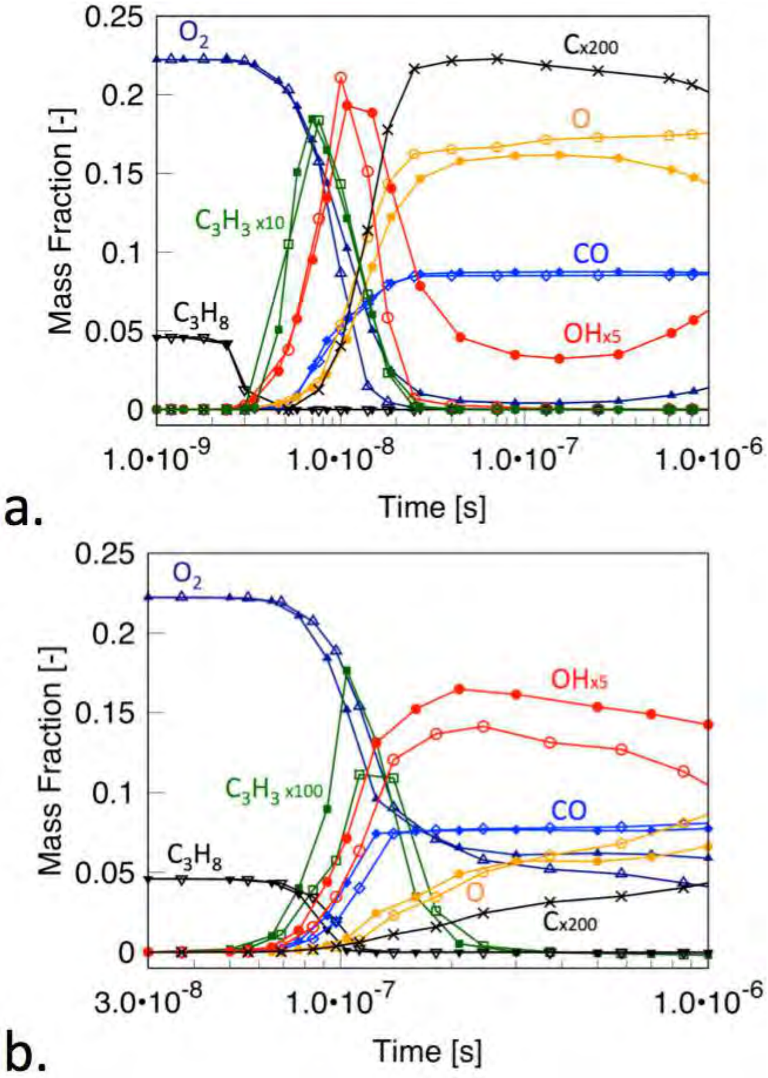

Figure 6.13: Evolution of relevant species mass fractions over time at points P_c (a) and P_u (b). P_u is located $0.31\ mm$ above P_c in the radial direction, see Fig. 6.4. Filled symbols are for COMB25 and empty symbols for MERGED34. Species C is only present in MERGED34.

Figure 6.13 provides a more detailed analysis of the flame initiation at points P_c and P_u (respectively in the center and just above the energy deposition zone, see Fig. 6.4). At P_c, combustion starts very rapidly ($2-3$ ns) in a perfectly mixed reactor regime and C_3H_8 is fully consumed after around 5 ns, i.e. before the activation of plasma chemistry. As a consequence, even though plasma kinetics have the largest thermal impact at P_c, they have no impact on the fuel consumption as shown by the two similar evolutions of the C_3H_8 mass fraction. In fact, the whole oxidation process is similar as evidenced by the evolutions of other species, such as C_3H_3. Differences on radical species appear later, after 10 ns, when temperature is high. As already explained, the O-OH balance is not well described by COMB25, but at this time, the local combustion is totally completed so that it is not affected by these radical differences. The contribution of the dissociated species C, ignored by the COMB25, is also marginal.

At point P_u where combustion occurs in a propagating premixed flame regime, discrepancies are also small. O and C mass fractions tend to increase after the flame passage as temperature rises slowly by diffusion from the energy deposition zone. Conversely, remaining O_2 progressively decreases due to dissociation reactions. The main impact of plasma kinetics is however observed at P_u: the over prediction of OH and O mass fractions causes slightly earlier combustion (see C_3H_8 and O_2 profiles). As P_u is still in a high temperature plasma zone, the slight difference on the O-OH balance is also visible.

Plasma reactivity during ignition is then proven true, but limited in time and space. Its influence on the flame initiation is extremely small: the initial position of the flame kernel observed in Fig. 6.12 (b) is hardly modified by plasma chemistry. Thus, no significant difference in temperature fields is observed with or without plasma chemistry after tens of microseconds: the flame propagation speed and direction are similar and the flame appears to be independent of plasma reactions.

6.8 High temperature Energy Deposition model for LES: A new methodology

Results of this section can be particularly useful to derive spark/laser ignition models in the context of LES. The standard Energy Deposition (ED) model [151] reviewed in Sec. 5.5.2 is interesting to mimic ignition by recovering a kernel of size comparable to experiments hundreds of microseconds after ignition. But the early phase of ignition is totally ignored. On the contrary, the 2-step Energy Deposition model presented in Sec. 6.2 allows to capture many important features of spark or laser ignition. For instance, the strong shock wave after breakdown and induced convective motion influencing the initial flame position and propagation velocity are accounted for. Species dissociations and recombinations are also recovered as the high density breakdown energy deposition is simulated.

Of course, applying the 2-step Energy Deposition model in LES ignition simulations of realistic combustor designs is still out of reach considering the very refined grid and short time-step required. However, in a first approach, it is possible to simply adapt the standard 1-step ED model to encompass more early-time effects. As demonstrated in Sec. 6.7, the influence of the plasma kinetics on the flame initiation is very limited making the use of a combustion-plasma scheme useless in a LES context. Analytically reduced chemistries containing O_2 dissociation such as COMB25, are complex enough for such studies to recover the main effects of radicals creation on flame initiation. To recover other early-time effects (very high temperature just after breakdown, shock wave, induced convective motion influencing the flame kernel), the 1-step formalism of the standard ED model is kept but the energy is deposited in a much smaller volume and in a much shorter time. This new methodology is called ED_HT (Energy Deposition for High Temperature). It must be clarified that the objectives of the ED and ED_HT models are very different. The ED model is a convenient way to circumvent the complex early phase of ignition and focus on larger time scales. The ED_HT model intends to describe the early phase of ignition by simplifying only proven unimportant features on the flame initiation. Thanks to the much shorter deposition time scale, the ED_HT model allows for example to account for the early flame kernel/turbulence interactions that are sometimes decisive for the ignition outcome.

In the standard ED model, the input energy is imposed to respect energy transfer efficiencies in agreement with the literature ($10 - 30$ % efficiencies). It accounts in particular for energy losses by the shock wave [78, 86, 87, 88, 89], a phenomenon which is not explicitely modeled with this approach. With the ED_HT model, a shock wave is actually created due to the denser energy deposition. Its strenght is directly linked to the time and space scales chosen for the energy deposition (but always lower than that of a real spark-induced shock wave). The input energy with ED_HT should thus be greater than with the ED model because some of the energy lost by the shock wave can be explicitely simulated with ED_HT, instead of being fully modelled with ED. Besides, energy transfer efficiencies must still account for other sources of neglected losses such as thermal conduction at electrodes in the context of spark ignition, or radiation. The much smaller energy deposition volume and much shorter deposition time lead to very high temperatures just after breakdown ($T > 10000\ K$), as found in the literature. Therefore, viscosity and thermal conductivity of the mixture should be derived using adequate models such as the D'Angola law [19]. Indeed, as previously said, classical viscosity laws such as the Sutherland law [160] or power law do not behave correctly as they don't account for species dissociations occuring above 3000 K. All thermodynamic properties can be extracted from the reference NASA database [135]. If necessary, extrapolations can be performed to obtain species properties at high temperatures reached in the LES calculation.

6.9 Conclusions

Two Analytically Reduced Chemistries along with an appropriate 2-step Energy Deposition model have been derived to study the impact of plasma kinetics during ignition using DNS of propane-air ignition in an anode-cathode configuration. The importance of the ED model has been highlighted on both non-reacting and reacting cases: the short temporal and spatial scales of spark ignition should be reproduced by the model to correctly catch initial flame position and propagation velocity. The impact of plasma chemistry on the mixture temperature and composition is clearly demonstrated during the first microseconds of ignition, significantly lowering the temperature in the narrow energy deposition zone between electrodes by way of endothermic dissociation reactions. However, the contribution of plasma chemistry to combustion initiation is marginal as most radical production at high temperature appears after fuel oxidation starts, and the increase of radicals in the plasma is not sufficient to modify combustion chemistry. Nevertheless, results show that the accuracy of the chemical description of combustion is of prime importance to catch the correct ignition delay time and initial flame kernel propagation. In this context, Analytically Reduced Chemistries such as COMB25, in particular containing O_2 dissociation, represent a good compromise between accuracy and cost and are a promising approach to study complex chemical phenomenon in flames.

Considering these results, an improved version of the standard 1-step ED model has been proposed in order to reproduce the most important features of flame initiation in the context of LES simulations. This ED_HT model will be used in Chap. 8 dedicated to LES of two-phase ignition of the KIAI single burner.

In addition to these results, and as a perspective to the DNS presented above, the PLASMA38 scheme has also been coupled to an ARC dedicated to n-heptane/air oxidation in order to demonstrate the feasibility of two-phase spark ignition simulations including a detailed plasma kinetics. This simulation is illustrated in Fig. 6.14. The n-heptane/air mixture ($\phi_g = 0.5$, $\phi_l = 0.5$) is initially at rest and at atmospheric conditions. Fuel droplets are uniformly initiated in the domain with a constant initial diameter $d_p = 15\ \mu m$. A lagrangian formalism is used to describe the evolution of the dispersed phase. Figure 6.14 shows a field of fuel mass fraction with droplets coloured by their diameter. This first pilot simulation has proven its potential to recover some important features of spark ignition in mists of fuel droplets. For instance, droplet

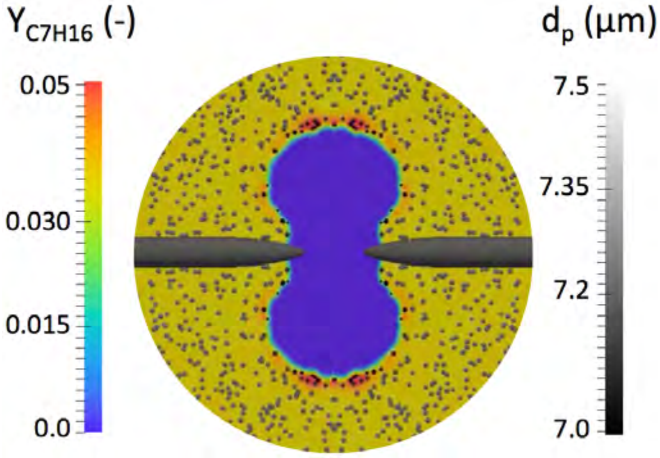

Figure 6.14: Ignition of an n-heptane/air mixture at atmospheric conditions ($\phi_g = 0.5$, $\phi_l = 0.5$). Fuel droplets are uniformly initiated in the domain with a constant initial diameter $d_p = 15\ \mu m$.

entrainment by induced inward flow along electrodes, droplets accumulation ahead of the flame front, and pre-evaporation of the mixture by the shock-induced thermal elevation are found. Some phenomena such as droplet deformation or splitting [88, 125] are of course not recovered and would require further model developments. Another essential perspective would be to study ignition in turbulent conditions, as radical species transport after ignition could lead to new conclusions.

Part III

Flame growth and propagation towards the nearest injector

Chapter 7

Literature review

Contents

7.1 Stochastic behaviour of ignition 114

7.2 Local competition between flammability and turbulence . . 115

7.2.1 Early laminar phase 115

7.2.2 Fully turbulent regime 116

7.2.3 Flame growth in spray mists 118

7.3 Kernel evolution in recirculating flows 119

7.3.1 Premixed flows 120

7.3.2 Non-premixed flows 123

7.3.3 Spray flows 123

7.4 Ignition probability prediction models 126

7.4.1 Models based on properties at the spark position 126

7.4.2 Models based on kernel trajectory 128

7.5 Conclusions 130

Kernel growth and propagation towards the nearest fuel injector is the second phase of ignition occurring in aeronautical combustors following the flame kernel generation investigated in Part. II. The objective of this chapter is to propose a literature review on this phase of ignition.

The outcome of the first phase of ignition is directly linked to both the igniter properties and the local flow properties. The kernel is often generated by placing the heads of the spark plug in a flammable environment. Aeronautical spark plugs deliver a huge amount of energy to ensure the formation of a flame kernel. This phase is therefore less crucial than the flame growth phase that presents a stochastic behaviour due to the highly turbulent non-premixed flow (see Sec. 7.1). Flame extinction might happen at any time until the flame is stabilized due to the local competition between flammability and turbulence (see Sec. 7.2). To obtain a successful flame growth phase, the initial kernel should survive and grow while being convected by the turbulent flow (Sec. 7.3) in the combustor until reaching its stabilized position in the chamber. Thus, from an initial sparking position, the flame faces very variable flow conditions (mixture composition and turbulence) depending on its stochastic trajectory. As a consequence, being able to predict numerically the ignition probability P_{ign} of a given spark is therefore very challenging and is the focus of Sec. 7.4.

7.1 Stochastic behaviour of ignition

According to Mastorakos [121], an inherent property of forced ignition is its random character, each ignition sequence being different from another due to many sources of stochasticity. The level of stochasticity increases with the complexity of the flow surrounding the spark:

- In perfectly premixed quiescent conditions, randomness comes from the igniter. The targeted energy a spark plug should provide is subject to fluctuations from one spark to the other due to variable losses in the electrical circuit. Shot-to-shot variations in laser energy are also reported [79]. In both cases, an energy below the MIE can can be deposited, which may lead to an ignition failure.

- In a non-premixed quiescent or laminar flow, fluctuations of equivalence ratio must be considered. At the same sparking position, the mixture could be flammable at one time but under the lean flammability limit just after, when a pocket of air crosses the ignition region for instance. This brings stochasticity for the early kernel creation phase (see Sec. 5) but also for the kernel growth phase as a kernel might be initiated in a flammable region but then propagated until reaching a non-flammable region potentially leading to late extinction. In order to characterize this randomness, Birch [169] introduced the Flammability Factor F_f defined as

  $$F_f = \int_{z_{lean}}^{z_{rich}} P(z) dz \tag{7.1}$$

  with $P(z)$ the PDF of mixture fraction. F_f represents the probability of the mixture to be inside the limits of flammability over time. Spray ignition is similarly affected by the local fluctuations of gaseous mixture fraction but the randomness of local droplet properties (diameter, velocity, liquid volume fraction) are also necessary [124] to accurately characterise F_f. The Flammability Factor is often strongly correlated to P_{ker}, which is only the probability of generating a flame kernel. P_{ker} differs from P_{ign} which is the probability of igniting the whole combustion chamber.

- Finally, in non-premixed (spray) turbulent flows, velocity fluctuations must also be taken into account [92]. First, local turbulence may increase the flame surface enhancing its consumption speed. However, too strong stretch may on the contrary quench the flame. The limit between flame enhancement and flame shrinking mainly depends on the relative size of the kernel compared to the turbulent structures it faces [170] but also depends on the local flammability. This competition between both mecanisms has been mainly investigated in simple infinite

> domain, as described in Sec. 7.2. Velocity fluctuations may also lead to different kernel trajectories, starting from the same ignition position. Several studies on kernel growth in internal combustion engines [171], jet configurations [151, 172] and recirculating flows have been carried out to understand the link between kernel convection and ignition probability. Section 7.3 focuses on recirculating flows as they are more representative of the flow in aeronautical combustors.

In summary, in the most complex situation of spark ignition in a spray turbulent environment, kernel creation is subject to randomness so $0 \leq P_{ker} \leq 1$. Once initiated, the kernel trajectory may considerably vary so that the kernel may encounter very different conditions in terms of flammability and turbulence level. Late quenching of the kernel or full ignition might thus occur ($P_{ign} \leq P_{ker}$).

7.2 Local competition between flammability and turbulence

7.2.1 Early laminar phase

In the early phase of flame growth, which intersects with the creation phase (see Sec. 5), the kernel expansion is laminar because of the short length scale of the kernel and the short time scale. Following a spark ignition or a laser ignition, the kernel has an ellipsoidal shape close to a spherical shape. In this laminar phase, the kernel is stretched only by curvature effect (no tangential strain contribution) [5]:

$$\kappa = \frac{2}{r_k}\frac{dr_k}{dt} \tag{7.2}$$

with κ the flame stretch and r_k the kernel radius. With this stretch evolving proportionally to $1/r_k$, gradients of fuel mass fraction and temperature appear near the flame front. Depending on the competition between heat and species diffusivity, stretch can enhance the flame consumption speed S_c if flame cooling is slower than fuel feeding or reduce it otherwise. The fuel based Lewis number $Le_F = \lambda/(\rho C_p D_F)$ comparing heat diffusivity $\lambda/(\rho C_p)$ and fuel diffusivity D_F is thus important. For $Le_F < 1$, flame consumption speed is increased by increasing stretch, and the contrary is observed for $Le_F > 1$. During this short phase, turbulence has no effect on the flame, contrary to the mixing properties. For non-premixed mixtures, the flammability factor F_f is crucial. Misfires can be found in overall flammable mixtures because local non-flammability can be found, even rarely. P_{ker} has then been shown to be correlated to F_f even if not perfectly equal [92]. An already developed kernel can also be quenched if at some point a non-flammable pocket of fresh gases crosses the front. Even when staying inside the flammability limits, mixture inhomogeneities have an impact on the initial laminar

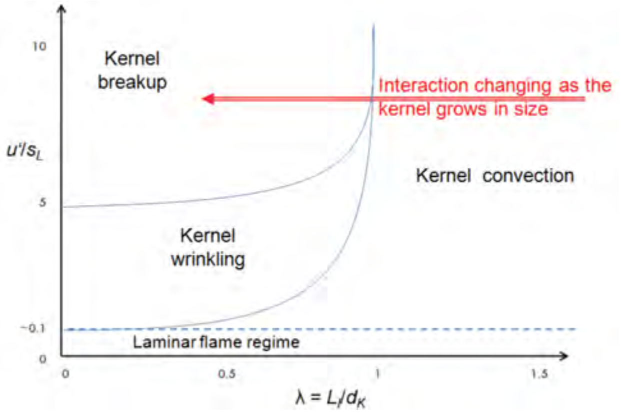

Figure 7.1: Turbulence kernel interaction regime map as proposed by Reddy et al. [174].

kernel growth. In a stratified flow where $z_{lean} < z < z_{st}$, heat release inhomogeneities are observed [173] and lead to local stretch of the kernel, enhancing its development compared to a kernel in a premixed mixture at the same global equivalence ratio. For rich cases ($\phi_{glob} > 1$), a triple flame behaviour is recovered and drives the kernel growth rate [121]. The stretch induced by local heat release inhomogeneities is however negligible compared to the aerodynamic stretch that the flame progressively faces while growing. Initially, the kernel size is very small so all turbulent scales are larger than the kernel size. At this moment, the kernel is only convected by eddies without much wrinkling of the front as shown on the right part of the turbulence kernel interaction regime map proposed by Reddy et al. [174] and shown in Fig. 7.1. As its size increases, the kernel starts interacting with smaller (relatively to its size) turbulent scales that may wrinkle the flame front. Akindele et al. [103] investigated the transition from laminar to turbulent regimes by characterizing the influence of turbulence on the kernel with an effective thermal diffusivity making the transition between the laminar and fully turbulent regimes:

$$D_{turb} = 0.44u'l_t \left(1 - \exp\left(-\frac{u't}{0.44l_t}\right)\right) \tag{7.3}$$

with u' and l_t the turbulent intensity and turbulent integral length scale respectively.

7.2.2 Fully turbulent regime

Turbulence can then have a positive impact or be detrimental to kernel expansion depending on its intensity and characteristic length scale [174]. This kernel-turbulence interaction is similar to flame-turbulence interaction that has been widely studied in the literature [5, 175]. Moderate turbulent intensity increases the flame surface area and consequently the consumption speed. This is referred as the kernel wrinkling regime

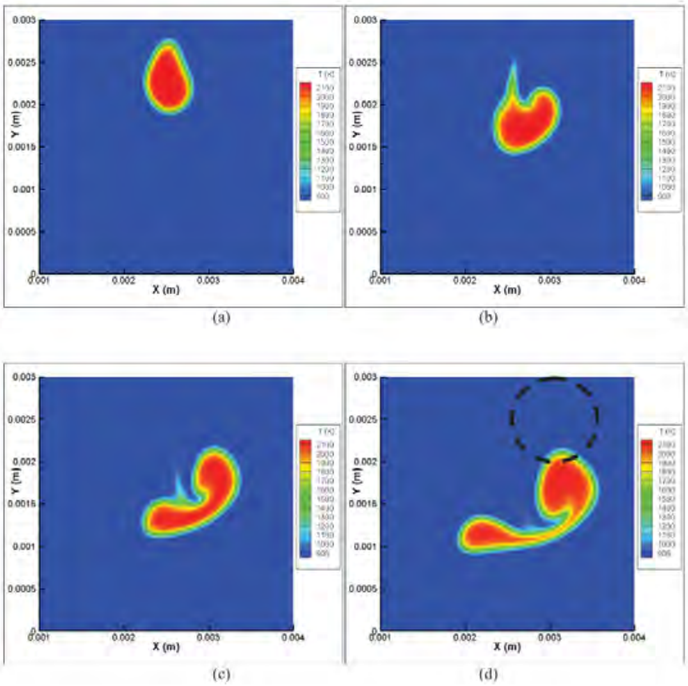

Figure 7.2: Interaction of a flame kernel with an eddy of length scale comparable to the kernel size [174].

in the diagram of Reddy et al. [174]. However, for ignition, turbulence has often a detrimental impact on kernel growth, leading to local or global quenching. Too main extinction mechanisms can be distinguished:

- Even at low intensity, large turbulent structures can wrinkle the flame surface up to a point where the kernel can be dislocated by a local front quenching creating smaller independent sub-kernels [170]. This is illustrated in Fig. 7.2 where a kernel of characteristic size equivalent to the integral length scale is broken in two pieces. As small kernels are more prone to thermal diffusion, extinction of these sub-kernels are likely to occur.

- Small vortices (small enough to enter the preheat layer of the flame but too large to enter the reactive layer) are responsible for another extinction mechanism investigated by Jenkins et al. [176] who performed 3D DNS of kernel propagation in a turbulent flow and analysed their results in terms of contribution of stretch to the weighted flame displacement speed S_d^* introduced by Echekki et al. [177]. The main conclusion is that the displacement speed is found to be almost not correlated to tangential strain but negatively correlated to curvature created by small eddies as shown in Fig. 7.3. Negative values of S_d^* are even found, which represents regions where the flame thickness is locally increasing, potentially leading to extinction as heat is diffused away from the reaction zone faster than it is

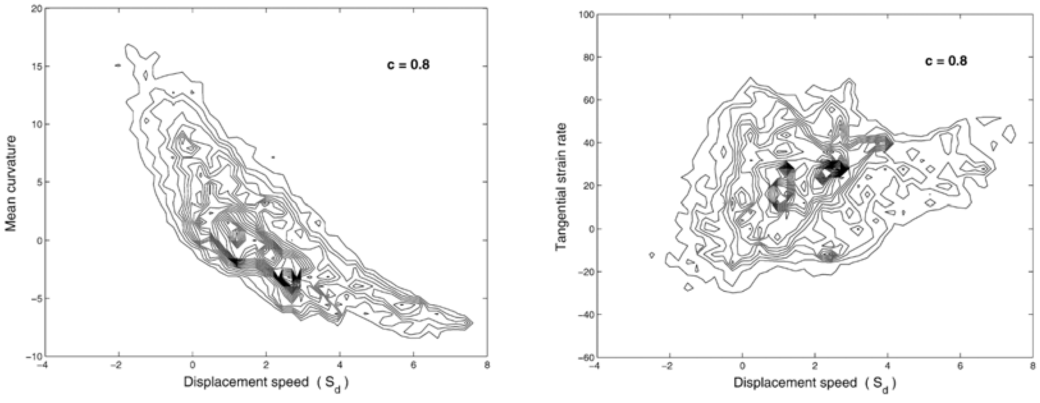

(a) (b)

Figure 7.3: Correlation of displacement speed S_d on a kernel front isosurface at $c = 0.8$. (a) Joint PDF of S_d and mean curvature. (b) Joint pdf of S_d and tangential strain rate [176].

produced.

For extremely high turbulent intensities, flame quenching is independent of the local mixture fraction. However, the impact of turbulence may be affected by the local mixture fraction in the case of moderate turbulence intensities. This has been demonstrated by Abdel-Gayed [178] in premixed flow, rewriting the Karlovitz number as

$$Ka = 0.157 \left(\nu \frac{u'^3}{l_t} \right)^{1/2} \frac{1}{{S_l^0}^2} \tag{7.4}$$

with u' the turbulent velocity magnitude, ν the kinematic viscosity, l_t the integral length scale and s_l^0 the laminar flame velocity. Abdel-Gayed considered a large number of experiments and highlighted a critical Karlovitz number $Ka_c = 1.5$ common to all experiments above which quenching occurs. The quenching limit is then function of the local equivalence ratio due to the use of S_l^0 in the definition of Ka. For near stoichiometric mixtures, turbulence intensity can be much higher without leading to flame quenching. Although this has been shown in a premixed context, comparing turbulent to chemical time scales is still relevant in non-premixed gaseous and spray flames so this general trend stays valid even if of course, Ka_c may vary.

7.2.3 Flame growth in spray mists

Recent studies focused on the ignition of quiescent or turbulent mists of fuel droplets. As for non-premixed gaseous ignition, early flame creation is almost only controlled by fluctuations of the overall equivalence ratio at the sparking location [124]. Spray ignition is often characterized by an initial non-flammable gaseous mixture as fuel is mainly liquid. Wandel et al. [179] showed that depending on the initial energy given to the mixture E_{ign}, different scenarii may happen. With too low energy, droplet evaporation is insufficient to reach the lean flammability limit. Then the energy is directly diffused so that ignition never starts. With higher energy, a small flammable region is created and a flame kernel is initiated. However, the heat release rate is not enough to compensate both thermal diffusion and surrounding droplet evaporation. Thus, quenching occurs ultimately, in particular if fuel is available as large droplets because they would require more energy to be evaporated. Finally, with an important initial energy deposition, a large kernel is generated that releases enough energy to evaporate droplets in front of the flame and allows a sustainable flame propagation. Droplet evaporation can then be a controlling parameter only at early time when the kernel is still weak. Neophytou et al. [180] also investigated the growth of a flame kernel in a turbulent droplet-laden mixing layer with DNS. The mixture was globally rich ($\phi_{glob} = 2$) leading to the creation of an edge flame following spark ignition. The contribution of stretch to the weighted flame displacement speed S_d^* (negative correlation with curvature) was shown to remain valid for spray flames. Moreover, the triple flame displacement speed was of the order or lower than the laminar flame speed of the equivalent stoichiometric gaseous flame. This means that flame propagation is mostly due to the turbulent motion of the flow.

Esclapez [1] summarized the three main regimes of kernel quenching in Fig. 7.4. Regardless of the turbulence level, kernel extinction due to mixture inhomogeneities is possible. Similarly, independently of the local equivalence ratio, extreme turbulence intensity may lead to flame quenching by the interaction of the kernel with large scale eddies as well as with vortices smaller than the kernel size. For moderate turbulent intensities, the local kernel expansion arises from the competition between mixture fraction and turbulence. According to Mastorakos [121], the regions of highest ignition probability in a combustor are those close to stoichiometry and with weak enough local turbulence. This would correspond to quiescent recirculation zones in typical industrial burners. However, if initially located in such favourable zone, the kernel could be convected rapidly to more adverse conditions for flame growth. Understanding potential kernel pathways is then essential to draw the ignition probability map of a given combustor and is addressed in Sec. 7.3.

7.3 Kernel evolution in recirculating flows

In this section, only recirculating flows representative of aeronautical combustors are considered. The incoming air velocity in a typical combustion chamber is much higher than the turbulent flame velocity. To allow 1- a quiescent flame kernel growth, 2- its

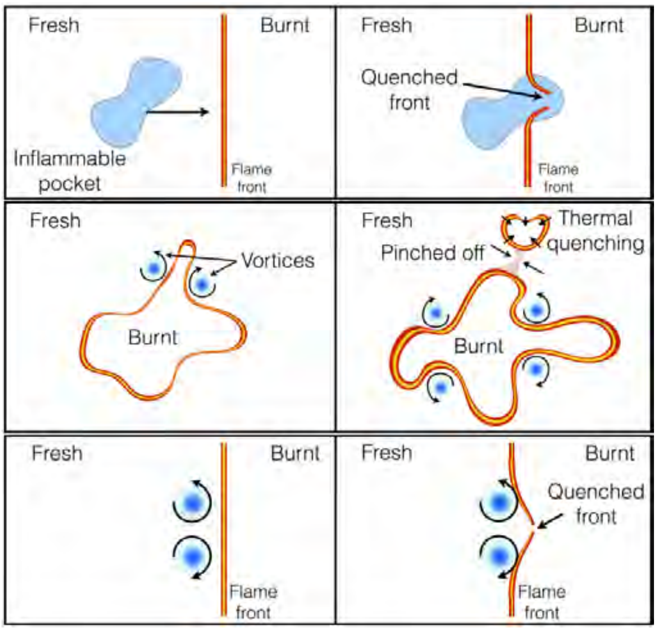
Fresh
Burnt
Inflammable pocket
Flame front
Fresh
Burnt
Quenched front
Flame front
Fresh
Vortices
Burnt
Fresh
Thermal quenching
Pinched off
Burnt
Fresh
Burnt
Flame front
Fresh
Burnt
Quenched front
Flame front

Figure 7.4: Summary of the three main flame kernel quenching mechanisms in non-premixed flows, from Esclapez [1]. (Top) mixture heterogeneity, (middle) kernel fragmentation by large scale turbulence, (bottom) stretch quenching of the flame front by small turbulent structures.

upstream propagation, and 3- its stabilisation at the injector nozzle, combustors are designed to generate both inner and outer recirculation zones as sketched in Fig. 7.5. To do so, the incoming air should have an important radial component induced either by a bluff body or by a swirled injection system. With the latter, often chosen in aeronautical devices, the incoming air also has an important azimuthal component. The high axial velocity Jet Zone (JZ) separates two recirculation zones defined by negative axial velocity: the Inner Recirculation Zone (IRZ) and the Corner or Outer Recirculation Zone (CRZ/ORZ). With such flow topology, kernel trajectories can be various, moreover considering the stochastic nature of turbulent flow.

This section presents the main results of experimental and numerical studies that investigated kernel growth in recirculating flows, often in an attempt to gather local flow properties and potential kernel trajectories to build the ignition probability map of the studied combustor. Premixed, non-premixed and spray ignitions have been studied and results are presented in this order.

7.3.1 Premixed flows

Ahmed [183] investigated experimentally the premixed version of the configuration of Ahmed et al. [181] sketched in Fig. 7.5a. Bach et al. [184] considered the bluff body configuration opened to atmosphere of Kariuki et al. [185]. Cordier et al. [186] used

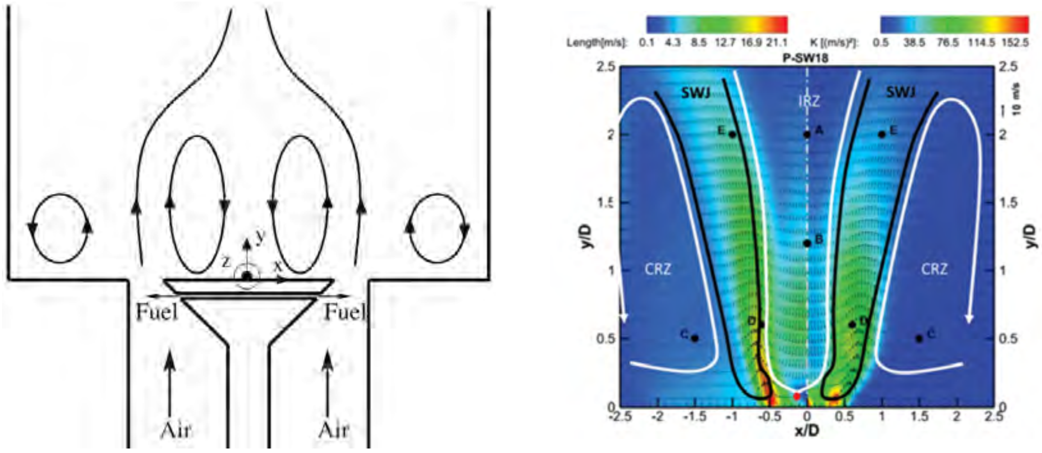

(a)

(b)

Figure 7.5: (a) Bluff body configuration of Ahmed et al. [181]. (b) Swirled configuration of Cordier et al. [182]. Both configurations have been studied in premixed, non-premixed and two-phase conditions.

a premixed swirled confined burner [182] presented in Fig. 7.5b to investigate kernel growth. The three experiments used methane-air mixtures and mainly differ by the burner geometry. Several conclusions were drawn from these studies. First, P_{ign} is correlated to Ka, P_{ign} being high where Ka is small [184]. Second, the mean velocity direction at the sparking position is important as shown by Bach et al and Cordier et al. It has to be in direction of the bluff body to obtain high ignition probability. Moreover, misfire was found to occur when the early flame kernel crossed the shear layer to reach the bottom of the IRZ. Ahmed [183] proposed a sketch of potential spark scenarii, reported in Fig. 7.6a. Whereas no ignition was reported in the CRZ, ignition probability was high in the IRZ. Starting from there, the kernel is convected upstream towards the bluff-body and the flame may then be pushed downstream by the jet. Ignition probability maps were experimentally drawn for the configurations of Ahmed et al. [181] and Cordier et al. [186] and are displayed in Fig. 7.6b (Left) and Fig. 7.7a (Right) respectively. The ignition probability is shown to be high in quiescent recirculation zones and reduces progressively when moving towards the jet zone. Ahmed also reported the detrimental effect of increasing the bulk inlet air velocity as it increases the turbulence level, shrinking the ignitable region. Finally, Esclapez [1] performed 10 LES of ignition at three different positions in the KIAI premixed configuration of Cordier et al. [182] and also evidenced a large range of kernel trajectories. Ignition failure was found to be induced by too strong flame/turbulence interactions that dislocate the kernel and leads to its quenching by diffusion.

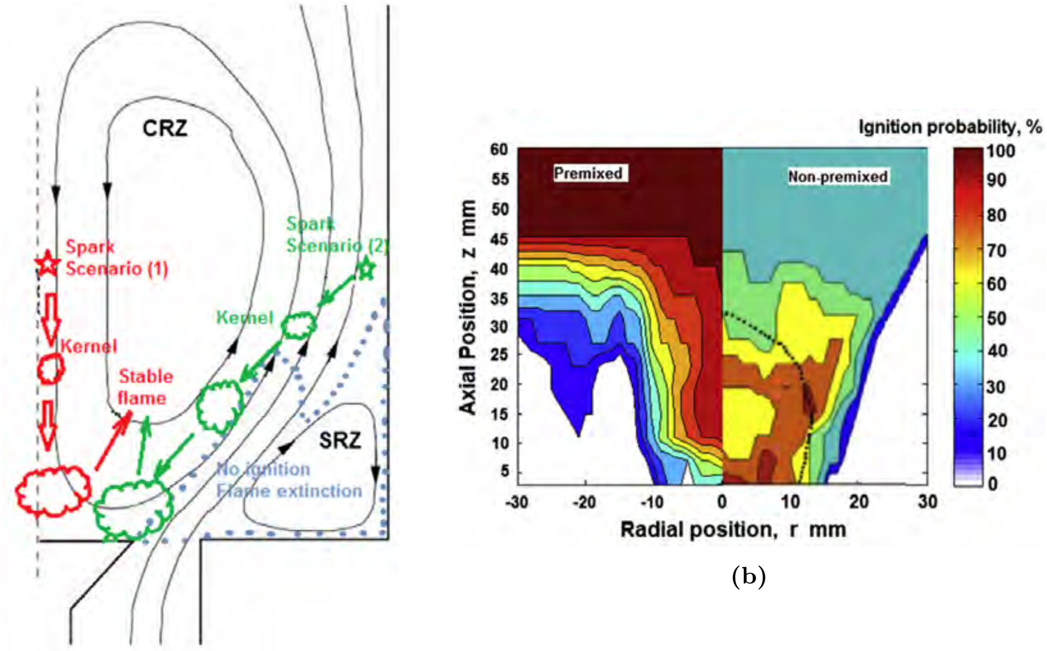

(a)

(b)

Figure 7.6: (a) Sketch of potential spark scenarii in the premixed configuration of Ahmed et al. [181]. (b) Comparison of ignition probability map in premixed and non-premixed cases extracted from Ahmed [183].

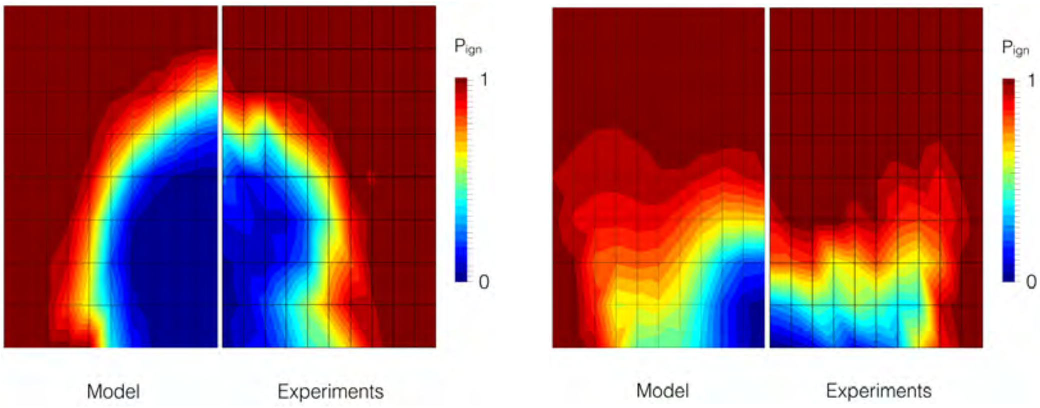

(a)

(b)

Figure 7.7: Ignition probability maps in the configuration of Cordier et al. [182]. The comparison between the experimental probability map and prediction by the numerical model of Esclapez [1] is shown for both (a) premixed and (b) non-premixed configurations.

7.3.2 Non-premixed flows

The two configurations from Ahmed et al. and Cordier et al. were also studied in non-premixed conditions to further study the impact of mixture inhomogeneities on ignition probability. In both configurations, reporting the ignition probability map for premixed and non-premixed cases (Fig. 7.6b left & right for Ahmed and Figs. 7.7a right & 7.7b right for Cordier) highlights the impact of fuel heterogeneities on ignition. In low strain rate regions, high ignition probability comes with near stoichiometric mixture while in high turbulence regions, this detrimental effect controls the outcome of ignition regardless of the mixing properties at these locations. Ahmed et al. [181] distinguished three scenarii of failure: 1- No spark generation, 2- flame kernel initiation followed by rapid flame convection downstream and blow off and 3- flame propagation and stabilization at the bluff body followed by global flame extinction. This confirms the necessity to study kernel trajectories to be able to predict kernel convection in unfavourable zones. Moreover, P_{ign} correlated quite well with the flammability factor map F_f even if ignition could occur when sparking in low flammable region. Such cases are explained by a kernel that survives enough (if low turbulence is encountered) while being advected in a much more favourable zone to growth.

Two LES studies of the non-premixed configuration of Ahmed et al. [181] were also performed: Triantafyllidis et al. [187] performed 6 LES from two positions with either one-step or detailed chemistry plus a Conditionnal Moment Closure (CMC) model and Subramanian et al. [188] used tabulated chemistry plus a presumed subgrid-scale (SGS) probability density function model to perform 20 LES from 5 spots but on quite coarse meshes. The stochastic behaviour of ignition was recovered by Subramanian et al. [188] as they showed that ignition success or failure could occur when sparking at the same position, only depending on the initial flow condition, leading to two different initial kernel trajectories. Both numerical studies recovered the main mechanisms and kernel trajectories. For instance when sparking from the CRZ, the flame initially moves towards the bluff-body, then to the shear layer and eventually re-enters the CRZ. Triantafyllidis et al. [187] also pointed out the need to use detailed chemistry. If one-step chemistry allowed to obtain a qualitative agreement on ignition behaviour, the flame growth rate was only recovered with detailed chemistry.

7.3.3 Spray flows

Finally, several studies aimed to get closer to real aeronautical conditions by employing liquid fuel injection systems. An academic swirled spray burner called MERCATO, equiped with a kerosene pressure swirl atomizer, was set up at ONERA and studied

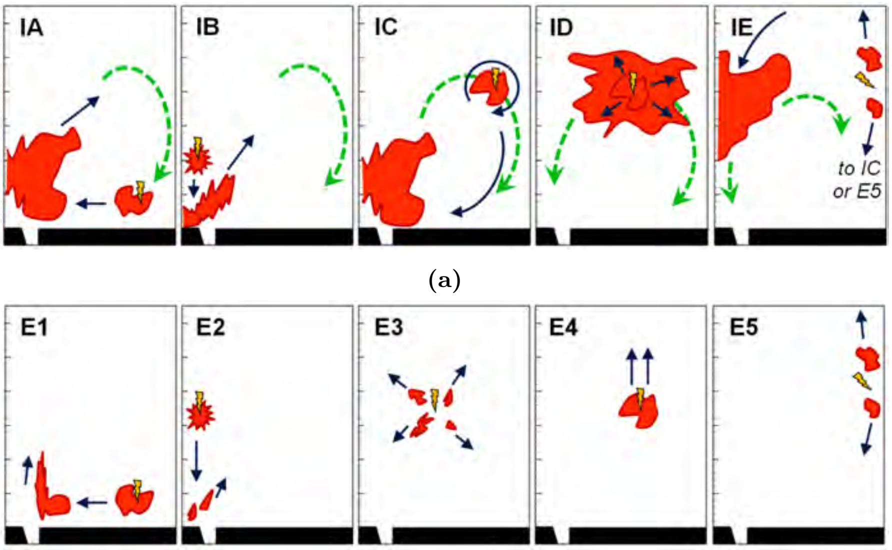

(a)

(b)

Figure 7.8: Sketch of the main mechanisms of (a) successful and (b) failed ignition sequences observed in the KIAI-Spray configuration of Marrero-Santiago [2]. Black arrows represent initial kernel convection. Green dashed arrows illustrate later flame growth direction.

experimentally [189] and numerically [139, 140, 189, 190] using RANS and LES simulations. The same kernel trajectories as in Ahmed et al. [181] were found. Marrero-Santiago et al. [191, 192] recently adapted the gaseous KIAI configuration of Cordier et al. [182] to be used with a n-heptane liquid pressure swirled injector in ultra lean conditions $\phi_{glob} = 0.61$. In order to avoid liquid fuel film formation on the combustor walls that would prevent any direct flame visualisation, air and liquid were pre-heated, also limiting the impact of liquid phase on ignition behaviour. Marrero-Santiago [2] proposed a classification of mechanisms leading to either ignition success or failure, shown in Fig. 7.8. A large variety of trajectories was found: the kernel could be trapped by the ORZ, pushed downstream by the JZ, or even divided in two parts that each follows its own trajectory. This explains why investigating ignition probability by only considering local flow properties [193] is inappropriate even if P_{ign} is shown to be closely related to F_f or to a map of turbulent kinetic energy. Indeed, the experimental ignition probability map provided by Marrero-Santiago, shown in Fig. 7.9, clearly showed that the highest ignition probability was found in the quiescent and always flammable ORZ while the IRZ with higher turbulence level and a mixture fraction near the lean flammability limit showed very poor ignition performances. A strong gradient of ignition probability was found in the JZ separating the ORZ and the IRZ. High velocities were encountered in the JZ but the spray was also dense, potentially providing a large amount of fuel, favourable to ignition. Letty et al. [194] and Marchione et

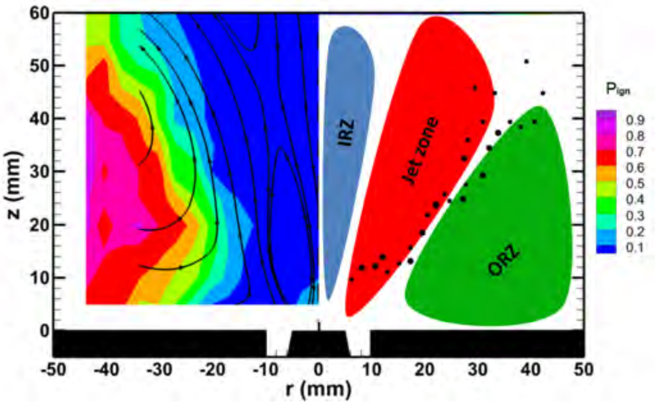

Figure 7.9: (Left) Ignition probability map of the KIAI-Spray (n-heptane-air, $\phi_{glob} = 0.61$) configuration of Marrero-Santiago [2] with streamlines of the mean airflow. (Right) Sketch of the three main zones of the swirled-confined flow.

al. [195] also investigated the adapted version for spray ignition of the configuration of Ahmed et al. [181] using n-heptane providing the experimental ignition probability map shown in Fig. 7.10 (Right). After identifying the same kernel trajectories than in the non-premixed case, Marchione et al. focused on spray ignition, highlighting that when sparking in the spray zone, ignition was eased with smaller droplets for the same global equivalence ratio. Besides, highest ignition probability was found in regions where the total (gas+liquid) mixture fraction provided the highest flammability factor. This n-heptane spray burner was also studied numerically by Tyliszczak et al. [196] using a LES/CMC approach. Performing 16 simulations for each one of the 20 positions investigated, numerical ignition probabilities could be compared to experimental ones showing a relatively good agreement even if authors conceded that further developments and validation were needed to improve results.

On more realistic configurations representative of aeronautical combustors, Read et al. [197, 198] investigated experimentally lean-direct-injection gas-turbine combustor while Jones et al. [199] studied a realistic gas turbine sector with LES simulations (subgrid-scale probability density function model, lagrangian formalism for the liquid phase and 4-step global scheme). The same mechanisms of ignition failure than observed in lab-scale experiments were recovered: 1- rapid disintegration, 2- flame irremediably convected downstream, 3- flame split in multiple kernels and 4- no stabilization at injector. However, Read et al. [198] explained that in his work, initial kernel velocities were much less important on ignition outcome than in many laboratory-scale experiments, suggesting that more high-quality measurements in realistic gas-turbine combustion systems were required.

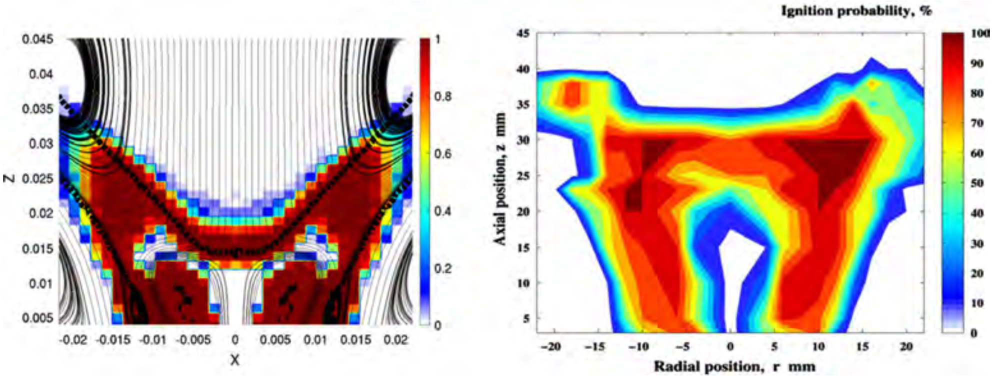

Figure 7.10: Ignition probability maps of the two-phase n-heptane-air ($\phi_{glob} = 0.90$) configuration of Ahmed et al. [181]. (Left) Predicted map of Neophytou et al. [200]. (Right) Experimental map of Marchione et al. [195].

7.4 Ignition probability prediction models

In the design of aeronautical combustors, the position of the spark plug is essential to optimise ignition and re-ignition capacities as shown in Sec.7.3. Performing a posteriori experimental series of ignition sequences for a lot of spark position as in academical apparatus would be too time and money consuming for industrial gas turbines. Thus, engineers try to anticipate the spark plug best position as early as possible in the conception process. Numerical simulations could be used in that way to help predicting the ignition probability map of a given combustor. Two solutions are possible:

- "Brute-force LES": Perform many LES of ignition sequences at each spark position investigated [151, 201]. This method gives the best predictions but is very costly as statistical convergence requires to study a large number of ignition sequences at each position.

- Low order model: Build much faster low-order models that do not require to perform reacting simulations. Only numerical fields extracted from one simulation of the cold flow preceding ignition are used. This promising method has been investigated by many research groups and the different models are described here after.

7.4.1 Models based on properties at the spark position

As it was shown that P_{ker} is closely related to local flow properties at the sparking position [2, 181], a first class of low-order models only uses local properties of the cold flow prior to ignition to obtain a first guess of the ignition probability map. Birch et al. [193] were the first to link the flammability factor F_f to P_{ker}. Eyssartier et al. [202] developed a methodology, called I-CRIT-LES, to encompass more local cold flow information and include spark properties to build an ignition probability map in two-phase single burner configurations. Five successive criteria must be fulfilled to obtain a successful ignition:

- The gaseous mixture at the spark time and position of interest should be flammable.
- The energy transmitted to the gas by the discharge should be high enough to sustain a hot gas kernel until combustion occurs.
- If the two previous conditions are fulfilled, combustion can start. The flame kernel can only grow if the vaporisation of liquid fuel and combustion are fast enough to offset diffusion effects.
- Near the walls, the flame should not be quenched.
- To propagate upward, the turbulent flame speed should be greater than the local flow speed.

Applying these criteria on multiple instantaneous non-reacting solutions allows to obtain a probability map of the combustion chamber. The I-CRIT-LES model was applied on the two phase flow MERCATO configuration [203] showing overall good agreement with the experimental ignition probability map except on the injection axis. Linassier et al. [204] developed a very similar method also based on successive criteria, mainly modifying the kernel growth criterion. Compared to Eyssartier et al. [202], a better estimation of P_{ign} was obtained in the IRZ.

If point-wise models already provide good indication whether ignition is possible or not at a given position, they neglect all mechanisms involving kernel convection, that were shown to be very important in recirculating flows. These models are therefore accurate to estimate P_{ker} but not sufficient for a precise evaluation of P_{ign}. For example, when sparking in a non-flammable mixture, a kernel can be rapidly convected in a flammable region, leading to ignition success. A point-wise low-order model would predict a zero ignition probability at such point. Moreover, a crucial factor of kernel growth is missing in the models of Eyssartier et al. [202] and Linassier et al. [204]: potential quenching of the flame kernel by too high turbulence intensity is not considered. Low-order models accounting for kernel displacement in combustors and introducing a Karlovitz number to account for potential kernel shrinking can account for these two crucial aspects and provide more reliable probability map.

7.4.2 Models based on kernel trajectory

In trajectory-based methods, the kernel is tracked using either conserved scalar as in the work of Wislon et al. [205] or lagrangian particles as for Weckering et al. [206] or Neophytou et al. [200]. An important assumption of all models accounting for kernel trajectory is that they are based on either instantaneous or mean cold flow velocity fields. This means that the flow is supposed to be unaffected by the flame, which is acceptable for small kernels, but becomes wrong when the kernel is too large as burnt gas expansion is known to modify considerably the velocity field. In the SPINTHIR model of Neophytou et al. [200], inspired by the work of Richardon [207], an initial spark volume is imposed in the domain. Flammable cells inside this volume "generate" burning particles than are tracked using a stochastic Langevin model based on a time-averaged non-reacting solution. Particles can extinguish as function of the local Karlovitz number encountered. When a particle arrives in a flammable fresh gas cell, this cell is switched from state "cold gas" to state "burnt gas" and another flame particle is created and tracked. At the end, if the burnt gas volume reaches an arbitrary critical volume, ignition is considered successful. The resulting numerical ignition probability map is compared to the experimental one in a counter flow configuration and in the bluff-body burner of Ahmed et al. [181] operated with methane and n-heptane. As shown in Fig. 7.10 for the burner operated with n-heptane, results are in fair agreement with experiments. The SPINTHIR model has also been recently evaluated in the premixed bluff body configuration of Bach et al. [208] showing good agreemtent on ignition probability maps with the experiment. The SPINTHIR model however shows several weakness. In terms of performance, in order to get a full ignition probability as presented in Fig. 7.10 (Left), a large number of tries should be run to get a reasonable statistical convergence. Moreover, the ignition probability is very dependant on parameters such as the mesh resolution or the arbitrary critical burnt gas volume. Finally, only two particle states (burning state or extinguished) are possible, meaning that when a flame particle reaches a non-flammable cold gas cell, the flame extinguishes and the cell stays in "cold state". Soworka et al. [209] improved this last point by adding a third possible state: "hot gases". Then, when a flame particle reaches a non-flammable cold gas cell, its state is switched to "hot gases" state and may further ignite neighbouring flammable cold cells. In order to avoid any dependence on grid resolution, Cordier et al. [210] also extended the SPINTHIR model [200] by only considering flame particles. Kernel particles are first created in an arbitrary spark volume, and then tracked using a Langevin model based on instantaneous cold flow velocity fields of the chamber considered. To model flow stochasticity, a new velocity field is randomly picked from the experimental database regularly. As in the SPINTHIR model, particles facing a too high local Karlovitz number extinguish to account for possible quenching. A kernel volume is associated to each particle. The kernel growth rate is then calculated as function of the local turbulent flame speed. When the size of the kernel reaches the local integral length scale, the particle is divided in two particles conserving the initial flame volume. Particle evolution is tracked in time and criteria on their number and position in the chamber at the end of the calculation is used to obtain the ignition probability. This model has been compared to the experimental ignition probability map of the premixed configuration of Cordier [182], showing that the main trends were recovered except in high turbulent zones such as the Jet Zone.

Another trajectory based model was developed by Esclapez [1]. The idea of the model is to compute the space and time evolution of the kernel position and its radius. This kernel position tracking is performed using its presence PDF $P_{pres}(x,t)$ as well as the first and second moments of the non-reacting flow LES fields. Initially, the kernel presence PDF is Gaussian centred around the sparking position with a characteristic size close to the initial plasma volume. Then the position PDF tracking needs three main assumptions. First, as for other models, statistics of the non-reacting flow (mean and fluctuations) are used, which is acceptable as long as thermal expansion is negligible for small kernels. Second, the cold flow velocity components are assumed to follow a Gaussian distribution which has been shown to be a reasonable approximation by Pope [211]. Finally, the self-propagating velocity S_d of the flame is considered low compared to its absolute velocity, which has also been verified for small kernels in turbulent flows [180]. With these assumptions, the probability of displacement of a kernel from one position to another position of the chamber can be reconstructed and finally, $P_{pres}(x,t)$ is simply the sum of all possible trajectories of kernels presence PDF arriving at x:

$$P_{pres}(x,t) = \sum_{n=1}^{N} P_{pres}(x_n, t-dt) V(x_n) \quad P(x_n, x)$$

with the first term being the probability of being at point x_n at time $t-dt$ and the second term being the PDF of displacement from position x_n to position x. N is the number of nodes with a non-zero probability of presence at time $t-dt$. Note that P_{pres} is normalized : $\int P_{pres} dx = 1$. While the kernel presence PDF is tracked, its radius is also evaluated over time taking into account potential quenching (by turbulence or inflammable mixture) and using an analytical flame growth rate. To do so, three statistical indicators are used:

- The flammability factor F_f reconstructed using a composite PDF of cold flow mixture fraction based on its mean and RMS values.

- The mean flammable mixture fraction $\bar{z}|_{z_{lean}<z<z_{rich}}$ which is more representative than the classical mean mixture fraction when reactive properties should be evaluated for instance. The evaluation of $\bar{z}|_{z_{lean}<z<z_{rich}}$ is directly linked to F_f.
- A classic Karlovitz number Ka as defined by Abdel-Gayed et al. [178]. In the Ka definition, the laminar flame speed required is estimated at $\bar{z}|_{z_{lean}<z<z_{rich}}$. An arbitrary value of critical Karlovitz number $Ka_c = 4.5$ above which quenching is supposed to occur is chosen.

Using these indicators, one can reconstruct the conditioned kernel presence PDF:

$$P_{pres,cond}(x,t) = F_f(x).C_{Ka}(x).P_{pres}(x,t)$$

with $C_{Ka}(x) = 1$ if $Ka(x) < Ka_c$ and $C_{Ka}(x) = 0$ otherwise. During the first moments of ignition, the temperature of the kernel rises well above the adiabatic temperature. Until the kernel temperature decreases to the adiabatic temperature, no quenching is considered as the energy surplus is important. During this phase, the kernel radius evolution is computed analytically in 0D considering that the kernel displacement is negligible. It stays at the spark location. From the moment the kernel temperature falls back the adiabatic temperature, the kernel displacement and radius are tracked using its conditioned presence PDF $P_{pres,cond}(x,t)$ and associated radius PDF. The kernel growth rate is deduced from the turbulent flame velocity [212], flame quenching is considered where $Ka > Ka_c$, and an arbitrary kernel radius $r_{k,c}$ above which ignition is successful is used. $r_{k,c} = 15\,mm$, close to the integral length scale, is retained by Esclapez. The final probability P_{ign} of ignition success at one position is then obtain by integrating $P_{pres,cond}(x,t)$ over the entire domain and over time up to time t:

$$P_{ign}(t) = \int\limits_{t=0}^{t} \int_x P_{pres,cond}^{r_k(x,t)>r_{k,c}}(x,t)dx\,dt.$$

$P_{ign}(t)$ starts at zero and grows progressively up to its converged value when all potential kernels are either quenched or above $r_{k,c}$. The ignition probability map predicted by the model has been compared to the experimental map given by Cordier [182] on the KIAI configuration. The comparison is shown respectively in Fig.7.7a and Fig. 7.7b for both premixed and non-premixed cases. The ignition probability map is globally well reproduced for the premixed case but less accurately in the non-premixed configuration. Besides, results are quite sensitive to the critical $r_{k,c}$ value chosen.

7.5 Conclusions

The flame growth phase and propagation towards the nearest injector is the most critical phase in an entire hight altitude relight sequence of gas turbine in case of accidental engine failure. The kernel creation phase is normally well mastered as a very important energy can be provided by the spark plug. The light-round phase is also known to be reliable. The majority of ignition failures actually occurs in this phase as the flame is still weak and might face detrimental flow conditions. Besides, this phase also presents an important stochastic behaviour induced by high levels of turbulence making its comprehension difficult. The local kernel development at every position of a combustor has been identified in the literature to be controlled by few parameters such as the local flammability of the mixture and the turbulence intensity. Moderate turbulence intensity might enhance the flame growth, but if too strong, the kernel could be quenched. In particular, when the mixture fraction is near flammability limits, the heat of combustion produced is lower than the turbulent thermal diffusion. Starting from the spark plug position, the flame growth and subsequent propagation are then driven by the local flow properties that evolve with the kernel trajectory in the combustor. Nevertheless, too few detailed studies focusing on the mechanisms of ignition in realistic configurations are reported in the literature. The comprehension of this phase is thus still a challenge nowadays. Another major challenge for engineers is to be able to predict early in the engine conception phase the probability of ignition as function of the spark position. This way, an optimization of the spark plug position can be done. Many LES could be performed at each intended position, but the associated cost would be too high. Low order numerical tools, that only require cold flow properties as input, and that are able to predict the probability of ignition starting from a given position in the chamber have therefore been developed to help engine manufacturers. Most advanced tools obviously need to take into account both local competition between flammability and turbulence intensity, and statistics of potential kernel trajectories.

To increase our knowledge on the mechanisms driving ignition success or failure in such conditions, Chap. 8 is dedicated to performing LES of two-phase ignition sequences in the academic KIAI-Spray burner representative of aeronautical combustors. Before performing these ignition sequences, our numerical set-up is validated against experimental data on the non-reacting and reacting flows of the same configuration. It allows to evaluate the capacity of LES to accurately reproduce spray flames. Finally, the objective of Chap. 9 is the development of a trajectory-based model for ignition probability prediction in realistic two-phase combustors following the work of Esclapez [1].

Chapter 8

LES of two-phase ignition of the KIAI single burner

Contents

8.1 Objectives 133
8.2 Experimental set-up 134
8.3 Numerical set-up 137
8.4 Non-reacting flow analysis 142
  8.4.1 Flow dynamics 142
  8.4.2 Gaseous and liquid fuel distribution 146
8.5 Stable reacting flow 149
  8.5.1 Flow dynamics and flame position 149
  8.5.2 Two-phase unsteady flame structure 152
8.6 Quantitative comparison of spray ignition sequences between LES and experiments 154
  8.6.1 Experimental ignition probability map 154
  8.6.2 Two-phase flow conditions at P1 before ignition 156
  8.6.3 Ignition sequences 157
8.7 Identification of key mechanisms controlling ignition success or failure 159
  8.7.1 Experimental classification of observed scenarii 159
  8.7.2 Decomposition of ignition/extinction scenarii in elementary mechanisms 161
  8.7.3 Detailed analysis of elementary mechanisms 163
  8.7.4 Local Kernel Growth (LKG) mechanism 163
  8.7.5 Local Kernel Shrinking (LKS) mechanism 168
  8.7.6 Kernel Convection 171
8.8 Conclusions 174

8.1 Objectives

Many experiments are dedicated to studying the flame growth phase of ignition in academic burners, trying to reproduce the main features of real burners [181, 183, 186]. Numerical investigations of the same academic burners are performed [187, 188, 201, 213] to supplement experimental analysis. However, very few experimental or numerical studies dedicated to the second phase of ignition in two-phase flows are found in the litterature [194, 195, 196, 214].

The objectives of this chapter are then multiple:

- Validate the numerical set-up by comparison versus experimental data in non-reacting and stable reacting flows.
- Show the ability of LES to reliably investigate the physics of spray ignition by again comparing with measurements.
- Increase our knowledge on the mechanisms driving two-phase ignition success or failure in a configuration representative of aeronautical combustors. This knowledge is particularly useful to derive ignition probability prediction models such as the one of Chap. 9.

The chapter organisation follows this order after the experimental and numerical set-ups description.

This chapter is adapted from two articles. One is published in [215] and available in Appendix. C:
F. Collin-Bastiani, J. Marrero-Santiago, E. Riber, G. Cabot, B. Cuenot, B. Renou, A joint experimental and numerical study of ignition in a spray burner, Proceedings of the Combustion Institute (2018),
https://doi.org/10.1016/j.proci.2018.05.132
The other one is in preparation for submission to Combustion & Flame :
J. Marrero-Santiago, F. Collin-Bastiani, E. Riber, G. Cabot, B. Cuenot, B. Renou, On the mechanisms of flame kernel extinction or survival during aeronautical ignition sequences. Experimental and numerical analysis.

8.2 Experimental set-up

Experimental facility The experimental configuration studied here is the two-phase flow version of the gaseous KIAI set-up [186], called KIAI-Spray configuration, experimented by J.Marrero Santiago [2] at CORIA, France. It is confined with quartz windows, allowing full optical access (Fig. 8.1 Left). The injection system, sketched in Fig. 8.2, is composed of a simplex pressure atomizer (Danfoss, 1.46 kg/h, 80° hollow cone) and an external annular swirling air co-flow with inner and outer diameters of 10 and 20 mm respectively. The radial swirler is composed of 18 rectangular (6 mm x 8 mm) channels inclined at 45° with a corresponding Swirl number of 0.76 [186].

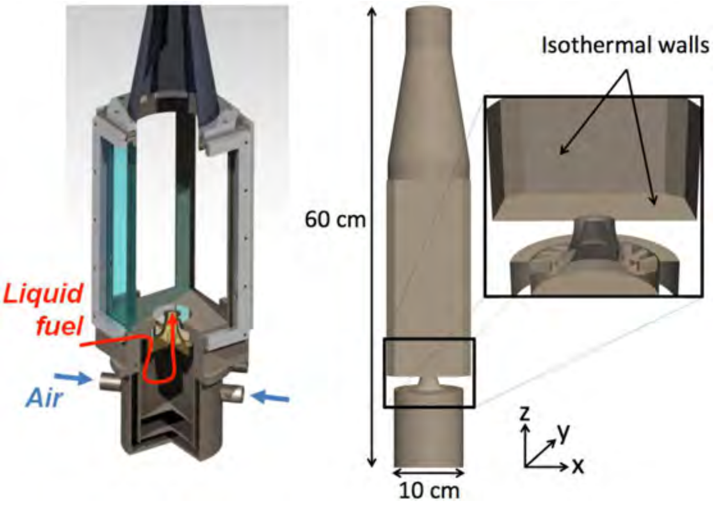

Figure 8.1: (Left) Cut of the KIAI-Spray burner. (Right) Computational domain for LES with a zoom on the injection system.

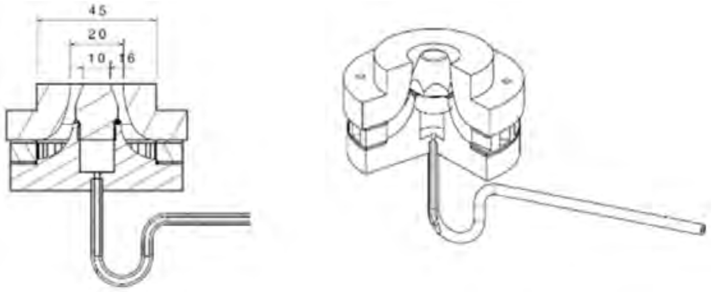

Figure 8.2: Sketch of the injection system of the KIAI-Spray configuration: simplex pressure atomizer + external annular swirling air co-flow with inner and outer diameters of 10 and 20 mm. Taken from [2].

Because of the pressure difference across the simplex atomiser ($\approx 8\ bars$) and also due to the design of the atomiser, the injected liquid is very quickly atomised when entering the combustion chamber as shown by the Shadowgraphy image presented in Fig. 8.3. The destabilisation of the liquid sheet and generation of filaments in the first 2 mm after injection (primary atomisation) is well captured as well as the following secondary atomisation leading to almost only spherical droplets after 4 mm.

Two operating conditions are investigated in this chapter. The first one focuses on the *flame* case which is the steady reacting case, and the second one on all *ignition* cases and the associated *non-reacting* flow all ignition sequences start from. Air and liquid fuel (n-heptane) mass flow rates, controlled by thermal and Coriolis mass flow controllers are summarized in Tab. 8.1 for the two cases. Both correspond to an experimental Reynolds number of $Re = 14797$. The chamber is operated at ambient pressure. In order to avoid run-off by liquid fuel at the windows and perform quantitative diagnostics, preheated air is injected at temperature $T_{air} = 416 \pm 3\ K$ whereas

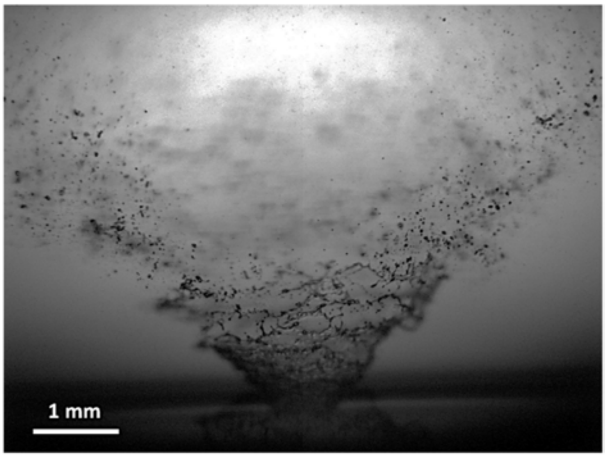

Figure 8.3: Shadowgraphy image in the KIAI-Spray burner showing primary and secondary atomisation above the simplex pressure atomizer. Taken from [2].

	flame	*non-reacting* & *ignition*
$\dot{m}_{Air}$ (g/s)	8.2	8.2
$\dot{m}_{Fuel}$ (g/s)	0.28	0.33
ϕ_{glob}	0.52	0.61

Table 8.1: Experimental mass flow rates of air and fuel in the *flame*, *non-reacting* and *ignition* conditions, and associated global equivalence ratio ϕ_{glob}.

liquid fuel is heated by surrounding air and injected at temperature $T_{fuel} \approx 350\ K$. Both operating points are representative of ultra-lean conditions. For *ignition* cases, before triggering any spark, the system reaches a stable internal window temperature of $T_{wall} = 387\ K$, which is constantly measured by a thermocouple and controlled to ensure the repeatability of all ignition sequences.

Experimental diagnostics and ignition procedure Many diagnostics are used experimentally:

- Phase Doppler Anemometry (PDA) measurements are applied to characterize the fuel droplet size and size-classified velocity, as well as the air velocity in reacting conditions.
- High Speed Particle Image Velocimetry (HS-PIV) is used to extract velocity measurements of the non-reacting flow.
- OH-PLIF is applied to the reacting flow in order to characterize the spray flame structure.

- During ignition sequences, a high-speed camera is used to capture the kernel motion inside the chamber and the total spontaneous flame emission.

Concerning the ignition procedure, the mixture is ignited by a laser-induced spark in selected locations inside the burner. The experimental set-up is similar to the one used in [216]. The energy deposited by the spark is evaluated around 405 mJ from the measurements of the reference and transmitted laser pulse energies. This high value is necessary to ensure a wide range of ignition events within the domain in such ultra-lean conditions. The spark can be approximated by an ovoid of $\approx\ 1-2\ mm$. An experimental ignition probability map of the chamber is built in order to identify the favourable and unfavourable regions for the ignition of the KIAI-Spray burner. For each spark position, 30 independent ignition tests are performed to build the local ignition probability. More details about diagnostics and the ignitier system can be found in [192, 214, 215, 217].

Note that contrary to Part. II that focuses on spark ignition, laser ignition is used here because it is non-intrusive and because spark position can be changed easily. However, as explained throughout Chap. 5, laser and spark ignitions share many common points. The ED_HT methodology for Energy Deposition in LES calculations proposed in Sec. 6.8 is thus suitable for laser ignition too and will be used in this chapter to mimic energy deposition.

8.3 Numerical set-up

Numerics and boundary conditions The KIAI-Spray burner is investigated numerically using LES with the code AVBP co-developed by CERFACS and IFPEN (www.cerfacs.fr/avbp7x). AVBP solves the LES-filtered fully compressible reacting Navier-Stokes equations. For the gas phase, the third order in time and space Taylor-Galerkin scheme [48] is used for the *non-reacting* and *flame* simulations. *Ignition* simulations of Sec. 8.6 are performed using the second order in time and space Lax-Wendroff scheme [47] to save CPU time and the more accurate Taylor-Galerkin scheme is used for *ignition* sequences of Sec. 8.7. The computational domain displayed in Fig. 8.1 (Right) contains the inlet pipe, the swirlers, the injection veins, the combustion chamber and the convergent at the outlet. The Navier-Stokes Characteristic Boundary Conditions [46] are used for inlet and outlet boundary conditions while the combustor walls are considered as no-slip and isothermal ($Tw = 387\ K$ for *non-reacting* and *ignition* cases and $Tw = 1000\ K$ for the *flame* case). A uniform velocity profile is imposed at the air inlet, naturally producing the swirled flow in the combustor thanks to the swirler geometry. Turbulent subgrid stresses are modeled using the SIGMA model [29].

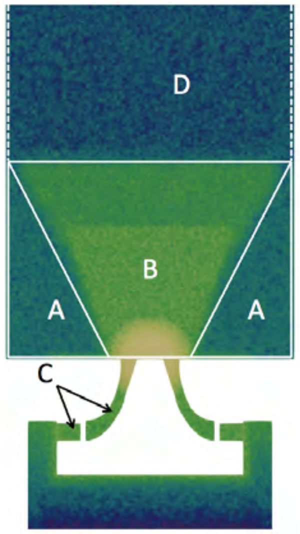

(a)

	non-reacting	*flame*	*ignition*
N_{cells} (Millions)	21.4	77.9	105.0
Δ_x (A) (mm)	0.8	0.65	0.35
Δ_x (B) (mm)	0.5	0.35	0.35
Δ_x (C) (mm)	0.4	0.4	0.4
Δ_x (D) (mm)	1.2	0.8	0.8

(b)

Figure 8.4: Cut of the generic mesh topology and associated minimum cell sizes in each zone for all meshes.

Meshes Fully unstructured grids are generated for the three cases: *non-reacting*, *flame*, and *ignition* simulations. A generic mesh topology is given in Fig. 8.4a. Associated minimum cell sizes in each zone presented are given for all meshes in Table 8.4b along with the total number of tetrahedral cells. The *non-reacting* mesh is the coarsest one as no thin reaction zone must be resolved, but only turbulent structures, mainly in the shear layer region (zone B). The *flame* mesh is particularly refined near the a-priori known flame region (zone B), contrary to the *ignition* mesh for which a homogeneous refinement of the entire bottom part (zones A+B) of the combustor is needed as the kernel trajectory during the ignition sequence is not known. The swirler vanes and convergent (zone C) are always very refined. Far downstream (zone D), the mesh is progressively coarsened as this zone is not of particular interest in this study.

Liquid phase modelling A Lagrangian approach is chosen for the spray description. A first order explicit scheme is used for the time advancement of the liquid phase. The Schiller & Naumann [57] correlation is used for the drag force. The Spalding evaporation model [58] is used with the complex transport coefficients evaluation of Sierra et al. [52] and the Abramzon & Sirignano [62] correction. The droplet interaction with walls is modelled with a simple elastic rebound methodology as spray-wall interactions are limited due to the pre-heating employed. Finally, as in the numerical study of the jet spray configuration of the KIAI burner [218], the FIM-UR injection model (see Sec. 4.5) of Sanjosé et al. [64] is used and the injection droplet size distribution is fitted to experimental data using a Rosin-Rammler distribution:

$$RR\left(d_p\right) = q\frac{d_p^{q-1}}{X^q}\exp\left[-\left(\frac{d_p^q}{X}\right)\right] \tag{8.1}$$

$$X = \frac{\Gamma(1+2/q)}{\Gamma(1+3/q)}d_p^{SMD}. \tag{8.2}$$

The parameter describing the spread of the distribution is set to $q = 2.3$ and the chosen SMD is $d_p^{SMD} = 31\ \mu m$. Γ is the standard Gamma function.

Combustion modelling For the *flame* and *ignition* cases, the n-heptane fuel oxidation is described using an Analytically Reduced Chemistry named $ARC\_25\_C_7H_{16}$ derived from the *detailed* mechanism of Jerzembeck et al. [219] using the reduction tool YARC [43]. The Jerzembeck mechanism is already a simplified version of the comprehensive LLNL mechanism [159]. Targetted quantities for the reduction were unstrained laminar flames (speed, adiabatic temperature and major species and heat release rate profiles) as well as strained laminar flames (dependence of S_c on stretch) on a wide range of equivalence ratio. The $ARC\_25\_C_7H_{16}$ comprises 25 transported species, 27 species in Quasi-Steady State Approximation and 210 irreversible reactions. All species are detailed in Tab. 8.2 for the sake of completeness. The simplified transport methodology described in Sec. 3.1.3 is used, with species Schmidt numbers $S_{c,k}$ fitted targetting the laminar unstrained flame speed on the entire flammable range of equivalence ratio. A summary of its performances on canonical gaseous laminar flames using the Software Cantera [166] is given in Fig. 8.5. Normalized species mass fraction profiles on a 1D laminar unstrained premixed flame ($T = 298\ K$, $P = 1\ bar$, $\phi = 1.0$) are accurately retrieved with the $ARC\_25\_C_7H_{16}$ compared to the detailed Jerzembeck mechanism. S_l^0 is correctly recovered on the entire range of flammability and compares well with experimental measurements from [220] on the same operating point. The influence of fresh gas temperature is also well captured with the $ARC\_25\_C_7H_{16}$ compared to the detailed mechanism. Finally, in the context of ignition where kernel-turbulence interactions are decisive, the response of $ARC\_25\_C_7H_{16}$ to strain must be assessed. This is done on a 1D laminar strained premixed flame in the KIAI-Spray conditions: a fresh premixed n-heptane/air mixture at $T = 413\ K$ and $\phi = 0.61$ is injected on one side whereas combustion products (at $\phi = 0.61$) are injected on the other side. The strain rate a is varied to cover representative values found in the KIAI configuration by changing the fresh and burnt gases inlet velocities u_f and u_b:

$$a = \frac{u_f + u_b}{d} \tag{8.3}$$

with d the distance between the two opposed injection points. The $ARC\_25\_C_7H_{16}$ correctly reproduces the detailed mechanism behaviour with less than 15% error on

Fuel/Oxidizer	n-heptane/Air
Detailed mechanism	LLNL [159, 219]
Number of transported species/reactions/QSS	25/210/27
Transported species	H H_2 O O_2 OH H_2O HO_2 H_2O_2 CH_3 CH_4 C_2H_2 C_2H_4 C_2H_6 C_3H_4-a C_3H_6 C_4H_6 n-C_7H_{16} CO CO_2 CH_2O CH_3OH CH_2CO HOCHO C_4H_8-1 N_2
Schmidt number	0.123 0.206 0.482 0.741 0.491 0.550 0.746 0.751 0.674 0.677 0.814 0.772 0.992 1.065 1.031 1.266 1.985 0.750 0.955 0.858 0.878 1.015 1.033 1.252 0.705
QSS species	CH CH_2(S) CH_2 C_2H_3 C_2H_5 C_3H_2 C_3H_3 C_3H_5-a n-C_3H_7 C_4H_7 p-C_4H_9 C_5H_9 C_5H_{10}-1 C_5H_{11}-1 C_6H_{12}-1 C_7H_{15}-2 HCO CH_3O CH_3O_2 CH_3O_2H HCCO CH_2CHO C_2H_5O $C_2H_5O_2$ CH_3CO n-$C_3H_7O_2$ p-$C_4H_9O_2$

Table 8.2: Summary of the $ARC\_25\_C_7H_{16}$ scheme.

the consumption speed on the entire range of strain rates. Species chemical time-scales of all transported species of $ARC\_25\_C_7H_{16}$ are given in Fig. 8.6, and compared to the LES integration time step $\Delta t = 2e^{-8}$ s corresponding to our KIAI-Spray set-up. CH_3 and C_4H_8-1 are very stiff to integrate temporally while the fuel *n*-C_7H_{16} is also very close the Δt. For this reason, CH_3 & C_4H_8-1 are integrated implicitly following the methodology of Jaravel [41]. Furthermore, in order to improve the stability of the explicit time integration for other species (especially for *n*-C_7H_{16}), 3-5 explicit sub-iterations are used for the chemical system in one LES time-step [41, 221]. The over-cost associated to this chemical sub-cycling remains low for such reduced number of sub-iterations.

For both *flame* and *ignition* cases, the ultra-lean operating point and the very refined mesh allow to fully resolve the flame front with at least 5 grid points in the flame thickness, and neglect the subgrid-scale wrinkling of the flame. A posteriori verification shows that the contribution of the subgrid-scale Turbulent Kinetic Energy (TKE) is under 5% of the total TKE in the whole flame region.

Energy Deposition modelling The standard ED model [151] is used for ignition sequences of Sec. 8.6 with parameters summarized in Tab. 8.3. The ED_HT energy deposition model presented in Sec. 6.8 is only used for ignition sequences of Sec. 8.7 as it was derived latter. Parameters of the ED_HT model are also given in Tab. 8.3. For the standard ED model, the input energy is fixed to order to recover a kernel of accurate

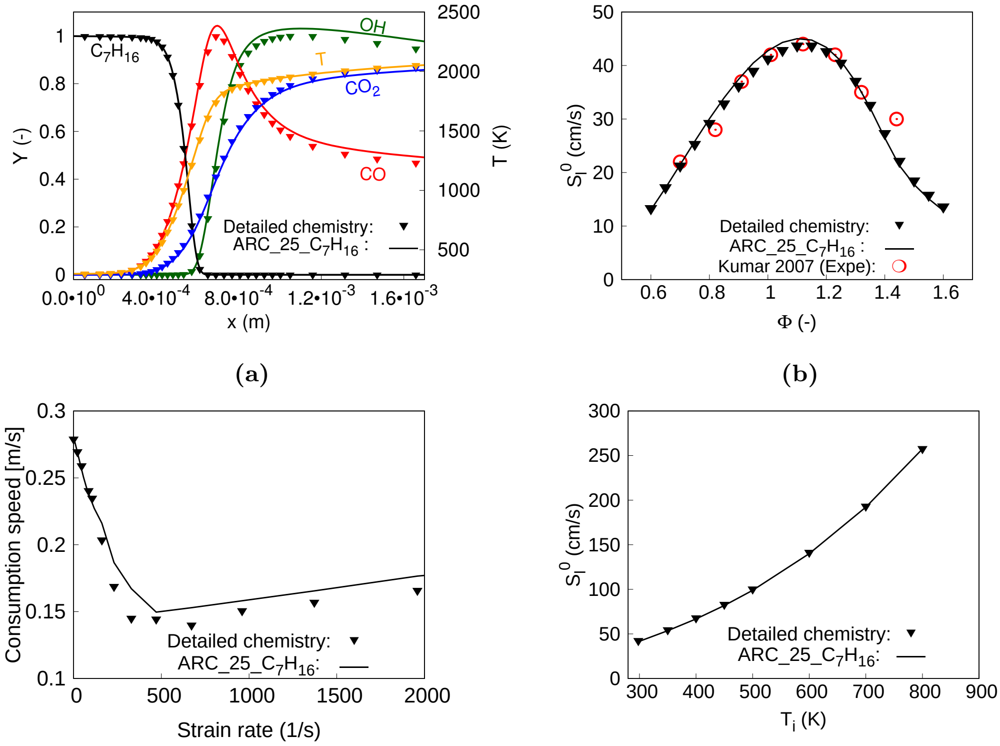

(a) **(b)**

(c) **(d)**

Figure 8.5: Validation of the $ARC\_25\_C_7H_{16}$. (a) Normalized species mass fraction profiles on a 1D laminar unstrained premixed flame ($T = 298\ K$, $P = 1\ bar$, $\phi = 1.0$). (b) S_l^0 as function of ϕ on a 1D laminar unstrained premixed flame ($T = 298\ K$, $P = 1\ bar$). (c) Global consumption speed versus strain rate on a 1D laminar strained premixed flame ($T = 413\ K$ and $P = 1\ bar$, $\phi_{glob} = 0.61$ representative of the KIAI configuration). (d) S_l^0 as function of T on a 1D laminar unstrained premixed flame at $P = 1\ bar$, $\phi = 1.0$.

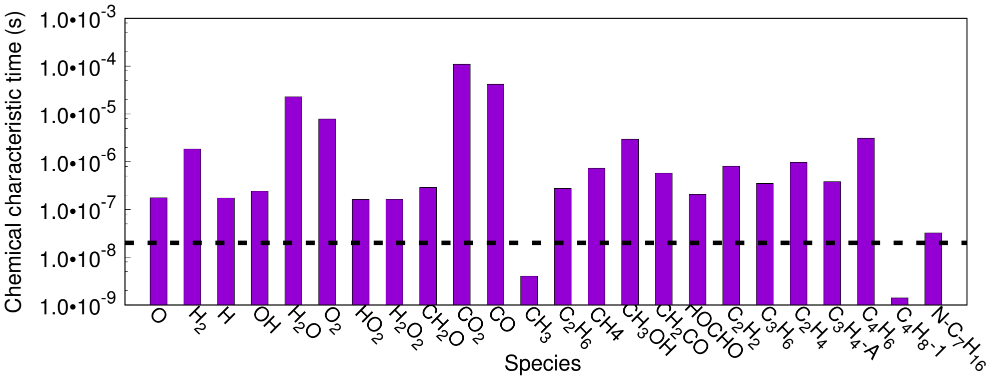

Figure 8.6: Species chemical time-scales computed on 1D laminar unstrained premixed flame with the $ARC\_25\_C_7H_{16}$ mechanism. The LES integration time step $\Delta t = 2e^{-8}\ s$ corresponding to the KIAI-Spray set-up is added with a black dashed line.

	Standard ED model	ED_HT
ED sphere diameter	8 mm	5.5 mm
ED time	100 μs	2 μs
ED energy	25 mJ	80 mJ

Table 8.3: ED parameters of the standard ED model used in Sec. 8.6 and of the improved ED_HT model used in Sec. 8.7.

size compared to experiments hundreds of microseconds after the laser ignition. Using 25 mJ leads to the desired behaviour and to an energy transfer efficiency of 6 % close to the experimentally observed efficiency of 7 % – 15 % [78, 79, 90] for laser ignition. For the ED_HT model, the input energy is set to obtain a 10 % energy transfer efficiency from the spark energy to the energy left in the flame kernel after few microseconds. Canonical 3D ignition tests, not presented here, in the KIAI-spray conditions showed that using a 80 mJ input energy led to 40.5 mJ left in the kernel (desired 10 % energy transfer efficiency) and 39.5 mJ taken by the shock wave. It represents a 49.3 % energy transmission coefficient to the shock wave which is slightly lower than standard literature values (50 – 80 %). This is explained by the under-estimated power of the shock created in the ED_HT model compared to real spark-induced shock waves. For both energy deposition model, the laser-induced spark region is refined during the early instants following energy deposition with a typical cell size $\Delta x = 0.17$ mm, leading to a larger grid. Once the kernel is large enough, the flow is interpolated on the reference grid to simulate the full ignition sequence.

8.4 Non-reacting flow analysis

8.4.1 Flow dynamics

Cuts of the three components of non-reacting flow mean gaseous velocity are shown in Fig. 8.7. A flow topology typical of highly swirled configurations is recovered with the IRZ, ORZ and spray-SJZ clearly identified in Fig. 8.7a showing the axial velocity. The isoline $U_{axial} = 0$ drawn in black separates well each zone. The IRZ is closed downstream because of the convergent at the outlet. The radial and azimuthal velocities are very important in the SWJ due to the swirled injection system. The radial velocity cut allows to observe the bottle-neck shape of the reverse flow: the IRZ is very thin at low axial position and only opens downstream almost reaching lateral walls. Finally, the velocity magnitude is the lowest in the ORZ.

Numerical mean gaseous and liquid velocity profiles are compared with experiments in Fig. 8.8. The three axial sections used are drawn in Fig. 8.19 A. Gaseous profiles match experimental ones with good precision at the three heights. Liquid profiles

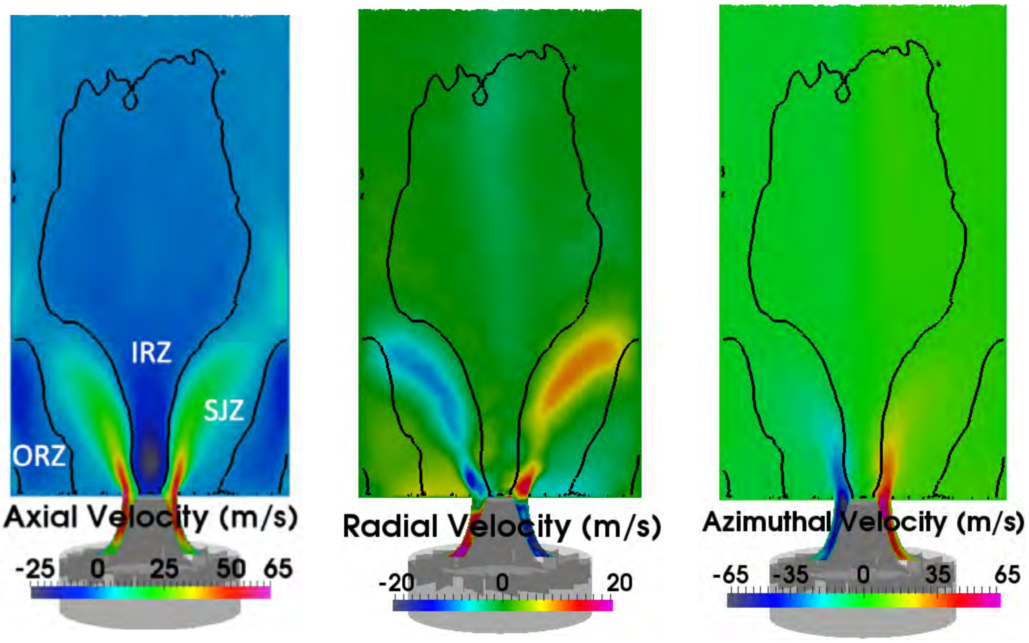

(a) (b) (c)

Figure 8.7: Cut of the non-reacting flow mean gaseous velocity. (a) Axial component. (b) Radial component. (c) Azimuthal component. An isoline $U_{axial} = 0$ is drawn in black.

are shown for two droplet diameter classes: $d_p \in [10; 20]$ μm and $d_p \in [30; 40]$ μm. Smaller droplets almost act like tracers in the gaseous flow while bigger droplets are more inertial and much less influenced by the gaseous phase at low axial positions. The LES swirled FIM-UR droplet injection model reproduces well the important radial and azimuthal liquid velocities for both droplet classes at low positions induced by the experimental injection system. A small under-estimation of the axial liquid velocity is observed at $z = 15$ mm for large droplets but this difference rapidly vanishes. All these profiles also demonstrate that LES recovers well the opening angle of both the air jet and the spray for small and large droplets.

Gaseous and liquid velocity fluctuation profiles are also presented in Fig. 8.9. The same axial stations and droplet classes are used for the comparison with experiments. An overall very good agreement is also found on the three components of velocity fluctuations. A small under-estimation of liquid velocity fluctuations is observed in general. That may be explained by the lack of injection velocity fluctuation used in the numerical set-up. Liquid velocity fluctuations are therefore only due to turbulence in LES while experimentally, the simplex pressure atomizer also induces an intrinsic randomisation of the inlet liquid velocity. Nevertheless, the comparison between LES and experiments shows a very good agreement on the aerodynamic of the gaseous and liquid phases.

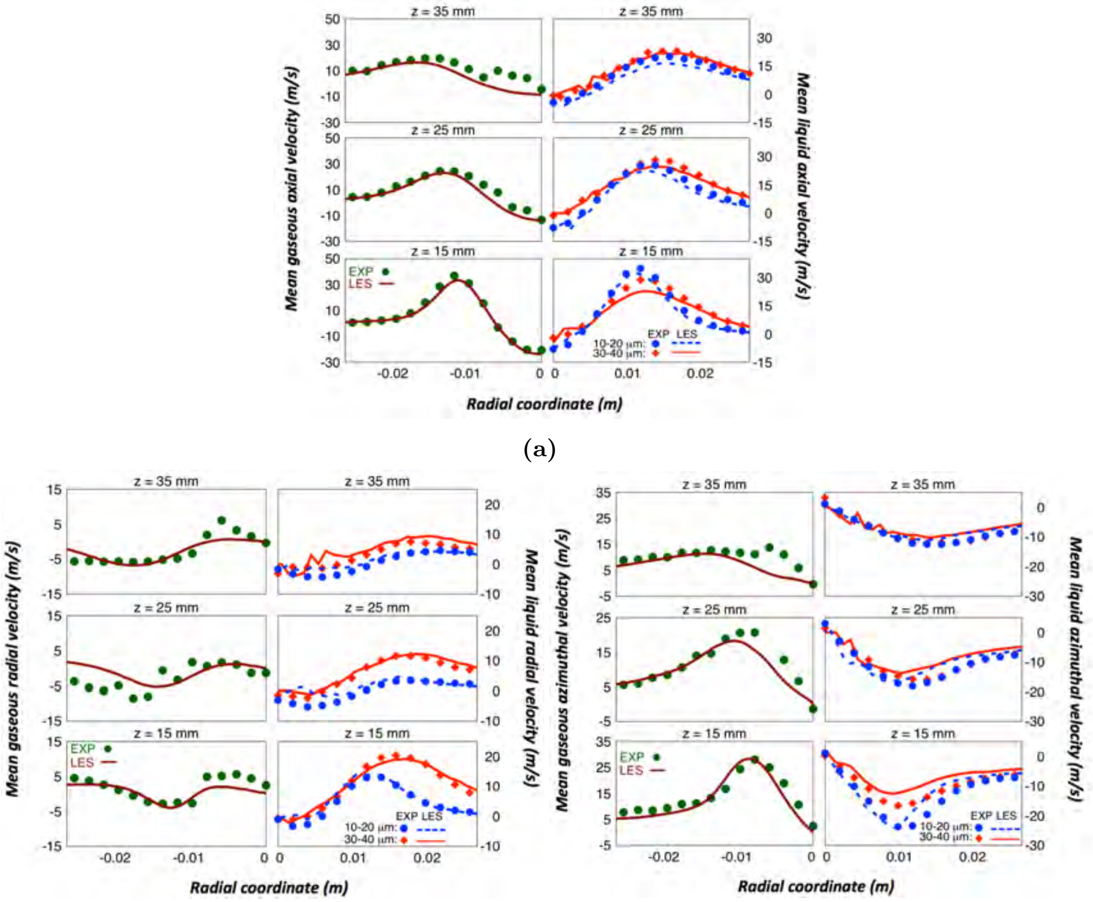

(a)

(b)

(c)

Figure 8.8: Mean gaseous and liquid velocity profiles of the non-reacting flow. (a) Axial component. (b) Radial component. (c) Azimuthal component.

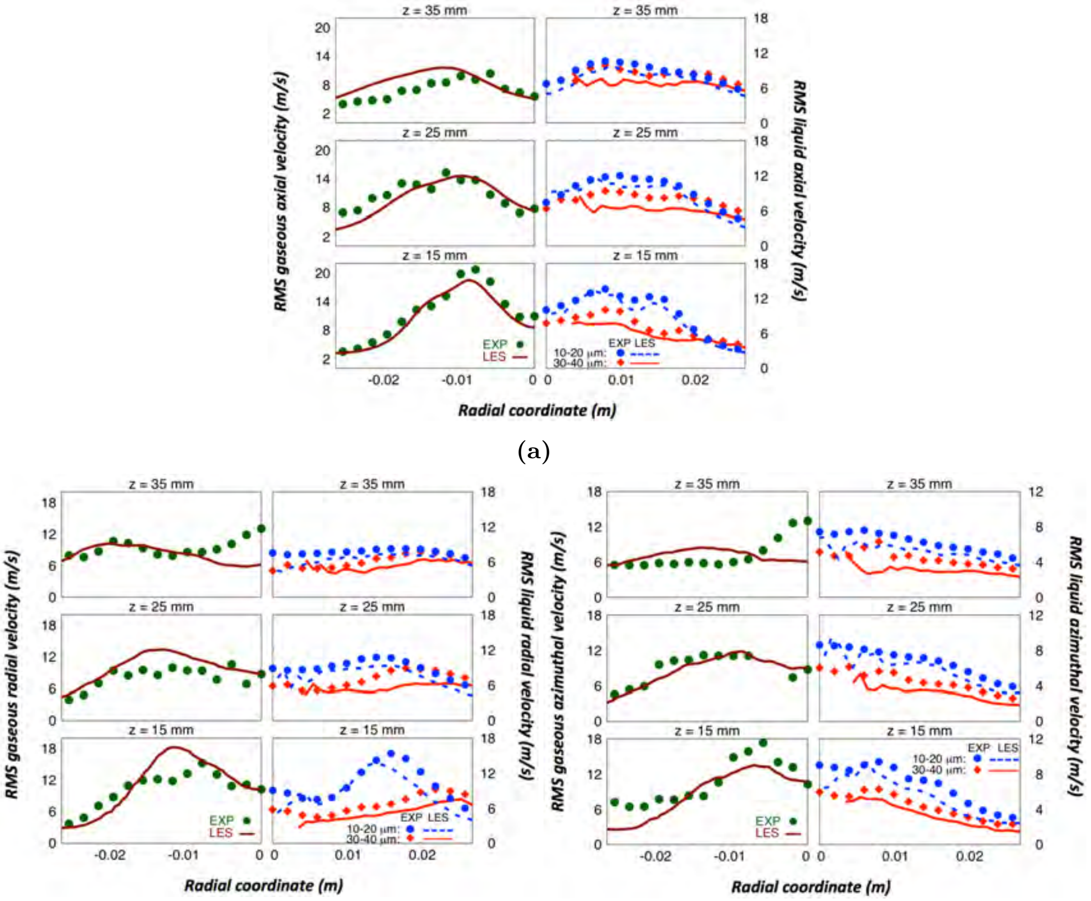

(a)

(b)

(c)

Figure 8.9: Gaseous and liquid velocity fluctuation profiles of the non-reacting flow. (a) Axial component. (b) Radial component. (c) Azimuthal component.

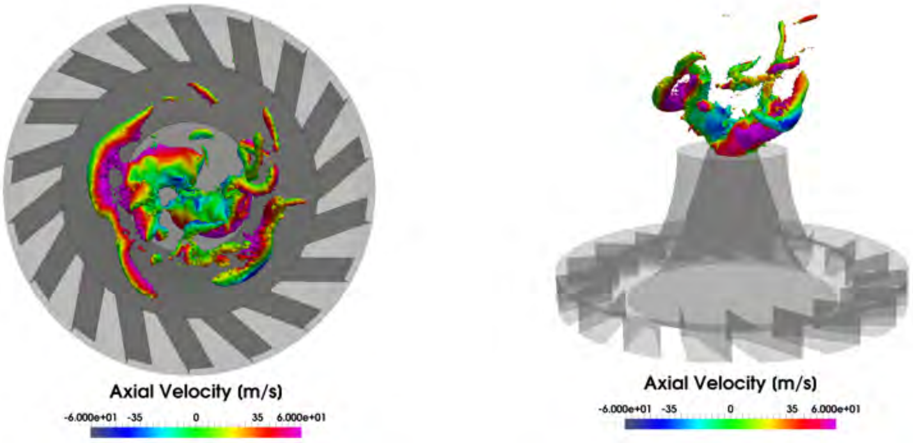
Axial Velocity (m/s)
-6.000e+01
-35
0
35
6.000e+01

(a) Top view

(b) Side view

Figure 8.10: PVC represented by an iso-surface of pressure $P = 100\,200\,Pa$, coloured by axial velocity.

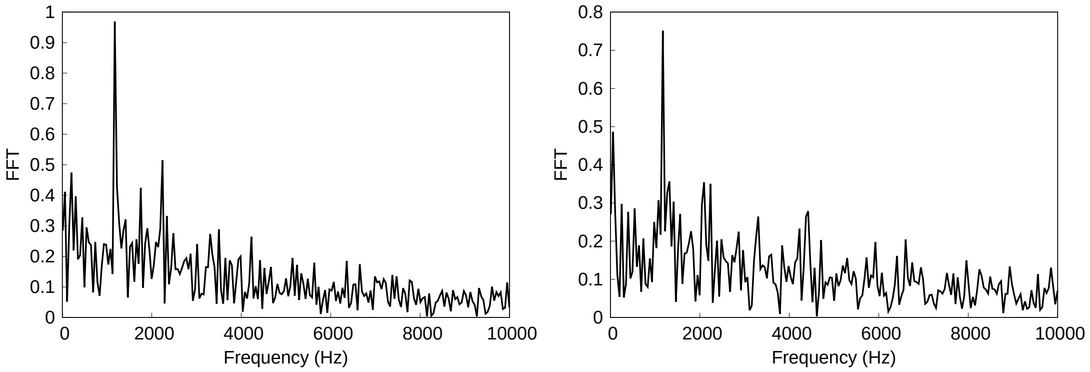

(a) Axial velocity signal **(b) Equivalence ratio signal**

Figure 8.11: FFT spectra of (a) axial velocity and (b) equivalence ratio of a probe in the PVC region ($x = 7\ mm; z = 10\ mm$) in the KIAI-Spray configuration.

The swirl number of our configuration being above the super-critical swirl number ($S_w = 0.76 > S_{w,c} = 0.707$ [222]), the KIAI-Spray non-reacting flow can face hydrodynamic instabilities. Instabilities are visible in our *non-reacting* case as large scale coherent structure, called precessing vortex core (PVC) [223], in the inner shear layer between the SJZ and the IRZ and in the outer shear layer between SJZ and the ORZ. This PVC is shown in Fig. 8.10 by an iso-surface of pressure $P = 100\,200\,Pa$, coloured by axial velocity. The top view highlights the high gradient of axial velocity on the outer PVC branch separating the SJZ and the ORZ. The PVC is made of two opposed branches in the inner shear layer. FFT spectra of time series of axial velocity and equivalence ratio at a probe in the PVC region ($x = 7\ mm; z = 10\ mm$) are presented in Fig. 8.11. These plots reveal periodic oscillations, associated to the PVC hydrodynamic instability. The peak activity is found at 1200 Hz close to the value of 1150 Hz found in the gaseous non-premixed version of th KIAI configuration [1] with the same swirl number ($S_w = 0.76$).

8.4.2 Gaseous and liquid fuel distribution

The mean fuel distribution in the chamber is investigated in Fig. 8.12 by separating the gaseous and liquid contributions. The total ($\phi_{tot} = \phi_g + \phi_l$) equivalence ratio is also reported. ϕ_g is well correlated to the flow topology: the mean gaseous equivalence ratio in the ORZ is close to the global equivalence ratio of the chamber $\phi_{glob} = 0.61$ while the SJZ and the IRZ are much leaner as the residence time of droplets in these zones is smaller and not sufficient for their complete evaporation. The spray angle (80°) is visible on the ϕ_l field. Just above the injection system, the very dense spray leads to a locally very rich mixture ($\phi_l > 20$). This is confirmed by the cut of mean liquid volume fraction α_l shown in Fig. 8.13a. At low axial stations ($z < 10\ mm$) in the SJZ,

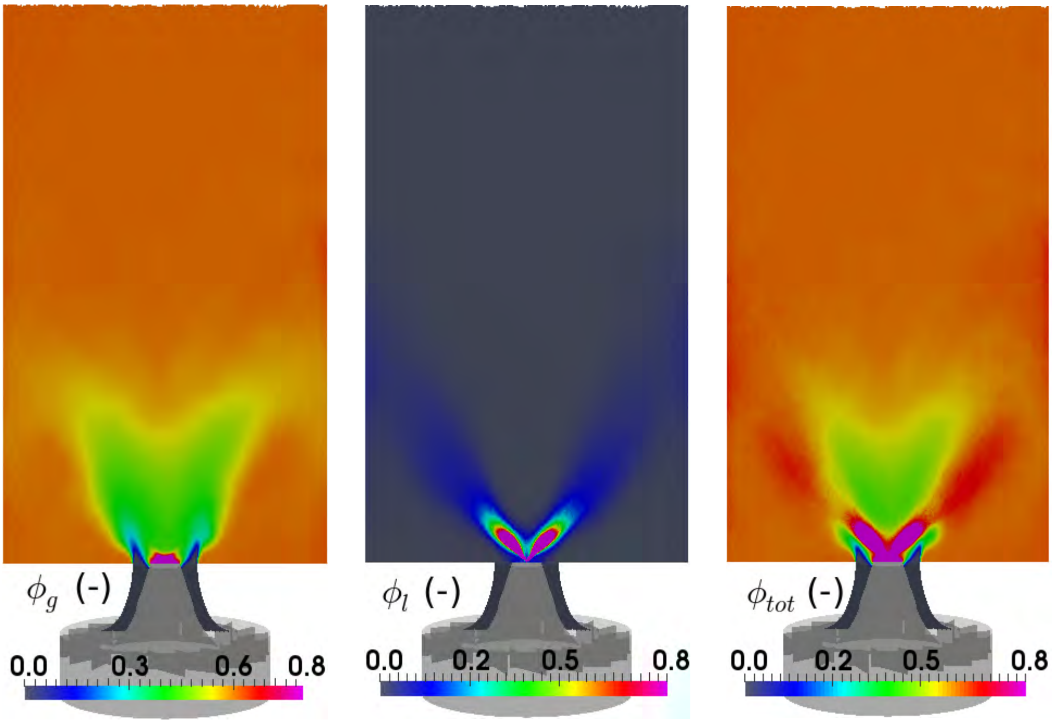

(a) (b) (c)

Figure 8.12: Cuts of the non-reacting flow mean equivalence ratio. (a) Gaseous, (b) Liquid and (c) Total (gaseous+liquid) equivalence ratio.

$\alpha_l > 1e^{-4}$ is reached in the spray core. The spray is more dilute downstream and in a large part of the ORZ with $1e^{-5} < \alpha_l < 1e^{-4}$. Typical associated fuel evaporation rate in this zone is around $\dot{m}_{evap} = 0.1 - 1\ kg.s^{-1}.m^{-3}$ as illustrated by Fig. 8.13b. Due to evaporation, the liquid equivalence ratio reduces near $\phi_l = 0.1$ at high axial position of the SJZ and even $\phi_l < 0.05$ in the lower part of the ORZ and in the IRZ. In these later zones, the liquid volume fraction is almost negligible with $\alpha_l < 1e^{-6}$ so that almost only gaseous fuel is found.

The poly-dispersion of the spray is assessed by looking in Fig. 8.14 at distributions of droplet diameter at two points in the chamber highlighted in Fig. 8.13a. P_A is located at $r = 18\ mm, z = 35\ mm$, downstream in the spray injection direction, while P_B is located at $r = 0\ mm, z = 10\ mm$, just above the injection system at the bottom of the IRZ. P_A presents a mean droplet diameter of $d_p = 16.7\ \mu m$, much smaller than in P_B ($d_p = 23.2\ \mu m$). The very differently shaped experimental PDFs of droplet diameter at these two points are well recovered by LES validating the FIM-UR model and calibrated injection droplet size distribution.

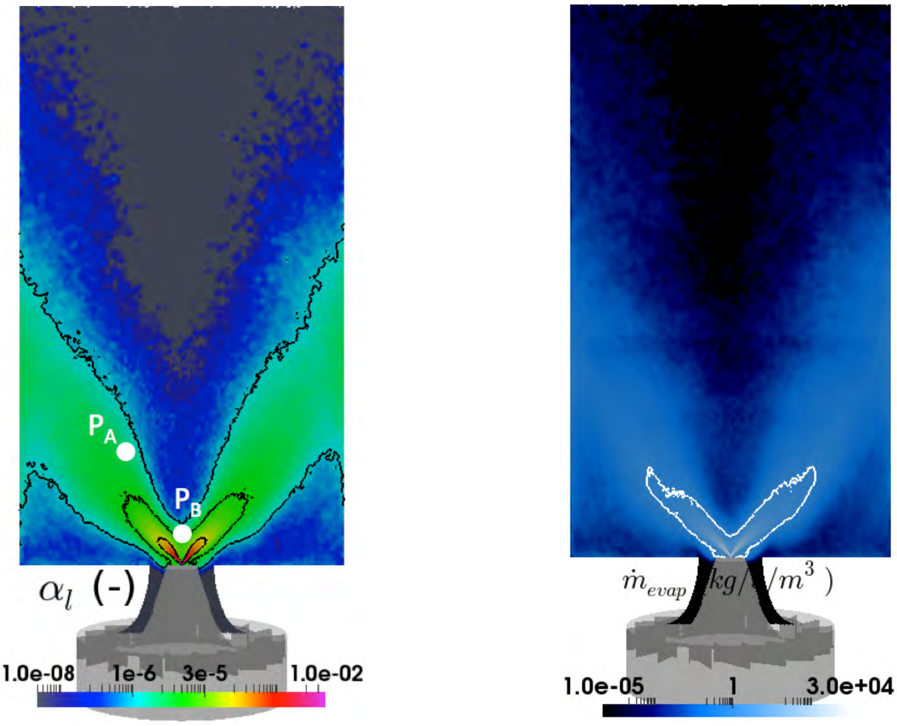
P_A
P_B
α_l (-)
1.0e-08
1e-6
3e-5
1.0e-02
$\dot{m}_{evap}$ ($kg/s/m^3$)
1.0e-05
1
3.0e+04

(a) (b)

Figure 8.13: Cut of the non-reacting flow mean (a) liquid volume fraction with iso-$\alpha_l = 1e^{-4}$, $1e^{-5}$, $1e^{-6}$ and (b) evaporation rate with an iso-$\dot{m}_{evap} = 1\,kg/s/m^3$. Positions P_A & P_B are used in Fig. 8.14.

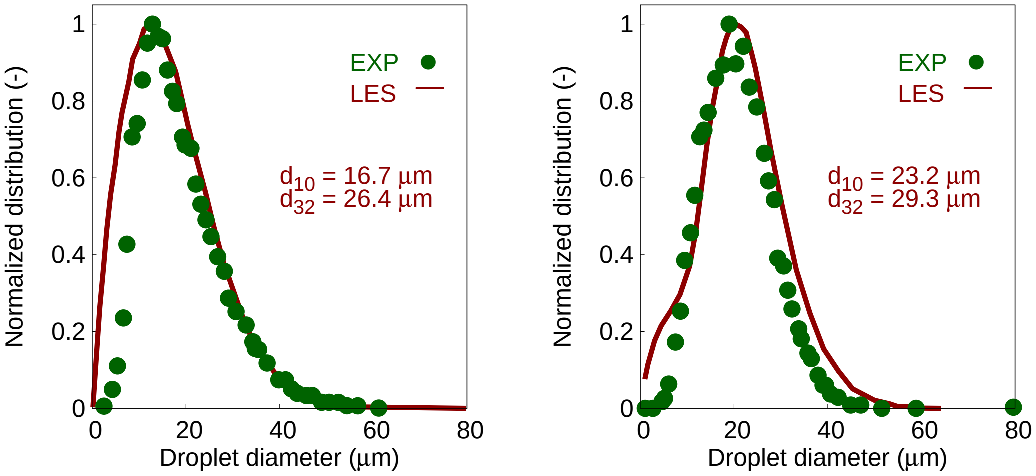

(a) (b)

Figure 8.14: Comparison between experimental and LES normalized distribution of non-reacting flow droplet diameter at two points highlighted in Fig. 8.13a: (a) P_A: $r = 18\ mm, z = 35\ mm$, (b) P_B: $r = 0\ mm, z = 10\ mm$.

8.5 Stable reacting flow

8.5.1 Flow dynamics and flame position

Before addressing the complex transient *ignition* phase, the structure of the stabilized lifted M-shape spray flame is studied to present the main characteristics of this reacting flow. First at the three stations downstream the injector ($z = 15, 25, 35\ mm$, see Fig. 8.19), numerical and experimental radial profiles of mean gaseous velocities as well as liquid velocities per diameter class are compared in Fig. 8.15. The typical features of a swirled-stabilized combustion chamber remain in the presence of the flame, with the IRZ and the ORZ. Thermal expansion leads to strong mean axial velocities in the combustion chamber with maximal velocities up to 45 m/s. The reverse flow is a little bit under-predicted in LES and at higher stations, the axial velocity is under-estimated compared to experiments. As in the *non-reacting* case, size-classified droplet mean axial velocity profiles show that small droplets ($d_p \in [10; 20]\ \mu m$) almost follow the carrier phase unlike large ones ($d_p \in [30; 40]\ \mu m$) which are more inertial close to the injector tip. The difference between small and large droplet axial velocity reduces downstream in the chamber. Unlike the azimuthal velocity component that is perfectly recovered by LES compared to experiments for both gaseous and liquid phases, the radial velocity profiles do not match. The small impact of droplet size on the liquid mean radial velocity is however found. The overall agreement between experiments and LES is fairly good showing the capability of LES to catch the main behaviour of the two-phase flame in the KIAI-Spray burner.

Gaseous and liquid velocity fluctuation profiles of the *flame* case are also presented for the three velocity components and the same three axial stations in Fig. 8.16. The reacting flow exhibits high turbulence intensity due to both the IRZ and the flame unsteadiness. Except for the radial component at the lowest axial position, these high levels of fluctuations are very accurately predicted by LES.

The comparison between an axial cut of mean $OH-PLIF$ image from experiments and the mean OH mass fraction from LES (maximum value: $Y_{OH} = 4e^{-4}$) is shown in Fig. 8.17 in order to qualitatively observe the mean flame shape. The flame structure is analyzed in details in Sec. 8.5.2. The normalized vertical profiles (on the red dashed line shown in Fig. 8.17) of OH mass fraction from experiments and LES are presented in Fig. 8.18 to quantitatively assess the flame height in LES versus experiments. The very good agreement on the mean flame shape and height does not explain the small differences on axial and radial velocity profiles observed between experiments and LES. The same differences were observed on the KIAI-Spray jet flame [218] and this point is still under investigation. In particular, the impact of chemistry modelling and the

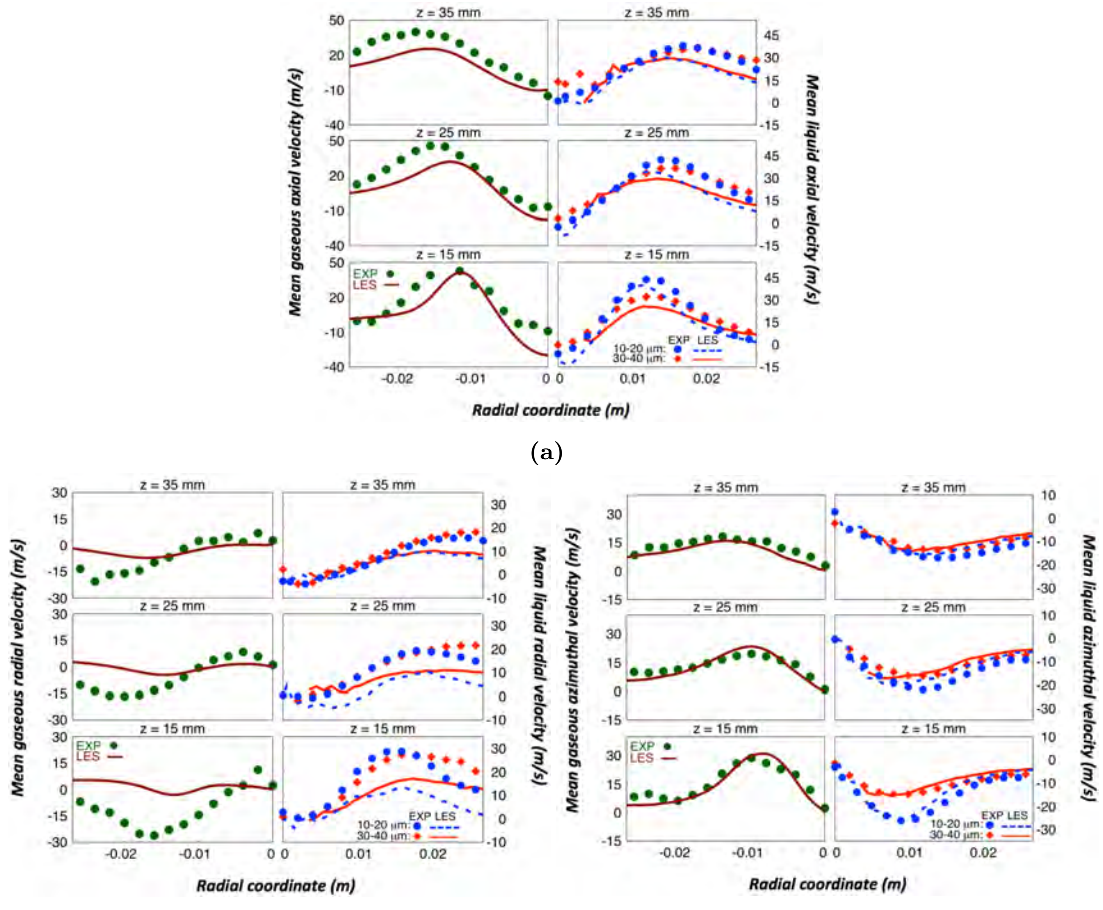

(a)

(b)

(c)

Figure 8.15: Mean gaseous and liquid velocity profiles of the stable flame case. (a) Axial component. (b) Radial component. (c) Azimuthal component.

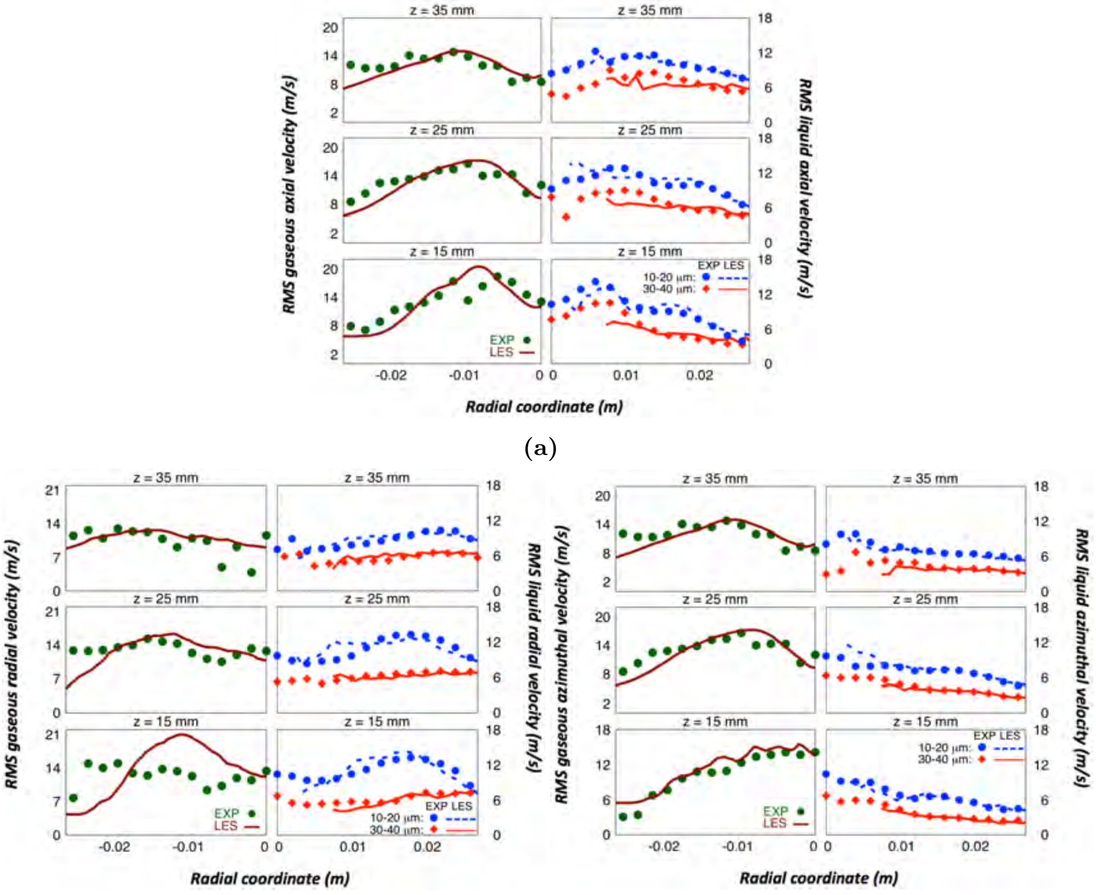

(a)

(b)

(c)

Figure 8.16: Gaseous and liquid velocity fluctuation profiles of the stable flame case. (a) Axial component. (b) Radial component. (c) Azimuthal component.

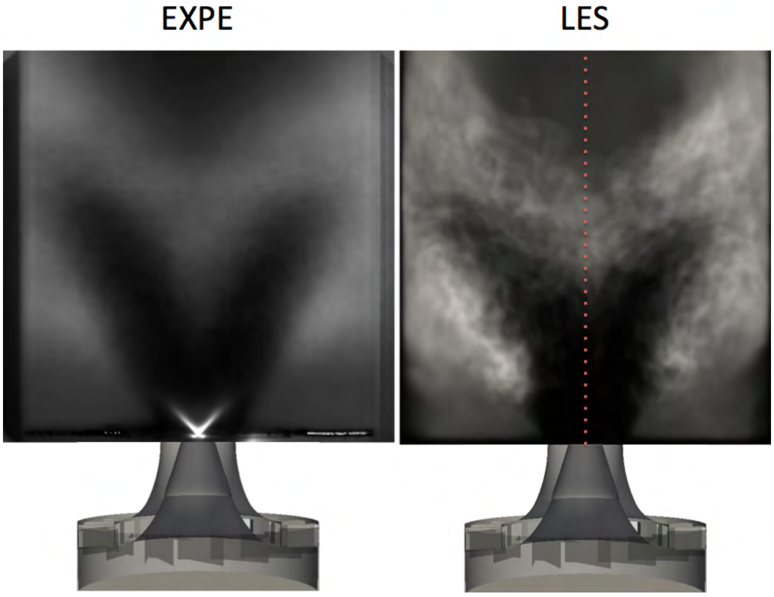

Figure 8.17: Comparison between an axial cut of mean $OH-PLIF$ image from experiments and the mean OH mass fraction from LES (maximum value: $Y_{OH} = 4e^{-4}$) in the stable flame case. The thin red dashed line shows where the data of Fig. 8.18 are extracted from.

absence of subgrid-scale combustion model on these differences have been shown to be negligible.

8.5.2 Two-phase unsteady flame structure

The lifted M-shape spray flame exhibits a strong unsteadiness, resulting in very different structures that can be seen both experimentally and numerically. Figure 8.19 displays the three main structures of this fluctuating flame, comparing experimental OH-PLIF images on the top and instantaneous fields of OH mass fraction directly extracted from LES, since the ARC_25_C_7H_{16} chemical scheme contains the OH species. In all

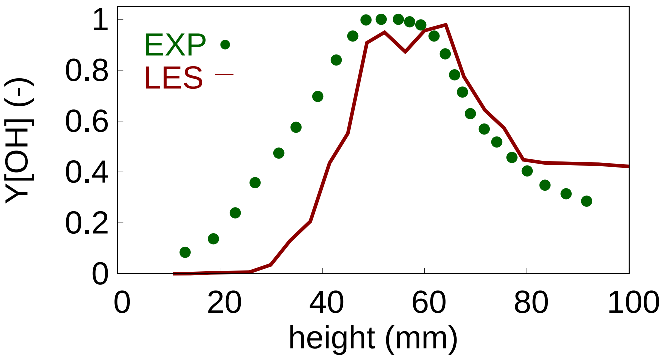

Figure 8.18: Normalized vertical profiles (line shown in Fig. 8.17) of OH mass fraction from experiments and LES in the stable flame case.

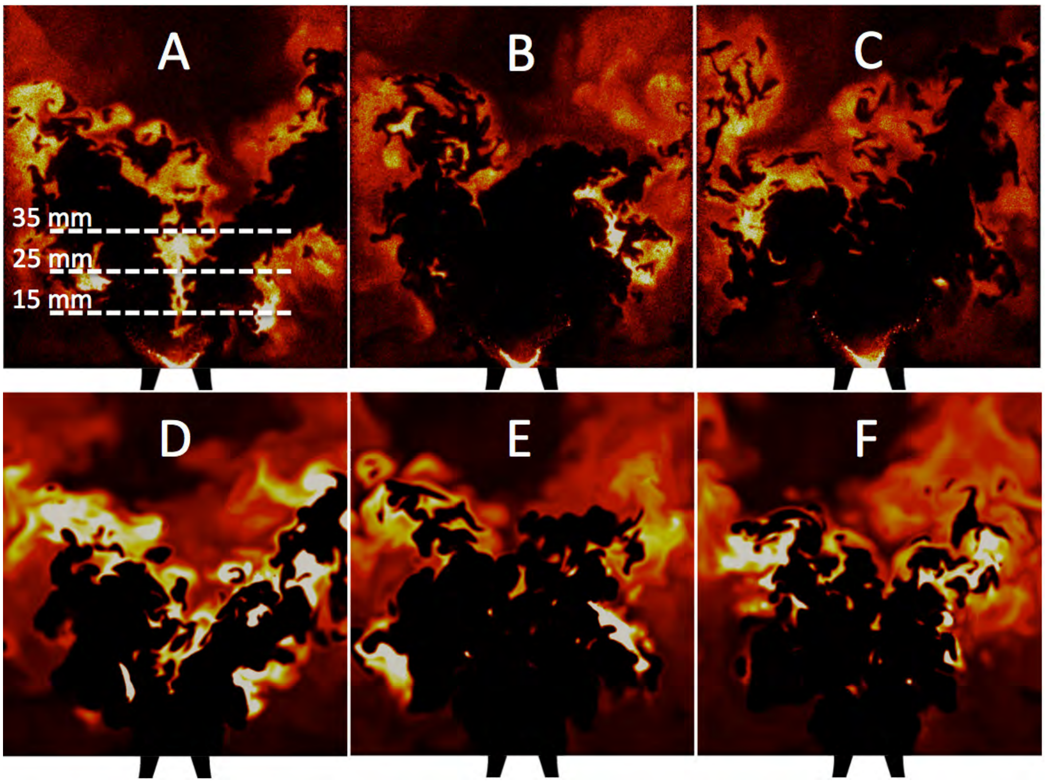

Figure 8.19: Stable flame case. A-B-C: Experimental OH-PLIF images D-E-F: Instantaneous fields of OH mass fraction from LES, with maximum value $Y_{OH} = 0.001$. Dimensions of visualization boxes are $90\ mm \times 94\ mm$.

pictures, different regions can be distinguished: 1) Black regions downstream the injector highlight fresh gases. 2) Low color intensity (in the ORZ and at the top of each image) characterizes burnt gases with diffused OH traces remaining. 3) High color intensity is typical of near post flame region containing a lot of OH produced by the flame. 4) The flame front can be localized by the sharp OH gradient regions and decomposed in two parts: an outer flame front separating the ORZ and the fresh gases branches with the lowest point of this front called the leading edge; and an inner flame front between the fresh gases and the IRZ, with the lowest point of this front called the stabilization point. 5) If droplets are not visible on the images, their impact on the flame is strong. The wrinkling of the flame is partly due to the turbulent behaviour of the dispersed phase. Even local extinctions may originate from fuel droplets crossing the flame front and leading to mixtures too rich to burn.

Figures 8.19 (A and D) show very low stabilization points just above the fuel injector with well defined M-shaped flames. Both right branches reach the wall far downstream. Figures 8.19 (B and E) highlight situations where the stabilization point is far downstream ($z \approx 40$ mm). In these cases, the flame is much more compact exhibiting large fresh gas pockets accumulated between the injector and the inner flame front. Finally, Figs. 8.19 (C and F) allow to highlight flame shapes with leading edges being high ($z \approx 35$ mm, left side of both images). In such situation, fresh gases are not blocked by the outer flame front and thus feed the ORZ. The available fuel will then be consumed attracting the leading edge upstream, thus promoting the flame position intermittency.

8.6 Quantitative comparison of spray ignition sequences between LES and experiments

In this section, a join experimental and numerical study is proposed to assess the ability of LES to reliably investigate the physics of spray ignition in a configuration reproducing the complex features of real burners. The experimental ignition probability map of the KIAI-Spray configuration is first discussed in order to select the ignition point used for ignition sequences. non-reacting flow conditions at the chosen point are recalled before comparing the experimental and LES ignition sequences in terms of flame kernel evolution over time and overall ignition timings.

8.6.1 Experimental ignition probability map

Ignition probability is evaluated experimentally as a function of the spark location and the results are provided in Fig. 8.20 (Left). The ignition probability map is closely linked to the main features of such swirled configuration. Indeed, ignition is almost impossible in the center of the burner corresponding to the IRZ, and until $r < 20$

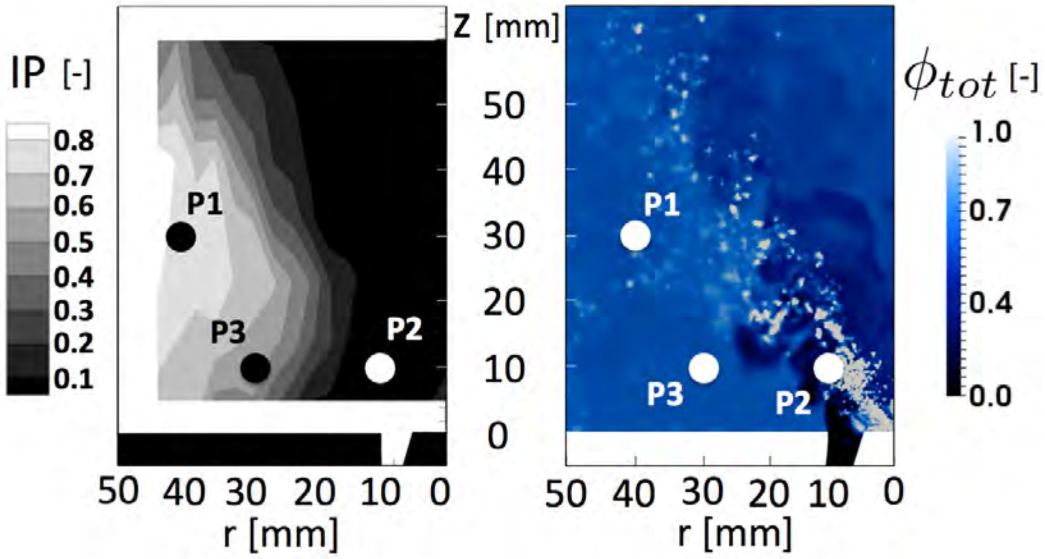

Figure 8.20: (Left) Experimental ignition probability map. (Right) Numerical instantaneous field of total (gaseous + liquid) equivalence ratio in the non-reacting flow. P1, P2, P3 indicates the location where spray ignition sequences are detailed in this chapter.

mm. The probability then gradually grows from $r \approx 20\ mm$ to $r \approx 30\ mm$ to reach a plateau of maximum ignition probability around $70-80\%$ in the ORZ. The very lean conditions considered in this work make ignition very difficult because the weak initial flame kernel is vulnerable to spatial and temporal variations of the local flow properties in terms of turbulent intensity, gaseous equivalence ratio and droplets number density that depend on the spark location.

Figure 8.20 (Right) shows a numerical instantaneous field of total (gaseous + liquid) equivalence ratio for one half of the combustion chamber obtained after the filling of the combustor is completed (500 ms physical time). A very lean homogeneous region ($\phi_{tot} = 0.45$) is observed in the IRZ, together with a lean homogeneous mixture, close to the global equivalence ratio ϕ_{glob} in the ORZ. The spray-jet region exhibits intense ϕ_{tot} fluctuations, with accumulation of droplets in the region of low gaseous vorticity. Note that the color scale is saturated to a maximum value of $\phi_{tot} = 1.0$ to better identify droplets, although the equivalence ratio reaches values up to $\phi_l = 20$ in the vicinity of liquid injection.

Based on this experimental ignition probability map, point P1 is chosen for the joint experimental-numerical analysis of spray ignition. P1 is located in the ORZ (see Fig. 8.20) at position $r = 40\ mm; z = 30\ mm$ and experimentally shows a high ignition probability of 80%.

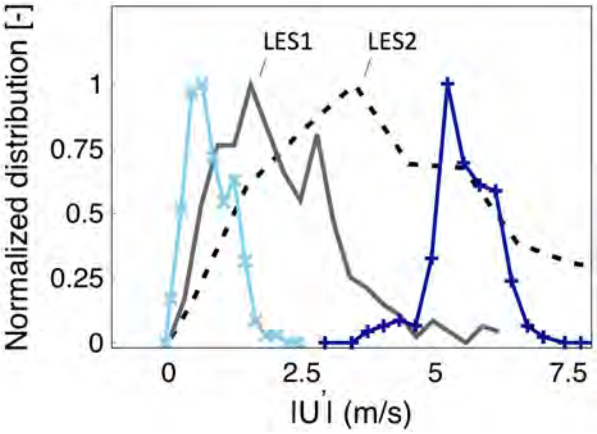

Figure 8.21: Normalized distributions of absolute velocity fluctuations on the non-reacting flow at point P1. Curves with symbols are experimental distributions (HS-PIV measurements) representative of low and high turbulence levels found near P1. LES distributions correspond to ignition trials shown in Fig. 8.23.

8.6.2 Two-phase flow conditions at P1 before ignition

At point P1 the mixture exhibits a rather homogeneous ϕ_{tot} distribution close to the global equivalence ratio ($\phi_{glob} = 0.61$) as discussed in Sec. 8.4.2. From time to time however, pockets of high ϕ_{tot} reach the vicinity of P1, indicating the presence of evaporating droplets. Interaction of droplets with the developing flame may therefore occur and will be discussed later.

Although point P1 is located in a region of low turbulent kinetic energy compared to the air jet [214], it exhibits non-negligible velocity fluctuations which significantly vary with time. This is illustrated in Fig. 8.21 which displays the experimental normalized distribution of two-component absolute velocity fluctuations in the neighbourhood of P1 (within a square of 5 mm length) for low and high turbulence levels with respect to the levels found near P1.

Two LES of ignition sequences (referred to as LES1 and LES2 in the following) are performed at point P1, starting at two different instants (t_1 and t_2 respectively) of the established *non-reacting* flow. Both instants are chosen to describe the flow variability around P1 observed experimentally. At both instants, P1 is surrounded with a lean gaseous mixture $\phi_{tot} \approx \phi_{glob}$. The two instants mainly differ by the turbulence intensity in the vicinity of P1, as shown in Fig. 8.21, where the normalized distributions of the three-component absolute gaseous velocity fluctuations recorded around P1 in both LES are also shown. The two numerical initial conditions are in between the experimental range, centred around 1.5 m/s and 3.5 m/s respectively. Note that the range of velocity fluctuation magnitude obtained numerically is not as wide as in the experiments, and the distributions are less peaked, which may be due to the much longer investigation

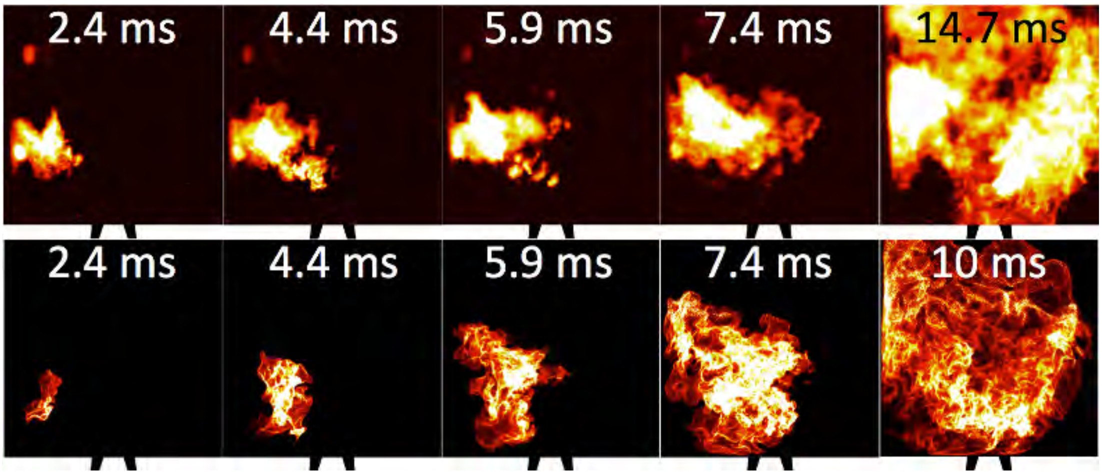

Figure 8.22: (Top): Experimental spontaneous flame emission sequence at P1 (EXP1). (Bottom): Numerical integrated heat release during ignition sequence at P1 (LES1). Dimensions of visualization boxes are $98\ mm \times 98\ mm$.

time in the experiments allowing to catch rare moments of locally very low and very high turbulence intensity. Furthermore, strict comparison between experimental and numerical distributions would be inaccurate recalling that they are respectively based on 2D and 3D velocity fields. Still, Fig. 8.21 shows that LES and experiments both highlight the same mechanisms influencing the kernel growth, being here turbulence intermittency.

8.6.3 Ignition sequences

Among the 30 experimental ignition tests at position P1, 9 high-speed videos were recorded, 8 of which reported successful events. Only two experimental sequences, named EXP1 and EXP2, are used here together with the two numerical ignition sequences (LES1 and LES2). These sequences EXP1 and EXP2 correspond respectively to the shortest and longest trials among the 9 recorded ones. EXP1 lies in the low range of turbulence intensity while EXP2 is triggered in the high range of turbulence intensity at P1.

Figure 8.22 (Top) shows the high-speed images of the flame kernel for EXP1. The visualization box size is $98\ mm \times 98\ mm$ for all images in the figure and shows both halves of the chamber. At $t = 2.4\ ms$ the kernel develops around P1 and has little distortion due to the initial low turbulence. Interaction with fuel droplets can be identified as intense luminous patterns. By $t = 4.4\ ms$, the kernel has sufficiently expanded to come close to the spray branch. At $t = 5.9\ ms$, a part of the flame kernel evolves towards the spray nozzle keeping a strong azimuthal motion. Intense, luminous parts in the images reveal the presence of a strong fuel stratification. At further times, the flame propagates and expands in all directions, in particular towards the injector.

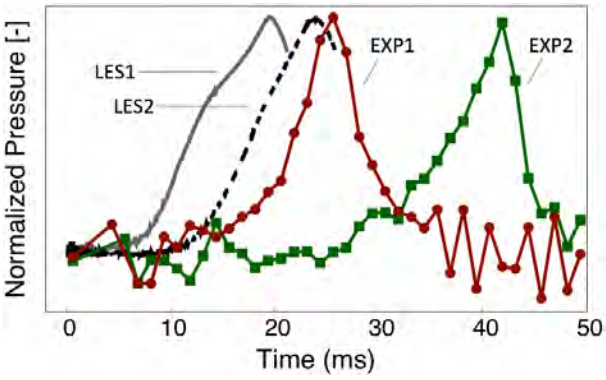

Figure 8.23: Temporal evolution of pressure at P1 for the experimental sequences EXP1 and EXP2, and the numerical sequences LES1 and LES2.

By $t = 14.7$ ms the flame has reached the opposite wall. This behaviour is characteristic of an ignition by spray branch. Once attached to the spray cone, the flame describes a spiral motion due to the swirling flow and finally reaches the injector. The bottom part of Fig. 8.22 illustrates the numerical sequence LES1, where the integration of the heat release through the entire volume of the chamber allows to track the evolution of the flame kernel. All the successive steps of kernel growth experimentally observed are reproduced numerically, assessing the capacity of LES to reproduce the mechanisms involved in ignition by spray branch.

The capacity of LES to accurately predict ignition delay times is now evaluated by plotting in Fig. 8.23 the temporal evolution of the pressure in the combustion chamber for the four experimental and numerical ignition sequences. First comparing with Fig. 8.21, a general trend can be observed: higher turbulence intensity before ignition leads to longer ignition delay, both experimentally and numerically. EXP2 and LES2 show very teared kernels due to high strain limiting the kernel growth during the first 10 ms for LES2 and for 20 ms for EXP2. This confirms the detrimental impact of the initial turbulent field at spark location on the flame kernel growth highlighted in [121, 201] for gaseous flames. However, the difference between the two numerical delay times is smaller than for the two experimental ignitions. This may be due to the closer and wider velocity fluctuation distributions of LES1 and LES2 compared to the two experimental ones. Yet, as soon as the flame holds on the injector ($t = 14.7$ ms for EXP1 and $t = 10$ ms for LES1 in Fig. 8.22), the agreement between LES and experiments is very good, the slope of the increase in pressure being very similar for the 4 experimental and numerical ignition sequences. Note that the total ignition delays predicted by the two LES are shorter than for experiments, the difference being mostly due to the kernel phase. Since this phase is the most stochastic phenomenon, many other LES sequences with various turbulence intensities and spray densities should be performed to quantitatively compare with the experiments.

This coupled numerical-experimental investigation shows the capacity of LES to investigate spray ignition in realistic configuration reproducing real burners geometries. In the next section, it is thus proposed to continue this joint work by focusing on the still incompletely understood mechanisms controlling ignition success or failure in such configurations. For this purpose, LES allows to analyse very deeply ignition sequences, bringing complementary information that cannot be extracted from experiments alone.

8.7 Identification of key mechanisms controlling ignition success or failure

8.7.1 Experimental classification of observed scenarii

Thanks to high-speed visualisations of flame kernel development initated from many points of the chamber, Marrero Santiago [2] reduced in his PhD all observed sequences in the KIAI-Spray set-up to 10 scenarii as discusses in Sec. 7.8. 5 successful ignition (IA-IE) scenarii and 5 extinction scenarii (E1-E5), have been revealed. These ten scenarii are placed in Fig. 8.24 as function of the spark position where they have been observed. Ignition and extinction scenario regions often overlap evidencing the stochasticity of ignition. Different scenarii leading to the same outcome can also occur at one position. These scenarii, briefly introduced in Sec. 7.8, are described here along with Fig. 8.25 sketching each one. Plain arrows indicate the typical initial trajectories of the kernel while green dashed arrows are representative of the trajectories of the developed kernel in a second stage. Interested readers are referred to [2] for more details.

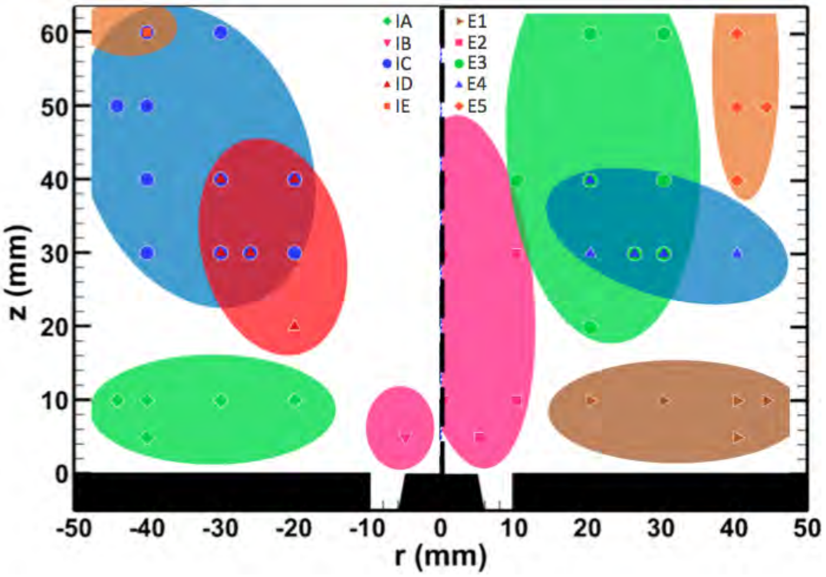

Figure 8.24: Map of (Left) Ignition scenarii and (Right) Extinction scenarii in the KIAI-Spray chamber.

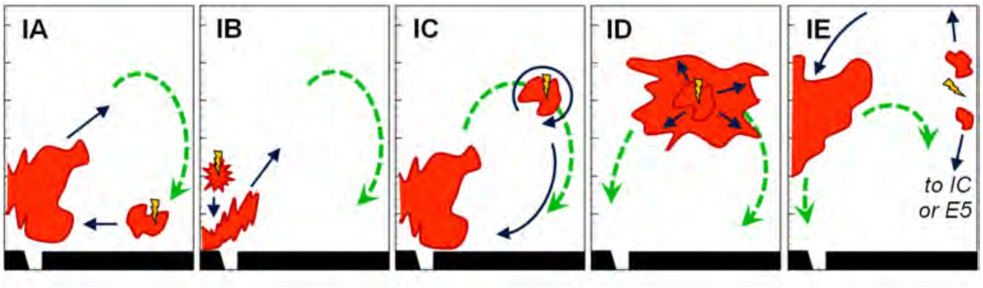

(a)

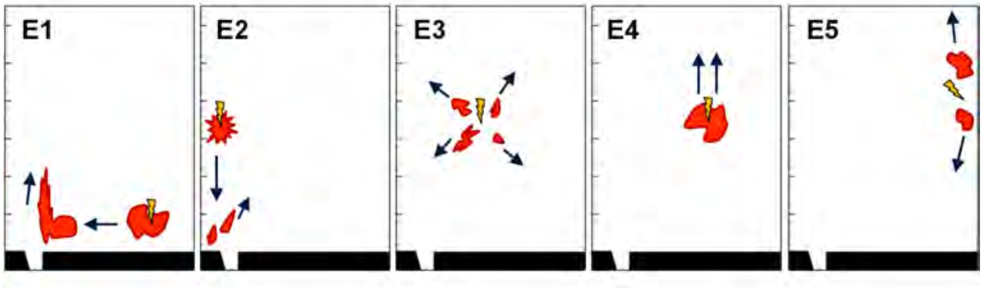

(b)

Figure 8.25: Sketch of the different observed (a) ignition and (b) extinction scenarii. Plain arrows indicate the typical initial trajectories of the kernel while green dashed arrows are representative of the trajectories of the developed kernel in a second stage.

- The *Delayed-Shearing Ignition Mode*, labelled IA, occurs in the bottom of the ORZ. The mean flow brings the kernel towards the spray-SJZ. The kernel has time to grow by travelling in the ORZ. When reaching the spray-SJZ, it faces detrimental high turbulence levels and is pushed downstream by the mean air jet. If the kernel survives, it is trapped again in the ORZ, igniting the whole chamber.

- The *Delayed-Shearing Extinction Mode*, labelled E1, is very similar to the *Delayed-Shearing Ignition Mode*. Here, due to a shorter residence time in the ORZ before reaching the spray-SJZ, the kernel do not survive in this last turbulent region. IA is preferential for $r > 30\ mm$ and E1 is preferential for $r < 30\ mm$.

- The *Prompt Cone-Ignition Mode*, labelled IB, hardly happen as the IRZ and bottom part of the spray-SJZ are generally lean regions presenting very high detrimental velocity fluctuations. If, exceptionally, good conditions are found at the spark position, a flame kernel may develop and would be immediately convected downstream and finally captured by the ORZ, as in IA.

- The *Prompt-Continuous-Shearing Extinction Mode*, labelled E2, is the most probable event taking place in the IRZ or at low axial positions of the spray-SJZ.

Kernels triggered here most of the time don't survive as they are immediately stretched by the turbulent shear layer.

- The *Long-ORZ-Growth Ignition Mode*, labelled IC, is very common since it takes place in the large ORZ or on top of the spray-SJZ. The smooth or slightly deformed kernel is rapidly captured by the mean ORZ flow. It evolves quiescently traversing the entire ORZ along the combustor wall. The end of the sequence is equivalent to the *Delayed-Shearing Ignition Mode*.

- The *Multi-Shearing Extinction Mode*, labelled E3, occurs in the spray-SJZ at mid radial positions $r \in (10, 30)\ mm$ and for $z > 20\ mm$. Here, turbulence is still high, and despite immediately interacting with fuel droplets, the kernel is quickly broken into several wrinkled small pieces. They most of the time extinguish rapidly.

- The *Spray-Branch Ignition Mode*, labelled ID, takes place when sparking on top of the spray-SJZ, or in the ORZ close to the spray branch. The kernel encounters acceptable turbulence levels and the presence of fuel droplets able to feed it. The flame front propagates upstream towards the injector through the spray branch and ultimately enters the IRZ and ORZ.

- The *Starving-Blowout Mode*, labelled E4, occurs on top of the spray-SJZ or ORZ. The kernel can sometimes be convected downstream by the still important mean flow velocity without being captured by the ORZ.

- The *Downstream-to-IRZ Ignition Mode*, labelled IE, has been rarely observed. It may occur along the combustor wall, at the limit between the top of the ORZ and the spray-SJZ. The kernel can be separated in two pieces here, one captured by the ORZ, then following already described paths, and the other one convected upstream. If this last one survives long enough, it can be trapped by the IRZ from the top and ignite the chamber.

- The *Clean-Division Mode*, labelled E5, occurs at the same place than the *Downstream-to-IRZ Ignition Mode*. After the kernel separation, both sub-kernels are too weak to survive, even if located in favourable regions. They thus extinguish in few milliseconds.

8.7.2 Decomposition of ignition/extinction scenarii in elementary mechanisms

To go a step further, and propose a simpler and possibly more universal classification of ignition/extinction mechanisms, the scenarii of Sec. 8.7.1 are now decomposed. In all

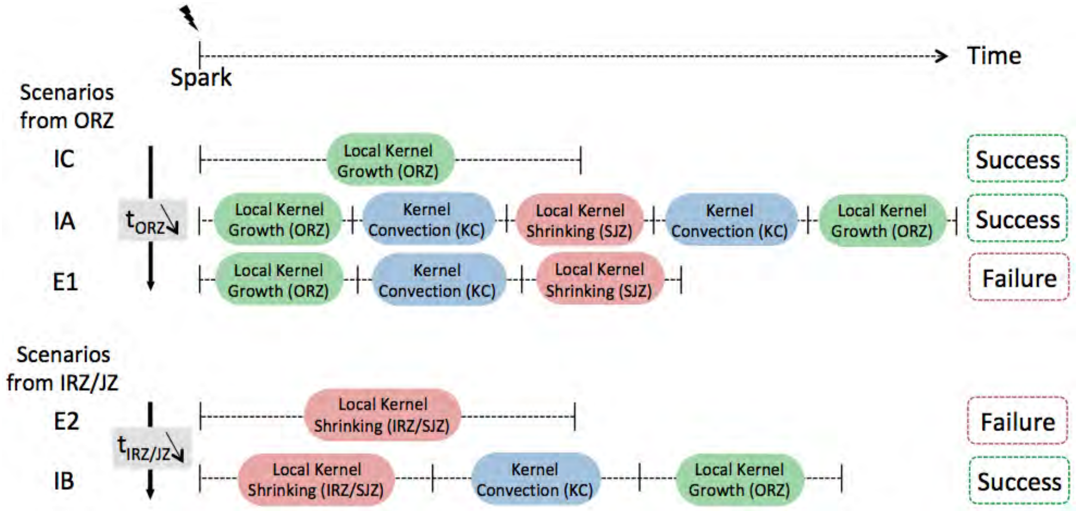
Spark
Time
Scenarios from ORZ
IC
IA
E1
t_{ORZ}↘
Local Kernel Growth (ORZ)
Kernel Convection (KC)
Local Kernel Shrinking (SJZ)
Success
Failure
Scenarios from IRZ/JZ
E2
IB
$t_{IRZ/JZ}$↘
Local Kernel Shrinking (IRZ/SJZ)

Figure 8.26: Sketch of the reconstruction of five configuration-dependent scenarii using universal elementary mechanisms.

scenarii, the kernel ability to survive or even expand is function of the local properties encountered along its trajectory. From this observation, three elementary mechanisms are proposed to reconstruct any ignition or extinction scenario:

- Local Kernel Growth (LKG)
- Local Kernel Shrinking (LKS)
- Kernel Convection (KC)

Figure 8.26 shows the decomposition of five scenarii found in our KIAI-Spray configuration using universal elementary mechanisms. The IC mode is merely a LKG process. Indeed, the residence time t_{ORZ} in the ORZ allows a long LKG leading to a strong kernel. In the IA mode, t_{ORZ} is reduced and the shorter LKG does not allow the kernel to stabilize. A KC process then brings the kernel in the SJZ, where it undergoes LKS until getting back in the ORZ where a LKG is again triggered, leading finally to ignition. Further reduction of t_{ORZ} leads to a too small kernel at the end of the first LKG process to survive the following LKS, and extinction occurs (E1 scenario). Similarly, when sparking in the IRZ, the E2 mode and the IB mode are easily converted in a combination of these three elementary mechanisms, the outcome being related to the residence times $t_{IRZ/SJZ}$ in the IRZ/SJZ respectively.

LKG and LKS processes are analyzed in the following section to highlight the associated local flow properties and kernel behaviour. The decisive role of kernel convection is also discussed.

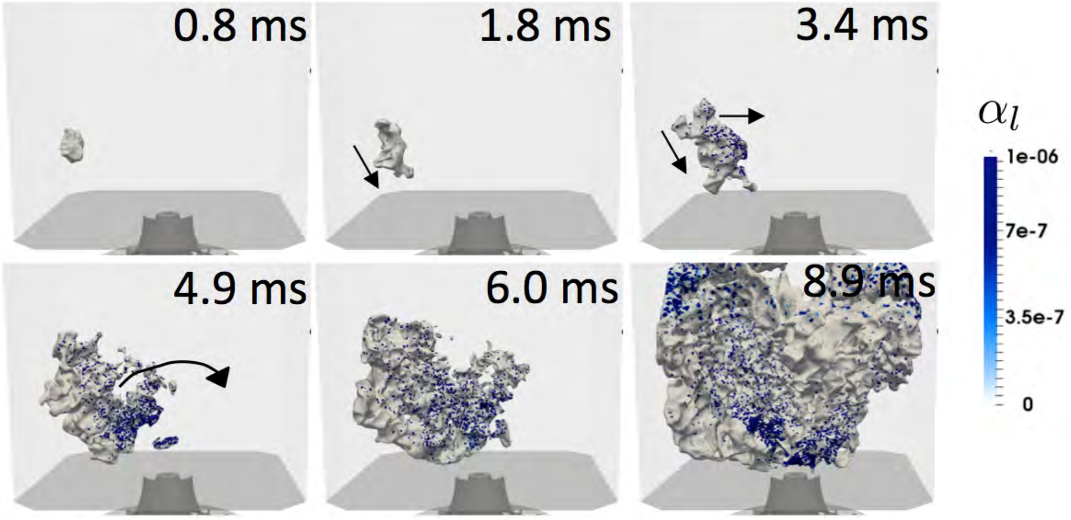

Figure 8.27: LES sequence P1-S. Flame front visualization (iso-$T = 1500\ K$) coloured by liquid fuel volume fraction.

8.7.3 Detailed analysis of elementary mechanisms

In this section, each elementary mechanism is analyzed using series of LES of ignition in the KIAI-Spray configuration. The sparking time and location are varied and some ignition sequences are wisely selected to highlight specific characteristic behaviours.

To characterize the local kernel-turbulence interactions and possible causes of extinction, two indicators will be used in the following. First the kernel surface over kernel volume ratio S_k/V_k, which increases with the degree of deformation of the kernel by large turbulent structures: an abrupt increase of S_k/V_k occurs when the kernel separates in several sub-kernels. Second, the density-weighted flame displacement speed $S_d^* = \frac{\rho}{\rho_f} S_d$ [177, 224] where ρ and ρ_f are respectively the local and fresh gases densities is used to evaluate the interaction between the flame and small vortices and possible extinction. S_d^* represents the difference between the convective speed and the flame front speed. The density-weighted form is preferred to account for gas expansion through the flame front. When small vortices are able to penetrate the preheat layer of the flame, the flame is thickened by the enhanced diffusion process, and negative S_d^* [225] may appear, if the rate of thermal diffusion dominates that of heat release. This is often associated to flame extinction [226].

8.7.4 Local Kernel Growth (LKG) mechanism

The LKG mechanism is well illustrated by the ignition at P1 ($r = 40\ mm, z = 30\ mm$), called P1-S, shown in Fig. 8.27. The kernel initially develops smoothly in the ORZ for the first microseconds. Around 1.8 ms, it is slowly convected to the bottom of the ORZ thanks to the recirculation motion. In the meantime, the kernel also develops

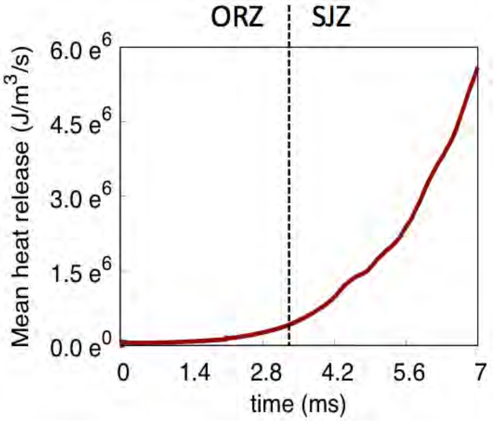

Figure 8.28: LES sequence P1-S: Temporal evolution of mean heat release in the whole chamber.

towards the top of the spray zone, as evidenced by the level of liquid volume fraction at the flame. The kernel then extends azimuthally due to the main swirl motion while being convected upstream along the Spray/Jet Zone to finally reach the injector nozzle after 8.9 ms. As shown by Fig. 8.28, the mean heat release in the whole chamber grows monotonously during the sequence showing an easy ignition. This LES sequence actually recovers the IC scenario highlighted experimentally. It can be decomposed in two phases: the quiescent kernel growth in the ORZ ($t < 2 - 3$ ms) and the turbulent kernel growth in the SJZ ($t > 2 - 3ms$).

8.7.4.1 LKG in the ORZ

The initial state is described with PDFs of flow and fuel/air mixing properties in a sphere of $r = 6$ mm around P1 shown in Fig. 8.29a and Fig. 8.29b with red plain lines. P1 is characterized by very quiescent conditions: the three velocity components are centred around 0 m/s and the velocity fluctuations are almost null, not exceeding 1 m/s. As already explained in Sec. 8.4.2, the gaseous equivalence ratio at P1 is quite constant around $\phi_g = 0.58$, near the global equivalence ratio. The few droplets found in this zone are characterized by a heterogeneous size distribution from $r = 5$ μm to $r = 20$ μm and are mainly at equilibrium with the gas as shown by the low relative velocity.

Figure 8.31a shows the mean gaseous equivalence ratio encountered by the kernel (at $c = 0.65 \pm 0.15$, where c is the progress variable based on the temperature) during the sequence. It confirms that during the first $2 - 3$ ms, the kernel sees a low gaseous equivalence ratio ($\phi_g \approx 0.55$). The temporal evolution of mean heat release at the kernel surface ($c = 0.65 \pm 0.15$) is shown in Fig. 8.31b. The heat release stabilizes after the initial peak associated to a sur-adiabatic phase following the spark. The mean gaseous equivalence ratio found at the position of droplets is logically higher, near ≈ 0.7. The

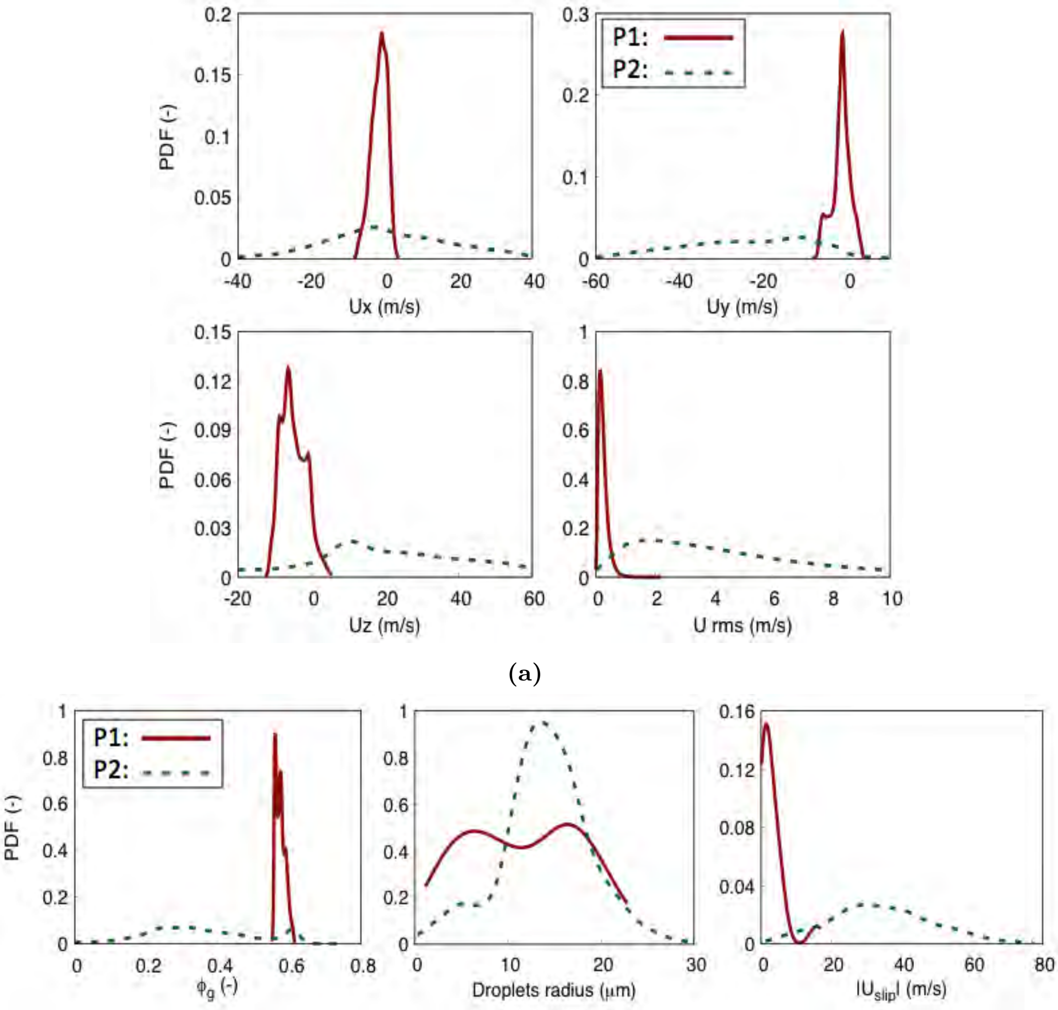

(a)

(b)

Figure 8.29: PDFs in a sphere of $r = 6\ mm$ around the sparking position for sequences P1-S and P2-F, at $t = 0\ s$ of (a) the three velocity components and RMS velocity, (b) gaseous equivalence ratio, droplets radius and relative velocity between droplets and the gas.

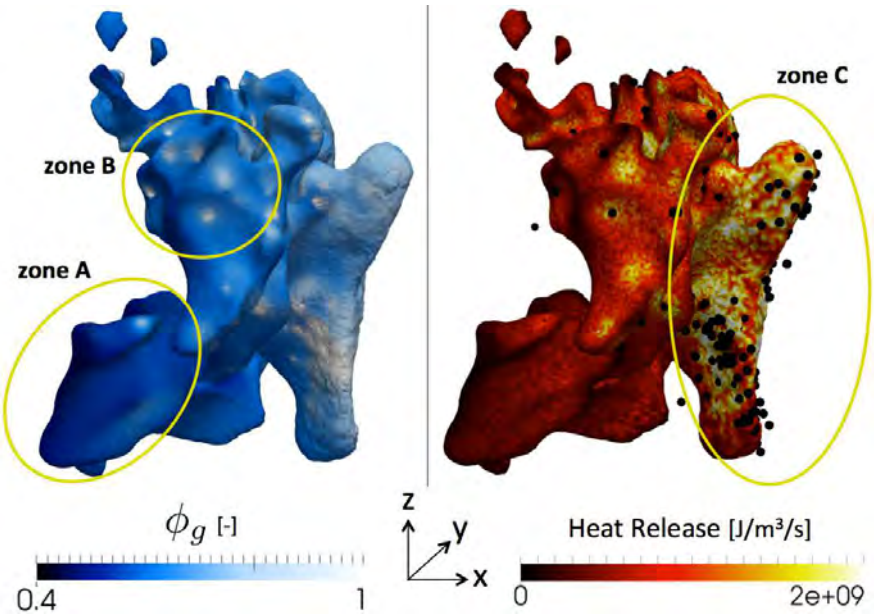

Figure 8.30: Zoom on a typical flame kernel in its early development stage near the ORZ - spray SJZ (iso-contour of progress variable $c = 0.5$ after 3.5 ms during sequence LES1 of Sec. 8.6.3) colored by (Left) gaseous equivalence ratio and (Right) heat release. Evaporating fuel droplets in this zone are represented on the right side by black spheres.

presence of droplets also matches with higher heat release. This link was also found in LES1 and LES2 investigated in Sec. 8.6.3 and can be better appreciated with Fig. 8.30 showing a visualisation of typical flame kernel in its early development stage near the ORZ - spray SJZ. The flame contour is colored by gaseous equivalence ratio (Left) and heat release (Right). Evaporating fuel droplets are represented by black spheres in Fig. 8.30 (Right). Three regions can be distinguished. In zone A where there are very few particles, the liquid fuel evaporation rate is not sufficient to compensate the gaseous fuel consumption, and the flame can not survive. The heat release is very low and the flame locally extinguishes. In zone B, fast single droplet evaporation occurs near the flame, generating a locally rich gaseous mixture and possibly high heat release in cases of individual burning droplets. However, the contribution of these isolated droplets to the main flame is marginal. The major impact of evaporating fuel droplets on the flame kernel is found in zone C. The spray is dense in this region, leading to high and flammable gaseous equivalence ratios. This region is the most reactive one, evidencing the preferential direction of the kernel towards zones of high fuel droplet number density. However, concerning P1-S, the overall low droplet number density near the kernel at that time makes the impact of droplets negligible in this case, similarly to zone A of B in Fig. 8.30.

The time evolution of S_d^* computed at $c = 0.35 \pm 0.15$, representing the preheat zone

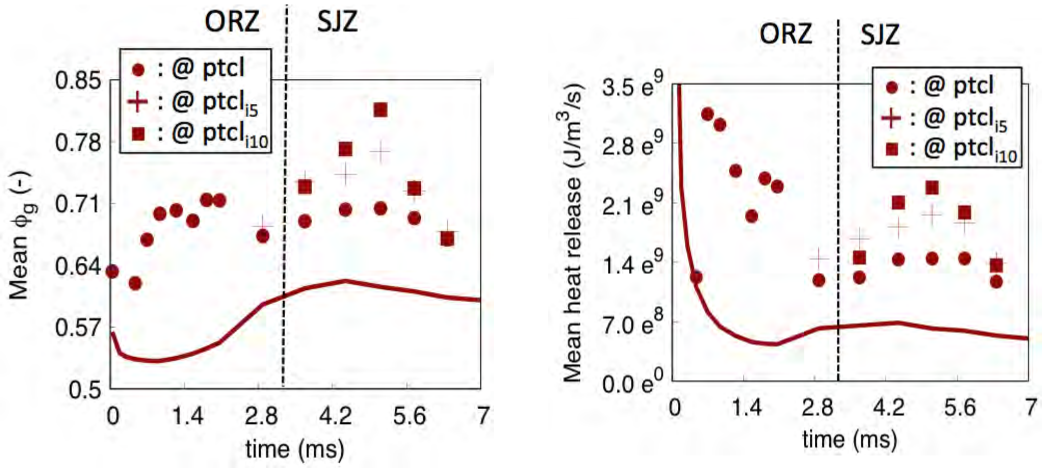

(a) (b)

Figure 8.31: LES sequence P1-S. Temporal evolution of (a) mean gaseous equivalence ratio and (b) mean heat release at $c = 0.65 \pm 0.15$. Symbols identify the mean value at the position of droplets located on the kernel surface $c = 0.65 \pm 0.15$: circles for all droplets, crosses for droplets having more than 5 droplets within $1\ mm$, squares for droplets having more than 10 droplets within $1\ mm$.

of the flame, and of S_k/V_k are shown respectively in Fig. 8.32b and Fig. 8.32a. S_k/V_k and S_d^* drop during the first $1\ ms$ in accordance with the almost spherical expansion observed in Fig. 8.27. The flame displacement speed stabilizes around $S_d^* \approx 0.07\ m/s$, i.e. close to the laminar flame speed at $\phi_g \approx 0.55$.

8.7.4.2 LKG in the SJZ

When arriving in the SJZ, the kernel encounters higher gaseous equivalence ratio up to $\phi_g = 0.63$ due to the much higher number density of droplets in the spray zone ($t > 3\ ms$ in Fig.8.31a). This beneficial increase of local equivalence ratio is however balanced by a lower flammability factor resulting from intermittent pockets (not shown) of lean mixtures. Although the SJZ has a high turbulence intensity, it does not affect S_k/V_k because the kernel is already large enough compared to the scales of turbulence, which can thus deform locally the kernel but can not break it in pieces. S_d^* also stays around $0.07\ m/s$ indicating no major effect of turbulence on the flame propagation.

8.7.4.3 Summary of Local Kernel Growth mechanism

The above analysis shows that the LKG mechanism, although mostly favoured by high ϕ_g and low u', may also appear for low ϕ_g / low u' (as in the ORZ) or high ϕ_g / high u' (as in the SJZ), provided that the positive effect on LKG (low u' or high ϕ_g) dominates

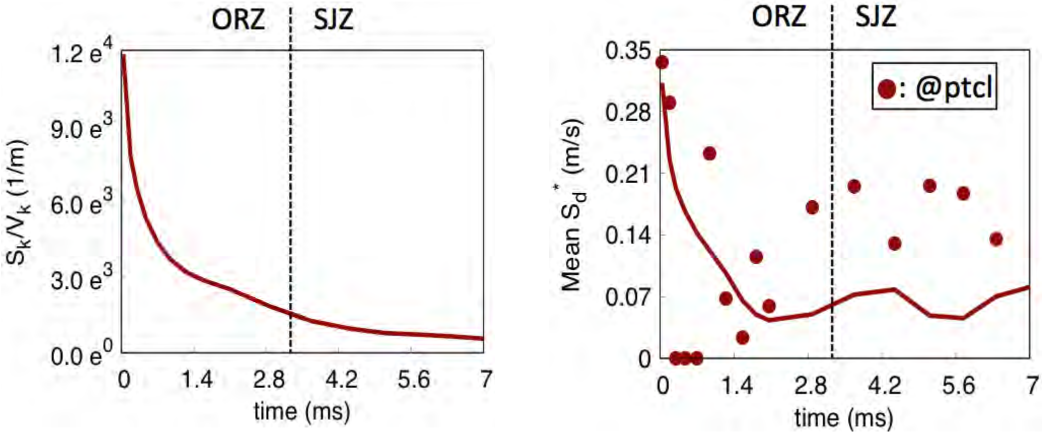

(a) (b)

Figure 8.32: LES sequence P1-S: Temporal evolution of (a) kernel surface over kernel volume ratio, and (b) mean density-weighted flame displacement speed S_d^* in the preheat zone of the flame defined as $c = 0.35 \pm 0.15$, with points representing the mean S_d^* at the position of droplets located in this zone.

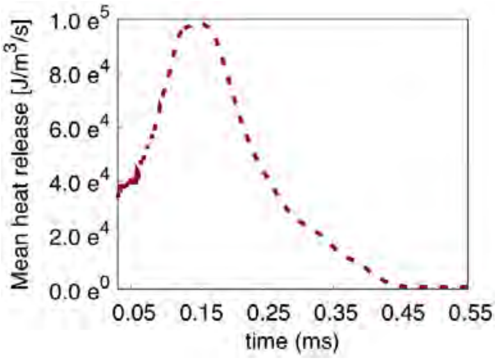

Figure 8.33: LES sequence P2-F. Time evolution of the mean heat release in the whole chamber.

8.7.5 Local Kernel Shrinking (LKS) mechanism

The LKS mechanism is studied with the sequence sparked at point P2 ($r = 10\ mm, z = 10\ mm$), called P2-F.

8.7.5.1 Overview of P2-F sequence

PDFs of initial flow and fuel/air mixing properties in a sphere of $r = 6\ mm$ around P2 are shown respectively in Fig. 8.29a and Fig. 8.29b with green dashed lines. As the sparking position is located in the core of the SJZ, the kernel immediately faces the most intense turbulent intensity in the whole chamber, reflected by the widespread velocity PDF. The PDF of gaseous equivalence ratio found is also quite broad, as recirculating gases from the ORZ and penetrating the SJZ create pockets of rich gases in an overall lean zone. The droplets radius distribution around P2 peaks at 15 μm, and droplets

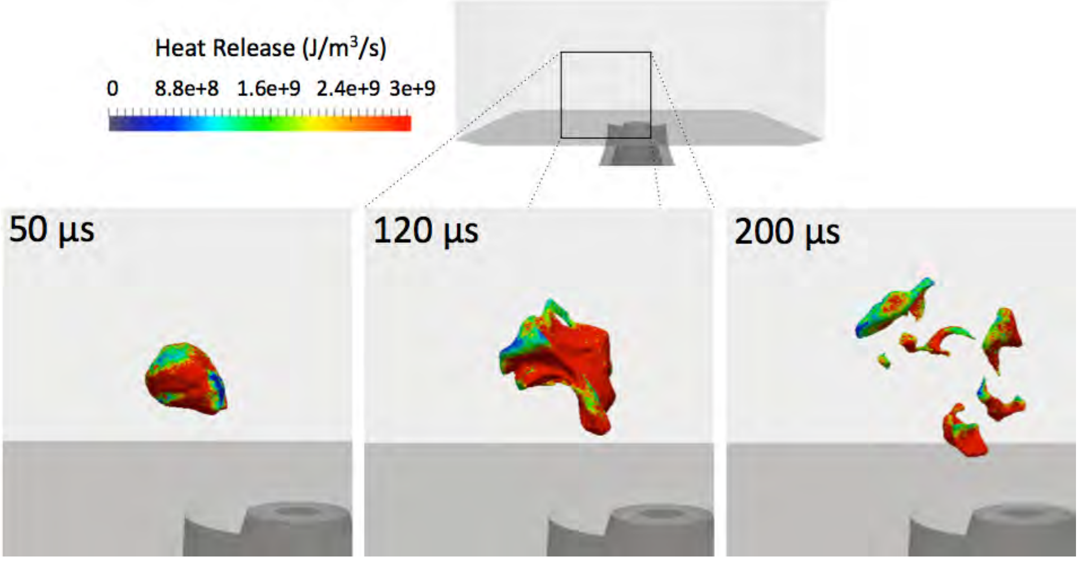

Figure 8.34: LES sequence P2-F. Flame front visualization (iso-$T = 1500\ K$) coloured by heat release.

are not in equilibrium with the gas as indicated with the non-zero slip velocities.

The sequence is short as the kernel quenches rapidly in less than 1 ms, as shown in Fig. 8.33. The general evolution of the flame is presented in Fig. 8.34. After 50 μs, the kernel starts to loose its initial spherical shape. After 120 μs it is already much shredded by large turbulent structures and is finally divided in multiple parts after only 200 μs, leading to its total extinction at $\approx$ 500 μs. This kernel fragmentation is perfectly similar to the one observed experimentally for spark positions close to P2 [2]. During the lifetime of the kernel, the droplets density on the kernel surface ($c = 0.65 \pm 0.15$) shown in Fig. 8.35a is relatively constant near $8e^8$ $drop/m^{-3}$. In the same time, the gaseous equivalence ratio at the kernel stays under the lean flammability limit, always under $\phi_g = 0.4$ as shown in Fig. 8.36a. In fact, an important part of heat release is produced by diffusion flames as shown in Fig. 8.35b with the Takeno Index [12]. Diffusion flames appear when droplets cross the flame front and evaporate in the burnt gases. Reaching around 50 % of the total heat release during the first 50 μs, the contribution of diffusion combustion reduces progressively as droplets evaporate, and premixed combustion represents at the end 90 % of the total heat release. The temporal evolution of mean heat release in the flame ($c = 0.65 \pm 0.15$) is shown in Fig. 8.36b. As for sequence P1-S, the presence of droplets creates spots of higher heat release.

8.7.5.2 Kernel-turbulence interaction

As the mixture properties seen above are able to sustain a flame, the reason for LKS and ignition failure is to be linked to the fragmentation of the kernel (Fig. 8.34). The temporal evolution of S_k/V_k and S_d^* computed at $c = 0.35 \pm 0.15$ shown respectively in

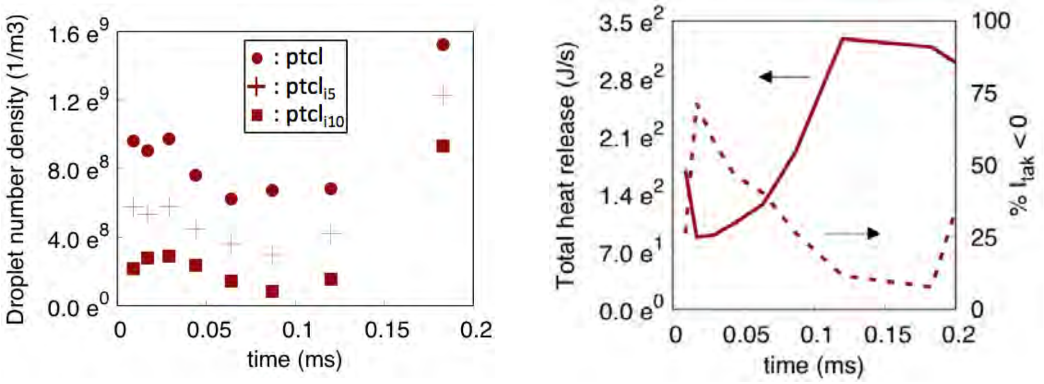

(a)

(b)

Figure 8.35: LES sequence P2-F: (a) Temporal evolution of the mean droplet number density on the kernel surface defined as $c = 0.65 \pm 0.15$. Circles identify all droplets, crosses identify only droplets having more than 5 droplets within $1\ mm$, squares stand for droplets having more than 10 droplets within $1\ mm$. (b) Temporal evolution of the total heat release in the whole chamber, and the % of heat release conditioned by negative Takeno Index.

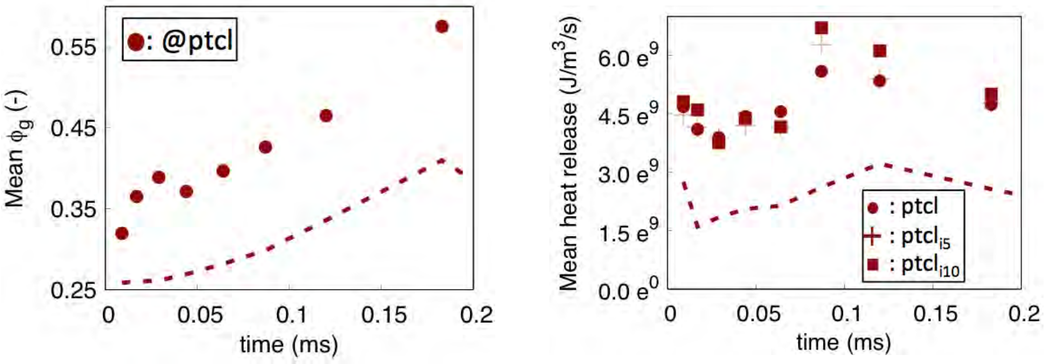

(a)

(b)

Figure 8.36: LES sequence P2-F. Temporal evolution of (a) mean gaseous equivalence ratio and (b) mean heat release seen by the flame identified by $c = 0.65 \pm 0.15$. Symbols identify the mean value at the position of droplets located on the kernel surface considered: circles for all droplets, crosses for droplets having more than 5 droplets within $1\ mm$, squares for droplets having more than 10 droplets within $1\ mm$.

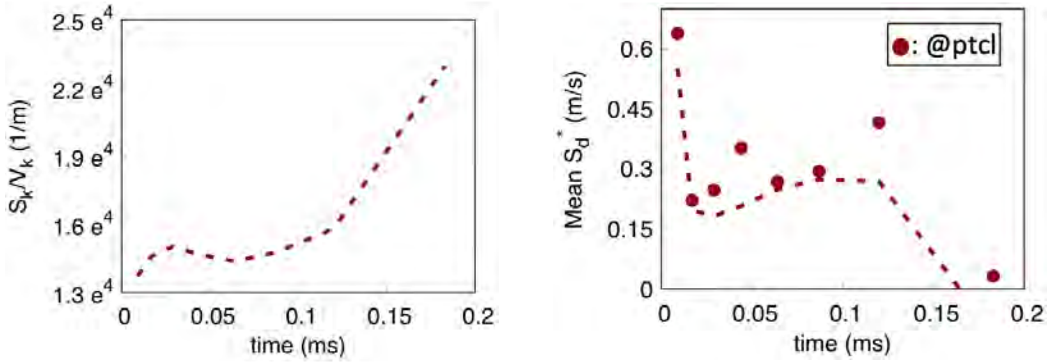

(a) (b)

Figure 8.37: LES sequence P2-F: Temporal evolution of (a) kernel surface over kernel volume ratio, and (b) mean density-weighted flame displacement speed S_d^* in the preheat zone volume defined as $c = 0.35 \pm 0.15$, where points represent the mean S_d^* at the position of droplets located in this zone.

Fig. 8.37a and Fig. 8.37b confirm the process. The increase of S_k/V_k, indicating kernel fragmentation occurs near 100 μs. At that time, the mean heat release still increases, showing that fragmentation itself is not the direct cause of extinction. It however leads to smaller sub-kernels which are much more subjected to thermal quenching. This reflects in the mean S_d^* which drops drastically at 150 μs, corresponding to the sudden drop of mean heat release. Compared to sequence P1-S and the LKG mechanism, it appears that LKS is the result of low ϕ_g and high u'.

8.7.6 Kernel Convection

As explained in Sec. 8.7.2, kernel convection is the third mechanism involved in ignition. It plays a critical role when carrying the kernel from a zone promoting LKG to a zone promoting LKS or vice versa. To illustrate the importance of kernel convection, two sequences both sparked at P3 ($r = 30\ mm, z = 10\ mm$), in the bottom part of the ORZ, are analyzed. One successful sequence, called P3-S, follows the IA scenario (see Sec. 8.7.1) while the failed sequence, called P3-F, exhibits a E1 scenario. The only difference between the two sequences is their sparking time.

PDFs of the initial radial $x-$velocity component in the direction of the injector, velocity fluctuation, gaseous equivalence ratio and droplet radius in a sphere of $r = 6\ mm$ around P3 are shown in Fig. 8.38 for both sequences. Both kernels of P3-F and P3-S actually see similar initial conditions in terms of flammability conditions, velocity fluctuations and droplet presence. The most important difference concerns the initial flow velocity in the direction of the injector: For P3-S it peaks around $-1\ m/s$ and never goes below $-6\ m/s$, while for P3-F it peaks around $-7\ m/s$, never exceeding $-2\ m/s$. This means that the kernel of sequence P3-S is convected towards the injector

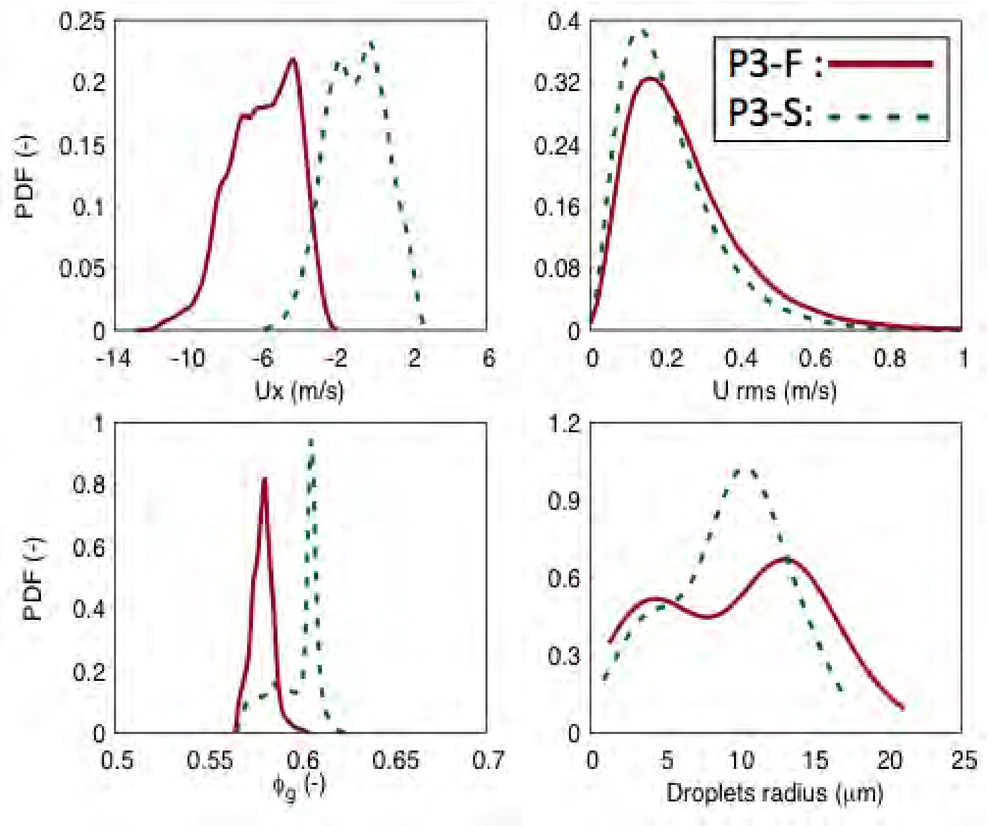

Figure 8.38: LES results: PDF of velocity towards the injector axis, RMS velocity, gaseous equivalence ratio and droplets radius in a sphere of $r = 6\ mm$ around the sparking position for sequences P3-F and P3-S, at $t = 0\ s$.

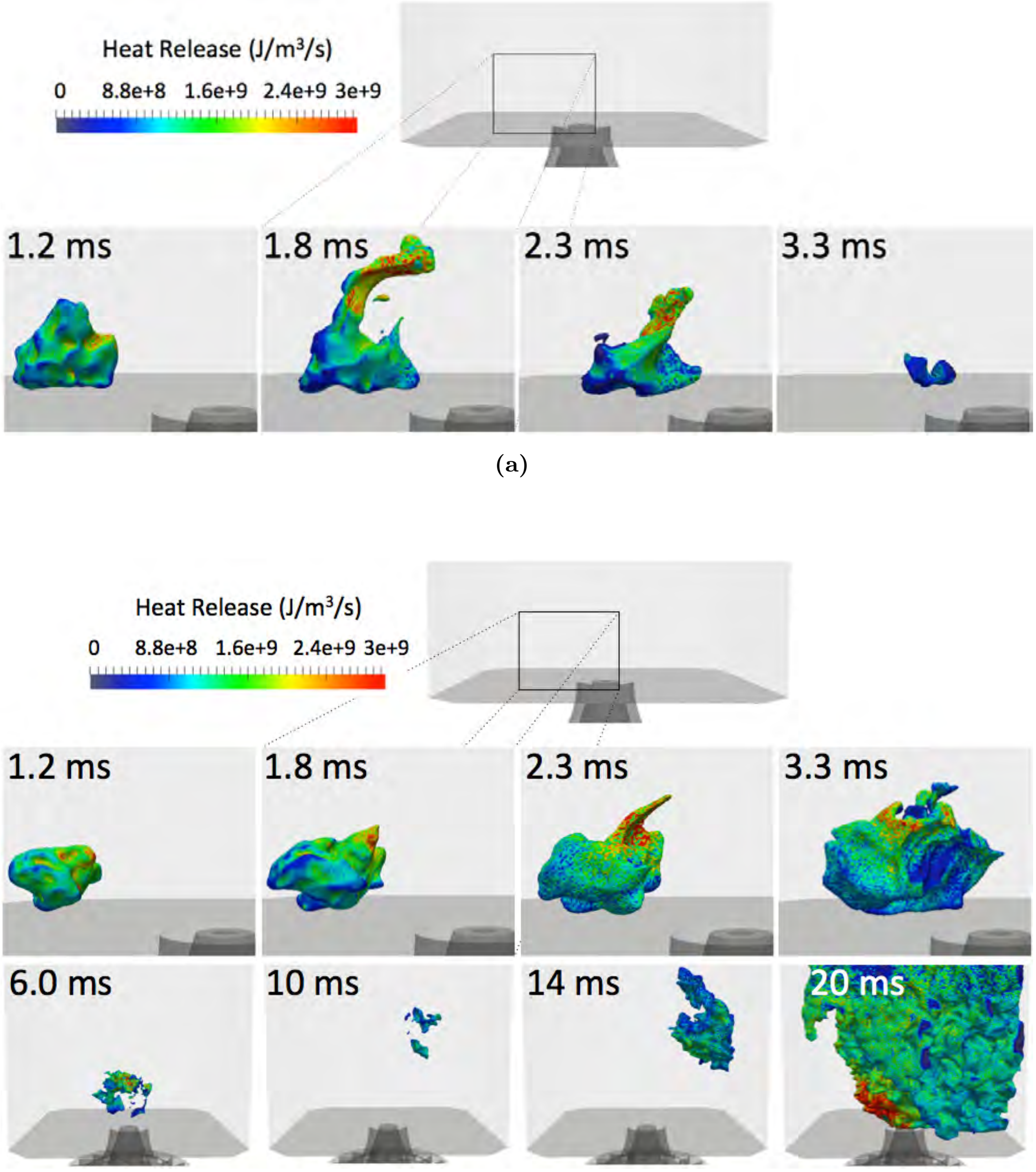
Heat Release (J/m³/s)
0
8.8e+8
1.6e+9
2.4e+9
3e+9
1.2 ms
1.8 ms
2.3 ms
3.3 ms
Heat Release (J/m³/s)
0
8.8e+8
1.6e+9
2.4e+9
3e+9
1.2 ms
1.8 ms
2.3 ms
3.3 ms
6.0 ms
10 ms
14 ms
20 ms

(a)

(b)

Figure 8.39: Flame front visualisations (iso-$T = 1500\ K$) coloured by heat release of LES ignition sequences (a) **P3-F** and (b) **P3-S**.

much more slowly than the kernel of sequence P3-F. The longer residence time t_{ORZ} of the kernel of sequence P3-S results in a longer LKG mechanism characteristic of the ORZ. This t_{ORZ} difference is visible in Fig. 8.39a and Fig. 8.39b showing the flame front evolution of sequences P3-F and P3-S respectively: when arriving in the SJZ when high kernel-turbulence interactions are expected, the kernel in P3-S is more than twice larger than in sequence P3-F, because it arrives there with a 1 ms delay. As a consequence, the kernel-turbulence interactions have more impact on the kernel of P3-F which thus experiences a LKS.

8.8 Conclusions

Two-phase flow lean aeronautical ignition has been investigated on an academic burner representative of real configurations by means of two-phase ignition LES simulations. non-reacting flow and stable flame regimes have been first analyzed to study the flow topology, droplet size distribution, gaseous and liquid velocities, and the flame structure. A typical swirled non-reacting flow topology made of an IRZ, ORZ and spray-SJZ is found. The reacting case exhibits a lifted M-shape flame. Simulations have been compared to experimental results, finding a general very good agreement between both approaches.

A joint experimental and numerical study has then be conducted at a selected sparking point of the ORZ. Both long and short ignition sequences have been similarly recovered as function of the turbulent intensity level existing in the local flow prior to sparking. The overall agreement has demonstrated the accuracy of LES to study ignition in realistic burners.

Therefore, it has been proposed to continue this joint work to focus on the identification of generic mechanisms inducing either ignition success or failure. Identified scenarii observed experimentally on the KIAI-Spray set-up have been proven to be all explained by three very generic mechanisms transposable to any similar burner: Local Kernel Growth (LKG), Local Kernel Shrinking (LKS), and Kernel Convection (KC). A LKS mechanism is characterized by detrimental turbulence kernel interactions prevailing over potentially good flammability conditions, contrary to a LKG mechanism. KC is the decisive parameter transporting the kernel from LKG to LKS zones and inversely. A detailed numerical investigation of ignition sequences starting from three points in the chamber has allowed to deeply characterize these elementary mechanisms and to demonstrate the kernel evolution when facing each one of them. The local beneficial effect of the presence of droplets has also been tackled. The flame kernel development is enhanced by the presence of droplet clusters (found in the spray-SJZ essentially) but negligibly by isolated droplets crossing the flame front. Thanks to the coupled numerical-experimental work, a reliable investigation of the underlying physical mechanisms of spray ignition has been provided, and a methodology to analyse them has been demonstrated.

Chapter 9

Prediction of two-phase ignition probability

Contents

9.1 Objectives 177

9.2 Test configuration 178

9.2.1 Experimental configuration 178

9.2.2 Large Eddy Simulation set-up 179

9.2.3 Non-reactive LES results 180

9.3 Model for Ignition STatistics (MIST) 182

9.3.1 Quenching criteria 182

9.3.2 Initial kernel 186

9.3.3 Kernel trajectories: Prediction of the kernel probability of presence 187

9.4 Application to the KIAI burner 189

9.4.1 Comparison with experimental ignition probability maps . . . 189

9.4.2 Comparison with two-phase reacting LES ignition sequences . 191

9.5 Application to a real combustor 194

9.5.1 Industrial configuration and operating points 194

9.5.2 Two phase cold flow topology for the two operating points . . 196

9.5.3 Parameters used for MIST 197

9.5.4 Comparison of relight performance at two flight altitudes . . 199

9.5.5 Optimisation of the spark plug position 201

9.6 Conclusions 208

9.1 Objectives

Because of its stochastic nature, ignition is often evaluated experimentally using ignition probability P_{ign} maps [181, 186]. Numercially, direct prediction of the ignition probability using LES has been proven feasible [201] but can seldom be used for design purposes due to the numerical cost and return time associated with LES simulations. Several methodologies have been developed to provide a rapid and computationally cheap evaluation of the ignition probability. These methods are reviewed in Sec. 7.4.

They can be sorted into two classes: models based solely on local properties of the non-reacting flow and models tracking the spatio-temporal evolution of the ignition kernel (and subsequent flame development). Pointwise models are computationally cheap and provide estimation of P_{ker} but fails to capture the transient motion of the flame kernel, thus are not able to predict P_{ign} in regions dominated by convection. Many attempts of the second class have been proposed in the litterature [200, 205, 206, 207, 209, 227]. They were able to capture transient flame kernel motion and expansion, but were found sensitive to arbitrary success criteria and the multiple simulations required to obtain converged statistics significantly increase the computational cost.

In this work, it is proposed to go a step further along the same line, with the development a method that directly extracts flame kernel motion statistics from time-averaged cold flow quantities. This allows to built reliable full ignition maps and to determine the optimum position of the igniter.

In the following, the model is derived and applied to the lean swirled experimental burners KIAI and KIAI-Spray operated in premixed, non-premixed and two-phase flow modes [186, 215]. The model outputs and performances are discussed and the model is ultimately used on an industrial combustion chamber, showing its value on a very complex configuration.

This chapter is adapted from an article in preparation for submission to Combustion & Flame :
L. Esclapez, F. Collin-Bastiani, E. Riber, B. Cuenot, A statistical model to predict ignition probability
The initial development of the model was done in [1]. The contribution of this PhD work to the model is its improvement, in particular its adaptation to two-phase flow, and its application to the KIAI-Spray burner and industrial configuration.

9.2 Test configuration

9.2.1 Experimental configuration

The experimental configuration employed to evaluate the model performances is the already presented KIAI set-up, later updated for two-phase flows [2] (KIAI-Spray). In gaseous conditions, the injection system is composed of a central jet (d = 4 mm) nested within the annular swirl stream (D_{in} = 9 mm, D_{ext} = 20 mm) of the swirler. In premixed mode, both the central tube and the plenum are fed with a methane/air mixture whereas in non-premixed mode the central jet is fed with pure methane and the plenum is fed with air.

	Premixed	Non-premixed	Spray
Central jet $\dot{m}_{Air}$ (g/s)	0.224	-	-
Plenum $\dot{m}_{Air}$ (g/s)	5.37	5.43	8.2
Central jet $\dot{m}_{Fuel}$ (g/s)	0.009	0.234	0.33
Plenum $\dot{m}_{Fuel}$ (g/s)	0.233	-	-
$S_{w,Expt.}$	0.76	0.76	0.76
ϕ_{glob}	0.75	0.75	0.61
P_{in} (bars)	1.0	1.0	1.0
T_{in} (K)	300	300	416
T_{Fuel} (K)	-	-	350

Table 9.1: Summary of experimental operating conditions in premixed, non-premixed and spray modes. Incoming air and fuel mass flow rates from the central jet and the plenum, experimental swirl number $S_{w,Expt.}$ (evaluated at the combustion chamber inlet), global equivalence ratio ϕ_{glob}, inlet pressure P_{in} and temperature T_{in}, and n-heptane inlet temperature for the spray case.

All experimental operating conditions of premixed, non-premixed and spray modes are summarized in Tab. 9.1. Compared to spray cases investigated in Chap. 8, air and fuel are not preheated for the gaseous cases and a richer regime is studied. To measure the fuel mole fraction field in non-premixed mode, planar laser induced fluorescence (PLIF) based on acetone is used. It is recalled that ignition is triggered by laser-induced breakdown allowing a non-intrusive control of the deposit location, duration and strength. Ignition probability maps are constructed using 50 ignitions tries at each deposit location for the gaseous cases resulting in a maximum error of about 7,2% [228], and using 30 ignitions tries at each deposit locations for the spray case.

9.2.2 Large Eddy Simulation set-up

All simulations are performed with the solver AVBP [229, 230]. The third order accurate in space and time numerical scheme TTGC [48] is used. Inlet and outlet boundary conditions are treated according to the NSCBC formulation [231]. Walls are considered adiabatic non-slipping in gaseous cases at atmospheric conditions and treated as non-slipping iso-thermal ($Tw = 387\ K$) in the preheated spray mode, which induces very few differences concerning the cold flow. Turbulent subgrid stresses are modeled using the SIGMA approach [29]. For gaseous cases, chemistry is described with a 2-step formalism and the thickened flame approach as presented in Esclapez *et al.* [201]. For the spray case, ARC chemistry is used without dedicated combustion model as detailed in Sec. 8.3. In the spray mode, a Lagrangian approach is retained for the dispersed phase description. Details are provided in Sec. 8.3. The domain is discretized into a fully unstructured mesh using around 22 million tetrahedral elements (details given in

Sec. 8.3). The axial direction is referred to as the z-axis, corresponding to the main flow direction, while the x-axis and y-axis denote the transverse directions. Space dimensions are non-dimensionalized by $D_{ext} = 20\ mm$.

9.2.3 Non-reactive LES results

The flow pattern shown in Fig. 9.1 for the gaseous case in very similar the spray case (see Sec. 8.4) and is therefore not described again. Detailed comparison of the non-reacting LES prediction against experiments for the premixed and non-premixed case have been reported in a previous works [1, 232]. Similar comparison is presented in Sec. 8.4.1 for the spray case. A very good agreement is found authorizing the development of the ignition model.

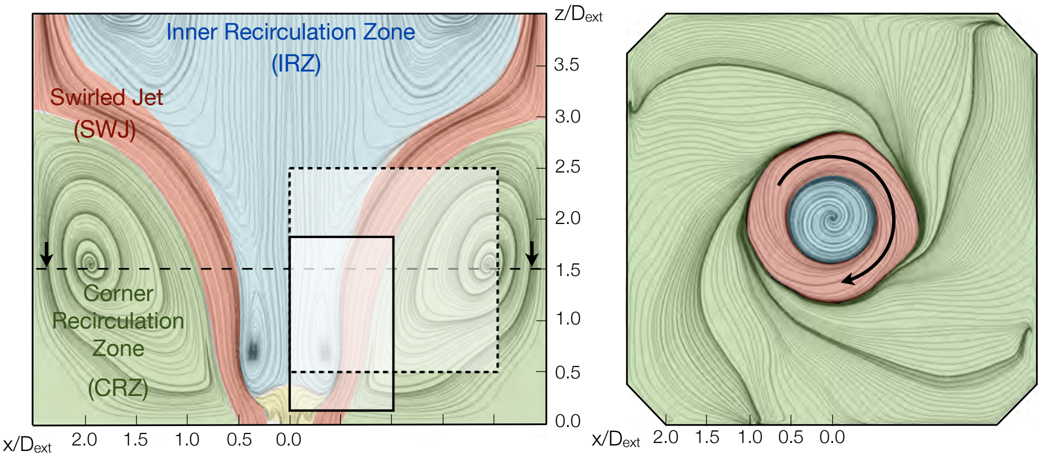

Figure 9.1: Time-averaged pseudo-streamlines in a central x-normal plane (left) and z-normal plane (right) for the non-premixed case. Red: Swirled Jet Zone (SJZ), Blue: Inner Recirculation Zone (IRZ), Green: Outer Recirculation Zone (ORZ). The black plain and dashed boxes respectively indicate the experimental ignition maps for gaseous and spray cases.

A focus is now made on mixing, which is important for ignition. Figure 9.2 (left) shows the mean flammability factor field. Since the overall equivalence ratio is flammable, F_f is unity in most of the combustion chamber where all species are well mixed, and reaches 0 only at the methane and air inlets. Intermediate values of F_f are found in the wake of the air swirled jet, between the rich injection and lean ORZ. The IRZ is mostly filled with premixed flammable mixture. The mixture fraction PDF extracted along the arrows (a) and (b) (Fig. 9.2 (right) show the variety of z distribution and the strong inhomogeneity in these zones. In the spray case, evaporation and mixing effects reflect on the gaseous and liquid equivalence ratio maps ϕ_g and ϕ_l, shown in Fig. 9.3. Due to the preheated conditions, droplets evaporate quickly leading to $\phi_l > 1$ in the SJZ for $z/D_{ext} < 1$. Almost no droplets are found in the upper part of the SJZ and even less in the IRZ and ORZ. The entire ORZ is characterized by a very homogeneous gaseous equivalence ratio close to the global value $\phi_{glob} = 0.61$, whereas the IRZ is leaner (ϕ_g ¡ 0.5), close to the lean flammability limit.

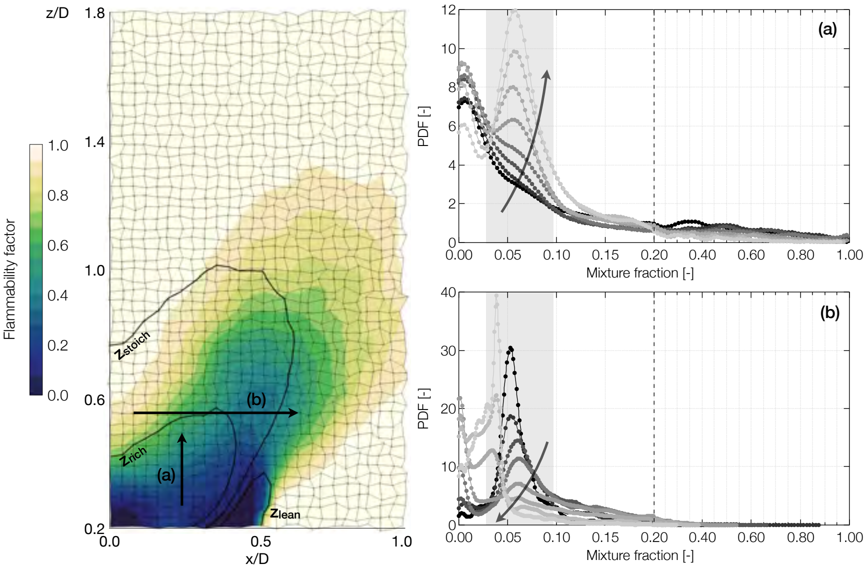

Figure 9.2: Non-premixed case. Mean flammability factor field (left) with z-isolines and $P(z)$ at several locations in the mixing region (right). The grey area highlights the flammable mixture zone.

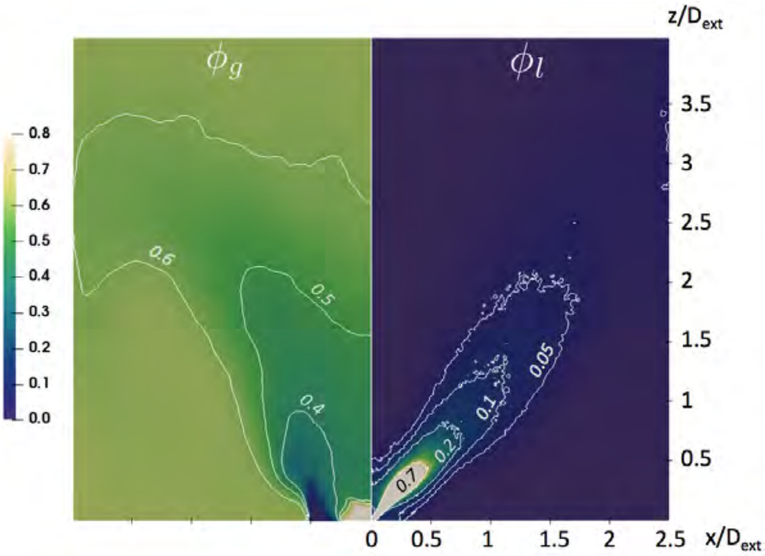

Figure 9.3: Spray case. Maps of the cold flow gaseous equivalence ratio ϕ_g (left) and liquid equivalence ratio ϕ_l (Right).

9.3 Model for Ignition STatistics (MIST)

In contrast with previous methodologies [200, 202, 204], the objective here is to take into account the flame kernel displacement by constructing trajectory statistics from the flow statistics. Combining these kernel motion statistics with local flow properties then leads to the ignition probability. The model can be decomposed in the following steps:

1. Perform a non-reacting CFD simulation to obtain the first two statistical moments of the velocity components ($\overline{u_i}$, u_i') and mixture fraction ($\overline{z}$, z'). Liquid volume fraction statistics ($\overline{\alpha_l}$, α_l'), mean droplet diameter $\overline{d_p}$, and mean droplet velocity $\overline{u_l}$ are also required for the spray case. In LES, statistics are obtained via time-averaging.
2. Compute quenching criteria from the non-reacting flow statistics.
3. Use the spark characteristics to evaluate the kernel initial size and the time required for cooling from the sparking temperature to the burnt gas temperature. This step is performed in 0D assuming that the kernel temperature evolution is dictated by the balance between heat release rate and turbulent dissipation.
4. Starting from the state defined in step 3, compute the temporal evolution of kernel statistics, by combining the evolution of the kernel probability of presence P_{pres} constructed from step 1 statistics with the quenching criteria of step 2. The kernel size evolution is also computed to determined when it has grown sufficiently to ensure a successful ignition.

Note that step 1 may be performed with any approach to predict statistics or even with measurements.

9.3.1 Quenching criteria

Like previous ignition probability models, two major mechanisms leading to kernel quenching are considered: mixing [169] and flame stretching [200, 205].

9.3.1.1 Mixture composition

Gaseous cases Several ignition studies in non-premixed flow in the literature clearly point out the fact that the flammability factor F_f is a critical parameter [169, 181, 200], closely related to the probability of creating a sustainable flame kernel. The flammability factor is well defined for gaseous configurations (see Eq. 7.1). It is the integral of the mixture fraction PDF $P(z)$ between the lower (z_{lean}) and upper (z_{rich}) flammability limits. As performed in experimental studies [169, 193], time-averaged statistics

$\overline{z}$, z' obtained from the non-reacting LES are used to construct the flammability factor. It is however necessary to assume a shape for $P(z)$. In free jets, the combination of the Gaussian and Dirac functions provides a fairly good estimate of F_f [233]. For more complex flows such as swirled flows, the large variety of mixture fraction distributions (see Fig. 9.2) is better represented by a combination of the log-normal and Beta distributions:

$$F_{f,model} = \gamma F_{f,\beta} + (1-\gamma) F_{f,logN}. \tag{9.1}$$

In this expression,

$$F_{f,logN} = \frac{1}{2}\left[\mathrm{erf}\left(\frac{\ln(z_{rich})-\mu}{\sqrt{2}\,\sigma^2}\right) - \mathrm{erf}\left(\frac{\ln(z_{lean})-\mu}{\sqrt{2}\,\sigma^2}\right)\right] \tag{9.2}$$

is the flammability factor evaluated using a log-normal repartition function with μ and σ the log-normal law parameters computed from $\overline{z}$ and z' and

$$F_{f,\beta} = I_{z_{rich}}(\alpha,\beta) - I_{z_{lean}}(\alpha,\beta) = \frac{B_{z_{rich}}(\alpha,\beta)}{B(\alpha,\beta)} - \frac{B_{z_{lean}}(\alpha,\beta)}{B(\alpha,\beta)} \tag{9.3}$$

is the flammability factor evaluated using a Beta distribution where $B_z(\alpha,\beta)$ is the incomplete β function of parameters α and β given by:

$$\alpha = \overline{z}\left(\frac{\overline{z}(1-\overline{z})}{z'} - 1\right) \quad \text{and} \quad \beta = (1-\overline{z})\left(\frac{\overline{z}(1-\overline{z})}{z'} - 1\right). \tag{9.4}$$

The blending factor γ is evaluated using:

$$\gamma = 0.5\left(1 + \tanh\left(\frac{z' - 0.15}{0.04}\right)\right) \tag{9.5}$$

A second important quantity to characterize the mixture is the value of z_{mean} within the flammability limits, i.e. the conditional mean flammable mixture fraction $\overline{z}_{flam}$, given by:

$$\overline{z}_{flam} = \frac{\int_{z_{lean}}^{z_{rich}} zP(z)\,dz}{F_f} \tag{9.6}$$

Taking $P(z)$ as the composite PDF introduced previously, $\overline{z}_{flam}$ is found:

$$\begin{aligned}\overline{z}_{flam} = \Bigg(&\gamma \int_{z_{lean}}^{z_{rich}} \frac{1}{B(\alpha,\beta)} z^{\alpha}(1-z)^{\beta-1}\,dz \\ &+(1-\gamma)\int_{z_{lean}}^{z_{rich}} \frac{1}{\sigma\sqrt{2\pi}} \exp^{-\frac{(\ln(z)-\mu)^2}{2\sigma^2}}\,dz\Bigg) / F_{f,model}\end{aligned} \tag{9.7}$$

The accuracy of the predicted values of F_f and $\overline{z}_{flam}$ in non-premixed mode compared to the actual values obtained from the LES is assessed in [1].

Spray cases In addition to the directly available gaseous fuel, F_f must take into account the liquid fuel that evaporates in the kernel. Following the work of Rochette *et al.* [15] who analyzed two-phase laminar flame structures, the characteristic evaporation time

$$\tau_{ev} = \frac{\rho_l d_p^2}{8\rho_g D_F \ln\left(1+B_M\right)} \tag{9.8}$$

is compared to the characteristic combustion time $\tau_c \approx \delta_l^0 / S_L^0$ with δ_l^0 the laminar flame thickness and S_L^0 the laminar flame speed at the local ϕ. In Eq. 9.8, ρ_l and ρ_g are the liquid and gaseous densities, d_p the droplets diameter, D_F the fuel diffusivity, B_M the Spalding mass transfer number. Two archetypes of two-phase kernels are distinguished: weakly evaporation-controlled flames and evaporation-controlled flames:

- A weakly evaporation-controlled flame corresponds to the situation where the gaseous mixture fraction in the fresh gas is above the lean flammability limit ($\phi_g > \phi_{lean}$), or where liquid fuel evaporates very promptly:

  $$U^* \frac{\tau_{ev}}{\tau_c} < 1 \tag{9.9}$$

  with $U^* = u_l/u_g$ the relative velocity between fuel droplets and the carrier phase. Such a flame is very close to a purely gaseous flame and F_f is estimated as in the gaseous case with Eq. 9.1 where $\overline{z} = \overline{z_{eff}}$ includes rhe evaporation fuel consumed in the flame of thickness very close to δ_l^0, [15]:

  $$\overline{z_{eff}} = \overline{z_g} + \left(\frac{\delta_l^0}{\max\left(\delta_{ev}, \delta_l^0\right)} \right)^{2/3} \overline{z_l} = \overline{z_g} + \Gamma\, \overline{z_l} \tag{9.10}$$

  with $\delta_{ev} = u_l * \tau_{ev}$ the evaporation length, and $\overline{z_l}$, $\overline{z_g}$ the mean liquid and gaseous mixture fractions. The fluctuating mixture fraction z'_{eff} originates from turbulent mixing and spray local evaporation. It is assumed here that mixture fraction fluctuations resulting from cold flow evaporation are negligible compared to fluctuations due to turbulent mixing and evaporation in the flame, so that z'_{eff} is given by:

  $$z'_{eff} = \underbrace{z'_g}_{\substack{\text{turbulent}\\\text{mixing}}} + \underbrace{\Gamma \frac{\rho_l}{\rho_g} \alpha'_l}_{\substack{\text{evaporation}\\\text{in the flame}}} \tag{9.11}$$

  where z'_g and α'_l are simply taken from the cold flow statistics.

  Finally, the conditional mean flammable mixture fraction $\overline{z}_{flam}$ is calculated as in gaseous flows using Eq. 9.6.

- An evaporation-controlled flame corresponds to the case where the gaseous mixture fraction of the fresh gas is below the lean flammability limit and evaporation is the limiting process compared to combustion:

  $$U^* \frac{\tau_{ev}}{\tau_c} > 1 \tag{9.12}$$

  The consumption rate is much lower than in a weakly evaporation-controlled flame and the liquid fuel is burnt as soon as it is evaporated, leading to:

  $$\overline{z_{eff}} = \overline{z_l} + \overline{z_g}, \tag{9.13}$$

  $$z'_{eff} = z'_g + \frac{\rho_l}{\rho_g}\alpha'_l. \tag{9.14}$$

  The flammability factor F_f and the conditional mean flammable mixture fraction $\overline{z}_{flam}$ are again respectively estimated as in the gaseous case with Eqs. 9.1 and 9.6. Note that the rich flammability limit is never reached for evaporation-controlled flames.

9.3.1.2 Flame stretch

Turbulence may be responsible of significant quenching due to fragmentation of the flame kernel (see Sec. 8.7.5). Following the previous work of [205] and [200], a criterion based on the Karlovitz number is used. The estimation of Ka is taken from [178]:

$$Ka = 0.157\,(\nu\varepsilon)^{1/2}\,\frac{1}{{S_L^0}^2} \tag{9.15}$$

where ε is the turbulent dissipation and ν is the kinematic viscosity. S_L^0 can be locally estimated using the $\overline{z}_{flam}$. For spray cases, S_L^0 is replaced by the two-phase laminar flame speed S_L^{tp} proposed in [15]. For weakly evaporation-controlled flames, $S_L^{tp} \approx S_L^0(\overline{z}_{flam})$. For evaporation-controlled flames, S_L^{tp} is much smaller that S_L^0 and can be estimated by replacing τ_c by τ_{ev}:

$$S_L^{tp} = \frac{\delta_l^0}{\tau_{ev}}, \tag{9.16}$$

where δ_l^0 is evaluated at $\phi_g = 1$ for cases involving both diffusion and premixed flame structures.

In LES, ε is defined as:

$$\varepsilon = 2\nu_{tot} S_{i,j}\bar{}S_{i,j} \tag{9.17}$$

where $S_{i,j}$ is the deformation tensor

$$S_{i,j} = \frac{1}{2}\left(\frac{\partial u_i}{\partial x_j} + \frac{\partial u_j}{\partial x_i}\right) \tag{9.18}$$

and $\nu_{tot} = \nu + \nu_t$ However, evaluating ε from the mean velocity field is inadequate. Therefore, under the hypothesis of Gaussian instantaneous velocity distribution around

$\overline{u_i}$ with a variance u_i', many instantaneous velocity fields $\tilde{u}$ are reconstructed based on the non-reacting flow time-averaged data. ε is then the average of all individual dissipation rate tensor $\tilde{\varepsilon}$ associated to each $\tilde{u}$ field. 20-50 reconstructed $\tilde{u}$ fields are generally sufficient to ensure a converged ε tensor. The validity of the hypothesis of Gaussian shaped velocity is provided in [1].

Quenching occurs when the Karlovitz numebr is above a critical value Ka_c. The determination of Ka_c is crucial. A value of $Ka_c = 1.5$ is reported in the literature [178, 200] for premixed flames. [186] uses $Ka_c = 4.5$ based on the agreement of the ignition model with experimental data. This value is retained in the present work.

9.3.2 Initial kernel

Following the spark discharge, the transition between the hot plasma and a self-sustained flame kernel occurs at temperatures largely above the burnt gas temperature [72]. A detailed description of this transition requires to take into account complex physico-chemical interactions and is out of the scope of the present model. Here, the initial kernel development is split in two phases: the kernel growth is first sustained by the high temperature associated to the energy deposit, then it is driven by combustion. During the first phase, the kernel can survive a non-flammable mixture or strong turbulence. This phase lasts for the time required for the kernel to cool down to the burnt gas temperature. Given the amount of deposited energy ε_i and the deposit size Δ_s, the maximum kernel temperature $T_{k,max}$ is given by (assuming no reaction during the short deposition duration):

$$T_{k,max} = T^0 + \frac{1}{\rho_g C_p} \frac{\varepsilon_i}{(2\pi)^{3/2}\sigma_s^3} \tag{9.19}$$

where $\sigma_s = \Delta_s / 2\sqrt{ln 10^4}$ for a Gaussian shape of the deposit. T^0 and ρ_g are the fresh gas temperature and density. The kernel temperature then evolves following a 0-dimensional temperature balance:

$$\frac{dT}{dt} = \dot{\omega}_T(\overline{z}_{flam}) + \frac{D_{th}}{r_k^2}(T^0 - T) \tag{9.20}$$

The first term of the RHS results from combustion and is evaluated at the deposit location using the laminar flame speed at the mean flammable mixture fraction $\overline{z}_{flam}$:

$$\dot{\omega}_T(\overline{z}_{flam}) = \frac{Y_F(\overline{z}_{flam}) \mathcal{Q}_r S_L^0(\overline{z}_{flam})}{C_p \delta_l^0(\overline{z}_{flam})} \tag{9.21}$$

with $\mathcal{Q}_r$ the heat of combustion. The second term represents the diffusive heat loss, with the thermal diffusivity given by [103]:

$$D_{th} = D_{lam} + D_{turb} = \frac{\lambda}{\rho C_p} + 0.44 u' l_t \left(1 - \exp\left(-\frac{u't}{0.44 l_t}\right)\right). \tag{9.22}$$

The turbulent diffusivity progressively increases with time from 0 to its fully developed value [103]. Finally, the kernel growth is taken into account following a laminar asymptotic growth [101]:

$$\frac{dr_k}{dt} = \frac{T_b}{T^0} S_L^0(\overline{z}_{flam}). \tag{9.23}$$

with T_b the burnt gas temperature. Resolving Eq. 9.20, with flow properties at the spark location, leads to the kernel cooling time t_{CD}. For two-phase flows, S_L^0 is simply replaced by S_L^{tp} in Eqs. 9.21 and 9.23.

9.3.3 Kernel trajectories: Prediction of the kernel probability of presence

Instead of explicitly computing multiple individual event trajectories and construct a probability *a-posteriori* [200], the probability for a kernel of size r_k to be at the position $\boldsymbol{x}_k$ at time t, written $P_{pres}(\boldsymbol{x}_k, r_k, t)$, is directly constructed by integration of the probability density function $p(\boldsymbol{x}, r, t)$ around that position and radius. In order to construct $p(\boldsymbol{x}, r, t)$ and its temporal evolution, four main hypothesis are required:

- the local velocity components follow a Gaussian distribution (the validity of this hypothesis is evaluated in [1]),
- Kernel trajectories can be described with a Markov displacement approach,
- Velocity statistics of the non-reacting flow remain valid during the first milliseconds after the spark,
- the self-propagating velocity of the flame is low compared to the flame displacement velocity.

Following the second hypothesis, the position $\boldsymbol{x}_k(t)$ of a kernel of size r_k is given by the Langevin stochastic differential equation (SDE) [234]:

$$\frac{\mathrm{d}\boldsymbol{x}_k(t)}{\mathrm{d}t} = \mu(\boldsymbol{x}_k) + \sigma(\boldsymbol{x}_k)\eta(t), \tag{9.24}$$

where the initial kernel position $\boldsymbol{x}_k(t = 0) = \boldsymbol{x}_0$ is the spark position. The function $\mu(\boldsymbol{x}_k)$ corresponds to the deterministic motion while the second term introduces the turbulence effect. $\eta(t)$ is a white noise (stationary, Gaussian random process with zero mean and delta Dirac autocorrelation). The temporal evolution of the PDF of the kernel position $p(\boldsymbol{x}, r_k, t)$ is governed by the Fokker-Planck equation associated with the above Langevin equation [235]:

$$\frac{\partial p(\boldsymbol{x}, r_k, t)}{\partial t} = -\frac{\partial}{\partial \boldsymbol{x}}(\mu(\boldsymbol{x}) p(\boldsymbol{x}, r_k, t)) + \frac{\partial^2}{\partial \boldsymbol{x}^2}\left(\frac{\sigma^2(\boldsymbol{x})}{2} p(\boldsymbol{x}, r_k, t)\right) \tag{9.25}$$

where the first term on the RHS represents the mean drift of $p(\boldsymbol{x}, r_k, t)$ by the underlying flow, while the second term represents turbulent diffusion. The parameters $\mu(\boldsymbol{x})$ and $\sigma^2(\boldsymbol{x})$ are related to the flow statistics as: $\mu(\boldsymbol{x} = \bar{u}$ and $\sigma^2(\boldsymbol{x}) = u'dt$. Eq. 9.25 is numerically integrated in space and time in the computational domain of the LES. Additionally, $p(\boldsymbol{x}, r, t)$ is discretized in the kernel radius space using N_{sec} sections as depicted in Fig. 9.4, in which $p(\boldsymbol{x}, r, t)$ is constant and equal to $p_i(\boldsymbol{x}, t)$ for the i-th section. The lower and upper sections min and max radius correspond to failed and successful ignition events respectively. During the calculation, the conservation of the total probability yields:

$$P_{tot}(t) = \int_V \int_r p(\boldsymbol{x}, r, t)\ dr\ dv = 1. \tag{9.26}$$

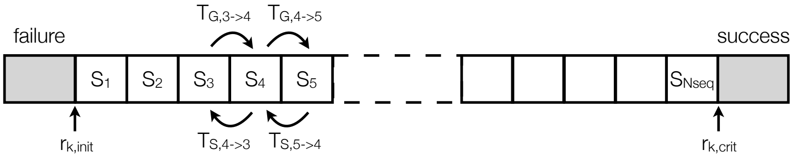

Figure 9.4: Breakdown of the kernel size space into sections with transition rates between consecutive sections.

Transition between two consecutive sections is driven by the kernel growth rate (T_G) or shrinking rate (T_S). The kernel growth and shrinking transition rates for section i are given by:

$$T_{G,S_i \rightarrow S_{i+1}}(\boldsymbol{x}, t) = \int_{r_i^{upp} - \delta_{G,r}}^{r_i^{upp}} p_i(\boldsymbol{x}, t) dr \tag{9.27}$$

$$T_{S,S_i \rightarrow S_{i-1}}(\boldsymbol{x}, t) = \int_{r_i^{low}}^{r_i^{low} + \delta_{S,r}} p_i(\boldsymbol{x}, t) dr \tag{9.28}$$

where $\delta_{G,r} = S_t(\boldsymbol{x})\delta_t$ is the kernel size growth increment during a time interval δ_t with $S_t(\boldsymbol{x})$ the local turbulent flame speed, and $\delta_{S,r} = D_{th}(\boldsymbol{x})/\overline{r}_i\delta_t$ is the kernel size shrinking increment during a time interval δ_t with $D_{th}(\boldsymbol{x})$ the local thermal turbulent diffusivity, and r_i^{low} and r_i^{upp} are the radius section i lower and upper bound, respectively. The turbulent flame speed is evaluated following [182, 212]:

$$S_t = S_L^0 + n \left(\frac{u'}{S_L^0} \right)^c \cdot S_L^0 \tag{9.29}$$

where n and c are the model constants evaluated by [182]. Even if developed in the context of premixed flames, this expression is also used for non-premixed and spray cases as considering an enhancement of the consumption speed by turbulence is still meaningful. S_L^{tp} is used instead of S_L^0 in spray mode.

The balance of each section then depends upon the time after deposit and the local flow properties:

	Premixed	Non-premixed	Spray
$r_{k,crit}$ [m]	0.01	0.01	0.008
$r_{k,init}$ [m]	0.001	0.0008	0.001
Ka_c	4.5	4.5	4.5
N_{seq}	12	12	12

Table 9.2: Summary of the model physical and numerical parameters.

- if $t < t_{CD}$, the kernel is not subjected to extinction and the net of change of $p_i(\boldsymbol{x}, t)$ during a time interval δ_t is given by:

$$\dot{Q}_i = T_{G,S_{i-1}\to S_i} - T_{G,S_i\to S_{i+1}} \tag{9.30}$$

- if $t >= t_{CD}$, the net change of $p_i(\boldsymbol{x}, t)$ for locations where $Ka > Ka_c$ writes:

$$\dot{Q}_i = T_{S,S_{i+1}\to S_i} - T_{S,S_i\to S_{i-1}} \tag{9.31}$$

  while for location where $Ka < Ka_c$, the net change $\dot{Q}_i$ writes:

$$\dot{Q}_i = F_f(\boldsymbol{x})(T_{G,S_{i-1}\to S_i} - T_{G,S_i\to S_{i+1}}) - (1 - F_f(\boldsymbol{x}))(T_{S,S_{i+1}\to S_i} - T_{S,S_i\to S_{i-1}}) \tag{9.32}$$

Kernels in the first section moving to the failed probability, or in the last section moving to the success probability, are removed from the calculation. At the end, all the $p_i(x, t)$ are null, corresponding to the end of the calculation. The probability of ignition when sparking at x_0 is then known as P_{ign}.

9.4 Application to the KIAI burner

The model is now applied to the three operating conditions listed in Table 9.1. The model parameters used for each case are listed in Table 9.2.

9.4.1 Comparison with experimental ignition probability maps

The result obtained with MIST for the premixed case are compared to the experiment in Fig. 9.5a. The map corresponds to the solid line box in Fig. 9.1. The shape of the ignition probability contours predicted by the model are in fairly good agreement with the experimental result: a large region of low ignition probability is found along axis of the injection system up to an axial position of $z/D_{ext} = 1.4$. The shape of this region is found to globally follow the limits of the IRZ, indicating that transport effects from downstream position towards the injector nozzle are responsible for this low ignition probability. Indeed, in this case the only extinction criterion is stretch, illustrated

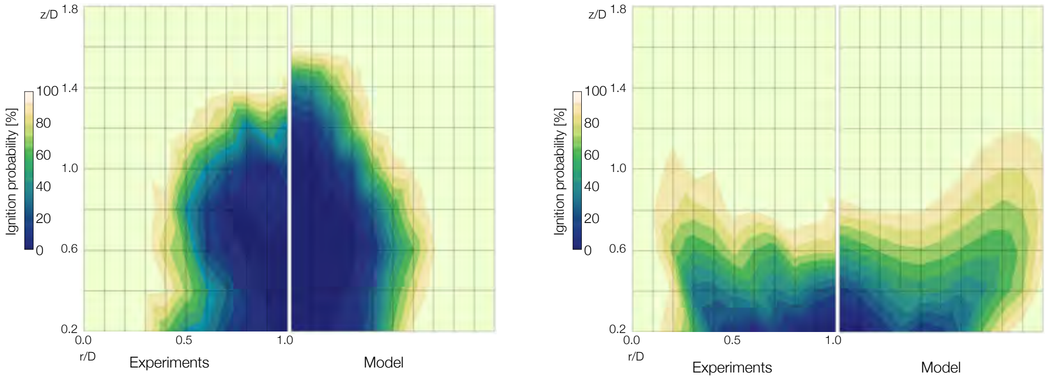

(a) (b)

Figure 9.5: Comparison between experimental (left) and model (right) ignition probability maps in the solid-line box of Fig. 9.1 for (a) premixed and (b) non-premixed cases.

in Fig. 9.6 (left) with the Karlovitz number. The region of Karlovitz number above the critical value $Ka_c = 4.5$, close to injection, is much smaller than the low ignition probability region, indicating that kernels move upstream where they are quenched. Aside from this central region, the ignition probability is 1 in the upper part of the combustion chamber as well as in the ORZ.

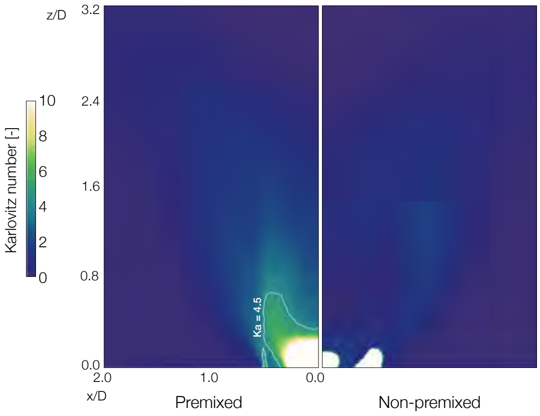

Figure 9.6: Karlovitz number contours in a central cut plane through the computational domain in the premixed and non-premixed cases.

The non-premixed case results are compared against experiment in Fig. 9.5b, where a good agreement is observed: the low ignition regions are located close to the pure methane central jet and in the wake of the pure air SJZ. In contrast with the premixed case, the low ignition probability region does not extend within the IRZ: in this case, the region of high Karlovitz number is more confined due to the near stoichiometric conditions in the lower part of the IRZ, as illustrated in Fig. 9.6. The contours of ignition probability closely follow those of the flammability factor depicted in Fig. 9.2, indicating that the kernel survival is mainly controlled by mixing effects. However, the analysis of the model results and the LES of ignition [201] shows that ignition can occur even with locally detrimental conditions at the spark location.

The comparison between experimental and model ignition probability maps for the spray case is proposed in Fig. 9.7. The comparison is proposed in the dashed box of Fig. 9.1. The agreement is quite satisfactory between both maps. The same overall topology of ignition probability is recovered: 1- The entire IRZ is characterized by very low P_{ign} values under 0.1, 2- the ORZ is the most ignitable region of the chamber, with $P_{ign} > 0.7$ near the lateral wall, 3- the gradient of P_{ign} is more or less coincident with the spray-SJZ. The predicted map shows a slightly larger low-P_{ign} zone, with the stiff gradient of probability shifted by around 0.5 D_{ext} towards the ORZ. Still, the gradient is correctly inclined, following the SJZ.

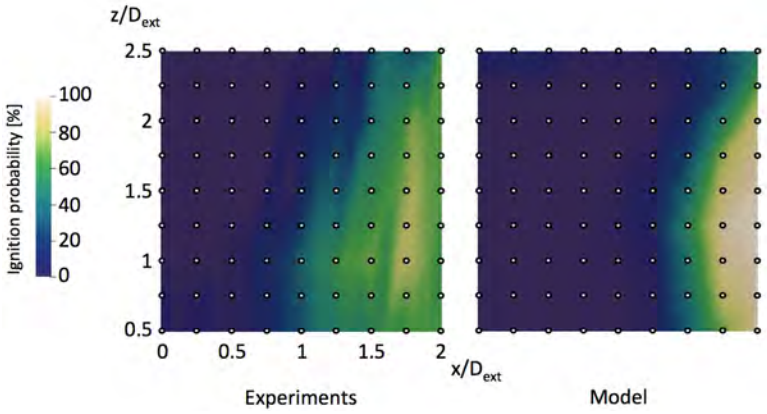

Figure 9.7: Spray case. Comparison between experimental (Left) and model (Right) ignition probability maps in the dashed box of Fig. 9.1.

This topology of P_{ign} is strongly related to local non-reacting flow properties shown in Fig. 9.8. The very homogeneous flammable mixture along with low Karlovitz number (thanks to low velocity fluctuation levels) found in the ORZ explain to a large extent the very high ignition probability. On the contrary, the IRZ and the bottom of the spray-SJZ are much leaner, and present higher velocity fluctuations. When combined, these detrimental conditions lead to a local Karlovitz number over the critical value $Ka > 4.5$, and explain why the IRZ and the bottom of the SJZ are almost not ignitable.

9.4.2 Comparison with two-phase reacting LES ignition sequences

P_{ign} and P_{ker} are sometimes very different and the final outcome of an ignition sequence does not only depend on local properties at the spark location. To illustrate how MIST recovers such complex ignition behaviour, results from the LES of spray ignition named P3-S already discussed in Sec. 8.7.6 and sparked at $x/D_{ext} = 1.5$, $z/D_{ext} = 0.5$ are analysed. The experimental ignition probability found at this position is $P_{ign,exp} = 50$ %. Snapshots of the flame front (iso-$T = 1500$ K) coloured by the heat release rate

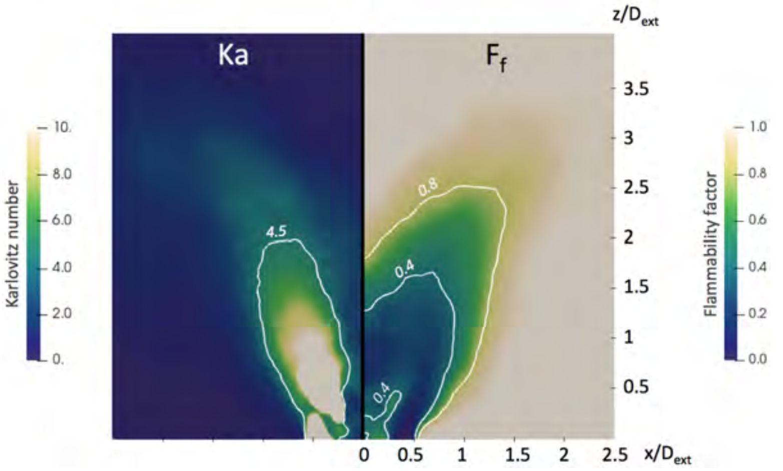

Figure 9.8: Spray case. Maps of reconstructed Karlovitz number (Left) and flammability factor (Right).

are given in Fig. 9.9 at different times after the spark. Starting from the bottom of the ORZ, the kernel is first convected towards the injector (a) by the recirculating flow. In this phase, the kernel grows as it encounters favourable local conditions. When arriving above the air inlet (b), the flame kernel subjected to very high velocity fluctuations, may quench rapidly. The kernel is then convected downstream by the SJZ (c) and is still strongly shredded in this turbulent zone. If able to survive, the kernel finally reaches the much favourable top part of the ORZ (d) after 10 ms, where it grows quickly to extend over the entire ORZ and SJZ (e), and eventually ignite the full chamber and establish a stable flame. This sequence is only one successful event among all ignition scenarii which have been obtained from the same sparking position, with many different outcomes: fast ignition in the ORZ when the residence time in this zone increases, fast misfire in the bottom part of the SJZ if this residence time is too small, or late misfire in the top part of the SJZ for the intermediate case.

Figure 9.10 shows in (a)-(c) the perspective and top views of the ignition position P3. The ignition probability given by the model at this point is 40 %, close to the experimental value (50 %). (b)-(d) represent the iso-surface of all positions of the chamber where $r_{k,crit}$ has been reached at the end of the calculation, regardless of the time after spark. It is remarkable to observe that the model is able to recover the wide range of flame kernel trajectories and for example to catch late ignition in the top part of the ORZ, corresponding to Fig. 9.9 (d).

Figure 9.11 provides a front view of the iso-volume of mean flame kernel radius $\bar{r_k} > 1\ mm$, coloured by $\bar{r_k}$ at three times after the spark. After 1 ms (b), the kernel convection phase in the bottom part of the ORZ is found, similarly to the reacting LES sequence. At this early time, the mean kernel size is $\bar{r_k} \approx 3\ mm$ and progressively increases. After 3 ms (c), the larger iso-volume shows the dispersion of the kernel

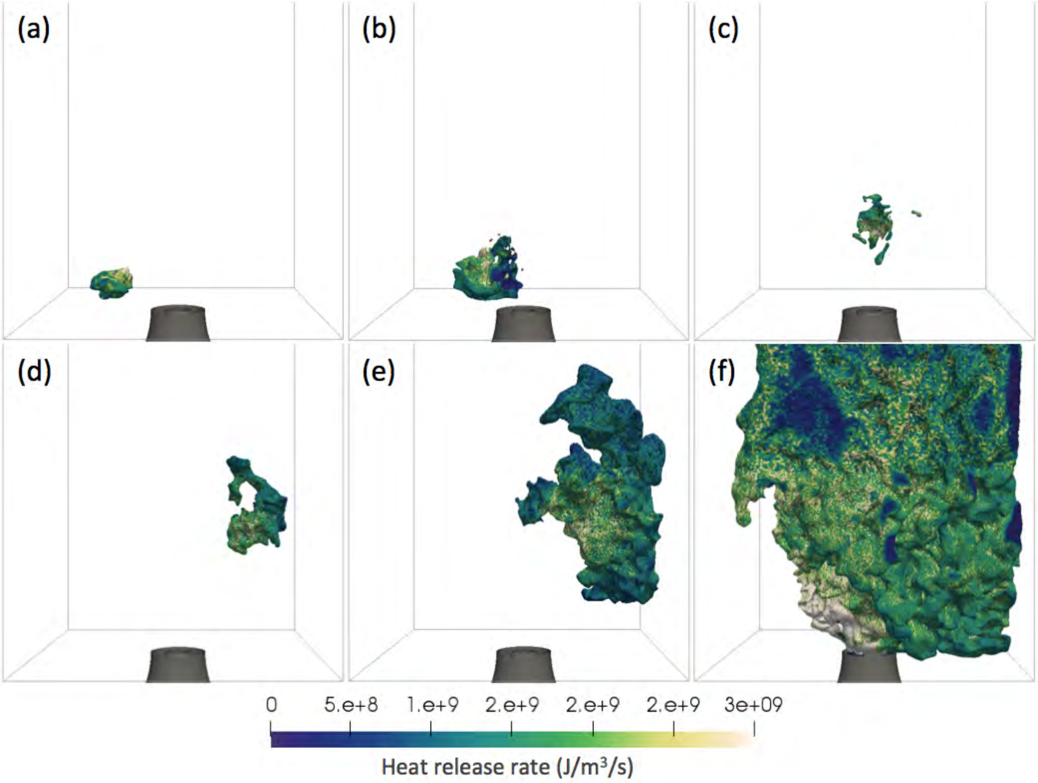
(a)
(b)
(c)
(d)
(e)
(f)
0
5.e+8
1.e+9
2.e+9
2.e+9
2.e+9
3e+09
Heat release rate (J/m³/s)

Figure 9.9: LES of spray ignition sequence sparked at P3. Flame front visualisation (iso-$T = 1500\ K$) coloured by heat release. Time after spark: (a) $1.7\ ms$, (b) $3.7\ ms$, (c) $7.7\ ms$, (d) $13\ ms$, (e) $16\ ms$, (f) $20\ ms$.

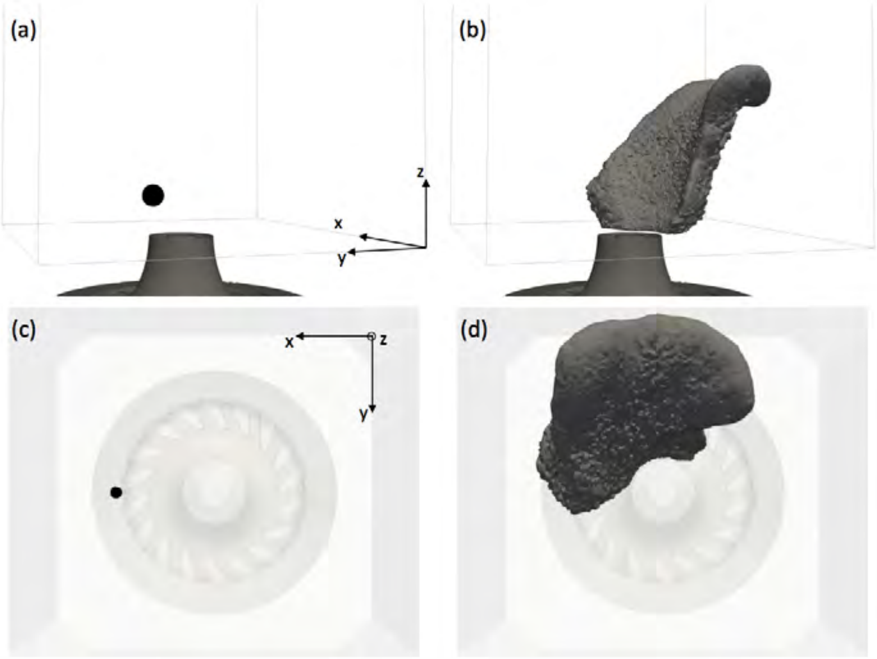
(a)
z
x
y
(b)
(c)
x
z
y
(d)

Figure 9.10: Spray case. (a)-(c) Perspective and top views of the ignition position P3. (b)-(d) Final iso-surface of all positions where $r_{k,crit}$ was reached.

trajectories. Kernels staying longer in the favourable ORZ grow much more than those that entered the adverse SJZ earlier. This is demonstrated by $\bar{r_k}$ reaching 7 mm in the ORZ while remaining below $\bar{r_k} \approx 5$ mm in the SJZ. The most advanced points of the iso-volume (towards the SJZ) correspond to kernels leaving the ORZ most rapidly, thus having the lowest $\bar{r_k}$, near 3 mm. After 7 ms (d), kernels that stay longer in the ORZ reach $\bar{r_k} = r_{k,crit} = 8$ mm. On the contrary, kernels convected downstream in the SJZ grow more slowly as in Fig 9.9 (c), showing that the model is able to recover the complex phases highlighted by the reacting LES sequence.

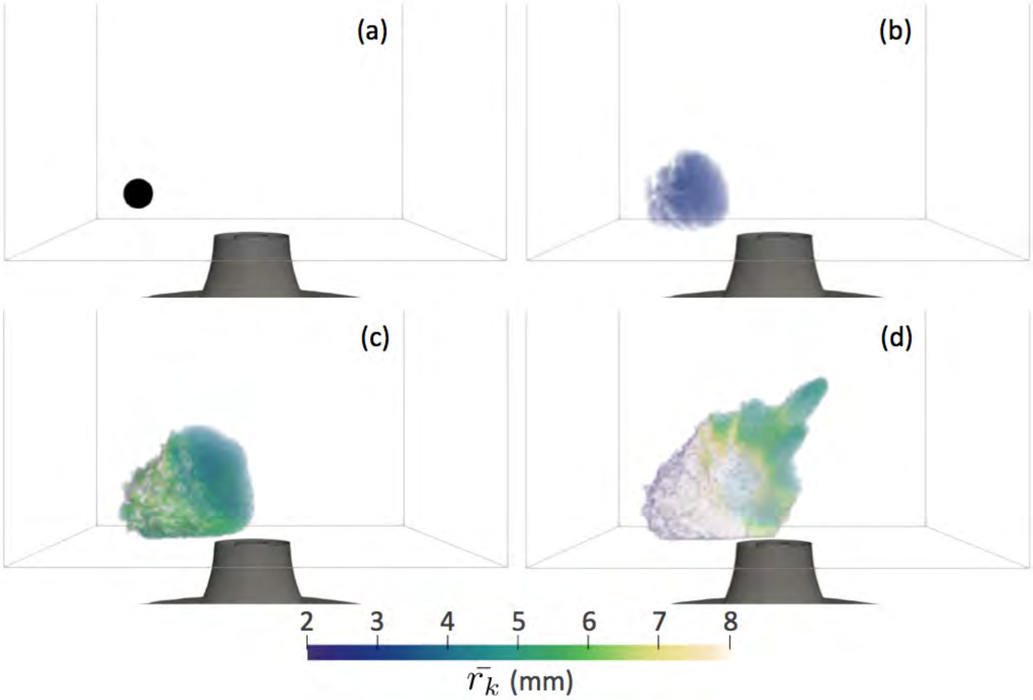

Figure 9.11: Spray case. (a) Front view of the ignition position $x/D_{ext} = 1.5$, $z/D_{ext} = 0.5$. Iso-volume of the mean flame kernel radius after 1 ms (b), 3 ms (c) and 7 ms (d).

9.5 Application to a real combustor

9.5.1 Industrial configuration and operating points

After assessing the validity of MIST in the academic KIAI configuration in Sec. 9.4, MIST is now applied to a real industrial combustor. The global view of the configuration is presented in Fig. 9.12. Geometry details including the injector system, as well as exact operating conditions, will not be provided here for confidentiality purpose. The configuration is one sector of a standard Safran RQL (Rich Burn, Quick Mix, Lean Burn) annular combustion chamber. The flow topology in this configuration is shown in an axial cut (injector-spark plug plan) displayed in Fig. 9.13a. The air entering the

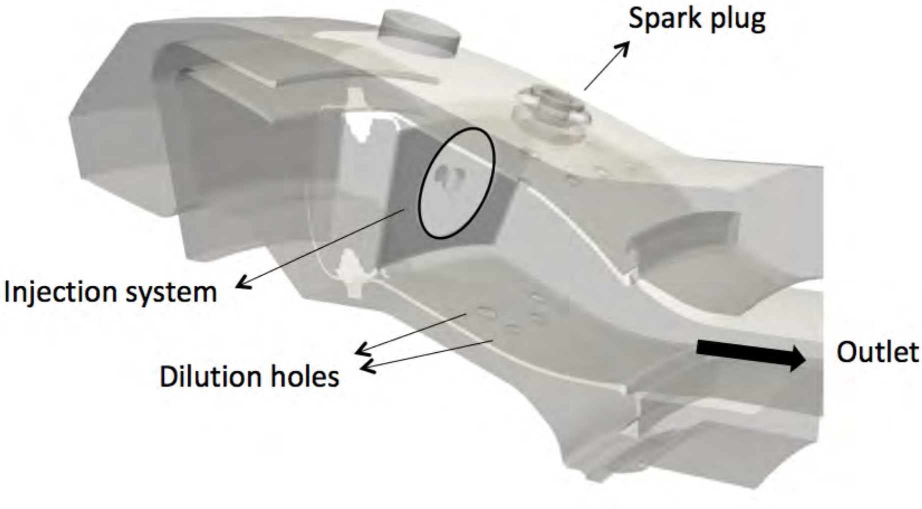

Figure 9.12: Global view of the industrial configuration studied.

chamber by the injection system generates a flow topology similar to the KIAI configuration, with a swirled jet zone (SJZ) separating the inner recirculation zone (IRZ) from the outer recirculation zones (ORZ). There are however two main differences with the KIAI configuration. First, bottom and top dilution holes split the chamber in two parts: the primary zone where combustion occurs in rich conditions and downstream the secondary zone where dilution and mixing of hot products with fresh air occur so that the remaining fuel burns in lean conditions. Second, two secondary flows can be distinguished: 1- a stream of pure air is injected along the top wall where the spark plug is attached. 2- a small transverse cooling air flow is also injected around the annular spark plug. These two air streams modify the flow in the spark plug region, which is not the case in the academic KIAI configuration which uses a laser spark. Finally, the upper wall of the combustor showing the relative position of the spark with dilution holes is detailed in Fig. 9.13b. The spark plug is located just upstream dilution holes, at the end of the primary zone.

The objective is to investigate the high altitude relight capabilities of this combustor at two different operating conditions (air inlet pressure and temperature) corresponding to two flight altitudes. Indeed, test campaign showed previously that these two operating points lead to different relight capabilities. At operating point OP-A corresponding to the lowest altitude, relight performance was shown better than at operating point OP-B, corresponding to a higher flight altitude. The capacity of MIST to reproduce this trend is first evaluated. Then MIST is used to help understanding the differences between the two operating points and to propose an optimisation of the spark plug location in order to improve the relight performances on both operating points.

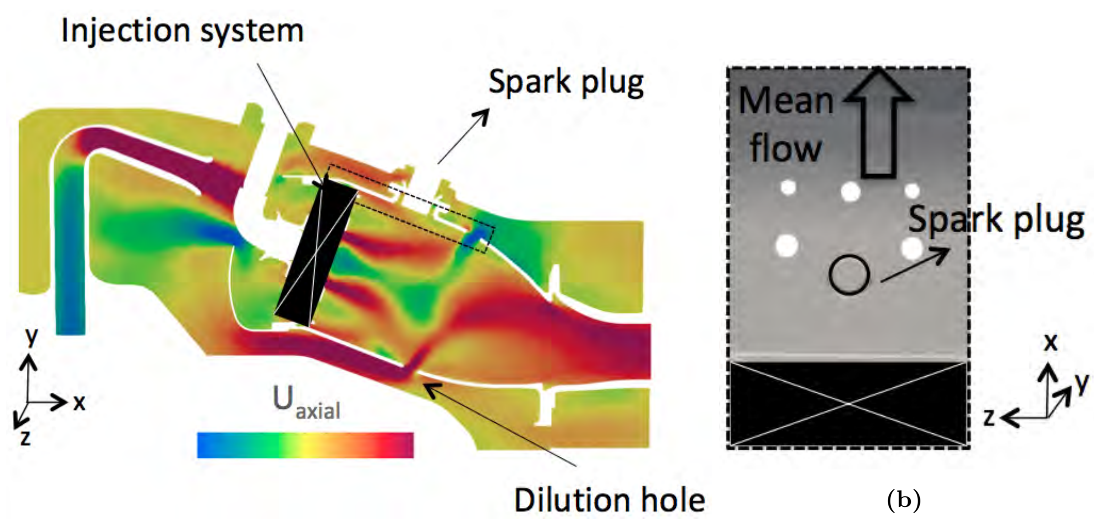

(a)

(b)

Figure 9.13: (a) Axial cut of the configuration coloured by mean axial velocity, on the injector-spark plug plan. The dashed zone is detailed in (b). (b) Zoom on the upper wall of the combustor showing the relative position of the spark plug with dilution holes.

9.5.2 Two phase cold flow topology for the two operating points

Figures 9.13a, 9.14a respectively show axial cuts of mean axial velocity and RMS velocity U_{rms} for OP-A. As OP-A and OP-B only differ by the inlet pressure-temperature conditions, the dynamic of the flow for both cases is very similar and therefore velocity fields for OP-B are not shown. In addition to the mean velocity field which shows classical SJZ, IRZ and ORZ, a region of very high velocity fluctuations appears in the dilution holes zone. The spark plug is located in the upper ORZ showing the lowest velocity fluctuations in the chamber. In Fig. 9.14b, the axial cut of mean liquid equivalence ratio ϕ_l for OP-A is presented. As OP-A and OP-B are representative of high altitude conditions, the inlet gas temperature for both cases is very low, so that the pre-evaporation of liquid droplets is limited for both cases and the field of ϕ_l is very similar for both operating points. ϕ_l is maximum close to the dense spray zone that follows the SJZ. The near-spark plug zone is very lean in terms of liquid fuel. Note that the injection spray angle is too narrow for droplets to impact the spark plug. This spray angle is an important parameter that is directly controlled by an input parameter of the cold flow LES calculation. A strong assumption is that for both OP-A and OP-B, this angle is kept constant.

Figure 9.15 compares axial cuts of gaseous equivalence ratio ϕ_g fields for both operating points, keeping the same colorscale. The cooling air stream around the spark plug leads to a bump of leaner mixture just below the spark-plug and the air flow along the upper wall is also responsible for a lean mixture in this near-wall region of

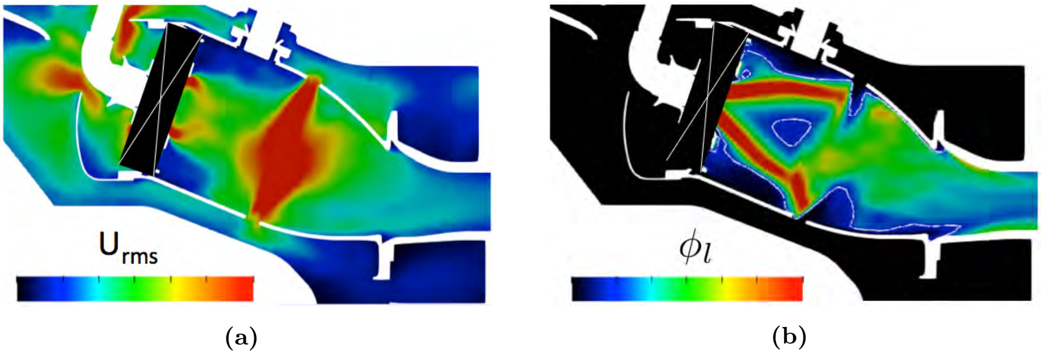

Figure 9.14: Axial cuts of (a) velocity fluctuations U_{rms} and (b) mean liquid equivalence ratio ϕ_l for OP-A. The fields for OP-B are very similar and therefore not shown.

the ORZ. The maximum value of ϕ_g obtained for OP-A is under the lean flammability limit. For OP-B, there is almost no liquid pre-evaporation, the maximum gaseous equivalence ratio being 10 times smaller than for OP-A. This difference in terms of pre-evaporated fuel is one of the main difference between OP-A and OP-B. The second important difference, closely related to evaporation, is the smaller mean droplet radius for OP-A than for OP-B with an average difference of $\Delta r_p = 2\ \mu m$ in the the near spark plug region of the ORZ. The two-phase combustion regime, I_{comb}, is directly linked to ϕ_g and r_p and is shown for OP-A and OP-B in Fig. 9.16. I_{comb} can characterize gaseous combustion ($I_{comb} = 0$), evaporation-controlled combustion ($I_{comb} = 1$), or weakly evaporation-controlled combustion ($I_{comb} = 2$), as described in Sec. 9.3. Differences observed between OP-A and OP-B are not sufficient to modify significantly the map of I_{comb}. Only the IRZ shows a different combustion regime between both cases. In the majority of the chamber, and especially near the spark plug, a weakly evaporation-controlled combustion is expected for both OP-A and OP-B. This result might be surprising as the very low temperature was expected to slow down evaporation so that it could be the limiting factor. However, as shown by the axial cut of characteristic evaporation time τ_{ev} for OP-B displayed in Fig. 9.17, τ_{ev} is very small in the whole ORZ as droplets are small in this zone. τ_{ev} is then smaller than the characteristic chemical time at the lean flammability limit leading to a weakly evaporation-controlled combustion regime. The IRZ is the only zone evidencing an evaporation-controlled combustion because of the bigger droplets found there.

9.5.3 Parameters used for MIST

For all MIST applications on this RQL combustor, the same set of parameters is used and gathered in Tab. 9.3. The critical radii of definitive extinction and ignition are respectively based on typical flame thickness and integral length scale representative

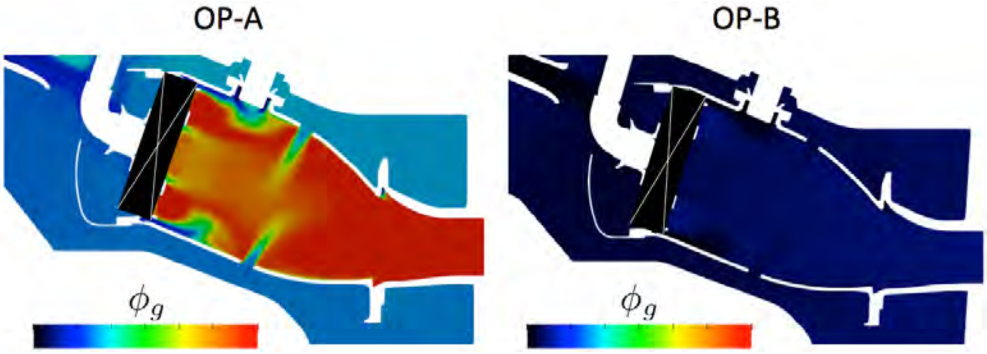

Figure 9.15: Comparison of axial cuts of gaseous equivalence ratio ϕ_g fields between OP-A and OP-B.

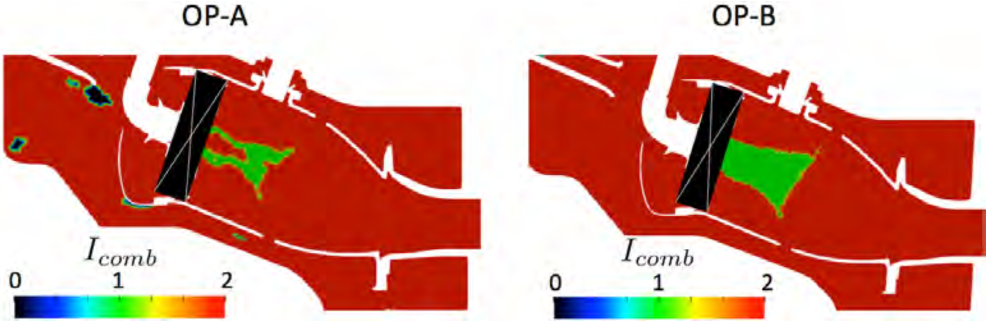

Figure 9.16: Comparison of axial cuts of two-phase combustion regime I_{comb} fields between OP-A and OP-B.

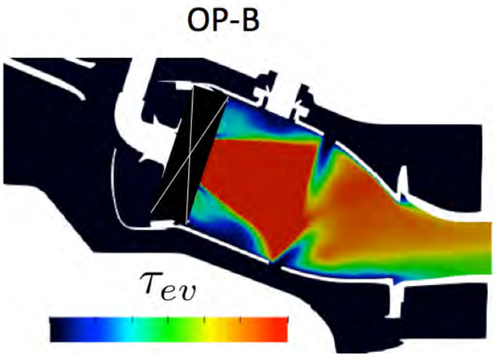

Figure 9.17: Axial cut of characteristic evaporation time τ_{ev} field for OP-B.

Parameter	Value
$r_{k,crit}$ [m]	0.008
$r_{k,init}$ [m]	0.001
Ka_c	4.5
N_{seq}	12
T_b (used for τ_{ev})	1900 K
t_{CD}	1 ms

Table 9.3: Summary of the model physical and numerical parameters used for the industrial application.

of the configuration. An important parameter of the model is the initial radius of the kernel. As estimating the size of the spark early in the sequence ($t << 1$ ms) is not easy, the geometric dimension of the spark plug has been used as a first guess, which leads to an initial kernel radius of around $3-5$ mm. All the simulations have been based on an initial radius of 5 mm due to time limitations. However, to further assess the robustness of MIST, the impact of this parameter should be tested. The initial kernel is centred at a distance of 4.5 mm from the spark plug surface so that the energy deposition is flush to the spark plug surface. The time-averaged cold flow solutions from LES performed by Safran Aircraft Engines and described in Sec. 9.5.2 associated to both OP-A and OP-B are used. The Euler-Euler formalism was used for these calculations with standard models for drag and evaporation.

9.5.4 Comparison of relight performance at two flight altitudes

Statistical indicators constructed thanks to cold flow properties are now compared between OP-A and OP-B. Figures 9.18, 9.19 and 9.20 show comparisons of flammability factor F_f, laminar two-phase flame speed S_l^{tp}, and Karlovitz number Ka respectively. Following the comparison of the two-phase cold flow, only small differences are found between the two operating points. If OP-B presents a higher flammability factor in the IRZ than OP-A, the bump of almost zero F_f just below the spark plug is smaller for OP-A. In the rest of the chamber, the mean value of flammability factor is quite homogeneous, centred around 0.5 in both cases. For two phase laminar flame speed, OP-A is characterized by a quite homogeneous value of around 0.4 m/s in the ORZ except for the bump below the spark plug, while OP-B presents a more heterogeneous distribution of S_l^{tp}, with a mean value a bit lower than for OP-A. This difference is partly explained by the droplet size distributions difference. In the IRZ, S_l^{tp} is very low for both cases, explained by the large droplets found there leading to a slow evaporation-controlled combustion mode. Finally, the maps of Karlovitz number for OP-A and OP-B shown in Fig. 9.20 are quite similar. The saturated value $Ka > 10$

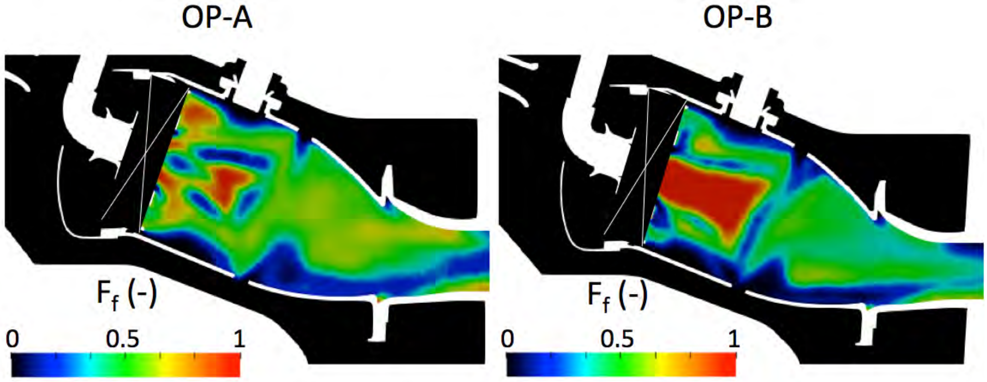

Figure 9.18: Comparison of axial cuts of flammability factor F_f fields between OP-A and OP-B.

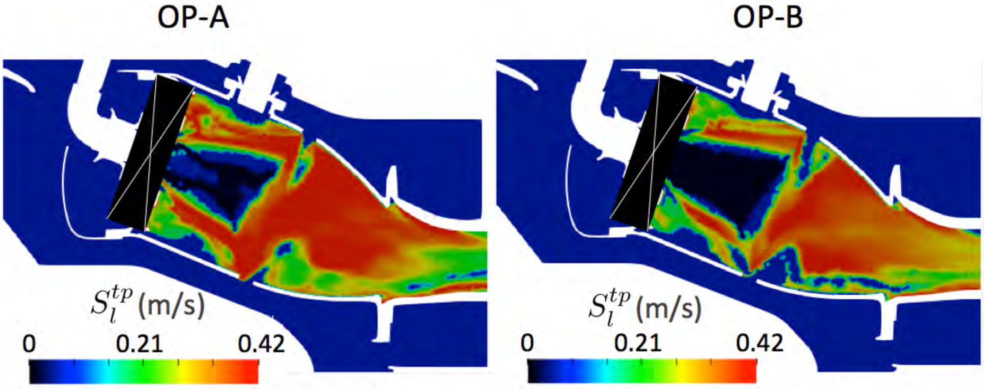

Figure 9.19: Comparison of axial cuts of laminar two-phase flame speed S_l^{tp} fields between OP-A and OP-B.

found in the IRZ is directly related to the very small S_l^{tp} found in this zone. As seen in Fig. 9.14a, the transverse cooling air coming from dilution holes generates important velocity fluctuations causing a prohibitive Ka value for flame propagation. Finally, for both OP-A and OP-B, a similar (marginally wider for OP-A) thin layer of relatively low Ka number is found along the upper wall. This favourable environment for flame growth is very small for both cases, which means that the kernel must grow up to the critical radius of definitive ignition (8 mm here) before leaving this low-Ka area to lead to a successful ignition. The small size of the zone also has another important consequence: contrary to the KIAI case where the kernel develops for a long time, here, the kernel either quenches or grows rapidly ($t < 4$ ms in any case). Thus, only local flow conditions near the spark plug determine the outcome of ignition. The kernel trajectory is less important in this industrial configuration and therefore no analysis of kernel trajectories are given here as they do not bring relevant information here.

The ignition probabilities computed by MIST for both OP-A and OP-B are given in the two first columns of Tab. 9.4, relatively to P_A which is not provided for confidentiality purpose. The ignition probability of OP-B is found around 45 % lower

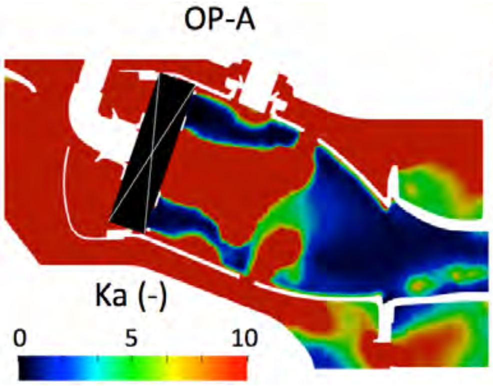

Figure 9.20: Comparison of axial cuts of Karlovitz number Ka fields between OP-A and OP-B.

Operating point	OP-A	OP-B	OP-A-noSP	OP-B-noSP
Ignition probability	P_A	0.55 P_A	1.1 P_A	0.4 P_A

Table 9.4: Ignition probability computed by MIST for cases including the spark plug geometry OP-A, OP-B and cases neglecting for the spark plug geometry OP-A-noSP and OP-B-noSP. All ignition probabilities are expressed as function of the ignition probability P_A for OP-A.

than the one of OP-A, which is the qualitative trend observed during the experimental test campaign. This difference of ignition probability is however smaller than the one observed experimentally. Because of the complex method to compute the ignition probability, it is not possible to decouple the effect of each statistical indicator. It is the combination of the differences for the 3 parameters F_f, Ka, and S_l^{tp} that leads to the 45 % lower ignition probability for OP-B compared to OP-A. In terms of CPU-time, obtaining the ignition probability for one spark plug position requires around 1 hour on 36 processors. This promising result shows the capacity of MIST to recover very costly and time-consuming experimental results with a simple numerical tool having a very short restitution time. Besides, MIST allows to analyse quantitatively some crucial parameters driving ignition such as fields of flammability factor and Karlovitz number in complex two-phase flows.

As MIST is able to recover at least qualitative trends in terms of ignition probability, an optimisation study of the spark plug position is carried out to investigate the potential improvement of relight performance on both operating points, but of course more specifically for OP-B.

9.5.5 Optimisation of the spark plug position

The flow topology and mixing properties around the spark plug are affected by the cooling air stream around the spark plug. To properly investigate other spark positions with MIST, a new time-averaged cold flow solution associated to each new spark position should be used. This would require important CPU resources and long restitution times annihilating the interest of MIST. Therefore, the strategy here is to use only one time-averaged cold flow solution for which the spark plug geometry and its cooling air flow are neglected. The different spark positions are investigated in Sec. 9.5.5.2, after assessing the assumption made on the geometry in Sec. 9.5.5.1.

9.5.5.1 Impact of the simplification of the spark plug geometry

In practice, neglecting the spark plug geometry and its cooling air flow consists in removing them from the geometry and keeping only the dilution holes on the upper wall. Figure 9.21 presents axial cuts of flammability factor F_f, laminar two-phase flame speed S_l^{tp} and Karlovitz number Ka of the time-averaged cold flow for OP-A with this geometry simplification, called OP-A-noSP. These three fields can be directly compared to left snapshots of Figs. 9.18, 9.19 and 9.20 to assess the impact of the geometry simplification made. The comparison is proposed here only for OP-A as the comparison for OP-B leads to the same conclusions. Only minor differences can be found between OP-A and OP-A-noSP in the majority of the chamber. These differences are mainly due to a different time averaging between both solutions. Near the spark plug zone, differences are more important. The bump found in OP-A, characterized by a non-flammable mixture because of the incoming cooling air and leading to low F_f, low S_l^{tp}, and high Ka, is of course not recovered in OP-A-noSP. Only the cooling film along the upper wall is reproduced compared to OP-A. The area of low-Ka near the upper wall is very similar to the one of OP-A, except again the little bump that is logically not captured. The impact of this geometry simplification on ignition probability is shown in Tab. 9.4 where the ignition probability for both OP-A-noSP and OP-B-noSP are expressed in function of P_A. The relative error made by neglecting the spark plug geometry is under $\pm$ 30 % for both operation points. Even if it affects the quantitative estimation of ignition probabilities, neglecting the spark plug geometry is therefore a reasonable strategy that allows to investigate qualitatively new spark positions at a very limited cost keeping the same time-averaged cold flow simulation.

9.5.5.2 Investigation of new spark positions

Many new spark positions are studied to evaluate if the standard position of the spark plug could be optimized. A particular focus is made on operating condition OP-B, as it presents the lowest ignition probability. The reference position of the spark plug, corresponding to the study of Sec.9.5.4 is called position P_2 in the rest of this section. The investigated positions are gathered in 3 classes:

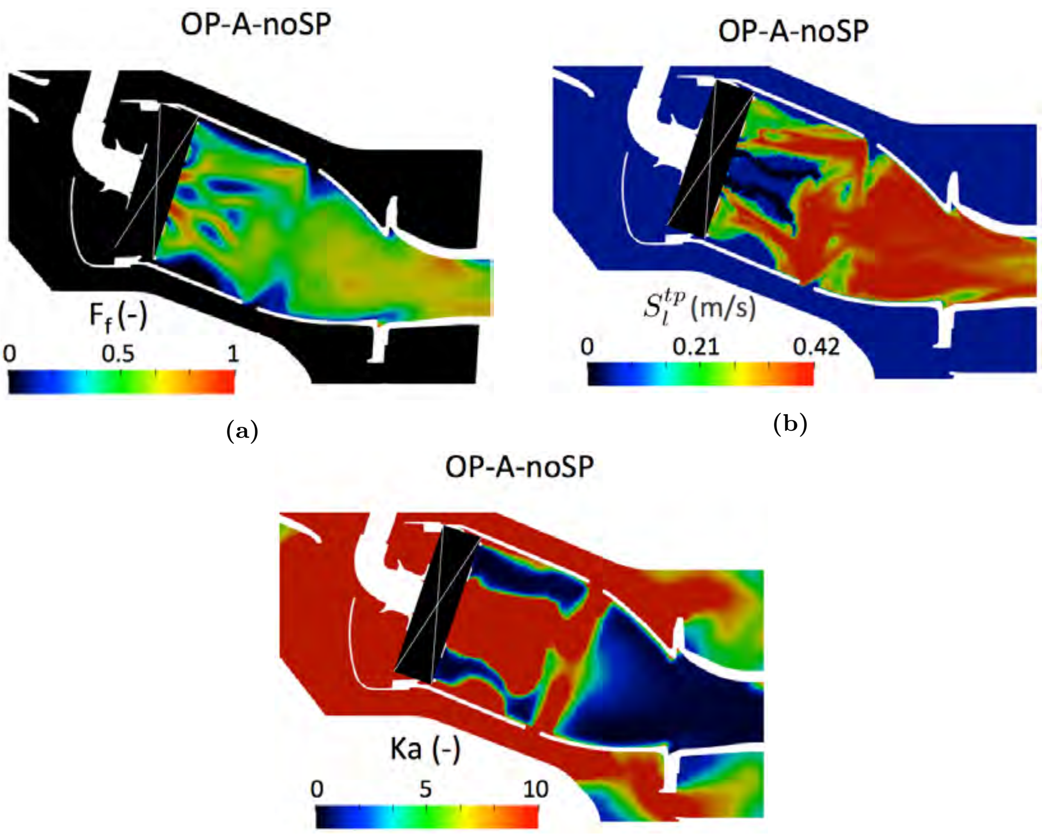

(a) (b)

(c)

Figure 9.21: Axial cuts of mean (a) flammability factor F_f, (b) laminar two-phase flame speed S_l^{tp} and (c) Karlovitz number Ka for OP-A-noSP.

- Displacement normal to the spark plug axis.
- Lateral displacement around the initial spark plug position.
- Spark plug located in the inter-injector plan.

Displacement normal to the spark plug axis: P_1 - P_3

During a real spark discharge, the plasma is created at the surface of the spark plug, flush to the wall. Then a typical convective motion induced by the shock produced by the spark and presented for instance in Fig. 6.9 of Chap. 6 pushes in less that hundreds of microseconds the kernel of burnt gases generated in the normal direction to the spark plug. This initial kernel convection cannot be captured by the cold flow solution used here. Representing this complex phase within a MIST study is not feasible and therefore requires to fix arbitrary the initial distance of the kernel from the wall. This point is furthermore crucial when recalling the presence of the cooling film along the upper wall. Starting from P_2, two first positions are tested, varying only the distance to the wall of the kernel initiated in MIST: P_1 is located closer to the wall at a distance of 3 mm instead of 4.5 mm for P_2, and P_3 is at a distance of 10 mm. Figure 9.22 shows axial cuts of Karlovitz number and turbulent flame speed for OP-B-noSP. The position of P_1, P_2 and P_3 are noted. The closest point to the wall, P_1, is located in the film region, characterized by very unfavourable conditions for kernel growth. P_2 is on the transition between the film region and the favourable low-Ka zone. Finally, P_3 is found in the core of this low-Ka region, also corresponding to a relatively high and homogeneous turbulent flame speed around 1.5 m/s. The kernel starting from P_3 can then easily and rapidly grow, contrary to P_2 and even more to P_1. In this latter case, the kernel must be convected quickly in a zone more favourable to its growth, otherwise it can be quenched almost immediately staying near P_1.

The predicted ignition probability starting from P_1 and P_3 for both configurations OP-A-noSP and OP-B-noSP are given in Tab. 9.5 along with the ones found for all tested positions. As in Tab. 9.4, ignition probabilities are expressed as function of the ignition probability P_A starting from P_2 for OP-A. In this table, points where ignition probability is multiplied or divided by at least a factor 2 compared to P_2 are respectively highlighted in green and red to highlight interesting variations. The initial distance to the wall appears to be a crucial parameter directly driving the final ignition probability. A strong gradient of ignition probability is observed between P_1 and P_3 corresponding to the transition between the film and the low-Ka ORZ area. This observation is valid for both operation points OP-A and OP-B. Therefore, it appears that generating a kernel as far as possible from the cooling film on the upper wall of the combustion

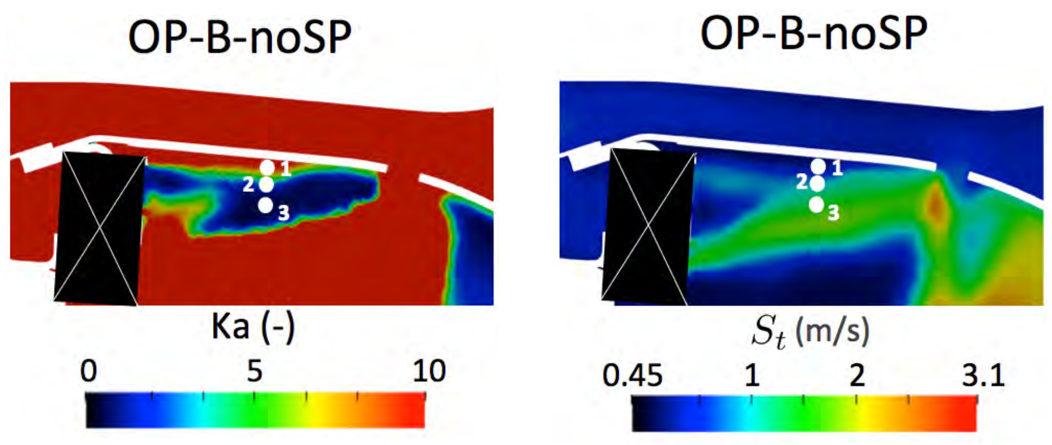

(a)

(b)

Figure 9.22: Axial cuts of mean (a) Karlovitz number Ka and (b) turbulent flame speed S_t for OP-B-noSP.

Position	$P1$	$\boldsymbol{P2}$	$P3$	$P4$	$P5$	$P6$	$P7$
OP-A-noSP	0.2 P_A	**1.1** P_A	3.6 P_A	1.2 P_A	1.8 P_A	1.2 P_A	1.7 P_A
OP-B-noSP	0.05 P_A	**0.4** P_A	1.9 P_A	0.2 P_A	0.7 P_A	0.4 P_A	0.6 P_A

Position	$P8$	$P9$	$P10$	$P11$	$P12$	$P13$	$P14$
OP-A-noSP	2.5 P_A	0.7 P_A	3.1 P_A	3.2 P_A	4.2 P_A	3.2 P_A	7.4 P_A
OP-B-noSP	0.6 P_A	0.05 P_A	1.8 P_A	1.1 P_A	2.0 P_A	1.8 P_A	0.9 P_A

Table 9.5: Predicted ignition probability for all tested spark positions and for both configurations OP-A-noSP and OP-B-noSP. The real spark position corresponding to results of Tab. 9.4 is P_2. All other positions are shown in Figs. 9.22, 9.23, 9.24. All ignition probabilities are expressed as function of the ignition probability P_A starting from P_2 for OP-A. Points where ignition probability is multiplied or divided by at least a factor 2 compared to P2 are highlighted in green and red respectively.

chamber allows to increase notably the ignition probability. In practice, that would imply to use an intrusive spark plug inside the combustor instead of using it flush to the wall. Obviously, this modification might also affect the flow topology of the flow. This is not accounted for by MIST when considering ignition from P_3 as the spark plug geometry is neglected. This recommendation should thus be read with care and would require further investigations, not engaged for time reason, to confirm this point. Note that another solution would be to use a spark plug flush to the wall equipped with a system able to push quickly the generated kernel in the normal direction to the spark plug.

Lateral displacement of the spark plug around its initial position: P_4 - P_{13}

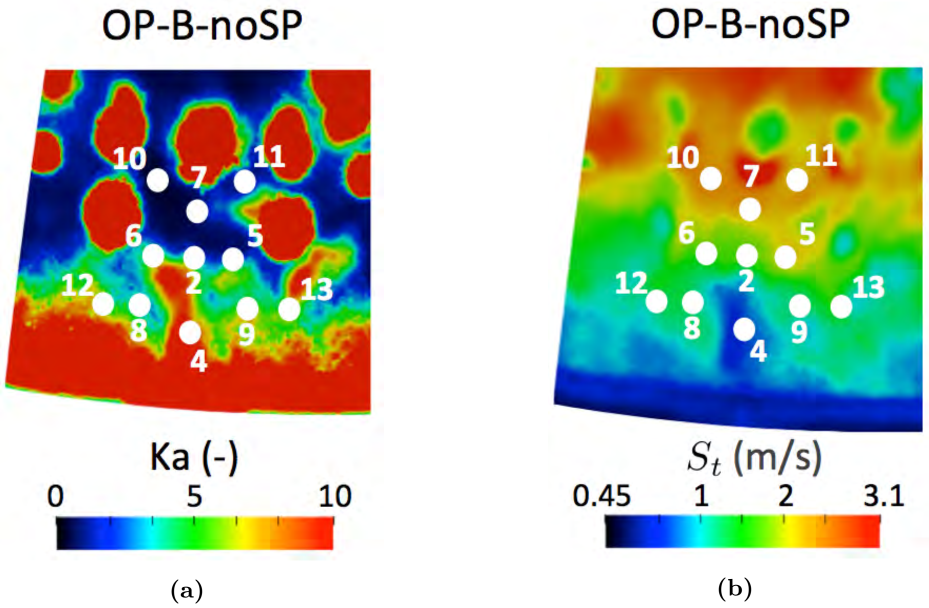

Figure 9.23: Cuts along the top wall ($d = 4.5\ mm$) of mean (a) Karlovitz number Ka for OP-B-noSP, (b) turbulent flame speed S_t for OP-B-noSP. Investigated positions from P_4 to P_{13} are localised.

After investigating the influence of the distance to the wall, only lateral displacement of the spark plug relatively to P_2 is considered here, keeping the same distance to the wall: $4.5\ mm$. Figure. 9.23 shows for OP-B-noSP the iso-surface $d = 4.5\ mm$ along the top wall colored by Karlovitz number and turbulent flame speed. All investigated positions from P_4 to P_{13}, highlighted by white points, are located on this iso-surface. Ignition probabilities starting from each point for both OP-A-noSP and OP-B-noSP are given in Tab. 9.5. As explained in Sec. 9.5.4, local flow conditions near the spark plug almost entirely determine the ignition probability in both OP-A and OP-B as the kernel survival time and trajectory are very limited. Thus, ignition probabilities found can be explained by using Fig. 9.23.

Ignition at P_4, P_8 and P_9 presents a variation of ignition probability compared to P_2 that behaves differently for OP-A-noSP and OP-B-noSP. This is due to the presence near the injector plan of a tail of high-Ka and low-S_t rising downstream up to $P_2 - P_6$ for OP-B-noSP that is not found for OP-A-noSP. This tail can be noticed in Fig. 9.22a showing a cut of Karlovitz number for OP-B-noSP while no such tail is found in Fig. 9.21c showing the same cut for OP-A-noSP. The proximity to this tail of points P_4 and P_9 makes their associated ignition probability much lower than P_2 for OP-B-noSP while they stay almost constant for OP-A-noSP. For P_8, the ignition probability is multiplied by more than a factor 2 compared to P_2 for OP-A-noSP while it is only multiplied by 1.5 for OP-B-noSP.

Despite the immediate vicinity of dilution holes characterized by too extreme Karlovitz

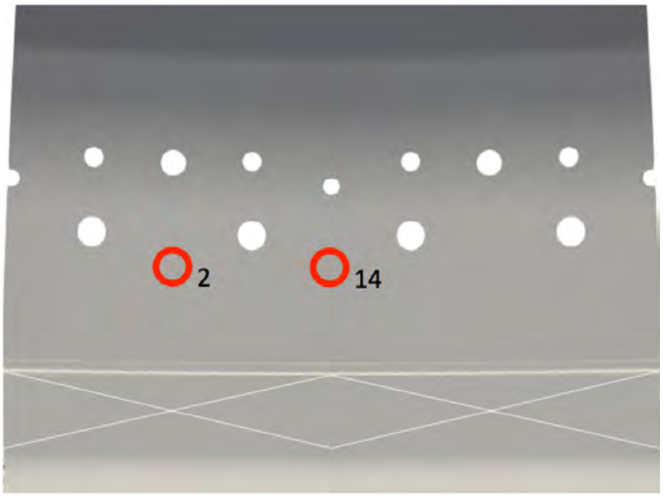

Figure 9.24: Zoom on the upper wall of the combustor showing the investigated spark position P_{14}, with position P_2 recalled.

number, P_{10} and P_{11} present very interesting local conditions: a low Karlovitz value ($Ka < 2$) associated to a high turbulent flame speed ($S_t > 2\ m/s$). This combination leads to an important increase of the ignition probability compared to point P_2 as the ignition probability is multiplied by almost three for OP-A-noSP and more than 2.5 for OP-B-noSP. However, fitting the large spark plug so close to dilution holes raises feasibility issues for practical applications.

Finally, locating the spark plug at P_{12} or P_{13} under dilution holes brings the highest increase of ignition probability compared to P_2. MIST anticipates an ignition probability multiplied by 3-4 for OP-A-noSP and by a factor of 4-5 for OP-B-noSP. Located in the primary and secondary dilution holes plan, P_{12} and P_{13} are indeed in a zone of homogeneous and globally favourable turbulent flame speed near 1.5 m/s. They are also upstream dilution holes, giving them the opportunity to grow before reaching this zone by axial convection. Kernels starting from P_{12} or P_{13} also have the opportunity to expand azimuthally. As placing the spark plug at P_{12} or P_{13} is feasible in practice, these two points are potentially good candidates to optimize the spark plug position.

Spark plug positioned in the inter-injector plan: P_{14}

One spark plug position, P_{14}, is finally tested in the inter-injector plan as shown in Fig. 9.24. Using only one sector of the annular burner, P_{14} would be located on the axisymmetric boundary of the domain. For numerical issues, the domain as well as cold flow solutions are duplicated in order to obtain a 2-sector configuration on which MIST is used[1]. P_{14} is put on the same axial distance from the bottom of the chamber than P_2. The inter-injector region does not present extreme turbulent flame speed values as shown in Fig. 9.25b. However, almost the entire inter-injector region is characterized by a very low flammability factor and a very high value of Karlovitz number as presented in Fig. 9.25c and 9.25a for OP-B-noSP. P_{14} is however very close to the bottom part of the inter-injector region where the flammability factor is acceptable and the Karlovitz number is very low. Thus, a kernel initiated from P_{14} can grow easily if initially convected to this area, leading to an ignition probability multiplied by 2 compared to P_2 for OP-B-no-SP. For operating point OP-A, the low-Ka high-F_f zone is even wider, leading to an increase by a factor of 6-7 of the ignition probability compared to P_2.

---

[1] In real burners, the sector containing the spark plug is a little bit different than other standard sectors. This difference is not taken into account here. As a first step, identical adjacent sectors are

However, the reliability of this last MIST result must be lowered considering that the flow topology near the inter-injector plan is certainly misrepresented because of the sector duplication applied. More important, a strong assumption of the MIST methodology is raised here: when a kernel reaches the critical radius of definitive ignition (set at 8 mm here), ignition is considered definitely successful. MIST is not dedicated to investigate the phase of upstream kernel propagation towards the injectors of the chamber. Thus, MIST supposes this phase automatically achieved. Investigated points P_1-P_{13} are all located above the injector, where the flammability factor is quite homogeneous around $F_f \approx 0.5$ or higher for both OP-A and OP-B. In such flammable conditions, assuming the upstream kernel propagation phase successful is reasonable. However, concerning P_{14}, this assumption is no more valid as the high flammability region at the bottom of the inter-injector plan is not connected to injectors by a continuous region of sufficiently flammable mixture. Therefore, this strong assumption must be remembered to avoid drawing inaccurate conclusions.

9.6 Conclusions

A trajectory-based model for ignition probability prediction in realistic two-phase combustors has been developed following the initial work of Esclapez [1]. It only uses time-averaged flow field quantities, reducing its computational cost. Cold flow statistics coming from experiments can also be used instead of LES results. Flame kernel displacement are directly taken into account by constructing a statistic of its trajectories. Then the local risk of kernel quenching is evaluated using indicators (Karlovitz number, flammability factor, mean flammable mixture fraction) that highlight inappropriate mixture composition and aerodynamic stretch. The temporal evolution of the kernel position, via its presence PDF P_{pres}, and of its size are computed to estimate

---

considered in order to simply duplicate fields to use MIST in the inter-injector

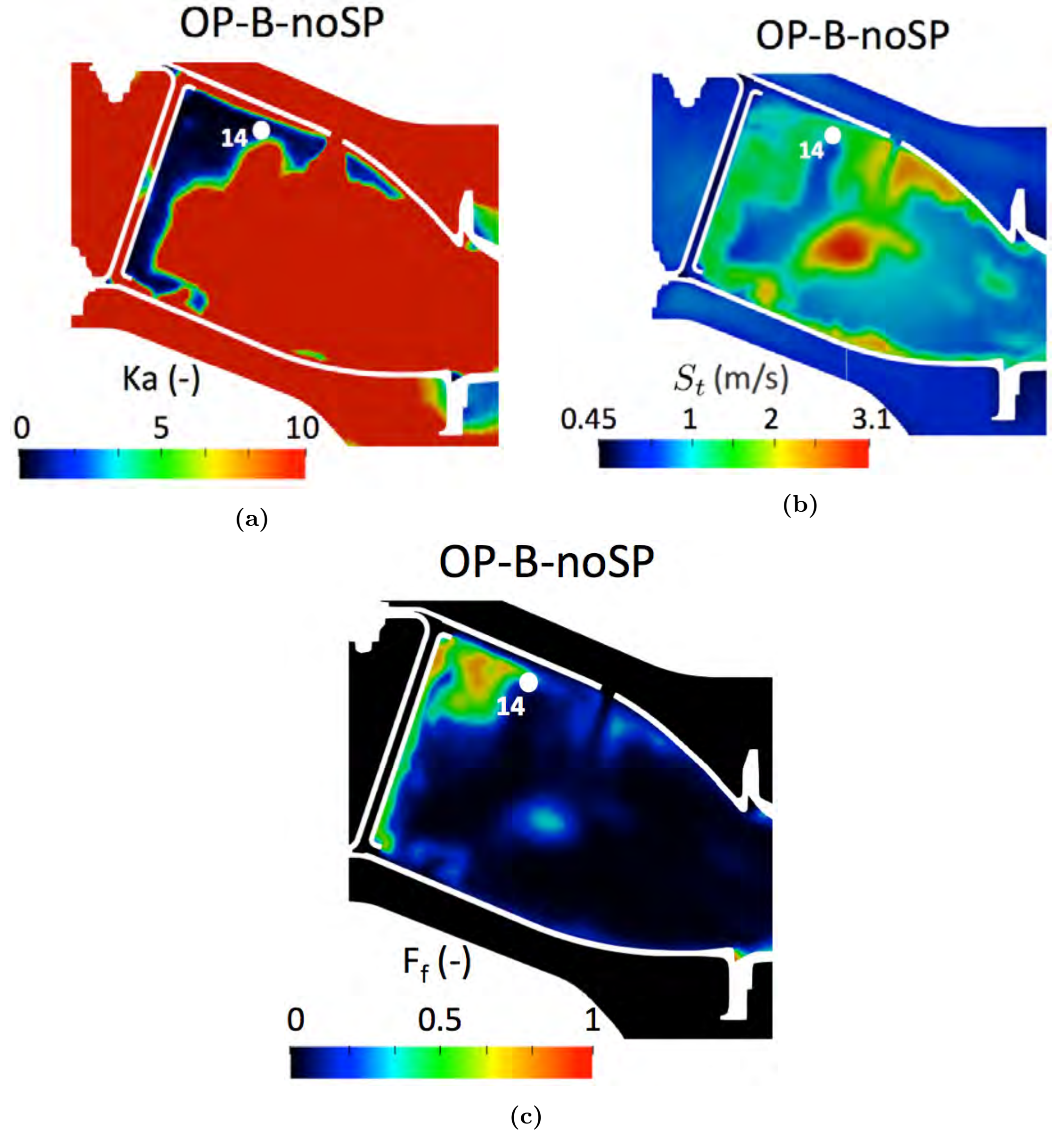

(a)

(b)

(c)

Figure 9.25: Axial cuts on the inter-injector plan of (a) Karlovitz number Ka for OP-B-noSP, (b) Turbulent flame speed S_t for OP-B-noSP (c) Flammability factor F_f for OP-B-noSP.

whether the kernel extinguish or is able to grow sufficiently to insure a successful ignition. The model of course rely on few arbitrary chosen parameters. The dependency of results on numerical parameters has been shown quite low. On the contrary, results are obviously sensitive to physical parameters ($\mathrm{r}_{k,crit}$, $\mathrm{r}_{k,init}$) definition. The knowledge gained in Chap. 7 and 8 is then essential.

The model has been applied on the gaseous premixed and non-premixed KIAI set-up but also its two-phase version KIAI-Spray. By progressively increasing the complexity of the set-up, it was shown that the model correctly captures the aerodynamic stretch (premixed version) and the mixture fraction inhomogeneities (non-premixed and spray versions). Experimental ignition probability maps have been recovered fairly well, capturing correctly the gradient of ignition probability. The importance of considering kernel trajectory statistics has been underlined on the spray case, by comparing model results with a reacting LES ignition sequence. The model is able to catch with very good accuracy the wide range of flame kernel trajectories, that directly controls the final ignition probability in this academic burner.

Finally, the model has also been applied on an industrial configuration to investigate high altitude relight capabilities, in conditions representative of two aircraft altitudes. The ability of MIST to retrieve the correct trend on ignition performance in such complex combustors for these two operating points has been assessed. An optimisation study of the spark plug position has then been conducted to improve relight performance on both operating points. In terms of CPU-time, obtaining the ignition probability starting from one position requires around 1 hour on 36 processors, making it useful early in the industrial combustor design process.

Part IV

Light-round

Chapter 10

Literature review

Contents

10.1 Multi-burners non-reacting flow topology 214

10.2 Overview of inter-sector flame propagation 215

10.2.1 Arc and radial propagation modes 215

10.2.2 Leading Point behaviour 217

10.3 Mechanisms driving flame propagation 218

10.3.1 Injector-to-injector distance 218

10.3.2 Thrust effect 219

10.3.3 Flame wrinkling and turbulent flame speed 220

10.3.4 Swirling motion 220

10.3.5 Spray injection 220

10.3.6 Wall heat losses 221

10.3.7 Near lean flammability limit 221

10.4 Conclusions 222

The final phase of ignition is the light-round,following the flame kernel generation (see Part. II), and the flame growth and propagation to the nearest fuel injector (see Part. III). This phase has been much less studied in the past compared to the two previous phases, mostly because even if light-round failure might occur, most of ignition failures happen earlier in the relight sequence. Still, improving our fundamental knowledge of the light-round phase is necessary to guarantee that blow off does not happen during high altitude relight and also to anticipate changes of combustor design or fuel types. Studying this third phase is however much more expensive that the two others. Experimentally, designing an annular test configuration is much more complicated than a single burner. Numerically, the LES of a full ignition sequence in an annular combustor is very expensive and was not feasible until the last decade: the first LES of a full combustion chamber reported in the litterature is the work of Boileau et al. [236] in 2008.

This chapter summarizes the conclusions of all known studies on gas turbine light-round. First, the typical non-reacting flow topology of multi-burner configurations is presented in Sec. 10.1. Then the phenomenology of inter-sector flame propagation in annularly or linearly arranged swirling burners is explained in Sec. 10.2 and finally, Sec. 10.3 proposes a focus on all important parameters driving flame propagation.

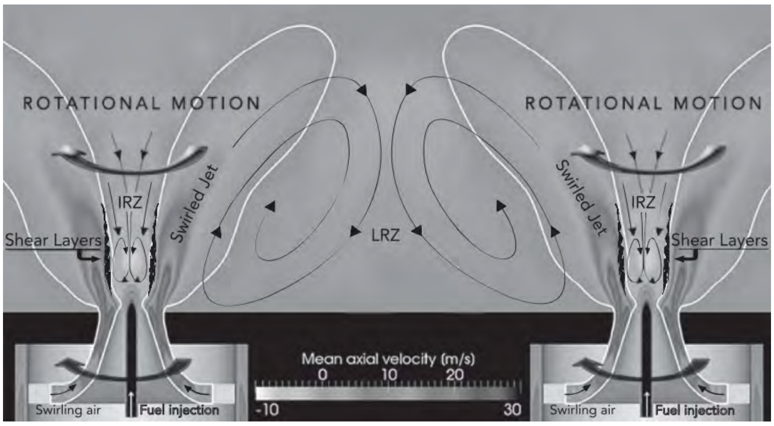

Figure 10.1: Typical topology of the swirled non-reacting flow in a muti-burners configuration. An Inner Recirculation Zone (IRZ) and a Swirled Jet Zone (SJZ) are found above each injector. Between two injectors, a Lateral Recirculation Zone (LRZ) is formed. Extracted from Barre et al. [238].

10.1 Multi-burners non-reacting flow topology

Cordier et al. [237] and Barre et al. [238] investigated inter-sector propagation both experimentally and with LES in the KIAI linear set-up, made of three to five linearly arranged non-premixed swirling burners in atmospheric and globally lean conditions. The typical topology of such swirled non-reacting flow is sketched in Fig. 10.1. The same topology is found in annular combustors, and a linear arrangment is chosen to simplify the set-up. An Inner Recirculation Zone (IRZ) and a Swirled Jet Zone (SJZ) are found above each injector, similarly to a mono-injector burner. Between adjacent injectors, a Lateral Recirculation Zone (LRZ) is formed. The mixing properties are of course different in each zone. The SJZ in generally richer than both recirculation zones. The spacing between injectors also plays an important role on the fuel repartition in the chamber. When increasing this spacing, the SJZ penetrates further downstream and LRZ are larger, higher and leaner. On the contrary, IRZ tend to be shorter and richer. In the Coria Linear Swirled Spray Burner (CLSSB) which is the adaptation of the KIAI linear set-up presented in Fig. 10.1 for spray ignition, Marrero-Santiago et al. [239] extendred to two-phase flows the dependencies of aerodynamics and fuel (liquid and gas) distribution to injector distance. It was found that in the lean regime ($\phi_{glob} = 0.61$), when the injector-to-injector distance is too high, the mixture in the LRZ can drop below the flammability limit. This may slow down or even prevent flame propagation from one injector to an other.

10.2 Overview of inter-sector flame propagation

10.2.1 Arc and radial propagation modes

Mechanisms involved in the light-round are directly linked to the injector-to-injector distance. Barre et al. [238] showed that two different flame propagation modes are possible. For small spacings (below $150\,mm$ in their case), a purely radial, rapid and safe propagation is observed as the LRZ is flammable. Above a critical distance ($160\,mm$), the propagation is more complex, ignition is longer and failure might happen. In this mode, called arc propagation, the flame first develops on the injector closest to the ignition system, then moves downstream in the axial direction of the injector, spreads radially and eventually reaches the neighbouring injectors from the top of their IRZ thanks to the bridge connecting rich SJZ branches. This arc propagation mode is illustrated in Fig. 10.2 comparing an experimental sequence and a LES simulation for the same inter-injector gap. This comparison also shows the excellent predictive capability of LES for such ignition sequences. Kumar et al. [240] showed the capacity of a numerical set-up including URANS modeling, detailed chemistry and adaptive mesh refinement technique to qualitatively reproduce the flame propagation in this configuration. In the experimental two-phase CLSSB configuration, Marrero-Santiago [214] also identified the same two propagation modes as function of the inter-sector distance.

Bourguoin et al. [241] also found a radial propagation mode in their experimental set-up MICCA, consisting in an annular combustor operated in lean premixed regime with a fixed inter-injector distance of $7\,cm$. LES of the same experimental set-up were made by Philip et al. [242]. A very good qualitative and quantitative agreement was found for the flame front shape and motion, as well as for the ignition delay of the chamber, using the two combustion models [243]: DTFLES and FTACLES. In particular, five phases were identified:

- After the spark, a small flame kernel forms and expands rapidly in the fresh mixture.
- The flame front propagates to the surrounding burners forming an arch. The arch opens up as soon as its top reaches the exit of the chamber.
- Then, two fronts propagate independently on both sides of the burner, in a burner-to-burner propagation mode. In the previous phase and also this one, the inter-injector distance controls the propagation mode, being radial or arc.
- The two flame fronts finally merge on the opposite side of the burner.
- Burnt gases are evacuated and the steady state is reached.

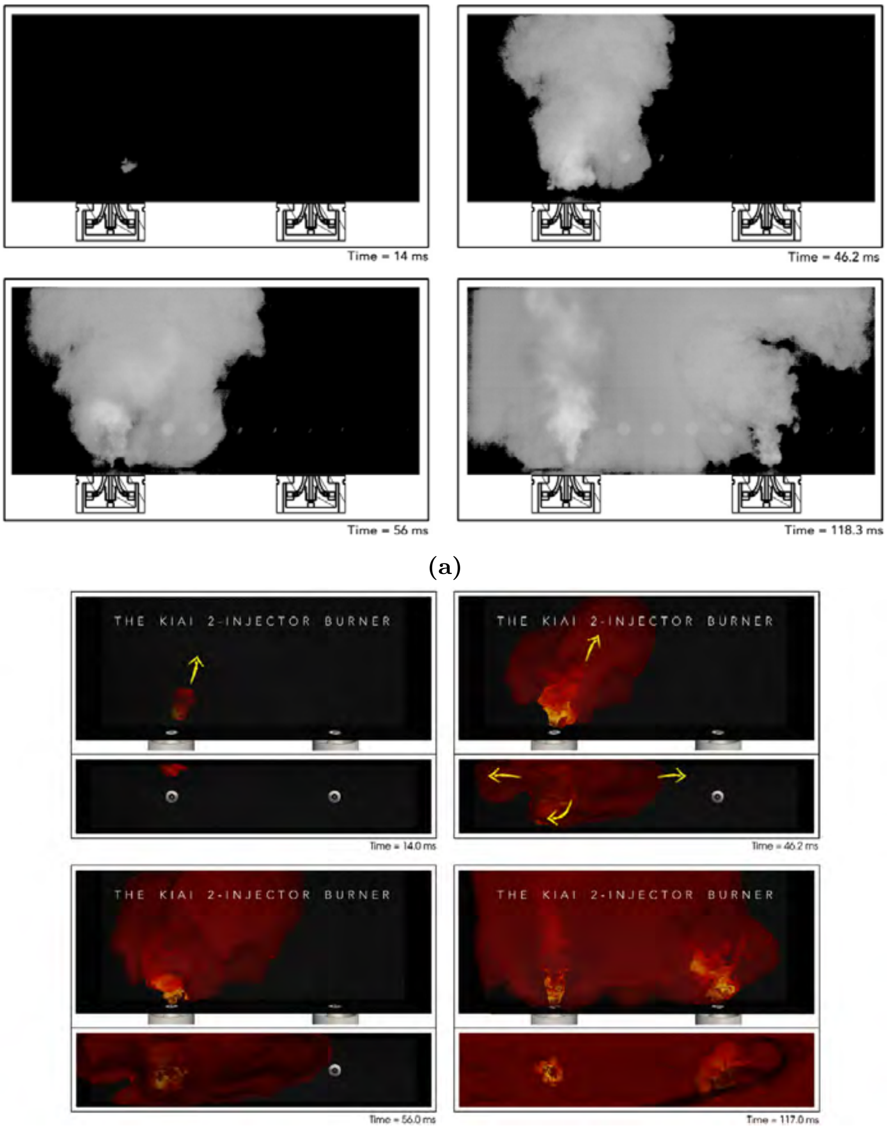
Time = 14 ms
Time = 46.2 ms
Time = 56 ms
Time = 118.3 ms
THE KIAI 2-INJECTOR BURNER
Time = 14.0 ms
Time = 46.2 ms
Time = 56.0 ms
Time = 117.0 ms

(a)

(b)

Figure 10.2: Visualisation of the flame expansion for a high injector-to-injector distance evidencing an arc propagation mode for both (a) experiment and (b) LES simulation. Extracted from Barre et al. [238].

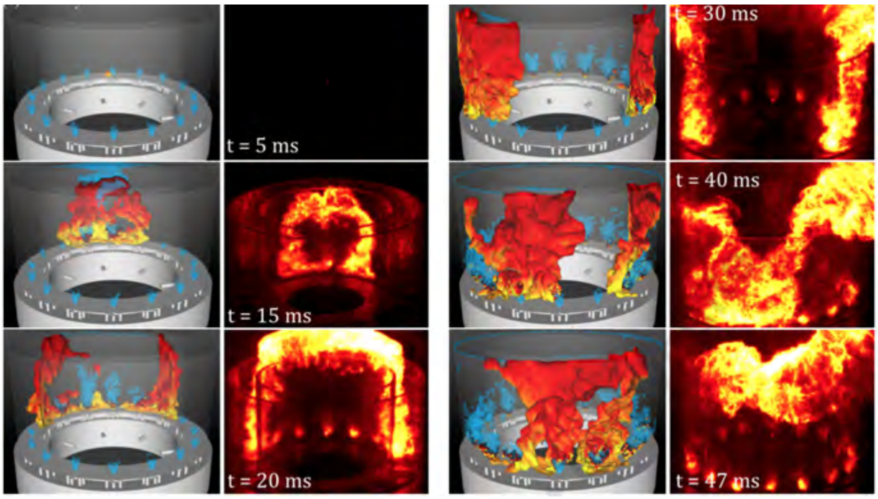

Figure 10.3: Comparison between experimental and numerical flame position at six instants of a light-round. Extracted from Lancien et al. [245].

These five phases were also found in the annular MICCA-spray set-up dedicated to spray ignition and experimented by Prieur et al. [244] for $0.8 \leq \phi_{glob} \leq 1.0$. LES of this MICCA-spray configuration were performed by Lancien et al. [245] with an Eulerian formalism for the dispersed phase. The two-phase light-round is qualitatively similar to the premixed gaseous one of Bourguoin et al. [241]. The five phases were found similar in the experiment and in the simulation [246], with a more pronounced deceleration in the final stages found in the simulation leading to a slight delay of about 10 % in the final front merging. The comparison between experimental and numerical flame position evolution during the light-round of the MICCA-spray set-up is presented in Fig. 10.3 and illustrates well the five phases of the light-round, as well as the ability of LES to reproduce the light-round also in spray condition.

10.2.2 Leading Point behaviour

Flame propagation is often studied with the evolution of Leading Point (LP) of the flame (the most advanced position of the flame in the azimuthal direction for annular set-ups or in the radial direction for a linear arrangement). As demonstrated by Lancien et al. [246], tracking the flame evolution by its LP position or by using sector-integrated heat release gives identical results. This suggests that flame propagation may be controlled by the leading-point. In the pioneer work of Boileau et al. [236], LES of an ignition sequence in a full annular industrial Safran Helicopter gas turbine was done with liquid fuel injection. Rich atmospheric conditions were applied and an Eulerian formalism was used for the dispersed phase. In his work, the LP was shown to first move axially reaching high axial position and to finally fall back and propagate azimuthally, staying in the bottom part of the chamber, near the injectors as the presence of the swirling flow enhances its propagation. Similarly, in the LES of the MICCA-spray configuration, Lancien et al. [246] concluded that for the first third of the sequence the LP is lifted up due to the arch-like flame. Then its axial position oscillates until around half of its trajectory, where the LP definitely drops down near the backplane. Looking at the mixture fraction along the LP trajectory, the LP showed a mixture systematically richer than the lean ϕ_{glob}.

10.3 Mechanisms driving flame propagation

Kao et al. [247] studied experimentally the spray ignition of a linear arrangement of burners. To demonstrate that there are many mechanisms driving flame propagation, non-dimensional numbers were introduced, describing the effect of inter-injector spacing, fuel/air ratio, turbulence, and also gas temperature for evaporation. These numbers were S/D, A/F, Re, and $\frac{T_{air}-T_F^{boil}}{T_F^{boil}-T^F}$ respectively with S the inter-swirler spacing, D the diameter of swirler exit, A/F the air-fuel ratio, Re the Reynolds number, T_{air} and T^F the inlet air and fuel temperature and T_F^{boil} the fuel boiling temperature. In the following, a list of the main ignition-controlling parameters proposed in the literature is given.

10.3.1 Injector-to-injector distance

As already discussed in Sec. 10.1 and Sec. 10.2, the injector-to-injector spacing is an essential factor as it influences the flow dynamics and mixing properties. The propagation mode (arc or radial) is directly influenced by this distance. A critical distance may be found to distinguish between both modes: $160\,mm$ was found by Barre et al. [238] in gaseous premixed conditions while Marrero-Santiago et al. [214] proposed $130\,mm$ for spray ignition. In this last study, the authors explain that the sudden change in propagation mode should not be associated to a critical distance but rather to a critical mixture fraction in the LRZ. This criterion is much more generic and allows to understand the behaviour of other configurations in the literature [248].

The two propagation modes (arc and radial) are well correlated to the ignition delay time (based on pressure measurements) as shown in Fig. 10.4. Ignition delay times in the two-phase CLSSB configuration are given for different fuels as a function of the injector spacing [2]. The change of propagation mode is directly identified by the change of the slope. For low injector-to-injector distance, the ignition delay time is almost independent of the injector spacing and is only controlled by the thrust effect (see Sec. 10.3.2) while the arc mode is characterized by a linear dependence of the delay time on the spacing.

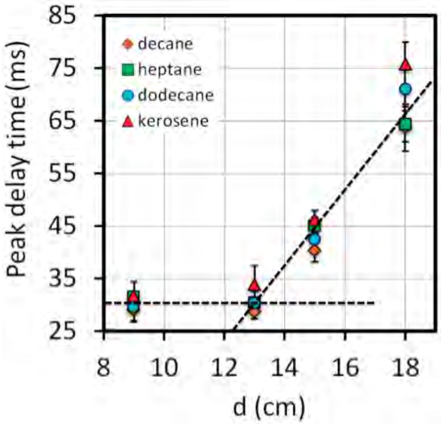

Figure 10.4: Ignition delay time in the CLSSB configuration for four fuels with variable volatility and four injector-to-injector spacings. Extracted from Marrero-Satiago [2].

In an annular lean premixed combustor with variable distance between injectors, Machover et al. [248] also retrieved the two modes as function of the injector distance. The arc (sawtooth) mode was recovered only for large inter-injector distance inducing low flammability in the LRZ. In all other annular configurations studied in the literature, only the radial propagation mode was found as the injector-to-injector distance was short.

10.3.2 Thrust effect

The absolute flame displacement velocity during light-round is a key parameter that has been investigated by many authors. In the early work of Boileau et al. [236], it was already explained that the main mechanism driving light-round is the burnt gas expansion that pushes the two opposite flame branches in the azimuthal direction. The absolute flame displacement speed is thus much greater than the turbulent flame velocity until the two branches merge. Bourguoin et al. [241] also found that the burnt gas expansion controls the flame motion during light-round in its annular premixed set-up so that $S_a = (\rho_u/\rho_b)S_d$ with S_a the absolute flame speed, S_d the flame displacement speed, and ρ_u, ρ_b respectively the fresh and burnt gas densities. This key thrust effect has been also evidenced experimentally and numerically in linear and annular arrangement of burners, for premixed, non-premixed and spray ignition (Barre et al. [238], Prieur et al. [244], Lancien et al. [245], Machover et al. [248]). The fresh gas velocity is modified at a distance of several sectors ahead of the flame due to volumetric expansion. Few cases were however found not driven by the burnt gas expansion, typically for very high injector distance [239], or in non-premixed ultra lean ($\phi_{glob} \leq 0.4$) conditions [227, 249]. In all cases not showing any thrust effect, the mixture fraction in the

LRZ was found below the lean flammability limit. The mechanism driving such cases is discussed in Sec. 10.3.7.

10.3.3 Flame wrinkling and turbulent flame speed

As already discussed in details in Sec. 7.2, turbulence enhances the flame propagation by increasing the flame surface. This effect was evidenced by Marrero-Santiago et al. [239] who found more wrinkled flames for small injector-to-injector distances. Bourguoin et al. [241] showed that the overall ignition time reduces with increasing bulk velocity leading to higher turbulence intensity but insisted on the fact that the delay time difference is actually more related to the kernel development phase rather than the light-round phase. As detailed in Sec. 7.2, turbulence can also be detrimental to flame propagation, especially when the kernel is small. This detrimental effect was shown in the lean premixed annular burner of Bach et al. [184].

10.3.4 Swirling motion

The swirling motion imposed by the injectors plays a grat role on the behaviour of flame propagation. Bach et al. [184] explained that in their annular premixed burner, the flame propagates further along the outer or inner wall according to the injector swirl number and orientation. This leads to a non-symmetrical propagation that was also observed later by Bourguoin et al. [241] but also in linear set-ups by Barre et al. [238] and Marrero-Santiago et al. [214] for instance. The orientation of the swirl of the closest injector to the spark is particularly important as it drives the initial flame trajectory.

10.3.5 Spray injection

Boileau et al. [236] compared the same ignition sequence with liquid and gaseous fuels. A faster flame propagation was obtained with the gaseous fuel, mostly due to the first injector ignition because of the added evaporation time. Recently, the annular MICCA-spray set-up was used by Prieur et al. [244] with premixed gaseous propane-air and liquid n-heptane and n-dodecane fuels presenting respectively high and low volatilities. Here also, premixed gaseous injection yielded the shortest ignition delay, and more volatile liquid fuel induced a shorter delay. The observed ignition delay differences were attributed to the laminar two-phase velocity s_l^{tp} assumed smaller than the equivalent gaseous s_l^0. Using correlations taken from Neophytou et al. [14], the 20 % difference in ignition delay between propane-air and n-heptane-air cases was well correlated to a similar difference between s_l^0 of the propane-air mixture and s_l^{tp} of the n-heptane mixture. Marrero-Santiago et al. [214] also used liquid fuels of variable volatilities in his two-phase CLSSB linear set-up. The fuel type effect was found more important in the arc mode. As in Prieur et al. [244], a higher volatility reduces the ignition delay. In this case, delay times obtained with the n-dodecane fuel showed an increase of $14 - 21\,\%$ with respect to the case with n-heptane fuel.

In the LES of Lancien et al. [245], rapid evaporation of droplets ahead of the flame led to a premixed-controlled combustion mode. More interesting, it was also evidenced that the gaseous equivalence ratio in the fresh gases between the beginning and the end of the light-round rises much faster than predicted by a 0D evaporation calculation. This enhanced evaporation may be attributed to the high turbulence generated by the thermal expansion. According to authors, a better liquid phase description is required to investigate more deeply this point, for instance by considering poly-dispersion with a Lagrangian formalism, which will be done in this work in Chap. 12. As in gaseous cases, ignition perturbs the flow up to 3 injectors ahead of the flame, with a significant impact on the sprays that are inclined in the azimuthal propagation direction. The liquid and gaseous properties encountered by the flame are therefore modified compared to the ones of the non-reacting flow making the analysis of the light-round sequence complex. Marrero-Santiago et al. [239] explained that in the arc mode, thermal expansion effect on droplets, as observed by Lancien et al. [245] for radial propagation, is limited. Indeed, the transport of droplets from high (SJZ) to low (LRZ) density zones to homogenize the mixture fraction is almost impossible if zones are too distant.

10.3.6 Wall heat losses

The influence of wall heat losses in the light-round process was investigated only in the MICCA-spray burner for $\phi_{glob} = 0.89$ by Prieur et al. [3] and Lancien [4]. In practice, in atmospheric or even depressurized low-temperature conditions, walls are cold compared to the flame temperature. High heat losses occur at the walls due to the temperature difference. However, in case of high-altitude engine failure, the relight procedure is immediately engaged. The combustor walls are thus still hot when the light-round occurs, limiting heat losses. However, after few seconds, wall temperature drops and ignition is more difficult. It was shown with numerical simulation that ignition delay is larger with wall heat losses because of the lower azimuthal velocity generated by the lower burnt gases volumetric expansion.

10.3.7 Near lean flammability limit

In ultra-lean ($\phi_{glob} \leq 0.4$) conditions, Machover et al. [227, 249] did found any thrust effect in linear or annular arrangement of burners. In these two experiments, because of the mixture fraction in the LRZ that is near or under the lean flammability limit, the flame propagation is controlled by the probability that a flame fragment travels from one burner to the following. The distance between the burners is therefore the most important factor. Bridges between adjacent SJZ must be created by close enough injectors to facilitate the flame transport. The influence of the bulk air velocity is much more limited. As no gas expansion is found in such case, the flame velocity is of the order of the turbulent flame velocity. As can be expected, an increase of the velocity with global equivalence ratio is found due to a higher probability of flame fragment transport between burners as flammability is higher. When dealing with such lean conditions, ignition might fail during the light-round. Machover et al. [249] observed that the steady-state flame stability limits are wider than the ignitability limits in terms of mixture fraction. However, by decreasing the inter-burner spacing, they become closer because the LRZ are richer. As the flame propagation is directly driven by its probability to survive and to be convected, trajectory based numerical models presented in Sec. 7.4 can be used to track the flame evolution even in the light-round phase but only when no thrust effect is found. This was done by Machover et al. [250] using the model of Neophytou et al. [200] in an annular non-premixed configuration operated in ultra-lean conditions ($\phi_{glob} \leq 0.4$). The low order model correctly retrieved trends such as the impact of injectors distance and ignition delays. Good prediction of delays was especially found for large inter-burner spacing and leaner equivalence ratio.

10.4 Conclusions

The final phase of an aeronautical ignition or relight sequence is the inter-sector flame propagation. Although much less work has been devoted to this phase compared to the previous ones, some trends can be identified from the literature. It was found that the global behaviour of this phase is controlled by few parameters. For high global equivalence ratio and low injector-to-injector spacing, a flammable mixture is found in the whole chamber. In such case, the flame brush follows the Leading Point and propagates radially in the lower part of the chamber enhanced by richer mixture fraction and favourable turbulent flows induced by swirled injectors. The flame velocity is in such case controlled by the burnt gas volume expansion, leading to velocities much higher than the turbulent flame speed. When lowering the global equivalence ratio and increasing the injector-to-injector spacing, the propagation switches to an arc mode. Lateral Recirculation Zones separating injectors are lean and the flame advances from one injector to its neighbouring injector preferentially thanks to the bridge possibly connecting adjacent rich jet branches. In such conditions, the flame velocity is of the order of the turbulent flame velocity, controlled by its probability to survive and to be convected. No more thrust effect is observed. Therefore, ignition failure might even occur during light-round for extremely low global equivalence ratio considered or too high inter-injector distance.

Light-round sequences in spray conditions have recently been investigated experimentally in two academic configurations: the linear CLSSB set-up of Marrero-Santiago et al. [214] and the annular MICCA-spray set-up of Prieur et al. [244] which has also been studied numerically by Lancien et al. [245]. As shown in these works, the light-round sequence can be strongly affected by the heterogeneous droplet distribution in the chamber. Starting from the results already obtained in these two configurations, the objective of the next two chapters(11 and 12) is thus to continue investigating the light-round phase and in particular the influence of liquid fuel distribution and volatility.

Chapter 11

Inter-sector flame propagation: CORIA Linear Swirled Spray Burner

Contents

11.1 Objectives **225**
11.2 Experimental set-up **226**
11.3 Numerical set-up **228**
11.4 Influence of the inter-injector spacing on ignition **230**
11.4.1 Non-reacting flow 230
11.4.2 Ignition sequences 235
11.5 Influence of fuel volatility **243**
11.6 Conclusions **245**

11.1 Objectives

This chapter is dedicated to the study of inter-injector two-phase flame propagation in a linearly arranged multi-burner. The main relevant studies of multi-injector spray flame propagation were reviewed in Chap. 10. Following the experimental work of Marrero-Santiago et al. [2, 214, 239], the objective here is to perform LES of ignition in the multi-burner set-up as a complementary study. The linear arrangement is considered for its simplicity compared to an annular set-up for which the flame dynamics is more complex. The MICCA-Spray annular configuration will be studied in Chap. 12.

After introducing the experimental and numerical set-ups, the crucial effect of the injector-to-injector distance which changes both the flow dynamics and the local fuel distribution in the chamber is assessed on the non-reacting flow topology and ignition behaviour and results are compared to experiments. The objective of this comparison is also to show the capacity of LES to investigate two-phase light-round sequences. Two-phase flow related parameters such as the influence of liquid fuel distribution and volatility on ignition, are finally discussed.

11.2 Experimental set-up

The experimental configuration studied is the Coria Linear Swirled Spray Burner (CLSSB) which is the two-phase flow version of the KIAI linear set-up [237, 238]. It has been experimented by J.Marrero Santiago [2, 214, 239] at CORIA, France. A picture of the set-up is given in Fig. 11.1. It is a confined chamber with a large black metallic window at the back, a large frontal quartz window allowing optical access and two lateral small quartz windows mounted on metallic supports. Similarly to the KIAI-spray configuration, a convergent exhaust nozzle is used to avoid external air recirculation. Air convergent ducts and spray atomizer systems are all the same and identical to the ones of the KIAI-Spray configuration presented in Sec. 8.2. The number of injectors (air convergent + spray atomizer) can be changed from 3 to 5, and the injector-to-injector distance d is also variable. Three configurations will be studied in this work: 3 injectors with $d = 18\ cm$, 4 injectors with $d = 15\ cm$, and 5 injectors with $d = 9\ cm$. A front view of the $d = 18\ cm$ configuration equipped with three injectors is shown in Fig. 11.2. The main flow regions are highlighted. Each injector has its own Inner Recirculation Zone and Swirled Jet Zone. Injectors are separated by Lateral Recirculation Zones. Top views of the three investigated cases are sketched in Fig. 11.3 giving the dimensions of each configuration. All swirlers, named from 1 (left) to 5 (right), are oriented in the same direction and contrary to the KIAI-Spray set-up where a laser was used, ignition is triggered by an aeronautical spark plug delivering $450 mJ/pulse$ in a single-spark mode. The spark plug is centred on the second injector in all cases and its exact position is reported in Tab. 11.1 for the three configurations. $z = 0\ m$ corresponds to the bottom wall of the chamber, ($x = 0\ m$, $y = 0\ m$) corresponds to the position of injector 2 for the $d = 18\ cm$ case, to the position of injector 3 for the $d = 9\ cm$ case, and to the middle point between injectors 2 & 3 for the $d = 15\ cm$ case.

To ensure good ignition performance, the operating conditions are modified compared to the KIAI-Spray configuration: air and liquid fuel mass flow rates per injector are respectively set to 6.86 g/s and 0.316 g/s leading to a higher global equivalence ratio of $\phi_{glob} = 0.7$ for all cases. Two fuels are used to study the impact of liquid fuel volatility: n-heptane and n-dodecane. The chamber is operated at ambient pressure, with preheated air ($T_{air} = 416 \pm 3\ K$) and fuel ($T_{fuel} \approx 350\ K$). All ignition tests were performed after reaching a stable internal window temperature of $T_{wall} = 387\ K$. HS-PIV (aerodynamics), toluene PLIF (mixture fraction ditribution) and high speed flame visualisation described in [2, 239] were used for measurements.

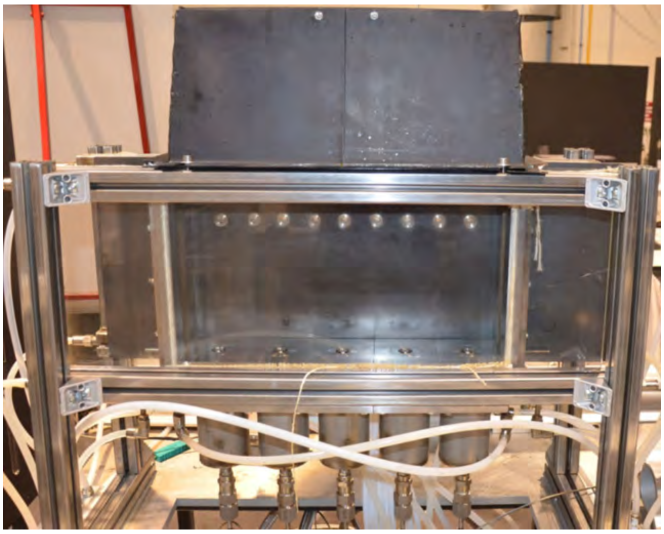

Figure 11.1: Picture of the Coria Linear Swirled Spray Burner (CLSSB). Extracted from [2].

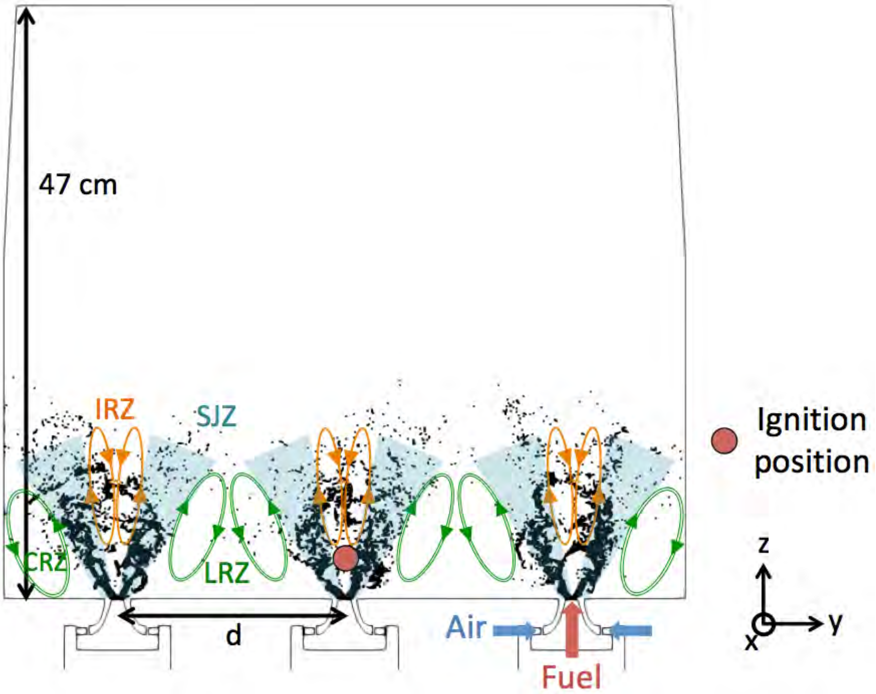
47 cm
IRZ
SJZ
CRZ
LRZ
d
Air
Fuel
Ignition position
z
y
x

Figure 11.2: Scaled front view of the $d = 18\ cm$ configuration.

Configuration	d = 18 cm	d = 15 cm	d = 9 cm
x (m)	-0.045	-0.045	-0.045
y (m)	0.0	-0.075	-0.09
z (m)	0.023	0.023	0.023

Table 11.1: Position of the spark plug for the three configurations studied.

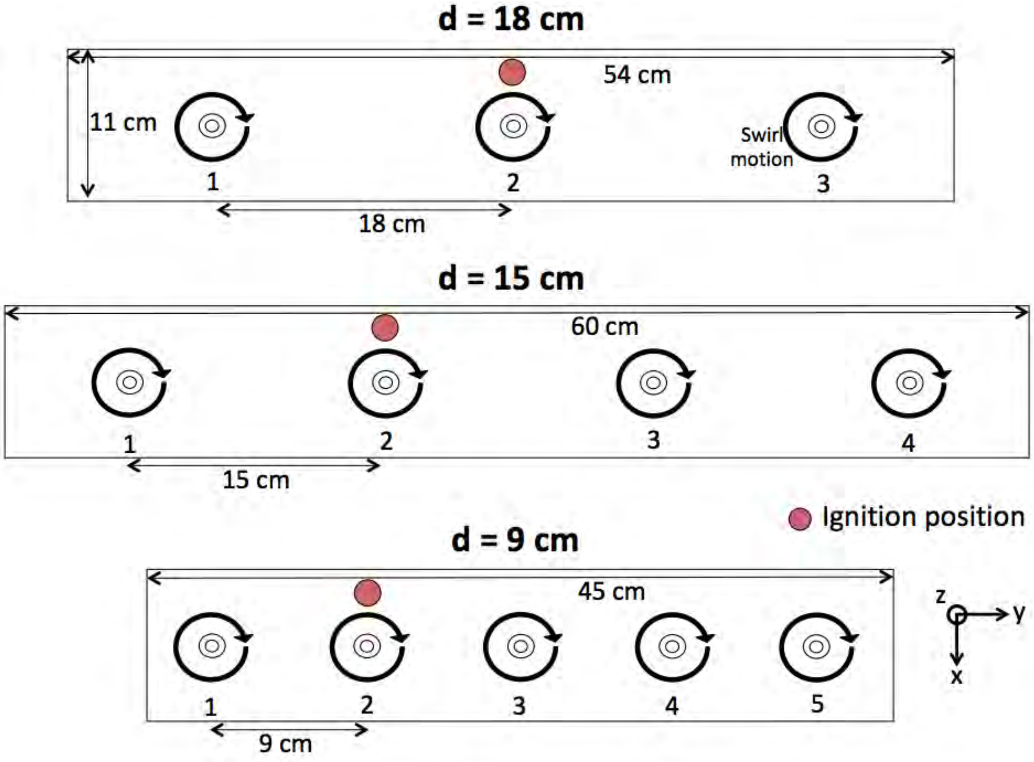

Figure 11.3: Scaled top views of the three investigated cases.

11.3 Numerical set-up

The three inter-injector distances are studied using n-heptane fuel (non-reacting flow and ignition), and the $d = 18$ cm non-reacting flow is also investigated using n-dodecane. The numerical set-up is very close to the one used in the KIAI-Spray configuration (see Sec. 8.3 for details). The AVBP code is used with the third order in time and space Taylor-Galerkin scheme [48] for all LES. Similarly to the KIAI-Spray case, the computational domain contains the inlet pipe, the swirlers, the injection veins, the combustion chamber and the convergent at the outlet. The same NSCBC boundary conditions and SIGMA models are used. Lateral combustor walls are defined as no-slip and isothermal at $Tw = 387$ K.

Fully unstructured grids are generated, with the same topology illustrated in Fig. 11.4 taking the example of the $d = 18$ cm case. The mesh characteristics for the non-reacting flow simulations are similar to the ones of the KIAI-Spray set-up. Cell sizes associated to ignition sequences are given in Table 11.2. The corresponding total number of tetrahedral cells are 122 M cells for the $d = 9$ cm case, 149 M cells for the $d = 15$ cm case and 131 M cells for the $d = 18$ cm case. Considering the large dimensions of the combustor, resolving the flame front without combustion model would require too important HPC resources. For this reason, the minimum cell size in the entire bottom part of the chamber (zone A) is set to 0.8 mm and the Thickened Flame (TF)

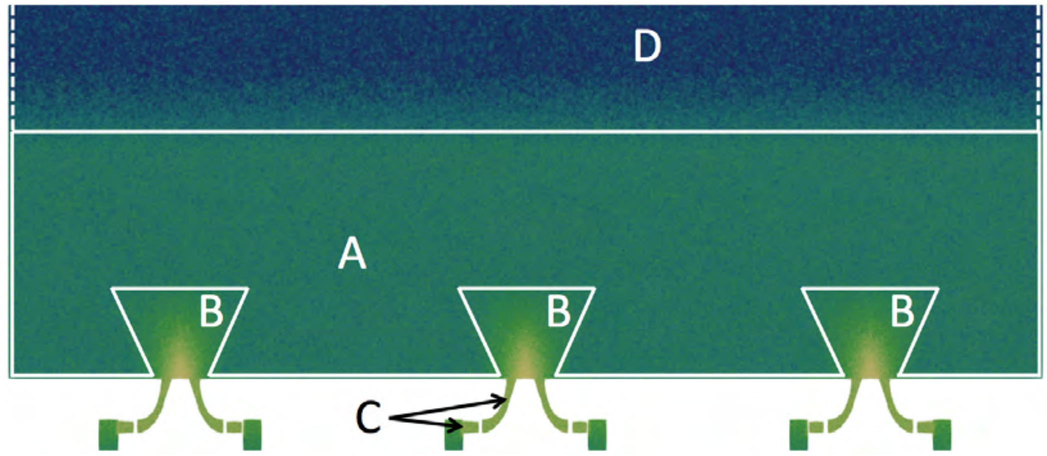

Figure 11.4: Cut of the CLSSB mesh topology, presented in the $d = 18\ cm$ case.

Zone	A	B	C	D
$\Delta_{x,min}\ (mm)$	0.8	0.2	0.4	1.2

Table 11.2: Minimum cell size in each zone of the CLSSB mesh topology.

model [33] is used (details are provided below). Zone B surrounding dense spray regions is more refined. Indeed, the TF model has been derived in the context of gaseous flames. Therefore, even if its extension to spray flames has already been justified by Boileau [63] and Paulhiac [17], it is preferred to limit the thickening factor ($F < 3$). Finally, the swirler vanes and convergent are well refined to guarantee the correct flame dynamics, while downstream regions are progressively coarsened.

The exact same Lagrangian approach than for the KIAI-Spray study is chosen for the spray description (see Sec. 8.3) and is not detailed here. Note that as demonstrated by Paulhiac [17] (Sec. 4.3.3), the two-phase TFLES model implies the application of F to evaporation and drag.

The n-heptane fuel oxidation is described using the $ARC\_25\_C_7H_{16}$ scheme derived and validated in Sec. 8.3. The Dynamic Thickened Flame model (DTFLES) [40] is retained so that the combustion model only impacts the flame region. The relaxation thickening sensor based on the fuel source term is used as proposed by Jaravel [41] for ARCs. A tabulation of 1D flame properties (s_l^0, δ_l^0 and $|\dot{\omega}_F|$) as function of ϕ_g is used to obtain the local thickening factor required to have at least 5 grid points in the flame thickness. The Charlette efficiency function [37] is chosen in its static version ($\beta = 0.5$) to recover the unresolved flame wrinkling.

The standard ED model [151] is used in this section instead of the ED_HT model (Sec. 6.8) as studying the inter-injector propagation does not require a very detailed and costly modelling of the early flame kernel growth. Table 11.3 summarizes the ED

ED sphere diameter	9 mm
ED time	25 μs
ED energy	50 mJ

Table 11.3: ED parameters of the standard ED model used.

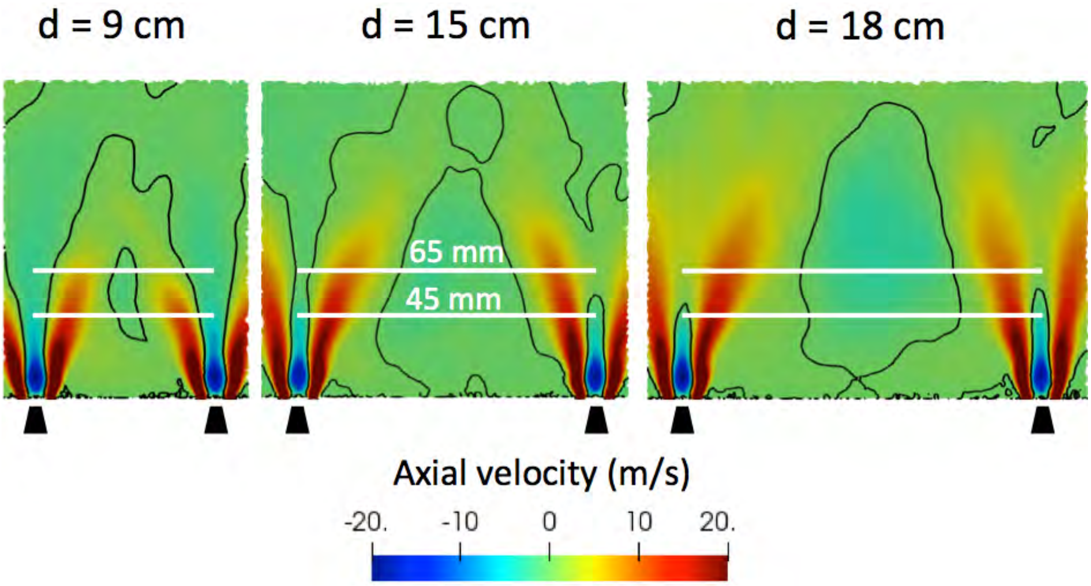

Figure 11.5: Cuts of non-reacting flow mean axial velocity for the three inter-injector spacings. An iso-contour of $U_{axial} = 0$ is drawn in black. The two white horizontal lines show where the data of Fig. 11.6 are extracted from. The injectors position is recalled below each figure.

parameters used here. The input energy corresponds to an energy transfer efficiency of 11 % in the range of standard values from the literature. Note that when coupling the ED model with the TFLES model, misfiring could occur if the deposited energy is too diffused (the thermal diffusion coefficient is multiplied by the thickening factor F). To avoid this side effect, the TFLES model is switched on only after the chemical run-way: in practice the thickening factor F is limited to one until the maximum temperature in the domain reaches a given temperature corresponding to chemical run-away.

11.4 Influence of the inter-injector spacing on ignition

11.4.1 Non-reacting flow

The flow topology is much sensitive the inter-injector distance d. Cuts of non-reacting flow mean axial velocity for the three inter-injector spacings investigated are provided in Fig. 11.5. The black line shows an iso-contour of $U_{axial} = 0$ and injectors position are recalled below each figure. Note that for the three cases, the shown axial velocity field is the one between injectors 2 and 3. The IRZ height and width tend to decrease with increasing d, so that when at $d = 9\ cm$ the IRZ is open, it is closed and much smaller at $d = 18\ cm$ with a height below 60 mm. The case $d = 15\ mm$ is intermediate with a very thin but still open IRZ above injector 2 and a closed IRZ above injector 3 (these different behaviours are attributed to an insufficient LES averaging time). Contrary to the IRZ, the highly turbulent jet zone is wider when increasing d. Its height almost doubles from $d = 9\ cm$ to $d = 18\ cm$. Finally, the LRZ area is also increased with d. At $d = 9\ cm$, the LRZ is very small, trapped between the two adjacent SJZ which are really close to each other. On the contrary for $d = 18\ cm$, neighbouring SJZ are far away, leaving a lot of space for the LRZ to develop. The LRZ height increases so much that the "gap" between adjacent SJZ is only found at very hight axial position ($z < 150\ mm$) contrary to the $d = 9\ cm$ case where neighbouring SJZ intersect much lower in the chamber ($z \approx 70\ mm$). These flow topology differences varying the injector-to-injector distance are of course expected to influence the ignition behaviour.

Validation of the LES non-reacting flow gaseous aerodynamics versus experiment is proposed in Fig. 11.6. Mean and RMS axial velocities as well as mean radial (y-direction) velocity are compared on horizontal profiles (lines shown in Fig. 11.5) for (a) $d = 9\,cm$, (b) $d = 15\,cm$ and (c) $d = 18\,cm$. The position of injectors 2 and 3 are recalled below each plot. An overall good agreement is found between LES and experiments. The angle of the SJZ is perfectly recovered for $d = 9\ cm$ but seems a little bit too large compared to experiment for $d \geq 15\ cm$. RMS velocities are slightly over-estimated in the LES, especially in the spray jet zone. Note that experimental profiles were measured with HS-PIV *without* considering the spray. This may explain the observed differences especially in the dense spray regions where droplet induced turbulence is captured by LES and ignored in experiments. It is particularly interesting to see that for $d \geq 15\ cm$, the LRZ is very quiescent with RMS velocities remaining below 2 m/s in this large zone. On the contrary, for $d = 9\ cm$, no such low RMS velocity plateau is found in the LRZ, RMS velocities being always above 4 m/s.

The non-reacting flow mixture fraction distribution in the chamber is another key parameter of ignition. This is especially true in the present lean configuration $\phi_{glob} = 0.7$. Local spots of non-flammable mixture can be found and prevent the flame propagation. The comparison between experimental (Toluene-PLIF diagnostics) and LES cuts of equivalence ratio for the three inter-injector spacings is shown in Fig. 11.7 Note that ϕ_g is used for experiments and ϕ_{tot} for LES but except in the first 10 mm above the injector, ϕ_{tot} is very similar to ϕ_g. This comparison shows important discrepancies. The most important one is the rich SJZ branches found in the experiments up to 50 mm for the three d values, while in LES, the total equivalence ratio in spray jet branches is around $\phi_{tot} = 0.8$ except in the first 10 mm above the injector where the dense spray leads to a liquid equivalence ratio above $\phi_l = 20$. With increasing d

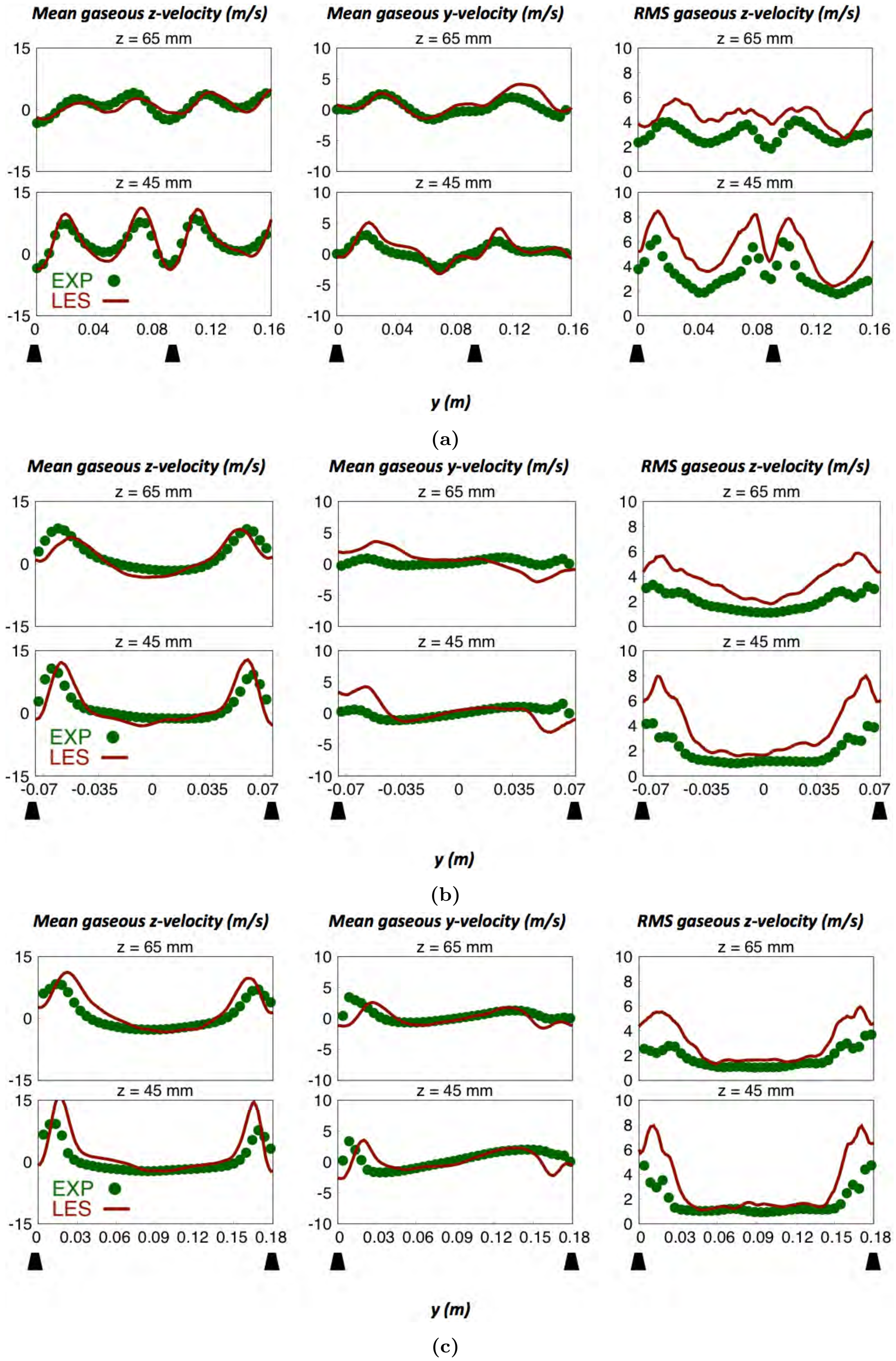

(a)

(b)

(c)

Figure 11.6: Comparison between experiments and LES of horizontal profiles (lines shown in Fig. 11.5) of non-reacting flow mean and RMS gaseous axial velocity and mean gaseous radial velocity for (a) $d = 9\,cm$, (b) $d = 15\,cm$, (c) $d = 18\,cm$.

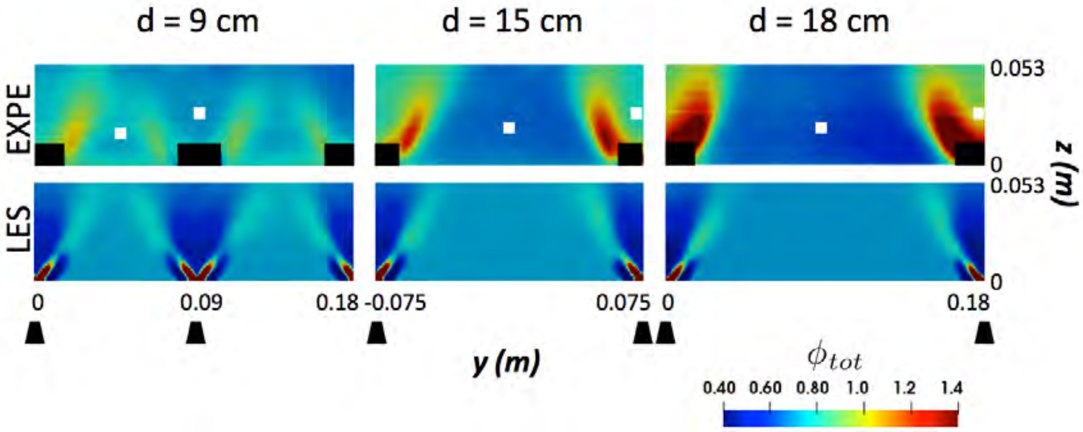

Figure 11.7: Comparison between experimental and LES cuts of equivalence ratio for the three inter-injector spacings. ϕ_g is used for experiments and ϕ_{tot} for LES but except in the first $10\ mm$ above the injector, ϕ_{tot} is very similar to ϕ_g. White squares show where the data of Fig. 11.8 are extracted from.

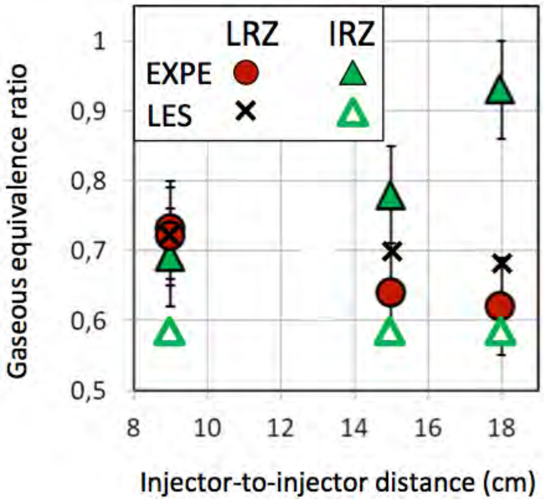

Figure 11.8: Comparison between experiments and LES of the gaseous equivalence ratio found in the IRZ and LRZ (exact zones shown in Fig. 11.7). Error bars indicate the given experimental measurement uncertainty.

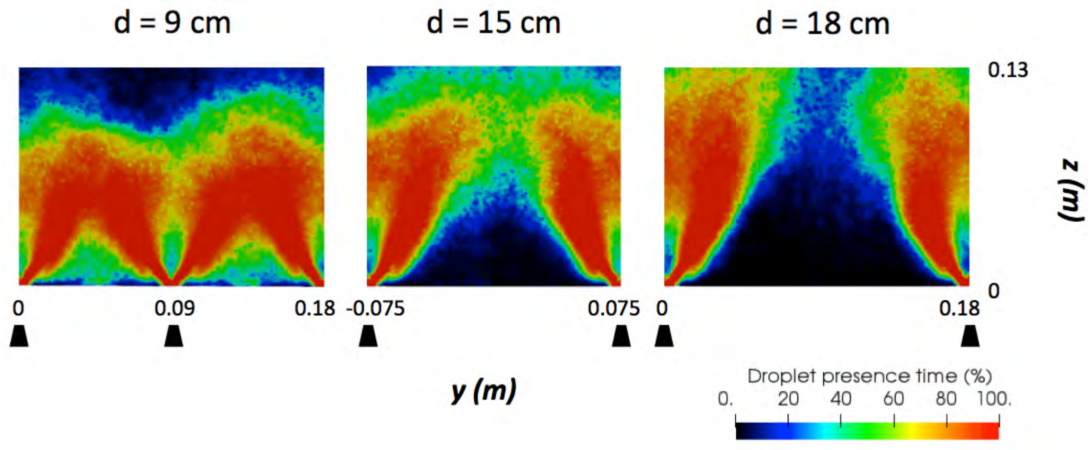

Figure 11.9: Cuts of droplets presence (% of time) for the three inter-injector spacings.

values, the experimental ϕ_g found in the IRZ increases a lot (from 0.69 to 0.92 changing d from 9 cm to 18 cm) while in LES, this value stays perfectly constant at a very lean value $\phi_{tot} = 0.59$). This is quantified in Fig. 11.8 summarising the experimental and LES gaseous equivalence ratio found in the IRZ and LRZ (exact zones shown by white squares in Fig. 11.7). Finally, for $d = 9$ cm, equivalence ratios found by LES and experiments in the LRZ are in good agreement at $\phi_g = 0.72$. When increasing the inter-injector distance d, the LRZ mixture fraction is progressively homogenized and reduced, which is found experimentally and numerically. For $d = 18$ cm, LES predicts $\phi_g = 0.69$ in the central core of the LRZ while experiments give $\phi_g = 0.62$.

Overall, the influence of the injector-to-injector distance on the mixture fraction distribution seems to be much more important in experiments than predicted by the LES. The important differences found on equivalence ratio between LES and experiments was already found in the KIAI-spray configuration, where the droplet size distributions were however in good agreement at two different positions in the chamber. The evaporation model was also validated in a previous study [218] of the unconfined version of the KIAI-Spray set-up. Differences might partially be explained by the Toluene-PLIF diagnostics which introduce some problems to filter sub-pixel droplets from the vapour phase in moderately dense spray zones. According to Marrero Santiago [2]: "the spray branch reveals a denser droplet concentration towards the nozzle where Toluene-PLIF can only be qualitative". As the droplet concentration in the IRZ is also important, quantitative experimental evaluation of ϕ_g is this zone must also be taken with care. To illustrate qualitatively the presence of droplets in the CLSSB configuration, cuts of droplets presence (% of time when at least 1 droplet is found in the cell volume) are presented in Fig. 11.9 for the three inter-injector spacings. It can qualitatively be used to identify zones where Toluene-PLIF is less accurate.

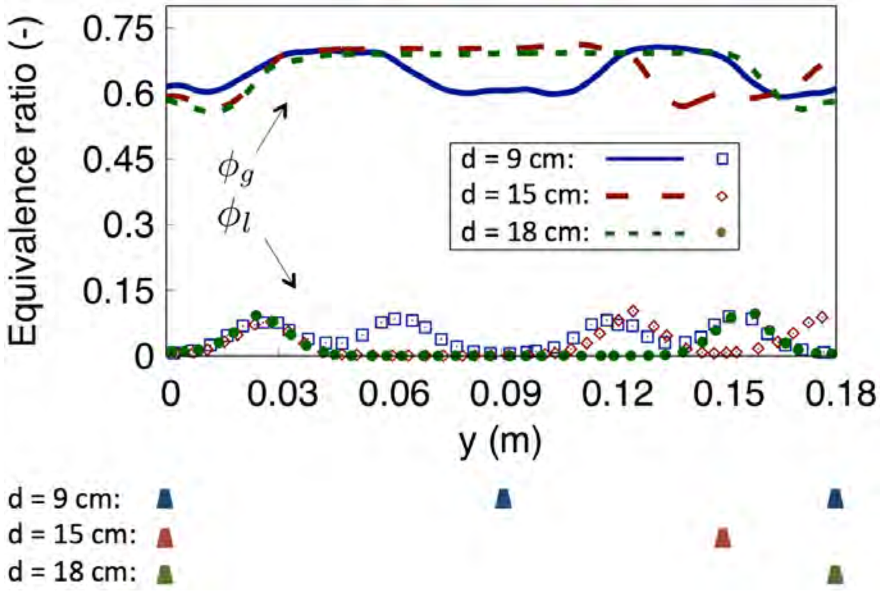

Figure 11.10: Profiles along the line $z = 45\,mm$ of gaseous and liquid equivalence ratios for the three inter-injector spacings. The respective injectors position is recalled below the figure. Note that profiles and injectors position of the case $d = 15\ cm$ are shifted to align injector 2 with the other configurations.

Figure 11.9 also confirms that for $d = 9\ cm$, dense spray branches of adjacent injectors communicate directly at a height of $z \approx 50\ mm$. This is no more the case for $d = 15\ cm$ and even less for $d = 18\ cm$ for which injector SJZs are well separated by the lean LRZ with no droplets left. At $z = 45\ mm$ (see Fig. 11.5), profiles of ϕ_g and ϕ_l for the three inter-injector spacings are plotted in Fig. 11.10. The respective injectors position is recalled below the figure. Note that profiles and injectors position of the case $d = 15\ cm$ are shifted to align injector 2 with the other configurations. This clarifies that $\phi_l = 0$ in the LRZ for $d \geq 15\ cm$ while for $d = 9\ cm$, the minimum liquid equivalence ratio in the LRZ is around $\phi_l = 0.05$. It also confirms the LES result of Fig. 11.8: in the IRZ, an increase of d is not associated to an increase of gaseous equivalence ratio, contrary to what is supported by experiments.

11.4.2 Ignition sequences

Ignition sequences using n-heptane fuel are now analysed for the three inter-injector distances. As reference, Fig. 11.11 presents experimental high-speed spontaneous flame emission images during one ignition trial for each injector spacings. LES sequences for $d = 9\ cm$, $d = 15\ cm$ and $d = 18\ cm$ are respectively shown in Figs. 11.12, 11.13 and 11.14. For each, flame front visualizations (iso-$T = 1400\ K$) coloured by heat release are shown, along with fuel droplets.

For $d = 9\ cm$, Fig. 11.12 shows that the flame is immediately convected to the

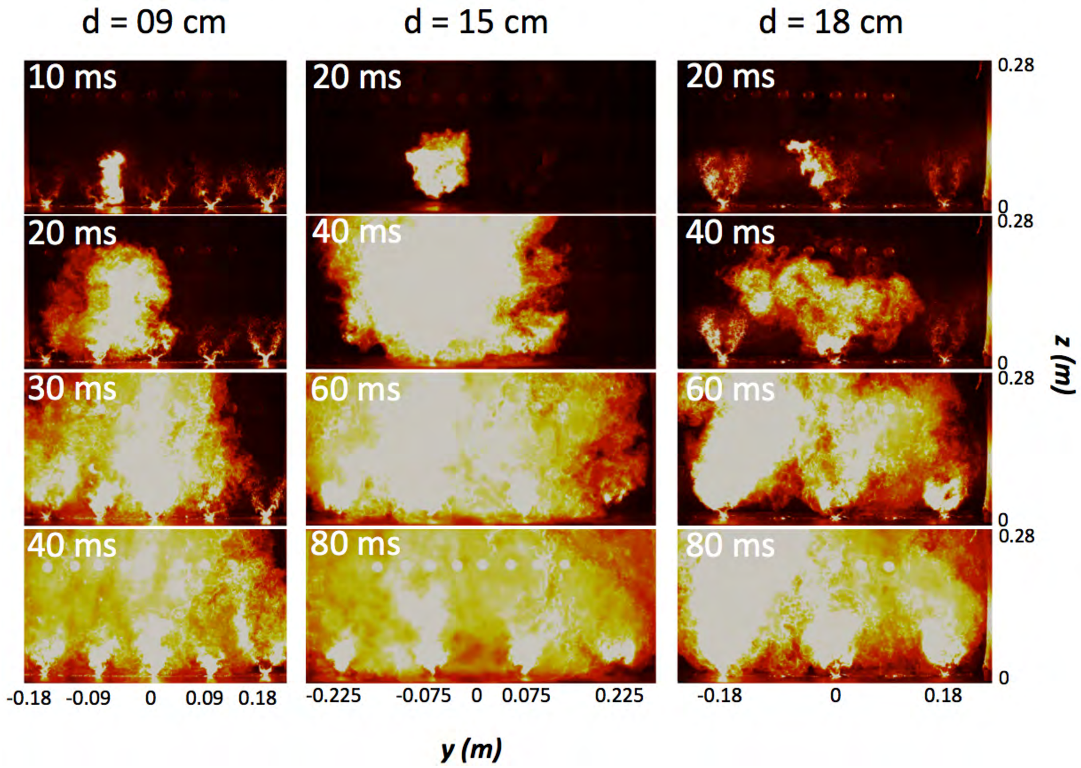

Figure 11.11: Experimental high-speed spontaneous flame emission images during one ignition trial for each injector spacings.

right, while staying low in the chamber. The beginning of the sequence is actually slow as the kernel volume between 10 ms and 20 ms is almost constant contrary to the experimental visualization where the flame expansion is very fast in this period. After 20 ms, the flame starts propagating to the right and left directions with a clear radial mode, similarly to the gaseous KIAI-linear configuration investigated by Barre et al. [238]. The flame stays very low ($z < 14$ cm) in the chamber at 30 ms compared to experiments in which it reaches $z = 28$ cm at that time. Vertical flame fronts propagating radially along the bottom wall are found to reach injectors 1 and 4 after 40 ms, corresponding approximately to the experimental snapshot at 30 ms. Finally, in the LES sequence, the very wrinkled flame front reaches the right chamber wall after around 50 ms.

At this point, it is important to stress that ignition sequences always present an important stochasticity so that comparing experimental and LES trials one by one is not expected to give quantitative agreement. The main source of stochasticity arises from the turbulent flow, responsible for the differences of the flow at sparking time. This is illustrated in Fig. 11.15 providing PDFs of velocity components around the ignition position for the three injector spacings, for both average non-reacting flow and instantaneous field at the time of sparking. In the $d = 9$ cm case, the flow around the spark position at the sparking time is very different than the average field, although

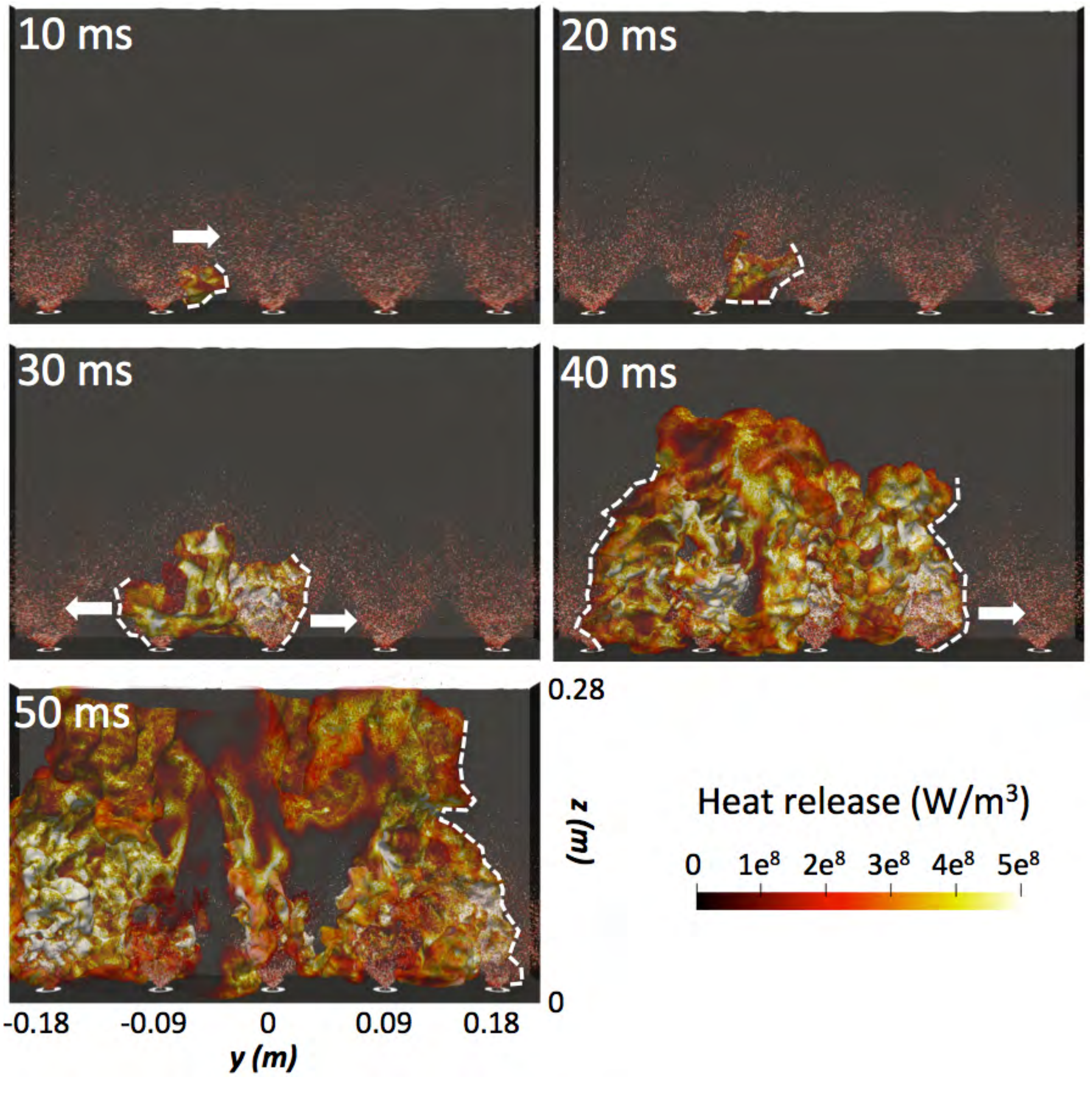
10 ms
20 ms
30 ms
40 ms
50 ms
0.28
z (m)
0
-0.18
-0.09
0
0.09
0.18
y (m)
Heat release (W/m³)
0
1e8
2e8
3e8
4e8
5e8

Figure 11.12: $d = 9\ cm$, **n-heptane ignition sequence. Flame front visualization (iso-**$T = 1400\ K$**) coloured by heat release. Fuel droplets are also added. Thin dashed line help distinguishing the flame front.**

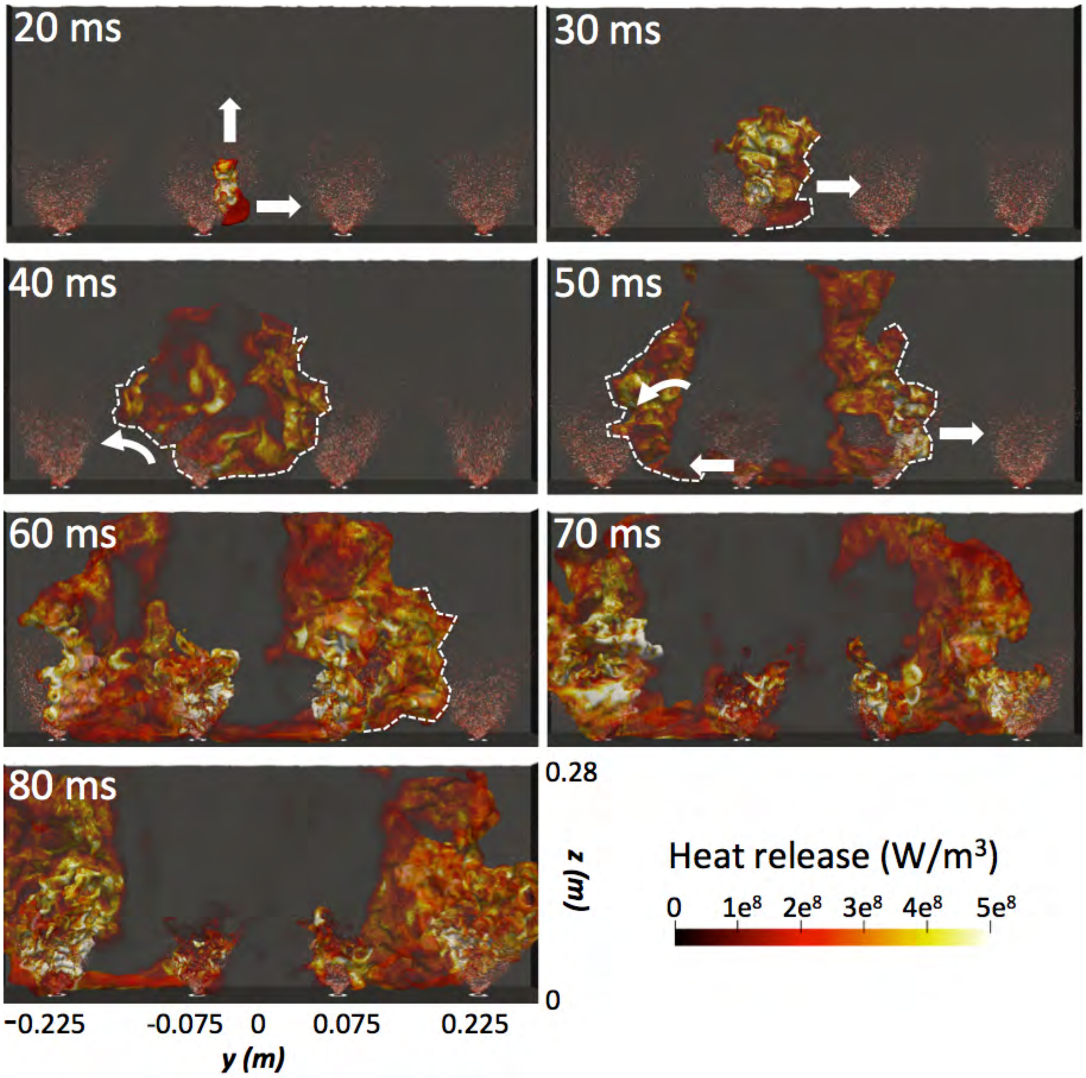

Figure 11.13: $d = 15\ cm$, **n-heptane ignition sequence. Flame front visualization (iso-**$T = 1400\ K$**) coloured by heat release. Fuel droplets are also added.**

the spark position is in a quiescent recirculating zone presenting low fluctuation levels. In particular, the axial Uz velocity is much lower than the average value, which explains partly why the flame stays initially very low in the chamber compared to the experiment. Besides, the radial Uy velocity around the spark position at the sparking time is much higher ($\approx 5\ m/s$) than the average value centred around 2 m/s. This high initial radial velocity, attributed to the swirl motion in this half of the chamber, explains the initial rapid displacement of the flame towards injector 3.

For $d = 15\ cm$, Fig. 11.15 highlights that the flow around the spark position at the sparking time is very close to the mean non-reacting flow. Thus, it is not surprising to observe in Fig. 11.13 that the initial axial and radial flame expansion do not deviate from the experiment as much as the $d = 9\ cm$ case (Fig. 11.11). At $t = 30\ ms$, the radial propagation mode of the right flame branch is clearly evidenced, corresponding to the experimental behaviour. Experimentally at 40 ms, the flame path between injector 2 and injector 1 comes off the bottom wall but stays at relatively low axial stations ($z < 70$ cm) making the distinction between a radial or arc mode difficult. According to the droplet presence map given in Fig. 11.9, $z = 70$ cm actually corresponds to the bottom part of neighbouring spray branches bridge, making the assumption of an arc mode realistic in this case. This hybrid arc-radial propagation mode is well recovered numerically at 40 ms. The left branch of the flame also joins the spray-SJZ of injector 1 at $z \approx 70$ cm. Following this leading arc mode, a secondary radial mode is found at 50 ms, evidenced by the flame crossing the LRZ towards injector 1. In the positive y direction, the radial mode continues and injector 4 is ignited at around $t = 70$ ms instead of 60 ms for the experimental trial presented. Finally, the mean heat release of the flame in the $d = 15$ cm is much smaller than the flame of case $d = 9$ cm. This was expected considering the decreased thermal power of the chamber induced by the removal of one injector along with the increase of the volume of the combustor.

For the last case $d = 18$ cm, as for $d = 15$ cm, the flow around the spark position at the sparking time is very similar to the average non-reacting flow. The radial Uy velocity as well as the velocity Ux in the chamber transverse direction are very low, respectively centred around -1 m/s and 0 m/s. The axial velocity component is just slightly higher around 2 m/s. Therefore, the created kernel tends to stay close to the sparking location. Figure 11.14 shows a kernel slowly convected downstream after 20 ms, only reaching the spray zone after 25 m/s. This is also highlighted by Fig. 11.16 showing the evolution of the Leading Point (LP) of the right flame branch going towards positive y during the three ignition sequences. The x-position of the LP in the $d = 18$ cm case does not separate from the back wall until 25 ms. This slow early flame development found with LES seems in good agreement with experiments showing a small flame still in the neighbourhood of injector 2 after 20 ms. Note that Fig. 11.16 also highlights the impact of the average swirl motion induced by the alignment of swirls all oriented in the same direction. For all configurations, the LP position of the branch propagating in the positive y direction stays in the half $x < 0$ m corresponding to a swirled-induced mean $Uy > 0$ m/s flow. This leads to a non-symmetric propagation already observed [214, 241]. Once the flame reaches the highly turbulent SJZ of injector 2, it expands in all directions. After 30 ms, the right branch of the flame inclines and goes up to $z = 180$ mm as indicated by the axial position of the LP shown in Fig. 11.16. This is much higher than the dense spray zone of the adjacent injector 3 (see Fig. 11.9). Therefore the flame transport by this arc mode is slowed as the flame does not catch the adjacent SJZ. Note that such a high arc propagation mode would be very dangerous in an industrial burner where dilution holes may quench the flame at such high locations. Independently of this arc mode

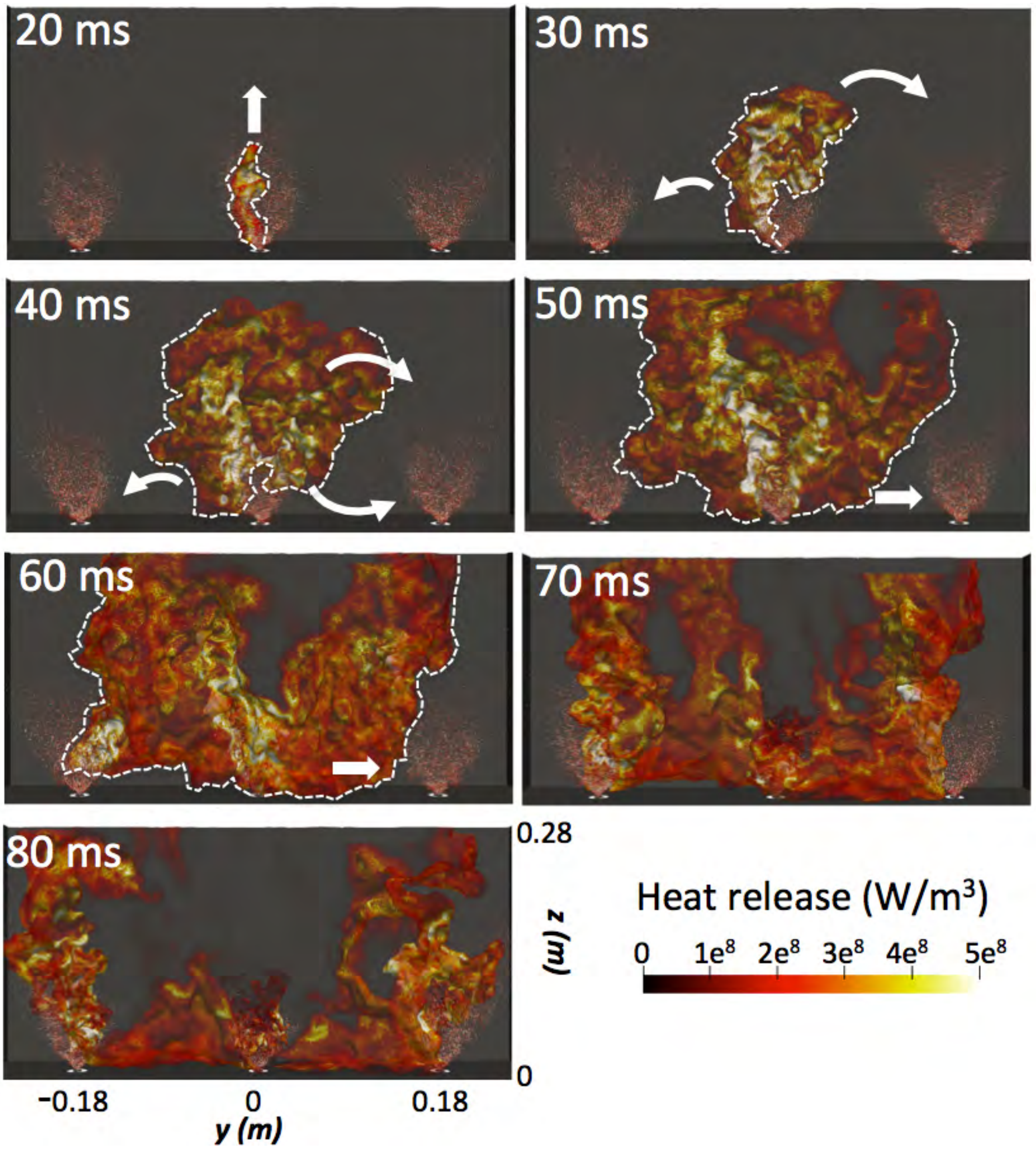
20 ms
30 ms
40 ms
50 ms
60 ms
70 ms
80 ms
0.28
z (m)
0
-0.18
0
0.18
y (m)
Heat release (W/m³)
0
1e⁸
2e⁸
3e⁸
4e⁸
5e⁸

Figure 11.14: $d = 18\ cm$, **n-heptane ignition sequence. Flame front visualization (iso-**$T = 1400\ K$**) coloured by heat release. Fuel droplets are also added.**

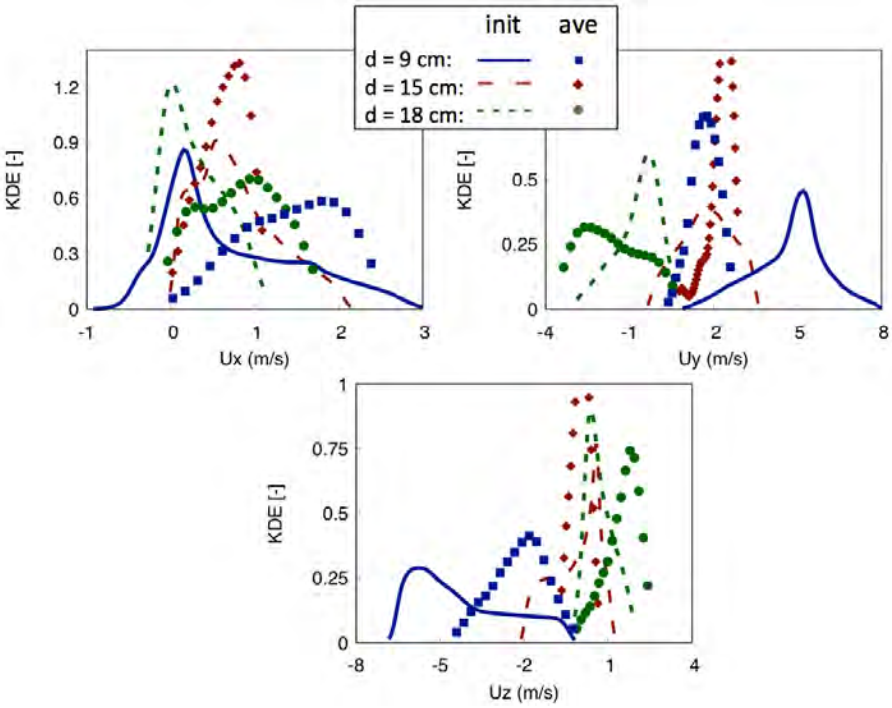

Figure 11.15: PDFs of the three velocity components in a sphere ($r = 9\ mm$) centred around the ignition position for the three injector spacings. Symbols correspond to the average non-reacting flow while lines correspond to instantaneous fields at the time of sparking.

occurring at high axial positions, the flame also propagates towards injector 3 by the LRZ following a late radial propagation mode as evidenced at $t = 40 - 60\ ms$. Such a radial mode for this high injector spacing is made possible by the flammable mixture of the LRZ around $\phi_g \approx 0.69$ according to LES (see Fig. 11.8). However, the very low turbulence activity in the LRZ implies a turbulent flame velocity much lower than when propagating through SJZs. Finally, injector 3 is ignited from the bottom wall following the late radial mode, which is eventually faster than the arc mode occurring at too high axial locations. Injector 1 is ignited at around 60 ms following a very classic arc mode initiated at 30 ms. The ignition timing of injector 1 as well as the height of this arc mode bridge ($z \approx 90 - 100\ mm$) are in good agreement with the experimental sequence. Furthermore, Fig. 11.9 shows that this height actually corresponds to the bottom of the bridge joining neighbouring spray branches for $d = 18\ cm$.

All propagation modes found are summarized in Tab. 11.4 for the three injector spacing. For small spacing, only the radial propagation mode is found. When increasing this spacing, a low arc mode appears between injectors 2 and 1 as observed experimentally, along with radial modes for the flame propagation towards injector 4. Finally, when increasing further the spacing d, the prevailing mechanism is the arc mode. During injectors 2 → 3 propagation, the very slow and unsafe high arc

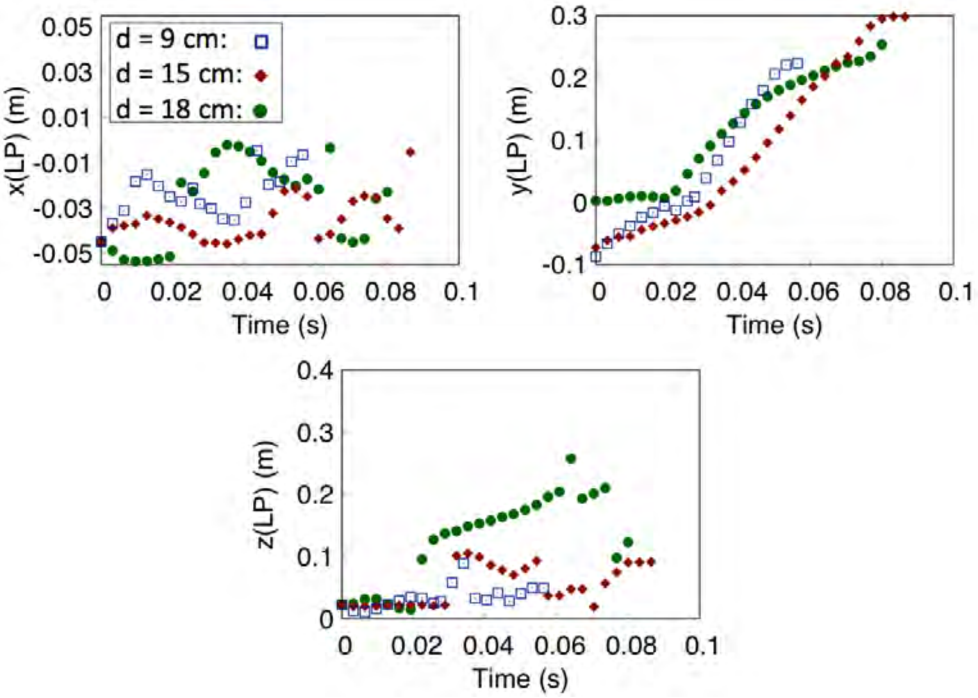

Figure 11.16: Evolution of the Leading Point position (corresponding to the right flame branch going towards $+y$) during the three ignition sequences using n-heptane. Note: Ignition spark positions may be found in Tab. 11.1.

mode allows a radial propagation mode to develop lately. These differences of flame propagation modes reflect on ignition delay times. A comparison with experiments is made in Fig. 11.17 where the flame propagation speed for the three injector spacings for LES (1 sequence) is compared to experiments (mean value over 20 trials for each case). In the experiment, this is calculated as the distance between the spark position and the furthest injector divided by the time required to ignite this furthest injector. Numerically, as the time when an injector is fully ignited is difficult to define precisely, it is replaced by the time at which the LP reaches the y-position of the furthest injector as given in Fig. 11.16. Therefore the LES propagation speed is by definition slighlty over-estimated compared to experimental values. Still, a good agreement is found between experiments and LES, both showing the decrease of propagation speed when increasing d. Discrepancies for $d \geq 15$ cm are higher than for $d = 9$ cm, which was expected. Indeed, for $d = 9$ cm, the radial propagation mode is controlled by the burnt gases thermal expansion [238] leading to a very high velocity around 5.6 m/s. For $d \geq 15$ cm, thermal expansion is no more the driving mechanism: arc propagation modes are mostly controlled by the fluctuating turbulence and mixing properties encountered by the flame along its trajectory. This leads to more fluctuating ignition times and discrepancies might be explained by the non-averaged LES value extracted from only 1 simulation instead of 20 trials for experiments.

	$d = 9\ cm$	$d = 15\ cm$	$d = 18\ cm$
INJ 2 → 1	Radial	Low arc	Low arc
INJ 2 → 3	Radial	Radial	High arc + Radial
INJ 3 → 4	Radial	Radial	-
INJ 4 → 5	Radial	-	-

Table 11.4: Propagation modes between injectors for each injector-to-injector spacing.

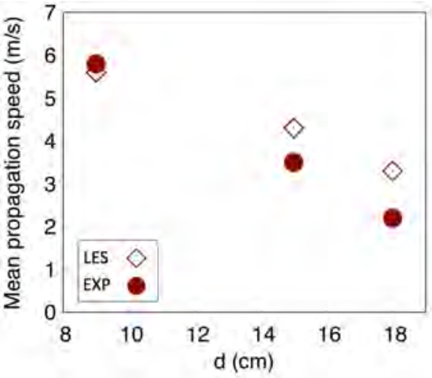

Figure 11.17: Flame propagation speed for the three LES ignition sequences with n-heptane and associated experimental mean values over 20 trials for each case.

11.5 Influence of fuel volatility

In order to investigate the impact of fuel volatility, a simulation of the non-reacting flow using n-dodecane instead of n-heptane is performed. It is expected that using the much less volatile n-dodecane fuel results in different liquid and gaseous fuel distributions in the chamber. Cuts of total equivalence ratio for both n-heptane and n-dodecane are compared in Fig. 11.18. The differences observed are actually very low. It is important to notice here that the air and fuel pre-heating ($T_{air} = 416 \pm 3\ K$ and $T_{fuel} \approx 350\ K$) used in our configuration smooths variations that could be observed at atmospheric conditions for instance. Still, discrepancies are visible on the profiles along the line $z = 45\,mm$ of gaseous and liquid equivalence ratios presented in Fig. 11.19. The most significant difference appears in the IRZ where $\phi_g = 0.5$ with n-dodecane instead of $\phi_g = 0.6$ with n-heptane. So close to the lean flammable limit, such small difference may lead to very different behaviours if a kernel is trapped in the IRZ. In the spray-SJZ, the liquid equivalence ratio reaches $\phi_l = 0.16$ with n-dodecane instead of $\phi_l = 0.10$ with n-heptane. Finally, the LRZ is very similar for both fuels with an almost null liquid contribution to the local equivalence ratio.

To focus on the liquid phase, cuts of droplets presence (% of time) for both fuels are provided in Fig. 11.20. The slower evaporation process with n-dodecane is well

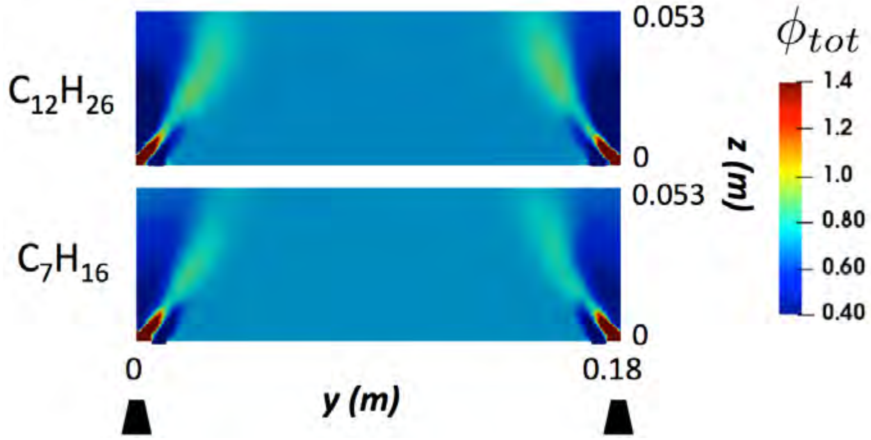

Figure 11.18: Cuts of total equivalence ratios for both n-heptane and n-dodecane.

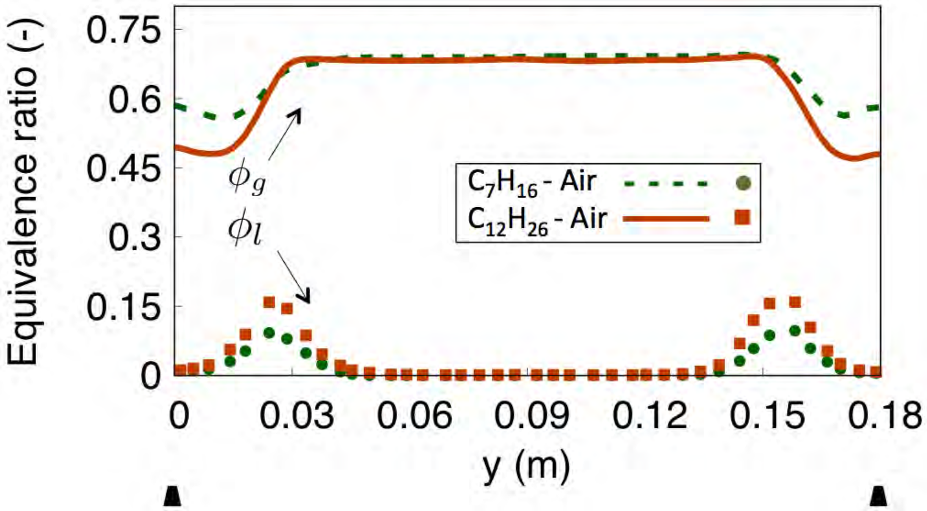

Figure 11.19: Profiles on the line $z = 45\,mm$ of gaseous and liquid equivalence ratios for both n-heptane and n-dodecane.

identified as dense spray zones are limited to $z = 120\ mm$ with n-heptane instead of $z = 180\ mm$ with the n-dodecane. Droplets are sometimes detected in the lower part of the LRZ with n-dodecane which is not the case with n-heptane. Finally, spray zones of adjacent injectors are well separated with n-heptane while, because droplets residence time is higher with n-dodecane, a bridge is formed between adjacent injectors. This change of topology may be important if an arc propagation mode occurs with such large injector spacing. As fuel is available in the form of liquid droplets with n-dodecane in this inter-injector region, energy losses to evaporate the fuel may penalize the flame propagation compared to an ignition with n-heptane where gaseous fuel is directly available. This behaviour is experimentally observed as n-dodecane delay times are increased by $14 - 29\ \%$ with respect to n-heptane [2].

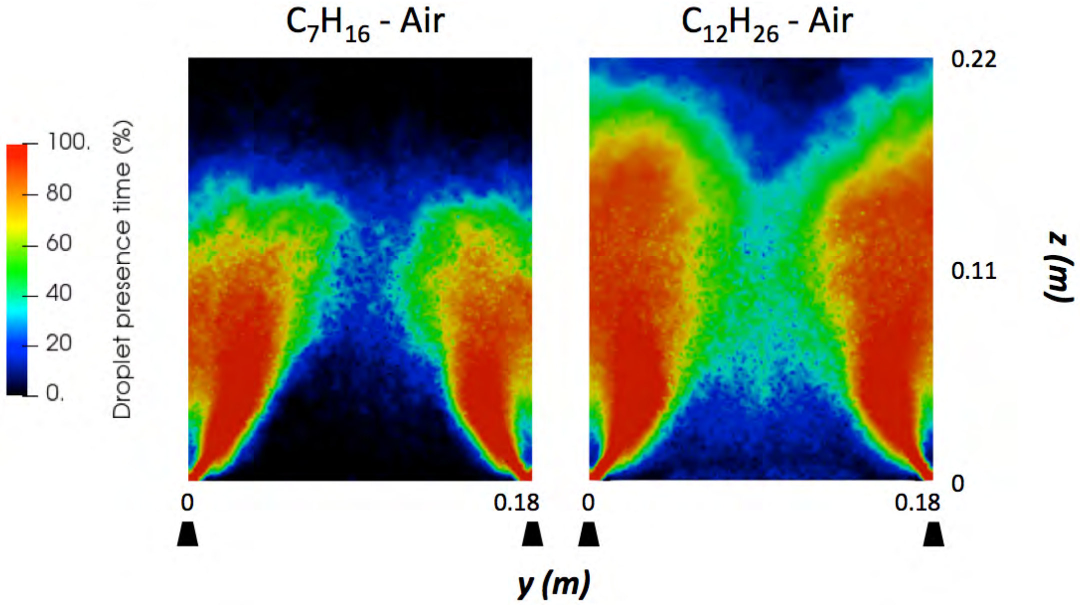

Figure 11.20: Cuts of droplets presence (% of time) for n-heptane and n-dodecane.

11.6 Conclusions

The Coria Linear Swirled Spray Burner (CLSSB) [2, 214, 239] has been investigated with LES. This configuration has been used with 3, 4 or 5 similar injectors, leading to different injector-to-injector spacings d. The impact of d on the non-reacting flow topology in terms of aerodynamics and fuel-air mixing has shown lower velocity fluctuations throughout the chamber and disconnected swirled jet zones between adjacent injectors for higher spacing. Similarly, droplets distribution in the chamber is changed with d and dense spray zones of neighbouring injectors are found to be directly connected only for $d = 9\ cm$. Nevertheless, the gaseous fuel equivalence ratio distribution is less influenced by d. For instance, the very quiescent lateral recirculation zone is filled with a flammable mixture of similar equivalence ratio independently of d.

The impact on ignition of flow and mixing topologies induced by a change of d have then been discussed by performing reacting LES ignition sequences for three different values of d. Flame propagation modes have been found to strongly depend on the spacing d, in good agreement with the literature, showing mainly a radial mode for low d and progressively more arc-like modes when increasing the injectors spacing. The $d = 18\ cm$ case highlighted in particular an interesting arc mode where the flame quickly moves downstream in the axial direction. As the SJZ of adjacent injectors are not able to early catch fragments of the flame, the sequence takes longer time to ignite the entire chamber. Flame propagation speeds, directly linked to the propagation mode for each d value, are in good agreement with experiments. A radial propagation mode is mainly controlled by burnt gases expansion leading to fast ignition and very small variability. On the contrary, an arc mode is driven by local flame-turbulence interaction and mixing properties along the flame path. Local quenching can often occur in overall lean configuration, leading to longer ignition and more variability on ignition delay times and induced propagation speed.

Finally, the impact of the fuel volatility has been assessed by looking at the non-reacting flow using a less volatile fuel (n-dodecane instead of n-heptane). The liquid and gaseous fuel distributions in the chamber are changed, mainly leading to a leaner IRZ and a higher droplets density in the LRZ with n-dodecane compared to n-heptane. Energy losses to evaporate the fuel slow down the flame propagation with a less volatile fuel. However, differences appear very limited in the present case as air and fuel are pre-heated.

The good overall agreement compared to experiments demonstrates the reliability of LES to study inter-injector spray flame propagation in complex burner geometries. Future work should be devoted to perform the ignition sequence with n-dodecane and compare with n-heptane. Differences are expected to be limited ($14 - 29$ % relative difference found experimentally on propagation speed) but this could be a first step toward cold depressurized high-altitude relight conditions where the impact of fuel volatility will be much higher.

Chapter 12

Light-round: MICCA annular combustion chamber

Contents

12.1 Objectives 247

12.2 Experimental set-ups 248

12.3 Numerical set-up 250

12.4 Validation of the non-reacting and stable flame cases on the SICCA configuration 254

12.4.1 Validation on the non reacting SICCA-U 254

12.4.2 Validation on the stable flame in the SICCA-C 256

12.5 MICCA-Spray light-round 259

12.5.1 Non-reacting flow 259

12.5.2 Ignition dynamics and timings 261

12.5.3 Burnt gas expansion effect 264

12.5.4 Leading point dynamics 265

12.5.5 Flame-spray interactions 268

12.6 Conclusions 271

12.1 Objectives

This chapter focuses on light-round in the MICCA-Spray configuration. Its annular shape makes it well representative of real combustors but diagnostics are limited due to the annular geometry with transparent walls. Therefore, a single injector set-up has been built for validation purposes. As reviewed in Chap. 10, studies of annular light-round are limited and very recent (Bach et al. [184], Machover et al. [248]). The MICCA set-up, investigated experimentally by Bourguoin et al. [241] and numerically by Philip et al. [242], was adapted in 2017 to two-phase flows by Prieur et al. [3, 244]. This MICCA-Spray configuration is today the only academic annular combustor operated in two-phase conditions. In parallel with the experimental work of Prieur, Lancien et al. [4, 245, 246] studied the light-round process on this configuration using LES with the Eulerian formalism for the description of the dispersed phase.

Two objectives are pursued in this chapter:

- Investigate two-phase light-round in a realistic annular two-phase combustor.
- Assess the impact of the liquid phase description by comparing LES with the Lagrangian (EL) formalism to the results of Lancien obtained with the Eulerian (EE) approach. EL and EE simulations are thus systematically compared throughout this chapter.

The chapter starts with the description of the experimental set-ups (single and multiple injector burners) and numerical details. Non-reacting and stable flame validation cases are then presented on the single burner set-up. Finally, the MICCA-Spray ignition simulation performed with the EL formalism is analysed and compared to experiments and the LES - EE simulation.

12.2 Experimental set-ups

Experimental facility

The MICCA-Spray configuration was experimented by K.Prieur [3] at EM2C laboratory, France. It is the two-phase version of the already existing MICCA set-up [251]. A snapshot of the configuration is presented in Fig. 12.1 (left). It is an annular combustor confined with two coaxial quartz windows of diameters 300 *mm* and 400 *mm* and height 200 *mm* allowing direct visualisation of the flame propagation during the ignition sequence. No convergent is placed at the outlet. The annular plenum is fed by 8 air injectors (1 visible in the picture). Air enters the combustion chamber from the plenum thanks to 16 identical swirled injectors detailed in Fig. 12.1 (center). For each injector, air goes through one of the 6 vertical inner tubes and the corresponding radial swirler. Air then joins axially the combustion chamber by a small cavity. This set-up leads to a Swirl number of $Sw = 0.68$. The fuel enters directly the small cavity ahead of the combustion chamber by a simplex atomizer placed with a 6 *mm* recess compared to the chamber bottom wall. Note that the arc length between consecutive injectors is 6.9 *cm* which is lower than the inter-injector distances investigated in the three CLSSB configurations (d = 9 *cm* - 18 *cm*) of Chap. 11. A top view of the MICCA-Spray configuration is shown in Fig. 12.16. Injectors are numbered from 1 to 7 in the H+ combustor half and from -1 to -7 in the H- half. The injector closest to the spark is injector 0 and the opposite one, from where visualisations are obtained is injector 8. For each injector, a sector can be defined as for instance sectors 4 and -2 sketched in Fig. 12.16. The swirl orientation of all injectors is the same and is also reported for injectors 1 and 2.

Configuration	**SICCA-U**	**SICCA-C**	**MICCA-Spray**
$\dot{m}_{Air}$ (g/s)	1.942	1.942	30.21
$\dot{m}_{Fuel}$ (g/s)	0.1111	0.1111	1.778
ϕ_{glob}	0.87	0.87	0.89

Table 12.1: Air and liquid fuel mass flow rates for the three configurations investigated with corresponding global equivalence ratios.

The MICCA-Spray configuration was operated at atmospheric pressure, and both air and liquid fuel (n-heptane) were injected at 298 K. Air and liquid fuel mass flow rates are reported in Tab. 12.1. The gaseous flow rate corresponds to a Reynolds number of $Re = 19580$ and a global equivalence ratio of $\phi_{glob} = 0.89$ is reached.

The annular shape of the combustor makes quantitative diagnostics difficult, apart from direct visualisation of the flame propagation during ignition. In order to characterize the aerodynamics and spray structure with optical diagnostics, and also to serve as a validation database for numerical simulations, a confined mono-injector version of the MICCA-Spray configuration, called SICCA-C, has been built. The SICCA-C set-up is shown in Fig. 12.1 (right). It is a tubular burner confined with a quartz window of diameter 70 mm and height 150 mm. The injector is exactly similar to the one of the MICCA-Spray. A third configuration has been studied experimentally by simply removing the quartz tube from the confined SICCA-C set-up. The obtained unconfined version of the SICCA burner is called SICCA-U. The SICCA-C and SICCA-U set-ups are also operated at atmospheric pressure without any air or liquid pre-heating. Identical mass flow rates are used for both configurations and are given in Tab. 12.1. The global equivalence ratio is very close to the MICCA-Spray combustor. In this Chapter, the SICCA-U configuration will be used to assess our LES set-up in terms of gaseous and liquid velocity profiles and droplet size distributions. The SICCA-C configuration will be used to compare experimental and numerical stable reacting flows to validate our LES combustion models. Finally a simulation of the light-round will be performed and compared to experiments as well as the previous LES of the MICCA-Spray configuration.

Experimental diagnostics and ignition procedure

Experimental diagnostics used for comparison with LES results are summarized here.

- Phase Doppler Anemometry (PDA) measurements were performed to characterize the fuel droplet size and velocity profiles for both air and fuel droplets in the

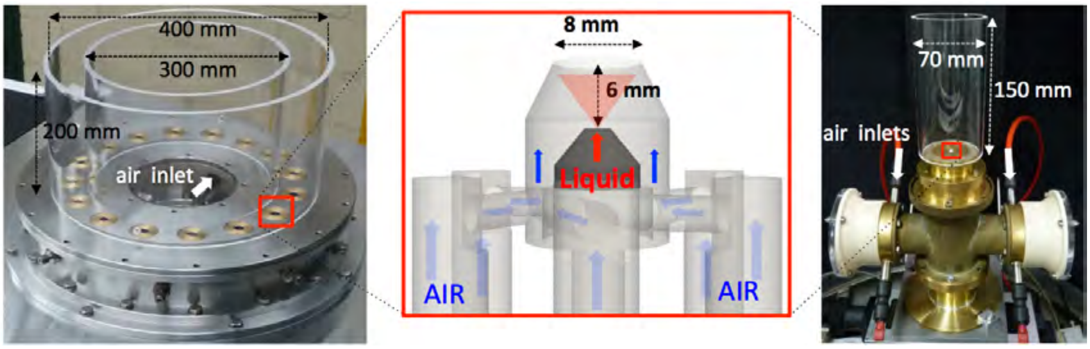

Figure 12.1: Photographies of the (left) MICCA-Spray and (right) confined SICCA-Spray configurations. The unconfined SICCA-Spray version is simply obtained by removing the quartz tube from the confined SICCA-Spray set-up. Zoom on the swirler and injection systems used for all configurations (center).

SICCA-U configuration.

- A high-speed camera equipped with a CH^* filter for chemiluminescence was used to visualize the stable flame in the SICCA-C configuration. Particle Image Velocimetry (PIV) was used to measure gaseous velocity in this stable flame regime.

- The SICCA-C internal wall temperature was measured by using thermochromic paint and exposing it to the flame for 5 min. The axial profile as function of the height is shown in Fig. 12.2.

- The MICCA-Spray ignition sequence was recorded with a high-speed camera Phantom V2512 equipped with a CH^* filter and located on the opposite side to the spark location.

Experimentally, ignition was triggered with a spark plug releasing around 25 mJ and fixed at the bottom of the outer wall around 10 mm from the center of the closest injector.

For complementary details on the MICCA-Spray, SICCA-U and SICCA-C configurations and experimental diagnostics, readers are refered to the PhD of K.Prieur [3].

12.3 Numerical set-up

Numerics and boundary conditions

The three configurations are investigated numerically using LES with the code AVBP co-developed by CERFACS and IFPEN (www.cerfacs.fr/avbp7x). For the gas phase, the third-order in time and space Taylor-Galerkin scheme [48] is used. The

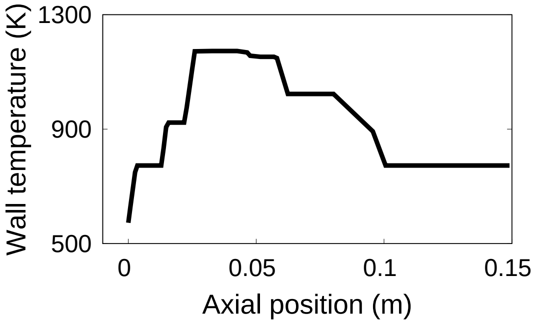

Figure 12.2: Axial profile of the SICCA-C internal wall temperature in presence of the flame.

computational domain contains the plenum with the air inlets, the swirlers, the combustion chamber for the MICCA-Spray and SICCA-C, and a large atmosphere used at the outlet (directly after the swirlers for the SICCA-U set-up). The Navier-Stokes Characteristic Boundary Conditions [46] are used for inlet and outlet boundary conditions. All MICCA-Spray and SICCA-C walls are considered as no-slip and adiabatic. For the MICCA-Spray configuration, modeling lateral walls as adiabatic is chosen to be representative of immediate relight of the combustor just after flame-out. Indeed, walls are considered still hot, making heat losses at the wall negligible. The influence of the walls temperature on the light-round in the MICCA-Spray configuration has been studied by T.Lancien [4]. For the SICCA-C stable flame case, isothermal walls are used. The experimental profile shown in Fig. 12.2 is imposed on lateral walls and a fixed temperature $Tw = 410\ K$ is set for the bottom wall as it is cooled by a water cooling cycle. Turbulent subgrid stresses are modeled using the SIGMA model [29].

Meshes

Fully unstructured grids are generated for the three configurations. A generic mesh topology is given in Fig. 12.3a and associated minimum cell sizes in each zone of Fig. 12.3a are given for all meshes in Table 12.3b along with the total number of tetrahedral cells. The SICCA-U mesh is the coarser one as only turbulent structures, mainly in the shear layer region (zone B), are to be resolved. For confined combustors, the minimum cell size in the entire bottom part of the chamber (Zone A) is set to 0.5 mm and the Thickened Flame (TF) model [33] is used (details provided below). As for the CLSSB meshes of Chap. 11, Zone B surrounding highly turbulent regions is particularly refined to limit thickening factors in these dense spray regions. The swirlers vanes and cavity ahead of the chamber (zone C) are always very refined. Far downstream (zone D), the mesh is progressively coarsened as this zone has no interest. With these requirements, the total number of tetrahedral cells for the MICCA-Spray configuration

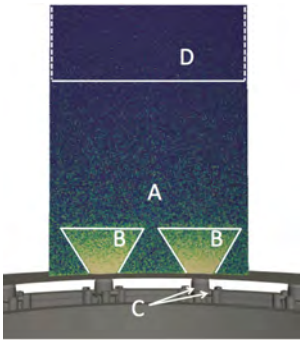

(a)

	SICCA-U	*SICCA-C*	*MICCA*
N_{cells} (Millions)	17.5	19.1	323.2
Δ_x (A) (mm)	0.7	0.5	0.5
Δ_x (B) (mm)	0.4	0.4	0.4
Δ_x (C) (mm)	0.4	0.4	0.4
Δ_x (D) (mm)	1.0	1.0	1.0

(b)

Figure 12.3: (a) Cut of the generic mesh topology and (b) associated minimum cell sizes in each zone of the MICCA-Spray mesh. A two-sector slice in the radial median plan of the annular chamber is shown. Meshes for the unconfined and confined SICCA versions follow the same topology.

reaches 323 M cells. Note that the same cell sizes are used for the MICCA-Spray and SICCA-C configurations in order to validate the numerical set-up to be used in the MICCA-Spray configuration on the smaller SICCA-C set-up.

Liquid phase

The Lagrangian (EL) formalism is used for the spray description. In order to assess the impact of the liquid phase formalism, an effort has been made to reduce as much as possible numerical set-up differences with the EE LES of Lancien [4, 245, 246]. In particular, the numerical domain, mesh characteristic sizes, numerics and boundary treatments are kept similar.

The same drag (Schiller & Naumann [57] correlation) and evaporation (Spalding model [58], complex transport coefficients evaluation of Sierra et al. [52] and Abramzon & Sirignano [62] correction) models used for the KIAI-Spray and CLSSB set-ups are used. The two-phase Thickened Flame model is used, which implies the application of F on drag and evaporation [17] (Sec. 4.3.3). The droplets interaction with walls is modelled with simple elastic rebound except inside the cavity ahead of the chamber. In this cavity, the high droplet density makes interactions with walls important. Complex interaction regimes [54] are however not taken into account, replaced by a simpler slip condition along the wall. As the number of particles is high without fuel and air preheating, 1 numerical particle is used to represent 10 similar fuel droplets (same size, temperature, velocity, etc) in order to reduce the computational cost. This choice is a trade-off between numerical cost and dispersed phase statistical convergence.

Finally, the FIM-UR injection model (see Sec. 4.5) of Sanjosé et al. [64] is used and the injection droplet size distribution is fitted on experimental data using a Rosin-

Rammler distribution. For this purpose, experiments on the SICCA-U configuration performed with the liquid atomizer nozzle pushed downstream by 6 mm to be flush with the cavity exit are used. This way, the calibration of the injection droplet size distribution is not impacted by droplets-wall interaction. An optimisation of the injected Rosin-Rammler distribution parameters is performed by targeting PDFs of droplets size at few points ahead of the injection. The final Rosin-Rammler distribution parameters are set to $q = 1.3$ and $d_p^{SMD} = 18\ \mu m$. The mean half-angle of the injection spray cone is also taken from the same experiment when the air flow was temporarily blocked. Direct evaluation from tomographic visualisation gives spray half-angle of 16°.

Combustion modelling

For the reacting SICCA-C and MICCA-Spray configuration, in order to compare results with the one of T.Lancien [4, 245, 246], the same two-step global scheme for n-heptane oxidation is used (2S_C_7H_{16}_DP) [17]. The scheme correctly reproduces the adiabatic temperature and 1D unstrained laminar flame speed for a wide range of operating conditions including the one studied here. It is made of six species (C_7H_{16}, O_2, N_2, CO_2, H_2O, CO) and two reactions (C_7H_{16} oxidation into CO and CO-CO_2 equilibrium). Validation details may be found in [17]. A very good agreement was obtained in the range $\phi = 0.4 - 1.5$ at atmospheric conditions (relative errors below 4 % in terms of laminar flame speed and adiabatic temperature).

The Dynamic Thickened Flame model (DTFLES) [40] is retained to only thicken the flame region. A thickening sensor based on the C_7H_{16} oxidation reaction rate is used. As for the CLSSB set-up, a tabulation of 1D flame properties (s_l^0, δ_l^0 and $\dot{q}$) as function of ϕ_g is used to obtain the local thickening factor required to have at least 5 grid points in the flame thickness. The Charlette efficiency function [37] is chosen in its static version ($\beta = 0.5$) to recover the unresolved flame wrinkling.

MICCA-Spray initialisation and ignition procedures

Before performing the ignition sequence of the MICCA-spray configuration, a non-reacting flow is established. This is performed considering only a periodic 45°, 2-sector domain corresponding to 1/8 of the full MICCA-Spray set-up, allowing to drastically reduce computational cost. Indeed, if aerodynamics rapidly reach a statistical steady state (100 ms), gaseous and liquid mixture fraction distributions in the entire combustor require around 1 s of physical time to be statistically converged because of the slow fuel evaporation rate at atmospheric conditions. Once the two-phase non-reacting flow is converged (after 1.425 s in our case), the solution is duplicated 7 times to recover

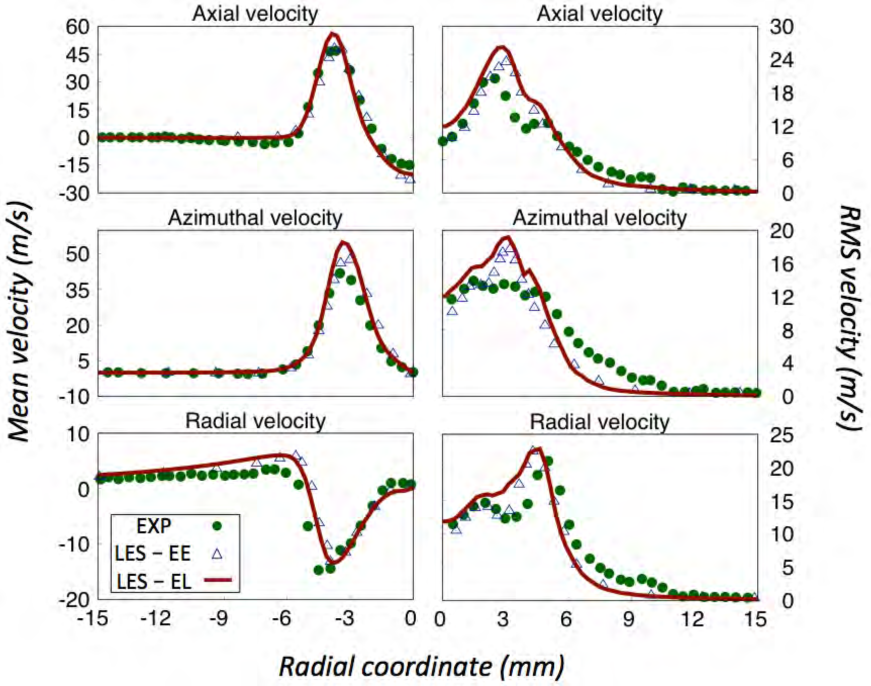

Figure 12.4: Radial profiles of mean and RMS gaseous velocities at $z = 2.5\ mm$ in the SICCA-U configuration. LES results with the EL formalism are compared with experiment and LES simulations with the EE formalism [4]. The position $z = 2.5\ mm$ is visualized in Fig. 12.8 on the similar SICCA-C configuration.

the 360° MICCA-Spray geometry. The simulation is continued for few milliseconds on the full configuration to destroy coherent non-physical flow structures that may have arisen from the use of a periodic bi-sector.

Finally, the standard ED model [151] is used to trigger ignition as studying the light-round does not require a more precise modelling. A kernel of diameter $d \approx 10\ mm$ is initiated at the experimental spark plug position.

12.4 Validation of the non-reacting and stable flame cases on the SICCA configuration

12.4.1 Validation on the non reacting SICCA-U

The SICCA-U configuration can not stabilize a flame in the absence of recirculating flow induced by lateral walls. The flow topology of this configuration is then very different from that of the MICCA-Spray configuration and is not the object of this study. However, as this non-reacting configuration has been well characterized experimentally [3], it is thus employed to validate our general LES set-up.

Radial profiles of mean and RMS gaseous velocities at $z = 2.5\ mm$ in the SICCA-U configuration are presented in Fig. 12.4. LES results with the EL formalism are com-

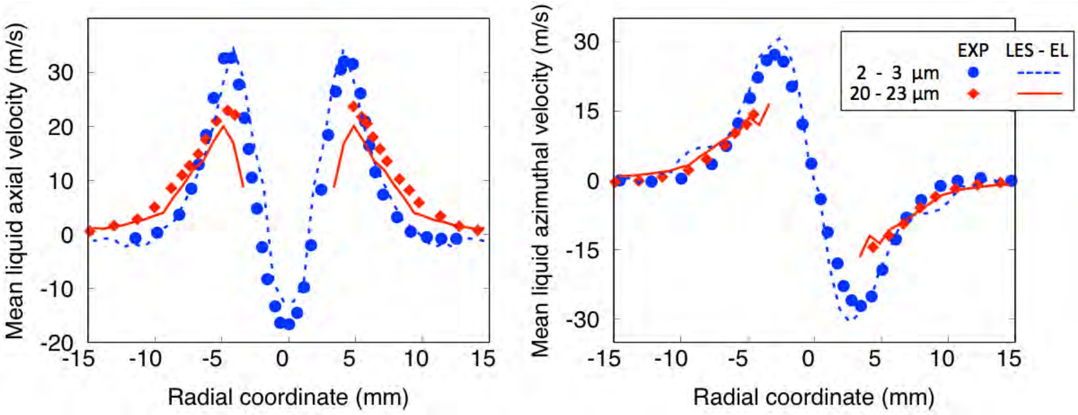

Figure 12.5: Radial profiles of mean liquid velocities at $z = 7.5\ mm$ for two droplet size classes ($d_p \in [2;3]\ \mu m$ and $d_p \in [20;23]\ \mu m$). Only LES results with the EL formalism are compared with experiment as the EE formalism does not provide size-classified data. The line $z = 7.5\ mm$ is shown in Fig. 12.8 on the similar SICCA-C configuration.

pared with experiment and LES simulations with the EE formalism [4]. The position $z = 2.5\ mm$ is visualized in Fig. 12.8 on the similar SICCA-C configuration. Note that measurements of the gaseous flow were performed in the absence of the spray, while LES results were obtained with the spray. However, it has been shown in [3] that the influence of droplets on the mean air velocity field is limited in this configuration. An overall good agreement is found between experiment and LES results for the three velocity components. Slightly higher velocity fluctuations are found in both LES simulations in the air jet zone, which may result from the presence of droplets in the LES.

Profiles of mean liquid velocities at $z = 7.5\ mm$ (position also shown in Fig. 12.8) for two droplet size classes ($d_p \in [2;3]\ \mu m$ and $d_p \in [20;23]\ \mu m$) are shown in Fig. 12.5. Only LES results with the EL formalism are compared with experiment as the EE formalism does not provide size-classified data. Experimental and numerical data are not presented where the droplet density is too low, namely in the range $r \leq 3.5\ mm$. Experimental velocity profiles are well recovered with LES for both droplet size classes. The same conclusion than in the KIAI-Spray configuration can be highlighted: smaller droplets are much less inertial than larger ones and therefore much less influenced by the gaseous phase. The important radial and azimuthal liquid velocities induced by the injection system are correctly modelled by the LES swirled FIM-UR droplet injection model. The opening angle of the spray outside the cavity (half-angle of $\approx 31^o$) is also well retrieved, and appears to be different from the FIM-UR half-angle of 16°. This last point will be further discussed in Sec. 12.4.2.

Finally, the numerical injection droplet size distribution (Rosin-Rammler distribu-

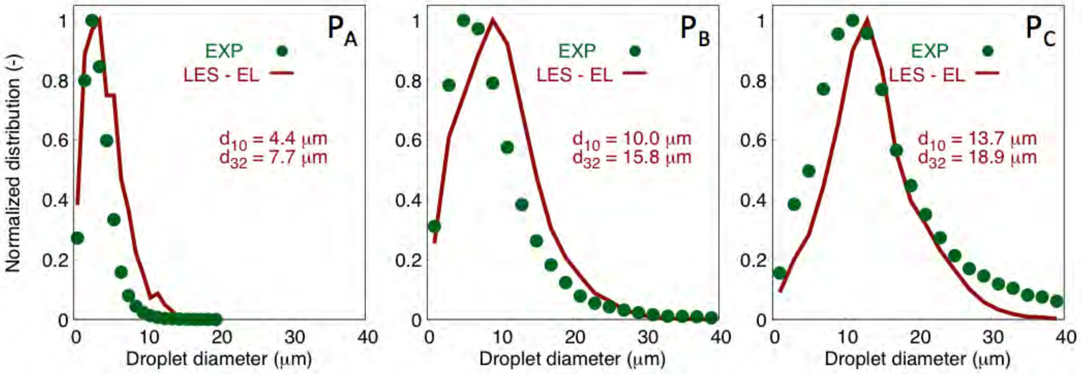

Figure 12.6: Comparison between experimental and LES normalized distribution of droplet diameter at three points (P_A, P_B and P_C respectively from left to right) of the SICCA-U configuration. Points P_A, P_B and P_C are shown in Fig. 12.8. P_A: $r = 0\ mm, z = 7.5\ mm$; P_B: $r = 7\ mm, z = 7.5\ mm$; P_C: $r = 10\ mm, z = 7.5\ mm$.

tion with parameters: $q = 1.3$, $d_p^{SMD} = 18\ \mu m$) is assessed by comparing experimental and LES distributions of droplet diameter at three points (P_A: $r = 0\ mm, z = 7.5\ mm$; P_B: $r = 7\ mm, z = 7.5\ mm$; P_C: $r = 10\ mm, z = 7.5\ mm$) of the SICCA-U configuration in Fig. 12.6. Their position relatively to the injector is shown in Fig. 12.8. Droplets at P_B are slightly too large in LES compared to experiments but the difference remains acceptable. Droplet distributions are very heterogeneous with Sauter Mean Diameters of 7.7 μm and 18.9 μm respectively at P_A and P_C located in the IRZ and spray-SJZ. LES distributions match well experimental ones at the three positions showing the performance of the FIM-UR model with chosen injection parameters.

12.4.2 Validation on the stable flame in the SICCA-C

The SICCA-C stable flame case is now investigated to validate our modelling approach, based on two-step global scheme (2S_C$_7$H$_{16}$_DP), DTFLES model with parameters evaluated locally, and static Charlette efficiency function ($\beta = 0.5$).

Figure 12.7 shows a cut of mean axial gaseous velocity, with the iso-$U_{axial} = 0$ drawn in black to identify the ORZ, IRZ and spray-SJZ. An iso-$Hr = 4e^7\ W/m^3$ is added in white to localize the mean flame position. A lifted M-shape flame stabilizes as in the KIAI-Spray set-up. The topology is actually very similar to the one of the KIAI-Spray configuration, extensively investigated in Sec. 8.5. Two differences may be noted. First the IRZ is not closed here, because no convergent exit is used contrary to the KIAI-Spray configuration. Second, the recirculating flow reaches the liquid injector nozzle with important negative values ($U_{axial} < -25\ m/s$) at low axial positions. Thus, the gaseous flow coming from the cavity ahead of the combustor is blocked by the strong reverse flow and only enters the chamber by a thin outer annular section leading there

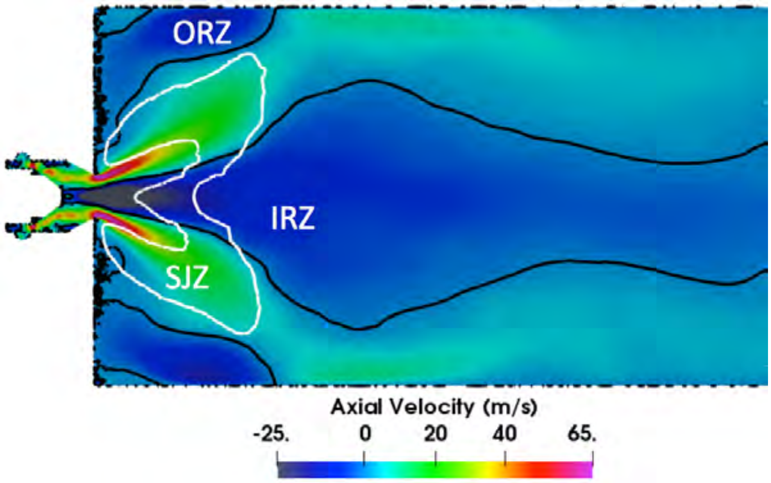

Figure 12.7: Cut of mean axial gaseous velocity in the SICCA-C configuration (stable flame). An iso-$U_{axial} = 0$ is drawn in black to identify the recirculation zones, and an iso-$Hr = 4e^7\ W/m^3$ is added in white to localize the mean flame position.

to high axial velocities ($U_{axial} > 50\ m/s$). Injected droplets are also immediately pushed back by the reverse flow and impact the lateral walls of the cavity whatever their injection angle is. They are finally carried out by the positive axial gaseous flow through the outer annular section to feed the combustion chamber.

The mean flame position and shape found in LES are compared in Fig. 12.8 to experiment and the previous LES - EE [4]. The experimental flame shape is visualized with an averaged Abel transform and LES flames are represented by average heat release rates. Outer flame branches almost stabilize on the injector tip for both LES simulations which is not the case in the experiment. Still, the lifted M-shape spray flame is well recovered in both simulations, with heights of the central foot and of the flame top very close to experiment, as qualitatively shown by the two white lines on the three images. The most reacting region in the LES - EL simulation appears to be the bottom part of flame branches while it is located in the central top region of the flame in the LES - EE simulation. This might be due to the poly-dispersity taken into account in the LES - EL leading to small droplets evaporating rapidly and so fuel available at the exit of the cavity. In the LES - EE simulation, fuel is evaporated higher in the chamber so that the heat release rate is maximum at higher location. Overall, this lifted M-shape flame is also much very correlated to the thermal boundary condition applied on lateral and bottom walls as demonstrated in [4].

A quantitative validation of the SICCA-C stable flame case is proposed in Fig. 12.9. Radial profiles of mean gaseous axial velocity at two heights (lines shown in Fig. 12.8) are given. LES results with the EL formalism are compared with experiment and results from LES - EE. Profiles are fairly well recovered at both positions evidencing the burnt

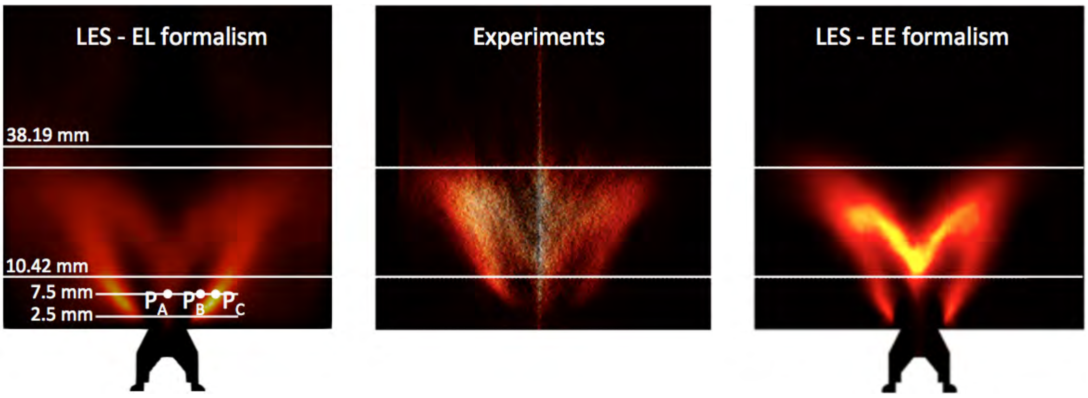

Figure 12.8: Average flame shape comparison on the SICCA-C configuration. Present LES result (left) with the Euler-Lagrange formalism, experiment [3] (center) and previous LES result with the Eulerian formalism [4] (right). The experimental flame shape is visualized with an averaged Abel transform and LES flames are represented by average heat release rates.

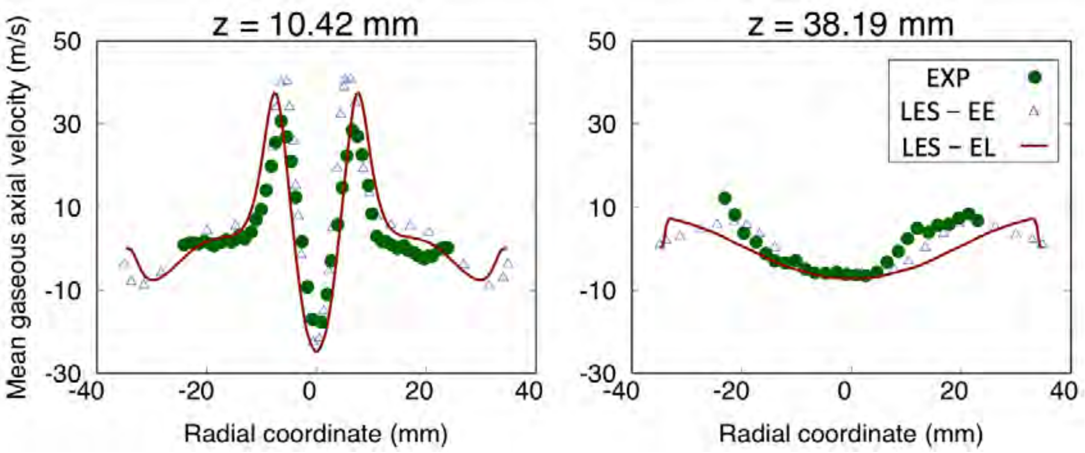

Figure 12.9: Radial profiles of mean gaseous axial velocity at two heights (lines shown in Fig. 12.8). LES results with the EL formalism are compared with experiment and LES simulations with the EE formalism [4].

gas expansion induced by the flame and producing very important axial velocities at $z = 10.42\ mm$. At 38.19 mm, the flow is more quiescent with a small reverse flow in the IRZ ($U_{axial} \approx -5\ m/s$) well found by LES compared to experiment. These profiles along with qualitative flame shape comparison validate the numerical and modelling approach, allowing to investigate now an ignition sequence in the annular MICCA-Spray configuration.

12.5 MICCA-Spray light-round

12.5.1 Non-reacting flow

The gaseous and liquid fuel distributions prior to ignition are presented in Fig. 12.10 comparing central cuts of gaseous equivalence ratio ϕ_g for LES with the EL and EE formalisms. An iso-$\phi_g = 0.7$ is drawn in white on both cuts. Similarly, Fig. 12.11 compares fields of liquid volume fraction α_l found with the two dispersed phase formalism. Both calculations are well converged, with a homogeneous gaseous mixture fraction in the whole combustor. A clear difference is visible on both gaseous and liquid distributions: the mean gaseous equivalence ratio found in the chamber with the EE formalism is very close to $\phi_g = 0.89$ while it is around $\phi_g = 0.8$ for the EL formalism. The height of the iso-$\phi_g = 0.7$ is also much smaller with the EE formalism. This is related to the evaporation process which appears faster in the case of the EE calculation. This is confirmed with the liquid volume fraction fields: in the LES - EE simulation, the liquid totally evaporates at mid-height of the combustion chamber while droplets are still found at the exit of the combustor with the EL formalism. Note that the direct comparison between LES - EL and LES - EE α_l fields is made difficult as the EL formalism does not provide statistically converged data at locatio of very low droplet density, contrary to the EE formalism, which directly computes statistical moments. The presence of droplets far downstream in the EL simulation may be explained by the poly-dispersity of the spray described in the Lagrangien formalism. In the EE calculation, the injection diameter is fixed at 15.3 μm after a dedicated optimisation study [4]. With the injection droplet size distribution used (Rosin-Rammler with $q = 1.3$, $d_p^{SMD} = 18\ \mu m$) in the EL formalism, large droplets are also injected, which need more time to fully evaporate and thus have longer residence times in the chamber, allowing them to reach high axial positions.

Differences in evaporation may also be attributed to the model, using different parametrization in both simulations: $Sc^{evap}_{C_7H_{16}} = 1.3431$, $Pr^{evap}_{C_7H_{16}} = 0.97648$ for the EL simulation and $Sc^{evap}_{C_7H_{16}} = 0.69$, $Pr^{evap}_{C_7H_{16}} = 0.735$ for the EE simulation. This leads to substantial discrepancies on the evaporation time of fuel droplets. Single droplet evaporation times in cold ($T_{air} = 300\ K$) and hot ($T_{air} = 1500\ K$) conditions for $d_p = 15.3\ \mu m$, $T_p = 300\ K$ for both parametrizations are gathered in Tab. 12.2. Reference evaporation times obtained with detailed evaluation of the transport coefficients (called detailed) are also reported, as well as times obtained with simplified transport coefficients evaluation (called simplified). Evaporation times are correctly recovered with the parametrization of the EL calculation in both cold and hot conditions. For the parametrization of the EE simulation, a non-negligible difference arises in hot condition, even more important in cold condition. Evaporation seems too fast in this case,

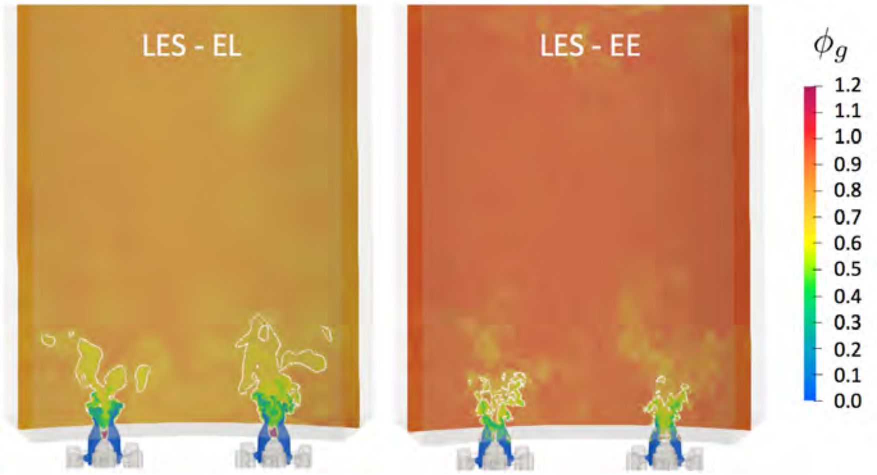

Figure 12.10: Comparison between LES with the EL and EE formalisms of central cuts of instantaneous gaseous equivalence ratio ϕ_g in the MICCA-Spray non-reacting flow. An iso-$\phi_g = 0.7$ is drawn in white on both cuts.

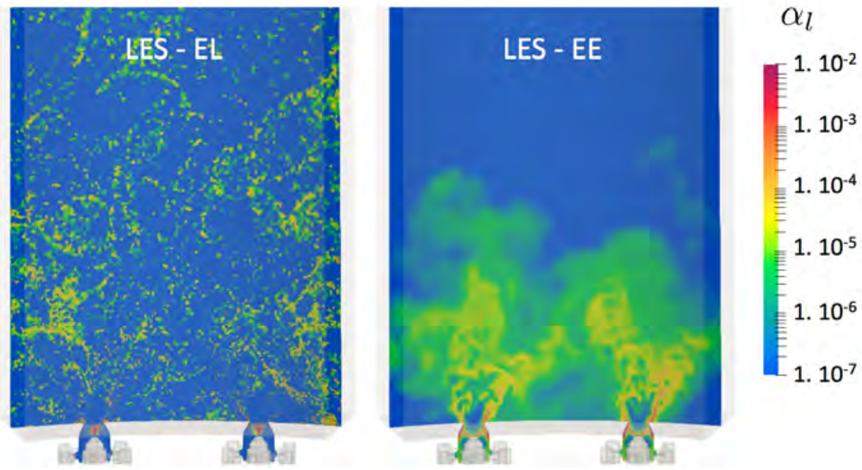

Figure 12.11: Comparison between LES with the EL and EE formalisms of central cuts of instantaneous liquid volume fraction α_l in the MICCA-Spray non-reacting flow.

Case	$T_{air} =$ 300 K	$T_{air} =$ 1500 K
Detailed transport	19.9 ms	0.50 ms
Simplified transport	17.9 ms	0.23 ms
$Sc^{evap}_{C_7H_{16}} = 1.343$, $Pr^{evap}_{C_7H_{16}} = 0.976$ (EL)	18.8 ms	0.52 ms
$Sc^{evap}_{C_7H_{16}} = 0.690$, $Pr^{evap}_{C_7H_{16}} = 0.735$ (EE)	12.8 ms	0.37 ms

Table 12.2: Single droplet evaporation times in cold and hot conditions for EL and EE parametrizations along with reference evaporation times obtained with detailed and simplified transport coefficients. $T_p = 300\ K$ **and** $d_p = 15.3\ \mu m$ **(similar to LES - EE injection diameter).**

which can explain differences observed in Fig. 12.10 and Fig. 12.11. These important discrepancies should be kept in mind when analysing ignition sequences.

12.5.2 Ignition dynamics and timings

The MICCA-Spray light-round sequence is qualitatively shown in Fig. 12.12. The flame shown by volume rendering of heat release is presented at 8 instants during the sequence and compared to the experimental flame evolution. Note that both sequences are synchronized on the ignition time of injector 1 ($t_{ign}^{inj\ 1} = 0\ ms$) (shown in Fig. 12.16) to eliminate possible discrepancies on ignition phases 1 and 2 which are not the focus of this chapter.

The overall experimental flame evolution is recovered with a very good accuracy in LES. In particular, the five main steps of the light-round, already found in the purely gaseous MICCA configuration (see Sec. 10.2.1) are also found experimentally and numerically in this two-phase flow set-up:

- The flame kernel expands rapidly in the fresh mixture ($t \leq 5\ ms$).
- The flame propagates to the neighbouring burners forming an arch that opens when it reaches the exit of the chamber ($5\ ms \leq t \leq 10\ ms$).
- The two flame fronts propagate independently, igniting burners in a radial propagation mode allowed by the small inter-injector distance ($10\ ms \leq t \leq 25\ ms$).
- The two flame fronts finally merge on the opposite side of the igniter location ($t = 30\ ms$) showing a good symmetry of the light-round propagation in both halves of the combustor.
- Burnt gases are evacuated and the steady state is reached ($t > 30\ ms$).

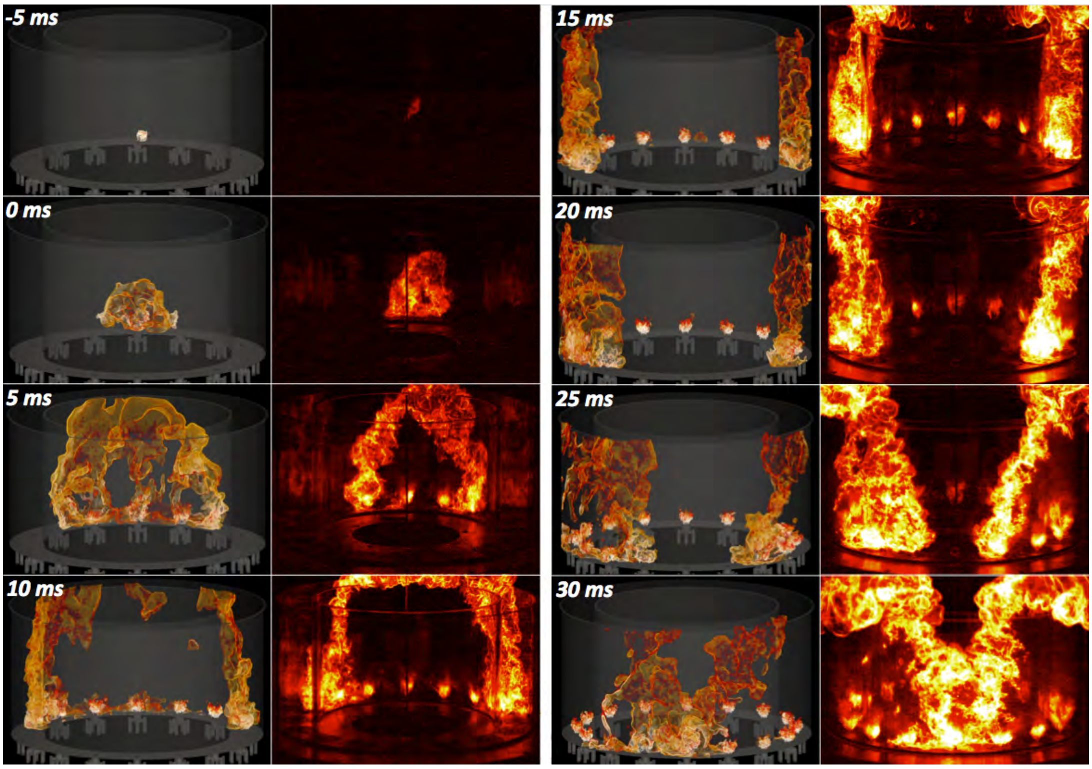

Figure 12.12: Comparison between (left) LES and (right) experimental flame evolution during the light-round sequence. The experimental visualisation is obtained with a high-speed camera equipped with a CH^* filter. The LES flame is shown by a volume rendering of heat release.

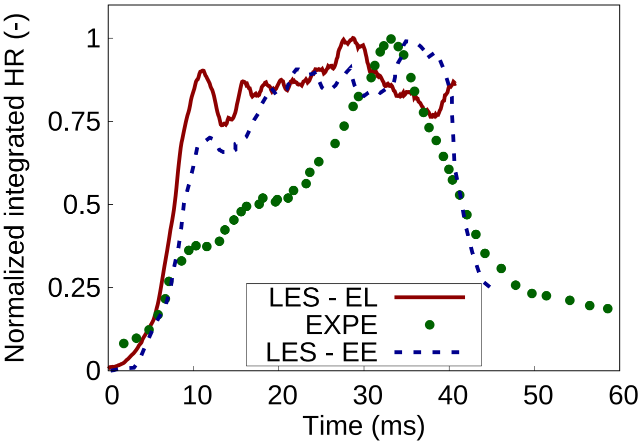

Figure 12.13: Temporal evolution of the integrated heat release in the combustion chamber from LES and total light intensity of the experimental sequence.

A first quantitative comparison between temporal evolution of the integrated heat release in the combustion chamber for LES simulations and total light intensity obtained from the experimental images is proposed in Fig. 12.13, where both sequences are synchronized on the ignition time of injector 1. Both LES sequences are quite similar and present the same shape of heat release evolution with a strong early increase corresponding to the second phase of the light-round and then a more steady heat release (phase III) until the two fronts merge (phase IV). The peak of heat release actually occurs before the merging in the LES - EL case, contrary to the LES - EE simulation. The timing of the peak of heat release is slightly under-estimated with the LES - EL simulation compared to the experimental one (-4 ms). The LES - EE over-estimates this timing but to a lesser extent. Again, the direct comparison of one experimental and one numerical ignition sequence is always delicate as ignition is a very stochastic phenomenon. However, the very small inter-injector distance of the MICCA-Spray configuration leads to a small variability of the ignition time as the flame propagation is mainly controlled by burnt gas expansion. The experimental curve presented in Fig. 12.13 is then very representative of the average timing (± 2 ms) and other simulations are expected to provide similar ignition sequences.

A more deeper analysis of the ignition timing of each sector is now performed. Figure 12.14 provides ignition timings of each sector for both halves H+ and H- for the LES - EL and the LES - EE simulations, and two sets of experimental timings (corresponding to two independent sequences) are reported for the H- half. The time at which a given sector is ignited is defined with the Leading Point (LP) advancement. The LP is defined as the most advanced point in the azimuthal direction (θ angle defined

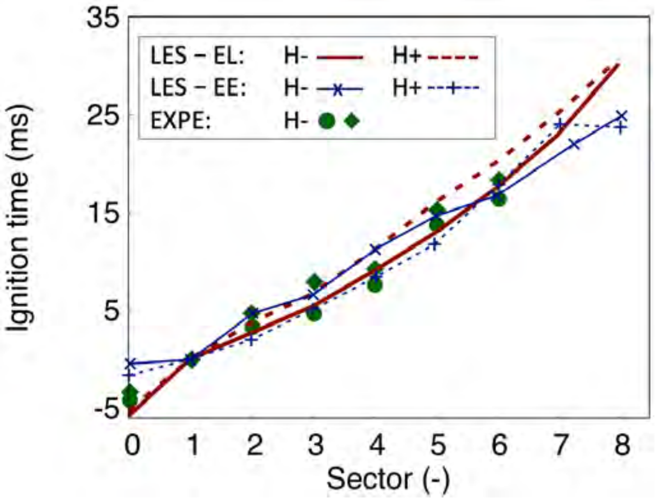

Figure 12.14: Ignition timings of each sector for both halves H+ and H- for the LES - EL and LES - EE simulations. Two sets of experimental timings (corresponding to two independent sequences) are also reported for the H-half.

in Fig. 12.16) on the $c = 0.9$ flame iso-surface. The time at which the LP reaches the θ angle of a given injector defines the corresponding sector ignition delay time. The obtained values are close to the times at which the integrated heat release in each sector is maximum [4]. Experimentally, timings are given by the time at which the light intensity in the given sector is maximum. Note that again, timings are synchronized on the ignition timing of injector 1 ($t_{ign}^{inj\ 1} = 0\ ms$). An excellent agreement is found between experimental and numerical ignition timings for both simulations up to sectors ±6. This shows that the two-phase flame propagation speed is very accurately recovered during the propagation phase of the two opposite flame fronts. The flame speed is constant up to injector 6. After this point, a clear slowdown of the flame is visible for the LES - EL simulation, corresponding to the time when the two flame fronts face each other at injector 8. This slowdown seems almost absent in the LES - EE simulation. Therefore, the ignition timing of sector 8 is much higher for LES - EL than for LES - EE.

12.5.3 Burnt gas expansion effect

To understand the slowdown of the flame propagation just before the fronts merging for LES - EL, unfolded central cuts of azimuthal gaseous velocity at three moments during light-round are shown in Fig. 12.15. The injector nearest to the spark position is located on both sides of each cut, and injector 8 is in the center. U_θ is positive from left to right. A black iso-$Hr = 2e^8\ W/m^3$ allows to track the flame front position. This figure clearly demonstrates the already studied burnt gas expansion effect. At

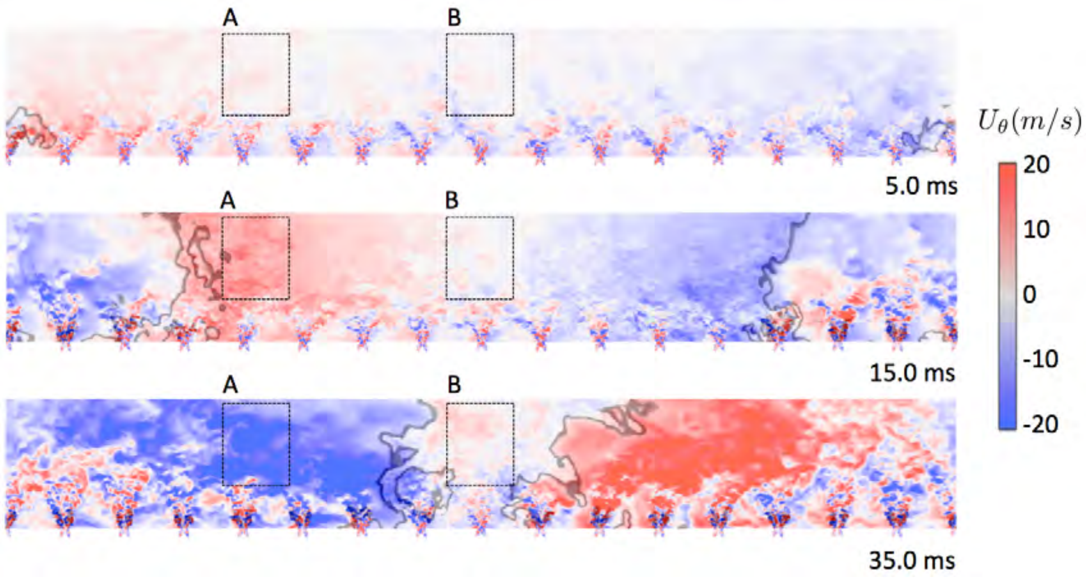

Figure 12.15: Unfolded central cuts of azimuthal gaseous velocity at three moments during light-round. Injector 0 (nearest to spark position) is on both sides of each cut, and injector 8 is in the center. U_θ is positive from left to right. A black iso-$Hr = 2e^8\ W/m^3$ allows to track the flame front position.

$t = 5\ ms$, the azimuthal velocity in boxes A and B is almost null far from the flame. At $t = 15\ ms$, box A is just in front of the flame front, in the cold gas side. The azimuthal velocity in this zone reaches very high values showing that the flame is accelerated by this burnt gas expansion. The average velocity (between branches H+ and H-) of the LP from sectors 2/-2 to sectors 6/-6 is 15.6 m/s, 50 times higher than the laminar flame speed at $\phi = 0.89$ at atmospheric conditions, and one order of magnitude higher than the turbulent flame speed. Box B being still too far from the flame, no effect is detected there. After the passage of the flame at $t = 35\ ms$ in box A, a strong reverse azimuthal flow occurs. This classic burnt gas expansion effect already found in previous similar configurations is however not recovered above injector 8, in box B. Indeed, at 35 ms, box B is in the fresh gas region, just between the two flame branches coming symmetrically from both sides. The strong azimuthal velocities induced in front of both flame fronts inhibit each other leading to a negligible U_θ at this time. This explains the slowdown of the flame propagation observed in Fig. 12.14 for both branches H+ and H-. The merging of flame fronts is then no more controlled by burnt gas expansion but by turbulent flame propagation. Why this slowdown effect is not observed in LES - EE is explained now.

12.5.4 Leading point dynamics

H+ and H- LPs trajectories in the axial x-y plane for both LES - EL and LES - EE simulations are reported in Fig. 12.16. The spark position is recalled. The fronts prop-

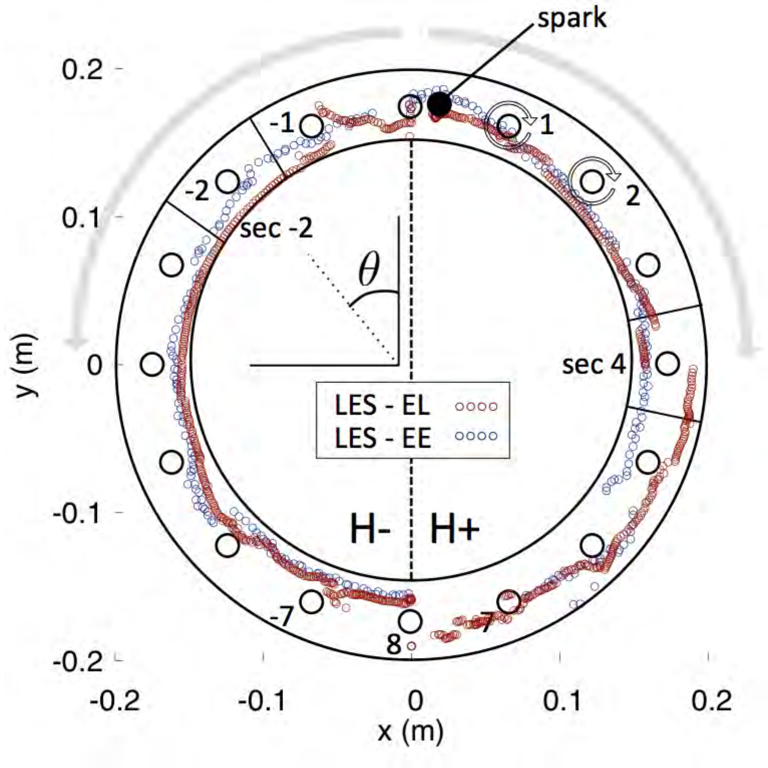

Figure 12.16: H+ and H- leading point trajectories in the axial x-y plane for both LES - EL and LES - EE simulations.

agate in both halves from the top to the bottom. The impact of the swirl orientation on the LP trajectory is strong. On the H- part, the LPs of both LES - EL and LES - EE simulations follow the inner combustor wall, pushed there by the mean flow generated by the swirlers. On the H+ side, the mean flow along the inner combustor wall goes from injector 8 to injector 0. Leading points first follow the shortest path along the inner wall but then switch from the inner wall to the more favourable outer wall during the sequence, near injector 4 for LES - EL and between injectors 5 and 6 for LES - EE. The advantageous mean flow induced by swirlers along the external wall offsets the longer distance to go on this side.

In the LES - EE simulation, the H+ LP stops at injector 7 indicating that the front merging occurs near this injector, instead of near injector 8 as in experiments and in LES - EL. This non-symmetry might explain why no slowdown is observed in Fig. 12.14 at injector 8: the H- front does not decelerate when crossing sector 8 as the opposite H+ front is still located ahead of sector 7.

H+ and H- leading points trajectories in the radial z-θ plane for both LES - EL and LES - EE simulations are presented in Fig. 12.17. H+ leading points have a very similar evolution in the z-θ plane: the LP stays in the bottom of the chamber near $z = 25\ mm$ most of the time, except around $\theta = 90\ ^o$ corresponding to injector 4. On

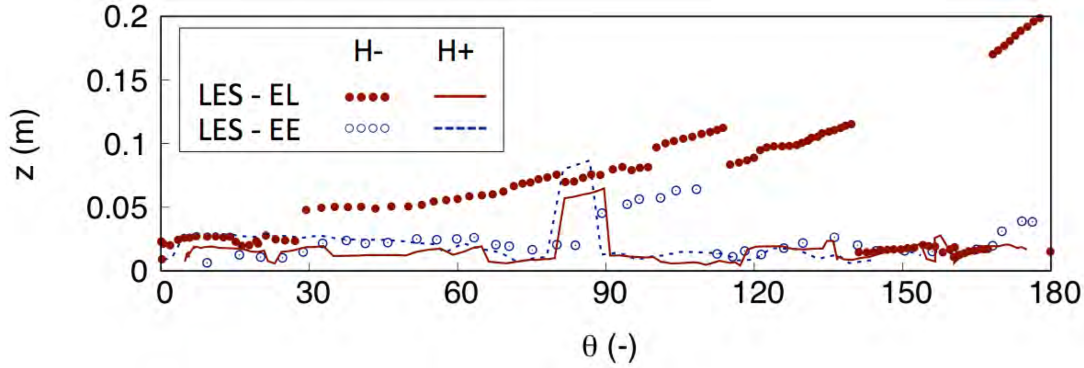

Figure 12.17: H+ and H- leading point trajectories in the radial z-θ plane for both LES - EL and LES - EE simulations.

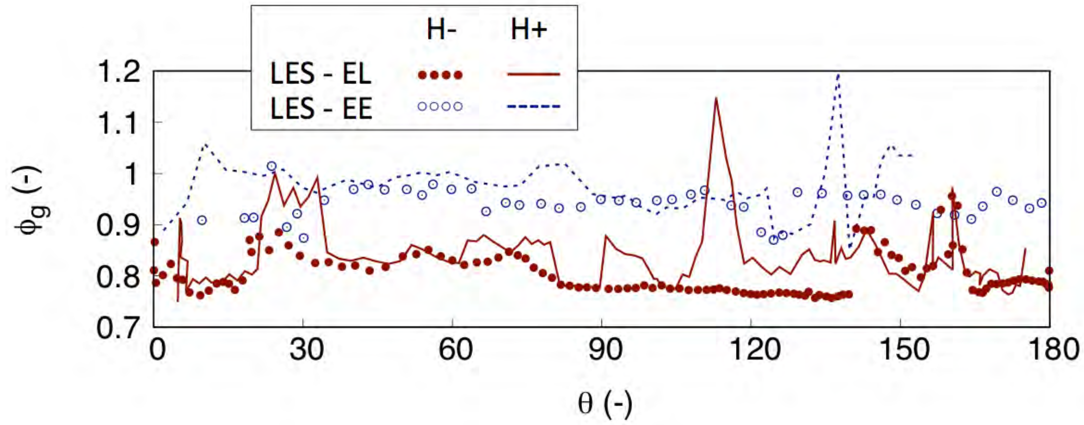

Figure 12.18: Evolution of the gaseous equivalence ratio found at the H+ and H- leading points as function of θ for both LES - EL and LES - EE simulations.

the contrary, the H- LP of the LES - EL simulation goes higher, reaching $z = 120\ mm$ at $\theta = 140\ ^o$. At the end, the LP goes back to a low axial location before returning above $z = 150\ mm$. This discontinuity shows the presence of two advanced flame positions after $\theta = 120\ ^o$, one in the bottom part of the chamber, and the other higher. This can be visualized in Fig. 12.12 at $t = 25\ ms$ where the H- front (left side) is vertical so that the LP can oscillate from low to high locations. The H+ front (right side) seems more inclined, leading to a LP established in the lower part of the combustor. The rather well established vertical fronts in the LES - EL simulation contribute to promoting the slowdown of the flame at the end as the burnt gas expansion inhibition is higher in this case. Experimentally, fronts are more inclined at the end of the light-round. Therefore, cold gases expelled ahead of each front are not directly opposed but are ejected in the axial direction. The burnt gas expansion effect is then less reduced during the front merging than found in LES - EL.

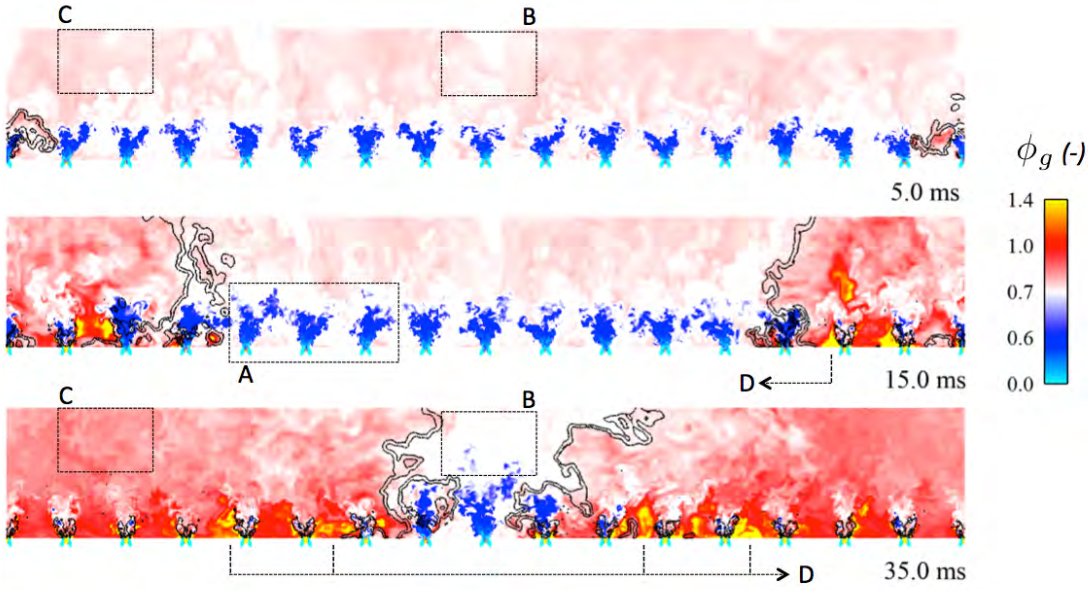

Figure 12.19: Unfolded central cuts of gaseous equivalence ratio at three moments during light-round. An iso-$c = 0.9$ allows to track the flame front position.

12.5.5 Flame-spray interactions

As the leading points of branches H+ and H- are found at different heights for LES - EL, it is expected that they encounter different flow conditions on their way. In particular, the evolution of the gaseous equivalence ratio found at the H+ and H- leading points as function of θ for LES - EL and LES - EE is given in Fig. 12.18. For the LES - EL run, it is clear that the H- LP sees a much more homogeneous ϕ_g than the H+ LP. Indeed, the H- LP moves above turbulent spray injectors bringing mixture heterogeneities. The H+ LP trajectory crosses inter-injector LRZs and encounters spots of high gaseous equivalence ratio. ϕ_g fluctuations are only found for the H- leading point between $\theta = 140\ ^o$ and $\theta = 165\ ^o$, corresponding exactly to the moment the LP goes temporarily to the bottom of the combustor.

Concerning the LES - EE simulation, a significant difference is observed with the LES - EL in terms of average ϕ_g at the LP position. This is of course linked to the discrepancy regarding pre-evaporation already discussed in Fig. 12.10. The different formalism and evaporation parameters for the LES - EE simulation lead to a higher non-reacting flow evaporation of droplets and thus to a higher ϕ_g at the LP position.

To continue investigating the mixture fraction distribution in the chamber not only focusing on the leading points, unfolded central cuts of gaseous equivalence ratio at three moments during the LES - EL light-round are provided in Fig. 12.19. An iso-$c = 0.9$ allows to track the flame front position. Similarly, cuts of liquid volume fraction are shown in Fig. 12.20 keeping the same colorscale than in Fig. 12.11. First, boxes C of Fig 12.19 confirm that after the flame passage, the complete evaporation of droplets

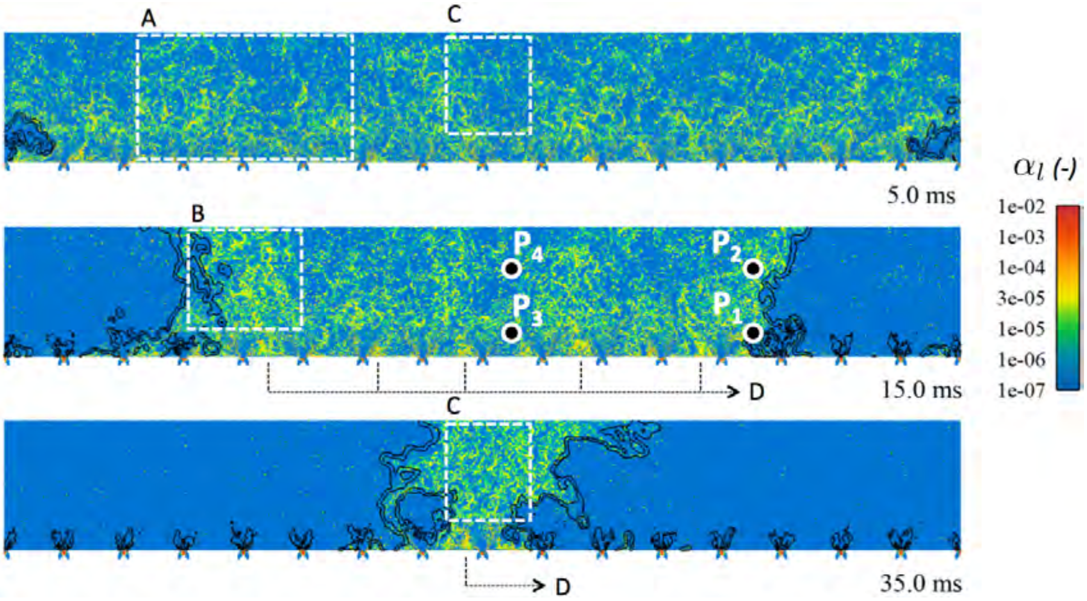

Figure 12.20: Unfolded central cuts of liquid volume fraction at three moments during light-round. An iso-c = 0.9 allows to track the flame front position. Points P_1, P_2, P_3, P_4 investigated in Fig 12.21 are also positioned.

lead to a homogeneous mixture fraction near $\phi_g = 0.89$ instead of $\phi_g = 0.8$ for the non-reacting flow. Box A of Fig. 12.20 helps discriminating denser spray regions in the bottom part of the chamber and less populated regions higher in the combustor as cold flow evaporation is more advanced.

Box A of Fig. 12.19 at $t = 15\ ms$ highlights that the topology of sprays up to three injectors ahead of the flame front are inclined due to the burnt gas expansion effect. This was also found in the LES - EE case [4]. Droplets are pushed by the strong azimuthal flow way before the flame reaches them. Consequently, droplets tend to leave their spray-SJZ and sometimes accumulate in LRZs creating spots of high alphal highlighted in Fig. 12.20 by arrows D. Therefore, after the flame passage, spots of very rich ϕ_g are created in the bottom of LRZs, as droplets fully evaporate. These spots are stressed out in Fig. 12.19 by arrows D. LRZs are actually richer than the rest of the chamber after the flame passage, near $\phi_g = 1.0$. Droplets found at higher locations and expelled by the front propagation create dense spray regions in front of the flame during the entire light-round as in box B of Fig. 12.20. At 35 ms, when both fronts get closer around injector 8, the droplet density above injector 8 is much higher than initially as outlined by boxes C of Fig. 12.20. In the same time, the gaseous equivalence ratio above injector 8 also reduces slightly as evidenced by boxes B of Fig. 12.19. Indeed, cold gas at $\phi_g = 0.8$ is pushed downstream by the burnt gas effect and replaced by fresh air injected from neighbouring injectors. As droplets have less time to evaporate compared to the non-reacting flow filling stage, the mixture is leaner

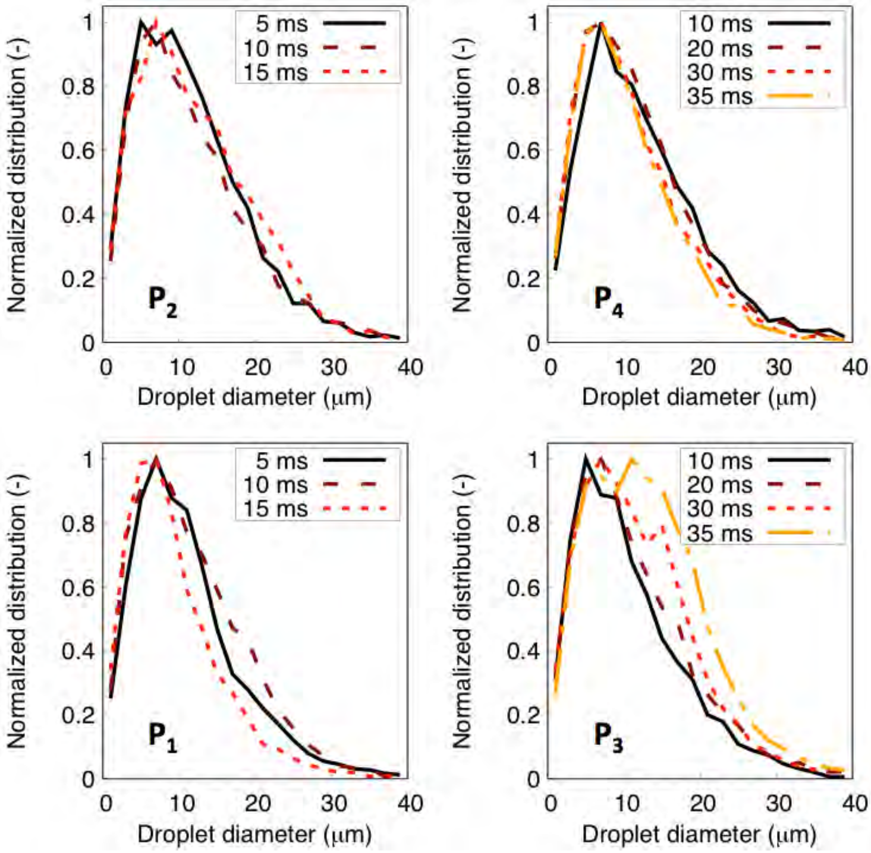

Figure 12.21: Evolution of the droplets diameter PDF before the flame passage at points P_1, P_2, P_3, P_4 shown in Fig. 12.20.

at the end of the light-round sequence. In conclusion, at the end of the light-round, the fresh mixture trapped between both flame fronts above injector 8 is leaner and has more droplets. The consequence is a reduced flame propagation speed contributing to the flame slowdown, even if this effect is secondary compared to the inhibition of the azimuthal flows generated by the opposite propagating fronts.

Finally, droplets diameter PDF at points P_1, P_2, P_3, P_4 shown in Fig. 12.20 are presented in Fig. 12.21 at 4 times before the flame passage. PDFs at P_1, P_2 and P_4 stay almost unchanged up to the flame passage, showing that the burnt gas expansion does not have a significant preferential effect on large or small droplets. The only marked modification occurs at point P_3, in the LRZ near injector 8. The droplets diameter PDF progressively shows the presence of more large droplets in front of the flame which can be explained by a faster evacuation of small droplets in the axial direction. Still, the poly-dispersity of the spray does not seem determinant in this configuration. This was actually expected considering the very narrow droplet diameter distributions encountered as emphasized in Fig. 12.6.

12.6 Conclusions

After successfully validating the numerical set-up on a single injector burner compared to available experimental data, light-round at atmospheric condition and $\phi_{glob} = 0.89$ has been studied in the annular MICCA-Spray configuration [3, 244] using LES with the Lagrangian formalism for the liquid phase. Results have been compared to experiment but also to LES performed with the Eulerian formalism [4, 245, 246].

The ignition behaviour is found to match very well the experimental sequence. Adding the complexity of liquid fuel does not change the overall sequence compared to gaseous fuel. The same five steps of ignition are recovered in agreement with experiments. Ignition timings show a very good agreement between experiment and LES for the first 6 sectors where experimental data are available. The timing of heat release peak is however shorter in the simulation compared to experiment ($-4\ ms$) for which total light intensity is measured. The major role of burnt gas expansion has been demonstrated and the analysis of the leading points trajectory has allowed to highlight the importance of the swirlers orientation. All these light-round features have been similarly found in previous gaseous ignition cases showing that using liquid fuels does not modify drastically the ignition behaviour in this configuration.

Using a liquid fuel however directly controls the gaseous mixture fraction and liquid fuel distributions. The choice of the formalism for the dispersed phase description is essential to correctly recover these distributions. A first difference attributed to the liquid phase formalism has been found between both LES - EL and LES - EE on the non-reacting flow filling before ignition. A globally leaner mixture is found with the EL simulation, due to either a different evaporation calibration and/or the addition of poly-dispersity. Consequently, during the ignition sequence, the flame faces a leaner cold mixture in the LES - EL simulation, as shown by the leading points properties over time. Still, some features of the light-round in two-phase conditions emphasized experimentally are identically recovered with both formalisms. For instance, dense spray regions up to three injectors ahead of the flame are inclined, modifying the mixture seen by the flame compared to the non-reacting quiescent flow. Droplets also tend to accumulate in LRZs creating spots of rich mixtures in the bottom of the chamber. These spots are a key factor of the leading points trajectory and overall flame propagation.

Chapter 13

General Conclusions

This PhD thesis is dedicated to the study of two-phase flow ignition in aeronautical gas turbines. The complex transient ignition phase is still a major challenge for researchers even in simple configurations because of the wide range of physics and time-space scales involved. Ignition relight is also a key process for engine manufacturers as it drives future combustor designs aiming at reducing fuel consumption and pollutant emissions. This work follows the PhD of L. Esclapez [1] who limited his work to gaseous flows. Taking into account the liquid fuel is a necessary evolution to better understand the behaviour of real combustors ignition process as it changes the fuel distribution in the chamber and adds the evaporation process to the already long list of physics involved. A Lagrangian formalism is used throughout this work for the dispersed phase allowing to account for spray poly-dispersity, known to be a decisive feature of spray ignition. A second key improvement is to consider a better chemistry description than standard Globally Reduced Chemistries [22] previously used, which are not designed to describe accurately complex phenomena such as ignition. Analytically Reduced Chemistry [23, 24] is considered in this thesis as it represents a good compromise between cost and accuracy.

This PhD work was performed in the context of the TIMBER project (Two-phase Ignition and propagation in Multi-BurnER combustors) gathering Safran Group and laboratories CERFACS, CORIA and EM2C but also the FAMAC project (Ignition Fundamentals for Internal Combustion Engines) regrouping Continental and CERFACS, CORIA, EM2C, IFPen, and LAPLACE laboratories. In this context, the three main phases of ignition have been investigated with Large Eddy Simulations. Available experimental data were used to validate numerical results and perform joint studies:

- About the kernel creation phase, a focus was made on the influence of the plasma chemistry as this feature is often neglected in numerical simulations. For this purpose, a simple anode-cathode configuration [158] operated in gaseous conditions was chosen. Experimental data from C. Lacour, CORIA were used for validation. The impact of plasma chemistry on the mixture temperature and composition is clearly demonstrated during the first microseconds of ignition but actually appears marginal on the combustion initiation as most radical production at high temperature appear after fuel oxidation starts. Encompassing a detailed plasma chemistry description is therefore an acceptable assumption. Nevertheless, the accuracy of the chemical description of combustion is of prime importance to capture the correct initial flame kernel propagation. Analytically Reduced Chemistries, in particular containing O_2 dissociation, represent a very promising solution.

- On the second ignition phase (kernel growth and propagation to the nearest injector), the two-phase swirled confined mono-injector KIAI-Spray burner [2], operated by J. Marrero-Santiago in CORIA, was investigated. A joint experimental and numerical study proved the accuracy of LES to study ignition in such realistic burners. Generic mechanisms inducing either ignition success or failure were identified. Each one was deeply characterized together with the subsequent kernel evolution. The local beneficial effect of the presence of droplet clusters on the kernel growth was emphasized. It was found that the most important parameter driving this phase is turbulence, as it controls the stochasticity of ignition. Predicting the outcome of an ignition sequence is therefore a challenge, hardly solved by performing numerous LES sequences due to a prohibitive cost. A trajectory-based model for ignition probability prediction in realistic two-phase combustors was thus developed and successfully applied in the academic KIAI-Spray configuration and an industrial combustor. Its potential to be used during the design process is demonstrated thanks to its moderate cost.
- The inter-sector flame propagation phase was studied considering two set-ups: the Coria Linear Swirled Spray Burner [2] operated by J. Marrero-Santiago and the MICCA-Spray configuration experimented by K. Prieur [3] at EM2C. In this last one, LES results obtained by T. Lancien [4] at EM2C using the Eulerian formalism for the liquid phase were reported for comparison. The choice of the dispersed phase formalism is essential to correctly recover gaseous and liquid fuel distributions. The poly-dispersity encompassed in Lagrangian calculations of the spray represents a key add-on in this sense. Nevertheless, compared to gaseous conditions, it is demonstrated that the injector-to-injector spacing [252] and the burnt gas expansion effect [243] stay the two main features driving two-phase light-round as they mainly control the flame speed and the injector-to-injector propagation mode.

This work is a reliable contribution to the understanding of the underlying physical mechanisms of spray ignition. LES coupled to Analytically Reduced Chemistry and the Lagrangian formalism for the spray has shown its capacity to investigate such phenomenon. Presented results however underline a limited influence of the liquid phase on ignition. This is explained by the atmospheric conditions considered in all studied configurations, and injected air and liquid fuel even pre-heated in the KIAI-Spray study for experimental technical issues. As a general perspective of this work, depressurized low-temperature conditions should be investigated to be more representative of crucial relight conditions at high altitude. With such operating conditions, the influence of fuel evaporation on the ignition process is expected to be higher, significantly affecting ignition performance. This will actually be focused in the APLAREP project in which Safran Group, CERFACS and CORIA are continuing their collaboration.

Bibliography

[1] L. Esclapez, *Numerical study of ignition and inter-sector flame propagation in gas turbine.* PhD thesis, 2015. 9, 14, 15, 18, 119, 120, 121, 122, 129, 131, 146, 178, 180, 183, 186, 187, 208, 273

[2] J. M. Santiago, *Experimental study of lean aeronautical ignition. Impact of critical parameters on the mechanisms acting along the different ignition phases.* PhD thesis, 2014. 18, 124, 125, 126, 134, 135, 136, 159, 169, 178, 218, 219, 225, 226, 227, 234, 244, 245, 274

[3] K. Prieur, *Dynamique de la combustion dans un foyer annulaire multi-injecteurs diphasique.* PhD thesis, Université Paris-Saclay, 2017. 18, 221, 247, 248, 250, 254, 255, 258, 271, 274

[4] T. Lancien, *Etude numerique de lallumage diphasique de foyers annulaires.* PhD thesis, Université Paris-Saclay, 2018. 18, 32, 221, 247, 251, 252, 253, 254, 255, 257, 258, 259, 264, 269, 271, 274

[5] T. Poinsot and D. Veynante, *Theoretical and Numerical Combustion.* Third Edition (www.cerfacs.fr/elearning), 2011. 23, 24, 26, 27, 49, 115, 116

[6] S. M. Candel and T. Poinsot, "Flame stretch and the balance equation for the flame surface area," *Combust. Sci. Technol.* , vol. 70, pp. 1–15, 1990. 25

[7] R. W. Bilger, S. H. Starner, and R. J. Kee, "On reduced mechanisms for methane-air combustion in nonpremixed flames," *Combust. Flame*, vol. 80, pp. 135–149, 1990. 26

[8] A. N. Kolmogorov, "The local structure of turbulence in incompressible viscous fluid for very large reynolds numbers," *C. R. Acad. Sci. , USSR*, vol. 30, p. 301, 1941. 28

[9] N. Peters, *Turbulent combustion.* Cambridge University Press, 2001. 30

[10] R. G. Abdel-Gayed, D. Bradley, M. N. Hamid, and M. Lawes, "Lewis number effects on turbulent burning velocity," *Proc. Combust. Inst.* , vol. 20, pp. 505–512, 1984. 30

[11] B. Cuenot and T. Poinsot, "Effects of curvature and unsteadiness in diffusion flames. implications for turbulent diffusion flames," *Proc. Combust. Inst.* , vol. 25, pp. 1383–1390, 1994. 30, 31

[12] T. Takeno, M. Murayama, and Y. Tanida, "Fractal analysis of turbulent premixed flame surface," *Experiments in Fluids*, vol. 10, pp. 61–70, 1990. 31, 169

[13] D. R. Ballal and A. H. Lefebvre, "Flame propagation in heterogeneous mixtures of fuell droplets, fuel vapor and air," *Proc. Combust. Inst.* , vol. 18, pp. 321–327, 1981. 33

[14] A. Neophytou and E. Mastorakos, "Simulations of laminar flame propagation in droplet mists," *Combust. Flame*, vol. 156, no. 8, pp. 1627–1640, 2009. 34, 220

[15] B. Rochette, E. Riber, and B. Cuenot, "Effect of non-zero relative velocity on the flame speed of two-phase laminar flames," *Proc. Combust. Inst.* , 2018. 34, 184, 185

[16] A. Wood, W. Hwang, and J. Eaton, "Preferential concentration of particles in homogeneous and isotropic turbulence," *International journal of multiphase flow*, vol. 31, no. 10-11, pp. 1220–1230, 2005. 36

[17] D. Paulhiac, *Modélisation de la combustion dun spray dans un bruleur aéronautique.* PhD thesis, 2015. 37, 56, 61, 75, 229, 252, 253

[18] J. Hirschfelder, C. Curtis, and B. Bird, *Molecular Theory of Gases and Liquids.* John Wiley & Sons, 1954 ed., 1954. 41

[19] A. D'angola, G. Colonna, C. Gorse, and M. Capitelli, "Thermodynamic and transport properties in equilibrium air plasmas in a wide pressure and temperature range," *The European Physical Journal D*, vol. 46, no. 1, pp. 129–150, 2008. 42, 81, 92, 108

[20] K. K. Kuo, *Principles of combustion.* Hoboken, New Jersey: John Wiley & Sons, Inc., 2005 Second Edition. 43

[21] B. Franzelli, *Impact of the chemical description on direct numerical simulations and Large Eddy Simulations of turbulent combustion in industrial aero-engines - TH/CFD/11/101.* PhD thesis, Université de Toulouse, France - MeGeP Dynamique des Fluides, 2011. phd. 44

[22] B. Franzelli, E. Riber, M. Sanjose, and T. Poinsot, "A two-step chemical scheme for kerosene-air premixed flames," *Combust. Flame*, vol. 157, pp. 1364–1373, 2010. 44, 273

[23] P. Pepiot and H. Pitsch, "An efficient error-propagation-based reduction method for large chemical kinetic mechanisms," *Combust. Flame*, vol. 154, pp. 67 – 81, 2008. 45, 91, 273, 303

[24] T. Jaravel, E. Riber, B. Cuenot, and G. Bulat, “Large eddy simulation of an industrial gas turbine combustor using reduced chemistry with accurate pollutant prediction,” *Proc. Combust. Inst.* , vol. 36, no. 3, pp. 3817–3825, 2017. 45, 90, 91, 273, 303

[25] T. Løvs, D. Nilsson, and F. Mauss, “Automatic reduction procedure for chemical mechanisms applied to premixed methane/air flames,” *Proc. Combust. Inst.* , vol. 28, no. 2, pp. 1809–1815, 2000. 45

[26] T. Løv Acta Astronautica s, P. Amnéus, F. Mauss, and E. Mastorakos, “Comparison of automatic reduction procedures for ignition chemistry,” *Proc. Combust. Inst.* , vol. 29, no. 1, pp. 1387–1393, 2002. 45

[27] J. Smagorinsky, “General circulation experiments with the primitive equations: 1. the basic experiment.,” *Mon. Weather Rev.* , vol. 91, pp. 99–164, 1963. 48

[28] F. Ducros, F. Nicoud, and T. Poinsot, “Wall-adapating local eddy-viscosity models for simulations in complex geometries,” in *ICFD*, pp. 293–300, Baines M. J., 1998. 48

[29] F. Nicoud, H. Baya Toda, O. Cabrit, S. Bose, and J. Lee, “Using singular values to build a subgrid-scale model for large eddy simulations,” *Phys. Fluids* , vol. 23, no. 8, p. 085106, 2011. 48, 137, 179, 251

[30] K. N. C. Bray and J. B. Moss, “A closure model for the turbulent premixed flame with sequential chemistry,” *Combust. Flame*, vol. 30, pp. 125–131, 1977. 49

[31] V. Moureau, B. Fiorina, and H. Pitsch, “A level set formulation for premixed combustion LES considering the turbulent flame structure,” *Combust. Flame*, vol. 156, no. 4, pp. 801–812, 2009. 49

[32] B. Fiorina, R. Vicquelin, P. Auzillon, N. Darabiha, O. Gicquel, and D. Veynante, “A filtered tabulated chemistry model for les of premixed combustion,” *Combust. Flame*, vol. 157, no. 3, pp. 465–475, 2010. 49

[33] O. Colin, F. Ducros, D. Veynante, and T. Poinsot, “A thickened flame model for large eddy simulations of turbulent premixed combustion,” Tech. Rep. HEP/123-qed, CERFACS, 1999. 49, 50, 51, 229, 251

[34] A. W. Cook and J. J. Riley, “A subgrid model for equilibrium chemistry in turbulent flows,” *Phys. Fluids A*, vol. 6, no. 8, pp. 2868 – 2870, 1994. 49

[35] A. W. Cook and J. J. Riley, “Subgrid scale modeling for turbulent reacting flows,” *Combust. Flame*, vol. 112, pp. 593 – 606, 1998. 49

[36] P. S. Volpiani, *Modèle de plissement dynamique pour la simulation aux grandes échelles de la combustion turbulente prémelangée.* PhD thesis, Université Paris-Saclay, 2017. 51

[37] F. Charlette, D. Veynante, and C. Meneveau, "A power-law wrinkling model for LES of premixed turbulent combustion: Part I - non-dynamic formulation and initial tests," *Combust. Flame*, vol. 131, pp. 159–180, 2002. 51, 229, 253

[38] F. Charlette, C. Meneveau, and D. Veynante, "A power-law flame wrinkling model for les of premixed turbulent combustion part ii: dynamic formulation," *Combust. Flame*, vol. 131, no. 1-2, pp. 181–197, 2002. 51

[39] G. Wang, M. Boileau, D. Veynante, and K. Truffin, "Large eddy simulation of a growing turbulent premixed flame kernel using a dynamic flame surface density model," *Combust. Flame*, vol. 159, no. 8, pp. 2742–2754, 2012. 51

[40] J.-P. Légier, T. Poinsot, and D. Veynante, "Dynamically thickened flame LES model for premixed and non-premixed turbulent combustion," in *Proc. of the Summer Program* , pp. 157–168, Center for Turbulence Research, NASA Ames/Stanford Univ., 2000. 52, 229, 253

[41] T. Jaravel, *Prediction of pollutants in gas turbines using large eddy simulation.* PhD thesis, 2016. 52, 140, 229

[42] D. G. Goodwin, H. K. Moffat, and R. L. Speth, "Cantera: An object-oriented software toolkit for chemical kinetics, thermodynamics, and transport processes," *Caltech, Pasadena, CA*, 2009. 53

[43] P. Pepiot, *Automatic strategies to model transportation fuel surrogates.* PhD thesis, Stanford University, 2008. 53, 139

[44] T. Schønfeld and M. Rudgyard, "Steady and unsteady flows simulations using the hybrid flow solver avbp," *AIAA J.* , vol. 37, no. 11, pp. 1378–1385, 1999. 53

[45] N. Lamarque, *Schémas numériques et conditions limites pour la simulation aux grandes échelles de la combustion diphasique dans les foyers d'hélicoptère.* Phd thesis, INP Toulouse, 2007. 53

[46] T. Poinsot and S. Lele, "Boundary conditions for direct simulations of compressible viscous flows," *J. Comput. Phys.* , vol. 101, no. 1, pp. 104–129, 1992. 53, 97, 137, 251

[47] P. D. Lax and B. Wendroff, "Systems of conservation laws," *Commun. Pure Appl. Math.* , vol. 13, pp. 217–237, 1960. 53, 137

[48] O. Colin and M. Rudgyard, "Development of high-order taylor-galerkin schemes for unsteady calculations," *J. Comput. Phys.* , vol. 162, no. 2, pp. 338–371, 2000. 53, 137, 179, 228, 250

[49] G. Marta, *Development and validation of the Euler-Lagrange formulation on a parallel and unstructured solver for large-eddy simulation.* PhD thesis, Institut National Polytechnique de Toulouse-INPT, 2009. 56

[50] F. Jaegle, *LES of two-phase flow in aero-engines.* PhD thesis, Université de Toulouse - Ecole doctorale MEGeP, CERFACS - CFD Team, Toulouse, December 2009. 56

[51] J.-M. Senoner, *Simulations aux grandes échelles de lécoulement diphasique dans un brûleur aéronautique par une approche Euler-Lagrange.* PhD thesis, INPT, 2010. 56

[52] P. Sierra Sánchez, *Modeling the dispersion and evaporation of sprays in aeronautical combustion chambers.* PhD thesis, 2012. 56, 60, 138, 252

[53] G. Chaussonnet, *Modeling of liquid film and breakup phenomena in Large-Eddy Simulations of aeroengines fueled by airblast atomizers.* PhD thesis, École Doctorale Mécanique, Énergétique, Génie civil et Procédés (Toulouse , 2014. 56

[54] N. Iafrate, *Simulation aux grandes échelles diphasique dans les moteurs downsizes à allumage commandé.* PhD thesis, 2016. 56, 252

[55] J. D. Schwarzkopf, M. Sommerfeld, C. T. Crowe, and Y. Tsuji, *Multiphase flows with droplets and particles.* CRC press, 2011. 57, 58

[56] C. W. Oseen, *Hydrodynamik.* Leipzig, 1927. 58

[57] L. Schiller and A. Nauman, "A drag coefficient correlation," *VDI Zeitung*, vol. 77, pp. 318–320, 1935. 58, 138, 252

[58] D. B. Spalding, "The combustion of liquid fuels," in *4th Symp. (Int.) on Combustion*, pp. 847–864, The Combustion Institute, Pittsburgh, 1953. 58, 138, 252

[59] R. S. Miller, K. Harstad, and J. Bellan, "Evaluation of equilibrium and non-equilibrium evaporation models for many-droplet gas-liquid flow simulations," *Int. J. Multiphase Flow* , vol. 24, no. 6, pp. 1025–1055, 1998. 59

[60] C. Wilke, "A viscosity equation for gas mixtures," *The journal of chemical physics*, vol. 18, no. 4, pp. 517–519, 1950. 60

[61] W. E. Ranz and W. R. Marshall, “Evaporation from drops,” *Chem. Eng. Prog.*, vol. 48, no. 4, p. 173, 1952. 61

[62] B. Abramzon and W. A. Sirignano, “Droplet vaporisation model for spray combustion calculations,” *Int. J. Heat and Mass Transfer* , vol. 9, pp. 1605–1618, 1989. 61, 138, 252

[63] M. Boileau, *Simulation aux grandes échelles de l'allumage diphasique des foyers aéronautiques.* Phd thesis, INP Toulouse, 2007. 61, 229

[64] M. Sanjosé, J. Senoner, F. Jaegle, B. Cuenot, S. Moreau, and T. Poinsot, “Fuel injection model for euler–euler and euler–lagrange large-eddy simulations of an evaporating spray inside an aeronautical combustor,” *Int. J. Multiphase Flow* , vol. 37, no. 5, pp. 514–529, 2011. 63, 138, 252

[65] E. Gutheil, “Numerical analysis of the autoignition of methanol, ethanol, n-heptane and n-octane sprays with detailed chemistry,” *Combust. Sci. Technol.* , vol. 105, no. 4-6, pp. 265–278, 1995. 67

[66] J. Warnatz, “The structure of laminar alkane-, alkene-, and acetylene flames,” vol. 18, no. 1, pp. 369–384, 1981. 67

[67] C. K. Westbrook, J. Warnatz, and W. J. Pitz, “A detailed chemical kinetic reaction mechanism for the oxidation of iso-octane and n-heptane over an extended temperature range and its application to analysis of engine knock,” vol. 22, no. 1, pp. 893–901, 1989. 67

[68] J. Griffiths, D. Coppersthwaite, C. Phillips, C. Westbrook, and W. Pitz, “Autoignition temperatures of binary mixtures of alkanes in a closed vessel: Comparisons between experimental measurements and numerical predictions,” vol. 23, no. 1, pp. 1745–1752, 1991. 67

[69] A. H. Lefebvre, *Gas Turbines Combustion.* Taylor & Francis, 1999. 67, 76

[70] R. Clements, P. Smy, and J. Dale, “An experimental study of the ejection mechanism for typical plasma jet igniters,” *Combust. Flame*, vol. 42, pp. 287–295, 1981. 67

[71] G. Joulin, “Point-source initiation of lean spherical flames of light reactants: an asymptotic theory,” *Combust. Sci. Technol.* , vol. 43, no. 1-2, pp. 99–113, 1985. 68

[72] R. Maly and M. Vogel, “Initiation and propagation of flame fronts in lean ch4-air mixtures by the threemodes of the ignition spark,” in *17th Symp. (Int.) on Combustion*, pp. 821–831, The Combustion Institute, Pittsburgh, 1978. 68, 71, 72, 74, 89, 90, 91, 186

[73] S. Refael and E. Sher, “A theoretical study of the ignition of a reactive medium by means of an electrical discharge,” *Combust. Flame*, vol. 59, no. 1, pp. 17–30, 1985. 68, 73, 74, 81, 89, 90

[74] M. Lim, R. Anderson, and V. S. Arpaci, “Prediction of spark kernel development in constant volume combustion,” *Combust. Flame*, vol. 69, no. 3, pp. 303–316, 1987. 68, 73, 90

[75] E. Sher, J. Ben-Ya’ish, and T. Kravchik, “On the birth of spark channels,” *Combust. Flame*, vol. 89, no. 2, pp. 186–194, 1992. 68, 81, 82, 90

[76] M. N. Plooster, “Shock waves from line sources. numerical solutions and experimental measurements,” *Phys. Fluids* , vol. 13, no. 11, pp. 2665–2675, 1970. 69

[77] M. Kono, K. Niu, T. Tsukamoto, and Y. Ujiie, “Mechanism of flame kernel formation produced by short duration sparks,” *Proc. Combust. Inst.* , vol. 22, no. 1, pp. 1643–1649, 1989. 70, 89, 98

[78] T. Phuoc and F. White, “An optical and spectroscopic study of laser-induced sparks to determine available ignition energy,” *Proc. Combust. Inst.* , vol. 29, pp. 1621 – 1628, 2002. 70, 71, 72, 108, 142

[79] D. Bradley, C. G. W. Sheppard, I. M. Suardjaja, and R. Woolley, “Fundamentals of high-energy spark ignition with lasers,” *Combust. Flame*, vol. 138, pp. 55–77, 2004. 70, 71, 72, 114, 142

[80] C. Ternel, *Contribution au développement de l’allumage par laser pour les moteurs à combustion interne.* PhD thesis, Université de Rouen, France, 2006. 70, 71, 91

[81] S. Nakaya, S. Iseki, X. Gu, Y. Kobayashi, and M. Tsue, “Flame kernel formation behaviors in close dual-point laser breakdown spark ignition for lean methane/air mixtures,” *Proc. Combust. Inst.* , vol. 36, no. 3, pp. 3441–3449, 2017. 70, 71

[82] D. Verhoeven, “Spark heat transfer measurements in flowing gases,” *Revue de l’Institut Français du Pétrole*, vol. 52, no. 4, pp. 453–464, 1997. 71

[83] H. El-Rabii, G. Gaborel, J.-P. Lapios, D. Thevenin, J. Rolon, and J.-P. Martin, “Laser spark ignition of two-phase monodisperse mixtures,” *Opti. Comm.*, vol. 256, no. 4-6, pp. 495–506, 2005. 71

[84] B. Sforzo, A. Lambert, J. Kim, J. Jagoda, S. Menon, and J. Seitzman, “Post discharge evolution of a spark igniter kernel,” *Combust. Flame*, vol. 162, no. 1, pp. 181–190, 2015. 71, 81, 91

[85] T. Mantel, *Contribution à la modélisation de la combustion dans les moteurs à allumage commandé avec prise en compte de la phase d’allumage.* PhD thesis, Université de Rouen, France, 1993. 71, 91

[86] R. George, *Développement de nouvelles stratégies dallumage laser: application à la propulsion aéronautique et/ou spatiale.* PhD thesis, Université Paris-Saclay, 2017. 71, 108

[87] S. Brieschenk, R. Hruschka, S. O’Byrne, and H. Kleine, “High-speed time-resolved visualisation of laser-induced plasma explosions,” in *28th International Congress on High-Speed Imaging and Photonics*, vol. 7126, p. 71260N, International Society for Optics and Photonics, 2009. 71, 108

[88] G. Gebel, T. Mosbach, W. Meier, and M. Aigner, “Laser-induced blast waves in air and their effect on monodisperse droplet chains of ethanol and kerosene,” *Shock Waves*, vol. 25, no. 4, pp. 415–429, 2015. 71, 78, 108, 110

[89] R. Teets and J. Sell, “Calorimetry of ignition sparks,” *SAE transactions*, vol. 97, pp. 371–383, 1988. 71, 72, 108

[90] D. H. McNeill, “Minimum ignition energy for laser spark ignition,” *Proc. Combust. Inst.* , vol. 30, no. 2, pp. 2913–2920, 2005. 72, 142

[91] S. Mouriaux, *Large Eddy simulation of the turbulent spark ignition and of the flame propagation in spark ignition engines.* PhD thesis, Université Paris-Saclay, 2016. 72, 80

[92] E. Mastorakos, “Ignition of turbulent non-premixed flames,” *Prog. Energy Combust. Sci.* , vol. 35, no. 1, pp. 57–97, 2009. 72, 114, 115

[93] I. Glassman, *Combustion.* New York: Academic Press, 1987. 73

[94] M. Champion, B. Deshaies, G. Joulin, and K. Kinoshita, “Spherical flame initiation: Theory versus experiments for lean propane-air mixtures,” *Combust. Flame*, vol. 65, no. 3, pp. 319–337, 1986. 73, 83

[95] B. Deshaies and G. Joulin, “On the initiation of a spherical flame kernel,” *Combust. Sci. Technol.* , vol. 37, p. 99, 1984. 73

[96] K. Kailasanath, E. Oran, and J. Boris, “A theoretical study of the ignition of premixed gases,” */cf*, vol. 47, pp. 173–190, 1982. 73, 89

[97] E. S. Oran and J. P. Boris, “Detailed modelling of combustion systems,” *Prog. Energy Combust. Sci.* , vol. 7, no. 1, pp. 1–72, 1981. 73

[98] T. M. Sloane, “Numerical simulation of electric spark ignition in atmospheric pressure methane-air mixtures,” *Combust. Sci. Technol.* , vol. 73, pp. 367–381, 1990. 73, 80

[99] T. M. Sloane, “Numerical simulation of electric spark ignition in methane-air mixtures at pressures above one atmosphere,” *Combust. Sci. Technol.* , vol. 86, pp. 121–133, 1992. 73

[100] T. Kravchik and E. Sher, “Numerical modeling of spark ignition and flame initiation in a quiescent methane-air mixture,” *Combust. Flame*, vol. 99, pp. 635–643, 1994. 73, 75, 80, 89

[101] P. Boudier, S. Henriot, T. Poinsot, and T. Baritaud, “A model for turbulent flame ignition and propagation in spark ignition engines,” in *Twenty-Fourth Symposium (International) on Combustion* (T. C. Institute, ed.), pp. 503–510, 1992. 73, 83, 84, 187

[102] J. Tagalian and J. B. Heywood, “Flame initiation in a spark-ignition engine,” *Combust. Flame*, vol. 64, no. 2, pp. 243–246, 1986. 73

[103] O. Akindele, D. Bradley, P. Mak, and M. McMahon, “Spark ignition of turbulent gases,” *Combust. Flame*, vol. 47, pp. 129–155, 1982. 73, 116, 186, 187

[104] G. F. Ziegler, E. P. Wagner, and R. R. Maly, “Ignition of lean methane-air mixtures by high pressure glow and arc discharges,” vol. 20, no. 1, pp. 1817–1824, 1985. 73

[105] D. R. Ballal and A. H. Lefebvre, “The influence of flow parameters on minimum ignition energy and quanching distance,” *Proc. Combust. Inst.* , vol. 15, pp. 1473–1481, 1974. 73, 74

[106] S. Pischinger and J. B. Heywood, “A model for flame kernel development in a spark-ignition engine,” in *23rd Symp. (Int.) on Combustion*, pp. 1033–1040, The Combustion Institute, Pittsburgh, 1990. 74

[107] R. Maly, "Ignition model for spark discharges and the early phase of flame front growth," in *18th Symp. (Int.) on Combustion*, pp. 1747–1754, The Combustion Institute, Pittsburgh, 1981. 74

[108] C. Beck, R. Koch, and H. Bauer, "Identification of droplet burning modes in lean, partially prevaporized swirl-stabilized spray flames," *Proc. Combust. Inst.* , vol. 32, p. in press, 2009. 75

[109] K. Annamalai and W. Ryan, "Interactive processes in gasification and combustion. part i: liquid drop arrays and clouds," *Prog. Energy Combust. Sci.* , vol. 18, no. 3, pp. 221–295, 1992. 75

[110] J. Bellan and K. Harstad, "Ignition of non dilute clusters of drops in convective flows," *Combust. Sci. Technol.* , vol. 53, no. 2-3, pp. 75–87, 1987. 75

[111] D. Ballal and A. Lefebvre, "Ignition of liquid fuel sprays at subatmospheric pressures," *Combust. Flame*, vol. 31, pp. 115–126, 1978. 76

[112] D. R. Ballal and A. H. Lefebvre, "Ignition and flame quenching of flowing heterogeneous fuel-air mixtures," *Combust. Flame*, vol. 35, pp. 155–168, 1979. 76, 77

[113] D. R. Ballal and A. H. Lefebvre, "A general model of spark ignition for gaseous and liquid fuel-air mixtures," in *Eighteenth Symposium (International) on Combustion* (T. C. Institute, ed.), pp. 1737–1747, 1981. 76, 77

[114] S. K. Aggarwal and A. Sirignano, "Ignition of fuel sprays: deterministic calculations for idealized droplet arrays," *Proc. Combust. Inst.* , no. 20, pp. 1771–1780, 1984. 76, 77

[115] C. Graves, L. TANG, and J. Skifstad, "Ignition of a fuel spray by a hot surface," *AIAA J.* , vol. 24, no. 12, pp. 1994–2001, 1986. 76, 77

[116] S. Hayashi, S. Kumagai, and T. Sakai, "Propagation velocity and structure of flames in droplet-vapor-air mixtures," *Combust. Sci. Technol.* , vol. 15, pp. 169–177, 1976. 76, 77

[117] A. K. Singh and C. E. Polymeropoulos, "Spark ignition of aerosols," vol. 21, no. 1, pp. 513–519, 1988. 76, 77

[118] S. Aggarwal and K. Nguyen, "Ignition behavior of a fuel spray flowing in a tube," *Chem. Eng. Comm.*, vol. 88, no. 1, pp. 23–29, 1990. 76, 77, 78

[119] K.-P. Lee, S.-H. Wang, and S.-C. Wong, “Spark ignition characteristics of monodisperse multicomponent fuel sprays,” *Combust. Sci. Technol.* , vol. 113, no. 1, pp. 493–502, 1996. 76

[120] S. K. Aggarwal, “A review of spray ignition phenomena: present status and future research,” *Prog. Energy Combust. Sci.* , vol. 24, no. 6, pp. 565–600, 1998. 76

[121] E. Mastorakos, “Forced ignition of turbulent spray flames,” *Proc. Combust. Inst.* , vol. 36, no. 2, pp. 2367–2383, 2017. 76, 114, 116, 119, 158

[122] D. R. Ballal and A. H. Lefebvre, “Ignition and flame quenching of quiescent fuel mists,” *Proc. R. Soc. Lond. A* , vol. 364, pp. 277–294, 1978. 77

[123] S. K. Aggarwal, “Ignition behavior of a multicomponent fuel spray,” *Combust. Flame*, vol. 76, no. 1, pp. 5–15, 1989. 78, 79

[124] P. M. de Oliveira, P. M. Allison, and E. Mastorakos, “Ignition of uniform droplet-laden weakly turbulent flows following a laser spark,” *Combust. Flame*, vol. 199, pp. 387–400, 2019. 78, 114, 118

[125] G. C. Gebel, T. Mosbach, W. Meier, M. Aigner, and S. Le Brun, “An experimental investigation of kerosene droplet breakup by laser-induced blast waves,” *J. Eng. Gas Turb. and Power* , vol. 135, no. 2, p. 021505, 2013. 78, 80, 110

[126] T. M. Sloane and P. D. Ronney, “A comparison of ignition phenomena with detailed and simplified kinetics,” *Combust. Sci. Technol.* , vol. 88, pp. 1–13, 1992. 79, 81

[127] E. Sher and J. C. Keck, “Spark ignition of combustible gas mixtures,” *Combust. Flame*, vol. 66, no. 1, pp. 17–25, 1986. 80

[128] M. Benmouffok, *Caractérisation théorique du plasma lors de l’application d’un courant impulsionnel: application à l’allumage des moteurs.* PhD thesis, Université Paul Sabatier-Toulouse III, 2016. 81

[129] T. Jaravel, J. Labahn, B. Sforzo, J. Seitzman, and M. Ihme, “Numerical study of the ignition behavior of a post-discharge kernel in a turbulent stratified crossflow,” *Proc. Combust. Inst.* , 2018. 81

[130] D. R. Stull and H. Prophet, “JANAF thermochemical tables, 2nd Edition,” Tech. Rep. NSRDS-NBS 37, US National Bureau of Standards, 1971. 81

[131] J. Schulz, K. Gottiparthi, and S. Menon, “Ionization in gaseous detonation waves,” *Shock Waves*, vol. 22, no. 6, pp. 579–590, 2012. 81

[132] P. Teulet, J. Gonzalez, A. Mercado-Cabrera, Y. Cressault, and A. Gleizes, "One-dimensional hydro-kinetic modelling of the decaying arc in air-pa66-copper mixtures: I. chemical kinetics, thermodynamics, transport and radiative properties," *J. Phys. D: Appl. Phys.* , vol. 42, no. 17, pp. 175–201, 2009. 81, 92, 303

[133] I. Kossyi, A. Y. Kostinsky, A. Matveyev, and V. Silakov, "Kinetic scheme of the non-equilibrium discharge in nitrogen-oxygen mixtures," *Plasma Sources Sci. Tech.*, vol. 1, no. 3, p. 207, 1992. 81, 92, 303

[134] L. J. Kieffer and G. H. Dunn, "Electron impact ionization cross-section data for atoms, atomic ions, and diatomic molecules: I. experimental data," *Rev. Modern Physics*, vol. 38, no. 1, p. 1, 1966. 81, 92, 303

[135] B. J. McBride, S. Gordon, and M. A. Reno, "Coefficients for calculating thermodynamic and transport properties of individual species," *Report No. TM-4513, NASA, 1993*, 1993. 81, 91, 109, 303

[136] M. Thiele, S. Selle, U. Riedel, J. Warnatz, and U. Maas, "Numerical simulation of spark ignition including ionization," in *Twenty-Eighth Symposium (International) on Combustion* (T. C. Institute, ed.), pp. 1177–1185, 2000. 81

[137] O. Yaşar, "A new ignition model for spark-ignited engine simulations," *Parallel computing*, vol. 27, no. 1-2, pp. 179–200, 2001. 81

[138] R. Mendez Rojano, "Study of spark plug ignition," tech. rep., CERFACS, 2015. 81, 97

[139] G. Linassier, *Etude expérimentale et numérique de lallumage des turboréacteurs en conditions de haute altitude.* PhD thesis, Toulouse, ISAE, 2012. 83, 124

[140] A. Bruyat, *Influence de l'évaporation de gouttes multicomposant sur la combustion et des effets diphasiques sur l'allumage d'un foyer aéronautique.* PhD thesis, Toulouse, ISAE, 2012. 83, 124

[141] Z. Tan and R. D. Reitz, "An ignition and combustion model based on the level-set method for spark ignition engine multidimensional modeling," *Combust. Flame*, vol. 145, no. 1-2, pp. 1–15, 2006. 83

[142] J. M. Duclos and O. Colin, "Arc and kernel tracking ignition model for 3D spark ignition engine calculations," in *Fifth Int. Symp. on Diagnostics, Modelling of Combustion in Internal Combustion Engines (COMODIA)*, (Nagoya, Japan), pp. 343–350, 2001. 84, 85

[143] S. Richard, O. Colin, O. Vermorel, A. Benkenida, C. Angelberger, and D. Veynante, “Towards large eddy simulation of combustion in spark ignition engines,” *Proc. Combust. Inst.* , vol. 31, pp. 3059–3066, 2007. 85

[144] O. Colin and K. Truffin, “A spark ignition model for large eddy simulation based on an {FSD} transport equation (issim-les),” *Proc. Combust. Inst.* , vol. 33, no. 2, pp. 3097 – 3104, 2011. 85

[145] O. Colin, M. Ritter, C. Lacour, K. Truffin, S. Mouriaux, S. Stepanyan, B. Lecordier, and P. Vervisch, “Dns and les of spark ignition with an automotive coil,” *Proc. Combust. Inst.* , 2018. 85

[146] T. M. Sloane, “The effect of selective energy deposition on the homogeneous ignition of methane and its implication for flame initiation and combustion enhancement,” *Combust. Sci. Technol.* , vol. 42, no. 3-4, pp. 131–144, 1985. 85

[147] T. J. Poinsot, “Flame ignition in a premixed turbulent flow,” in *Annual Research Briefs* , pp. 251–272, Center for Turbulence Research, NASA Ames/Stanford Univ., 1991. 85

[148] M. Baum and T. Poinsot, “Effects of mean flow on premixed flame ignition,” *Combust. Sci. Technol.* , vol. 106, no. 1-3, p. 19, 1995. 85

[149] N. Chakraborty and R. S. Mastorakos, E. Cant, “Effects of turbulence on spark ignition in inhomogeneous mixtures: A direct numerical simulation(DNS) study,” *Combust. Sci. Technol.* , vol. 179, no. 1-3, pp. 293–317, 2007. 85

[150] W. Jones and V. Prasad, “Les-pdf simulation of a spark ignited turbulent methane jet,” *Proc. Combust. Inst.* , vol. 33, no. 1, pp. 1355–1363, 2011. 85

[151] G. Lacaze, E. Richardson, and T. J. Poinsot, “Large eddy simulation of spark ignition in a turbulent methane jet,” *Combust. Flame*, vol. 156, no. 6, pp. 1993–2009, 2009. 85, 86, 90, 91, 107, 115, 126, 140, 229, 254

[152] B. Enaux, *Simulation aux Grandes Echelles d’un moteur à allumage commandé-Evaluations des variabilités cycliques.* PhD thesis, 2010. 87

[153] B. Renou and A. Boukhalfa, “An experimental study of freely propagating premixed flames at various lewis numbers,” *Combust. Sci. Technol.* , vol. 162, no. 1, pp. 347–370, 2001. 87

[154] G. Lacaze, *Simulation aux Grandes Echelles de l’allumage de moteurs fusées cryotechniques.* PhD thesis, Institut National Polytechnique de Toulouse-INPT, 2009. 88

[155] S. P. Bane, J. L. Ziegler, and J. E. Shepherd, "Investigation of the effect of electrode geometry on spark ignition," *Combust. Flame*, vol. 162, no. 2, pp. 462–469, 2015. 89, 98

[156] B. Franzelli, E. Riber, and B. Cuenot, "Impact of the chemical description on a large eddy simulation of a lean partially premixed swirled flame," *C. R. Mécanique*, vol. 341, no. 1-2, pp. 247–256, 2013. 90

[157] F. Collin-Bastiani, O. Vermorel, C. Lacour, B. Lecordier, and B. Cuenot, "Dns of spark ignition using analytically reduced chemistry including plasma kinetics," *Proc. Combust. Inst.* , 2018. 90

[158] C. Lacour, A. Lo, J. Marrero, F. Lefebvre, P. Vervisch, A. Cessou, and B. Lecordier, *Characterisation of electric discharge in laminar flow with optical diagnostics*. Springer, 2016. 91, 96, 97, 273

[159] H. J. Curran, P. Gaffuri, W. J. Pitz, and C. K. Westbrook, "A comprehensive modeling study of iso-octane oxidation," *Combust. Flame*, vol. 129, no. 3, pp. 253–280, 2002. 91, 139, 140, 303

[160] W. Sutherland, "The viscosity of gases and molecular force," *Philosophical Magazine*, vol. 5, no. 36, pp. 507–531, 1893. 92, 108

[161] G. Jomaas, X. Zheng, D. Zhu, and C. Law, "Experimental determination of counterflow ignition temperatures and laminar flame speeds of c2-c3 hydrocarbons at atmospheric and elevated pressures," *Proc. Combust. Inst.* , vol. 30, no. 1, pp. 193–200, 2005. 92

[162] C. M. Vagelopoulos and F. Egolfopoulos, "Direct experimental determination of laminar flame speeds," in *27th Symp. (Int.) on Combustion*, pp. 513–519, The Combustion Institute, Pittsburgh, 1998. 92

[163] D. C. Horning, D. Davidson, and R. Hanson, "Study of the high-temperature autoignition of n-alkane/o/ar mixtures," *J. Prop. Power* , vol. 18, no. 2, pp. 363–371, 2002. 92

[164] P. Teulet, J. Gonzalez, A. Mercado-Cabrera, Y. Cressault, and A. Gleizes, "One-dimensional hydro-kinetic modelling of the decaying arc in air-pa66-copper mixtures: Ii. study of the interruption ability," *J. Phys. D: Appl. Phys.* , vol. 42, no. 18, pp. 185–207, 2009. 92, 303

[165] J. Manion, R. Huie, R. Levin, D. Burgess Jr, V. Orkin, W. Tsang, W. McGivern, J. Hudgens, V. Knyazev, D. Atkinson, *et al. NIST Chemical Kinetics Database, NIST standard reference database 17, version 7.0, Web address: http://kinetics.nist.gov*, 2008. 92, 303

[166] D. G. Goodwin, "Cantera code site," July 2009. 92, 139

[167] B. J. McBride and S. Gordon, "Computer program for calculation of complex chemical equilibrium compositions and applications ii. users manual and program description.," *Report No. 1311, NASA, 1994*, 1994. 92

[168] A. Lo, A. Cessou, C. Lacour, B. Lecordier, P. Boubert, D. Xu, C. Laux, and P. Vervisch, "Streamer-to-spark transition initiated by a nanosecond overvoltage pulsed discharge in air," *Plasma Sources Sci. Tech.*, vol. 26, no. 4, p. 045012, 2017. 96

[169] A. Birch, D. Brown, M. Dodson, and J. Thomas, "The turbulent concentration field of a methane jet," *J. Fluid Mech.* , vol. 88, no. 3, pp. 431–449, 1978. 114, 182

[170] N. Vasudeo, T. Echekki, M. S. Day, and J. B. Bell, "The regime diagram for premixed flame kernel-vortex interactionsrevisited," *Phys. Fluids* , vol. 22, no. 4, p. 043602, 2010. 114, 117

[171] B. Peterson, D. L. Reuss, and V. Sick, "On the ignition and flame development in a spray-guided direct-injection spark-ignition engine," *Combust. Flame*, vol. 161, no. 1, pp. 240–255, 2014. 115

[172] S. F. Ahmed and E. Mastorakos, "Spark ignition of a turbulent shear-less fuel–air mixing layer," *Fuel*, vol. 164, pp. 297–304, 2016. 115

[173] B. Renou, E. Samson, and A. Boukhalfa, "An experimental study of freely propagating turbulent propane/air flames in stratified inhomogeneous mixtures," *Combust. Sci. Technol.* , vol. 176, no. 11, pp. 1867–1890, 2004. 116

[174] H. Reddy and J. Abraham, "Influence of turbulence–kernel interactions on flame development in lean methane/air mixtures under natural gas-fueled engine conditions," *Fuel*, vol. 103, pp. 1090–1105, 2013. 116, 117

[175] R. Borghi, "On the structure and morphology of turbulent premixed flames," in *Rec. Adv. in Aerospace Sci.* (C. Bruno and C. Caseci, eds.), pp. 117–138, 1985. 116

[176] K. Jenkins, M. Klein, N. Chakraborty, and R. Cant, "Effects of strain rate and curvature on the propagation of a spherical flame kernel in the thin-reaction-zones regime," *Combust. Flame*, vol. 145, no. 1-2, pp. 415–434, 2006. 117, 118

[177] T. Echekki and J. H. Chen, "Unsteady strain rate and curvature effects in turbulent premixed methane-air flames," *Combust. Flame*, vol. 106, pp. 184–202, 1996. 117, 163

[178] R. G. Abdel-Gayed and D. Bradley, "Criteria for turbulent propagation limits of premixed flames," *Combust. Flame*, vol. 62, pp. 61–68, 1985. 118, 130, 185, 186

[179] A. P. Wandel, N. Chakraborty, and E. Mastorakos, "Direct numerical simulations of turbulent flame expansion in fine sprays," *Proc. Combust. Inst.* , vol. 32, no. 2, pp. 2283–2290, 2009. 118

[180] A. Neophytou, E. Mastorakos, and R. Cant, "Dns of spark ignition and edge flame propagation in turbulent droplet-laden mixing layers," *Combust. Flame*, vol. 157, no. 6, pp. 1071–1086, 2010. 119, 129

[181] S. F. Ahmed, R. Balachandran, T. Marchione, and E. Mastorakos, "Spark ignition of turbulent nonpremixed bluff-body flames," *Combust. Flame*, vol. 151, pp. 366–385, 2007. 120, 121, 122, 123, 124, 125, 126, 128, 133, 177, 182

[182] M. Cordier, *Allumage et propagation de flammes dans les écoulements fortement swirlés: études expérimentales et numériques.* PhD thesis, PhD thesis, INSA Rouen, 2013. 121, 122, 124, 129, 130, 188

[183] S. F. Ahmed, "The probabilistic nature of ignition of turbulent highly-strained lean premixed methane-air flames for low-emission engines," *Fuel*, vol. 134, pp. 97–106, 2014. 120, 121, 122, 133

[184] E. Bach, J. Kariuki, J. Dawson, E. Mastorakos, and H.-j. Bauer, "Spark ignition of single bluff-body premixed flames and annular combustors," in *51st AIAA Aerospace Sciences Meeting including the New Horizons Forum and Aerospace Exposition*, p. 1182, 2013. 120, 121, 220, 247

[185] J. Kariuki, J. R. Dawson, and E. Mastorakos, "Measurements in turbulent premixed bluff body flames close to blow-off," *Combust. Flame*, vol. 159, no. 8, pp. 2589–2607, 2012. 120

[186] M. Cordier, A. Vandel, G. Cabot, B. Renou, and A. M. Boukhalfa, "Laser-induced spark ignition of premixed confined swirled flames," *Combust. Sci. Technol.* , vol. 185, no. 3, pp. 379–407, 2013. 120, 121, 133, 134, 177, 178, 186

[187] A. Triantafyllidis, E. Mastorakos, and R. Eggels, “Large eddy simulations of forced ignition of a non-premixed bluff-body methane flame with conditional moment closure,” *Combust. Flame*, vol. 156, no. 12, pp. 2328 – 2345, 2009. 123, 133

[188] V. Subramanian, P. Domingo, and L. Vervisch, “Large eddy simulation of forced ignition of an annular bluff-body burner,” *Combust. Flame*, vol. 157, no. 3, pp. 579–601, 2010. 123, 133

[189] N. G. Rosa, G. Linassier, R. Lecourt, P. Villedieu, and G. Lavergne, “Experimental and numerical study of high-altitude ignition of a turbojet combustor,” *Heat Transfer Engineering*, vol. 32, no. 11-12, pp. 949–956, 2011. 124

[190] A. Eyssartier, *LES of two-phase reacting flows: stationary and transient operating conditions.* PhD thesis, 2012. 124

[191] J. M. Santiago, A. Verdier, G. Godard, A. Vandel, G. Cabot, M. Boukhalfa, and B. Renou, “Experimental study of laser ignition probability, kernel propagation and air and fuel droplet properties in a confined swirled jet-spray burner,” in *18th International Symposium on the Application of Laser and Imaging Techniques to Fluid Mechanics*, p. 84, 2016. 124

[192] J. Marrero-Santiago, A. Verdier, A. Vandel, G. Godard, G. Cabot, and B. Renou, “Spray ignition and local flow properties in a swirled confined spray-jet burner: experimental analysis,” *Proc. ILASS-Europe*, pp. 847–854, 2017. 124, 137

[193] A. D. Birch, D. R. Brown, and M. G. Dodson, “Ignition probabilities in turbulent mixing flows,” in *18th Symposium (Int.) on Combustion*, pp. 1775–1780, The Combustion Institute, Pittsburgh, 1981. 124, 126, 182

[194] C. Letty, E. Mastorakos, A. R. Masri, M. Juddoo, and W. O’Loughlin, “Structure of igniting ethanol and n-heptane spray flames with and without swirl,” *Exp. Thermal Fluid Sci.*, vol. 43, pp. 47–54, 2012. 124, 134

[195] T. Marchione, S. F. Ahmed, and E. Mastorakos, “Ignition of turbulent swirling n-heptane spray flames using single and multiple sparks,” *Combust. Flame*, vol. 156, pp. 166–180, Jan. 2009. 125, 126, 134

[196] A. Tyliszczak and E. Mastorakos, “Les/cmc predictions of spark ignition probability in a liquid fuelled swirl combustor,” in *51st AIAA Aerospace Sciences Meeting including the New Horizons Forum and Aerospace Exposition*, p. 427, 2013. 125, 134

[197] R. Read, J. Rogerson, and S. Hochgreb, “Relight imaging at low temperature, low pressure conditions,” in *46th AIAA Aerospace Sciences Meeting and Exhibit*, p. 957, 2008. 125

[198] R. Read, J. Rogerson, and S. Hochgreb, “Flame imaging of gas-turbine relight,” *AIAA J.* , vol. 48, no. 9, pp. 1916–1927, 2010. 125

[199] W. P. Jones and A. Tyliszczak, “Large eddy simulation of spark ignition in a gas turbine combustor,” *Flow, Turb. and Combustion* , vol. 85, no. 3-4, pp. 711–734, 2010. 125

[200] A. Neophytou, E. Richardson, and E. Mastorakos, “Spark ignition of turbulent recirculating non-premixed gas and spray flames: A model for predicting ignition probability,” *Combust. Flame*, vol. 159, no. 4, pp. 1503–1522, 2012. 126, 128, 178, 182, 185, 186, 187, 222

[201] L. Esclapez, E. Riber, and B. Cuenot, “Ignition probability of a partially premixed burner using {LES},” *Proc. Combust. Inst.* , vol. 35, no. 3, pp. 3133 – 3141, 2015. 126, 133, 158, 177, 179, 191

[202] A. Eyssartier, B. Cuenot, L. Y. Gicquel, and T. Poinsot, “Using les to predict ignition sequences and ignition probability of turbulent two-phase flames,” *Combust. Flame*, vol. 160, no. 7, pp. 1191–1207, 2013. 126, 127, 182

[203] R. Lecourt, G. Heid, and M. Zedda, “Ignition and extinction results at ambient conditions,” *Report, ONERA*, 2008. 127

[204] G. Linassier, A. Bruyat, P. Villedieu, N. Bertier, C. Laurent, O. Rouzaud, R. Lecourt, H. Verdier, and G. Lavergne, “Application of numerical simulations to predict aircraft combustor ignition,” *Comptes Rendus Mécanique*, vol. 341, no. 1-2, pp. 201–210, 2013. 127, 182

[205] C. Wilson, C. Sheppard, and H. Low, “A novel technique for predicting the ignition performance of an aero gas turbine combustion chamber,” 1999. 128, 178, 182, 185

[206] J. Weckering, A. Sadiki, J. Janicka, E. Mastorakos, and R. Eggels, “A forced ignition probability analysis method using les and lagrangian particle monitoring,” *Proc. Combust. Inst.* , vol. 33, no. 2, pp. 2919–2925, 2011. 128, 178

[207] E. S. Richardson, *Ignition modelling for turbulent non-premixed flows.* PhD thesis, University of Cambridge, 2007. 128, 178

[208] M. P. Sitte, E. Bach, J. Kariuki, H.-J. Bauer, and E. Mastorakos, "Simulations and experiments on the ignition probability in turbulent premixed bluff-body flames," *Combust. Theor. Model.* , vol. 20, no. 3, pp. 548–565, 2016. 128

[209] T. Soworka, M. Gerendas, R. Eggels, and E. Mastorakos, "Numerical investigation of ignition performance of a lean burn combustor at sub-atmospheric conditions," in *ASME Turbo Expo 2014: Turbine Technical Conference and Exposition*, American Society of Mechanical Engineers, 2014. 128, 178

[210] M. Cordier, A. Vandel, B. Renou, G. Cabot, M. Boukhalfa, and M. Cazalens, "Spark ignition of confined swirled flames: Experimental and numerical investigation," pp. V01AT04A028–V01AT04A028, 2013. 128

[211] S. B. Pope, *Turbulent flows.* Cambridge University Press, 2000. 129

[212] R. Abdel-Gayed, D. Bradley, and M. Lawes, "Turbulent burning velocities: a general correlation in terms of straining rates," *Proc. R. Soc. Lond. A*, vol. 414, no. 1847, pp. 389–413, 1987. 130, 188

[213] D. Barré, *Numerical simulation of ignition in aeronautical combustion chambers.* PhD thesis, 2014. 134

[214] J. Marrero-Santiago, A. Verdier, C. Brunet, A. Vandel, G. Godard, G. Cabot, M. Boukhalfa, and B. Renou, "Experimental study of aeronautical ignition in a swirled confined jet-spray burner," *J. Eng. Gas Turb. and Power* , vol. 140, no. 2, pp. 021502–11, 2017. 134, 137, 156, 215, 218, 220, 223, 225, 226, 239, 245

[215] F. Collin-Bastiani, J. Marrero-Santiago, E. Riber, G. Cabot, B. Renou, and B. Cuenot, "A joint experimental and numerical study of ignition in a spray burner," *Proc. Combust. Inst.* , 2018. 134, 137, 178

[216] C. Cardin, B. Renou, G. Cabot, and A. M. Boukhalfa, "Experimental analysis of laser-induced spark ignition of lean turbulent premixed flames: New insight into ignition transition," *Combust. Flame*, vol. 160, no. 8, pp. 1414–1427, 2013. 137

[217] J. Marrero-Santiago, A. Verdier, G. Godard, A. Vandel, G. Cabot, M. Boukhalfa, and B. Renou, "Experimental study of airflow velocity, fuel droplet size-velocity and flame structure in a confined swirled jet-spray flame," *Proc. ILASS-Europe*, pp. SIC–10, 2016. 137

[218] F. Shum-Kivan, J. M. Santiago, A. Verdier, E. Riber, B. Renou, G. Cabot, and B. Cuenot, "Experimental and numerical analysis of a turbulent spray flame structure," *Proc. Combust. Inst.* , vol. 36, no. 2, pp. 2567–2575, 2017. 138, 149, 234

[219] S. Jerzembeck, N. Peters, P. Pepiot-Desjardins, and H. Pitsch, “Laminar burning velocities at high pressure for primary reference fuels and gasoline: Experimental and numerical investigation,” *Combust. Flame*, vol. 156, no. 2, pp. 292–301, 2009. 139, 140

[220] K. Kumar, J. Freeh, C. Sung, and Y. Huang, “Laminar flame speeds of preheated iso-octane/o2/n2 and n-heptane/o2/n2 mixtures,” *Journal of propulsion and power*, vol. 23, no. 2, pp. 428–436, 2007. 139

[221] A. Felden, *Development of Analytically Reduced Chemistries (ARC) and applications in Large Eddy Simulations (LES) of turbulent combustion.* PhD thesis, 2017. 140

[222] H. Liang and T. Maxworthy, “An experimental investigation of swirling jets,” *J. Fluid Mech.* , vol. 525, pp. 115–159, 2005. 146

[223] M. Ruith, P. Chen, E. Meiburg, and T. Maxworthy, “Three-dimensional vortex breakdown in swirling jets and wakes: direct numerical simulation,” *J. Fluid Mech.* , vol. 486, pp. 331–378, 2003. 146

[224] H. Im, J. H. Chen, and J. Y. Chen, “Chemical response of methane air diffusion flames to unsteady strain rate,” *Combust. Flame*, vol. 118, pp. 204–212, 1999. 163

[225] M. Klein, N. Chakraborty, K. Jenkins, and R. Cant, “Effects of initial radius on the propagation of premixed flame kernels in a turbulent environment,” *Phys. Fluids* , vol. 18, no. 5, p. 055102, 2006. 163

[226] I. R. Gran, T. Echekki, and J. H. Chen, “Negative flame speed in an unsteady 2-d premixed flame: A computational study,” in *Proc. Combust. Inst.* , vol. 26, pp. 323–329, Elsevier, 1996. 163

[227] E. Machover and E. Mastorakos, “Experimental and numerical investigation on spark ignition of linearly arranged non-premixed swirling burners,” *Combust. Sci. Technol.* , vol. 189, no. 8, pp. 1326–1353, 2017. 178, 219, 221

[228] M. Smith, A. Birch, D. Brown, and M. Fairweather, “Studies of ignition and flame propagation in turbulent jets of natural gas, propane and a gas with high hydrogen content,” *Proc. Combust. Inst.* , vol. 21, pp. 1403–1408, 1986. 179

[229] L. Gicquel, N. Gourdain, J.-F. Boussuge, H. Deniau, G. Staffelbach, P. Wolf, and T. Poinsot, “High performance parallel computing of flows in complex geometries,” *Comptes Rendus Mécanique*, vol. 339, no. 2-3, pp. 104 – 124, 2011. 179

[230] L. Y. M. Gicquel, G. Staffelbach, and T. Poinsot, “Large eddy simulations of gaseous flames in gas turbine combustion chambers,” *Prog. Energy Combust. Sci.* , vol. 38, no. 6, pp. 782 – 817, 2012. 179

[231] T. Poinsot, T. Echekki, and M. G. Mungal, “A study of the laminar flame tip and implications for premixed turbulent combustion,” *Combust. Sci. Technol.* , vol. 81, no. 1-3, pp. 45–73, 1992. 179

[232] D. Barré, M. Kraushaar, G. Staffelbach, V. Moureau, and L. Gicquel, “Compressible and low Mach number LES of a swirl experimental burner,” *C. R. Acad. Sci. Mécanique*, vol. 341, pp. 277–287, 2013. 180

[233] R. Schefer, G. Evans, J. Z. anf A. Ruggles, and R. Grief, “Ignitability limits for combustion of unintended hydrogen releases: experimental and theoretical results,” *International journal of hydrogen energy*, vol. 36, no. 2426-2435, 2011. 183

[234] B. Boughton, J. Delaurentis, and W. Dunn, “A stochastic model of particle dispersion in the atmosphere,” *Boundary-Layer Meteorology*, vol. 40, no. 1-2, pp. 147–163, 1987. 187

[235] C. Gardiner, *Stochastic methods*, vol. 4. springer Berlin, 2009. 187

[236] M. Boileau, G. Staffelbach, B. Cuenot, T. Poinsot, and C. Bérat, “LES of an ignition sequence in a gas turbine engine,” *Combust. Flame*, vol. 154, no. 1-2, pp. 2–22, 2008. 213, 217, 219, 220

[237] M. Cordier, A. Vandel, B. Renou, G. Cabot, M. Boukhalfa, L. Esclapez, D. Barré, E. Riber, B. Cuenot, and L. Gicquel, “Experimental and numerical analysis of an ignition sequence in a multiple-injectors burner,” in *ASME Turbo Expo 2013: Turbine Technical Conference and Exposition*, pp. V01AT04A048–V01AT04A048, American Society of Mechanical Engineers, 2013. 214, 226

[238] D. Barre, L. Esclapez, M. Cordier, E. Riber, B. Cuenot, G. Staffelbach, B. Renou, A. Vandel, L. Y. Gicquel, and G. Cabot, “Flame propagation in aeronautical swirled multi-burners: Experimental and numerical investigation,” *Combust. Flame*, vol. 161, no. 9, pp. 2387 – 2405, 2014. 214, 215, 216, 218, 219, 220, 226, 236, 242

[239] J. Marrero-Santiago, A. Verdier, A. Vandel, G. Cabot, A. M. Boukhalfa, and B. Renou, “Effect of injector spacing in the light-around ignition efficiency and mechanisms in a linear swirled spray burner,” *Heat and Mass Transfer*, pp. 1–15, 2018. 214, 219, 220, 221, 225, 226, 245

[240] G. Kumar and S. A. Drennan, "A cfd investigation of multiple burner ignition and flame propagation with detailed chemistry and automatic meshing," in *52nd AIAA/SAE/ASEE Joint Propulsion Conference*, p. 4561, 2016. 215

[241] J.F Bourgouin and D. Durox and T. Schuller and J. Beaunier and S. Candel, "Ignition dynamics of an annular combustor equipped with multiple swirling injectors ," *Combust. Flame*, pp. 1–54, Feb. 2013. 215, 217, 219, 220, 239, 247

[242] M. Philip, M. Boileau, R. Vicquelin, T. Schmitt, D. Durox, J.-F. Bourgouin, and S. Candel, "Simulation of the Ignition Process in an Annular Multiple-Injector Combustor and Comparison With Experiments," *J. Eng. Gas Turb. and Power* , vol. 137, pp. 031501–9, Mar. 2015. 215, 247

[243] M. Philip, M. Boileau, R. Vicquelin, E. Riber, T. Schmitt, B. Cuenot, D. Durox, and S. Candel, "Large eddy simulations of the ignition sequence of an annular multiple-injector combustor," *Proc. Combust. Inst.* , vol. 35, no. 3, pp. 3159 – 3166, 2015. 215, 274

[244] K. Prieur, D. Durox, J. Beaunier, T. Schuller, and S. Candel, "Ignition dynamics in an annular combustor for liquid spray and premixed gaseous injection," *Proc. Combust. Inst.* , vol. 36, no. 3, pp. 3717–3724, 2017. 217, 219, 220, 221, 223, 247, 271

[245] T. Lancien, K. Prieur, D. Durox, S. Candel, and R. Vicquelin, "Large eddy simulation of light-round in an annular combustor with liquid spray injection and comparison with experiments," *J. Eng. Gas Turb. and Power* , vol. 140, no. 2, p. 021504, 2018. 217, 219, 221, 223, 247, 252, 253, 271

[246] T. Lancien, K. Prieur, D. Durox, S. Candel, and R. Vicquelin, "Leading point behavior during the ignition of an annular combustor with liquid n-heptane injectors," *Proc. Combust. Inst.* , 2018. 217, 218, 247, 252, 253, 271

[247] Y.-H. Kao, M. Denton, X. Wang, S.-M. Jeng, and M.-C. Lai, "Experimental spray structure and combustion of a linearly-arranged 5-swirler array," in *ASME Turbo Expo 2015: Turbine Technical Conference and Exposition*, pp. V04AT04A038–V04AT04A038, American Society of Mechanical Engineers, 2015. 218

[248] E. Machover and E. Mastorakos, "Experimental investigation on spark ignition of annular premixed combustors," *Combust. Flame*, vol. 178, pp. 148–157, 2017. 218, 219, 247

[249] E. Machover and E. Mastorakos, “Spark ignition of annular non-premixed combustors,” *Experimental Thermal and Fluid Science*, vol. 73, pp. 64–70, 2016. 219, 221, 222

[250] E. Machover and E. Mastorakos, “Numerical investigation of the stochastic behavior of light-round in annular non-premixed combustors,” *Combust. Sci. Technol.* , vol. 189, no. 9, pp. 1467–1485, 2017. 222

[251] J.-F. Bourgouin, *Dynamique de flamme dans les foyeres annulaires comportant des injecteurs multiples.* PhD thesis, Ecole Centrale de Paris (EM2C), 2014. 248

[252] D. Barre, L. Esclapez, M. Cordier, E. Riber, B. Cuenot, G. Staffelbach, B. Renou, A. Vandel, L. Y. Gicquel, and G. Cabot, “Flame propagation in aeronautical swirled multi-burners: Experimental and numerical investigation,” *Combust. Flame*, vol. 161, no. 9, pp. 2387 – 2405, 2014. 274

Appendices

Appendix A

Derivation of the combustion-plasma chemistry

In order to couple combustion and plasma chemistries, two chemical mechanisms must be merged: PLASMA38 and COMB25. COMB25 has been derived starting from the detailed LLNL mechanism [159] using a DRGEP method and Quasi-Steady State Approximations (QSSA) [23, 24]. It is made of 25 transported species (for which conservation equations are solved), 292 irreversible reactions and 16 species in QSSA (for which concentrations are calculated analytically). It is dedicated to propane combustion in air. Thermodynamic properties have been extracted from the NASA database [135] and extrapolated to $20,000\ K$ when necessary. The original set of plasma chemical reactions [132] contains 38 species and 334 irreversible reactions and has already been successfully used in previous plasma studies [164]. It is a comprehensive concatenation of elementary plasma reactions extracted from several publications of reference [133, 134, 165].

Hereafter are gathered details about the merging procedure leading to the mechanism named MERGED34 made of 586 irreversible reactions, 29 species in QSSA and 34 transported species.

- Among the 34 transported species of MERGED34, 14 species are essential as they appear in both combustion and plasma chemistries and constitute the coupling between the two chemistries: N_2, CH_2O, H, H_2, O, OH, H_2O, O_2, CO, CH_2, CO_2, CH_3, CH_4 and C_2H_2. 9 transported species come exclusively from the plasma database (C, N, C_2, CN, NH, NO, C_2H, NH_2, NCO) and 11 from the combustion part (HO_2, C_2H_4, C_2H_6, CH_2CO, C_3H_3, C_3H_4-A, H_2O_2, C_3H_5-A, C_3H_6, C_3H_8, C_4H_{10}).

- Among the 29 species in QSSA of MERGED34, 13 are charged species coming from PLASMA38 (e^-, H^+, C^+, O^+, N^+, O^-, H^-, CO^+, N_2^+, NO^+, O_2^+, OH^+, O_2^-). The remaining 16 species come from COMB25 (CH, CHO, CH_2GSG, CH_3O, $HCCO$, C_2H_3, CH_2CHO, C_2H_5, C_2H_3O-2, CH_3CO, C_3H_2, N-C_3H_7, $C_3H_6OOH_2$-1, I-C_3H_7, N-$C_3H_7O_2$, I-$C_3H_7O_2$).

- Among the 586 irreversible reactions of MERGED34, 40 reactions are common to both combustion and plasma databases:

$O{+}CO_2 \rightarrow CO{+}O_2$	$CO{+}O_2 \rightarrow O{+}CO_2$
$OH{+}H_2 \rightarrow H_2O{+}H$	$H_2O{+}H \rightarrow OH{+}H_2$
$OH{+}OH \rightarrow H_2O{+}O$	$H_2O{+}O \rightarrow OH{+}OH$
$H{+}O_2 \rightarrow O{+}OH$	$O{+}OH \rightarrow H{+}O_2$
$CH_2{+}O_2 \rightarrow H{+}H{+}CO_2$	$H{+}H{+}CO_2 \rightarrow CH_2{+}O_2$
$CH_2{+}O_2 \rightarrow CH_2O{+}O$	$CH_2O{+}O \rightarrow CH_2{+}O_2$
$CH_2{+}H_2O \rightarrow CH_3{+}OH$	$CH_3{+}OH \rightarrow CH_2{+}H_2O$
$HCO{+}H \rightarrow CO{+}H_2$	$HCO{+}HCO \rightarrow CH_2O{+}CO$
$HCO{+}OH \rightarrow H_2O{+}CO$	$HCO{+}CH_3 \rightarrow CH_4{+}CO$
$CH_3{+}O_2 \rightarrow CH_2O{+}OH$	$CH_2O{+}OH \rightarrow CH_3{+}O_2$
$CH_3{+}OH \rightarrow CH_2O{+}H_2$	$CH_2O{+}H_2 \rightarrow CH_3{+}OH$
$O{+}CH \rightarrow H{+}CO$	$H{+}CO \rightarrow O{+}CH$
$CH_4{+}O \rightarrow CH_3{+}OH$	$CH_3{+}OH \rightarrow CH_4{+}O$
$CH_4{+}OH \rightarrow CH_3{+}H_2O$	$CH_3{+}H_2O \rightarrow CH_4{+}OH$
$HCO{+}H_2 \rightarrow CH_2O{+}H$	$CH_2O{+}H \rightarrow HCO{+}H_2$
$CO_2{+}H \rightarrow CO{+}OH$	$CO{+}OH \rightarrow CO_2{+}H$
$CH_2{+}CH_4 \rightarrow CH_3{+}CH_3$	$CH_3{+}CH_3 \rightarrow CH_2{+}CH_4$
$H{+}CH_4 \rightarrow H_2{+}CH_3$	$H_2{+}CH_3 \rightarrow H{+}CH_4$
$CH_2{+}H \rightarrow CH{+}H_2$	$CH{+}H_2 \rightarrow CH_2{+}H$
$CH_2O{+}OH \rightarrow HCO{+}H_2O$	$HCO{+}CH_4 \rightarrow CH_2O{+}CH_3$

- When species are found in both databases, thermodynamic and transport properties of common species are taken from the combustion database. The same applies to rate coefficients of common reactions. In practice, differences are found to be negligible and do not affect the behaviour of the final merged mechanism.

Appendix B

Article on spark ignition (phase 1 of ignition)

F. Collin-Bastiani et al., DNS of spark ignition using Analytically Reduced Chemistry including plasma kinetics, Proceedings of the Combustion Institute (2018), https://doi.org/10.1016/j.proci.2018.07.008

DNS of spark ignition using Analytically Reduced Chemistry including plasma kinetics

F. Collin-Bastiani[a,c,*], O. Vermorel[a], C. Lacour[b], B. Lecordier[b], B.Cuenot[a]

[a] *CERFACS, 42 Avenue Gaspard Coriolis, 31057 Toulouse, France*
[b] *Normandie Univ, UNIROUEN, INSA Rouen, CNRS, CORIA, 76000 Rouen, France*
[c] *Safran Aircraft Engines, Rond-point Rene Ravaud, 77550, Moissy-Cramayel, France*

Abstract

In order to guarantee good re-ignition capacities in case of engine failure during flight, it is of prime interest for engine manufacturers to understand the physics of ignition from the spark discharge to the full burner lightning. During the ignition process, a spark plug delivers a very short and powerful electrical discharge to the mixture. A plasma is first created before a flame kernel propagates. The present work focuses on this still misunderstood first instants of ignition, i.e. from the sparking to the flame kernel formation. 3D Direct Numerical Simulations of propane-air ignition sequences induced by an electric discharge are performed on a simple anode-cathode set-up. An Analytically Reduced Chemistry (ARC) including 34 transported species and 293 reversible reactions is used to describe the coupled combustion and plasma kinetics. The effect of plasma chemistry on the temperature field is found to be non-negligible up to a few microseconds after the spark due to endothermic dissociation and ionization reactions. However its impact on the subsequent flame kernel development appears to be weak in the studied configuration. This tends to indicate that plasma chemistry does not play a key role in ignition and may be omitted in numerical simulations.

Keywords:
Spark ignition, Plasma kinetics, Analytically Reduced Chemistry

---

[*] Corresponding author:
Email address: `felix.collin@cerfacs.fr`
(F. Collin-Bastiani)

1. Introduction

In the current environmental context, major efforts are being made by the aeronautical industry to limit pollutant emissions such as NO_x, CO_2, or CO. An efficient solution to reduce NO_x formation is to operate at low temperature in the combustor primary zone by decreasing the mixture equivalence ratio. An important challenge for these low-NO_x combustors is to ensure operability and in particular relight capability in case of engine failure. Understanding the physics of spark ignition in flight conditions is therefore of prime interest for engine manufacturers. Spark ignition in an aeronautical engine can be divided in three main phases. The first phase is the kernel formation following the electric discharge at the spark plug; the second phase is the growth and propagation of the flame kernel up to the nearest fuel injector [1] and the third one is the intersector flame propagation [2]. The present study focuses on the first phase, i.e. the early instants of ignition, which has been rarely addressed in the literature [3–5]. At this stage, the very small scale of the kernel allows to use Direct Numerical Simulation (DNS) to describe and understand the main mechanisms driving this complex transient phenomenon.

In this first phase of ignition, a spark plug delivers a very short and powerful electrical discharge to the mixture, inducing the creation of a high temperature plasma [6] for a very short time and a subsequent propagating shock. This plasma has thus a thermal effect, a mechanical effect associated to the shock, and finally triggers a high chemical activity. To describe this last effect, suitable chemical kinetics should be used. Detailed mechanisms are however too complex and CPU-time consuming to be directly integrated in 3D DNS. One affordable solution is to use Analytically Reduced Chemistry (ARC) which keeps the main chemical paths of interest. ARCs have already been successfully used in the context of combustion [7, 8] and are particularly well suited for the study of ignition.

In this work, 3D DNS of the flame formation following the electric discharge in a simple configuration (two facing electrodes) using an ARC coupling combustion and plasma kinetics is performed. The objective is to study the effect of the plasma phase on ignition, in particular in terms of chemistry.

First, the derivation and validation of two ARCs are detailed (one for combustion only and another one describing both combustion and plasma chemistries), as well as the associated thermodynamic and transport properties. The development of an appropriate energy deposition model needed to mimic the spark discharge is then presented. Finally, DNS of the anode-cathode configuration are performed with and without plasma chemistry. Results are compared and analysed in terms of temperature and mixture composition evolution to understand the impact of the plasma phase.

2. Analytically Reduced chemistries

2.1. Combustion chemistry

Using a DRGEP method and Quasi-Steady State Approximations (QSSA) [7, 9], an ARC (called COMB25) made of 25 transported species (for which conservation equations are solved), 146 reversible reactions and 16 species in QSSA (for which concentrations are calculated analytically), dedicated to propane combustion in air, has been derived starting from the detailed LLNL mechanism [10]. Thermodynamic properties have been extracted from the NASA database [11] and extrapolated to $20,000\ K$ when necessary. For validation, COMB25 was used to compute laminar unstrained premixed flames at 1 bar and 298 K [12, 13]. A very good agreement with both the detailed mechanism and experimental data was obtained with less than 5 % relative error for equivalence ratios $0.6 < \phi < 1.4$. Mass fraction profiles of important species, such as C_3H_8, CO_2, CO but also OH and O that are known to be important for ignition, are also well predicted. In addition, ignition delay times at 1 bar and $\phi = 1$ were well recovered with relative errors under 15 % for $1,100\ K < T < 2,000\ K$ compared to both the detailed mechanism and experimental data [14].

2.2. Combustion-plasma chemistry

The original set of plasma chemical reactions [15], called PLASMA38 hereafter, contains 38 species and 183 reversible reactions and has been successively used in previous plasma studies [16]. PLASMA38 is here assessed at temperatures where ionization and dissociation reactions take place, i.e. for $T > 3,000\ K$. Constant pressure reactors are advanced in time and the final compositions obtained with the software Cantera [17] are compared to reference solutions given by the NASA Chemical Equilibrium with Applications (CEA) reference code [18]. Different test cases of increasing complexity have been considered. In the case presented here, the simulation starts at temperature T_{ini} with the equilibrium composition at T_{ini} given by the CEA code. It is then expected that the final temperature T_{final} and final composition X_{final} do not deviate from the initial

Table 1: Validation of PLASMA38. Relative errors between Cantera and CEA on the final temperature T_{final} and species molar fractions X^k_{final} obtained for various values of T_{ini}.

T_{ini} (K)	3,000	5,000	15,000	20,000
ε_T	$5.1\,e^{-4}$	$-3.2\,e^{-4}$	$-1.1\,e^{-2}$	$-7.1\,e^{-3}$
ε_X	$2.3\,e^{-3}$	$9.3\,e^{-3}$	$4.7\,e^{-2}$	$2.1\,e^{-2}$

state. Table 1 shows the relative errors on the temperature ε_T (Eq. 1) and species molar fractions ε_X (Eq. 2) obtained for various values of T_{ini}:

$$\varepsilon_T = \frac{T_{final} - T_{ini}}{T_{ini}} \tag{1}$$

$$\varepsilon_X = \frac{1}{N_{spec}} \sum_{k=1}^{N_{spec}} \frac{X^k_{final} - X^k_{ini}}{X^k_{ini}} \tag{2}$$

In the above expressions, N_{spec} is the number of transported species. In all cases of Tab. 1, the final temperature given by Cantera remains close to T_{ini} with less than 1 % relative error. The composition stays close to the equilibrium composition at T_{ini} with errors under 5 %. The electro-neutrality is preserved as well. Other test cases not presented here showed that even starting with a composition different from the equilibrium composition, the equilibrium state is recovered with good accuracy. This validates the plasma chemistry and associated thermodynamics in the tested conditions.

To couple combustion and plasma chemistries, PLASMA38 is simply merged to COMB25. All 13 charged species of PLASMA38, known to be very reactive, are put in QSSA. The resulting merged mechanism (named MERGED34) is finally made of 293 reversible reactions, 29 species in QSSA and 34 transported species. Among them, 13 species are essential as they appear in both combustion and plasma chemistries and constitute the coupling between the two chemistries. The merged mechanism was first evaluated for $T < 3,000\ K$ where combustion only is expected. MERGED34 was compared to the detailed LLNL mechanism and to COMB25 in terms of both laminar flame speed at 1 bar and 298 K and ignition delay time at 1 bar and $\phi = 1$ (not shown). No difference was observed confirming that plasma chemistry does not interfere with combustion chemistry at low temperatures. Similarly to PLASMA38, validations of MERGED34 at higher temperatures are based on constant pressure reactors simulated with Cantera, starting with a stoichiometric $C_3H_8 - air$ mixture at $T_{ini} = 300\ K$, and progressively increasing temperature up to $T_{final} = 10,000\ K$. The final composition is compared to the equilibrium composition at T_{final} given by the CEA code. The relative errors ε^k_X (Eq. 3) on the final molar fractions of the 4 major transported species k remaining at this temperature, are given in Tab. 2.

Table 2: Validation of MERGED34. Relative errors ε^k_X between Cantera and CEA on the molar fractions of the 4 major transported species k, starting with a stoichiometric $C_3H_8 - air$ mixture at $T_{ini} = 300\ K$.

species	C	N	O	H
ε^k_X	0.17	0.07	0.015	0.037

$$\varepsilon^k_X = \frac{X^k_{final} - X^k_{eq}(T_{final})}{X^k_{eq}(T_{final})} \tag{3}$$

An overall good agreement is obtained for the considered species. The mean relative error is 7 % with a maximum of 17 % for the atomic carbon molar fraction. These relative errors are acceptable for the targeted application of this work. This shows that the addition of species coming from the combustion scheme does not change high temperature chemical equilibrium.

3. Energy deposition model

The first phase of spark ignition can be itself divided in 3 main phases [5, 6, 19, 20]: during breakdown ($1 - 10\ ns$), a small amount of energy is delivered to the mixture. The energy deposition density is high as it occurs in a very small volume and for a very short time, and is very efficient. Temperatures up to $20,000\ K$ or more can then be reached in the inter-electrode zone leading to an intense shock wave, molecular dissociations and the creation of a radical pool. Following the breakdown, the arc phase lasts longer ($\approx 1\ \mu s$), but with lower energy deposition density and efficiency. Finally, the glow phase is characterized by a lower power compared to the arc phase and important losses due to conduction to the electrodes. However, the long duration of the glow phase ($\approx 1\ ms$) allows to transfer significant energy to the gas. This transfer is slow enough to allow the mixture to cool down by heat diffusion.

To properly model the phenomenology of a spark, an adaptation of the 1-step Energy Deposition (ED) model is used here [21]. It is based on a volumic source term $\dot{Q}$ added to the energy transport equation. Energy is deposited in 2 steps: the breakdown phase and the merged arc and glow phases, called glow hereafter for simplicity. The breakdown is too short to allow detailed measurements but the amount of electrical energy provided during this phase E_{bd} as well as the phase duration t_{bd} are known from experiments [22]. For the glow phase, the total electrical energy E_{glow} as well as the phase duration t_{glow} are also given experimentally [22]. In addition, it is observed that the electrical power is almost linearly decreasing. From these experimental observations, the time derivative of the electrical energy given to the electrodes $E_s(t)$ during the breakdown (Eq. 4) and glow (Eq. 5) phases are written respectively:

$$\frac{dE_s(t)}{dt} = \frac{E_{bd}}{t_{bd}} \tag{4}$$

$$\frac{dE_s(t)}{dt} = \frac{2\,E_{glow}}{{t_{glow}}^2}(t_{spark} - t). \tag{5}$$

with t_{spark} the end of the spark. The actual energy $E_{ign}(t)$ transferred to the mixture is then obtained by applying breakdown and glow efficiency coefficients:

$$E_{ign}(t) = \eta\, E_s(t) \tag{6}$$

$$E_{ign}(t) = \zeta\, E_s(t) \tag{7}$$

where η and ζ are estimated to 95 % and 30 % respectively, following the literature [6, 23–25]. The energy deposition volume is approximated by a cylinder between the two electrodes as represented in Fig.1.

4. Application to an anode-cathode configuration

4.1. Configuration and numerical set-up

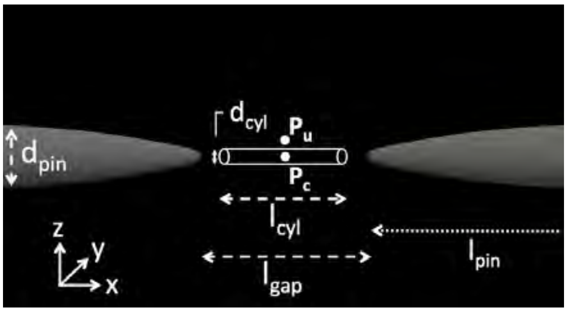

Figure 1: Sketch of the studied anode-cathode configuration.

The configuration studied here is an academic setup experimented at CORIA laboratory [22, 26]. It is made of two facing parabolic electrodes of length l_{pin} = 2.2 *cm* as illustrated in Fig. 1, with radius of curvature of 150 μm. The maximum diameter of the electrodes is d_{pin} = 1.6 *mm* and the electrode gap is l_{gap} = 3 *mm*. The volume is initially filled with an inert flammable propane-air mixture at $\phi = 0.75$ and at atmospheric conditions. Neglecting the temperature gradient between the two electrode heads, the configuration has a spherical symmetry (P_c [0,0,0] is the symmetry point). The numerical domain is thus reduced to $1/8^{th}$ of a sphere of radius 10 *cm*. The electrode surfaces are modelled as no-slip adiabatic walls. Indeed, losses at the walls are already accounted for by the efficiency coefficients η and ζ. The simulation is performed on a 2.1 million tetrahedral cells mesh with a characteristic grid size of 15 μm in the inter-electrodes gap. Such a small grid size is required during the breakdown phase to resolve the strong gradients and chemical source terms.

Table 3: Parameters for the ED model.

E_{bd}	5.0 mJ
t_{bd}	20 ns
E_{glow}	85 mJ
t_{glow}	2.6 ms

Simulations were performed with the code AVBP co-developed by CERFACS and IFPEN (www.cerfacs.fr/avbp7x). The second-order explicit Lax & Wendroff scheme was used with a time step imposed by the CFL number but also by the chemical system: time steps range from 0.2 *ns* during the breakdown phase to 2.5 *ns* in the glow phase. Chemistry sub-cycling was also used to improve the stability of the explicit time integration scheme. The ED model presented in Sec.3 was applied with parameters summarized in Tab. 3. The breakdown time t_{bd} was fixed at 20 *ns*, according to Lacour et al. [22]. The length of the energy deposition cylinder l_{cyl} is 2.4 *mm* and its diameter d_{cyl} is 150 μm, following experimental recommendations.

4.2. C_3H_8-air ignition sequence

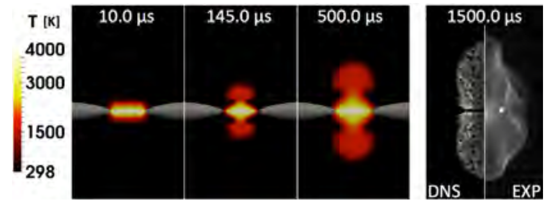

Figure 2: (Left): Temperature fields at 3 instants after the start of the ignition sequence, using COMB25. The same temperature fields are obtained with MERGED34 and are thus not shown. (Right): Integrated flame emission 1.5 *ms* after the ignition starts obtained numerically (with COMB25) and experimentally.

Two simulations were performed using COMB25 and MERGED34 to assess the impact of plasma kinetics on the ignition sequence. A first qualitative description of the flow motion during the ignition sequence with COMB25 is proposed in Fig. 2 (Left). The same evolution is observed with MERGED34 (not shown). After

10 μs, the flow is still governed by the gas expansion and the shock induced by the energy deposited during the breakdown. In later times, the depression following the shock wave induces an inward flow along the electrodes, forcing the hot gas region to expand in the radial direction (500 μs). This results in an elongated flame shape, forming a torus around the electrodes axis. Then the flame progressively evolves to a classical spherical flame, as observed experimentally.

During the ignition sequence, temperature and pressure in the energy deposition zone reach very high levels in a few nanoseconds. Such short time-scales must be reproduced by the ignition model, as does the 2-step ED model used in this work. Indeed, a simple 1-step model would delay too much the energy supply leading to an overestimation of the ignition time. Besides, the initial flame propagation is directly dictated by the convective motion induced by the shock. Considering a too large deposition volume would lead to a too weak shock and a wrong initial flame motion. To assess the validity of the ED model, the numerical ignition sequence is qualitatively compared to experimental visualizations (Fig. 2 Right) in terms of flame evolution at longer time ($\geq$ 1 ms). A good agreement is obtained, in particular in terms of flame velocity in the radial direction.

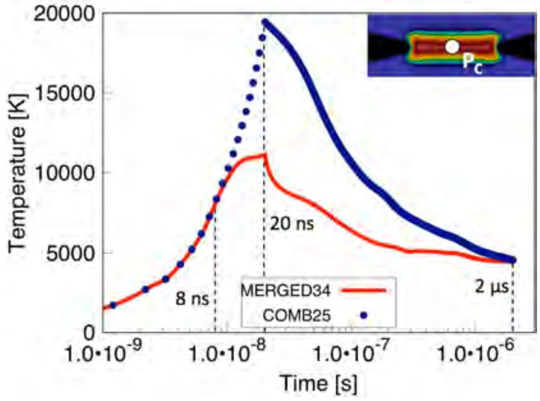

Figure 3: Evolution of the temperature at P_c versus time during the ignition sequence using MERGED34 and COMB25.

In order to quantify the impact of plasma kinetics, the time evolution of the temperature at P_c with and without plasma chemistry is displayed in Fig. 3 during the first 2 μs. To explain why plasma kinetics impact so drastically the temperature field, radial profiles (starting from P_c) of temperature and O_2, O, N_2 and N mass fractions obtained with MERGED34 are presented in Fig. 4 (top). Absolute differences between results of MERGED34 and COMB25 are also shown in Fig. 4 (bottom). 8 ns after ignition starts, the level of O_2 is similar in both simulations even if the temperature is high, close to $8,000$ K. Indeed, COMB25 contains part of the dissociation reactions such as H+O_2 $\rightarrow$ O+OH or OH+O_2 $\rightarrow$ HO_2+O. On the contrary, N_2 dissociation is present only in MERGED34. As N_2 dissociation has not started yet, no significant difference in mixture composition is observed explaining the similar temperature with both chemistries. After 20 ns, the dissociation process of O_2 is almost completed with MERGED34 as observed in Fig. 4: at P_c $[z = 0]$, $Y_{O_2} = 0.003$ and $Y_O = 0.16$. The conversion rate of O_2 into mono-atomic O is around 72 %. On the contrary, with COMB25, the dissociation process of O_2 is incomplete: $Y_{O_2} = 0.02$ at P_c and the O_2-O conversion rate is around 64 %. This is due to the simplified O_2 dissociation chemical pathways in COMB25, which produce OH instead of O. Around 36 % of the mass of oxygen atom is stored in other forms such as OH or CO. In MERGED34, where all O_2 dissociation chemical pathways are included, a smaller portion of the mass of oxygen atom, around 28 %, is stored in OH, CO, NO but also O^+ as ionisation reactions appear above $10,000$ K. Nevertheless, this discrepancy in the O_2 dissociation process remains small. The major difference between the two simulations concerns N_2 dissociation that is totally ignored in COMB25 and that starts around $7,500$ K. More than 20 % of the N_2 mass is transformed in N after 20 ns with MERGED34. As dissociation and ionisation reactions are strongly endothermic, neglecting this kinetic activity in COMB25 leads to a higher temperature ($19,200$ K compared to $11,100$ K with MERGED34) at P_c at the end of the breakdown. This thermal difference has a direct consequence on the mechanical effect: the shock amplitude is much higher with COMB25 (P_{max} = 84 bar) than with MERGED34 (P_{max} = 60 bar). At 2 μs, the exothermic recombination of N_2 is almost completed and the radial profiles of species mass fractions in both simulations are again very close leading to similar temperature levels ($\approx 4,500$ K) at P_c. From this moment, plasma effects become negligible again as temperature is too low to activate plasma reactions.

The impact of plasma chemistry on the heat release during ignition is shown in Fig. 5. Until the end of the breakdown, temperatures are very high with mostly endothermic reactions, so that only the negative heat release contribution is displayed in Fig. 5 a. At later times, exothermic combustion reactions occur and only the positive heat release contribution is displayed in Fig. 5 b. After 20 ns (i.e. at the end of the breakdown), the negative heat release is strong in the region heated by the energy deposition with MERGED34, indicating

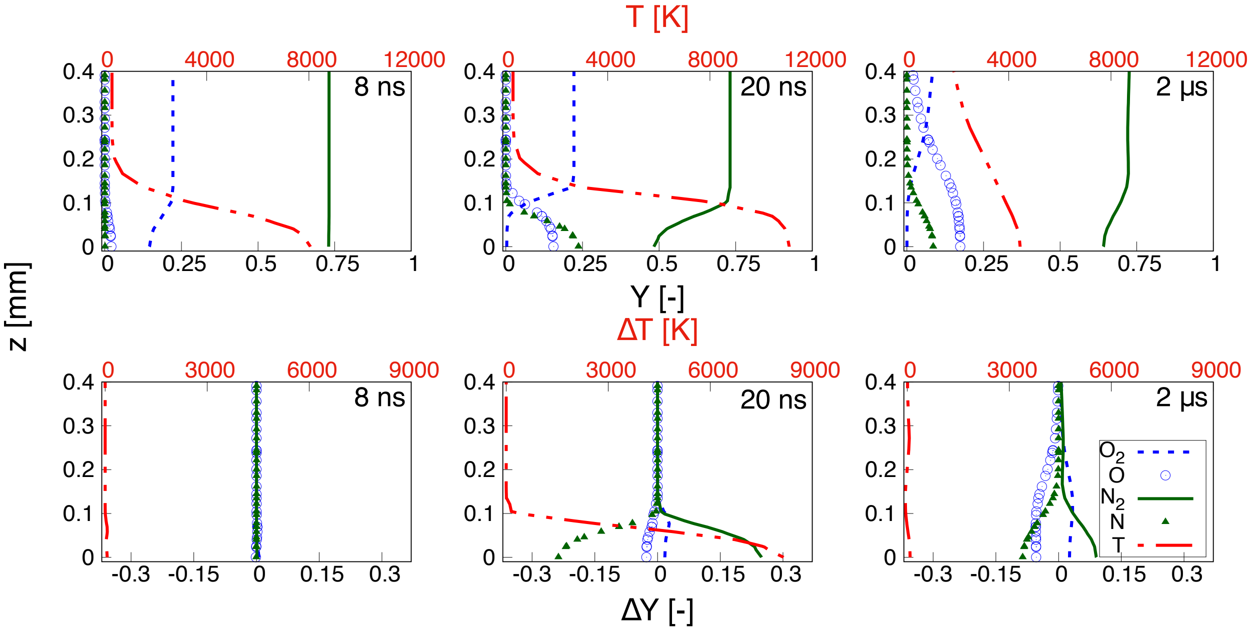

Figure 4: Radial profiles (at $x = 0$) of temperature and species mass fraction obtained with MERGED34 at three different instants of the ignition sequence (top) and absolute differences between calculations with COMB25 and MERGED34 (bottom). $\Delta T = T_{COMB25} - T_{MERGED34}$; $\Delta Y = Y_{COMB25} - Y_{MERGED34}$.

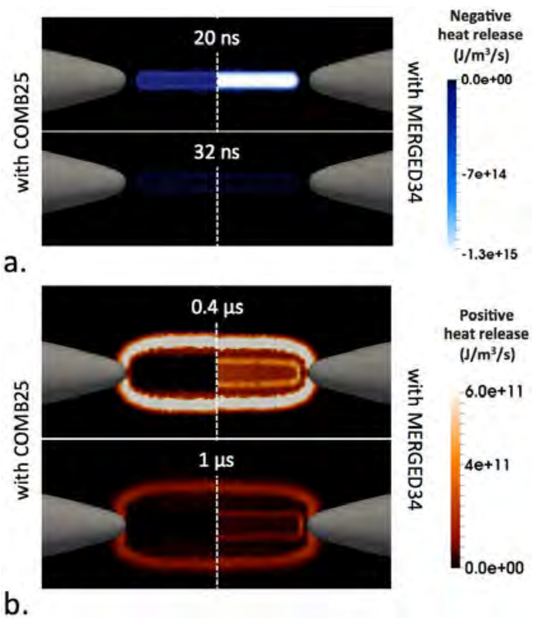

Figure 5: Fields of negative (a) and positive (b) heat release at different instants of the ignition sequence with the kinetic schemes COMB25 (left halves) and MERGED34 (right halves).

strong dissociation or ionization reactions. As already discussed, negative heat release is also present but lower using COMB25. After the end of the breakdown, the temperature starts to fall rapidly. At 32 ns, i.e., 12 ns after the end of the breakdown, the order of magnitude of negative heat release in the inter-electrode region has been reduced by a factor 100 showing that endothermic reactions have stopped. After tens of nanoseconds, first exothermic reactions appear. Two zones of reaction are highlighted in Fig. 5 (b): i) a zone of exothermic reactions around the energy deposition region, only present with MERGED34. This zone corresponds to molecule recombinations during the temperature drop following the breakdown phase. ii) An outer envelop of exothermic reactions, similar in both simulations. This positive heat release corresponds to the propagating flame created by the runaway of combustion reactions triggered at the border of the energy deposition zone by the hot gas kernel. Indeed, at this position, the temperature elevation is moderate ($1,000\ K < T < 2,000\ K$), too low to activate plasma chemistry but high enough for the mixture to burn.

Figure 6 provides a more detailed analysis of the flame initiation at points P_c and P_u (respectively in the center and just above the energy deposition zone, see Fig. 1). At P_c, combustion starts very rapidly ($2-3\ ns$) in a perfectly mixed reactor regime and C_3H_8 is fully consumed after around 5 ns, i.e. before the activation of plasma chemistry. As a consequence, even though plasma kinetics have the largest thermal impact at P_c, they have no impact on the fuel consumption as shown by the two similar evolutions of the C_3H_8 mass fraction. In fact, the whole oxidation process is similar as evidenced by the evolutions of other species, such as C_3H_3. Differences on radical species appear later, after 10 ns, when temperature is high. As already explained, the O-OH balance is not well described by COMB25, but at this time, the local combustion is totally completed so that it is not affected by these radical differences. The contribution of the dissociated species C, ignored by the COMB25, is also marginal. At point P_u where combustion occurs in a propagating premixed flame regime, discrepancies are also small. O and C mass fractions tend to increase after the flame passage as temperature rises slowly by diffusion from the energy deposition zone. Conversely, remaining O_2 progressively decreases due to dissociation reactions. The main impact of plasma kinetics is however observed at P_u: the over prediction of OH and O mass fractions causes slightly earlier combustion (see C_3H_8 and O_2 profiles). As P_u is still in a high temperature plasma zone, the slight difference on the O-OH balance is also visible.

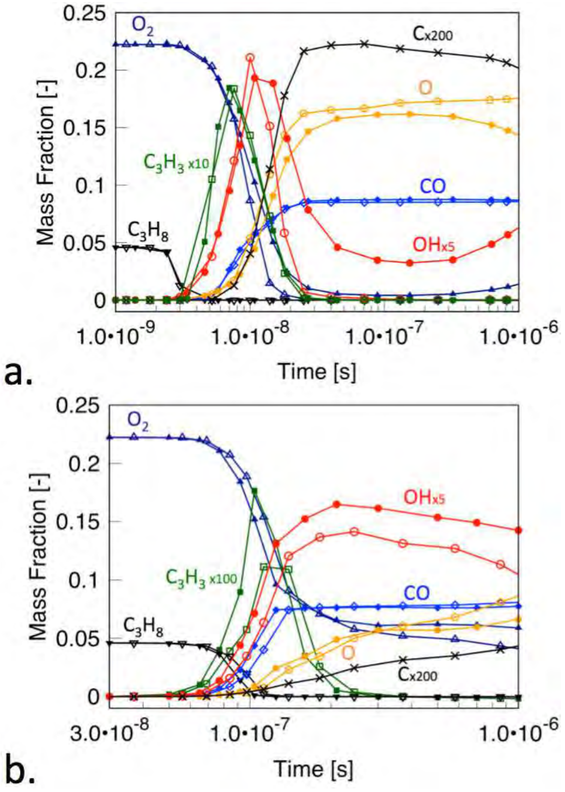

Figure 6: Evolution of relevant species mass fractions over time at points P_c (a) and P_u (b). P_u is located 0.31 mm above P_c in the radial direction, see Fig. 1. Filled symbols are for COMB25 and empty symbols for MERGED34. Species C is only present in MERGED34.

Plasma reactivity during ignition is then proven true, but limited in time and space. Its influence on the flame initiation is extremely small: the initial position of the flame kernel observed in Fig. 5 (b) is hardly modified by plasma chemistry. Thus, no significant difference in temperature fields is observed with or without plasma chemistry after tens of microseconds: the flame propagation speed and direction are similar and the flame appears to be independent of plasma reactions.

5. Conclusions

Two Analytically Reduced Chemistries along with an appropriate Energy Deposition model have been derived to study the impact of plasma kinetics during ignition using DNS of propane-air ignition in an anode-cathode configuration. First, the importance of the ED model has been highlighted: the short temporal and spatial scales of spark ignition should be reproduced by the model to correctly catch initial flame position and propagation velocity. The impact of plasma chemistry on the mixture temperature and composition is clearly demonstrated during the first microseconds of ignition, significantly lowering the temperature in the narrow energy deposition zone between electrodes by way of endothermic dissociation reactions. However, the contribution of plasma chemistry to combustion initiation is marginal as most radical production at high temperature appears after fuel oxidation starts, and the increase of radicals in the plasma is not sufficient to modify combustion chemistry. Nevertheless, results show that the accuracy of the chemical description of combustion is of prime importance to catch the correct ignition delay time and initial flame kernel propagation. In this context, Analytically Reduced Chemistries such as COMB25, in particular containing O_2 dissociation, represent a good compromise between accuracy and cost and are a promising approach to study complex chemical phenomenon in flames.

6. Acknowledgments

The authors thank P. Teulet from LAPLACE Laboratory (Toulouse, France) for providing the initial set of plasma reactions and P. Pepiot-Desjardins from Cornell University for the help and support with the YARC reduction tool. The authors gratefully acknowledge the financial support from Safran Aircraft Engines and the Agence Nationale de la Recherche (ANR) under the project FAMAC ANR-12-VPTT-0002. This work was granted access to the HPC resources of TGCC, CINES and IDRIS under the allocation A0032B10157 made by GENCI.

References

[1] E. Mastorakos, Prog. Energy Combust. Sci. 35 (1) (2009) 57–97.

[2] M. Philip, M. Boileau, R. Vicquelin, E. Riber, T. Schmitt, B. Cuenot, D. Durox, S. Candel, Proc. Combust. Inst. 35 (3) (2015) 3159–3166.

[3] T. Kravchik, E. Sher, Combust. Flame 99 (3) (1994) 635–643.

[4] K. Kailasanath, E. Oran, J. Boris, Combust. Flame 47 (1982) 173–190.

[5] S. Refael, E. Sher, Combust. Flame 59 (1) (1985) 17–30.

[6] R. Maly, M. Vogel, Proc. Combust. Inst. 17 (1) (1979) 821–831.

[7] T. Jaravel, E. Riber, B. Cuenot, G. Bulat, Proc. Combust. Inst. 36 (3) (2017) 3817–3825.

[8] B. Franzelli, E. Riber, B. Cuenot, C. R. Mécanique 341 (1-2) (2013) 247–256.

[9] P. Pepiot-Desjardins, H. Pitsch, Combust. Flame 154 (1) (2008) 67–81.

[10] H. J. Curran, P. Gaffuri, W. J. Pitz, C. K. Westbrook, Combust. Flame 129 (3) (2002) 253–280.

[11] B. J. McBride, S. Gordon, M. A. Reno, Coefficients for calculating thermodynamic and transport properties of individual species, Report No. TM-4513, NASA, 1993.

[12] G. Jomaas, X. Zheng, D. Zhu, C. Law, Proc. Combust. Inst. 30 (1) (2005) 193–200.

[13] C. M. Vagelopoulos, F. N. Egolfopoulos, Proc. Combust. Inst. 27 (1) (1998) 513–519.

[14] D. C. Horning, D. Davidson, R. Hanson, J. Propul. Power 18 (2) (2002) 363–371.

[15] P. Teulet, J. Gonzalez, A. Mercado-Cabrera, Y. Cressault, A. Gleizes, J. Phys. D: Applied Physics 42 (17) (2009) 175–201.

[16] P. Teulet, J. Gonzalez, A. Mercado-Cabrera, Y. Cressault, A. Gleizes, J. Phys. D: Applied Physics 42 (18) (2009) 185–207.

[17] D. G. Goodwin, H. K. Moffat, R. L. Speth, available at http://www.cantera.org (2017).

[18] B. J. McBride, S. Gordon, Computer program for calculation of complex chemical equilibrium compositions and applications ii. users manual and program description., Report No. 1311, NASA, 1994.

[19] M. Lim, R. Anderson, V. S. Arpaci, Combust. Flame 69 (3) (1987) 303–316.

[20] E. Sher, J. Ben-Ya'ish, T. Kravchik, Combust. Flame 89 (2) (1992) 186–194.

[21] G. Lacaze, E. Richardson, T. Poinsot, Combust. Flame 156 (10) (2009) 1993–2009.

[22] C. Lacour, A. Lo, J. Marrero, F. Lefebvre, P. Vervisch, A. Cessou, B. Lecordier, Proc. Appli. Laser Imaging Tech. Fluid Mech.

[23] B. Sforzo, A. Lambert, J. Kim, J. Jagoda, S. Menon, J. Seitzman, Combust. Flame 162 (1) (2015) 181–190.

[24] T. Mantel, Contribution à la modélisation de la combustion dans les moteurs à allumage commandé avec prise en compte de la phase d'allumage, Ph.D. thesis, Université de Rouen, France, 1993.

[25] C. Ternel, Contribution au développement de l'allumage par laser pour les moteurs à combustion interne, Ph.D. thesis, Université de Rouen, France, 2006.

[26] A. Lo, A. Cessou, C. Lacour, B. Lecordier, P. Boubert, D. Xu, C. Laux, P. Vervisch, Plasma Sources Sci. Tech. 26 (4).

Appendix C

Article on spray ignition (phase 2 of ignition)

F. Collin-Bastiani et al., A joint experimental and numerical study of ignition in a spray burner, Proceedings of the Combustion Institute (2018), https://doi.org/10.1016/j.proci.2018.05.132

A joint experimental and numerical study of ignition in a spray burner

F. Collin-Bastiani[a,c,*], J. Marrero-Santiago[b], E. Riber[a], G. Cabot[b], B. Renou[b], B. Cuenot[a]

[a] *CERFACS, 42 Avenue Gaspard Coriolis, Toulouse 31057, France*
[b] *Normandie Univ., UNIROUEN, INSA Rouen, CNRS, CORIA, 76000 Rouen, France*
[c] *Safran Aircraft Engines, Rond-point René Ravaud, Moissy-Cramayel 77550, France*

Abstract

Partly due to stringent restrictions on pollutant emissions, aeronautical engine manufacturers target lean operating conditions which raise new difficulties such as combustion stability as well as ignition and re-ignition at high altitude. The injection of liquid fuel introduces additional complexity due to the spray-flame interaction. It is then crucial to better understand the physics behind these phenomena and to develop the capacity to predict them in an industrial context. In this work, a comprehensive joint experimental and numerical investigation of the academic swirled-confined version of the KIAI-Spray burner is carried out. Experimental diagnostics, such as Phase Doppler Anemometry (PDA), Planar Laser Induced Fluorescence (OH-PLIF), high-speed visualization and high-speed particle image velocimetry (HS-PIV), together with Large Eddy Simulations coupled to Discrete Particle Simulations are used to study spray flame structure and spray ignition. The analysis of the swirled-stabilized spray flame highlights the main effects of the presence of droplets on the turbulent combustion, and the complementarity and validity of the joint experiment and simulation approach. Ignition sequences are then studied. Both experiment and simulation show the same behaviors, and relate the flame kernel evolution and the possible success of ignition to the local non reacting flow properties at the sparking location, in terms of turbulence intensity and presence of droplets.

Keywords:
Spray Flame, Ignition, Laser Diagnostics, Large Eddy Simulation

---

[*] Corresponding author:
Email address: `felix.collin@cerfacs.fr`
(F. Collin-Bastiani)

Preprint submitted to Proceedings of the Combustion Institute *December 4, 2017*

1. Introduction

The ignition process in gas turbines involves a wide range of parameters which makes it a multi-physical complex problem. New aeronautical burner designs demand a better knowledge of the mechanisms involved to ensure, for instance, re-ignition in altitude of lean-combustion engines. Real combustors operate with liquid fuel, inducing strong variations of local properties in terms of droplet size and velocity, and fuel vapor field. These parameters together with gas flow velocity and turbulence intensity govern the ignition mechanisms. Existing experimental studies on spray ignition [1–5] or investigations on the influence of parameters such as turbulence [6–8] are today still insufficient to identify and understand the real mechanisms of spray ignition. Large Eddy Simulation (LES) has been efficiently used to study such ignition but mostly in gaseous configuration [9, 10]. Coupled experimental and numerical analyses dedicated to spray ignition are therefore necessary to provide a valuable and deeper understanding of the processes taking place.

Ignition in aeronautical engines can be divided into four steps [11]: (i) energy deposition through a spark and its evolution into a flame kernel; (ii) kernel propagation; (iii) flame stabilization on one injector; (iv) injector-to-injector propagation of the flame. Phase (ii) appears to be critical since the flame kernel is exposed, depending on the spark location, to very different local two-phase flow turbulent properties that may be favorable or adverse for its survival. As for gaseous flames, this may be characterized by an ignition probability map. The main objective of this work is to investigate steps (ii) and (iii) of ignition in the presence of a spray in order to better understand and accurately predict spray ignition, which is still a difficult challenge.

To reach this objective, steps (ii)-(iii) of ignition of a single-injector swirled confined jet-spray burner are studied. After first studying the stabilized flame regime, numerical and experimental ignition sequences are compared at one ignition location wisely selected from the experimental ignition probability map. The analysis focuses on the influence of initial flow conditions on the kernel motion and shape as well as on the overall ignition timings.

2. Experimental setup

2.1. Experimental facility

Experiments were carried out in a two-phase flow version of the KIAI burner [12], confined with quartz windows that allow full optical access (Fig. 1 Left).

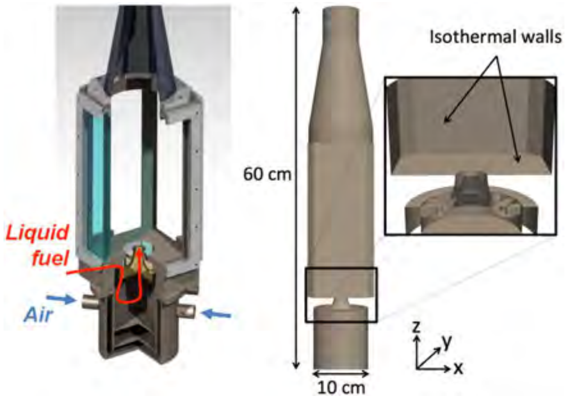

Figure 1: (Left) Cut of the KIAI-Spray burner. (Right) Computational domain for LES with detail of the injection system.

The system is composed of a simplex pressure atomizer (Danfoss, 1.46 kg/h, 80° hollow cone) and an external annular swirling air co-flow with inner and outer diameters of 10 and 20 mm respectively. The radial swirler is composed of 18 rectangular (6 mm x 8 mm) channels inclined at 45° with a corresponding Swirl number of 0.76 [12]. Air and liquid fuel (n-heptane) mass flow rates are controlled by thermal and Coriolis mass flow controllers. Preheated air is injected at temperature $T_{air} = 416 \pm 3\ K$ with a mass flow rate of $\dot{m}_{air} = 8.2\ g/s$ whereas liquid fuel is injected at temperature $T_{fuel} \approx 350\ K$ with a mass flow rate of $\dot{m}_{fuel} = 0.33\ g/s$, leading to a global equivalence ratio $\phi_{glob} = 0.61$ representing ultra-lean conditions. Under these operating conditions and without a flame, the system reaches a stable internal window temperature of $T_{wall} = 387\ K$, which is constantly measured by a thermocouple and controlled to ensure the repeatability of experiments. The mixture is ignited with a laser induced spark, by focusing a 532 nm laser beam in selected locations inside the combustion chamber. The spark properties are detailed in Section 2.3.

2.2. Experimental Diagnostics

PDA measurements were applied to characterize the fuel droplet size and size-classified velocity, as well as the air velocity in reacting conditions. For this, the air was seeded with $\approx 2\ \mu m$ olive oil droplets in order to increase the population of small droplets. The voltage in the photomultipliers was increased to privilege small droplet detection in this case. The group (0 - 5) μm then represented the air velocity due to its low Stokes number. The configuration used was a traditional refractive scattering configuration, detailed in [13].

OH-PLIF was also applied to the reacting flow in order to characterize the spray flame structure and for comparison with simulation. A Nd-YAG-laser operating at 532 nm was used to pump a tuneable dye laser (Quantel TDL90) supplied with Rhodamine 590 dye. The excitation wavelength was tuned to the $Q_1(5)$ transition line of the $A^2\Sigma^+(v' = 1) \leftarrow X^2\Pi(v'' = 0)$ band of OH at = 282.75 nm. The collection system consists of an EmICCD camera (PIMAX 4, Roper Scientific) with two colored glass filters (WG295 and UG11 from Schott). More details are provided in [14].

Regarding the non-reacting flow, HS-PIV was also used to extract the instantaneous 2D velocity fields, since ignition is a transient and stochastic phenomenon. The carrier phase was seeded far upstream with $< 2\,\mu m$ ZrO_2 particles. HS-PIV was applied on the airflow without spray presence on the XZ plane (vertical cut). Provided that the spray is not dense, the droplet presence does not modify significantly the airflow mean velocity; this was demonstrated in [14]. For the sake of concision, the reader is referred to [15] for more details.

2.3. Experimental ignition procedure

An experimental ignition probability map of the chamber was first performed in order to identify the favorable and unfavorable regions for the ignition of the KIAI-Spray burner. The mixture was ignited by a laser-induced spark in selected locations inside the burner using a focused 532 *nm* laser beam. A convergent lens of 200 *mm* focal length was used. The experimental setup is similar to the one used in [6]. The energy deposited by the spark is evaluated around 405 *mJ* from the measurements of the reference and transmitted laser pulse energies with two precision laser pyroelectric energy meters (Ophir: PE-25). This high value was necessary to ensure a wide range of ignition events within the domain in such ultra-lean conditions. The spark can be approximated by an ovoid of $\approx\ 1-2\ mm$. For each spark position, 30 independent ignition tests were performed to build a local ignition probability. In order to characterize the flame development, a CMOS Phantom V2512 high-speed camera was used to capture the kernel motion inside the chamber. The size of the recording region was 1280 x 800 *px*, with a magnification of 0.149 mm/px. The camera acquisition rate was 4 *kHz* with an exposure time of 240 μs. The total spontaneous flame emission was collected by the camera and a 532 *nm* rejection filter blocked the laser light. A dynamic pressure sensor at 10 *kHz* acquired the pressure signal synchronized with the high-speed imaging.

3. Numerical set-up

The KIAI-Spray burner was investigated numerically using LES with the code AVBP co-developed by CERFACS and IFPEN (www.cerfacs.fr/avbp7x). The computational domain displayed in Fig. 1 (Right) contains the inlet pipe, the swirlers, the injection veins, the combustion chamber and the convergent at the outlet. A fully unstructured grid was generated for the stabilized non-reacting and reacting cases, containing more than 60 million tetrahedral cells and where the smallest cells are located in the swirler vanes ($\Delta x = 0.4\ mm$) and in the shear layer region ($\Delta x = 0.3\ mm$). AVBP solves the LES-filtered fully compressible reacting Navier-Stokes equations. For the gas phase, the third order in time and space Taylor-Galerkin scheme [16] was used for the non-reacting and reacting steady flow simulations whereas the second order in time and space Lax-Wendroff scheme [17] was used for ignition sequences to save CPU time. The Navier-Stokes Characteristic Boundary Conditions [18] were used for inlet and outlet boundary conditions while the combustor walls were considered as non-slipping and isothermal ($Tw = 387\ K$ for the non reacting case and $Tw = 1000\ K$ for the reacting case). Turbulent subgrid stresses were modeled using the SIGMA model [19].

A Lagrangian approach was chosen for the spray description using the same sub-models for drag, evaporation and injection (FIM-UR model to mimic a simplex pressure atomizer) as in the numerical study of the jet spray configuration of the KIAI burner [20].

The *n*-heptane fuel oxidation was described using an Analytically Reduced Chemistry named ARC_25_C_7H_{16} derived from the skeletal mechanism of Jerzembeck *et al.* [21] using the reduction tool YARC [22]. It comprises 25 transported species, 27 species in Quasi-Steady State Approximation and 210 irreversible reactions. It was validated on one-dimensional gaseous laminar flames in atmospheric conditions and for equivalence ratios ranging from 0.6 to 1.6. The very refined mesh in the flame zone allows to fully resolve the flame front and neglect the subgrid-scale wrinkling of the flame.

Finally, the Energy Deposition (ED) model [23] was used to mimic the laser-induced ignition by recovering a kernel of accurate size compared to experiments hundreds of microseconds after the laser ignition. The corresponding deposition characteristic size is 8 *mm* and the total energy deposited is 25 *mJ* leading to an energy transfer efficiency in agreement with values from literature [24]. Following the ED procedure, the laser-induced spark region was refined during the early instants following energy deposition with a typical cell size $\Delta x = 0.17$ *mm*, leading to a larger grid containing about 70 millions tetrahedral cells. Once the kernel was big enough, the two-phase reacting flow was interpolated on the reference grid to simulate the full ignition sequence.

4. Stabilized spray flame

Before addressing the complex transient ignition phase, the structure of the stabilized lifted M-shape spray flame is studied to present the main characteristics of this reacting flow. First at three stations downstream the injector ($z = 15, 25, 35$ *mm*, see Fig. 3), numerical and experimental radial profiles of mean and RMS gaseous axial velocities as well as mean axial and radial liquid velocities per diameter class are compared in Fig. 2. The typical features of a swirled-stabilized combustion chamber remain in the presence of the flame, with strong Inner Recirculation Zone (IRZ) and Outer Recirculation Zones (ORZ). Thermal expansion leads to strong mean axial velocities in the combustion chamber with maximal velocities up to 45 m/s. The reacting flow exhibits high turbulence intensity due to both the IRZ and the flame unsteadiness. Size-classified droplet mean axial velocity profiles show that small droplets ($d_p \in [10; 20]$ μm) almost follow the carrier phase unlike large ones ($d_p \in [30; 40]$ μm) which are more inertial close to the injector tip. The difference between small and large droplet axial velocity reduces downstream in the chamber. There is little impact of the droplet size on the liquid mean radial velocity. The overall agreement between experiments and LES is fairly good showing the capability of LES to catch the main behavior of the two-phase flame in the KIAI-Spray burner. The main difference is the flame lift off height which is underestimated by LES, leading to an underestimation of the mean gaseous axial velocity, and consequently of the mean liquid axial velocity. Note that the same difference was observed on the KIAI-Spray jet flame [20] and that this point is still under investigation on both configurations. The radial acceleration due to thermal expansion is captured by LES but slightly under-estimated.

The lifted M-shape spray flame exhibits a strong unsteadiness, resulting in very different structures that can be seen both experimentally and numerically. Figure 3 displays the three main ones, comparing experimental OH-PLIF images on the top and instantaneous fields of OH mass fraction directly extracted from LES, since the ARC_25_C_7H_{16} chemical scheme contains OH species. In all pictures, different regions can be

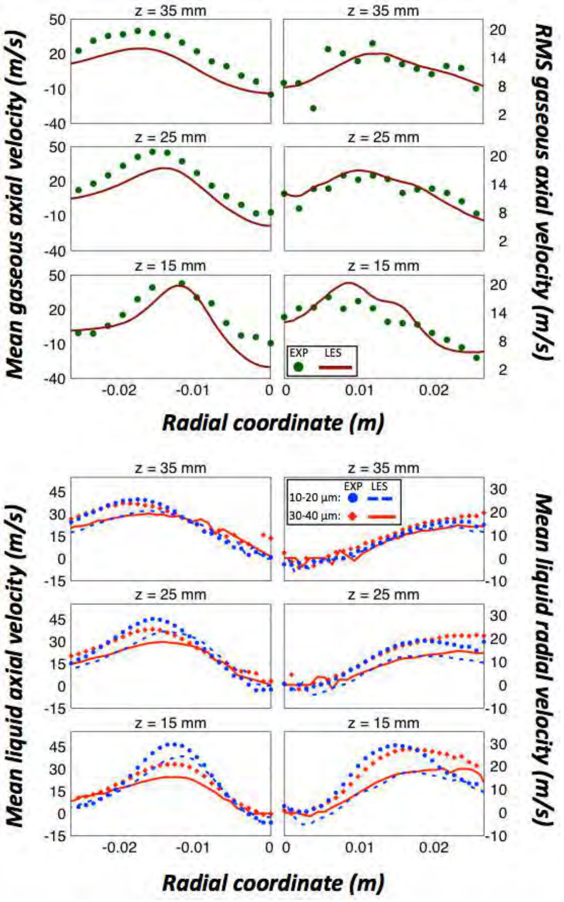

Figure 2: Comparison between experiments (symbols) and LES (lines) for the reacting flow. Radial profiles at 3 stations downstream the injector (see Fig. 3) of (Top): mean and RMS gaseous axial velocity. (Bottom): mean axial and radial droplet velocities for 2 diameter classes.

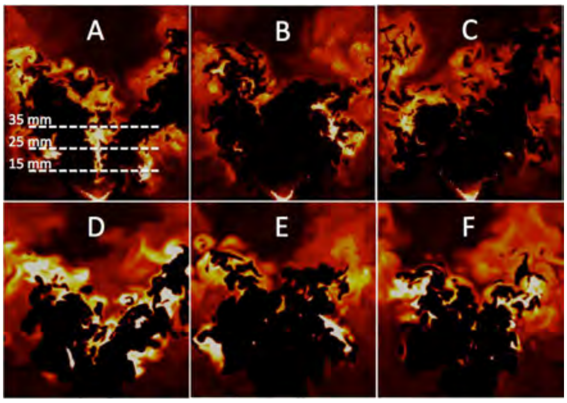

Figure 3: Reacting flow. A-B-C: Experimental OH-PLIF images. D-E-F: Instantaneous fields of OH mass fraction from LES, with maximum value $Y_{OH} = 0.001$. Dimensions of visualization boxes are 90 *mm x* 94 *mm*.

distinguished: 1) Black regions downstream the injector highlight fresh gases. 2) Low color intensity (in the ORZ and at the top of each image) characterizes burnt gases with diffused OH traces remaining. 3) High color intensity is typical of near post flame region containing a lot of OH produced by the flame. 4) The flame front can be localized by the stiff OH gradient regions and decomposed in two parts: an outer flame front separating the ORZ and the fresh gases branches with the lowest point of this front called the leading edge; and an inner flame front between the fresh gases and the IRZ, with the lowest point of this front called the stabilization point. 5) If droplets are not visible on the images, their impact on the flame is strong. The wrinkling of the flame is partly due to the turbulent behavior of the dispersed phase. Even local extinctions may originate from fuel droplets crossing the flame front and leading to too rich mixtures to burn.

Figures 3 (A and D) show very low stabilization points just above the fuel injector with well defined M-shaped flames. Both right branches reach the wall far downstream. Figures 3 (B and E) highlight situations where the stabilization point is far downstream ($z \approx 40$ *mm*). In these cases, the flame is much more compact exhibiting large fresh gas pockets accumulated between the injector and the inner flame front. Finally, Figs. 3 (C and F) allow to highlight flame shapes with leading edges being high ($z \approx 35$ *mm*, left side of both images). In such situation, fresh gases are not blocked by the outer flame front and thus feed the ORZ. The leading edge then comes down to consume the available fuel thereby continuing the flame position intermittency.

5. Ignition

5.1. Experimental ignition probability map

Ignition probability was evaluated experimentally as a function of the spark location and the results are provided in Fig. 4 (Left). The ignition probability map is closely linked to the main features of such swirled configuration. Indeed, ignition is almost impossible in the center of the burner corresponding to the IRZ, and until $r < 20$ *mm*. The probability then gradually grows from $r \approx 20$ *mm* to $r \approx 30$ *mm* to reach a plateau of maximum ignition probability around 70 – 80% in the ORZ. The very lean conditions considered in this work make ignition very difficult because the weak initial flame kernel is vulnerable to spatial and temporal variations of the local flow properties in terms of turbulent intensity, gaseous equivalence ratio and droplets number density that depend on the spark location.

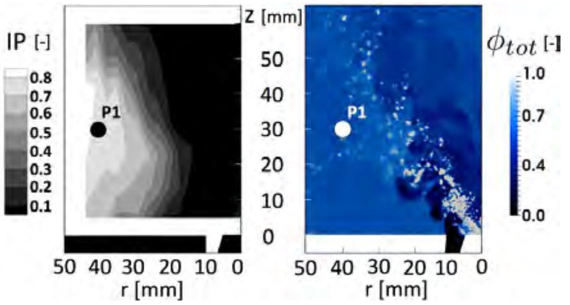

Figure 4: (Left) Experimental ignition probability map. (Right) Numerical instantaneous field of total (gaseous+liquid) equivalence ratio in the non reacting flow. P1 indicates the location where spray ignition sequences are detailed.

Figure 4 (Right) shows a numerical instantaneous field of total (gaseous+liquid) equivalence ratio for one half of the combustion chamber obtained after the filling of the combustor is completed (500 *ms* physical time). A very lean homogeneous region ($\phi_{tot} = 0.45$) is observed in the IRZ, together with a lean homogeneous mixture, close to the global equivalence ratio ϕ_{glob} in the ORZ. The spray-jet region exhibits intense ϕ_{tot} fluctuations, with accumulation of droplets in the region of low gaseous vorticity. Note that the color scale is saturated to a maximum value of $\phi_{tot} = 1.0$ to better identify droplets, although the equivalence ratio reaches values up to 20 in the vicinity of liquid injection.

Based on this experimental ignition probability map, point P1 is chosen for a joint experimental-numerical analysis of spray ignition. P1 is located in the ORZ (see Fig. 4) at position $r = 40$ *mm*; $z = 30$ *mm* and has a high ignition probability of 80%.

5.2. Two-phase flow conditions at P1 before ignition

At point P1 the mixture exhibits a rather homogeneous ϕ_{tot} distribution close to the global equivalence ratio ($\phi_{glob} = 0.61$). From time to time however, pockets of high ϕ_{tot} reach the vicinity of P1, indicating the presence of evaporating droplets. Interaction of droplets with the developing flame may therefore occur and will be discussed later. Although point P1 is located in a region of low turbulent kinetic energy compared to the air jet [13], it exhibits non-negligible velocity fluctuations which significantly vary with time. This is illustrated in Fig. 5 which displays the experimental normalized distribution of two-component absolute velocity fluctuations in the neighborhood of P1 (within a square of 5 *mm* length) for low and high turbulence levels with respect to the levels found near P1. To evaluate the role of the non-reacting flow state before sparking, two LES

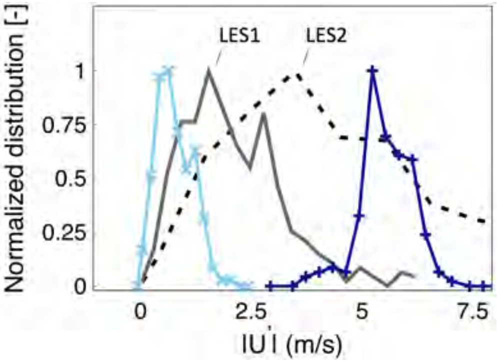

Figure 5: Normalized distributions of absolute velocity fluctuations on the cold flow at point P1. Curves with symbols are experimental distributions representative of low and high turbulence levels found near P1. LES distributions correspond to ignition trials shown in Fig. 8.

of ignition sequences (referred to as LES1 and LES2 in the following) were performed at point P1, starting at two different instants (t_1 and t_2 respectively) of the established non-reacting two-phase flow. Both instants were chosen to describe the flow variability around P1 observed experimentally. At both instants, P1 is surrounded with a lean gaseous mixture $\phi_{tot} \approx \phi_{glob}$. The two instants mainly differ by the turbulence intensity in the vicinity of P1, as shown in Fig. 5, where the normalized distributions of the three-component absolute gaseous velocity fluctuations recorded around P1 in both LES are also shown. The two numerical initial conditions are in between the experimental range, centered around 1.5 m/s and 3.5 m/s respectively. Note that the range of velocity fluctuation magnitude obtained numerically is not as wide as in the experiments, and the distributions are less peaked, which may be due to the shorter investigated time.

5.3. *Ignition sequences*

Among the 30 experimental ignition tests at position P1, 9 high-speed videos were recorded, 8 of which reported successful events. Only two experimental sequences, named EXP1 and EXP2, are used here together with the two numerical ignition sequences (LES1 and LES2). These sequences EXP1 and EXP2 correspond respectively to the shortest and longest trials among the 9 recorded ones. EXP1 lies in the low range of turbulence intensity while EXP2 was triggered in the high range of turbulence intensity at P1.

Figure 6 (Top) shows the high-speed images of the flame kernel for EXP1. The visualization box size is 98 *mm x* 98 *mm* for all images in the figure and shows both halves of the chamber. At $t = 2.4$ *ms* the kernel develops around P1 and has little distortion due to the initial low turbulence. Interaction with fuel droplets can be identified as intense luminous patterns. By $t = 4.4$ *ms*, the kernel has sufficiently expanded to come close to the spray branch. At $t = 5.9$ *ms*, a part of the flame kernel evolves towards the spray nozzle keeping a strong azimuthal motion. Intense, luminous parts in the images reveal the presence of a strong fuel stratification. At further times, the flame propagates and expands in all directions, in particular towards the injector. By $t = 14.7$ *ms* the flame has reached the opposite wall. This behavior is characteristic of an ignition by spray branch. Once attached to the spray cone, the flame describes a spiral motion due to the swirling flow and finally reaches the injector. The bottom part of Fig. 6 illustrates the numerical sequence LES1, where the integration of the heat release through the entire volume of the chamber allows to track the evolution of the flame kernel. All the successive steps of kernel growth experimentally observed are reproduced numerically, assessing the capacity of LES to reproduce the mechanisms involved in ignition by spray branch.

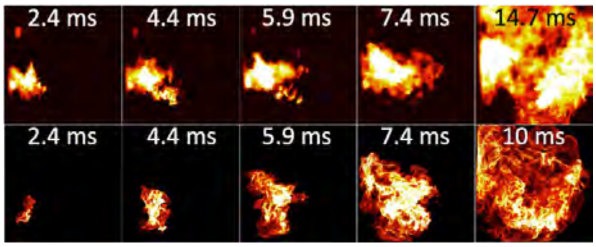

Figure 6: (Top): Experimental spontaneous flame emission sequence at P1 (EXP1). (Bottom): Numerical integrated heat release during ignition sequence at P1 (LES1). Dimensions of visualization boxes are 98 *mm x* 98 *mm*.

The interaction between the flame kernel and the fuel droplets noted in Fig. 6 is now detailed, looking in Fig. 7 at an instantaneous iso-contour of progress variable $c = 0.5$ (based on gaseous temperature) after 3.5 *ms* for LES1, colored by gaseous equivalence ratio (Left) and heat release (Right). Equivalence ratio is here based on the mixture fraction defined by Bilger [25]. Evaporating fuel droplets are represented by black spheres in Fig. 7 (Right). Three regions can be distinguished. In zone A where there are very few particles, the liquid fuel evaporation rate is not sufficient to compensate the gaseous fuel consumption, and the flame can not survive. The heat release is very low and the flame locally extinguishes. In zone B, fast single droplet evaporation occurs near the flame, generating a locally rich gaseous mixture and possibly high heat release in cases of indi-

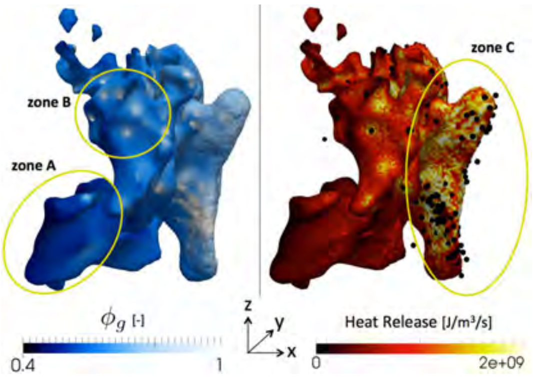

Figure 7: Zoom on the iso-contour of progress variable $c = 0.5$ after 3.5 *ms* during sequence LES1 colored by (Left) gaseous equivalence ratio and (Right) heat release. Evaporating fuel droplets in this zone are represented on the right side by black spheres.

vidual burning droplets. However, the contribution of these isolated droplets to the main flame is marginal. The major impact of evaporating fuel droplets on the flame kernel is found in zone C. The spray is dense in this region, leading to high and flammable gaseous equivalence ratios. This region is the most reactive one, evidencing the preferential direction of the kernel towards zones of high fuel droplet number density.

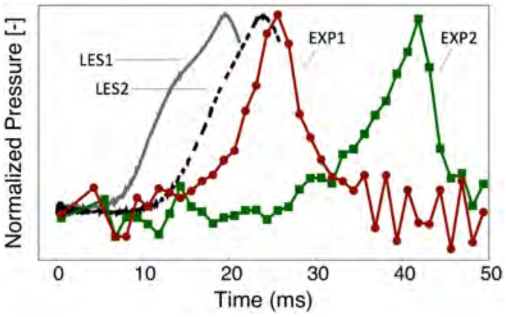

Figure 8: Temporal evolution of pressure at P1 for the experimental sequences EXP1 and EXP2, and the numerical sequences LES1 and LES2.

Finally, the capacity of LES to accurately predict ignition delay times is evaluated by plotting in Fig. 8 the temporal evolution of the pressure in the combustion chamber for the four experimental and numerical ignition sequences. First comparing with Fig. 5, a general trend can be observed: higher turbulence intensity before ignition leads to longer ignition delay, both experimentally and numerically. Both EXP2 and LES2 show very teared kernels due to high strain limiting the kernel growth during the first 10 *ms* for LES2 and for 20 *ms* for EXP2. This confirms the detrimental impact of the initial turbulent field at spark location on the flame kernel growth highlighted in [10, 11] for gaseous flames. However, the difference between the two numerical delay times is smaller than for the two experimental ignitions. This may be due to the closer and wider velocity fluctuation distributions of LES1 and LES2 compared to the two experimental ones. Yet, as soon as the flame holds on the injector (t = 14.7 *ms* for EXP1 and t = 10 *ms* for LES1 in Fig. 6), the agreement between LES and experiments is very good, the slope of the increase in pressure being very similar for the 4 experimental and numerical ignition sequences. Note that the total ignition delays predicted by the two LES are shorter than for experiments, the difference being mostly due to the kernel phase. Since this phase is the most stochastic phenomenon, many other LES sequences with various turbulence intensities and spray densities should be performed to quantitatively compare with the experiments.

6. Conclusions

Two-phase flow lean aeronautical ignition was investigated with various experimental techniques and with Large Eddy Simulations coupled to Discrete Particle Simulations. The reacting flow was first analyzed with PDA and OH-PLIF to study the droplet size distribution, the gaseous and liquid velocities, and the flame structure. This was compared to the numerical results, finding a general very good agreement between both approaches. Experimental ignition trials were then performed in order to obtain the ignition probability map in the chamber. The outer recirculation zone was found most favorable, presenting a minimum turbulent kinetic energy and a relatively homogeneous equivalence ratio. A joint experiment and numerical study was then conducted at a selected sparking point in this zone. Long and short ignition sequences as well as pressure signals (in both experiment and simulation) described the variability of the process and revealed a good agreement with the turbulent intensity level existing in the local flow prior to sparking. The local beneficial effect of the presence of droplets was also tackled. Thanks to the coupled numerical-experimental investigation, a reliable analysis of the underlying physical mechanisms of spray ignition has been provided, and a methodology to predict them has been demonstrated.

Acknowledgments

The authors gratefully acknowledge the financial support from Safran Aircraft Engines and the Agence Nationale de la Recherche (ANR) under the project TIMBER ANR-14-CE23-0009. This work was granted access to the HPC resources of TGCC under the allocations 2016153551 and & A0032B10157 made by PRACE and GENCI respectively. Alexis Vandel and Dr A. Verdier are warmly acknowledged for their help with experiments.

References

[1] T. Marchione, S. F. Ahmed, E. Mastorakos, Combust. Flame 156 (1) (2009) 166–180.
[2] C. Letty, E. Mastorakos, A. R. Masri, M. Juddoo, W. O'Loughlin, Exp. Thermal Fluid Sci. 43 (2012) 47–54.
[3] D. Ballal, A. Lefebvre, Proc. Combust. Inst. 18 (1981) 1737–1746.
[4] K. G. Moesl, K. G. Vollmer, T. Sattelmayer, J. Eckstein, H. Kopecek, J. Eng. Gas Turbines Power 131 (2) (2009) 021501–8.
[5] A. P. Wandel, Combust. Flame 161 (10) (2014) 2579–2600.
[6] C. Cardin, B. Renou, G. Cabot, A. M. Boukhalfa, Combust. Flame 160 (8) (2013) 1414–1427.
[7] S. F. Ahmed, R. Balachandran, T. Marchione, E. Mastorakos, Combust. Flame 151 (1-2) (2007) 366–385.
[8] S. S. Shy, C. C. Liu, W. T. Shih, Combust. Flame 157 (2) (2010) 341–350.
[9] D. Barré, L. Esclapez, M. Cordier, E. Riber, B. Cuenot, G. Staffelbach, B. Renou, A. Vandel, L. Y. Gicquel, G. Cabot, Combust. Flame 161 (9) (2014) 2387–2405.
[10] L. Esclapez, E. Riber, B. Cuenot, Proc. Combust. Inst. 35 (3) (2015) 3133–3141.
[11] E. Mastorakos, Proc. Combust. Inst. 36 (2) (2017) 2367–2383.
[12] M. Cordier, A. Vandel, G. Cabot, B. Renou, A. M. Boukhalfa, Combust. Sci. Tech. 185 (3) (2013) 379–407.
[13] J. Marrero-Santiago, A. Verdier, C. Brunet, A. Vandel, G. Godard, G. Cabot, M. Boukhalfa, B. Renou, J. Eng. Gas Turbines Power 140 (2) (2017) 021502–11.
[14] J. Marrero-Santiago, A. Verdier, G. Godard, A. Vandel, G. Cabot, M. Boukhalfa, B. Renou, Proc. ILASS-Europe (2016) SIC–10.
[15] J. Marrero-Santiago, A. Verdier, A. Vandel, G. Godard, G. Cabot, B. Renou, Proc. ILASS-Europe (2017) 847–854.
[16] O. Colin, M. Rudgyard, J. Comput. Phys. 162 (2) (2000) 338–371.
[17] P. Lax, B. Wendroff, Comm. Pure Appl. Math 13 (1960) 217.
[18] T. J. Poinsot, S. Lelef, J. Comput. Phys. 101 (1) (1992) 104–129.
[19] F. Nicoud, H. B. Toda, O. Cabrit, S. Bose, J. Lee, Phy. Fluids 23 (8) (2011) 085106.
[20] F. Shum-Kivan, J. M. Santiago, A. Verdier, E. Riber, B. Renou, G. Cabot, B. Cuenot, Proc. Combust. Inst. 36 (2) (2017) 2567–2575.
[21] S. Jerzembeck, N. Peters, P. Pepiot-Desjardins, H. Pitsch, Combust. Flame 156 (2) (2009) 292–301.
[22] P. Pepiot, Automatic strategies to model transportation fuel surrogates, Ph.D. thesis, Stanford University, USA (2008).
[23] G. Lacaze, E. Richardson, T. Poinsot, Combust. Flame 156 (10) (2009) 1993–2009.
[24] T. Phuoc, F. White, Proc. Combust. Inst. 29 (2) (2002) 1621–1628.
[25] R. Bilger, Proc. Combust. Inst. 22 (1) (1989) 475–488.